UNIVERSIDAD AUTÓNOMA DE MADRID
Departamento de Física Aplicada

Centro de Microanálisis de Materiales

ION BEAM DAMAGE BY ELECTRONIC EXCITATION WITH SWIFT HEAVY IONS IN LITHIUM NIOBATE: MECHANISMS AND NANOSTRUCTURING FOR PHOTONIC APPLICATIONS.

Memoria presentada para optar al Grado de

Doctor en Ciencias Físicas por

Miguel Luis Crespillo Almenara

Director:

Dr. José Olivares Villegas

(Instituto de Óptica, CSIC)

Tutor:

Prof. Aurelio Climent Font

Departamento de Física Aplicada. Universidad Autónoma de Madrid.

OCTUBRE 2011

UNIVERSIDAD AUTÓNOMA DE MADRID
Departamento de Física Aplicada

Centro de Microanálisis de Materiales

ION BEAM DAMAGE BY ELECTRONIC EXCITATION WITH SWIFT HEAVY IONS IN LITHIUM NIOBATE: MECHANISMS AND NANOSTRUCTURING FOR PHOTONIC APPLICATIONS.

by

Miguel Luis Crespillo Almenara

A dissertation submitted to the Sciences Faculty of
Universidad Autónoma de Madrid,
in partial fulfillment of the requirements for the
Degree of Doctor of Philosophy

Physics

Madrid, 11th October 2011.

Thesis Advisor:
Dr. José Olivares Villegas
(Instituto de Óptica, CSIC)

Thesis Tutor:
Prof. Aurelio Climent Font
Dept. Física Aplicada. UAM

A mi Padre y a mi Madre,

a Quienes les debo como hijo el mejor legado posible:
la enseñanza de los verdaderos principios y la cultura del esfuerzo,
el espíritu de sacrificio, la templanza ante el desaliento,
el afán de superación constante ante la adversidad,…
así como la satisfacción personal por el trabajo bien hecho, sin duda,
el mejor premio.

"The world little knows how many of the thoughts and theories which have been passed through the mind of a scientific investigador have been crushed in silence and secrecy by his own severe criticism and adverse examination; that in the most successful instantes not a tenth of the suggestions, the hopes, the wishes, the preliminary conclusions have been realized".

M. Faraday (1791-1867)

"Imagination is more important than knowledge. For knowledge is limited, whereas imagination embraces the entire World". (1930s)

"The important thing is not to stop questioning; curiosity has its own reason for existing". (1950s)

"There is a driving force more powerful than steam, electricity and atomic energy, the will".

"Try to become not a man of success, but try rather to become a man of value". (1950s)

"There are only two ways to live your life. One is as though nothing is a miracle. The other is as though everything is". (1940s)

A. Einstein (1879-1955)

Contents.

Aknowledgements.

"If I have seen further than other men, it is because I have stood on the shoulders of giants".
Isaac Newton (1642-1727).

I

O CAPTAIN! my Captain! our fearful trip is done;
The ship has weather'd every rack, the prize we sought is won;
The port is near, the bells I hear, the people all exulting,
While follow eyes the steady keel, the vessel grim and daring:
But O heart! heart! heart!
O the bleeding drops of red,…..

II

O Captain! my Captain! rise up and hear the bells;
Rise up - for you the flag is flung - for you the bugle trills;
For you bouquets and ribbon'd wreaths - for you the shores a-crowding;
For you they call, the swaying mass, their eager faces turning;
Here Captain! dear father!
This arm beneath your head;
It is some dream that on the deck,…

III

…..
The ship is anchor'd safe and sound, its voyage closed and done;
From fearful trip, the victor ship, comes in with object won;
Exult, O shores, and ring, O bells!
But I, with mournful tread,
Walk the deck my Captain lies,
Fallen cold and dead.

W. Whitman (1819-1892). "Leaves of Grass." (1900).
[193. O Captain! Mt Captain!.]

Finally, the work is finished, the Thesis is written. It has been a very long way since the beginning, filled with ups and downs and personal growth and changes. A big enterprise is rarely the work of one single person, and this Thesis is not an exception. Really, I am very lucky because of having the opportunity to enjoy Physics, not only from the textbooks, but from the day by day experiment, meetings, brainstormings and discussions, and I am in debt to a lot of people for making this dream comes true. Thus, I would like to express here my tribute to all of them who in one way or another helped me to do this job and to live through the years of my PhD.

In the first place, I would like to thank my advisors Dr. José Olivares and Prof. Fernando Agulló-López, not least for offering a fascinating and stimulating project, and allowing me to take part of a great research group, but for remaining actively involved in my work throughout my PhD and for always being available to give me guidance, support and encouragement. Thank you for giving me the opportunity to grow up as a scientist at your side. I am deeply grateful to you for all you have done for me. For your help in understanding the complex physics under study, for your deep concern in my experimental work and strong support in my personal life. Also for your patience when things went wrong because of me. Thank you for your enthusiasm and for teaching me experimental tricks, scientific approaches and how to face an unknown problem, in one word, how to make physics in a pragmatic way and with capital letters. Thank you for all of this. I appreciate it very much. My dearest Fernando, special words must be considered with you: thank you very much for showing me how to make Science. You were a constant source of inspiration and supported me always. Your careful supervision and valuable comments during the entire efforts with the research and writing the manuscript were critical to this work. You made me to give all of my best, and your restraint and compromise with this Thesis were fundamental pillars to go ahead. This Thesis would have never been possible without both of you, and I hope that it will cover at least a part of all those things you did for me.

I am also very lucky to have had the opportunity to work with Dr. Antonio Rivera whom I thank for never hesitating to apply his keen mind to various problems and impasses I came across. I am also grateful to the insightful comments and discussions during the all the PhD period. Moreover, I appreciate so much his friendship and support during all this time.

Thank you very much all the members of Non Lineal Optics Group at UAM-UPM, from the PhD students (now PhDs) to Professors (Javier Villarroel, Olga Caballero-Calero, Mercedes Carrascosa, Ángel García-Cabañes, Ángel Alcázar, Bruno Ramiro), for leaving me to take part of this family and living the building of the knowledge in this way.

I would like to mention the aid of my tutor Prof. Aurelio Climent, who opened me the doors of CMAM to develop my work and accepted me as a part of the accelerator staff without reservations; thank you very much for his help in matters administrative and academic at the University, and for trusting on me to perform this Thesis.

I am also grateful for the all the members of CMAM center, for contributing to make this work easier. I have to say that CMAM has been my home all this time and I would always remember the moments I lived there, and the friends I take with me. In this sense, Dr. Ángel Muñoz must be specially mentioned. Thank you for your generosity and your everlasting willingness for helping me. Thank you very much for learning from you so many things, and the most important one, allowing me to be your friend. Without any kind of doubt, you are one those great people holding me all this time, and part of this Thesis belongs to you. Besides, I cannot forget the friendship and support of two very special people, Dr. Jose Emilio Prieto and Dr. María Dolores Ynsa, for showing me the strength and courage to go ahead and for being there whenever I need it. Finally, an important remark must be noticed for the administrative, computacional, the scientific and the technical team of CMAM, for working so hard, helping me every day and trying to improve day by day. All the members of CMAM, past and present. Thank you!.

I have to acknowledge, evidently, to Dr. Alessandro Zucchiatti, head director of CMAM, who was a model of efficiency and dedication, helping me during all this time. I want to express you my sincerely gratitude too. Many thanks must be given to you for motivating and pushing me all the time. Thank you very much for your visits to my office almost each day, just before you go home in the late evening, during the time of the writing of the manuscript. Thank you for your stories all over the world, during different stages of your life, in different countries and seasons. Thank you for allowing me to live them through your memories and make me laugh so many times. In such a way, I could fly from my office chair for a while, and to give some extra oxygen to my tired brain. I will never forget your outstanding dinner at your home with your wife past December. I have to say, I had never eaten so extraordinary Italian meals, and I can still remember a wonderful story you told while you were lying in a wooden chair from South Africa. In the end, I have to say that it has been a real pleasure to work with you, your people and in your center; really, you must be proud of your work and the people under your supervision.

During these years, some short-time research stages were performed at GANIL (Caen, France) to carry out some the experiments of this Thesis. In this sense, I want to thank Prof. Marcel Toulemonde and Dr. Emmanuel Balanzat for their support during those several days. The first one deserves a special mention, because of his intense efforts on the experiments, being always ready for sharing with me his opinion. He received me with open arms. Thank you for your kindness, your time, and the fruitful discussions.

Several collaborators have been contributed to this Thesis in a significant way, I would like to mention them. In particular, I thank to all the members of Non Linear Optics of UAM, Dr. Gastón García from ALBA-CELLS, and Dr. Marco Bianconi from CNR-IMM (Bologna). I am very grateful for being able to use part of your valuable time in discussions and brainstorming. It has been really a pleasure to make Science with you.

In particular, I am deeply grateful to some Italian researchers who with some collaborations are nowadays in progress and anothers come from the past: Dr. Marco Bianconi from Bologna (CNR- Intituto per la Microelecttronica e Microsistemi) and Dr. Cinzia Sada and Dr. Marco Bazán (Università degli Studi di Padova), I can honestly say that I felt like at home during a visit there, I need to thank a lot for taking care of me, your kindness, patience and friendship.

I take advantage of this opportunity to thank all my Thesis colleagues, who shared good and bad moments, but it was great to have you nearby to pass them. Special comments are referred to Martin. Otto, so much time spent together during chemical etching processes and nanostructures characterization by AFM, and even, for a couple of months, roommates: thank you very much for your contagious enthusiasm, your strength, kindness, happiness, and sharing your clever ideas and bright intelligence. Roch Andrzejewski, my first friend at CMAM and roommate too, so many thanks for sharing your nigh conversations with me; Adriano Zabot, the Italian student, nice smiles and hard work for the last summer for your DiplomaThesis; and Javier Manzano, my colleague in the project, good luck with your thesis!.

Thank you, my dearest friends, who never let me down; because, even though, many months spend without seen you, our friendship is always where we have left it. Remarkable and careful mention receives Idoia. Thanks for all the shared moments, for your time, kindness and dedication, and for being always there when I called you. Thank you to all these special people

that have known to give me their space with the aim of forgetting of me for a while, learning to think in YOU.

Really, I am indebted to the following friends and colleagues for inspiring me with their intelligence and motivating me with their support; Dr. Victor Joco and Jorge Álvarez. Thank you for giving me much needed breaks during the writing of this dissertation and in life. You always make me smile, even at times when I am sure there is nothing to smile about. I appreciate your friendship, unwavering support and encouragement during this period.

In this sense, it is worthy to mention the special place that have reached during the last stage of the thesis writing the figure of a few extraordinary people at my new job, Julián Valencia, Pablo Varela and Fernando Marquez, who gave me the opportunity to learn many and useful lessons of life, wildlife and the complex human-being nature, interesting conversations and transmitting at any time the spirit of the job well done ("*in labore, suprema ars*"). Thank you for conquering my curious mind with your experiences and huge knowledges. Thank you for cheering me up and making me laugh more times. In one word, thank you very much for your friendship!.

Once I have arrived to this point, a special note must be done respect to Prof. Mario Jakas (he deserves a very special place), from whom everything started, and I want to express here my gratitude to him. Thank you for being my teacher, my friend, my advisor, etc…; thank you for encouraging me since the beginning of this adventure to go abroad without fear to risk. To spice me up when I was down, to inspire me to keep going and to always reach my goals; thank you for providing me with your priceless wisdom and advises, and for being always there to share the good moments and news. Thank very much to your wife, Alexa, too, always with enough time to listen my worries and advise me. Much time ago you have won a place in my heart. There are not words enough to tell you how fortunate I feel for having your unconditional friendship.

Finally, I would also like to thank immensely to my family for always encouraging and keeping me strong to pursue my interests, never refusing to buy me a book and indulging me years of unintelligible, one-sided conversations about science, and for allowing me to follow a dream. Thank you for dedicating so much time, efforts and sacrifices to my education. This is only a small reward after so long time. Thank you from the bottom of my heart, whose support I felt always and where I go. In particular I would like to express my greatest appreciation to my dad and mom, Miguel and Estrella, to whom I dedicate this Thesis. Without your love and support I would not be where I am today. The only sorrow that shadows my heart is the invaluable price that I have paid for the loneliness I have lived all these years having you far away from me. I am really proud of being your son, and it will be a great challenge for the rest of my life to turn into as valuable people as you. Thank you for teaching me from the childhood the value of hard work, getting stronger through personal effort giving my very best; and to learn to believe in myself with humility.

At the end of this long adventure, I can state I have got an enormous baggage full of knowledges, great memories and experiences, all of them recorded in the amber of memory, which will be remembered forever.

Once you have read this. I remember you reader that, YOU are who needs to trust on yourself and to look for the illusion inside you to finish YOUR Thesis. The doctorate, and to realize a PhD, is a very serious compromise with yourself. Each day one face challenges, and each day, one finds difficulties. The writing period of the manuscript means a great sacrifice and, besides, so much spirit and WILL. Look carefully the people around you; helps everybody who ever needs it, and receives from everybody as you can. The way is long, hard and, even, sometimes darkness appears, but it is not impossible; the goal will be reached thanks to all the people that are around you. I am sure YOU will never be alone.

Preface.

1.1. State of the art and motivation.
1.2. Overview and dissertation structure.
1.3. References.

1.1 State of the art and motivation.

The charged particles and ions are a very relevant structural damage agent to take into account, such as those produced in accelerators and those that are produced as secondary products by bombardment with neutrons in fission and fusion reactors. So far, calculations of the defects generated by charged particle irradiation mainly rely on the energy losses caused by elastic collisions between the incoming particle and the nuclei of the material [1, 2]. The basic physics is understood, and detailed simulations can be carried out [3, 4]. However, some classical experiments on alkali halide crystals [5, 6] using ionizing radiation (UV and X rays), as well as recent reports on inorganic insulators [7-16], and semiconductors [17-22], permit to envision that elastic nuclear collisions are only part of the irradiation damage story.

The structural damage induced by ion irradiation on dielectric materials and associated device degradation has been, so far, explained on the basis of collisional processes mostly ignoring the electronic excitation. Recent works, focused on lithium niobate, offers conclusive evidence that at high ion energy and moderate mass ($A > 15$) electronic excitation may induce a giant enhancement over the damage rate due to nuclear collisions. As a consequence the material becomes amorphized at irradiation fluences far below those required for nuclear collisions alone. These results are expected to have a deep impact on many applications.

The role of electronic excitation for the generation of point defects by swift ion irradiation on $LiNbO_3$ has been deeply studied, assessed and compared to the effect of elastic nuclear collisions. For sufficiently high stopping powers (S_e) the electronic generation rate is overwhelmingly dominant over the collision generation rate and leads to lattice amorphization at much lower irradiation fluences.

Nuclear accelerators originally planned for basic nuclear and atomic physics research invariably open up completely new perspectives in various fields, particularly in materials science and device technology. Low energy accelerators are now standard tools and their exploitation in engineering materials of all kinds of interest: electronic, tribological, and metallurgical etc. provide very fruitful activity. In this sense, in the past three decades numerous experiments at large scale accelerator facilities have greatly improved the understanding of the interaction of swift heavy ion with matter, and allow nowadays to use ion beams as a tool for structuring materials on the micro- and nanometric scale. Materials damage and devices degradation by ion bombardment are key issues to assure the performance and reliability of a number of present and future technologies, and, on the other hand, special mention deserves on its fundamental scientific interest as an exponent of radiation-matter interactions. Related to the involved technologies, they include, among others, radiation-resistant materials for fusion reactors, nuclear fission and fusion installations [23, 24], storage and immobilization of radioactive waste [25-27], lifetime of optical, electronic and optoelectronic components in space missions [28], ion-implantation for doping and material modification [29] as well as for smart-cut technologies [30], nanostructuring and nanopatterning of materials in electronics and phonics, and even, proton and heavy- ion therapy (C, O) in medicine [31, 32].

For high velocity ions ($v >> 0.1$ MeV/amu) energy is mostly deposited in the material by electronic excitation, being the electronic stopping power markedly dominant over the nuclear stopping power. In that energy range of some hundreds of MeV, a single heavy ion induces a continuous trail of damage with a few nanometer width and typically several tens of

micrometer length. Such ion tracks consist of material with properties that are drastically changed compared to the surrounding virgin bulk. Many different solids register particle tracks in particular all insulators such as polymers and inorganic solids, and some selected semiconductors and metals. Amorphous tracks of nanometer dimensions are, indeed, generated by single cosmic rays and high-energy ions in minerals, as well as, in dielectric and semiconductor crystals [7, 14, 20, 33-38]. To perform material patterning, fluences in the range of 10^6-10^{11} ions/cm^2 are sufficient and can easily be reached with usual beam intensity of some nA (corresponding to 10^{10} ions/s) or less. If track overlapping is necessary, fluences as large as 10^{14} ions/cm^2 can be achieved by using larger flux, where significant damage by elastic nuclear collisions is not expected [1], and therefore, additional processes, mainly of electronic origin, may contribute to severely enhance the damage rate. Consequently, ion beams could be an ideal instrument to modify under controlled conditions the physical and chemical properties on a nanometric scale with several advantages over other physical or chemical methods [1, 2, 39]. To date, research activities concerning ion tracks and their applications are mainly studied at large accelerator facilities delivering ions of energies above 2 MeV/u.

So far, the technological applications of ion irradiation mostly rely on the effects caused by nuclear collisions and ion implantation. In particular, research on ion implantation of transparent materials with light ions (H and He) has been mostly addressed to the modification the refractive index, allowing the fabrication of optical waveguides and a variety of integrated optical devices, although at the expense of quite high fluences (10^{16}-10^{17} at./cm^2). Recently, a growing interest is being paid to the material modifications induced by high-energy medium mass ions (*swift-heavy ions*) where electronic excitation is dominant over nuclear collisions. In this sense and using high enough fluences, a heavily damaged and/or amorphous surface layer has been very recently achieved on $LiNbO_3$ turning into a different way of processing optical waveguides (O, F, N) irradiations [8, 10, 40, 41] with energies around 5 MeV, as well as by silicon irradiations at 5, 7.5, and 30 MeV [10, 11, 41]. One attractive feature of those experiments for material processing is that the electronic excitation method requires much lower irradiation fluences for lattice damage and amorphization (around 10^{13}- 10^{14} at./cm^2), at least two orders of magnitude lower in comparison with nuclear collisions of the light ions implantation method, and generates impurity- free layers. Moreover, it offers other possibilities for tailoring refractive index profiles and so optical performance. A second branch of investigation has concerned the enhanced etching of $LiNbO_3$ as a consequence of the ion implantation induced defects [42-45]. The very high etching selectivity of the heavily damaged regions makes this process appealing for micromachining of $LiNbO_3$.

The aim of this Thesis work is to get a deeper insight in the mechanisms responsible of irradiation damage to materials induced by electronic excitation processes, showing their main features, and to identify the conditions under which they become dominant over the elastic collisions mechanism. It is worthy to notice that this research work appears in a rapidly evolving field, where recent developments are appearing daily. Although data are available for a number of inorganic insulators and semiconductors materials [7-22, 33-38], our results and analysis focus on $LiNbO_3$, an electro-optic and nonlinear dielectric material [46] with a crystal structure closely related to that of perovskites, where systematic and coherent data have being obtained.

Coming from a previous work [47], in which the results revealed the remarkable cumulative behaviour of the electronic excitation damage, we have point out our attention in the study of the irradiation species with stopping powers above the amorphization threshold (S_{th}). With this in mind, the structure of the electronic damage originated around the ion track, is discussed, tackling the problem realistically from diverse strategies. In this sense, the central amorphous core and the surrounding extensive halo containing point-like and extended defects, is studied going ahead from different ions energies regimes (E > 0.1 MeV/amu and E > 10 MeV/amu), using several experimental techniques like Rutherford Backscattering Spectroscopy in Channeling configuration (RBS/C), high resolution transmission electron microscopy (HRTEM) and atomic force microscopy (AFM); on the other hand, indirect methods through nanopores revealed after chemical etching, have been performed too. From another complementary perspective, the pursued purpose is to apply a recent theoretical scheme to discuss the RBS/C method for damage assessment and elucidate the relative role played by core and halo. The work is focused on $LiNbO_3$ for which a substantial amount of ion-beam irradiation data is available [48] . We propose an approach based on an exciton decay model [49] that allows one to calculate the concentration of point defects generated by every single ion impact. An overall back-scattering factor is introduced to quantify the de-channeled ion-beam fraction caused by the defects induced by irradiation (including both, core and halo).

Irradiations at very low fluences (~ 1 e12 cm^{-2}), as we call *single (isolated) track regime*, have been explored as part of the fundamental study, and with the aim of using the modifications of the damaged material, change in the physical properties - refractive index, in potential applications in waveguide structures. The main advantage of this procedure is that, for obtaining the resulting nanostructured material, the necessary fluence ranges decrease drastically compared to those for light ion implantation (He or H) of MeV energies [1]. On the other hand, ion tracks production of nanometric diameter size, in various crystalline materials by irradiating them with medium and high mass ions, is a research area that has received abundant attention in recent years, from the point of view of fundamental studies, up to its multiple applications, even coined the term "*ion track technology*" [34, 37, 38]. However, an important systematic research work must be developed to optimize the irradiation parameters (ion energy, fluence, angle of irradiadion, etc…), with the aim of tailoring the refractive index profiles and to obtain higher refractive index jumps and better optical confinement.

As conclusion, all the research work presented in this dissertation is a study developed with the aim of getting a more complete understanding of the complex processes that take part during the ion-matter interaction in the electronic excitation regime. With this in mind, the main substrate selected for the experimental tests has been lithium niobate, due to their interesting physical properties. Anyhow, in order to control these processes and their possible future technological applications, the mechanism by which they occur must be understood.

1.2 Overview and dissertation structure.

The organization of this dissertation is as follows, being its content briefly commented. Firstly, it has been structured in three main parts: *I. Introduction*, *II. Experimental Techniques* and *III. Results*.

The first part, *I. Introduction*, which is composed by *Chapters 1, 2 and 3*, is aimed to show a general introduction in which the most fundamental concepts are presented, providing to the reader the basis for the understanding of the results exposed throughout the whole Thesis.

Specifically, in *Chapter 1*, the concept of stopping power, the slowing down process (mechanisms of ion-matter interaction) of the ions into the matter will be described, showing the mechanism through the ions deposit their energy depending on the velocity range. The process of creation of amorphous tracks into the target from the irradiation with swift heavy ions will be described. In the theoretical framework, the main models that explain the damage created by the ions through the material due to their interaction with the electrons will be presented. This electronic damage will play the main role in all the processes described through the Thesis.

An introduction to the main properties of Lithium Niobate, the material substrate used in this dissertation, will be given within *Chapter 2*, where the most relevant electrical and optical properties of this material, as well as the growth techniques and its crystal structure are presented. Moreover, and special section is devoted to the specific chemical behaviour of Lithium Niobate and the basic chemical reactions used will be explained.

Finally, *Chapter 3* deals with the different micro-structuring techniques of Lithium Niobate and fabrication methods. So far, throughout this introductory Part of the Thesis we have presented, first the fundamental aspects of ion-matter interaction, as well as the modification of the physical properties of the irradiated materials; and secondly, the superior features of lithium niobate crystal, which give great importance, and make it a key material for fabrication of integrated optical devices. All of this leads us, in a natural way, to seek the synergy of the combination of both, through micromachining and defects engineering by different experimental techniques, obtaining new properties and optimizing the functionalization of the substrate.

The second part, *II. Experimental Techniques (Chapter 4)* describes the different experimental techniques used throughout this work, both, for the fabrication and for the characterization of the disordered structures and waveguides. A description of the facilities, as well as, the experimental conditions in which the irradiations were carried out, is presented.

Finally, the third part, *III. Results*, is devoted to the description of the original results of this Thesis work, which will be discussed in detail. It has been divided in four chapters (*Chapter 5 to 8*), due to the main results are based on essentially four experimental investigations.

In Chapter 5, *Kinetics of amorphization induced by swift ion beams in lithium niobate: The role of defective pre-amorphous areas (halos)*, is focused on the study of the structure of the damage on $LiNbO_3$ induced by dense electronic excitation of high energetic ion beams, that is the electronic regime, where the situation is poorly understood. The purpose is to critically discuss the main features about ion-beam amorphization of dielectric crystals, emphasizing the competition between the nuclear collision and electronic excitation routes.

We will address this situation from a double perspective, from one side, selecting experimental conditions with the aim of studying the kinetics of evolution of the damage with irradiation fluence, induced by ion bombardment with stopping power below and above the amorphization threshold; and, on the other one, a theoretical strategy is developed.

In Chapter 6, *Nanopores obtained by chemical etching on ion irradiated lithium niobate*, we present a systematical study into the formation of nanostructured pores generated by chemical etching after ion irradiation on lithium niobate. The different features of the nanopores obtained by chemical etching on ion-beam irradiated $LiNbO_3$ has been investigated for a variety of ions, energies and stopping powers in the electronic energy loss regime. The role of etching time and etching agent on the pore morphology, diameter, depth, and shape has also been studied.

The applied goal of this work is to find a powerful tool that allows us to obtain tailored-size nanostructured pores in an interesting material for optical applications like lithium niobate. Hence, this study is interesting both from the fundamental point of view and with the aim of optimizing and tailoring various technological potential applications like nanostructuring induced by ion beams.

The Chapter 7, *Recrystallization of amorphous nano-tracks and uniform layers generated in lithium niobate by swift-ion irradiations*, is devoted to the study of the recrystallization properties of the amorphous tracks and layers submitted to annealing processes. In this one we have provided systematic data on the kinetics of annealing of isolated amorphous tracks and homogeneous layers, which have been generated in $LiNbO_3$ by high-energy irradiation using low and moderate, or high fluence, respectively. Several ions, energies and stopping powers have been used. At variance with the heavily-damaged regions and layers generated by ion implantation, the tracks and layers investigated in this work are produced by electron excitation mechanisms.

The work is completed with the last Chapter of this Thesis, Chapter 8. *Thick optical waveguides in lithium niobate induced by swift heavy ions (~10 MeV/amu).* It deals with the description and discussion of a novel method to fabricate deep optical waveguides in $LiNbO_3$ using the electronic damage produced by very swift heavy ions (E ~ 10 MeV/amu) at ultralow irradiation fluences, much lower than normally used. This would allow the fabrication of much thicker waveguides (up to tens of microns). Such thick optical barriers suggest their application in the mid-Infrared range for astrophysics and other fields.

Finally, at the end of this dissertation, in Chapter 9. *Conclusions*, the main results and general conclusions drawn from this Thesis have been summarized.

1.3 References.

[1] P. D. Townsend, P. J. Chandler and L. Zhang, *"Optical Effects of Ion Implantation"*, Cambridge University Press, Cambridge, 1994.

[2] M. Nastasi, J. W. Mayer and J. H. Hirvonen, *"Ion-solid Interactions: Fundamental and Applications"*, Cambridge University Press, Cambridge, 1996.

[3] J. F. Ziegler, J. P. Biersack and U. Littmark, (Ed.), *The Stopping and Ranges of Ions in Solids*, Pergamon Press, New York, 1985.

[4] J. Ziegler, computer code SRIM version 2008, (http://www.srim.org).

[5] F. Agulló-López, R. C. Catlow and P. D. Townsend, *"Point Defects in Materials"*, Academic Press, London, 1984.

[6] R. T. Williams, and K. S. Song *"Self-trapped Excitons"*, Second edition, Springer-Verlag, Berlin, 1996.

[7] C. Trautmann, *"Modifications induced by swift heavy ions"*, Bull. Mater. Sci. 22 (1999) 679-686.

[8] G. G. Bentini, M. Bianconi, M. Chiarini, L. Correra, C. Sada, P. Mazzoldi, N. Argiolas, M. Bazzan and R. Guzzi, *"Effect of low dose high energy O^{3+} implantation on refractive index and linear electro-optic properties in X-cut $LiNbO_3$:Planar optical waveguide formation and characterization"*, J. Appl. Phys 92 (2002) 6477.

[9] T. Mohanty, N. C. Mishra, F. Singh, U. Tiwari and D. Kanjilal, *"Swift heavy ion irradiation induced modifications in sapphire"*, Nucl. Instr. Meth. B 212 (2003) 179-183.

[10] M. Bianconi, N. Argiolas, M. Bazzan, G.G. Bentini, M. Chiarini, A. Cerutti, P. Mazzoldi, G. Pennestri and C. Sada, *"On the dynamics of the damage growth in 5 MeV oxygen-implanted lithium niobate"*, Appl. Phys. Lett. 87 (2005) 072901.

[11] J. Olivares, G. García, F. Agulló-López, F. Agulló-Rueda, A. Kling, J.C. Soares, *"Generation of amorphous surface layers in $LiNbO_3$ by ion-beam irradiation: thresholding and boundary propagation"*, Appl. Phys. A 81 (2005) 1465-1469.

[12] F. Agulló-López, G. García and J. Olivares, *"Lattice preamorphization by ion irradiation: Fluence dependence of the electronic stopping power threshold for amorphization"*, J. Appl. Phys 97 (2005) 093514.

[13] G. García, F. Agulló-López, J. Olivares and A. García-Navarro, *"Monte Carlo simulation of damage and amorphization induced by swift-ion irradiation in $LiNbO_3$"*, J. Appl. Phys. 99 (2006) 053504.

[14] M. Toulemonde, W. Assman, C. Dufour, A. Meftah, F. Studer, and C. Trautmann, in: *"Ion Beam Science: Solved and Unsolved Problems"*. P. Sigmund, (Ed.), *The Royal Danish Academy of Sciences and Letters*, Copenhagen, 2006, pp. 263.

[15] A. Garcia-Navarro, F. Agulló-López, M. Bianconi, J. Olivares and G. García, *"Kinetics of ion-beam damage in lithium niobate"*, J. Appl. Phys. 101 (2007) 083506.

[16] J. Jensen, M. Skupinski, K. Hjort and R. Sanz, *"Heavy ion beam-based nano- and micro-structuring of TiO_2 single crystals using self-assembled masks"*, Nucl. Instr. Meth. B 266 (2008) 3113-3119.

[17] P. I. Gaiduk, F. F. Komarov and W. Wesch, *"Damage evolution in crystalline InP during irradiation with swift Xe ions"*, Nucl. Instr. and Meth. B 164–165 (2000) 377-383.

[18] F. Komarov, P. Gaiduk and A. Kamarou, *"Damage evolution and track formation in crystalline InP and GaAs during swift Kr and Xe ion irradiation"*, Vacuum 63 (2001) 657-663.

[19] W. Wesch, A. Kamarou and E. Wendler, *"Effect of high electronic energy deposition in semiconductors"*, Nucl. Instr. and Meth. B 225 (2004) 111-128.

[20] A. Kamarou, W. Wesch, E. Wendler, A. Undisz and M. Rettenmayr, *"Swift heavy ion irradiation of InP: Thermal spike modeling of track formation"*, Phys. Rev. B 73 (2006) 184107.

[21] W. Wesch, A. Kamarou, E. Wendler, A. Undisz and M. Rettenmayr, *"Effect of high electronic excitation in swift heavy ion irradiated semiconductors"*, Nucl. Instr. and Meth. B 257 (2007) 283-286.

[22] C. S. Schnohr, P. Kluth, A. P. Byrne, C. J. Foran and M. C. Ridgway, *"Comparison of the atomic structure of InP amorphized by electronic or nuclear ion energy-loss processes"*, Phys. Rev. B 77 (2008) 073204.

[23] E. R. Hodgson, *"General radiation problems for insulating materials in future fusion devices"*, J. Nucl. Mater. 258 (1998) 226.

[24] G. Vayakis, E. R. Hodgson, V. Voitsenya and C. I. Walker, *"Generic diagnostic issues for a burning plasma experiment"*, Fusion Science & Technology 53 (2008) 699-750.

[25] R. C. Ewing, W. Lutze and W. J. Weber, *"Zircon: A host-phase for the disposal of weapons plutonium"*, J. Mater. Res. 10 (1995) 243-246.

[26] I. Farnan, H. Cho and W.J. Weber, *"Quantification of actinide a-radiation damage in minerals and ceramics"*, Nature 445 (2007) 190.

[27] V. A. Skuratov, A. E. Efimov and K. Havancsak, *"Surface modification of $MgAl_2O_4$ and oxides with heavy ions of fission fragments energy"*, Nucl. Instr. and Meth. B 250 (2006) 245.

[28] C. Claeys, and E. Simoen, *"Radiation effects in advanced semiconductor materials and devices"*, Springer Series in Materials Science, Vol. 57, Springer, 2002.

[29] J. F. Ziegler, *"Ion implantation technology"*, North Holland, Amsterdam, 1992.

[30] M. Bruel, *"The history, physics, and applications of the smart-cut process"*, MRS Bull. 23 (1998) 35-39.

[31] J. Debus, Proposal for a dedicated ion beam facility for cancer therapy, Tech. rep., Report of DKFZ, GSI and FZR, September 1998.

[32] A. Wambersie, T. Auberger, R. A. Gahbauer, D. T. Jones and R. A. Pötter, *"A challenge for high-precision radiation therapy: The case for hadrons"*, Strahlenther. Onkol. 175 (1999) 122-128.

[33] R. L. Fleischer, P. B. Price, and R. M. Walker, *"Nuclear Tracks in Solids: Principles and Applications"*, University of California Press, Berkeley, CA, 1975.

[34] R. Spohr, in: *"Ion Tracks and Microtechnology: Basic Principles and Applications"*. K. Bethge, (Ed.), Vieweg, Braunchsweig, 1990.

[35] B. Canut, S. M. M. Ramos, R. Brenier, P. Thevenard, J.L. Loubet, M. Toulemonde, *"Surface modification of $LiNbO_3$ single crystals by swift heavy ions"*, Nucl. Instrum. Methods B 107 (1996) 194 -198

[36] G. Szenes, Z. E. Horvath, B. Pecz, F. Paszti and L. Toth, *"Tracks induced by swift heavy ions in semiconductors"*, Phys. Rev. B 65 (2002) 045206.

[37] M. Toulemonde, C. Trautmann, E. Balanzat, K. Horjt, A. Weidinger, *"Track formation and fabrication of nanostructures with MeV-ion beams"*, Nucl. Instr. Meth. B 216 (2004) 1-8.

[38] A. Meftah, J. M. Constantini, N. Khalfaoui, S. Boudjadar, J.P. Stoquert, F. Studer and M. Toulemonde, *"Experimental determination of track cross-section in $Gd_3Ga_5O_{12}$ and comparison to the inelastic thermal spike model applied to several materials"*, Nucl. Instrum. Methods B 237 (2005) 563-574.

[39] *"Ion Implantation-2000: Science and Technology"*, J.F. Ziegler, (Ed.), Lattice, Sunset Beach, CA, 2000.

[40] G. G. Bentini, M. Bianconi, L. Correra, M. Chiarini, P. Mazzoldi, C. Sada, N. Argiolas, M. Bazzan and R. Guzzi, *"Damage effects produced in the near-surface region of x-cut $LiNbO_3$ by low dose, high energy implantation of nitrogen, oxygen, and fluorine ions"*, J. Appl. Phys 96 (2004) 242.

[41] J. Olivares, G. García, F. Agulló-López, F. Agulló-Rueda, J.C. Soares and A. Kling, *"Optical investigation of the propagation of the amorphous–crystalline boundary in ion-beam irradiated $LiNbO_3$"*, Nucl. Instr. Meth. B 242 (2006) 534-537.

[42] C. I. H. Ashby, G.W. Arnold and P.J. Brannon, *"Ion-bombardment-enhanced etching of $LiNbO_3$ using damage profile tailoring"*, J. Appl. Phys. 65 (1989) 93.

[43] F. Schrempel, T. Gischkat, H. Hartung, E. -B. Kley and W. Wesch *"Ion beam enhanced etching of $LiNbO_3$"*, Nucl. Instr. Meth. B 250 (2006) 164-168.

[44] J. Reinisch, F. Schrempel, T. Gischkat and W. Wesch, *"Etching of Ion Irradiated $LiNbO_3$ in Aqueous Hydrofluoric Solutions"*, J. Electrochem. Soc. 155 (2008) D298-D301.

[45] M. Bianconi, F. Bergamini, G. G. Bentini, A. Cerutti, M. Chiarini, P. De Nicola and G. Pennestri, *"Modification of the etching properties of x-cut Lithium Niobate by ion implantation"*, Nucl. Instr. Meth. B 266 (2008) 1238-1241.

[46] K. K. Wong, (Ed.), *Properties of Lithium Niobate*, EMIS Data Review Series, INSPEC Exeter, 2002.

[47] A. García-Navarro, *"Irradiación con iones pesados de alta energía en dieléctricos para aplicaciones fotónicas: Guías de onda en $LiNbO_3$"*, PhD. Dissertation, Departamento de Física de Materiales, Universidad Autónoma de Madrid (UAM), Madrid, July 2007.

[48] A. Rivera, J. Olivares, G. García, J. M. Cabrera, F. Agulló-Rueda and F. Agulló-López, *"Giant enhancement of material damage associated to electronic excitation during ion irradiation: The case of $LiNbO_3$"*, Phys. Status Solidi A 206 (2009) 1109-1116.

[49] A. Rivera, A. Méndez, G. García, J. Olivares, J. M. Cabrera and F. Agulló-López, *"Ion-beam damage and non-radiative exciton decay in $LiNbO_3$"*, Journal of Luminescence 128 (2008) 703-707.

Part I.

Introduction.

Part I. Introduction.

In *Chapter 1* we will introduce several topics that will be useful for the understanding of the work presented throughout this PhD dissertation. Specifically, the interaction mechanisms of the ions with the matter, the slowing down process, and the processes of damage creation into the target will be briefly discussed. First, we will introduce some important physical magnitudes that result crucial for a further understanding of the stopping process, and the ion beam modification of materials (IBMM). The following Section cover the main features of the process of amorphous track (latent ion track) formation by irradiation with swift heavy ions, and describe, in the framework of the available theoretical models, the complex deposition processes through electronic interactions that create damage and modify the properties of the irradiated material.

Another Chapter (*Chapter 2*) will be devoted to the description of the main properties of the Lithium Niobate ($LiNbO_3$), being the material used as substrate in this research work. A brief review of the updated knowledge about $LiNbO_3$ properties will be made, as well as the fabrication method and the crystal defects present in the material. Finally, in *Chapter 3*, the fundamental physical principles of the theory of optical waveguides, the different manufacturing techniques and their technological applications will be briefly presented.

Chapter 1

General concepts.

1.1 Interaction of Ions with Matter.
1.2 Parameters of the ion-matter interaction.
1.3 Defects creation by elastic nuclear collisions.
1.4 Defect creation by Swift Heavy Ions: Materials modifications and track formation by electronic excitation.
1.5 Basic models of track formation by swift heavy ions.

1.1 Interaction of Ions with Matter.

All the work presented throughout this Thesis uses accelerated ions beams and their interaction with the material, (i.e., the processes to which an ion is subjected during its passage through the material), as a double tool, both for processing and analysis. It is therefore necessary, firstly, to define some physical quantities that will be used in the following Chapters, as well as to carry out an introduction on slowing down mechanism of ions through the matter and the parameters that govern this process. In this sense, this Section is devoted to establish some definitions and concepts that will be used throughout the text. A very basic theoretical background is needed in order to understand some of the discussions and to have a more clear picture of the concepts used in ion-matter interaction.

The irradiation process requires a study from a double perspective, one from the point of view of the projectile, and the other, related to the target. The story of the ion in the material does not provide information on the transformations suffered by the target material. However, it is necessary to understand how the energy is deposited in the matter in order to correlate the damage induced.

During the irradiation of a material by charged particles, these ones gradually transfer their energy to the target medium by successive interactions, which can lead to a damage creation of the target. The effects that a target may suffer after irradiation are due to, either the kinetic energy of the incident particle, or its potential energy (related to the charge of the projectile).

The main phenomena of slowing down of ions in matter are related to the effects induced by the deposition of kinetic energy through nuclear collisions and electronic mechanisms, which do not exclude the existence of other processes (like excitations, nuclear reactions and Cherenkov radiation), much less probable [1]. Thus, an energetic-swift ion, when traversing a solid slows down, distributing its energy into the material until it finally gets to rest. On its way through matter ion projectiles transfer their energy to the solid by two interaction processes: (1) by direct elastic collisions with the lattice atoms, [i. e. nuclear slowing down or nuclear energy loss, $S_n = (dE/dx)_n$] predominating at low energies (~1 keV/u), and (2) by electronic ionizations and excitations of atoms, i. e. inelastic interactions with target electrons [electronic slowing down or electronic energy loss, $S_e = (dE/dx)_e$] if the energy of the projectile is larger than ~ 0.1 MeV/u [2]. The latter will be the main mechanism in the first part of its trajectory, while, on the other hand, at the end of range, the nuclear energy loss will be the predominant process.

The processes involved in the interaction between the accelerated ion and the target material mainly depend on the ion velocity and the charges of the incident ions and atoms of the irradiated material. Overall, we can say that at low velocities (E < 0.01 MeV/u) [2] the energy loss is dominated by nuclear stopping power (S_n). Such collisions cause abrupt changes in the energy of the projectile and the direction of its path, leading to large angular scattering of the projectiles. Hence, the memory on the incident beam direction is rapidly lost and material alterations, which result from displacement cascades, are rather isotropic. The defect creation by elastic collisions is a direct consequence of Coulomb interaction between an incident ion and a target atom. Then, the number of displaced atoms can be calculated [3, 4].

On the other hand, at high velocities of the incident ion, (E > 0.1 MeV/u), energy loss is dominated by the electronic stopping power (S_e). Interaction with target electrons leads to excitation, ionization of the target atoms, and kinetic energy of ejected target electrons, being the incident beam direction retained. These electronic processes lead to a cuasi-continuum energy loss, leaving almost invariant the initial projectile direction. Hence, the stopping power depends on the ion velocity. This interaction is important at ion energies ≥ 1 MeV/u and primarily generates a hot electron gas around the straight ion trajectory. At 1 MeV/u, S_e is at least two orders of magnitude larger than S_n, being considered neglected. For swift ions (beam energy > 1 MeV/u), the energy is therefore mainly deposited on the electron subsystem of the irradiated material and consequently the number and mobility of the electrons play a crucial role [5] before the deposited energy is finally converted in atomic motion. If there exists an efficient coupling between the electron gas and the atoms of the solid, the latter can locally attain very high temperatures so that it melts within a few picoseconds.

These two regions are also referred to as the electronic and the nuclear stopping power regime[1]. **Figure 1 (a-c)** shows an example of the behaviour described, for several ions impacting on $LiNbO_3$, which describes the difference between the regions of low and high energy, and stopping powers that dominates in each one.

1.2 Parameters of the ion-matter interaction.

The most relevant parameters of the ion-matter interaction with the aim of defining an irradiation are the following:

- *Stopping power* (*dE/dx*), which depends on cross-sections of elastic and inelastic collisions,

- *Projected Ion Range* (R_p), the ion path length into the target, which depends on the ion velocity,

- *Density of deposited energy*, which depends on the ion velocity,

- *Irradiation Flux* (F), representing the number of incident particles sent to the target by unit area and per unit time (particles/cm^2 s),

- *Irradiation Fluence* (Φ), corresponding to the total number of particles received by the target per unit area (particles/cm^2).

1.2.1 The Stopping power and the Ion range.

As already mentioned, the slowing down of the incident charged particle into the target is produced, on one hand, by a direct interaction with the nuclei of target atoms and, on the other one, by an interaction with the electrons. The amount of energy lost by the ion during the slowing down in the material is then a characteristic parameter, called *Stopping Power* (S_e). The stopping power is a characteristic of the target medium and the incident particle (nature and

[1] In the electronic stopping power regime S_e is at least one order of magnitude greater than S_n. Both lines intersect at about $E_{ion} \sim 0.01$ MeV/u.

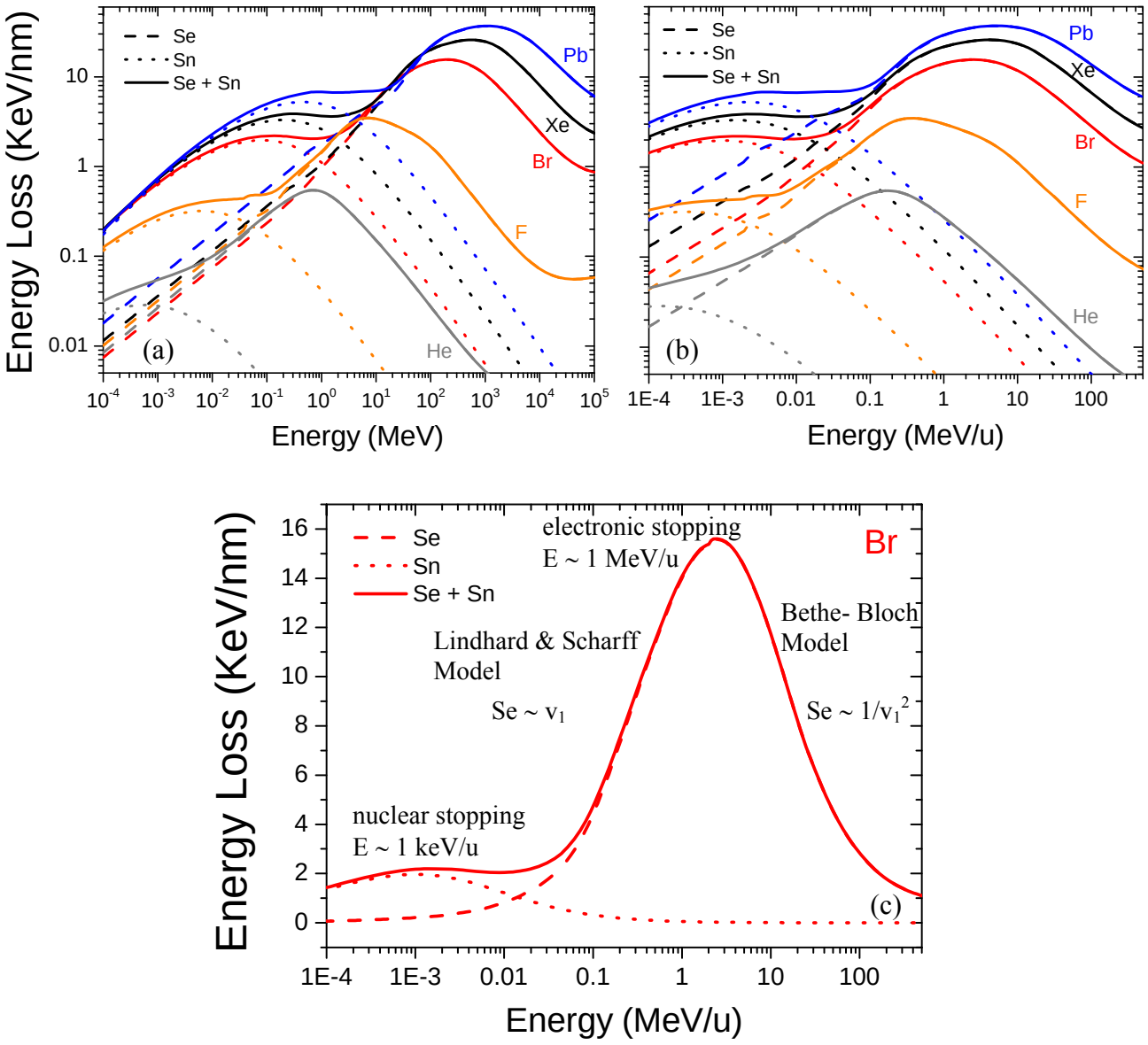

Fig. 1 (a-c). Distributions of electronic (dashed lines), nuclear (dotted lines) and total (solid lines) energy loss of ions listed in the leyend into $LiNbO_3$ crystals calculated by SRIM 2008 [6] as a function of the ion energy **(a)**, and the ion energy per atomic mass unit (specific energy) **(b)**. **(c)** Energy loss contributions for the case of Br ions into $LiNbO_3$ plotted versus the specific energy, showing the different energy regions (low and high energies), the Bragg peak and the dependency of the electronic stopping power on the ion velocity.

energy of the ion projectile). It is defined as a loss of energy of the projectile per unit length, i.e., S = dE/dx. It is expressed in *MeV cm²/mg* that can transform in *keV/nm* if we know the mass density of the material.

According to the collisional processes considered, elastic or inelastic interactions, a *nuclear stopping power* and an *electronic stopping power*, are respectively defined. The total stopping power (or energy loss) per unit length in the target, is obtained by adding the nuclear stopping powers (S_n) and electronic (S_e):

$$\left(\frac{dE}{dx}\right)_t = \left(\frac{dE}{dx}\right)_e + \left(\frac{dE}{dx}\right)_n \quad \textbf{(1)}$$

During the interaction, the velocity of the incident ion decreases and, at the stop, the ion is trapped in matter. It is then possible to determine the range (R_p) of the ion along its trajectory into the target, given by the relationship:

$$R_p = \int_0^{E_1} \left(\frac{dE}{dx}\right)^{-1} dE \quad \textbf{(2)}$$

where E_1 represents the initial kinetic energy of the particle as it enters into the target. The proposed route represents the projection of the ion path on the initial direction of the particle.

1.2.1.1 Nuclear Stopping power or elastic collisions.

The interactions between the incident ion and target atoms are treated, in general, as elastic collisions of two particles, governed by the laws of classical mechanics. The parameter that describes the ion-atom interactions, is the cross-section of collisional processes (σ *(T)*), defined as the probability that the projectile transfers an energy to a target atom during its interaction. Let us consider an incident ion with an initial kinetic energy E_1, atomic number Z_1, and mass M_1, and an atom from the target with atomic number Z_2 and atomic mass M_2, receiving a certain amount of energy T. Assuming a purely Coulomb-type interaction that applies to high energies, the collision cross-section is [1]:

$$\sigma(E_1, T_1) = \frac{(\pi Z_1 Z_2 e^2)^2 M_1}{T^2 E_1 M_2}, \text{ where } e^2 = 1.44 \text{ x } 10^{-7} \text{ eV/cm} \quad \textbf{(3)}$$

Then, the energy lost by nuclear collisions by the ion along its path, it is written:

$$\left(\frac{dE}{dx}\right)_n = N \int_{T_{\min}}^{T_{\max}} T\sigma(E_1, T)\, dT \quad \textbf{(4)}$$

where N is the number of atoms per unit volume, T_{min} corresponds to an minimum energy introduced to avoid divergence of the integral, and T_{max} is the maximum energy provided during a head-on collision: $T_{max} = (4M_1M_2E_1)/(M_1 + M_2)^2$. The expression of the nuclear stopping power, then, becomes:

$$-\left(\frac{dE}{dx}\right)_n = 2\pi N \frac{M_1}{M_2} \frac{Z_1^2 Z_2^2}{E_1} e^4 \ln \frac{T_{\max}}{T_{\min}} \quad \textbf{(5)}$$

1.2.1.2 Electronic Stopping power or inelastic collisions.

It should be emphasized that this situation is much more complex compared to the nuclear stopping regime where the energy is directly given to the lattice via atomic collisions. In this sense, the description of the inelastic interactions cannot be described as individual

interactions between two bodies, the ion projectile interacting at once with multiple electrons from the target, bound to their nuclei.

In the case of ions that we will use, the ions interact, in a first stage, with the electrons to which they will transfer a portion of their energy. These energetic electrons (called *δ-electrons*) move, mainly radially, inducing secondary ionization, carrying the energy initially transmitted from the incident ion at distances of tens of nanometers [7, 8]. The remaining ions throughout the trajectory of an incident ion are excited and ionized [9].

With the aim of having a qualitative description of the processes involved in the stopping force as a function of the ion velocity[2], we can consider what happens to a high energy ion which is penetrating into a solid target and steadily loosing energy[3]. We can distinguish three different velocity regimes in order to evaluate the electronic energy loss: they are defined in relation to the quantity $Z_1^{2/3} v_0$, where v_0 is the Bohr velocity ($v_0 = 2.2 \times 10^6$ m/s), and Z_1 is the atomic number of the incident ion. Considering v_1 as the projectile velocity, there are defined:

(a) High energy regime (when $v_1 >> Z_1^{2/3} v_0$): the *Bethe - Bloch region*.

(b) Intermediate energy regime (where $v_1 \approx Z_1^{2/3} v_0$): the *Bragg peak*.

(c) Low energy: velocity-proportional region (when $v_1 << Z_1^{2/3} v_0$) and the Nuclear stopping power regime.

(a) High energy regime ($v_1 >> Z_1^{2/3} v_0$): the Bethe - Bloch region.

In this case, at very high velocities, the incoming ion is completely stripped of all its electrons and, therefore, it can be considered as a point charge ($Z_1 e$) moving in an electron gas. The expression used in this case is the Bethe - Bloch´s formula [10]:

$$S_e = -\left(\frac{dE}{dx}\right)_e = \frac{4\pi e^4 Z_1^2 Z_2 N}{m_e v_1^2} L(v_1) \qquad \textbf{(6)}$$

where, NZ_2 is the electronic density of the target, m_e is the mass of the electron and I is the mean ionization potential. In this regimen the energy loss is proportional to $ln\ E/E_1$, where E_1 is the initial energy of the projectile, i. e. the stopping power is approximately proportional to the inverse of the square of the velocity ($S_e \sim 1/v_1^2$). This means that the energy loss decreases as the particle energy increases. This expression is valid for ions of very high velocity. Finally, the last term, $L(v_1)$, is the so-called *stopping number*, which groups a number of higher order and relativistic corrections. Further details on the expression far exceed the scope of the present work and they can be found in an excellent review from Ziegler [11].

[2] Note that, ignoring relativistic effects, $E = mv^2/2$, where m is the ion mass.

[3] It is worthy noticed that the description of the slowing down process of the ions carried out in this Section has been done considering an amorphous material, or a non-crystalline material oriented along a direction of symmetry. The specific consequences of irradiating a material in channeled configuration will be studied in detail in a following Chapter, during the exposition of Rutherford Backscattering Spectroscopy in Channeling configuration (RBS-C), which is one of the main characterization techniques used in this Thesis work.

(b) Intermediate energy regime (where $v_1 \approx Z_1^{2/3} v_0$.): the Bragg peak.

When the projectile velocity decreases, being its velocity comparable to that of the target electrons, the capture of electrons comes into competition with that of ionization. In this regime, the assumption of a fully stripped projectile is no longer valid and the *Bethe-Bloch formula* has to be modified. Its average electric charge is less than $Z_1 e$, and the electronic stopping power becomes lower than obtained according to the *Bethe´s formula*. A generally accepted solution is to extend the range of applicability of **Eq. (6)** by introducing the concept of an *effective charge*, Z_1^*, which can be calculated - as suggested by Bohr and demonstrated by L. C. Northcliffe [12] - assuming that an ion is stripped of all its electrons whose orbital velocities are smaller than the ion velocity:

$$\frac{Z_1^*}{Z_1} = 1 - \exp\left(\frac{-v_1}{v_0 Z_1^{2/3}}\right) \qquad \textbf{(7)}$$

This expression is derived from considering a Thomas-Fermi model for the atom, where the electron velocities scale as $Z_1^{2/3}$ - note that more empirical versions of **Eq. (7)** have been proposed, which yield a better fit to the experimental data [13]. **Eq. (7)** results in *fractional* values for the ion charge, that can be explained from a statistical point of view or directly considered as an *ad-hoc* correction that allows to extend to the lower energy range the applicability of the Bethe-Bloch formula.

In this velocity regime, two effects compete: on the one hand, there is the increase of stopping power with the diminution of velocity, as shown in **Eq. (6)** and, on the other hand, there is the diminution of the effective ion charge (see **Eq. 7**) which tends to diminish the stopping power as velocity decreases. At some point ($v_{peak} \approx 3v_0 Z_1^{2/3}$), both effects compensate, producing the smooth maximum - often called *Bragg peak* - which is characteristic of all stopping curves vs ion energy. At velocities below the Bragg peak the stopping power decreases as the ion energy decreases.

(c) Low energy: velocity-proportional region ($v_1 << Z_1^{2/3} v_0$) and the Nuclear stopping power regimen.

To this point the ion is slowed down in a quasi-continuum way and collisions with the nuclei of the material are highly improbable[4] events. Therefore, the trajectory of the ion is approximately straight.

At the end of the ion trajectory, and for energies below the *Bragg peak* (tipically at E ~ 1 keV/u) the nuclear stopping contribution, is no longer negligible and, therefore, the stopping force has to be calculated accounting for both electronic, S_e, and nuclear S_n contributions. At

[4] In average, one per 10^6 incident ions will be backscattered after collisions with target atoms. This will be the proportion of incident ions to be measured with the characterization technique of RBS (Rutherford Backscattering Spectroscopy), which will be detailed in a following Chapter. In channeling configuration (RBS-C), the measurement associated to the surface falls down up 95% in $LiNbO_3$, depending on the projectile and the energy used.

low speed, the ion has the greater part of its electrons. During the collision between the ion and target atom, the electron clouds of the two partners overlap, a rearrangement of electronic levels takes place during the interaction, leading to the formation of a quasi-molecule with its own electronics states. Only electrons weakly bound to the target contribute to the energy loss of the ion.

For the electronic stopping, the ion can be considered to be almost neutral at these velocities and, hence, S_e may be described under the framework of the J. Lindhard, M. Scharff and H. E. Schiott theory [14] - which predicts that the electronic stopping is proportional to the velocity of the ion:

$$S_e = -\left(\frac{dE}{dx}\right)_e = \frac{\xi_\varepsilon e^2 a_0}{2\pi\varepsilon_0^2}\frac{Z_1 Z_2}{\left(Z_1^{2/3}+Z_2^{2/3}\right)^{3/2}}\frac{v_1}{v_0} \quad \textbf{(8)}$$

where $\xi_\varepsilon \sim Z_1^{1/6}$, e is the electron charge, ε_0 is the dielectric permittivity of vacuum and a_0 is the Bohr length.

The nuclear stopping contribution becomes significant only at the lowest energies, and can be understood as the energy transfer from the moving ion to a target atom, considering a screened Coulomb potential due to the electrons around both the ion and target nuclei. The concept is rather simple, since one can assume a two- body collision. This potential can be expressed as a function of the distance between the ion and the target atom, r, as:

$$V(r) = \frac{Z_1 Z_2 e^2}{(4\pi\varepsilon_0)^2 r}\exp\left(\frac{-r}{a_0}\left(Z_1^{2/3}+Z_2^{2/3}\right)^{3/2}\right) \quad \textbf{(9)}$$

As a consequence of the comparable masses of the ion and the target nuclei - in contrast with the electronic stopping where the electron mass is much smaller than the mass of the ion - the nuclear stopping events are associated to noticeable deflections of the ion trajectory, where the ion may abruptly change its direction and the trajectory can no longer be considered as a straight line. Also, there will be major changes in the energy and momentum of the ion projectile after each collision. A very detailed work on nuclear stopping can be found, for example, in [15]. All these effects and experimental observations are taken into account when calculating an ion trajectory in a target material via the program SRIM [2, 6].

1.3 Defects creation by elastic nuclear collisions.

1.3.1 Basic theoretical principles. Effect into the solids by irradiation with material particles.

The main purpose of this Section is to determine changes induced by irradiation with material particles in the structure and properties of solid materials [16-18]. In this case the nuclear element corresponds to the bombarding particles that are used for damaging the solid and provide it with imperfections. Hence, the central problem that arises is the calculation of the number of such imperfections depending on the nature, energy and flux of bombarding particles.

The simplest types of defects which can be caused by radiation, are:

a) Vacancies: Empty places of the crystal network, due to the lack of the corresponding atom or ion.

b) Interstitials: Atoms or ions occupying a non regular position within the crystal.

c) Aggregates of these defects.

All these ones are related to punctual defects, in the sense of they refer to a microscopically localized position within the solid.

In brief, we show only the essential features of the Theory of Seitz and Koehler [19]. When an incident particle comes into contact with a solid produces (if the energy is high enough), atomic displacements giving rise to vacancy-interstitial pairs. In turn, these primary ones can create secondary displacements that lead to new defects. Admitting with Seitz that the following assumptions are satisfied:

a) The material can be understood as a disordered mean, i.e., without crystallographic regularity.

b) The energy invested in atomic excitation and ionization is negligible compared with that one in elastic processes[5].

c) The interaction process among atoms within the solid can be treated as binary collisions, while the rest of the medium remains unchanged.

Under these conditions, the following simple relationship for the number N of displacements created per unit time and unit volume can be written:

$$N = \Phi\, n_0\, \sigma_d\, \bar{\nu} \qquad \textbf{(10)}$$

where Φ is the flux of incident particles, n_0 is the number of atoms in the solid per unit volume, σ_d the cross-section for production of displacements, and $\bar{\nu}$ the average number of secondary displacements produced by each primary. As Φ and n_0 are known, the problem is to find expressions for σ_d y $\bar{\nu}$ depending on the type and energy of incident particles.

For the calculation of σ_d, the additional assumption is usually made, that there is a threshold energy E_d, such that, when an atom inside of solid receives an energy collision $T \geq E_d$, it is moved; whereas, if $T < E_d$, it remains in its place. Experiments have shown that in most cases, E_d takes values near of 25 eV. (A detailed description can be found in Ref. [16]).

Average number of secondary displacements produced per each primary one ($\bar{\nu}$).

In principle, this calculation is quite complicated; however, with the additional assumption that the lattice atoms that collide with each other can be treated as hard spheres, one may consider an integral equation for $\nu\,(T)$, which represents the number of secondary displacements created by each primary one of energy T.

[5] This hypothesis is approximately valid below a certain threshold energy E_d which can be taken equal to $A \times 10^3\ eV$ (A being the atomic mass of the bombarding particle).

In the case of $T << E_d$, it is verified:

$$\nu(T) = \frac{1}{2}\frac{T}{E_d} \tag{11}$$

From here, for $E >> E_d$, $\bar{\nu}(E)$ is given by the following expression:

$$\bar{\nu}(E) = \frac{1}{\sigma_d}\int_0^{T_{\max}} \sigma(T)\nu(T)dT = \frac{1}{2}\frac{\bar{T}}{E_d} \tag{12}$$

which tells us that the average number of displacements produced per each primary one is proportional to the average energy received by it in the collision[6]. Due to the limited scope of atoms of the solid within the crystal lattice (~ 100 atomic distances), all these displacements will appear very close together, resulting in a strongly disordered spatial region.

1.3.2 The phenomenology of the collisional cascades and the cooperative effects of cascades.

The formation of the first hit and displaced atom (*PKA*, "primary knock-on atom") is equivalent to the formation of an interstitial-vacancy pair (i-v), called *Frenkel pair*, and forms the basic structure of the damage. If the kinetic energy of *PKA* is the order of tens of *eV* or higher, it can keep moving through the crystal producing collisions with other atoms to form secondary displaced atoms, tertiary ones, etc…

Similar to the formation of Frenkel pairs, the total number of collisions takes place in a very short time (less than 10^{-13} s), during which the rest of the atomic lattice can be considered at rest. This event is known as a *cascade of collisions*.

In the first part of the cascade of collisions, when the *PKA* energy is still high, the individual collisions are relatively far apart each others, and the movement can be expressed through individual binary collisions. As the energy of atoms decreases the distance between collisions also decreases until it becomes comparable to interatomic distances.

Within the same cascade, and produced the first displaced atom or primary atom, there will be a number of events of atom-atom collisions, for which you can also define a mean free path between collisions. This mean free path will depend critically on the energy and the interaction potential. Depending on the type of interaction considered, calculations are made possible not only to estimate the number of displaced atoms, but also their spatial distribution. As the energy of the primary atom decays after successive binary collisions, these collisions occur at spatial intervals shorter and shorter until the distance between two collisions becomes comparable with interatomic distances. Then, a collective interaction begins.

A considerable amount of energy (eV/atom) is concentrated at the end of the path of *PKA*, in a very short time interval (≈ 10^{-13} -10^{-12} s) and a very small volume (10^4 atoms). This leads to a collective disarrangement in that region, and a random and irregular formation of

[6] The number of defects $\bar{\nu}(E)$ that can create this primary as a function of its energy *E* was originally given by Kinchin and Pease [3].

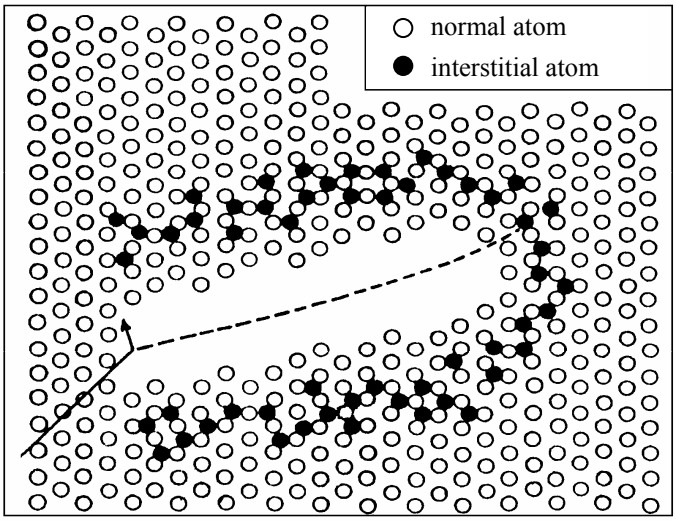

Fig. 2. Schematic of the *nude area* according to Brinkman. The solid line represents the projectile trajectory, and the dashed one, the primary atom path.

Event	Time-scale	Results
Binary collisions and energy transfer	< 0.1 ps	PKA
Collective displacement of atoms, cascade of displacements and spontaneous recombination	~ 0.1 ps	Cascade of collisions
Energy dissipation (spikes and cascade collapse)	~ 10 ps	Stable Frenkel pairs and nude areas
Interactions among defects by thermally activated movements	~ 10 ns	Recombination of individual defects, extended defects formation and microstructural changes

Table I. Different stages during the complete development of the cascade of collisions.

vacancies clusters surrounded by a layer of interstitials beyond the disturbed region (called *the nude area* according to Brinkman [20], see **Fig 2**. If the energy of the incident particle is very large, the cascade exhibits the tendency to separate into subcascades.

The complete development of the cascade of collisions can be schematically separated into several stages, which are summarized in **Table I**. The three first stages occur at times lower than 10^{-11} s and are determined by collisional processes. The resulting distribution of generated defects, isolated defects, Frenkel pairs, nude areas, is known as *primary damage state*. Subsequent process occurs at times > 10^{-8} s, and it is controlled by *diffusion processes*; the thermally activated motion of point defects produces changes in the microstructural state of the irradiated material.

1.3.3 Spatial distribution of damage produced in the collisional regime.

The most probable ranges of ions, $<R_I>$ and of defects, $<R_d>$, can be derived directly from mean values of energy losses given in tables by writing [21]:

$$<R_I> = \frac{1}{N_{at}} \int_0^E \frac{dE}{S_n(E) + S_e(E)} \quad \textbf{(13.a)}$$

$$<R_d> = \frac{1}{N_{at}} \int_{E_d}^E \frac{dE}{S_n(E)} \quad \textbf{(13.b)}$$

where N_{at} is the atomic density of the target.

Due to the stochastic nature of the nuclear stopping process, the depth distributions of implanted atoms and of energy transferred to nuclei, $f_I(E_I, R)$, by ions having a residual energy E_I at depth R, can be approximated by Gaussian functions in the case of amorphous or polycrystalline targets:

$$C(z) = \frac{\Phi S_u}{\sqrt{2\pi} N_{at} \Delta R_p} \exp\left(-\frac{(z - R_p)^2}{2\Delta R_p^2} \right) \quad \textbf{(14.a)}$$

$$C_{\max} = \frac{\Phi S_u}{\sqrt{2\pi} N_{at} \Delta R_p} \quad \textbf{(14.b)}$$

where N_{at} is the atomic density of the material, Φ, the irradiation dose, S_u, the unitary surface. R_p is the mean ion range projected onto the incident beam direction, and ΔR_p, its standard deviation. R_p is the center of the Gaussian and corresponds to the depth at which the implanted ion concentration is maximum. This atomic concentration denotes by C_{max}. These distributions are, however, estimated more accurately by using the transport equations defined by Lindhard and computing Monte-Carlo simulations of binary collision cascades with the SRIM code [2, 6].

Ion-beam damage to a crystalline solid in the form of atomic displacements is traditionally thought to arise predominantly from elastic collisions or nuclear stopping interactions [22]. Most of these elastic collisions occur in the end-of-range (*EOR*) region of the solid after the inelastic electronic processes have significantly slowed or almost stopped the implanted ions. At sufficiently high fluences (in the range 10^{15} - 10^{17} cm^{-2}) defect clustering develops and a quasi-amorphous layer develops monotonically at the end of the ion range, i.e. the region where the ions are implanted. Although the initiation of a definite amorphous phase is difficult to ascertain, it is generally accepted that it occurs for fluences around or slightly above 1 *dpa* (*displacements per atom*). The amorphization appears to be a gradual (monotonic) process resulting from the accumulation of successive displacement spikes, i.e., as the limit stage of a displacement spike. Moreover, the detailed structure of such an amorphous phase is also controversial and maybe not unique.

1.4 Defect creation by Swift Heavy Ions: Materials modifications and track formation by electronic excitation.

Until now we have described the changes undergone by the ions and the matter in the collisional regime, on the other hand, we must also to describe what happens in the target matter after the swift ions have passed through. The types of defects induced by a swift ion in a solid are determined by the type of solid, that is, these defects depends on the electronic structure of the material. Thus, the electronic collisions induce structural defects on insulators and semiconductors, while in the case of metals the deposited energy is rather dissipated through thermal energy without creating structural defects [1, 17].

As already mentioned, the defects created in the solid can be classified as follows:

1. Point defects - such as vacants, the interstitials or a combination of both as Frenkel pairs.
2. Extendend defects – emerged as consequences of defects in multiple electronic collisions, leading to the creation of *latent tracks*.

Several authors have tried to give an explanation for the creation of *latent tracks* in solids (insulators, metals, semiconductors). Models like *Coulomb Explosion* - or *Ion Spike* [19, 23, 24]-, and *the Thermal Spike Model* [25-29] have been proposed among others, which all of them will be studied in detail along this Chapter.

It has been explained above that, swift heavy ions (SHI) lose energy in materials mainly through inelastic collisions with the atomic electrons. Energetic ions passing through solids trigger a wide range of processes and cause permanent changes, i. e., structural damages induced by high electronic excitation, which are particularly interesting to both, for basic research investigations, and with respect to new types of technological applications. Along the trajectory, a trail of defects (point defects, defect clusters, structural phase transformation) known as *latent track* may be formed depending on the type of ion and its energy as well as the physical property of the materials. This damage is always created in the close vicinity of the trajectory of projectile. With the availability of high energy heavy ions from modern accelerators, swift heavy ion beams are proving to be of inmense use in various fields, particularly for modification of materials through dense electronic excitation following the slowing down of swift heavy ions in material.

Throughout this Thesis, irradiations with medium/high mass and high energy ions have been carried out, leading to the formation of amorphous tracks in $LiNbO_3$. The scenario of the creation of amorphous tracks with nanometric scales, using ions with high electronic stopping power (S_e > 5-6 keV/nm), is a field of study that is receiving much attention in the last 20 years [30, 31]. A great number of technological applications have been proposed placed in what has been so called *ion track technology* [32, 33], from dosimetry of fission fragments to molecular filters, passing through a variety of magnetic and electronic devices. This Section addresses the topic of ion tracks and considers the questions of their appearance and of their mechanisms of formation.

1.4.1 Structure of single tracks. Amorphous core and defective surrounding halo.

A fast heavy ion may lead to permanent material changes in a small volume surrounding the virtually straight ion path. The high electronic energy deposition gives rise to the formation of a chemical or structural defect cluster of cylindrical shape with an extremely large aspect ratio exceeding 1:1000. Such a defect cluster and its electronic and atomic precursors are denoted as *ion tracks*.

The discovery of ion tracks dates back to 1959 when Silk and Barnes published transmission electron micrographs of mica containing long, straight damage trails created by single fragments from the fission of ^{235}U [34]. Soon after that, it has been realized that ion tracks are narrow (< 5 nm), stable, chemically reactive centers of strain that are composed mainly of displaced atoms rather than of electronic defects [5]. It also became clear that these displaced atoms are not due to direct collisions between ions and the (screened) target nuclei, but are the result of the interaction of the projectile ions with the target electrons. Further experiments revealed that tracks were formed in insulators and badly conducting semiconductors, if the electronic stopping power (S_e) exceeded a material-dependent threshold value (S_{th}). At that time, no tracks could be detected in metals. The appearance of track effects in polymers is known since some decades [5] and has found widespread applications in the meanwhile [30]. The field has continuously developed both in basic understanding and in technological applications [5, 30, 35]. In this sense, the defect creation by swift heavy ions in the electronic stopping power regime in different materials whatever it is an insulator [36-49], semi-conductor [50-56] or conductor [57-61] has been extensively studied during the past decades. Except for insulators with an ionic bonding character, for example CaF_2 [62], pure metallic materials, as Ti [63] and several semiconductors [54], the highly localized energy deposited on electrons induced an amorphized track along the ion path, above a threshold value of the electronic stopping power (S_{th}).

Nowadays, it is known that other insulators, semi-conductors and even metallic glasses [58, 64-66] are also subject to materials modifications by heavy ions. This progress became possible when big ion accelerators delivered very heavy ions at stopping power maximum in order to overcome the large S_{th}-thresholds necessary for track formation in solids with metallic conductivity. Additional insight came from the effect of ion hammering in glasses bombarded with fast heavy ions [67, 68]. Overlapping ion tracks (at high fluences) may, e.g. lead to enhanced interface mixing effects. Furthermore, macroscopic material changes, such as plastic deformation or surface instabilities, are induced by the electronic energy deposition inside ion tracks [58, 66]. Individual ion tracks are explored as columnar defects for magnetic flux pinning and as quasi one-dimensional wires for electron field emission [69]. They are also used to trigger and control the nucleation of metal clusters in glass, similar as in the photographic process.

It should be emphasized that this situation is much more complex compared to the nuclear stopping regime where the energy is directly given to the lattice via atomic collisions. Once the projectile has reached its equilibrium charge state, there will be only minor fluctuations of its internal state and it will move with constant velocity along a straight-line trajectory until deep inside the solid. Thus, the projectile ion acts as a well defined and virtually

instantaneous source of strongly localized electronic excitation. In addition, the energy deposition of projectile is not homogeneous, but follows a radial distribution of approximately ~ $1/r^2$ (where *r* is the radial distance from the ion trajectory) [70]. Depending on the distance from the ion path, two regions can be characterized: (1) the *track core* of some nanometers, in which the energy density deposited on the electrons is ~ 20 eV/at (high density electronic excitations), and (2) the much larger *track halo* of some hundreds of nanometers, which receives at most ~ 0.2 eV/at (energy transportation by *δ-electrons*). Moreover, this energy density depends on the velocity of the beam (*velocity effect*): for high-velocity projectiles the energy deposition is smeared out into a larger radius [39]. Consequently for the same electronic energy loss, the energy density versus velocity can vary by one order of magnitude [9, 39]. That's to say, the initial spatial distribution of the energy imparted into the electron subsystem and the energy spectrum of electronic excitations determine the temperature of the local region near an ion path during thermalization of the excited region. Thus, for equal values of $(dE/dx)_e$, the ion with the higher velocity generates a larger radial distribution of the released electron energy in the stopping medium (because of an increase in the number and velocity of δ-electrons), and thus, lower density of the deposited energy, which causes the track to have a smaller radius[7] [39].

The formation of well-shaped cylindrical ion tracks requires electronic excitation levels surpassing material dependent thresholds (S_{th}). The precise values depend somewhat on the experimental track detection method, on ion velocity and irradiation temperature [32]. Below S_{th} the track structure deviates more and more from a cylindrical shape. At first, a track turns into a string of 'pearls' of defective material and, with decreasing S_e, eventually disappears in the background of defects originating from atomic displacements via S_n [32].

1.4.2 Ion track morphology in $LiNbO_3$ and other oxides.

Specifically, in the case of $LiNbO_3$, the dependence of the damage with the electronic stopping power of the incident ions, responsible for creating the tracks, have been widely examined [42, 43, 71, 72]. **Fig. 3** shows the radius of latent tracks as a function of electronic energy loss deduced from several physical characterizations[8] in two regimes of the energy of the incident ion. The energy density deposited in the solids is influenced by the projectile velocity, and thus, the damage created by the ions varies depending on the ion velocity: for a given electronic energy loss value the resulting track radius is larger at low than at high velocities, that is, at higher velocities the damage is smaller (*velocity effect*). From another point of view, it is

[7] For the same S_e value, the energy deposition is smeared out into a larger radius for high velocity projectiles. The reason for this *velocity effect* is that the maximum energy transferred to the electrons is $T_{max} = 2\ m_e\ v_{ion}^2$. The swifter the ion, the higher the fraction of the ion energy swept away from the core by these electrons for a given S_e value. The energy deposition is more localized for the low-velocity ions than for the high-velocity ones. Polymers are sensitive essentially to ionizations produced in the core, while damaging in metals results from lattice vibrations induced by elastic collisions of electrons outside the core. The damaging mechanisms of semiconductors and inorganic insulators are more intricate, since they involve various processes of electron-hole recombination and charge transfer.

[8] We point out that the experimental determination of the track radii shown in **Fig. 3** has been carried out through RBS-C measurements (Rutherford Backscattering Spectrometry in channeling configuration). In that case, it should be taken into account all the relevant considerations that will be detailed addressed in a following Chapter, which could result in an underestimation of the amorphization threshold of the electronic stopping power (S_{th}).

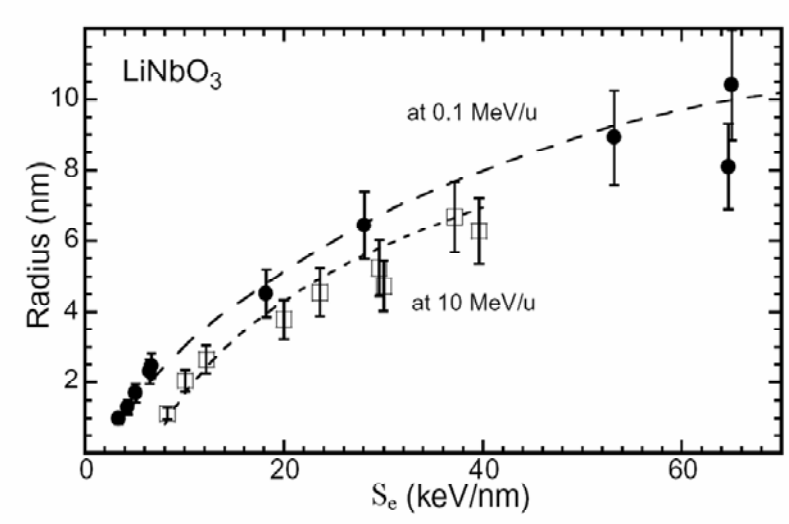

Fig. 3. The effective radius of the amorphous latent ion tracks (*R*) versus the electronic stopping power (S_e) for $LiNbO_3$. The two curves (circles and squares) correspond to the experimental points corresponding to low (energies ~ 0.1 MeV/u) and high energy (energies ~ 10 MeV/u) irradiation respectively. The plot has been obtained from [31]. The irradiations performed with beam energy at around 10 MeV/u come from [42], whereas that the irradiations with cluster beam at low velocity have been reported by [43, 73].

similar to state that, the threshold value of electronic stopping power increases with the ion energy.

Extrapolating the two plotted curves to a track radius R = 0, we will get two different values for the amorphization threshold, S_{th}. Hence, the threshold itself also depends on the ion velocity. The two curves correspond to measurements in the high velocity regime (10 MeV/u) and the low velocity regime (0.1 MeV/u). We will take an intermediate value, around S_{th} ~5 keV/nm, being the minimum value of electronic stopping power for the creation of an amorphous track. By this way, it will be considered throughout this work, always keeping in mind that it is an indicative value and it is velocity dependent.

One of the most important properties of tracks is their morphology as a function of the electronic energy loss (S_e). According to detailed studies of amorphous tracks in yttrium iron garnet ($Y_3Fe_5O_{12}$) [39], four different regions can be identified (**Fig. 4**). It is pointed out that these studies have been carried out through several experimental techniques, like high resolution transmission electron microscopy (HREM) [74] and chemical etching treatments in order to reveal the latent amorphous tracks [75]. From them, the shape of the latent tracks for different values of their radii can be described. In this sense, some important conclusions are: (1) close to the S_e threshold for damage creation, the track consists of extended spherical defects with a radius of about 1.5 nm, (2) on the other hand, if the radius of the track surpasses ~3 nm, the damage in the track becomes homogeneous, and further increases of S_e leads to a larger radius. For each ion a track appears on the surface[9] [45, 76].

[9] Each ion produces a small surface hillock of a few nanometers in height.

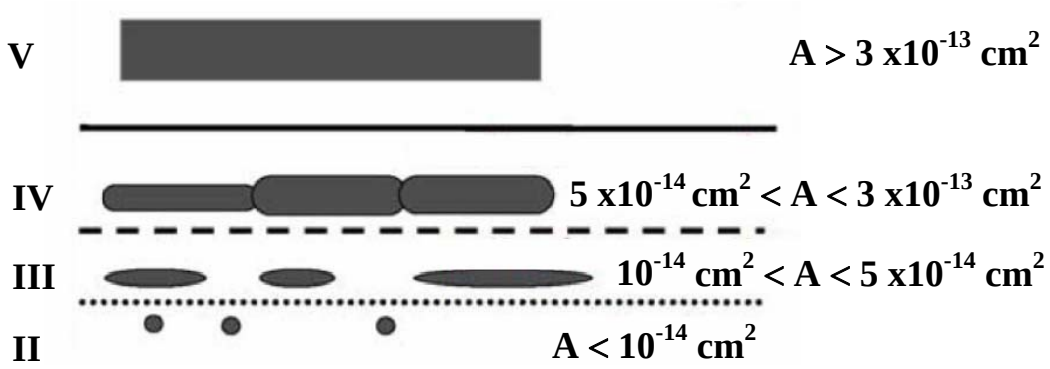

Fig. 4. Schematic of the track morphology showing the dependence on the damage cross section ($A = \pi R^2$), and thus, on the corresponding effective track radius. These results were obtained by high resolution electron microscopy (HREM) of irradiated $Y_3Fe_5O_{12}$. Figure obtained from Ref. [32, 39]. **Range II:** For $R < 0.6$ nm; $A < 10^{-14}$ cm^2, the electronic damage overcomes the nuclear damage. The extended defects are nearly spherical with a diameter of 1.5 nm. **Range III:** For $0.6 < R < 1.3$ nm; 10^{-14} cm^2 $< A <$ 5 x10^{-14} cm^2, by overlapping spherical effects, cylindrical defects of 3-nm diameter appear. **Range IV:** For $1.3 < R < 3.1$ nm; 5 x10^{-14} $< A <$ 3 x10^{-13} cm^2, the cylindrical defects overlap and the chemical etching of latent tracks begin to be efficient. **Range V:** For $R > 3.1$ nm; $A >$ 3 x10^{-13} cm^2, the defects are long cylinders of amorphous material and the damage is homogeneous inside the cylinder.

We have to remark that this S_e dependent track morphology was observed in several materials and seems to be a rather general feature [74].

1.4.3 Micro- and nanostructures formed by *ion track technology*. Applications of latent- and etched tracks.

One has to distinguish between the application of *latent*, i.e. as-implanted *ion tracks*, and *etched tracks*. Latent tracks emerge from the energy deposition of swift heavy ions inside a tiny target volume (‘*ion track core’*, ~10^{-15}-10^{-14} cm^3), and within an extremely short time (~10^{-17}- 10^{-15} s). These extraordinary transient conditions lead to dramatic modifications of the materials via chemical and structural changes, with accompanying heat and pressure pulses.

Amorphous tracks formed by electronic excitation are well aligned with beam direction and are themselves nanostructures, offering very interesting capabilities in nanotechnology [32, 77-81]. Four major strategies for latent track applications show up: (1) exploitation of the modified transport properties along ion tracks, (2) letting metallic atoms or clusters precipitate along the tracks, (3) exploitation of the material’s chemical changes, and (4) making use of ion-induced phase transitions [82, 83].

Dissolution of the latent track material by suitable chemical agents (‘etching’) leads to etched track formation; the so-called “etched tracks”, that is, generating nanopores. By careful selection of projectile, target, etchant, and etching conditions, etched tracks can be tailored towards any required shape, such as cylindrical, conical, or hyperbolic, transmittent (in thin foils) or non-transmittent, that can act as traps for foreign molecular species (sensors). On the other hand, etched tracks can be filled with other substances to form nanocomposite materials

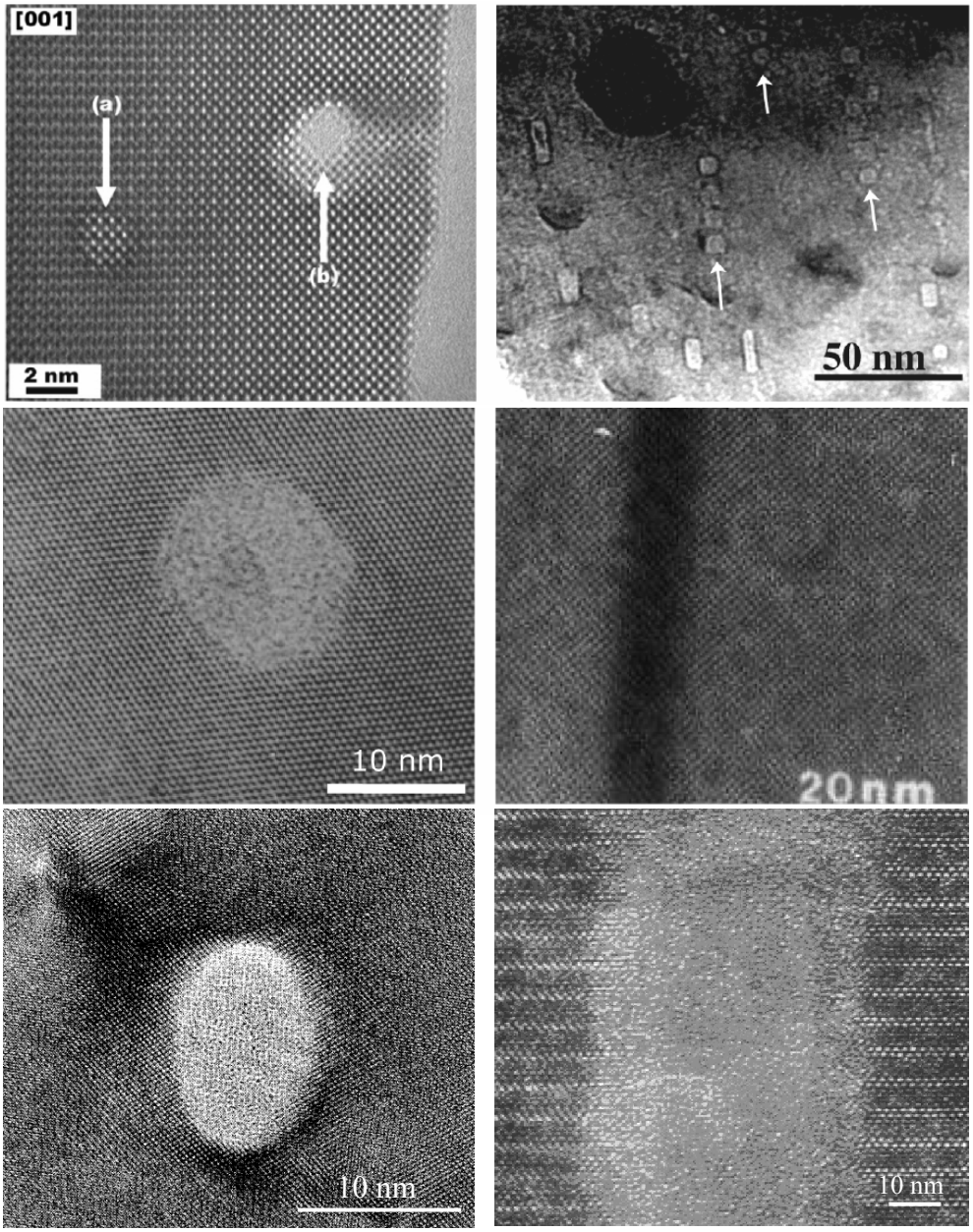

Fig. 5. High-resolution transmission electron microscopy images of ion tracks in non-amorphisable (top) and amorphisable (medium/bottom) insulators/semiconductors. Top left: Cross section of two tracks (*a* and *b*) in non-amorphisable SnO_2 irradiated with Cd ions (9 MeV/u) [84]. Top right: CaF_2 irradiated with Bi ions of 10 MeV/u. The arrows indicate the trajectories of non-continous facetted defect clusters [85]. Medium left: Cross section of a single track of a Pb ion in mica. The amorphous track zone is surrounded by the intact crystal matrix [50]. Medium right: Continuous amorphous track region created along the trajectory of a Xe ion (~24 MeV/u) in $Y_3Fe_5O_{12}$ [38]. Bottom left: Latent tracks of Dy ions (13 MeV/u) in GeS irradiated normal to the crystal surface [86]. Bottom right: Amorphous track in $Bi_2Sr_2CaCu_2O_8$ irradiated with swift Au ions [87].

with novel optical, electrical and magnetic properties; moreover, the embedded matter can be arranged as either massive wires (also called: 'fibers, fibrilles') or tubules, or it just can be dispersed discontinuously as small nanoparticles along the track length. There is a wide range of applications linked either to direct patterning of materials or to depositing material into the pores of etched ion track membranes [30, 80, 88].

1.4.4 Ion track formation process. Process of energy deposition.

The processes of track formation in the region of electronic energy loss are extremely complicated and are not yet completely understood with regard to a large number of points. The formation of ion tracks occurs as a series of processes which follow one another (see **Fig. 6**).

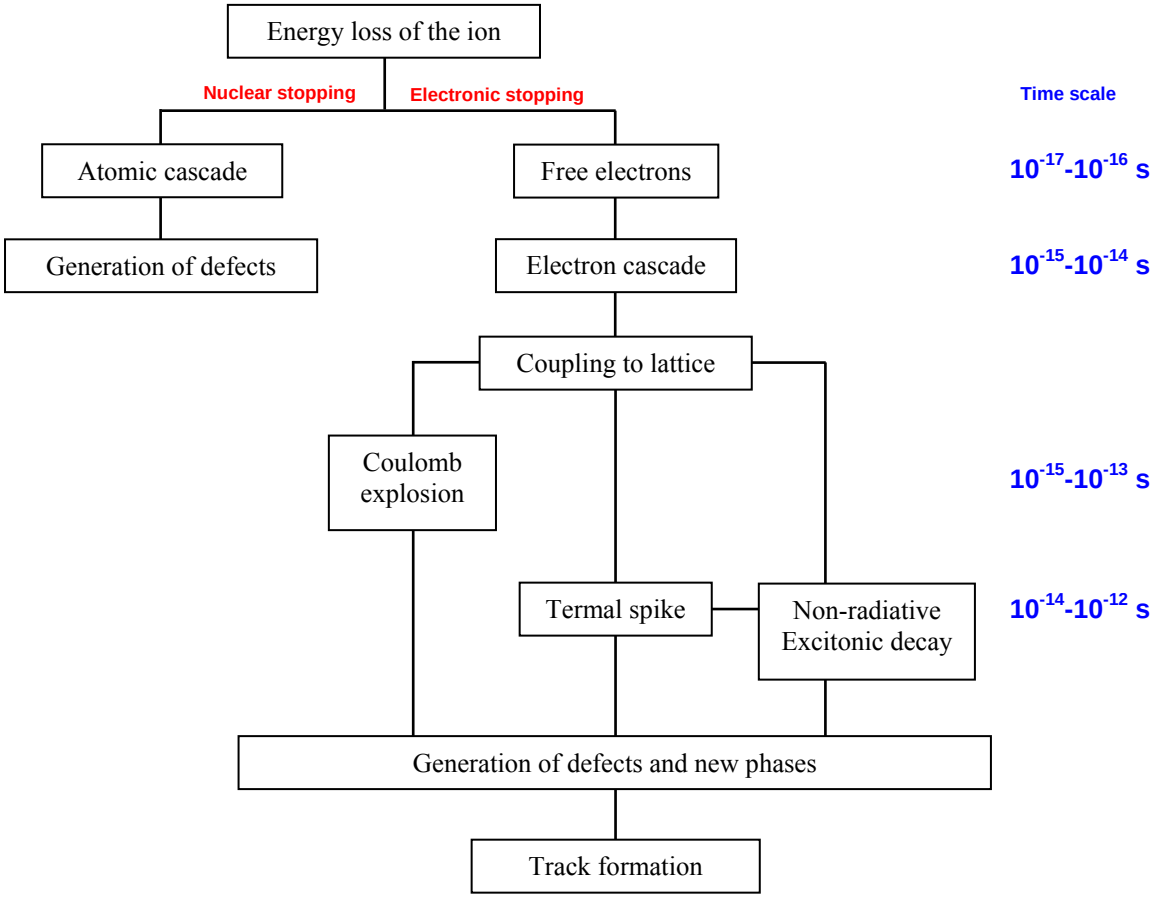

Fig. 6. Schematic of the most important processes in the formation of ion tracks, arranged according to primary and subsequent processes. The time-scale in which the processes occur is shown on the right-hand side.

Although the energy deposition of fast ions with the individual target electrons during the interaction time of around 10^{-17} to 10^{-16} s is well understood in theory, much less is known about the secondary processes which follow within 10^{-16} to 10^{-12} s. It is these secondary processes which are responsible for distributing the energy deposited by an ion throughout a cylindrical core zone with a diameter of several nanometers. Cooling and reordering processes within this zone last for around 10^{-10} s and eventually lead to the formation of permanent damage.

Fast ions create free electrons by ionization along their path. Approximately one-third of energy transferred by an ion is used for the excitation and ionization of the target atoms. The remaining two-thirds are converted to kinetic energy of the electrons, which, in turn ionize

further atoms and so initiate a cascade process. In insulators, for example, this process has a maximum range of up to one micrometer.

The energy transferred from fast ions to the electrons of the target atoms is of the order of 10^3 to 10^4 eV per lattice plane. This is an extremely high value, in comparison with the energy required to displace an atom from its position in the lattice (approximately 25 eV). The question of which subsequent processes transfer the energy deposited in the electronic system to the atomic lattice, and ultimately give rise to a zone of high defect density in the track, has not yet been completely elucidated. The most important parameters for both of the most discussed models of track formation (Coulomb explosion and Thermal spike) are the number and mobility of the free electrons, which are very different for insulators and for metals.

In order to gain deeper insight into the complex process involved in the final direct material modification, special emphasis is devoted to the short-time phenomena, from the initial ion energy loss processes to the electronic de-excitation mechanisms.

	Group I	Group II
Threshold	> 10 keV/nm	< 10 keV/nm
Which materials?	Metals (tracks need low κ); Semiconductors Si, Ge; A few insulators MgO, Al_2O_3, AlN.	Many insulators; Amorphous materials; High T_c superconductors
Class of mechanism	Need to affect a significant number of electrons involved in bonding	Self-trapping and related mechanisms
Nature of track	Fragmentary	Clear

Table II. Categories of tracks caused by swift heavy ions. This table draws a distinction between **Group I** and **Group II** behaviour.

Some interesting categories of material behaviour are summarized in **Table II** (for further details we strongly recommend Ref. [89], where, the available data for threshold stopping powers indicate two main classes of materials. The systematic differences in behaviour result from different coupling of the dense excited electrons, holes and excitons to atomic (ionic) motions, and the consequent lattice relaxation. The coupling strength of excitons and charge carriers with the lattice is crucial.

On the other hand, direct material modification needs an efficient mechanism for coupling the electronic excitations to lattice displacements. High levels of electronic excitation are the basis of a wide range of applications (see chapter 11 of Ref. [90]).

Only as a brief note about *femtosecond dynamics* (see a detailed description in Ref. [89], we can say that, a number of distinct stages can be identified, each of which has a characteristic time-scale. **Table III** summarizes the time-scales for the *relaxation stages*, which are described in more detail below.

It must be remarked that, *lattice relaxation* results from the change in interatomic interactions between atoms with highly excited electronic distributions. The structural modification under dense electronic excitation is initiated in the lattice relaxation stage. It is this stage that determines the *threshold stopping power (S_{th})*: the type of lattice relaxation depends

Relaxation stage	Time-scale
Charge redistribution	A few fs
Charge neutralization	< 0.01 ps (10 fs)
Electronic relaxation	< 0.5 ps (500 fs)
Lattice relaxation	< 1 ps
Heating	< 10 ps
Cooling	< 100 ps

Table III. Approximate time-scales for the completion of each relaxation stage. The times are representative. In metals, most of the important events occur between 0.1 and a few ps.

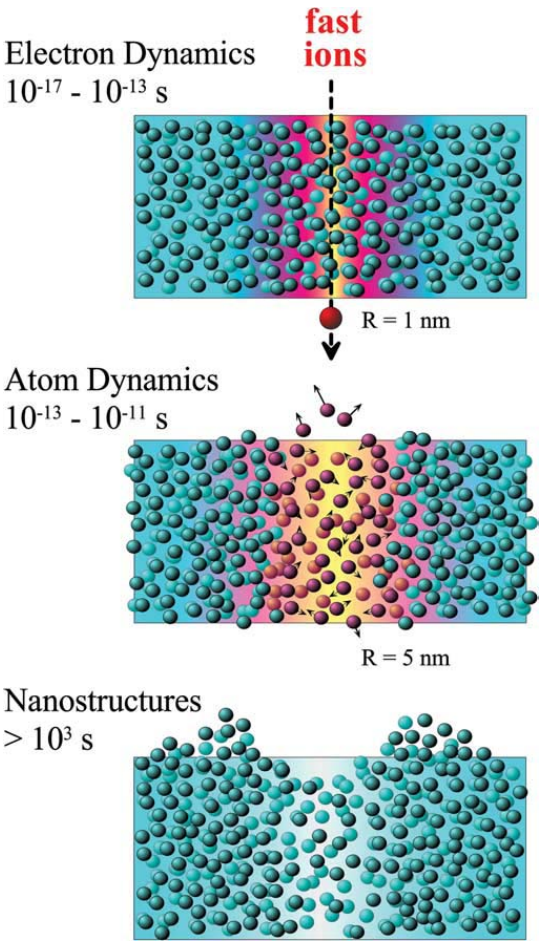

Fig. 7. Time evolution of an ion track. The initial excitation and ionization of atoms induces atomic motions, which freeze out and may lead to permanent rearrangements. In the bulk this may lead to structural or chemical modifications. At the surface craters or blisters on an atomic scale can be produced (from Ref. [91]).

on materials depending on whether excitons are self-trapped, or whether there is some other factor leading to energy localization, like an amorphous structure or pre-existing defects.

1.5 Basic models of track formation by swift heavy ions.

Since the beginning of 1950s several theoretical models have been proposed to explain the nanoscale modifications along the ion latent tracks induced in matter by the slowing down process of incident ions in the electronic stopping power regime, that is, due to the extremely dense induced electronic excitation.

In the following lines we will describe briefly those models, which have been developed in order to explain how the deposition of energy takes place and the modification of the material is produced.

1.5.1 Coulomb explosion model.

In this model, proposed by Fleischer et al. [23], it is assumed that the energetic incident ion creates along its path a cylindrical region of highly ionized matter. The highly repulsive electrostatic forces that act during the period before electrical neutrality is restored, giving rise to a violent explosion within 10^{-15} to 10^{-13} s. This phenomenon leads to the creation of an important disruption of a local region of the lattice. Energetic electrons are excited away from the track core very rapidly. This leads to charge separation and to high electric fields, which last a short time until electrical neutrality is recovered. Ion motion under these electric fields is one conceivable source of tracks.

The energy transfer for the insulating materials (~10 eV [92]) is the same order of magnitude as the threshold energy to produce atomic displacement, so that the process results in the creation of defects. However, in metals, due to rapid and strong screening of the disturbance by the conduction electrons, the energy transferred is estimated to be one or two orders of magnitude smaller [58]. In spite of it, we have to keep in mind that the concept of threshold of ionization energy refers to binary processes, and probably it is not relevant in the case under study, where the energy is transferred simultaneously to a large number of atoms along the ion path inside the target material.

It has been proposed a possible efficient mechanism for the conversion of the radial energy in lattice defects through low-frequency phonons [93]. The parameter that governs the defects creation is [92]:

$$\eta = \frac{Z_1^* v_0}{v} \qquad \textbf{(15)}$$

where the velocity effect has been taken into account, being Z_1^* is the effective charge of the projectile (**Eq. 7**) and v, v_0 is the ion and Bohr velocity, respectively. The model predicts that the damage cross-section through the electronic excitations should be proportional to η^8, this is, S_e^4. This behaviour has been observed experimentally for titanium and iron irradiated with swift heavy ions [94]. However, this dependence is not verified for the damage cross-sections for insulators irradiated at the low velocity regime ($\beta = v/c < 0.03$).

It is worthy to notice that some authors [28, 31] emphasize the fact that the time-scale in which the phenomenon of Coulomb explosion happens (10^{-15}-10^{-13} s) is shorter than the Thermal Spike (10^{-12} s), thus, we may assume that all the defects created by the former process will be annealed by the second one.

1.5.2 Inelastic Thermal Spike Model (i-TS).

This first theoretical model was proposed by Desauer in 1923 [95] and has since been expanded, modified and improved until today (e.g. when the Inelastic Thermal Spike (i-TS) model was presented [26, 27]). This model is based on considering that the amorphous tracks are created through the melting of the material and subsequent rapid cooling.

The i-TS model describes quantitatively the threshold of damage creation and the track size in insulators, taking into account the incident ion velocity [26, 31, 75]. It tries to establish a link between the initial energy deposition on the electrons and the resulting damage creation in the lattice. In this model, it is assumed that the induced track size results from a cylinder zone which contains sufficient energy E_m for melting (defined by the energy to reach the melting temperature plus the latent heat of fusion [26, 31]).

The i-TS model includes the electrons and the lattice of the target as two independent but coupled subsystems. The energy deposited by the projectiles serves as a heat source term and quickly spreads in the electron subsystem. The subsequent energy exchange from the hot electrons to the cold lattice is governed by the coupling constant g and by the temperature difference between the two subsystems.

According to the model, in the first stage, the deposition of the kinetic energy of the ions into the material is given to the electrons of the target atoms. The generation of tracks is a consequence of a strong collective electronic excitation followed by efficient energy transfer to the ionic lattice, and is based on thermally induced defects and subsequent rapid quenching, i.e. a phase transformation in a cylinder of some nanometers diameter. The basic idea of the inelastic thermal spike (i-TS) model is to treat the electrons and atomic nuclei of the lattice separately. The energy lost by the slowing down of a heavy ion when passing through the material excites the electrons of the target atoms *(δ-electrons*) in a time-scale of order of 10^{-16} s. Then, the thermalization happens by interaction with other electrons (electronic subsystem), in a characteristic timescale of the order of 10^{-15} s, and finally, they transfer their energy to lattice atoms (ionic subsystem) through electron-phonon coupling, reaching an equilibrium stage in the characteristic time of the vibrations of the lattice, typically about 10^{-12} s. In other words, the energy lost by the heavy ion, first is shared between electrons by the electron-electron interaction, and, then, is transferred to lattice atoms by electron-phonon coupling.

The generated vibrations due to the high energy density can be interpreted as a quasi-equilibrium with highly elevated temperature, which is assumed to be of Gaussian shape [96], reaching some 10^3 to 10^4 K - enough to melt a small portion of the lattice. The formation of a high-temperature cylinder along the incident ion path is assumed, the temperature of which could be higher than the melting and the vaporization temperatures. Due to the small volume of the cylinder, the cooling rate may reach $\sim 10^{14}$ Ks^{-1} so the molten matter cools down within $\sim 10^{-11}$ s and changes back to solid state, thus, leaving an amorphous track behind. In the framework of this model, the latent track is assumed to result from the rapid quenching of the entire cylinder of the molten matter, i. e., the nanotrack radius is defined by the cylinder along the ion track, which exceeds the melting temperature of the solid. Chronologically, the Ionic Spike (10^{-15} to 10^{-13} s) comes into play before the Thermal Spike (10^{-12} s) and one wonder whether or not the temperature rise anneals all the initial atomic displacements induced by the first process.

Mathematical description

The energy evolution process in the electron and lattice subsystems is mathematically described by two coupled differential equations [26, 27, 31, 32] governing the energy diffusion on the electron subsystem (**Eq. 16.a**) and lattice subsystem, respectively (**Eq. 16.b**). Since the trajectory of the projectiles can be regarded as straight, the equations are expressed in cylinder geometry with *t* being the time and *r* the radial distance from the ion path. A time-dependent thermal transient process is expressed:

$$C_e(T_e)\frac{\partial T_e}{\partial t} = \frac{1}{r}\frac{\partial}{\partial r}\left[rK_e(T_e)\frac{\partial T_e}{\partial r}\right] - g(T_e - T_a) + A(r,t) \qquad \textbf{(16.a)}$$

$$C_a(T_a)\frac{\partial T_a}{\partial t} = \frac{1}{r}\frac{\partial}{\partial r}\left[rK_a(T_a)\frac{\partial T_a}{\partial r}\right] + g(T_e - T_a) \qquad \textbf{(16.b)}$$

where $T_{(e,a)}$, $C_{(e,a)}$ and $K_{(e,a)}$ are the temperature, the specific heat and the thermal conductivity for the electronic ($_e$) and lattice ($_a$) subsystem, respectively. The energy exchange between the electronic and lattice subsystems is governed by the term: $g(T_e\text{-}T_a)$, being *g* the electron–phonon coupling constant [26-28, 40]. *A(r, t)* is the energy density per unit time supplied by the incident ions to the electronic subsystem at radius *r* and time *t* [8, 9].

$$A(r,t) = b \cdot S_e \cdot \exp\left(\frac{-(t-t_0)^2}{2s^2}\right) \cdot F(r) \qquad \textbf{(17)}$$

where *F(r)* is initial spatial energy distribution deposited into the electronic subsystem, which shape is given by the distribution of Waligorski et al. [9] and depends on the beam energy; *b* is a constant of normalization, $t_0 = \lambda / \vec{v}_e^*$ the corresponding time to the excited electron free mean path, lying in the order of ~ 10^{-15} s, and *s* the mean width of the Gaussian distribution, which can be assumed to be equal to t_0 [28], and *r* is the radial distance to the ion trajectory. *A (r,t)* is normalized to ensure that the integration in space and time is equal to the total energy loss S_e [27].

$$\int_{t=0}^{\infty}\int_{r=0}^{r=r_m} A(r,t)2\pi r dr dt = S_e \qquad \textbf{(18)}$$

where r_m is the maximum projected range for electrons perpendicularly to the ion path. The radiative recombination of electron–hole pairs is neglected.

As there is an important velocity effect in the damage creation [39], this model develops a complete numerical solution of the two equations [28], instead of partially [25] or totally analytical ones [97], in order to introduce directly the energy distribution on the electronic subsystem.

The thermodynamic parameters of the lattice used are those measured under equilibrium conditions, which are known and are extracted from the literature [98]. However, for the electronic subsystem is not as obvious, due to in an insulator there are not free electrons, which in principle they are unknown. In spite of this, the following drastic approximations are made, considering as valid the assumptions suggested by Baranov et al. [99]; they consist in assuming

that the excited electrons after the ion pass, which are in the conduction band, behave like free electrons in a metal. Consequently, there will be valid the resulting expressions for the electronic thermodynamic constants that come from the free electron gas Model [27], i.e., hot electrons in the conduction band of an insulator will behave like hot electrons in a metal, leading to an electronic diffusivity of $D_e \sim 2$ cm^2 s^{-1} and $C_e \sim 1$ J cm^{-3} K^{-1} [100]. The electronic thermal conductivity K_e is deduced from the product of the thermal diffusivity and the specific heat ($K_e = D_e C_e$).

$$C_e = \frac{3}{2} N_e k_B \approx 1 \text{ J cm}^{-3} \text{ K}^{-1} \quad \textbf{(19)}$$

$$K_e = C_e \cdot D_e = C_e \frac{1}{3} v_f l \approx 2 \text{ J cm}^{-1} \text{ s}^{-1} \text{ K}^{-1} \quad \textbf{(20)}$$

where k_B is Boltzmann´s constant; $N_e \sim 5$ x 10^{22} cm^{-3}, the density of excited electrons; $v_f \approx 10^8$ cm s^{-1}, the Fermi velocity; and l, the mean free path on electron-electron interaction.

The electron-phonon coupling constant g is unknown in the case of insulators. In any case, it is linked to the electron-phonon interaction mean time τ_a by the relation $\tau_a = C_e / g$, and to electron mean diffusion length λ of the deposited energy by the relation: $\lambda^2 = D_e \tau_a$ [26, 28].

$$\lambda^2 = D_e \cdot \tau_a = \frac{D_e \cdot C_e}{g} = \frac{K_e}{g} \approx \frac{2}{g} \quad \textbf{(21)}$$

As g is unknown, it is assumed that it is independent of the temperature and λ will be the only free parameter to fit in the model[10].

Studies in several oxides [31] have demonstrated the relationship between the parameter λ and the inverse of the energy band gap [26] ($E_g \approx 4$ eV for $LiNbO_3$). This behaviour is reasonable if we consider that the excited electrons transfer their energy to the valence electrons promoting them to the conduction band.

The thermodynamic parameters are described in [26] for insulators and in [26, 28] for metals. The main difference for these two material classes concerns the energy exchange between the electronic and atomic subsystems governed by $g(T_e - T_a)$. The energy deposited on the electrons is followed assuming the known thermal conductivity. Via the specific heat, the difference in temperature between the electron and lattice subsystems [T_e $(r, t) - T_a$ $(r, t-dt)$] multiplied by (g x dt) gives the part of the energy transferred to the atomic subsystem during dt. Subsequently, the energy is dissipated on the lattice subsystem, providing the energy per atom $E_a(r, t)$ and lattice temperature $T_a(r, t)$. In particular, in metals energy can be transferred from the hot lattice back to the electrons when $T_a > T_e$, while it is assumed to be inhibited in the case of insulators.

It is worthy to notice that, due to all terms in **Eq. 16.b** are temperature dependent, and there is a phase change from solid to liquid state in the material, this equation can be solved only numerically. However, the **Eq. 16.a** we can solve analytically, since we are considering the average values of the thermodynamic quantities ((**19**) (**20**) and (**21**)) over a wide range of

[10] A numerical version of this inelastic thermal spike code for insulators is now available under windows environment [29].

electron temperatures. This approach is valid for the interaction time between electron-electron, which is at least one order of magnitude less than the interaction time between the electron-phonon [25].

The solution of **Eq. 16.a** and **16.b** [27] gives us the temperature profile around the point crossed by the ion. As mentioned above, due to the small volume in which energy is deposited, the cooling rate can reach 10^{14} Ks^{-1}, so that the molten material cools down so quickly that starts to solidify at 10^{-11} s, and this causes, as the model, the amorphization of the material. Assuming that tracks in amorphizable insulators result from quenching of a molten phase, we can define the track radius as a cylinder, whose axis coincides with the ion path, and where the maximum temperature reached by the lattice is equal to, or greater than, the melting temperature of the material. Therefore, from the temperature profile is immediate to obtain the track radius. The evolution of the lattice temperature $T_a(t, r)$ around the projectile trajectory is deduced as a function of time (t) and space (r). The boundary conditions are fulfilled since the electronic energy deposition can be considered as constant along the ion trajectory.

Comments and concerns.

It is worthy to notice that, this last point turns into a weakness of the model since, in reality, the boundary between the amorphous region and the crystal is not abrupt, but it will create a damaged intermediate zone, but it will not have the same features of the amorphous material. There is experimental evidence - i. e. by electron microscopy [86], about the existence of this region, known as "*defective halo*" of the track, as well as the results which will be presented in this Thesis work.

Another problem is that the model assumes that when we are below the threshold of the electronic stopping power (S_{th}), from which the melting of the material happens, any damage is produced, although many experiments have shown that this is not true [86, 101, 102]. Furthermore, concretely in $LiNbO_3$ has been shown experimentally, as it has been investigated within our research group [103], the *cumulative nature of damage*, i. e., that defects created by irradiation below the amorphization threshold are added, thus, reaching by this way the total amorphization. A modified version of the Thermal Spike Model, which takes into account such behaviours, has recently been proposed [104, 105], and will be briefly described in a following Section (see **Section 1.5.4**).

Other concern is related to the definition of the temperature of the electronic subsystem in a situation clearly out of equilibrium (excited electrons), afterwards the pass of the ion, and when even they are not thermalized with the lattice, which occurs only after 10^{-12} s. However, some advocates of the model, state that the concept of temperature must not be understood faithfully, neither such as a measure of the deposited energy.

Respect to the velocity effect, described in a previous Section, it has been taken into account in the distribution of Waligorski [9] ($F(r)$ in **Eq. 17**)), which describes the distribution of initial energy deposited by the ion in the electronic subsystem, where appears explicitly the ion velocity. Therefore, the model does take into consideration this effect.

1.5.3 Thermal Spike by Szenes. The Analytical approach.

Another variant of the thermal spike model is developed by G. Szenes [96, 106-108]. The main assumption of the model is that there is a Gaussian temperature distribution in the ion induced spike (when the temperature of the lattice is maximum, approximately 10^{-12} s after the passage of the ion), which is characterized by its initial width *a(0)* and the efficiency *g* (gS_e is the fraction of the deposited energy transferred to the thermal spike, which contributes to the increase of the lattice temperature)[11].

The basic assumption of all thermal spike models is that around the trajectory of the high-energy ion a high-temperature region is formed in the material. In the following treatment, all temperatures refer only to the phonon system. It is assumed that when the temperature exceeds the melting point of the crystal a melt is formed. Due to its small diameter and the rapid cooling rate of the melt results in an amorphous structure when the melts solidifies.

Due to the electron-phonon interaction, the peak temperature of the spike T_p first grows up to its maximum value within a very short time (< 10^{-12} s) and then it decreases and the spike broadens as a result of heat conduction. We shall measure the time *t* from that moment when T_p is the maximum in the phonon system. Let us denote by T_{tg}, and *T(r, t)* the target temperature and the local temperature at a distance *r* from the ion trajectory. If *ΔT(r, t)* is the temperature increase in the thermal spike then $T(r, t) = \Delta T(r, t) + T_{tg}$. One of the main assumptions of this model is that the temperature increase along the ion trajectory *ΔT(r, t)* can be approximated by a Gaussian distribution:

$$\Delta T(r, t) = \frac{Q}{\pi a^2(T,t)} \exp\{- r^2 / a^2 (T, t)\} \qquad \textbf{(22)}$$

where $a^2(T, t)$ depends on thermal diffusivity and it is a parameter such that $a(T, 0) = a(0) =$ constant independent of *T* (initial width of the temperature distribution). It is essential for the model that at $t = 0$, **Eq. 22** simplifies to a Gaussian function. The value of *Q* can be obtained from the balance of energy

$$Q = \frac{gS_e - L\rho\pi R^2}{\rho c} \qquad \textbf{(23)}$$

where gS_e is the fraction of the energy deposited in the thermal spike, $R = R(t)$ is the radius of the melted zone, *c*, ρ, and *L* are the mean specific heat, the density, and the latent heat of phase transition, respectively.

A second assumption of the model is that the volume of the amorphous phase formed along the ion trajectory is proportional to the maximum volume of the melt. In the experiments usually the effective cylindrical radius of the amorphous tracks R_e is measured.

The model provides analytical relations between the effective track radius R_e and the electronic stopping power of the bombarding ion S_e, (for further details, see Ref. [108]). Thus, both, the track radius and the electronic stopping power are related through two remarkably

[11] The approach made in the framework of this model is used in a model recently developed within our research group [104]. It will be briefly shown in the following Section.

simple equations. One of them describes the track evolution and another one represents the condition for the formulation of ion-induced melt. By this way, at low electronic stopping power there is a threshold below which no amorphization is predicted.

1.5.4 Thermal-Spike extension model. Pre-amorphization stages and cumulative character of ion beam damage below electronic threshold

This model has been developed within the research group by Prof. Fernando Agulló-López, Dr. Gastón García and Dr. José Olivares Villegas [104]. It tries to explain some relevant features of the damage done by the ions through the electronic interactions, which are not described at all in the pre-existing models discussed till now, they are: (i) the cumulative nature of the electronic damage, and (ii) the dependence with the irradiation fluence of the threshold value of electronic stopping power for the production of amorphization, behaviour widely known through experimental evidence [101, 103, 109-111], (iii) moreover, it is worthy to notice this is the first attempt of describing the structure of the ion track, defining an internal *amorphous core*, where the reached temperature is above the melting ($T_c > T_m$), surrounded by a *defective point-like halo*, which temperature is below the melting ($T_h < T_m$).

The main purpose of this model is to extend the thermal-spike model [26, 108, 112], to discuss preamorphization stages in $LiNbO_3$, i. e., the generation of preamorphized regions during ion irradiation. This problem has not been investigated till now and the authors consider that thermal-spike models provide a suitable framework to deal with these stages and the transition to a fully amorphous crystal. It is appropriate to state here that it is not essential for the model to assume a thermal equilibrium distribution of atom velocities. The key point is to assume that the distribution can be adequately characterized by an average value or an effective temperature. Previous experimental data [101, 109, 111] and particularly those described in Ref. [104] show that a homogeneous amorphous layer with a sharp boundary is generated under irradiation for fluences above a critical value. Moreover, a threshold in the electronic stopping power appears to be required to initiate amorphization. All these data suggest that the formation of the amorphous layer is caused by electronic excitation mechanisms and, therefore, related to the generation of individual latent tracks. When a critical fluence corresponding to overlapping of such tracks is achieved, the layer is formed. On the other hand, it is shown [104] that the thickness of the amorphous layer increases with fluence, i. e., the inner boundary of the layer moves into the crystal. Thus, the preamorphization concept appears necessary to account for all these relevant results.

Theoretical model

The proposed model is based on the thermal-spike approach by Szenes [106, 108, 112]. It has the advantage of not requiring a detailed formulation of the electron and ion dynamics after irradiation accounting for the heat transport processes. Moreover, it can be easily extended to take into account preamorphization stages. The model is summarized here. It is only necessary to assume that the ion transfers an energy S_e per unit length to the electron system, and this energy is then transferred to the ionic lattice with a certain efficiency factor $g < 1$ independent of S_e. The transferred energy generates a certain temperature distribution $\Delta T =$

$\Delta T(r, t, S_e)$. At $t = 0$, when the excited electrons in the wake of the ion have given their energy to the lattice atoms, it is assumed a Gaussian distribution of the temperature:

$$\Delta T(r, 0, S_e) = \frac{Q}{2\pi a_0^2 \rho C} \exp\{- r^2 / 2 a_0^2\}, \quad \textbf{(24)}$$

where a_0 is the width of the initial Gaussian distribution, ρ the crystal density, and C the specific heat. $\Delta T = T - T_s$, T_s being the substrate temperature and $Q = gS_e$ the energy per unit length transferred to the ionic lattice. Thus, the evolution of the temperature profile $\Delta T = \Delta T(r, t, S_e)$, can be obtained for $t > 0$. The maximum temperature obtained for any $t > 0$ at a given distance r from the impact point is then[12] [108, 112]:

$$\Delta T_{max}(r, S_e) = \frac{gS_e}{2\pi a_0^2 \rho C} \exp\{- r^2 / 2 a_0^2\}, \qquad 0 < r < \sqrt{2}\, a_0, \quad \textbf{(25.a)}$$

$$\Delta T_{max}(r, S_e) = \frac{gS_e}{\pi e \rho C} \frac{1}{r^2}, \qquad r > \sqrt{2}\, a_0, \quad \textbf{(25.b)}$$

In particular, taking $\Delta T_{max} = \Delta T_m = T_m - T_s$, T_m being the melting temperature of the crystal, the critical required stopping power S_m is obtained through

$$\Delta T_m = \frac{gS_m}{2\pi a_0^2 \rho C}, \quad \textbf{(26)}$$

One can then calculate the radius of the region that has reached a temperature $T_{max} > T_m$, that is, defining the *core of the track*. The core radius R_c is thus

$$R_c^2 = r^2(T_m) = 2a_0^2 \log\frac{S_e}{S_m}, \qquad 0 \le R_c^2 \le 2a_0^2, \quad \textbf{(27.a)}$$

$$R_c^2 = r^2(T_m) = \frac{2a_0^2}{e} \log\frac{S_e}{S_m}, \qquad R_c^2 \ge 2a_0^2, \quad \textbf{(27.b)}$$

At any depth z the radius of the core is determined by the electronic stopping power curve $S_e(z)$. The track radius is then defined as the radius of a cylinder, whose axis coincides with the path of the ion, and where the maximum temperature reached by the lattice is equal to or greater than the melting temperature of the material. Therefore, from the temperature profile is immediate to obtain the radius of the track, corresponding to the radius of amorphization, R_c, described by **Eqs. 27.a** and **27.b**.

The key proposal of the model is that the defect structure of the region at and around the track is determined from the maximum temperature reached after the passage of the ion. The quenching rate is assumed to be fast enough to freeze the thermally generated defect concentration. In fact, although the melting point is not reached the concentration of intrinsic defects causing lattice disorder in the crystal may become very high and generate the *preamorphized region*. Moreover, the accumulation of these defects can turn into the total

[12] Notice that the maximum of those temperatures is attained at $r = 0$. $\Delta T_{max}(0, S_e) = \frac{gS_e}{2\pi a_0^2 \rho C}$

amorphization of the material, even when we are below the amorphization threshold for the electronic stopping power, S_{th}, which is defined mathematically as the value that causes a track radius equals to zero.

The model assumes that the concentration of intrinsic defects generated by the swift ion and responsible for the structural damage is given [17] by some effective Arrhenius law,

$$c(T)=A \exp\{-\varepsilon / kT\} , \quad \textbf{(28)}$$

This Arrhenius dependence is well established for the defect concentration achieved in thermal equilibrium at a temperature T. Then, ε is the formation energy of the responsible defect and A a factor related to the formation entropy s of the defect, $A = exp\{s/k\}$. However, in our case where thermal equilibrium is not guaranteed[13] the dependence should still apply with a different meaning for the parameter ε. In fact, **Eq. 28** simply states the probability for fast atoms with average kinetic energy $3\ kT/2$ to overcome a certain effective energy barrier ε and cause disorder. It is worthy to notice that it is not easy to decide on the kind of defects responsible for the thermally induced disorder and eventually the melting of the crystal [17, 113], and for that reason ε should be considered as an adjustable parameter.

On the other hand, in order to determine the lattice structure around the ion trajectory one should define a certain critical defect concentration to initiate or nucleate the melted and subsequently *amorphous phase* (*core,* c_m), as well as to characterize the damaged or *preamorphized regions* (*halo,* c_h) around the core, as we can see in **Fig. 8**. In many crystals the critical melting concentration c_m, derived from a comparison to experimental data [114], is roughly around 10^{-3} (normalized to atomic concentration). As to the so-called *preamorphized region* (*halo*), one may safely consider that they should contain a defect concentration $c_h / c_m \geq 10^{-3}$, i.e., c_h over 10^{-6}, which represents some typical background concentration of defects.

Keeping in mind these suppositions, one can obtain the temperature reached at this boundary (*halo*), and, following the same procedure used by Szenes in his model, the radius of the halo R_h at a depth z (see for more details Ref. [104]).

The other novel point of this model is to explain that the threshold of the electronic stopping power (S_{th}), above the amorphization of the material appears, decreases with the fluence, reflecting the cumulative nature of the electronic damage. The approach assumes that the radiation-induced defects at the damaged (*preamorphized*) regions add to those generated by another irradiation, i.e., damage is *accumulative*. This behaviour is well established for nuclear collision damage but it is less assured for electronic excitation damage. However, one may quote evidence of damage accumulation under swift-ion irradiation [115] as well as other types of electronic excitation [116]. Anyhow, the experimental data [101, 103, 104, 109-111] clearly point out to the generation of stable damage by electronic processes and also to the accumulative nature of such damage even below threshold.

The model proposes that irradiation introduces an electronic damage even when we are substantially below the amorphization threshold, generating *preamorfized regions*, as described above. The increase in thickness of the amorphous layer on going to higher fluences evidenced in Ref. [104] is not consistent with a fluence-independent threshold and clearly suggests that the

[13] In our case, we are clearly out-of-equilibrium, because the electrons transfer their energy to the lattice in a characteristic time of 10^{-12} s, not enough time for the lattice has reached its thermal equilibrium.

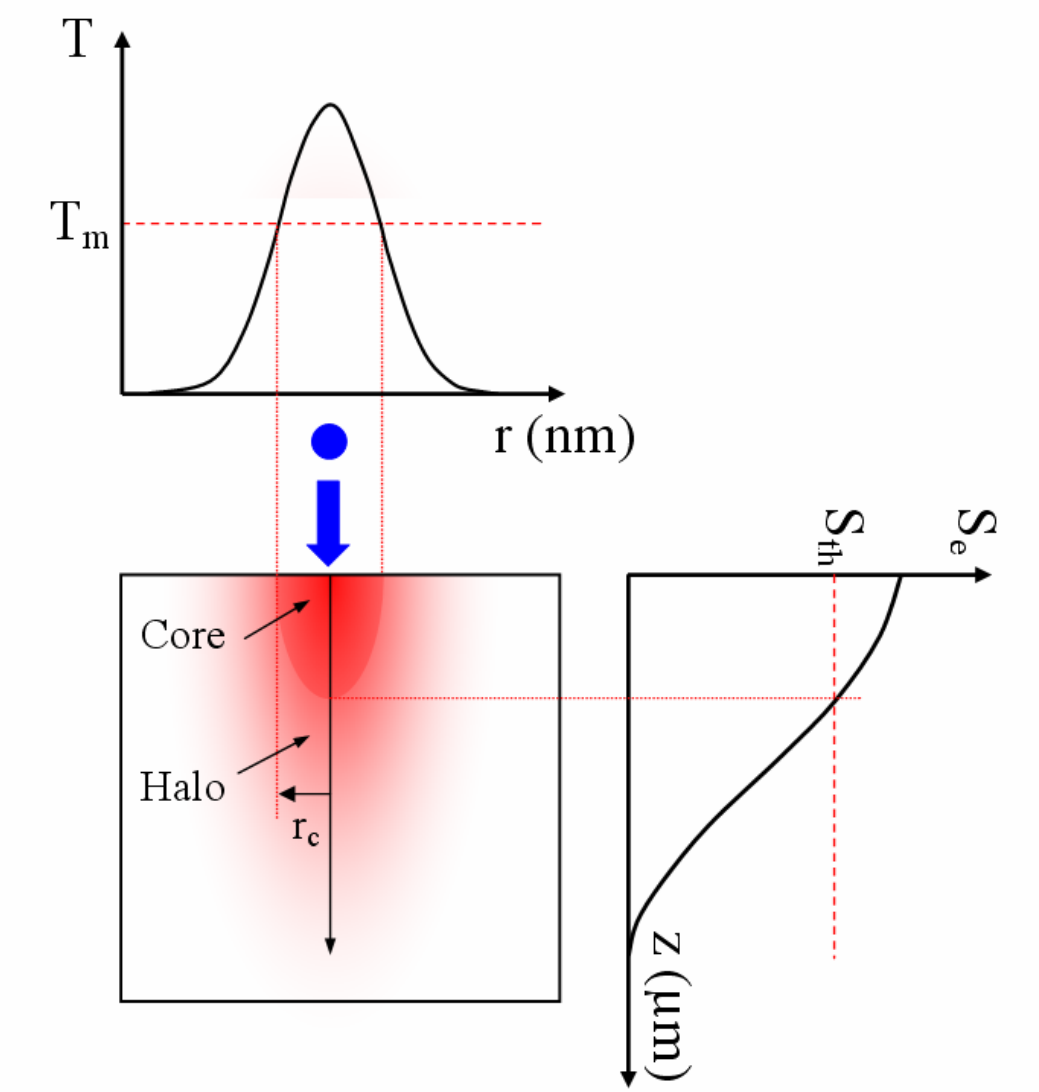

Fig. 8. Sketch of the thermal spike process. In the upper graph the radial Gaussian distribution of lattice temperature on the surface of the sample is plotted. The maximum lattice temperature is reached in the ion path. The melting temperature of the crystal is marked (T_m). In the bottom part a cross-section in depth of the crystal appears, in which the structure of the track reveals two well differenced regions: the *core* (*molten phase*, $T > T_m$) and the *defective halo* ($T < T_m$). To the right of the track profile, the electronic stopping power (S_e) curve vs the track depth is plotted. The dashed line marks the electronic threshold (S_{th}), which defines the amorphization threshold and, therefore, the effective track core.

threshold decreases with increasing fluence (*memory effect*). This effect implies a *synergy* between successive irradiations associated to either nuclear or electronic damage. The model proposes that irradiation introduces some substantial electronic damage below the threshold value for amorphization (*preamorphization stage*).

1.5.5 Monte Carlo simulation of damage and amorphization induced by swift-ion irradiation.

From the previous analysis we are able to know the effective damage threshold fluence-dependent on the surface of the sample. On the other hand, with this model it is possible to study the propagation of the boundary between amorphous and crystalline regions with the increasing fluence. In principle it is simply to translate the study from the surface to different depths in the sample, each ones corresponding to a value of S_e *(z)* obtained from simulations performed with SRIM software [2, 6]. However, there is a requirement that complicates the analysis: as the amorphous layer growths the material changes its density, being no longer known, and therefore, the electronic stopping power will change too.

In contrast, another weakness of the model is that it uses only average concentrations of defects as a function of depth in the sample, which means that does not take into account the statistical fluctuations, particularly important at low irradiation fluences. In order to solve these difficulties of the model, a Monte Carlo program has been developed [105], based on the same formulas applied to the analytical model previously described. This powerful tool allows us to calculate the number of defects created per each ion and the degree of amorphization reached for each depth, which allows us to describe the kinetics of amorphization as a function of the fluence before reaching the complete amorphization of the material. A complete explanation of the numerical recipe and the physical consequences far exceed the scope of this descriptive section, thus, a further detailed description can be found in Ref. [105]).

1.5.6 Excitonic models.

1.5.6.1 Exciton self-trapping model.

Electronic excitation is a powerful means to modify materials, since energy localization can occur by self-trapping or by some combination of trapping and self-trapping. The self-trapped exciton is an important example of a mechanism of energy localization. Such excitation and localization makes it possible for an amount of energy large enough to break bonds to be concentrated on a few atoms. Self-trapping of excitons takes place in many insulators, as reviewed by [117] and [90]. Itoh [118] (also Itoh and Stoneham [119]) suggested that exciton self-trapping is responsible for track registration in materials, notably SiO_2, which show a low threshold stopping power, smaller than 10 keV/nm. Such exciton self-trapping induces a large *lattice relaxation* and, of course, the local force constants, etc, will be altered immediately on excitation, even before self-trapping. At high exciton densities, approaching one exciton per cell, lattice order will not be maintained. At such densities, clusters of self-trapped excitons may contribute to the creation of new structures. There are no detailed calculations of the whole sequence of track formation, but one would anticipate that there are many electron-hole recombinations that do not cause modifications, especially in the early stages, and that some of the final damage processes resemble closely the behaviour at low excitation levels.

The electronic energy is imparted to the lattice during the *lattice relaxation stage*, before the *heating stage*. If self-trapping is crucial, then we expect different behaviour for systems in which self-trapping occurs and those in which it does not occur. The data are

enlightening. No self-trapping is observed in **Group I** materials, with their higher threshold stopping power. Self-trapping of excitons, or an equivalent lattice deformation upon electronic excitation, is observed in **Group II** materials.

1.5.6.2 Two-spikes model: Synergy between thermal spike and non-radiative exciton-decay mechanisms for ion damage and amorphization by electronic excitation.

The theoretical analysis of the lattice damage, and eventually amorphization, caused by heavy electronic excitation is a formidable task. The situation appears not only in ion beam irradiation but also in strong electronic and laser excitation. In this Section, we present a rather general framework for modelling the damage and amorphization induced by swift-ion irradiation. It combines concepts of the Exciton [119-121] and Thermal Spike [26, 106] models, and it includes a previous analytical approach [104]; all of them described in earlier Sections. The key physical question is how the energy stored after massive electronic excitation is transferred to the lattice and causes bond breaking and point defect formation. This Two-Spikes model has been extensively developed in Refs. [122-125]; moreover, in order to discuss within a more general perspective, taking as a reference the well-documented case of alkali halides [17, 90, 126, 127], the feasibility of the model has been successfully checked through the application to other dielectric or semiconductor materials like TiO_2 [128].

1.5.6.2.1 Main phenomenological features.

Unfortunately, at variance with the damage caused by nuclear collisions, the disorder produced in the electronic regime is poorly known and constitutes a matter of active controversy. Several theoretical models have been applied to the description of the amorphization caused by electronic excitation, such as Thermal Spike [26, 31], Coulomb explosion [129], or Molecular Dynamics (MD) calculations [130, 131]. So far, in spite of its simplicity, the Thermal Spike model has been mostly used to account for some relevant features of the amorphization process by single-ion impact. In this model the crystal does not develop any disorder (point defects) and keeps structurally unmodified unless the stopping power reaches a certain threshold value characteristic of the crystal. At this point the lattice melts and after rapid cooling becomes amorphous. The model has been able to explain in a reasonable way the dependence of the amorphous track diameter on electronic stopping power. However, this theoretical approach presents several flaws and shortcomings. Moreover, extensive experimental evidences [101, 103, 109-111] suggest that any adequate theoretical framework should take into account the following features:

a) First, the scheme is *binary* i. e., the regions of the crystal should only show two states, either fully crystalline or amorphous. On the contrary, there is extensive evidence that the crystal becomes strongly damaged even for irradiations below threshold (S_{th}) [86, 101, 102].

b) Moreover, the recent experiments performed in the high fluence regime have revealed an additional new feature of the ion-beam induced damage, namely its *cumulative character*. In other words, the damage produced by a certain fluence adds to that one generated

by a previous irradiation. In order to deal with this information the thermal spike model has been recently extended to address with the *preamorphization stage* [104, 105]. It is proposed that, below as well as above the electronic stopping threshold, one has to take into account the defects that are thermally generated. The threshold for track formation depends on the damage caused by prior fluence ϕ, so that the thickness of the amorphous layer generated by track overlapping increases with ϕ.

c) The generation rate involves an Arrhenius-type law whose exponent contains the intrinsic formation enthalpy of some suitable point defect. This dependence provides the *superlinearity* required by thresholding.

The predictions of the model are in reasonable accordance with the experiment [104, 105]. However, some difficulties of such model are connected with the need for thermal equilibrium and with the cumulative character of defect generation. Therefore, other alternative theoretical schemes should be explored. In order to explain all these features it is necessary to develop a model able to quantify the damage in terms of individual point defects.

In this Section it is briefly developed an alternative model based on the non-radiative decay of excitons that are self-trapped in the lattice. The model has been applied to $LiNbO_3$ where significant data have been gathered both in the single- and multiple-track regimes. Moreover, it allows for a comparison to the thermal spike models used so far.

The problem takes us back to the early days of photolitic (x-rays and UV) damage of ionic materials such as alkali halides [17], where it was ascertained that defects were created by non-radiative decay of localized (self-trapped) excitons. This idea was later recovered and discussed, at a qualitative level, as a reasonable mechanism to account for laser, electron, and swift-ion damage [119, 121, 132] in dielectric materials. The present work puts the model on a quantitative basis using features of the thermal spike model. The new synergic model appears quite promising and yields reasonable agreement with experiment for single impact as well as for high fluence irradiations. It may serve to promote a better understanding of electron excitation damage in dielectric materials.

The model is mostly phenomenological, although quantitative (provides the defect concentration). It takes into account the fraction of energy deposited as heat (thermal spike) as well as the fraction of energy deposited in the form of potential energy in electron-hole pairs, which in many cases readily get localized forming self-trapped excitons (exciton spike) [133] (i.e. O^- holes trapped at small electron polarons Nb^{4+}). The latter is often ignored despite it can be as high as 50% of the total energy. The model relies on the synergy between both spikes generated upon ion impact. It is proposed that the decay of these excitons may proceed either by light emission or non-radiative molecular dissociation leading to atomic disorder. A key parameter of the model is the energy barrier that separates bound and unbound regions of the excited state of the localized exciton. That is to say, the adiabatic potential energy surface (APES) for the excited state presents an energy barrier separating the bound and dissociated states. The high temperature reached at the thermal spike generated by the bombarding ion provides the necessary activation energy.

1.5.6.2.2 Some basic concepts: relationship between binding energy and gap energy.

Electronic excitation of a dielectric material implies the generation of conduction electron-valence hole pairs (excitons) that store a potential energy close to the band gap (E_g) of the material. It is often accepted that the number of excitons created by a given excitation energy W is, $N = W/I$, where I is an average ionization energy that can be roughly taken as 2 or 3 times the band gap, i. e. $I = 2\text{-}3\ E_g$. In other words, the deposited excitation energy W is split into a fraction stored as potential energy of the exciton system W_E and another fraction W_H deposited as heat, i. e. in the phonon system. These two fractions have quite different dynamics. Whereas the fraction W_H is the one considered in the dynamics of the thermal spike approach, the fraction W_E has been so far ignored. The ratio W_H/W is often defined as the heating efficiency factor g that lies typically 0.5-0.7. A first relevant consequence of this simple energetic balance is that the energy stored in the excitonic system is very significant and cannot be ignored when discussing the final fate of the excitation. In principle, one can consider three channels contributing to the decay of the exciton system, namely, radiative (photon) emission, non-radiative decay with phonon generation (additional heating) and non-radiative decay leading to permanent lattice damage (defects).

In order to evaluate the potential to convert this excitation energy to lattice defects, it is useful to relate the gap energy (E_g) to the binding energy of the material (E_b). Binding energy is, generally, defined as the energy required to separate the material in their component neutral atoms. This energy may be mostly ionic as for alkali and silver halides or mostly covalent as for many semiconductors. The two energies are comparable (in the case of alkali halides), indicating that the exciton decay may, indeed, lead to lattice damage. In other words, the energy stored in one single excitation (exciton) may be lower than the energy required to break the material.

The damage caused by electronic excitation is well known in Molecular Physics, as well as for many organic and inorganic materials. Molecular excitation by light may lead to decomposition (photodisociation). In fact, in some cases the excited state is disociative. A similar behaviour has been found in some dielectric crystals, such as alkali and lead halides and dihalides, silver halides, and so on, that decompose by light (photolysis) or ionizing radiation (radiolysis).

1.5.6.2.3 Physical bases of the exciton model. General criteria for applicability.

Alkali halides, having a wide electronic energy gap, constitute a classical and paradigmatic example of excitonic models for ionization damage and provide an adequate ground to discuss the rules that should apply to other more complex situations. After an extensive research effort it was concluded that Frenkel pairs can be generated by purely ionizing radiation (UV light, X-rays and gamma rays) through de-excitation of self-trapped (localized) excitons. The core of those excitons is constituted by a self-trapped hole at a X^- halogen site that forms a X_2^- molecule after relaxation and binding to a first-neighbour X^- ion [17, 90].

The self-trapped hole then acts as a recombination site for its electron partner through a coupled pair (exciton). Although the physics is complex, in brief, the luminescence emission of the exciton states operates in competition with the non-radiative defect-formation channel leading to the generation of a Frenkel pair. The primary efficiency for defect-formation has been measured as a function of temperature and can be explained by a peculiar structure of the potential energy curves leading to lattice recovery [126]. In other words, the efficiency is determined by an Arrhenius-type survival probability. This idea summarizes some key features of the exciton model, namely the occurrence of a non-radiative decay channel, which competes with the radiative emission. The non-radiative decay channel operates by overcoming a certain energy barrier in the relaxation profile leading to defect-formation.

On the basis of the information gathered for alkali halides one can now formulate some general rules to discuss exciton models in a more general context. Excitonic models propose that bond-breaking and point defect formation arise from the energy transferred from a single exciton (or maybe a cluster of close excitons) to the ionic lattice. In order to assure an efficient defect generation process from the non-radiative decay of the excitation energy stored at the exciton one should propose a few general criteria [127]:

(a) The excitation energy has to be well localized in a given lattice site so that the decay energy is transferred to a few atomic bonds, e.g. by forming a localized or trapped exciton. In fact, the occurrence of carrier as well as exciton self-trapping is a common feature [90, 135] in many dielectric (strongly polarizable) crystals, including halides, dihalides and binary or ternary transition metal oxides (e.g. MnO, NiO, $SrTiO_3$ and $BaTiO_3$. Electron or/and hole self-trapping is, often, a pre-requirement for exciton localization.

(b) One of the non-radiative de-excitation channels should lead to lattice reorganization, i.e., bond breaking and point defect-formation. This condition demands that the exciton energy is high enough to cause such a disorder. In other words, the energy stored in one single excitation (exciton) must be larger than the energy required to break one bond. In general, the operative channel may be thermally activated and requires the overcoming of a certain energy barrier. The energy necessary to overcome the barrier stems from the thermal spike, i.e., the energy deposited as heat.

(c) The lifetime of the bond breaking channel has to be short enough in comparison with that of other competing relaxation channels to assure the generation of point defects. This requires that the thermal energy barrier is low enough.

(d) The non-radiative de-excitation channel should represent a significant fraction of the total decay rate.

(e) The defects generated have to be separated far enough to avoid recombination and assure their survival.

1.5.6.2.4 General theoretical framework.

In the electronic losses regime (i.e. ignoring nuclear collisions), the energy deposited by the bombarding ion, proportional to S_e, is initially converted into kinetic energy of the excited electronic system, **Fig. 15**. Subsequently, this energy is transferred to the ionic lattice and eventually leads to creation of defects. For a given material one expects that the defect

concentration c should be a function of S_e and ϕ. When a critical concentration, $c = c_m$, is reached, the lattice collapses into an amorphous phase. In order to determine the function $c(\phi, S_e)$ one should take into account the main processes, **Fig. 15**, during the slowing down of electronic motion:

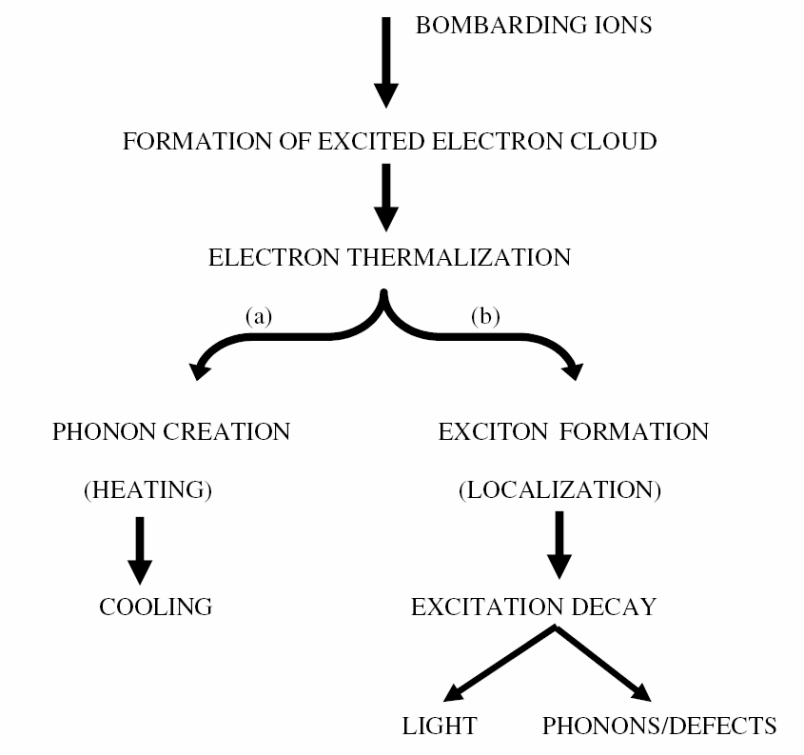

Fig. 15. Flow diagram showing the different physical channels of energy transfer following an ion impact event (from Ref. [123]).

(a) energy transfer to the crystal lattice (phonon creation),

(b) localization of the excitation energy as trapped excitons and finally,

(c) recombination of these excitons. This latter step leads to either light emission (radiative recombination), phonon creation (heating) or atomic displacement (defects). The two latter processes arise from non-radiative recombination.

Within this general scheme, one may consider two different alternative mechanisms to account for defect formation, i.e. *thermally induced generation of defects*, and *non-radiative exciton decay mechanism*.

1.5.6.2.4.1 Thermally induced generation of defects.

Disorder is generated through channel (a), i.e. by *thermal heating* and subsequent *quenching* (**Fig. 15.a**). This corresponds to a thermal spike approach (see Section 1.5.4, and Section D. Thermal-Spike extension model in Ref. [104]), where the key information is the temperature profile in the spike $T(t, r, S_e)$ that can be considered Gaussian

$$T(t, r, S_e) = T_0 \exp\{- r^2 / 2a^2(t)\} + T_s, \quad (45)$$

a being the width of the distribution and T_s the crystal temperature. The variable t stands for the time elapsed (during cooling) from the maximum temperature T_0 the spike axis. Local defect concentration is assumed to correspond to thermal equilibrium at the maximum temperature $T_m(r, S_e)$ reached at a distance r from the track axis, that can be readily calculated [104, 106]. The strong nonlinearity in the dependence $c(S_e)$ is, then, provided by the Arrhenius law that yields the local defect concentration $c(r, S_e)$ (**Eq. 40**),

$$c(r, S_e)=A \exp\{-\varepsilon / k\, T_m(r, S_e)\}\,, \tag{46}$$

ε being the thermal formation energy of the defects and A a constant. Using **Eqs. 45** and **46** we can obtain [104] the total number of defects per unit length generated (at a given depth) by a single ion impact with stopping power S_e. (**Eq. 44** in polar coordinates)

$$\bar{c}(\phi, S_e) = 2\pi\phi \int_0^\infty rc\left[T_{\max}(r, S_e)\right]dr\,, \tag{47}$$

Once the solution $c(\phi, S_e)$ has been obtained, one can readily determine the conditions for the generation of an amorphous layer. Taking into account the dependence $S_e(z)$ obtained from a SRIM program [2, 6], one may calculate the thickness of the amorphous layer as a function of fluence. The model has been described in detail in Section D. Thermal-Spike extension model and is in reasonable accordance with experimental data on Si-irradiated (7.5 MeV) $LiNbO_3$ at fluences $\leq 10^{14}$ cm^{-2} [104, 123].

1.5.6.2.4.2 Non-radiative exciton decay mechanism. Excitonic-decay model of damage: General formulation.

In this alternative scheme we assume that point defects, possibly consisting of broken or distorted, Nb-O_6 [136], are generated by non-radiative de-excitation of localized excitons (**Fig. 15.b**). The central assumption of the model is that every localized excitation at a Nb octahedron (exciton) has a reduced thermal stability in comparison to the unexcited crystal. As mentioned above, this type of process is well known in alkali halides, alkaline earth fluorides, and many oxides [135], as the mechanism responsible for generation of lattice defects under ionizing radiation (X-rays and UV light) [17] and it has been also proposed [119-121] to describe swift-ion damage. In the case of $LiNbO_3$, the information available is more scarce, although it is documented that electrons are self-trapped as polarons [17, 137] and that self-trapped excitons are very likely formed during irradiation. In fact, a blue intrinsic luminescence band at ~ 450 nm has been associated to electron-hole recombination at regular niobate groups [113, 138]. As for alkali halides it is proposed here that point defects are created via non-radiative decay of self-trapped excitons. However, there is a substantial difference between the two cases. For alkali halides, experiments mostly used low or moderate energy deposition levels and a *thresholding behaviour was not observed*. In our ion-beam experiments the occurrence of a well-defined threshold requires that in any suitable model the defect production rate should depend on the deposited energy (and so on S_e) in a *strongly superlinear way*. Therefore, in this model we are going to exploit the possible synergy between such excitonic mechanism and a thermal spike to account for the thresholding behaviour and for the main features of the damage and amorphization processes in $LiNbO_3$.

The theoretical scheme we propose is as follows: The first step in swift-ion bombardment is to generate, in about 10^{-16} s, an excited electron cloud along the ion trajectory.

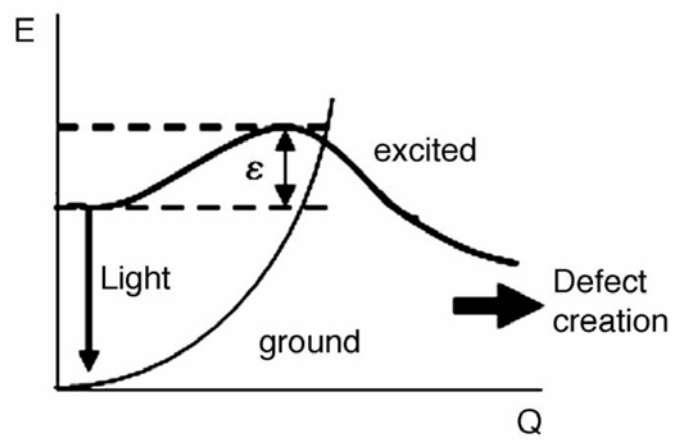

Fig. 16. Schematic level diagram for the localized exciton showing the energy *E* of the ground and excited electronic states of a self-trapped exciton as a function of a configurational coordinate *Q*. The energy barrier ε that must be overcome for non-radiative exciton decay and defect creation has been indicated (from Ref. [122]).

The number of electrons is estimated to be $N_e(z) = S_e(z)/I$, I being an effective ionization energy about 2-3 times the band-gap energy (E_g) of the material [119, 121]. These electrons initially exchange energy among themselves so that an effective electron temperature is reached, T_e (~10^{-15} s). The generated electrons very rapidly (in times well below 1 ps) transfer kinetic energy to the lattice (electron-phonon interaction processes enter into play to attain a common electron-lattice temperature, T_0), creating phonons (*thermal spike*), and generate new free electrons through atom ionization. After electron thermalization ("thermal equilibrium" stage at a time taken as $t = 0$), bound electron-hole pairs (excitons) are formed which become homogeneously localized (*self-trapped*) in the crystal lattice giving rise to an *excitation spike* that is coupled to the *thermal spike*. At this stage, mobile holes become captured at electrons self-trapped [17] as relaxed Nb^{4+} (small polarons) generate a homogeneous random distribution of self-trapped electron-hole pairs $Nb^{+4} - O^{-}$ (excitons) at some NbO_6 octahedral site [139-141]. It is assumed that the total number of excitons (electron-hole pairs) created by one single impact at a depth z is $N_X(z) = S_e(z)/I$. The final step is the exciton decay to the ground state via either light emission or non-radiative recombination, and restoring the perfect crystal structure during the rapid cooling caused by heat diffusion (~10^{-11} s). The non-radiative channel is considered to be the key process giving rise to lattice displacement in a way similar to the case of alkali halides. However, the *synergy* between the *thermal spike* and the *exciton decay* processes is essential to provide the *superlinearity* in the defect generation rate that is experimentally observed. In order to implement such a synergy one assumes for the exciton a schematic energy level diagram as illustrated in **Fig. 16**. It shows the adiabatic potential energy curves for the bound and (dissociated) excited electronic states as a function of an effective configurational coordinate (Q) for the ions. The excited level may lead to molecular dissociation and atomic displacement (Frenkel pair formation), either directly, or after overcoming a certain

potential energy barrier ε. This latter case provides a superlinear generation rate $\bar{c}(\phi, S_e)$, due to coupling between the two energy-loss channels (a) and (b). The high temperature reached in the spike provides the needed kinetic energy. Moreover, we will consider that excitons are homogeneously trapped at regular lattice sites (*homogeneous nucleation*) and all of them are equivalent for defect creation[14]. In its simpler form, the electron-hole recombination kinetics ($t > 0$) includes (a) a radiative channel (*photon emission*) corresponding to a well-documented broad band [138, 142, 143] peaked at 2.9 eV and (b) a dissociative (*non-radiative*) channel leading to point defect formation. In fact, oxygen-vacancy centers have been identified after irradiation in the electronic loss regime, either with high-energy electrons [144] or ions [145].

Using cylindrical coordinates *(r, z)* with the ion trajectory along the *z* axis, the rate equation for the decay of the local exciton concentration N_X generated by the impact, writes

$$\frac{dN_X(z,r,t)}{dt} = -N_X(z,r,t)\left\{\nu_0 \exp\left(-\frac{\varepsilon}{kT(z,r,t)}\right)+\frac{1}{\tau}\right\}, \tag{48}$$

ν_0 being a frequency factor, τ the radiative lifetime and *T (z, r, t)* stands for the evolution of the temperature profile in the spike. In spite of the scarcity of data, the competition between radiative and non-radiative processes expressed by **Eq. 48** is consistent with experimental data [113, 138] showing a thermally-activated decrease in the exciton emission band.

Some comments can be carried out respect the overall rate of exciton decay channels:

a) The non-radiative decay term in **Eq. 48** yields the defect generation rate, providing the required *strong nonlinear dependence of the damage rate on* S_e.

b) Once the spike has cooled down in times of the order of 10^{-11} s the radiative term having a longer lifetime will dominate and energy will be dissipated through light emission. Integration of that defect production rate over time and over the extension of the spike should yield the total number of defects created by the ion impact.

c) Finally, the model assumes that the irradiation triggers a lattice collapse and induces amorphization when the defect concentration reaches a critical value n_{th}. In a non-irradiated crystal the amorphization should just occur when the stopping power that determines the energy deposited in the spike equals the threshold level S_{th}. There are, indeed, well documented examples of defect-driven transitions [146].

Coming back to the rate equation (**Eq. 48**), in order to solve it, one also needs the initial condition $N_X(r, z, 0)$. It will be assumed that the shape of this exciton distribution matches the initial temperature profile and obeys the obvious relation

$$\int_0^\infty 2\pi r N_X(r,z,0)dr = N_e(z) = \frac{S_e(z)}{I}, \tag{49}$$

Possible exciton diffusion is ignored. The time-dependent temperature profile *T(r, z, t)* can be obtained from the microscopic coupled equations for the electron and phonon kinetics, as in the

[14] The model could be extended to cover the case where excitons are trapped at certain defective sites, previously existing or created by the irradiation (*heterogeneous nucleation*).

i-TS model by Toulemonde and coworkers [31]. However, ignoring the very first heating stage and starting at $t = 0$ (where the maximum spike temperature is reached), one may assume at every depth z that the temperature profile is gaussian around the trajectory [104, 107].

$$T(r, z, t) = T_s + \Delta T(0, z, t) \exp\{- r^2 / a^2(t)\}, \tag{50}$$

where T_s is the substrate temperature and

$$\Delta T(0,z,t) = \frac{a_0^2 \Delta T(0,z,0)}{a^2(t)}, \tag{51}$$

is the temperature increase caused by the ion impact. The time evolution of the profile width

$$a^2(t) = a_0^2 + \frac{4K}{\rho C} t, \tag{52}$$

is readily obtained from solving the heat conduction equation. K, C, and ρ, respectively, stand for the thermal conductivity, specific heat and mass density of the material. On the other hand, the initial temperature rise $\Delta T(0, z, 0)$ at the spike axis is related to the electronic stopping power $S_e(z)$ by [106]

$$\Delta T(0,z,0) = \Delta T_0(z) = \frac{g S_e(z)}{\pi a_0^2 \rho C}, \tag{53}$$

where g is an electron-phonon coupling parameter that measures the efficiency of energy transfer from the electronic system to the lattice. Thus, we need the fraction of the deposited energy invested in heat, $Q(z) = gS_e(z)$ $(g < 1)$, S_e being the electronic stopping power. Up to now [106, 107], the value of g was determined by the condition that at threshold, $S_e = S_{th}$, the reached peak temperature causes *melting* of the crystal (*thermal spike model*). In our present analysis, g is derived from the overall energetic balance:

$$S_e = E_p + Q = N_X E_g + Q = \frac{S_e E_g}{I} + g S_e \ , \tag{54}$$

where $E_p = N_X E_g$ is the *potential energy* stored in the exciton system.

Therefore,

$$g = 1 - \frac{E_g}{I}, \tag{55}$$

and thus,

$$\Delta T(0,z,0) = \Delta T_0(z) = T_0 - T_s = g \frac{S_e(z)}{\pi a_0^2 \rho C} = \left(1 - \frac{E_g}{I}\right) \frac{S_e(z)}{\pi a_0^2 \rho C}, \tag{56}$$

Assuming $I = 2.5\ E_g$, (I = 10 eV for $LiNbO_3$), we get $g = 0.6$, as previously used [107].

Next step will be to focus our attention on the defect-generation (non-radiative) channel of **Eq. 48**; one can write the rate of defect-generation as

$$\frac{dn}{dt} = N_X(r,z,t)\nu_0 \exp\left(-\frac{\varepsilon}{kT(r,z,t)}\right), \tag{57}$$

After time integration one obtains the concentration profile of point defects generated by every impact around the ion track, i.e. the overall radial distribution of the density of defects,

$$n(r,z) = \int_0^\infty dt\,\nu_0 N_X(r,z,t)\exp\left(-\frac{\varepsilon}{kT(r,z,t)}\right) \tag{58}$$

where $N_X(r, z, t)$ has to be obtained from a full solution of **Eq. 48** including the two decay terms. One important feature of the model is that **Eq. 58** predicts a strongly superlinear dependence of $n(r, z)$ on stopping power but without any definite threshold.

Once we have the expression to calculate de defect concentration profile the model goes a step further. It assumes that when that concentration overcomes a certain threshold value, $n \geq n_{th}$, the crystal lattice collapses and becomes amorphous (*defect driven transition* [146]); i.e., a defect-driven phase-transformation into an amorphous phase is triggered. In this case, the defect concentration reaches $n = N_{Nb}$, where N_{Nb} is the molecular (octahedral or Nb) density of the crystal ($N_{Nb} = 18.9$ *molec.* nm^{-3}). Consequently, the region of the track that fulfills that condition corresponds to the so-called *amorphous track core*. Outside that region the track contains an insufficient defect concentration to induce amorphization (*track halo*). The threshold concentration condition, $n = n_{th}$, should be the one generated when the stopping power reaches S_{th}, required to reach amorphization (*thresholding*). It is worthy to notice that, the model does not invoke melting as a necessary process for amorphization (as it is assumed in the *thermal spike model*), but here the condition is more general.

When the crystal is irradiated with a fluence ϕ (impact density), one has a random distribution of defect profiles, see **Eq. 58**. In order to analytically calculate the average defect concentration per unit volume, $N(z)$, we consider a high-enough fluence to guarantee track overlapping ($\phi > 10^{13}$ cm^{-2}),

$$N(z) = \phi \cdot n_L(z) = \int_0^\infty 2\pi r n(r,z)dr \tag{59}$$

being $n_L(z)$ the average linear defect concentration per impact at a depth z.

Chapter 2

Lithium Niobate. Summary of main physical properties and crystal structure.

2.1 Historical overview.

2.2 Crystal structure and properties.

2.3 Phases diagram and composition.

2.4 Lithium niobate growth techniques.

2.5 Defects in Lithium niobate.

2.6 Lithium niobate optical properties.

2.7 Lithium niobate electric properties.

This Chapter will summarize the main properties of the material used throughout the research work presented in this PhD dissertation: Lithium Niobate. This crystal has been widely studied [98] since it was first synthesized by B. T. Matthias and J. P. Remeika [147] in 1949. Nowadays there is an intense research effort centred in this important electro-optical material all over the world in order to use this crystal in the field of nonlinear optics for the fabrication of integrated optical devices because it possesses large electro-optical, piezoelectric and nonlinear optical coefficients; moreover, its use in other applications is performed, mainly in photonics. This interest is mainly due to its excellent and interesting optical properties, which makes $LiNbO_3$ suitable for a great variety of applications, such as such as optical waveguides [103, 136, 148-153], frequency doublers [154], miniature integrated electro-optics and all-optical devices [155, 156], polarization controllers, lasers, and very recently also photonic crystals. Benefiting from its good electro-optical, accusto-optical and nonlinear properties these devices can show remarkable properties such as nonlinear frequency conversion, ultrafast all-optical signal processing and single photon generation. Moreover, it also finds a great variety of uses in other fields, for instance, $LiNbO_3$ is used for electro-optical [157] and light modulating devices [158], commutators, multiplexers, filters [159] and holographic storage devices [160]. It has applications in the field of superficial acoustic waves (SAW) [161, 162], serving as filters in communication technology [163, 164] and is used as a substrate for Ti:Er:$LiNbO_3$ lasers [165], to name only a few[15].

On the other hand and from a fundamental point of view, it is worthy to notice that due to complexity an existing controversy on the explanation of the mechanisms of damage production (bond breaking and defect generation) by electronic excitation during swift-ion irradiation, it should be extremely necessary the election of a well-known properties material as substrate for the experiments. In addition, the Group within this research work is carried out, has a wide knowledge and great expertise on the different optical and structural characterization techniques for this material. All of these ingredients seem to point $LiNbO_3$ like an excellent candidate to perform the actual investigation. However, respect to this point, we have to remark that the fundamental research carried out by the Group is being extended to another materials from a double perspective, on one hand, with the aim of proving the general applicability and validity of the theoretical model developed for $LiNbO_3$ (the Excitonic Model), in rutile (TiO_2) [128], amorphous-silica (*a*-SiO_2) and quartz (*c*-SiO_2); and, on the another one, having in mind the use of the modified optical properties of the irradiated material by ion beams ($LiNbO_3$ [102, 103, 109, 167],(*a*-SiO_2) [168], $KGd(WO_4)_2$ [169, 170], quartz and $BaMgF_4$).

Finally, we can combine both topics, the very attractive piezoelectric and optical properties of Lithium niobate and that, ion irradiation modifies its physical and chemical properties (such as the refractive index, the etching behaviour, the chemical stability and the density due to radiation damage generating defects), which can be caused by both nuclear and electronic energy loss of the impinging ions [111, 171-182]. From them, it has been recently possible to develop in our Group, a new and successfully route for the fabrication of optical waveguides by swift ion irradiation [102, 103, 109, 167]. This method has been widely tested for $LiNbO_3$ demonstrating not only the feasibility but also a number of advantages such as substantially reduced ion fluences, which are several orders of magnitude lower than the standard method based on nuclear damage with light ion implantation [183-187]. As it was

[15] A good review about photonic applications of lithium niobate crystals can be found in Ref. [166]

above commented, later on the method was successfully applied to generate optical waveguides in another nonlinear optical crystal, $KGd(WO_4)_2$ [169, 170], slightly changing the irradiation conditions. This shows that the method could have a wide applicability to many other crystals with photonic interest. Moreover, in a further investigation, it has been successfully explored the use of the heavy ion irradiation method, in the electronic energy loss regime to even higher energies (~10 MeV/amu) and stopping powers [188]. This has allowed the fabrication of much thicker waveguides (up to tens of microns) with ultralow fluences ($< 10^{12}$ cm^{-2}), in order to get such thick optical barriers useful in the mid-IR, e.g. for astrophysical applications (or "Astrophotonics") [189, 190].

Thus, in summary, this Chapter is devoted to present a brief review of the structure, material and optical properties of $LiNbO_3$; as well as, the crystal defects present in the material and the most employed waveguide fabrication methods.

2.1 Historical overview.

Lithium niobate has been one of the most extensively studied materials in the last decades mainly due to its unique combination of ferroelectric and optical properties. Today, more than 400 papers are being published every year [191]. A very good review of its physical and chemical properties was already made by Rauber in 1978 [192].

In contrast to crystalline quartz, lithium niobate (LN) has not been found in nature. It was described for the first time in 1928 by Zachariasen [193], but it was not until 1949 that Mathias and Remeika discovered its ferroelectric properties studying single crystals grown from a flux [147]. However, systematic research on $LiNbO_3$ truly started in 1965, when both Fedulov [194] and Ballman [195] reported the successful growth of single crystals by the Czochralski technique, and then Nassau et al. [196, 197] and Abrahams et al. [198-200] published a five paper series on its physical properties in 1966.

Between 1965 and 1967 most of the basic experiments on acoustic wave propagation, electrooptic modulation, and bulk nonlinear laser optics - second harmonic generation (SHG) and optical parametric oscillation (OPA) - were performed. Between 1967 and 1980 extensive work was then devoted to improving the quality and homogeneity of grown samples, and to applications in photorefractive holographic storage, optical waveguides, and surface acoustic wave (SAWs) devices [192].

Around 1980 the industrial production of $LiNbO_3$ wafers was strongly increased, reaching world supply values. In 1984 the first $LiNbO_3$ waveguide modulator was commercialized, and in 1992 the first 100 mm long commercial quality waveguide was demonstrated.

On the other hand, and in a parallel way, it should be interesting to have a general outlook on the evolution along the years of the modification of the physical properties of lithium niobate by ion implantation, once the optical quality of the material has been accomplished.

The continuous improvement both in dimension and optical quality of LN wafers is connected with the widening of the spectrum of applications and the development of new devices, being demonstrated by the exponential growth of the number of publications devoted to this material during the last two decades [201]. It is around 1980 when the first pioneering

papers concerning the modification of the physical properties of LN by ion implantation were published [172, 177]. Since then a variety of ion species and energies have been tested for basic studies on damage formation by nuclear processes [180, 202, 203] and electronic processes in both subthreshold [109, 111, 204, 205] and ion track regime [41-43, 71].

From the application point of view, research on ion implantation of LN has been mostly addressed to the modification the refractive index, with the aim of producing waveguides with medium-mass ions at reasonable fluences [101, 103, 206-210]. A second branch of investigation has concerned the enhanced etching of LN as a consequence of the ion implantation induced defects [173, 176, 211, 212]. The very high etching selectivity of the heavily damaged regions makes this process appealing for micromachining of LN. The fabrication of both thin crystalline membranes by crystal ion slicing [213-215] and surface structures such as ridge waveguides [175, 216-218] has been demonstrated.

Nowadays ion implantation [179, 219, 220] can be considered sufficiently mature to enter in the production cycle, provided that the necessary knowledge for process design is attained.

2.2 Crystal structure and properties.

Lithium niobate is a crystalline solid belonging to the system Li_2O-Nb_2O_5, chemically very stable at room temperature, quite sensitive to humid surroundings. It is a quite hard solid (5 in the Mohs scale), with a fusion temperature of 1253ºC. Its refractive index is relative high (~2.3 in the visible spectra). Depending on its oxidation state, impurities content and their concentration, it presents a wide range of colours, from bright black when it is completely reduced to transparent when it is totally oxidized, going through brown and yellow in between. A summary of the main crystal properties is presented in **Table V**, which vary depending on the crystal stoichiometry, i.e. [Li]/[Nb] ratio [221, 222]. That is, the density of lithium niobate is dependent on Li content of the crystal. Abrahams and Marshal [223] reported that the density in a *congruent* $LiNbO_3$ crystal (48.45 mol% Li_2O) was 4.648 g/cm^3 and that in a *stoichiometric* crystal was 4.635 g/cm^3. Moreover, the composition depends also on the crystal orientation[16] [224].

One of the most remarkable features of $LiNbO_3$ is that it is a ferroelectric[17] material at room temperature. It has a very high Curie temperature, T_c, between 1050ºC and 1200ºC, depending on the crystal stoichiometry, i.e. [Li]/[Nb] ratio [221, 222]. $LiNbO_3$ structure is shown in **Fig. 17 (a, b)** over and below T_c.

The crystal structure of the material is slightly different in one and other phases. Crystal growth of lithium niobate by Czocharalski pulling method was reported by Ballman [195] in 1965. The detailed structure was determined by S. C. Abrams et al. in a series of papers [198, 225, 226] in 1966. We will describe both structures, bearing in mind that we will do for a *stoichiometric crystal*, i. e. the proportion of the atoms in the crystal exactly fulfils the formula $LiNbO_3$. In the case of *congruent composition*, which will be defined in a following Section, a relaxation of the crystal structure is induced.

[16] The equivalent *z-cut* has 48.47 mol% Li_2O. *x- cut* LN has the indicated 48.49 mol% Li_2O.
[17] *Ferroelectricity* consists in the emergence an intrinsic dipolar moment, referred to a *spontaneous polarization*, in the absence of an externally applied electric field.

Summary of General properties	
Intrinsic crystal properties	
Cristal structure	Trigonal, space group R_{3c}, point group 3m
Cell parameters	a = 5.148 Å, c = 13.863 Å
Density	$\rho = 4.64$ g/cm^3
Hardness	~ 5 Mohs
Thermal properties	
Melting point	$T_m \sim 1250$ ºC
Thermal expansion coefficients	$\parallel$a : 2.0 x 10^{-6} K^{-1} at 25 ºC
	$\parallel$c : 2.2 x 10^{-6} K^{-1} at 25 ºC
Thermal conductivity	4 W m^{-1} K^{-1} at 25 ºC
Thermal diffusivity	9 x 10^{-7} m^2 s^{-1}
Specific heat	0.633 J g^{-1} K^{-1}
Curie point	T_c = 1150ºC
Resistivity	2 x 10^{10} Ω - cm at 200 ºC
Pyroelectric coefficient	$p_3 = -6.4 (\pm 0.6) \times 10^{-5}$ C m^{-2} K^{-1}
Electrical properties	
Relative dielectric constant	$\varepsilon_{11}^T/\varepsilon_0 = 85$
	$\varepsilon_{33}^T/\varepsilon_0 = 29.5$
Piezo-electric coefficients	$d_{31} = -0.91 \pm 0.08$ pm/V
	$d_{33} = 8.1 \pm 0.2$ pm/V
	$d_{22} = 20.9 \pm 0.1$ pm/V
	$d_{51} = 70 \pm 3$ pm/V
Electro-optic coefficients	$r_{33}^T = 32$ pm/V, $r_{33}^S = 31$ pm/V
	$r_{13}^T = 10$ pm/V, $r_{13}^S = 8.6$ pm/V
	$r_{22}^T = 6.8$ pm/V, $r_{22}^S = 3.4$ pm/V
	$r_{51}^T = 32$ pm/V, $r_{51}^S = 28$ pm/V
Band gap	3.9 eV
Optical properties	
Absorption coefficient	≈ 0.1% cm^{-1} at 1064 nm
Transparency range	VIS/n-IR (~ 420 nm – 5.2 μm)
Optical anisotropy	Uniaxial negative, c-axis
Refractive indices:	$n_e = 2.146$, $n_o = 2.220$ at 1300 nm
	$n_e = 2.156$, $n_o = 2.232$ at 1064 nm
	$n_e = 2.203$, $n_o = 2.2286$ at 632.8 nm
Optical homogeneity:	$\Delta n \sim 5 \times 10^{-5}$ cm^{-1}
Birrefringence gradient	10^{-5} cm^{-1}
Non Linear Optic (NLO) coefficients	$d_{33} = 34.4$ pm/V
	$d_{31} = d_{15} = 5.95$ pm/V
	$d_{22} = 3.07$ pm/V

Table V. Table of basic properties of lithium niobate crystals. $LiNbO_3$ wafer parameters given by Photox Optical System, Ltd. The piezo-electric coefficients and the r_{51} electro-optic coefficient have been taken from [227]. The pyroelectric coefficient is taken from [228], and the band gap energy from [229].

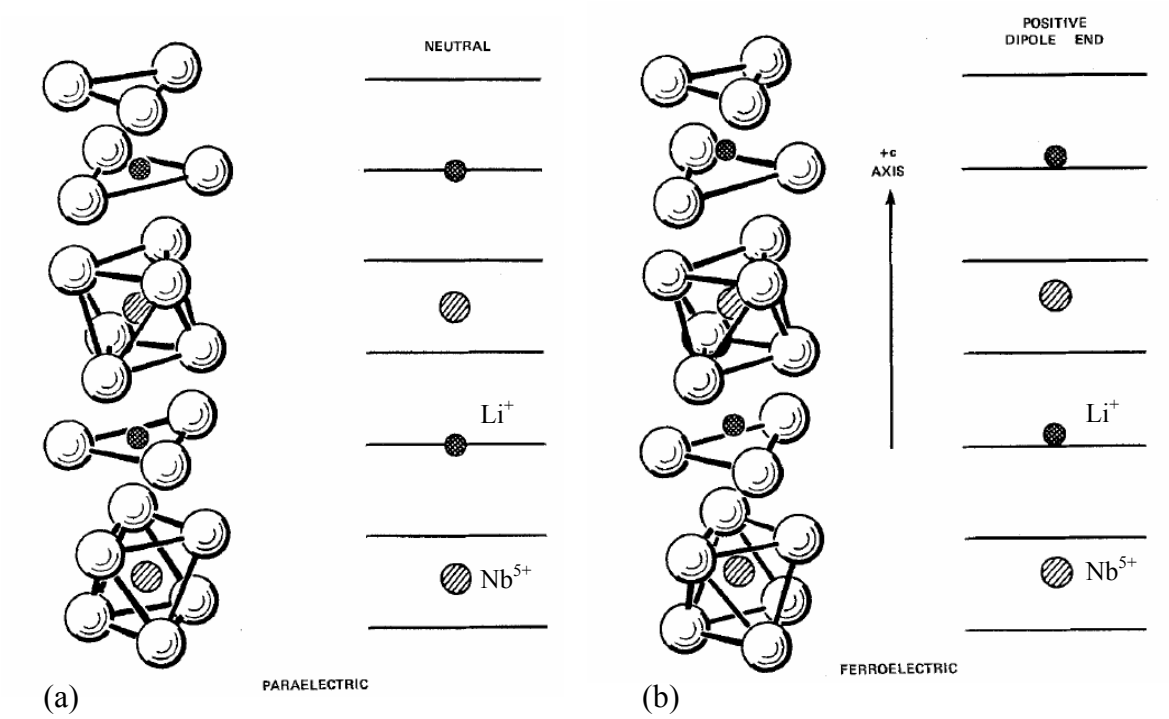

Fig. 17 (a, b). Crystallline structure of $LiNbO_3$: (a) paraelectric phase, (b) ferroelectric phase [225, 227, 230]. Positions of the lithium atoms (double cross-hatched circles) and the niobium atoms (single cross-hatched circles) with respect to the oxygen octahedra in the paraelectric ($T \geq T_C$) and ferroelectric phase ($T < T_C$) of lithium niobate. In (a), the positions of the lithium atoms are actually equally probable to be either above or below the oxygen layers by 0.37 Å. The lithium atoms shown are in the average position-in the oxygen layer. The horizontal lines in the diagram on the right represent the oxygen layers.

a) For temperatures over T_c (*paraelectric phase*), the crystal belongs to the spatial group rhombohedral (trigonal) $R\bar{3}c$, and corresponds to the punctual symmetry group $\bar{3}m(D_{3d})$, presenting inversion center [192, 227]. The crystal structure is a kind of distorted *perovsquite* [231]. The perovskite structure [232], it is ABO_3 where *A* is a lower (mono- or di-) and *B* a higher (tetra- or penta-) valency cation and *O* is oxygen. A perfect perovsquite structure is shown in **Fig. 18** in which the body-centered *B* cation is surrounded by an octahedra formed by the face-centered oxygen ions, and *A* cations occupy the corners of the cubic structure. In our case, for $T > T_c$, the distorted perovsquite is composed of oxygen octahedra sharing the adjacent faces, with the Li^+ atoms in an oxygen layer, that is *c/4* away from the Nb atom, and, in the center of one out of three octahedron, a Nb^{5+} atom. In turn, the lithium atoms are placed in the center of triangles formed also by the common oxygen atoms to two empty octahedra. These positions make the paraelectric phase non-polar [200]. We can see an outline of the structure in **Fig. 17 (a).**

b) For temperatures below T_c the structure changes to the so called *ferroelectric phase*. As the temperature decreases from the Curie temperature (T_c), the elastic forces of the crystal become dominant and force the lithium and niobium ions into new positions. The charge separation resulting from this shift of ions relative to the oxygen octahedra causes $LiNbO_3$ to exhibit *spontaneous polarization* at temperatures below 1150ºC.

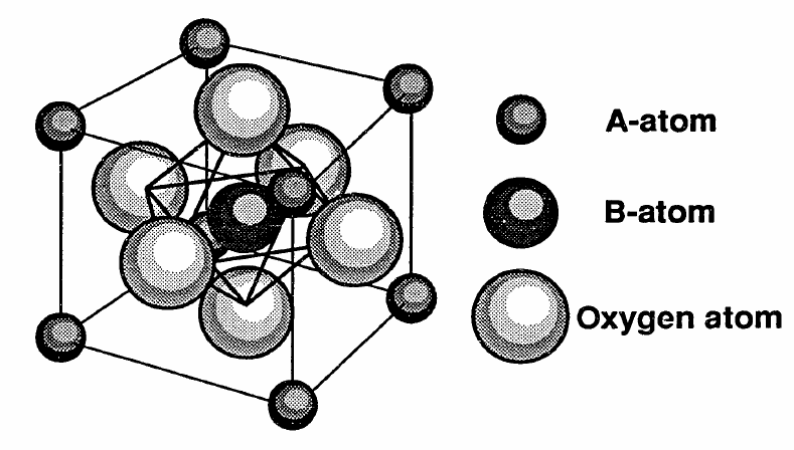

Fig. 18. Schematic of a perfect perovsquite structure.

In the ferroelectric phase a $LiNbO_3$ crystal exhibits three-fold rotation symmetry about its *c* axis. Thus, it continues being a member of the trigonal crystal system. In addition, it exhibits mirror symmetry about three planes that are 60º apart and intersect forming a three-fold rotation axis. These two symmetry operations then classify $LiNbO_3$ as a member of the $3m(C_{3v})$ point group, but no center of symmetry is present [227], which gives the crystal completely different properties to the *paraelectric phase*. It also belongs to the *R3c* space group [198].

In this case the crystal structure presents a similar one to the *paraelectric phase*, maintaining the octahedra formed by oxygen atoms, which are arranged in nearly hexagonal close-packed (HCP) planar sheets as shown in **Fig. 19** [198, 225, 226], except that the niobium and lithium atoms are displaced along the *c*-axis because of the lattice contraction due to the cooling, such as shown in **Fig. 17 (b)**: the niobium no longer occupy the center of the octahedron, while the lithium atom comes to occupy a position within another octahedron, but also shifted from its center.

In the trigonal system, two quite different unit cells can be chosen: *hexagonal* or *rhombohedral*. The conventional hexagonal unit cell in $LiNbO_3$ (a_H = 5.1483 Å, c_H = 13.8631 Å, and c/a = 2.693) contains six formula weights, while the conventional rhombohedral unit cell (trigonal, a = 5.4944 Å, α = 55º52´) contains only two formula weights [113, 192, 198, 225-227]. The octahedral interstices formed in this structure are one-third filled by lithium atoms, one-third filled by niobium atoms, and one-third vacant. In the +*c*-direction, the stacking sequence of cations in the interstices is: …Nb, vacancy, Li, Nb, vacancy, Li,…, and so on [198]. The distance of the Li^+ ion from the nearest oxygen plane in the ferroelectric phase is 0.37 Å. The asymmetry of the lattice structure makes $LiNbO_3$ a polar material. As is illustrated in **Fig. 17 (b)**, the oxygens are expressed in terms of oxygens triangles and oxygens cages.

On account of the movement of both cations in the same direction a *spontaneous polarization* of the crystal takes place in the direction of the *c*-axis, which is marked with a positive sign in the direction of movement of cations. This spontaneous polarization is what gives the character of the *ferroelectric crystal*, changing its symmetry. Thus, $LiNbO_3$ belongs to the broad class of displacement ferroelectrics. To reverse the orientation of the polarization, the Li^+ ions have to be displaced to the other side of its nearest oxygen triangle, while the Nb^{5+} ions can only move within the oxygen cages. The two stable positions (before and after reversal,

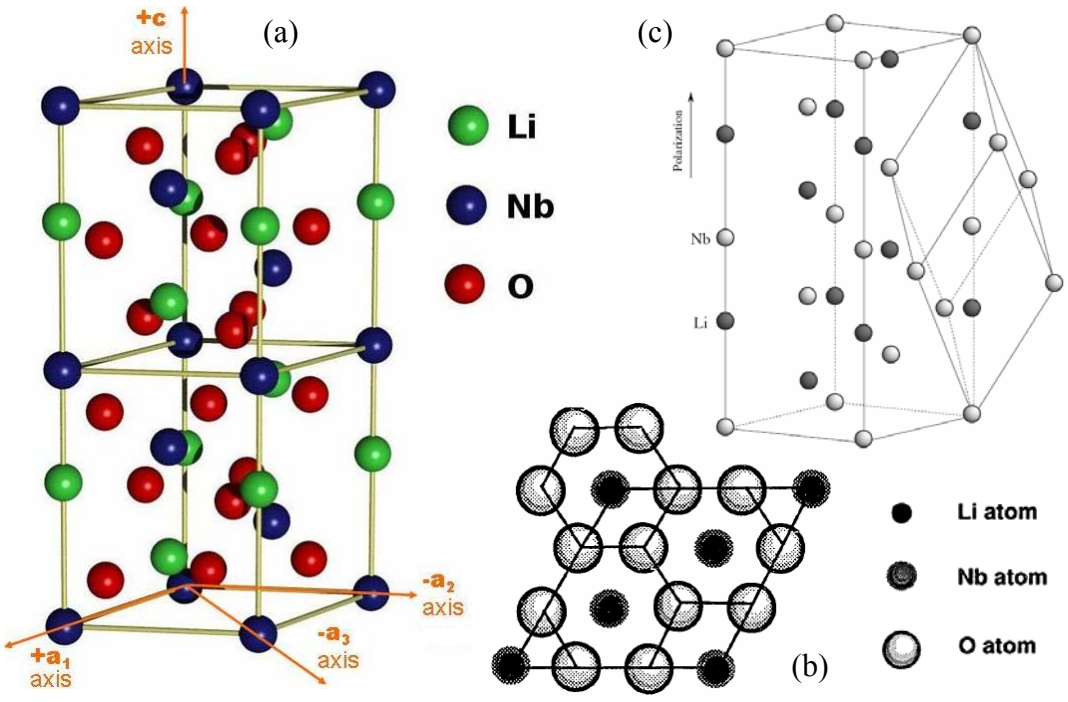

Fig. 19. Conventional rhombohedral unit cell and conventional hexagonal unit cell of ferroelectric $LiNbO_3$. (a) A hexagonal unit cell of $LiNbO_3$ structure with space group *R3c*, (b) represents the cell viewed down the polar axis. In its hexagonal representation, the equivalent in-plane unit vectors (a_1, a_2 a_3) are chosen such that they are perpendicular to the (*3m*) mirror planes of symmetry and enclose angles of 120º. The polarization direction determines the *c*-axis, perpendicular to the three directions. In (c) Li atoms are gray and Nb atoms are white. For the sake of clarity, the oxygen atoms are omitted.

Fig. 20) define the two possible directions of the *spontaneous polarization*, thereby defining $LiNbO_3$ a one-dimensional ferroelectric. The criterion of signs for the *spontaneous polarization* (and therefore the *c*-axis) is to assign the positive sign to the sense in which the shift of the positive charge takes place. In turn, the network of oxygen atoms undergoes a deformation: the triangles containing the lithium atoms in the paraelectric phase are contracted.

This structure makes $LiNbO_3$ an *uniaxial crystal*, where the refractive indexes in *x* and *y* directions are equal and referred to as the *ordinary index* (n_0) of $LiNbO_3$, but different to that of *z*, called *extraordinary index* (n_e). Spontaneous polarization of $LiNbO_3$ in the ferroelectric phase and its hyper-polarization are the origin of most of its interesting optical properties.

It has been commented above that, the initial definition for the *z*-axis is made during cooling down the crystal. Here, elastic forces press the atoms into their positions and the resulting positive end of polarity is named to be the +*z*-direction. This phenomenon is also known as the *pyroelectric effect*. An electric field arises as the temperature changes. The spontaneously induced polarization in *z*-direction is given by [228][18]

$$p_3 = \frac{\partial P_S}{\partial T} = -(6.4 \pm 0.6)x10^{-5} C \cdot m^{-2} \cdot K^{-1} \tag{60}$$

[18] More details will be preented in a following **Section 2.7.2**.

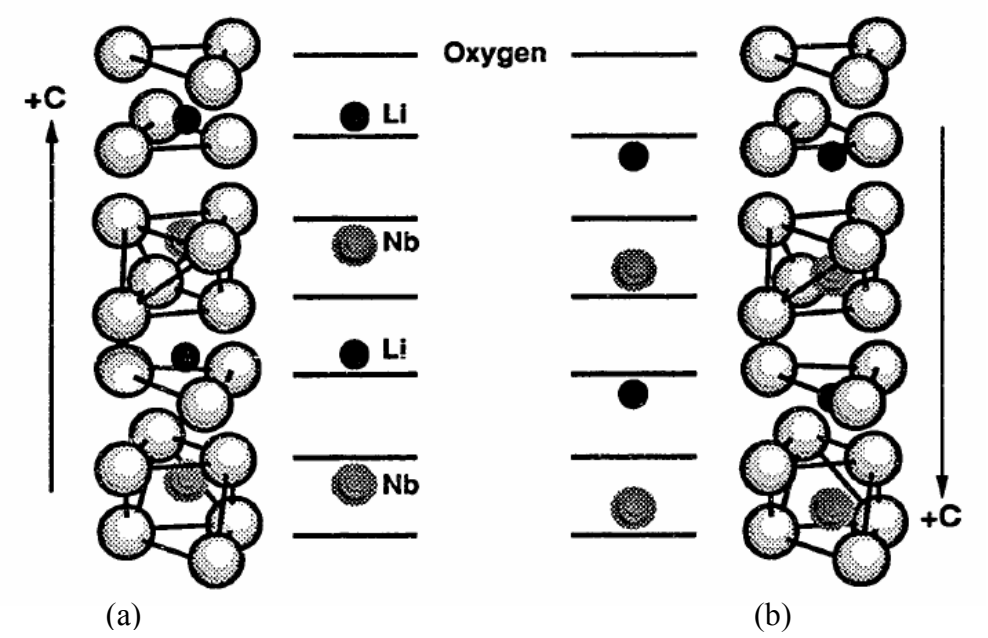

Fig. 20. Ferroelectric $LiNbO_3$ structure (a) before reversal, (b) after reversal.

To measure the polarity of the crystal ferroelectric phase, the *piezoelectric effect* can be exploited (this effect is explained more in detail in a following Section). Upon compression the +*z*-face (surface normal to *z*-axis in positive direction) gets charged negative because the lithium and niobium atoms are pushed closer to their paraelectric crystal sites leaving residual charges on either side.

Crystallographic projections of LN in principal directions and RBS/C studies.

It is worthy to notice that, the ferroelectric crystalline structure that has been described above will become apparent in our experiments of Rutherford Backscattering Spectroscopy in channelling configuration (RBS/C). The results will be shown throughout this Thesis work and the physical theoretical principles of this technique are described in a following Chapter. On the other hand, the experiments will be carried out on *z*-cut (which coincides with the optical *c*-axis) and *x*-cut congruent LN substrates.

In this point, and trying to advance some specific experimental details, we have to say that, whereas in the Chapter devoted to the study of the kinetics of amorphization *x*-/*z*- crystals were used for historical considerations and with the aim of investigate the anisotropy of the electronic damage respect to the crystallographic orientation; in the rest of the experimental research a determinated fixed orientation was selected. In this sense, in the Chapter in which the recrystallization and damage recovery through thermal treatment is studied, *z*-cut substrates were used to carry out the irradiations and the annealing process; however, due to the great piezoelectric interaction appeared between the AFM (Atomic Force Microscopy) probe and the *z*-cut surface, which would not allow the appropriate characterization of the nanostructures revealed after etching process, it was necessary to perform the investigation on *x*-cut substrates.

Figure 21 (a, b) show the projections of the crystal structure of $LiNbO_3$ in its *ferroelectric phase* aligned for channelling in the directions *z* and *x*, respectively. That is, the crystalline structure aligned with those directions "seen" by the projectil ions in the RBS/C

experiments. A great number of studies performed on the crystal structure of $LiNbO_3$ using the RBS/C experimental technique is found in the scientific literature [233-237]. In **Fig. 22**, the symmetry of a *z*-cut $LiNbO_3$ crystal is shown by means of a Rutherford Backscattering Spectrometry in channeling configuration (RBS/C)[19] [238].

On the other hand, it has been reported in the nuclear damage regime that, the defect concentration measured for a given ion fluence increases gradually with increasing fluence, and the damage is much higher in *x*-cut $LiNbO_3$ compared to *z*-cut simples (for details see [172, 176]). The higher backscattering yield for the *x*-cut is explained by a preferential rearrangement of the displaced Nb-atoms to vacant octahedral sites, which are situated close to the middle of the channel. These positions lead to a large "visibility" of the Nb atoms by the analyzing He-beam, i.e. a high backscattering yield is measured. In contrast, for the *z*-cut the rearranged Nb-atoms are shielded by Nb-atoms on regular lattice sites, which reduce the RBS-yield. In the electronic damage regime, it has been observed the same anisotropic behaviour for LN, where the *x*-cut shows higher damage by RBS than the *z*-cut for the same electronic stopping power and ion fluence; moreover, after a quantitative analysis of the out-of-plane swelling, due to the free expansion of the irradiated volume, it is observed that in *x*-cut samples is always higher than the measured on *z*-cut samples series. At the same time, the study carried out through various ion species and energies, reveals that the swelling effect depends on the fluence, the electronic stopping power and the range of the ions in agreement with the observations made in various oxides [42, 71, 239, 240]. However, in the case of the nuclear damage regime, the volume expansion seems to be independent of the crystal cut [241].

2.3 Phases diagram and composition.

$LiNbO_3$ has a melting point of 1253ºC [242] and a density of 4.64 g/cm^3. Both properties can vary according to the concentration ratio Li/Nb [243, 244]. Lithium niobate can be crystallized using a composition of the liquid phase within the range 45-58 mol Li_2O, resulting in crystals whose composition varies in the range of 48-50 mol Li_2O [242].

Lerner and colleagues [245] were the first to publish the $LiNbO_3$ phase diagram commonly accepted today. In the phase diagram of the Li_2O-Nb_2O_5 binary system (see **Figure 23**), there is a point close to the stoichiometry for which the concentration of Li_2O in the melting coincides with the concentration of Li_2O in the crystal. That is, there can be found a maximum in the solid-liquid curve corresponding to a concentration near the stoichiometric one (Li_2O 50%), but slightly different [242, 246]. This concentration corresponds to 48.490% molar of Li_2O in the crystal when the growth takes place along the *x*-axis, and 48.470% if it is grown along the *z*-axis [224]. The melt tends to crystallize at this concentration, known as *congruent*, where there is a deficiency of lithium with respect to the stoichiometric composition [242, 247]. In this congruent composition, the crystal growth takes place in an easy manner, resulting in crystals with high homogeneity, and consecuently, most of the crystals usually have such a composition. When the ratio [Li]/[Nb] in the crystal is equal to 1, the composition is called *stoichiometric*. Any other composition of the melt produces a variation on its composition

[19] These results were measured at the Centro de Microanálisis de Materiales (CMAM) by Andrés Redondo-Cubero. The experiment was performed with 3.5 MeV He^+ ions and minimum yield appears along the symmetry directions of the lattice.

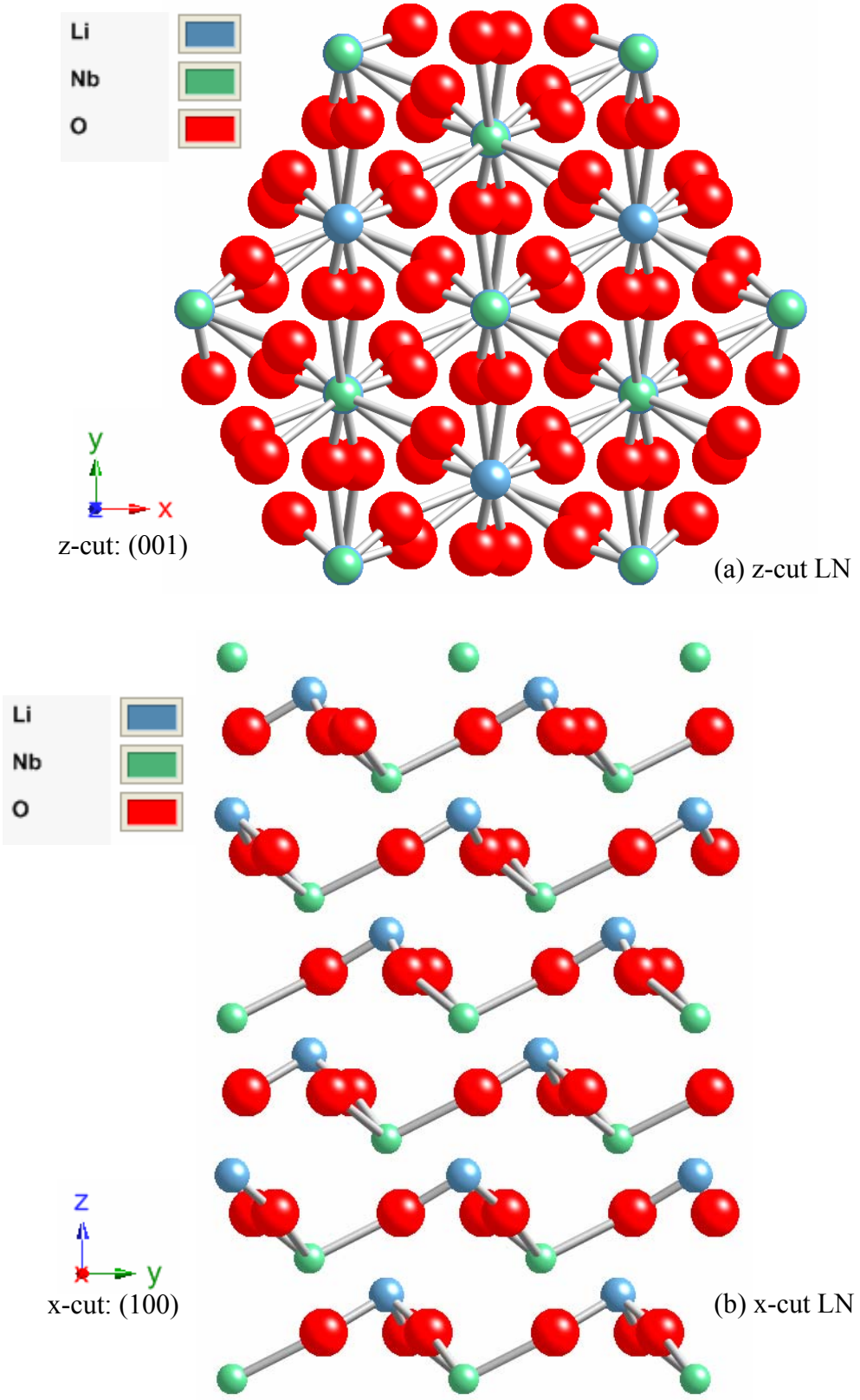

Fig. 21 (a, b). Projections of the crystal structure of ferroelectric $LiNbO_3$ oriented for channelling configuration, along: (a) *z*-cut, ***c***-axis [0001], (b) *x*-cut. From [248] using ilmenite ($FeTiO_3$) structure.

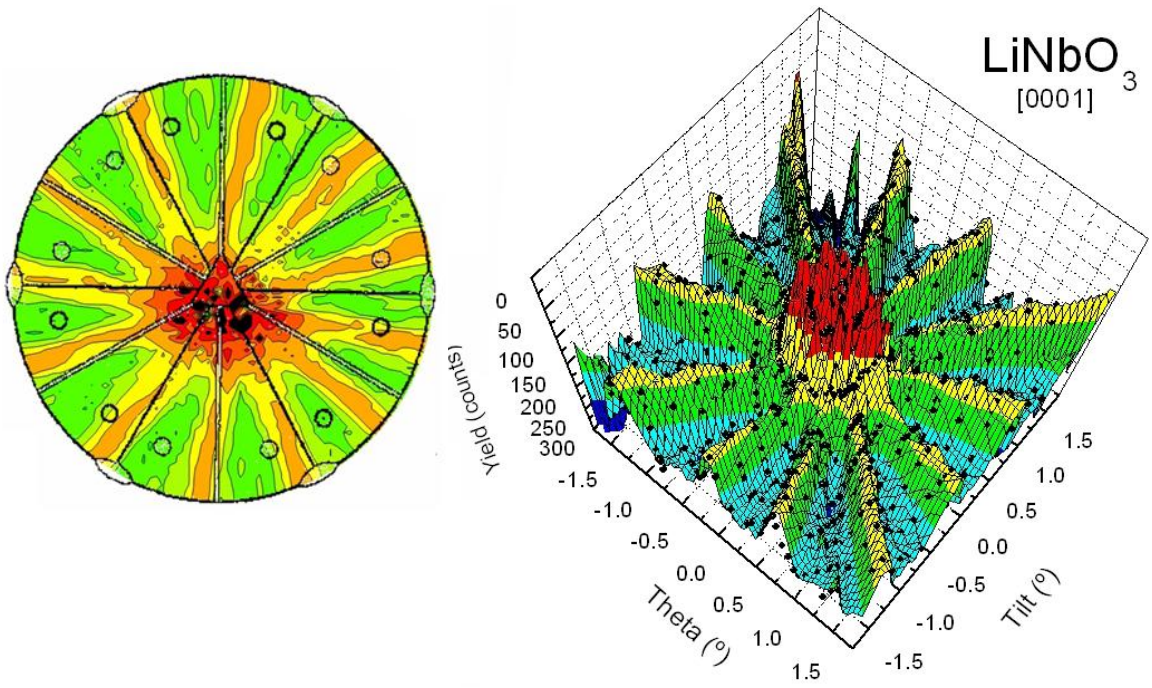

Fig. 22. (a) Comparison between the stereographic projection of a theoretical 3m (C_{3v}) lattice [249] and the actual experimental data. (b) Angular scan centered in the [0001] channel. Solid points represent the experimental data. The yield axis is inverted for a better view of the dip.

whiles the development of the crystal growth. And this variation is transferred to the crystal composition itself, affecting its physical properties.

2.4 Lithium niobate growth techniques.

2.4.1 Czochralski technique.

As it was mentioned earlier, the $LiNbO_3$ crystal was synthesized by first time by Matthias and Remeika in 1949 [147], but it was not until 1965 when the Czochralski technique [194, 195, 250] was implemented for growth crystals, when there were obtained large single crystals, with very good homogeneity and high structural quality, suitable for start to think about several applications. Ballman [195] was the first to grow $LiNbO_3$ using this technique.

Since 1965, the Czochralski method [194-196, 242, 250] has been the most employed growing technique for homogeneous, reproducible and rather bulky LN crystals, because of its versatility and simplicity [195]. This technique consists in the immersion of a single crystal seed of $LiNbO_3$ in a melt (at ~ 1260º C) with the components needed for the crystal. In the case of LN the melt usually comprises a mixture of Nb_2O_5 y Li_2CO_3 (the latter will be the physical source of Li_2O, after the decomposition and subsequent elimination of CO_2). Following, the seed is slowly rotated and vertically pulled out in such a way that the crystal growth proceeds around the seed, and a cylindric single-crystal is developed. For $LiNbO_3$, the pulling and rotation rates are typically 1-5 mm/h and 10-60 r.p.m, respectively. Once the crystal growth is finished, the cooling rate (~ 50º C/ h) must be strictly controlled to avoid fractures and cracks in the structure. Furthermore, this last part of the growth is usually made in oxygen atmosphere, to

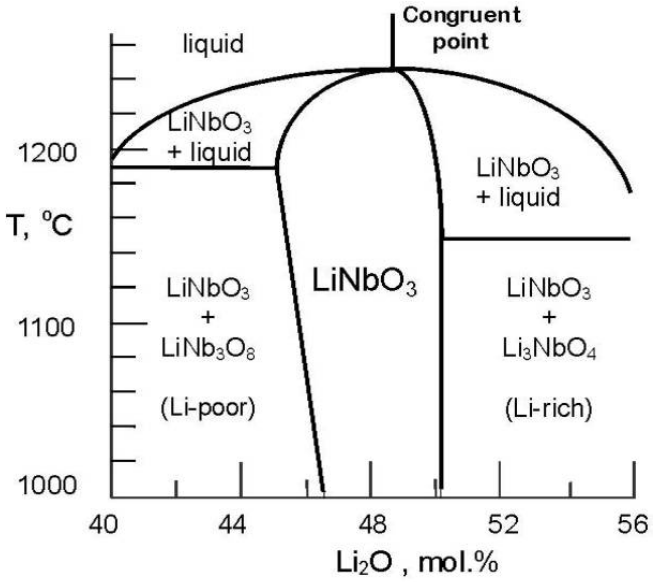

Fig. 23. (a) Phases diagram of Li_2O-Nb_2O_5 corresponding to $LiNbO_3$ formation [251]. The congruent composition, with 48.5 % of Li_2O, is the most common in the $LiNbO_3$ crystals by its homogeneity and easy of growth. (A historical reference can be found in [252, 253])

prevent Li losses due to the high temperature (> 1300º C) [195, 254, 255]. Nowadays, commercial crystals of 4 inches diameter and 50 mm thickness with a high homogeneity and good crystal properties are commercially available[20].

The $LiNbO_3$ crystals are usually grown in the *congruent* composition, due to it is the easiest way to grow it compared with other stoichiometries, as the composition of the crystal coincides with the melt [256]. It is worthy to notice that, the congruent composition was used throught all the experiments carried out in this Thesis work. As it was commented in a previous Section, it is very important that the composition of the crystal is constant since almost all its properties vary with its composition.

Despite of the natural trend of $LiNbO_3$ is the *congruent* composition, great efforts are made to obtain pure *stoichiometric* crystals (or quasi-stoichiometric) [256]. These processes are more difficult and several methods have been proposed, such as Czochralski growth with K_2O added to the melt [254, 255, 257, 258], the double crucible technique [259], and Vapor Transport Equilibrium (VTE) [260, 261].

2.4.2 Other crystal growth techniques for Lithium niobate.

Apart from the Czochralski crystal growth technique, which is the most widely used, there are other methods also used for $LiNbO_3$, for example the Stepanov technique [262-264]. Most of them are used for thin layers, as molecular beam epitaxy (MBE) [265], chemical vapour deposition (CVD) [266], liquid phase epitaxy (LPE) [267], magnetron sputtering [268] or laser ablation (PLD, pulsed laser deposition) [269, 270]. Also fiber optics made of $LiNbO_3$ have been developed [271, 272].

[20] In **Table V** a more detailed set of parameters for commercial congruent $LiNbO_3$ crystals are shown.

2.5 Defects in Lithium niobate.

In $LiNbO_3$ one of the key factors of its properties are the defects present in the crystal, as occurs for most materials. Most of these defects appear as a consequence of the crystal growth technique, but they can be also introduced on purpose to modify certain properties of the material in a controlled way.

The most used criterion to classify the defects of $LiNbO_3$ is to distinguish between *intrinsic* and *extrinsic defects*, which will be briefly described in this Section.

2.5.1 Intrinsic defects.

As it was mentioned before, the preferred composition for $LiNbO_3$ is the *congruent* one. This differs slightly from the *stoichiometric* one, having a deficit of Li, and the crystal needs some charge compensation mechanism. The *intrinsic defects* are those which appear during the growth of the crystal to compensate this lack of Li.

The study of these defects has produced different points of view with respect to their origin, such as niobium vacancies [273], oxygen vacancies [274] or lithium vacancies [275]. From the experimental perspective, a great number of measurements have been performed to clarify this point: nuclear magnetic resonance (NMR) [276], X-ray diffraction [277], etc.

On the other hand, recent studies based on density-fuctional theory calculations (DFT) of the $LiNbO_3$ different crystallographic surfaces [237] reveal the great interest placed to determine the chemical species present in each face and its dependency on the crystal stoichiometry. Not only fron a fundamental point of view, i.e, the origin of the physical properties, neither to optimize the applications obtained from the adecuated selection of the crystal substrate. In addition, we have to remark the added difficulty of the system under study, where the correct choice of the chemical potentials of the surface constituents plays an important role.

2.5.2 Extrinsic defects.

The presence of extrinsic defects is due to the addition of defects during the crystal growth technique (because of to impurities present on the melt, or in the atmosphere) or introduced after it. Ions such as Fe, H and others always appear in $LiNbO_3$ crystals grown with the Czochralski method, and their presence is inevitable [192]. Sometimes they are introduced on purpose to obtain doped $LiNbO_3$ in a controlled way. These *extrinsic defects* affect the optical properties of $LiNbO_3$ [278, 279], even in quantities as low as a few ppm.

2.5.3 Hydrogen.

Among all the impurities that can be found in $LiNbO_3$, hydrogen has a relevant importance due to the role that plays in both, the photorefractive thermal setting and the formation of waveguides, performed by the inclusion of hydrogen atoms in a layer of the crystal. Likewise, structural changes resulting in alterations in $LiNbO_3$ properties as the

refractive index, the conductivity in darkness, the photorefractive sensitivity or phase mismatch temperature for the second harmonic generation [280].

Hydrogen ions can be always found in $LiNbO_3$ in concentrations of $\sim 10^{19}$ cm^{-3}. Their addition to the composition of the crystal happens during its growth, due to the presence of H in the melt, in the atmosphere or both. As in other materials such as SiO_2 or TiO_2, the H ion is bonded to the oxygen, in the form of OH^- [244, 280]. These bonds are placed in planes formed by 6 oxygens normal to the ***c***-axis, along *O-O* directions.

As commented, higher concentrations of H produce changes in the structure of the crystal, modifying physical properties. To take advantages of these changes, different techniques have been developed to introduce massive H ions in the crystal: ion implantation ([H] $\sim 10^{20}$ cm^{-3} [281]) or proton exchange in an acid melt ([H] $\sim 10^{22}$ cm^{-3} [280, 282]). Both techniques produce the highest concentrations of H that can be achieved in $LiNbO_3$, but only in a few microns in depth. These amounts of H produce changes in the refractive index, which make these techniques very important ways of obtaining waveguide layers in $LiNbO_3$.

In the following lines will be briefly described these different methods, although in the spedific case of waveguides fabrication by ion implantation vs irradiation will be deeper studied in the following Chapter.

Waveguide fabrication by proton exchange.

Proton exchange is one of the most employed waveguide fabrication technique for the last years, because of its simplicity. The exchange process consists on the substitution of ions Li^+ with H^+. These incoming H^+ do not exactly replace the Li^+ ions, but are placed in the oxygen plane. Therefore, a new layer $H_xLi_{1-x}NbO_3$ appears in the surface of the $LiNbO_3$ substrate. Besides, this layer also gives rise to a certain stress in the *z*-axis, because of the difference between their crystal lattices [283, 284].

Given that $LiNbO_3$ is a photoelastic, piezoelectric and electro-optic material (as will be described later), different phenomena are produced in the crystal. The stress gives rise, due to the photoelastic effect, to change in the refractive index. At the same time, via the piezoelectric effect, an electric field is also produced, which in turn modifies the refractive index by means of the electro-optic effect. As a result, an increase in the extraordinary refractive index, where light can be guided, and a decrease in the ordinary index [285] takes place.

While the confinement of light only with extraordinary polarization is a clear limitation of such guides, they have excellent properties in other respects, like the high degree of confinement due to the high jump index, making them very useful for much of applications.

Waveguides fabrication by ion implantion.

Another common method for manufacturing waveguides in $LiNbO_3$ involves the implantation of accelerated light ions beams, typically He^+ and H^+ [183, 186, 286], with the aim of modifying the cristalline structure of the material. In this case, the refractive index remains almost unchanged with respect to the substrate in the area close to the surface (~1%).

The ion implantation uses light ions, usually He^+ or H^+, with energies of about 1 MeV and uses the damage they cause in the crystal lattice in the latter part of its path in the material, when they have little energy, and where they undergo collisions with lattice atoms (nuclear collision damage), as we have seen in **Chapter 1. Section 1.2.1**. This is due to the low collision cross-section of these ions at high energies (~ MeV), which does not produce alterations in the structure, only appearing punctual defects. By contrast, at the end of range of these ions, the collisions and the subsequent displacement of the lattice ions lead to the great disorder, which may include even the amorphization of the material. The produced disorder leads to a decrease in both the ordinary and extraordinary refractive indexes, up 10%, whose values depends on the implanted dose (typically between 10^{14} and 10^{17} at/cm^2). Therefore, the layer created in depth works as an optical barrier, creating a waveguide on the surface of the sample.

The incident ions pass through the region corresponding to the waveguide having high energy suffering only interactions with the electrons of the lattice, inducing ionization, but without creating severe damage, due to the electronic stopping power of the used ions (light ions: H, He) is too low (S_e < 1 keV/nm) to cause damage[21]. The defects that may arise in this area are easily removed by a subsequent thermal annealing. In this way, waveguides are obtained with optical losses as low as 0.2 dB/cm.

Hence, in the case of ion implantation, and unlike other methods such as *metals diffusion* or *ion exchange*[22], the waveguides are obtained by lowering the index in the stopping area, whose depth depends on the energy of the incident ions. Moreover, we have to remark that, the profile of the extraordinary refractive index is somewhat peculiar, because in the area where the defects concentrations are not very high, an increase in the index is verified [183].

The physical features of the waveguides (height, width and depth of the barrier) are easily tailored by playing with the energy and mass of the ions and the irradiation fluence, usually around 10^{16} - 10^{17} at/cm^2, high values that require high processing times.

It is worthy to notice that, recently, in the implementation process have also been used heavy ions (such as O^{3+} or Si^+), which has allowed obtain waveguides, reducing the needed implantation dose till values ≤ 10^{14} at/cm^2, thus, reducing significantly the exposition time [101, 206]. In the following Chapter this topic will be widely discussed.

2.6 Lithium niobate optical properties.

2.6.1 Linear optical properties.

2.6.1.1 Reflectivity and absorption edges.

Lithium niobate crystals, manufactured without applying any electric field during the growth process, pure and totally oxidized, are colorless and transparent. Reflectivity due to the high value of the refraction indices in the visible range, takes values of up to 15% at normal incidence. The internal transmittance is close to 100%, from 5.5 μm in the infrared range (that

[21] A more detailed quantiative study will be carried out in the following Chapter.
[22] A wide description about this waveguides fabrication method can be found in Refs. (Proton exchange [282], Ti diffusion [287, 288], Zn-diffusion [289]), which exceed the scope of this Thesis work.

is, the wavelength where the absorption associated to the lattice vibrations starts), to the ultraviolet absorption edge, at 330 nm [196, 290].

The band structure, as in other perovskite compounds, is characterized by the NbO_6 octahedra [291, 292]. Thus, it has been verified from studies based on the band structure of the crystal that, the absorption edge of $LiNbO_3$ can be explained by charge transfer between the *p-orbitals* of oxygen and *d-orbitals* of niobium, concretely, the fundamental optical absorption corresponds to electronic transitions from the valence band, formed by the *p-orbitals* of anions O_2^-, to the conduction band, formed by *d-orbitals* of Nb_5^+ cations [292, 293]. The absorption edge, is strongly dependent on the composition of the crystal, i.e., the [Li]/[Nb] rate in the crystal [294, 295], being shifted about 0.1 eV to higher energies in the stoichiometric case. It is worthy to notice that, despite of the anisotropy that introduces the structure of lithium niobate, the absorption edge is nearly isotropic, with no appreciable dichroism [292, 294].

2.6.1.2 Refractive indexes.

Lithium niobate is a *uniaxial* material, which therefore has two principal refractive indices: the *ordinary refractive index* (n_o), and the *extraordinary one*, (n_e), showing a strong negative birefringence of around: $n_e - n_o \sim -0.08$ [227, 290]. The *extraordinary refractive index* is related to the propagation of linearly polarized light, oscillating the electric field in the direction of optical axis, which coincides with the direction "*c*-axis" in the diagram in **Figure 17**. The *ordinary refractive index* is the corresponding to the electric field oscillating in the plane perpendicular to the optical axis. Both indices have been measured over a wide spectral range: from the ultraviolet region $\lambda \in (124 - 310)$ nm [296] to the near infrared region $\lambda \in (5 - 1000)$ μm [297, 298]. **Table VI** shows the refractive indices of congruent $LiNbO_3$, measured experimentally for several values of wavelengths [227].

There have been several studies on the actual refractive indices of $LiNbO_3$, which show great dispersion, which is mainly due to differences in the composition of the samples used [222, 299]. Both, the effect of the composition, as plasmons (UV), and the absorption associated with lattice vibrations (IR) are reflected in the generalized Sellmeier equation obtained by U. Schlarb and K. Betzler [300], as follows:

Wavelength, λ (nm)	Extraordinary Polarization (n_e)	Ordinary Polarization (n_o)
441.6	2.2887	2.3875
488.0	2.2561	2.3489
514.5	2.2422	2.3326
632.8	2.2028	2.2866
1060.0	2.1561	2.2323

Table VI. Ordinary and extraordinary refractive indices of $LiNbO_3$ in the congruent composition, from Ref. [227].

$$n_i^2 = \frac{50 + c_{Li}}{100} \times \frac{A_{0,i}}{\left(\lambda_{0,i} + \mu_{0,i}\left[f(T) - f(T_0)\right]\right)^{-2} - \lambda^{-2}} + \tag{61}$$

$$+ \frac{50 - c_{Li}}{100} \times \frac{A_{1,i}}{\left(\lambda_{1,i} + \mu_{1,i}\left[f(T) - f(T_0)\right]\right)^{-2} - \lambda^{-2}} + A_{UV} - A_{IR,i}\lambda^2$$

with

$$f(T) = (T + 273)^2 + \alpha\left[\coth\left(\frac{\widetilde{T}}{T + 273}\right) - 1\right] \tag{62}$$

Where i = *e, o* marks the polarization, c_{Li} the % molar Li_2O concentration (i.e., $c_{Li} \approx$ 48.48% in the case of congruent composition), λ the wavelength in nm, T the temperature in ºC and T_0 = 25.4 ºC. All the others are fitting parameters. **Eq. 61** is based on simulating the oscillator corresponding to electronic transitions that mark the absorption edge, as described in **Section 2.6.1.1**. In this equation, the first term is related to the NbO_6 structure, (the octahedra consist of oxygen atoms containing one atom of niobium inside), and the second to the Nb^{5+} in Li^+ places, i.e. *defects antisities*. Both terms are temperature dependent, given by **Eq. 62**. The third term deals with the contribution of the plasmons in the far UV (13 - 25.5 eV) [301] and it is independent of the polarization. This is because the anisotropic nature of $LiNbO_3$ is basically due to transitions below 7 eV [296], well below the previous value. Finally, the last term takes the infrared absorption into account.

As the study of the refractive index in $LiNbO_3$ is basically empirical and the adjustment of the parameters depends strongly on the nature of each crystal, a wide variety of Sellmeier equations for different stoichiometries and wavelength ranges can be found in literature (for more details see Ref. [113]). Depending on the crystal stoichiometry and the wavelength range one wants to work with, the ordinary and extraordinary refractive indices should be calculated with the appropriate Sellmeier equation. The fitting parameters of **Eq. 61** are shown in **Table VII**.

2.6.2 Nonlinear optical properties of Lihium Niobate.

Nonlinear media present several characteristics, such as a change of the refractive index with light intensity, interaction of photons and the alteration of the light frequency as it travels throughout the material. The medium is changed by the presence of the optical field and this transformation reciprocally modifies the optical field. $LiNbO_3$ is one of these nonlinear media, and this Section is devoted to briefly describe the main features of nonlinear phenomena in this material.

The interaction between the medium and light is described by the relation between the polarization density vector and the electric field vector. If the relation is nonlinear, then the medium is said to be nonlinear too, and the polarization density is written as:

$$P_i = \varepsilon_0\left[\sum_j \chi_{ij}^{(1)} E_j + \sum_{jk} \chi_{ijk}^{(2)} E_j E_k + \sum_{jkl} \chi_{ijkl}^{(3)} E_j E_k E_l + \ldots\right] \tag{63}$$

Extraordinary Polarization (n_e)	Ordinary Polarization (n_o)
$A_{0,e} = 3.9466 \times 10^{-5}$ nm^{-2}	$A_{0,o} = 4.5312 \times 10^{-5}$ nm^{-2}
$A_{1,e} = 8.3140 \times 10^{-5}$ nm^{-2}	$A_{1,o} = 2.7322 \times 10^{-5}$ nm^{-2}
$\lambda_{0,e} = 218.203$ nm	$\lambda_{0,o} = 223.219$ nm
$\lambda_{1,e} = 250.847$ nm	$\lambda_{1,o} = 260.26$ nm
$\mu_{0,e} = 7.5187 \times 10^{-6}$ nm/K^2	$\mu_{0,o} = 2.1203 \times 10^{-6}$ nm/K^2
$\mu_{1,e} = -3.8043 \times 10^{-5}$ nm/K^2	$\mu_{1,o} = -1.8275 \times 10^{-4}$ nm/K^2
$A_{IR,e} = 3.0998 \times 10^{-8}$ nm^{-2}	$A_{IR,o} = 3.6340 \times 10^{-8}$ nm^{-2}
$A_{UV} = 2.6613$	$A_{UV} = 2.6613$
$\alpha = 4.0238 \times 10^5$ K^2	$\widetilde{T} = 261.6$ ºC

Table VII. Parameters of the generalized Sellmeier equation at room temperature T_0 = 24.5º C for fitting the refractive indices of $LiNbO_3$. The coefficients of variation of temperature are also included [300].

In **Figure 24** it is shown the discussed fitting in the refractive indixes.

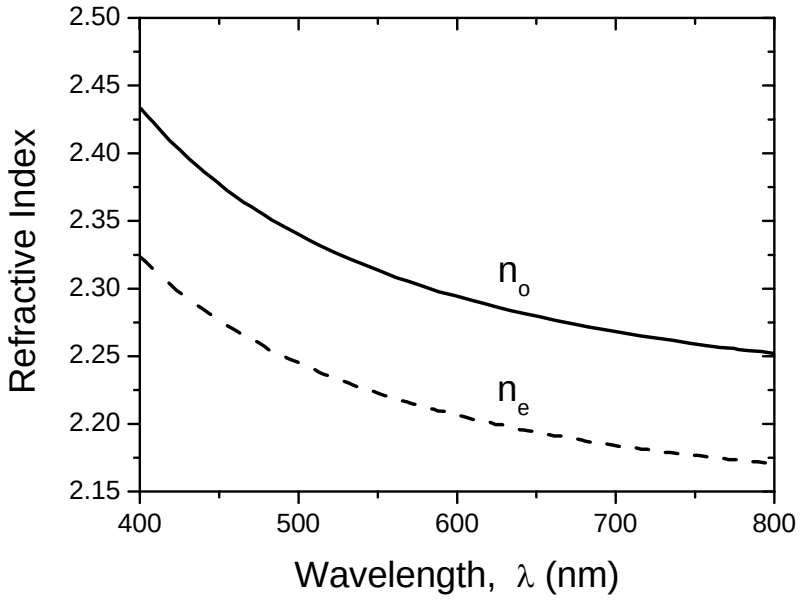

Fig. 24. Ordinary (solid line) and extraordinary (dashed line) refractive index of $LiNbO_3$ in the congruent composition obtained from the fitting of Sellmeier equation (**Eq. 61**) with the parameters listed in **Table VII**.

being the first term the linear response, fundaments of conventional optics, $\chi^{(2)}_{ijk}$ the second order nonlinear susceptibility, $\chi^{(3)}_{ijkl}$ the third order one, and so on. Some interesting applications associated with the second order term are the interaction of two monochromatic waves that

gives rise to a third one with a frequency equal to the sum or difference of the original frequencies (*frequency conversion*), frequency doubling of a monochromatic wave (*second harmonic generation*, *SHG*), etc. In the case of the third order term, it gives rise to *third harmonic generation, self-focusing, four wave mixing*, etc. These nonlinear phenomena are treated in detail in Refs. [302, 303].

We consider the general case in which the incident field is a sum of several monochromatic fields of frequencies ω_1, ω_2, ω_3, …, ω_p, that´s to say:

$$E_j(t) = \sum_{\alpha=1}^{p} E_j(\omega_\alpha)\cos(\omega_\alpha t + \varphi_\alpha) = \frac{1}{2}\left[\sum_{\alpha=1}^{p} \widetilde{E}_j(\omega_\alpha)e^{-i\omega_\alpha t} + \widetilde{E}_j^*(\omega_\alpha)e^{i\omega_\alpha t}\right] \tag{64}$$

Substituting **Eq. 64** in **63** appear several terms that account for the linear and nonlinear processes generated by the field in the material. In the case of nonlinear processes each of them correspond to a term of polarization, $\vec{P}$, oscillating at a frequency ω, given by a specified mixture of incident frequencies:

$$\omega = \sum_{\alpha} (\pm\omega_\alpha) \tag{65}$$

In the following we will describe briefly some of the nonlinear processes, particularly those with a greater potential applicability.

2.6.2.1 Second harmonic generation.

$LiNbO_3$ is a noncentrosymmetric material that presents a high $\chi_{ijk}^{(2)}$, and therefore, a high second order nonlinear response. The term of **Eq. 63** for the phenomenon of second harmonic generation is:

$$\widetilde{P}_i(2\omega_1) = \frac{\varepsilon_0}{2}\chi_{ijk}^{(2)}\widetilde{E}_j(\omega_1)\widetilde{E}_k(\omega_1) \tag{66}$$

Normally, since the tensor $\chi_{ijk}^{(2)}$ is symmetric against permutations of the indices *j* and *k* for any medium, it may be replaced by the matrix d_{il} dividing each term $\chi_{ijk}^{(2)}$ by 2, and using the following convention of index contraction: $jk \rightarrow l$ (11 → 1, 22 → 2, 33 → 3, 23 = 32 → 4, 13 = 31 → 5, 12 = 21 → 6), being **Eq. 66** as follows:

$$\widetilde{P}_i(\omega_1) = \varepsilon_0 d_{il}\widetilde{E}_l(\omega_1) \tag{67}$$

The terms of $\chi_{ijk}^{(2)}$ which are different from zero are indicated in contracted notation [227] in **Eq. 68**.

$$(\chi_{ij}) = \begin{pmatrix} 0 & 0 & 0 & 0 & \chi_{51} & -\chi_{22} \\ -\chi_{22} & \chi_{22} & 0 & \chi_{51} & 0 & 0 \\ \chi_{13} & \chi_{13} & \chi_{33} & 0 & 0 & 0 \end{pmatrix} \tag{68}$$

Frequently, in experimental works, the second order nonlinear coefficient, $d_{ij}^{(2)}$ is used instead of $\chi_{ij}^{(2)}$. The equivalence between them is simply $d_{ijkl}^{(2)} = \frac{1}{2}\chi_{ijkl}^{(2)}$. The values of the non-zero components of this tensor for commercial $LiNbO_3$ can be found in **Table V**. The magnitudes of these coefficients are high enough to allow the generation of second harmonic light with different methods: phase-matching [304, 305], quasiphase-matching in periodically polarized crystals [306-308], etc. In fact, $LiNbO_3$ has become on one of the reference materials for second order material applications.

2.6.2.2 Electro-optic or Pockels effect.

This is one of the most interesting optical effects of $LiNbO_3$. A change in the refractive index of a material due to the presence of an electric field is known as *electro-optic effect* [309]. Its importance comes from the large number of applications arising from this phenomenon, such as modulating devices [310-312] or switching ones [313]. Likewise, the electrooptical effect is crucial in the development of *photorefractive effect*, which we will discuss in a following **Section 2.6.2.4**.

In its ferroelectric phase, $LiNbO_3$ presents an index change proportional to the applied electric field, which is known as the *Pockels effect*. This proportionality varies slightly with the crystal composition [314].

The term of **Eq. 63** for this phenomenon is:

$$\widetilde{P}_i(\omega_1) = \widetilde{P}_i(\omega_1 \pm 0) = 2 \cdot \varepsilon_0 \cdot \chi_{ijk}^{(2)} \cdot \widetilde{E}_j(\omega_1) \cdot \widetilde{E}_k(0) \tag{69}$$

Although it is more commonly expressed in terms of change in the refractive index. Thus, it can be described as a third order tensor (r_{ijk}) as follows:

$$\Delta\left(1/n^2\right)_{ij} = \sum_k r_{ijk} E_k \tag{70}$$

Because of the *3m* punctual symmetry, only four of the components of the Pockels matrix (**Eq. 70**) are independent, r_{13}, r_{51}, r_{22} and r_{33}, according to the contracted notation for the electrooptic tensor [227]. Then, the contracted (r_{ij}) tensor writes in terms of these components as:

$$(r_{ij}) = \begin{pmatrix} 0 & -r_{22} & r_{13} \\ 0 & r_{22} & r_{13} \\ 0 & 0 & r_{33} \\ 0 & r_{51} & 0 \\ r_{51} & 0 & 0 \\ -r_{22} & 0 & 0 \end{pmatrix} \tag{71}$$

Expresing **Eq. 70** in terms of **Eq. 71** becomes:

$$\Delta\left(1/n^2\right)_l = \sum_k r_{lk} E_k \tag{72}$$

The values of these coefficients are very high (see **Table V**) and that makes $LiNbO_3$ one of the most employed materials for electro-optic devices.

In determining these electro-optic coefficients (**Eq. 71**), we must take into account the piezoelectric nature of lithium niobate[23] (see the following **Section 2.7.1**), whereby applying an electric field it tends to become distorted, what will also affect the refractive indices.

2.6.2.3 Photovoltaic effect.

This effect was discovered by A. M. Glass, D. von der Line and T. J. Negran in 1974 [232, 315]. They observed that in a $LiNbO_3$ crystal under illumination, if ***+c*** and ***-c*** faces were short-cut, appeared an electric current (j_{ph}), which was proportional to the light intensity (I) and to the absorption coefficient of the crystal (α). It occurs in crystals doped with donor impurities, (for example, Fe ions). The effect consists in the appearance of an electric current induced by light, which ionizes the donor impurities, bringing the electrons to the conduction band. Subsequently, due to the anisotropy of the crystal lattice, the electrons experience the potential difference created by impurities, since the distance between a substitutional defect and the Nb atom is different in $+c$ and $-c$, which causes a net electric current. That is, the photovoltaic current in ferroelectrics is due to the asymmetry of the charge transfer process resulting from the asymmetry of the crystal lattice (displacement of ions along the polar axis), which produces an asymmetric potential and a directional excitation of the photoelectrons [315, 316], thus, the current develops along the polar axis.

Charge carriers contributing to photovoltaic current can be excited from impurity centers within the band gap and directly from the valence band to the conduction band depending on the wavelength of light that is used. It is observed experimentally [315] that the magnitude of the photoinduced current density (j_{ph}) is proportional to the intensity of light that iluminate the material (I), and the absorption coefficient (α), as follows:

$$j_{ph} = \kappa \alpha I \tag{73}$$

being κ the corresponding proportional coefficient, known as *Glass constant*, which is dependent upon the nature of the impurity center, the photon energy of the incident light and the free path length of the carrier. More recently, and in order to get a clearer picture of the material parameters involved in this phenomena, Carrascosa *et al.* proposed a more specific expression [317, 318], which is

$$j_{ph} = e\, L_{pv}\, S_{ph}\, I\, [N_D] \tag{74}$$

where e is the value of the electron charge, L_{pv} is the effective photovoltaic transport length, S_{ph} the photoionization cross section of the active center, I the photon flux and $[N_D]$ the donor concentration ($[Fe^{2+}]$ in the case of $LiNbO_3$).

[23] Since in the experimental measurement of electro-optic coefficients are usually used electric fields that deform the material by *inverse piezoelectric effect*, that is, an applied electric field leads to deformation or mechanical stress.

2.6.2.4 Photorefractive effect. Optical damage.

The photorefractive effect was discovered by Ashkin *et al.* in 1966 [319] in $LiNbO_3$ and $LiTaO_3$. They detected that, when the crystal was illuminated with a high intensity laser beam, the light beam was expanded along the ***c***-direction. This nonlinear optical effect is due to the variation of refractive index produced under illumination in the material. That is, the photorefractive effect is a variation of the refractive index produced by a non uniform distribution of light intensity. The theory explaining this phenomenon supposes that there are impurities in the crystal, donors and acceptors of electrons [320].

To understand this effect, one has to consider different processes that occur under illumination: photoexcitation, transport, recombination, space charge distribution, electric field generation, and finally, refractive index change (by *electro-optic effect*) $\Delta n \sim 10^{-5}$.

The characteristic nonlocal photorefractive effect offers the possibility, if the illumination is not homogeneous, to record a refractive index pattern. This pattern is semi-permanent, but can also be erased with homogeneous illumination, without affecting the structure of the crystal, thus recovering the isotropic distribution of charge carriers, as in other holographic materials. The photorefractive effect is therefore used to multiple applications.

However, sometimes this refractive index change appears non intentionally in other linear or non linear applications of $LiNbO_3$ and generates beam distortions. In these cases, this undesirable effect is called *optical damage*. Basically, optical damage is the distortion of the light beam due to the *photorefractive effect*.

2.7 Lithium niobate electric properties.

The electric behaviour of $LiNbO_3$ is strongly related to the composition and defects of the crystal, both intrinsic and extrinsic (as can be seen in the *photorefractive effect*, **Section 2.6.2.4**). Therefore, from the study of the *electric conductivity*, information from the structure and transport mechanisms can be obtained, also related with the photovoltaic and photorefractive effects already mentioned. At room-temperature, the electric conductivity for congruent $LiNbO_3$ is $\sim 10^{-18}$ ohm/cm [321].

2.7.1 Piezoelectric effect.

This effect consists on the appearance of an electric field in the material caused by the creation of a mechanical deformation on it, and viceversa. Similarly, if you apply an electric field on the material, it will react deforming itself (*inverse piezoelectric effect*). The direct and inverse piezoelectric responses are described by a third-order tensor, δ_{ijk} , as follows:

$$P_i = \delta_{ijk}\sigma_{jk} \tag{75}$$

$$\varepsilon_{jk} = \delta_{ijk}E_i \tag{76}$$

where P_i, is the induced polarization by the effect, δ_{ijk} are the piezo-electric coefficients (see **Table V**) and σ_{jk} the stress tensor. If an electric field with E_i components is applied, an induced stress ε_{jk} will be generated. This effect depends on the stoichiometry of the crystal, decreasing with the increase of lithium concentration [322]. This effect has to be taken into account in the design of electro-optic devices, motion sensors, positioners [323]. For other applications, such as piezoelectric mirrors and components [323], or surface acoustic waves (SAW) devices [161], $LiNbO_3$ piezo-electricity is the key of their functionalism. Also, the piezoelectric effect must be taken into account when designing devices that have to work with the application of external electric fields.

2.7.2 Pyroelectric effect.

It consists in the generation an electric field induced by a variation in the temperature [324], and it is a result of the dependence of the *spontaneous polarization* (P_S) with temperature. In $LiNbO_3$, the pyroelectric effect is due to the movement of Li and Nb ions in relation to the levels of oxygen. As these ions are mobile only along the *c*-axis, the pyroelectric tensor has only cordinate p_3. If the crystal is heated, negative charge accumulates in its **+*c***-face. The dependence of this effect on the stoichiometry of the crystal is the same as in the case of the *piezo-electric effect* [322]. For the congruent composition at room temperature, the relation between the spontaneous polarization change and the change in the temperature is given by [228]:

$$p_3 \equiv \frac{\partial P_S}{\partial T} = -(6.4 \pm 0.6) \times 10^{-5} \frac{C}{m^2 K} \tag{77}$$

Chapter 3

Micro-structuring techniques of Lithium Niobate and waveguides fabrication methods.

3.1 Micro-processing techniques.

3.2 Refractive index tailoring.

So far, throughout this introductory Part we have presented, first the fundamental aspects of ion-matter interaction, as well as the modification of the physical properties of the irradiated materials; and secondly, the superior features of lithium niobate crystal, which give great importance, and make it a key material for fabrication of integrated optical devices. All of this leads us, in a natural way, to seek the synergy of the combination of both, through micromachining and defects engineering by different experimental techniques, obtaining new properties and optimizing the functionalization of the substrate.

In this sense, the term of *waveguide* stands between them, as well as its combination to get more complex devices. Thus, it seems appropriate first to shortly describe the concept of optical confinement in a material. Then, we will proceed to describe briefly the micromachinning techniques, putting a special emphasis on those related to ion beams.

Optical waveguides. Basic concepts.

Optical waveguides are defined like structures that allow the propagation of light being confined in a volume of characteristic dimensions of the order of the wavelength of light ($\lambda \sim 1$ micron), by total internal reflection process. The great confinement gained make the normal optical modes of propagation are few, well-differentiated and accessible to physical measurement and its practical use. Thus, the optical waveguides are essential components of optical and optoelectronic circuits, and integrated optical devices.

The first requisite for which the phenomenon of total internal reflection takes place is that the layer by which the ligh propagates through has a higher refractive index than the surroundings, and secondly, the dimensions of the confinement medium have to be in the order of the wavelength, typically of a few microns. In this medium, which may have different shapes, such as slabs (see **Figure 25.a**), stripes (**25.b**) or even cylinders (**25.c**) (as in optical fibers), light is transported is confined in the waveguide, without radiation into the surrounding media. The inner medium is usually referred to as *core*, *guide,* or *film* in the case of planar waveguides, and the upper and lower media are called the *cover* or *cladding,* and the *substrate,* respectively ($n_g > n_s > n_c$). Waveguides can be assembled on any dielectric material that provides the aforesaid properties, such as lithium niobate ($LiNbO_3$), silica (SiO_2), or lithium titanate ($LiTiO_3$), etc. As far as the core is concerned, it will be fabricated on $LiNbO_3$ substrates by means of different techniques (which will be briefly studied), mainly by doping a region close to the surface of the samples, which induce an increase in the refractive index and form the film or core of the waveguide. We can see in **Fig. 26** a schematic of the profile of an optical waveguide with constant refractive index, and the propagation of light through it, according to the geometric model.

Optical waveguides have been fabricated in various $LiNbO_3$ substrates using various techniques such as metal ion indiffusion (Ti, Zn, and Fe) [325, 326], proton exchange [327, 328], pulsed laser deposition (PLD) [329, 330], liquid phase epitaxy (LPE) [331], direct ultraviolet laser writing [332], ion beam techniques [e.g., ion etching, ion implantation, swift heavy ion irradiation, crystal ion slicing (CIS), etc.] [167, 183, 184, 214, 333], direct femto-second laser writing [334], optical induction (solitons, selective light illumination, etc…) [335], sol-gel [336], or combinations of a few of the above-mentioned methods [175, 217, 337]. The configurations of these guiding structures include not only the basic elements, such as 1D planar

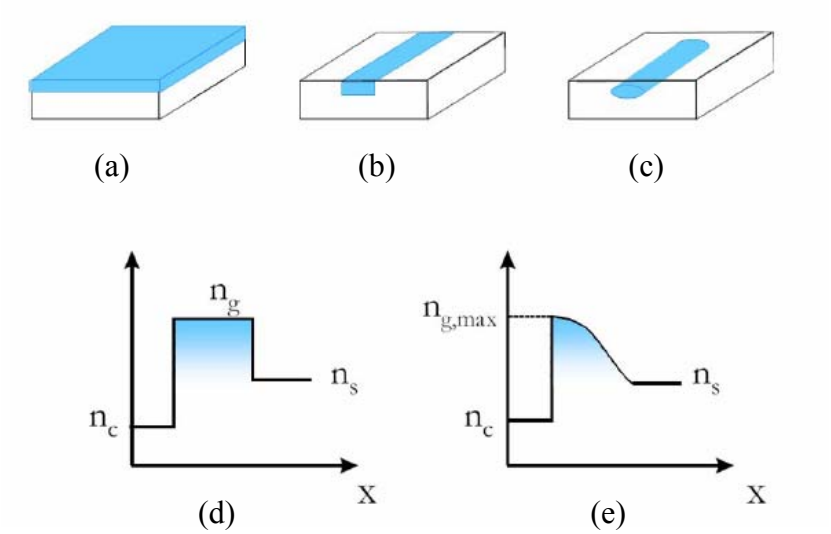

Fig. 25. Different geometries of waveguide structures: (a) planar (b) channel (c) channel and embedded. (d) and (e) Different *index profiles* (d) step profile (d) smooth profile.

waveguides or 2D channel or ridge waveguides, but also more complex structures such as photonic bandgap crystal slabs and microrings/microdisks. Based on these guiding structures, a number of well-designed functional devices such as waveguide modulators, waveguide lasers, electro-optical wavelength filters, nonlinear frequency converters, sensors, and microring resonators have been realized [338].

However, among other drawbacks associated to this techniques, it is worthy to mention that proton exchanged waveguides suffer from degradation of nonlinear optical figure of merit [339]; and, properties of waveguides developed by ion diffusion process strongly depend on exchange conditions as well as the quality of the substrate material [326].

In this sense, the possibility of introducing ion impurity at low temperature with accurate control of the energy, fluences, depth, and lateral concentrations of the dopants, which are sensitive to the waveguide structures, let ion implantation process to be an extensively attractive technique for waveguide fabrication [103, 340]. That is, as "physical" solutions, ion beam techniques offer intriguing versatility for photonic guiding structure fabrication in numerous optical substrates, including crystals, glasses, semiconductors, and organic materials, by means of diverse energetic ion beams with multiple species, energies, fluences, and beam sizes [167, 183, 184, 341-343]. $LiNbO_3$ crystals have received the most attention relative to other materials treated with ion beam technology. Different effects on $LiNbO_3$ lattices and structures are found for ion beams with different parameters as a result of diverse physical mechanisms. Ion-beam- processed $LiNbO_3$ wafers have shown well-preserved optical properties relative to those of bulk crystals. In addition, photonic structures and devices based on ion-beam-processed $LiNbO_3$ waveguides or thin films have exhibited promising prospects for various applications.

In this Chapter, I will focus my attention on photonic guiding structures in $LiNbO_3$ crystals produced by various ion beam techniques, giving a state-of-the-art summary of the field. It is worthy to notice that around 1980 the first pioneering papers concerning the

modification of the physical properties of LN by ion implantation were published [172, 177]. Since then, a variety of ion species and energies have been tested for basic studies on damage

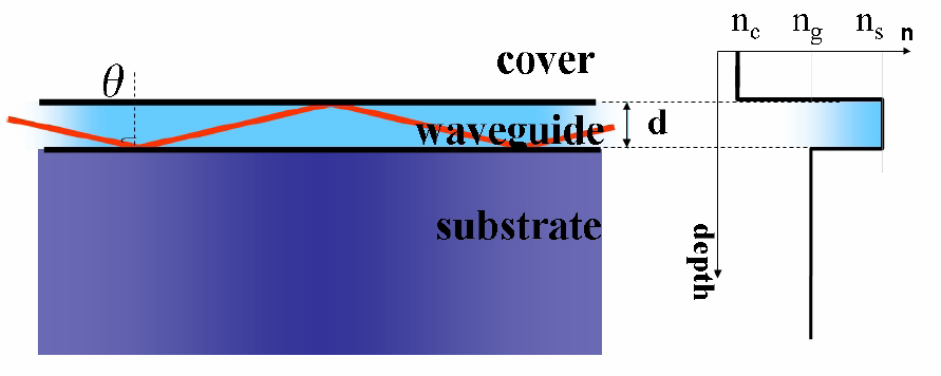

Fig. 26. Index profile and schematic view of a step planar waveguide.

formation by nuclear processes [180, 202, 203] (where the ion fluence of the order of 10^{16} ions/cm^2 or higher are necessary during light ion implantation (H or He) to form waveguides; an optical barrier will be built up on the material on implantation (at the end of the ions trajectory) due to damage induced by nuclear energy loss [111, 344]), and electronic processes in both subthreshold [109, 111, 204, 205] and ion track regime [41-43, 71].

The main modification effect when irradiating crystal samples is the damaging of lattice structure and/or modification of the refraction index, by means of causing nuclear and/or electronic damage. Usually consist on several subsequent processing steps like wet etching or thermal treatment to remove sacrificial volumes or layers [345].

The most important advantages of these ion beam techniques is that they are in a mature stage now, and allow micro-fabricating high quality devices, like very smooth thin films [213, 214, 218, 333, 346, 347], waveguides [348], or two-dimensional crystals [151], only to mention some examples, with spatial resolutions down to the nanometric scale [80, 349]. However, the major shortcoming is that they are intrinsically limited to surface two dimensional patterning, so that a direct three-dimensional structuring of bulk material without affecting its surface is not possible.

Finally, in order to get a more detailed scenario about the physical effects of various ion beam techniques on $LiNbO_3$, the refractive index changes in $LiNbO_3$ crystals induced by various energetic ion beams, and the fabrication methods, properties, and applications of ion-beam-processed $LiNbO_3$ photonic guiding structures, we strongly recommend a very complete and recent review from Chen [185], due to they are not subjet-matter of this Thesis work.

3.1 Micro-processing techniques.

3.1.1 Ion beam techniques.

Energetic ion beams affect the properties of target solid materials, including $LiNbO_3$, via different types of ion-solid interaction, as it has been studied throughout this **Part I**.

Although a great number of techniques can be named based in the ion beam based methods, we only focus our attention in those concerned with the scope of this Thesis work, let´s say ion implantation and swift heavy irradiation. However, **Table VIII** summarizes the various ionbeam techniques that are generally used to modify $LiNbO_3$ crystals, including their main parameters and the primary effects these methods have on the target materials.

Ion beam Techniques	Typical ion energy range	Main effects	Remarks related to $LiNbO_3$ crystals
Ion beam deposition	10 - 100 eV	Film deposition on the target	Not applicable for waveguide formation (poor qualities).
Ion beam etching/milling	0.5 - 2 keV	Etching or milling of the target surface	Relatively small-size ion beams; wide applicability to various substrates.
Ion implantation	100 keV - 6 MeV	Implantation into target, causing nuclear and electronic damages	Nuclear damage creating buried amorphous layer
Swift Ion Irradiation	12 MeV - GeV	Implantation into target, causing nuclear and electronic damages; electronic damage is dominant over the nuclear one.	Electronic damage causing buried amorphous layer even at low dose; threshold of electronic stopping power, $S_{th} \approx 5$ keV/nm.
Crystal Ion Slicing (CIS)	100 keV - 3 MeV	He ion implantation into target; nuclear damage creating strongly buried amorphized layer and bubbles that can be lift-off by wet etching or thermal treatment with wafer bonding.	Relatively large-scale thin films; freestanding membranes with thickness down to a few microns; thinner films requiring wafer bonding.
Focused Ion Beams (FIBs)	500 eV - 2 keV 2 MeV - 3 MeV	Milling or implantation, depending the energy and species of ions.	Beam diameter down to ~10 nm.

Table VIII. Techniques related to energetic ion beams and their main parameters.

3.1.1.1 Ion implantation.

Ions at energies above 100 keV are likely to penetrate into the substrate rather than sputter the target [350, 351]. Implanters, tandem accelerators, and so on are used to generate energetic beams of both light and heavy ions. The incident ions lose their energy mainly through electronic and nuclear energy-transferring mechanisms [183, 350]. The ions, implanted at different stopping powers determined by the ion mass, energy, and target materials, will cause damage through these two mechanisms. High-dose (typically above ~ 10^{16} ions/cm^2) light ions, typically referring to H or He particles, at energies of several keV to MeV induce an obvious

nuclear damage layer buried inside $LiNbO_3$ crystals [177, 183, 184, 286]. The electronic damage of light ion implantation mainly consists of point defects or color centers, which can be removed to some extent by thermal annealing at moderate temperatures of 200 - 400°C [183, 184]. However, heating treatments of $LiNbO_3$ in this temperature range do not destroy the nuclear damaged layers, and at most cause slight recovery of the disordered lattices in the region.

Some "*heavy*" ions, usually referring to *middle-light-mass* ion such as C, N, O, F, Si, Cl, Ni, or Cu at energies of several MeV, can cause relatively strong modifications in the implanted regions in $LiNbO_3$ even at lower doses of ~ 10^{14} atoms/cm^2. In these cases, the electronic stopping powers are much higher than those of light ions [101, 111, 206, 340, 352]. Nevertheless, low-dose heavy-ion-induced lattice disorders can also be removed by suitable thermal annealing (~ 200-300 °C). **Figure 27** shows the distributions of the electronic and nuclear energy deposition of 1.75 MeV He and 5 MeV O ions implanted into $LiNbO_3$ crystals from numerical simulations of SRIM 2008 (stopping and ranges of ions in matter [6]).

In this sense, we have to complete the framework giving a detailed scenario commenting that, effectively it has been explored the use of heavier ions, which in some of these irradiations was beginning to come into play the electronic damage as an important variable. In particular, results have been published with Si 3 MeV ions [206], Cu ions at 0.7, 1.4, 2.6 MeV (a multienergetic irradiation in order to achieve a homogeneous damage from the surface of the glass to the end of the range of Cu ions at 2.6 MeV) [353], O ions at 5 MeV [101], B ions at 3 MeV [208], Ni ions at 3 MeV [354], and C ions at 6 MeV [209]. **Figure 28** shows the electronic and nuclear stopping-power (S_e, S_n) of all the mentioned irradiations, where we found that S_e has much higher values than in the case of He implantations, because they are ions with a higher Z value (see **Eq. 6** and **9**). This, coupled with the fact that in order to increase the extraordinary refractive index of $LiNbO_3$ (as will be discussed later), the damage must be less than that the amorphization produces, makes the necessary fluences to produce waveguides by this menthod (~10^{14} at/cm^2), are several orders in magnitude lower than those used in the implantation method.

On the other hand, it is worthy to notice that, since $LiNbO_3$ is a crystalline material, ion beams with bombarding directions that are normal to the surface plane will create a "*channeling*" effect of incident ions into the substrate, particularly when the crystal wafers are cut along their crystallographic orientations[24] [355, 356]. This effect will bring about undesirable problems when one wishes to have accurate control of the implanted ion profiles in the crystal. In practice, the ion beams are usually tilted at a slight angle (for example, ~ 7°) from the sample surface normal planes for implantation into $LiNbO_3$ crystals, by which the channelling effect can be minimized [286]. Investigations of channeling irradiation in $LiNbO_3$ have also revealed that on-axis implantation causes a deeper damage peak and less damage than in off-axis cases [355, 356].

[24] A more detailed study on this effect will be given in a following Chapter. Really, we will use its properties not only during the irradiation samples, neither as characterization technique of the induced irradiation damage (RBS/C, Rutherford Backscattering Spectrometry in channeling configuration). Nevertheless, the effect of "ion channelling" during the irradiation with shift heavy ions is considered negligible.

We have to remember that, for the purpose of photonic applications, ion implantation has proven to be an efficient method for fabricating optical waveguide structures in many materials due to its accurate control of the refractive indices of the substrates [183, 184]; in fact, in some crystals with low phase transition temperatures or very stable chemical properties, ion

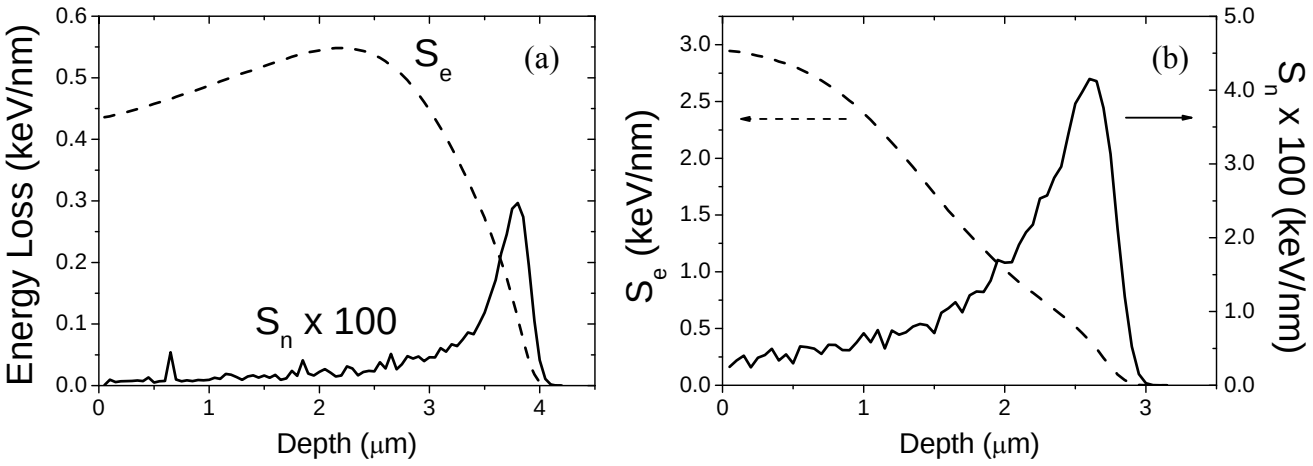

Fig. 27. Distributions of electronic (dashed lines) and nuclear (solid lines) energy deposition of (a) 1.75 MeV He and (b) 5 MeV O ions implanted into $LiNbO_3$ crystals calculated by SRIM 2008 [6].

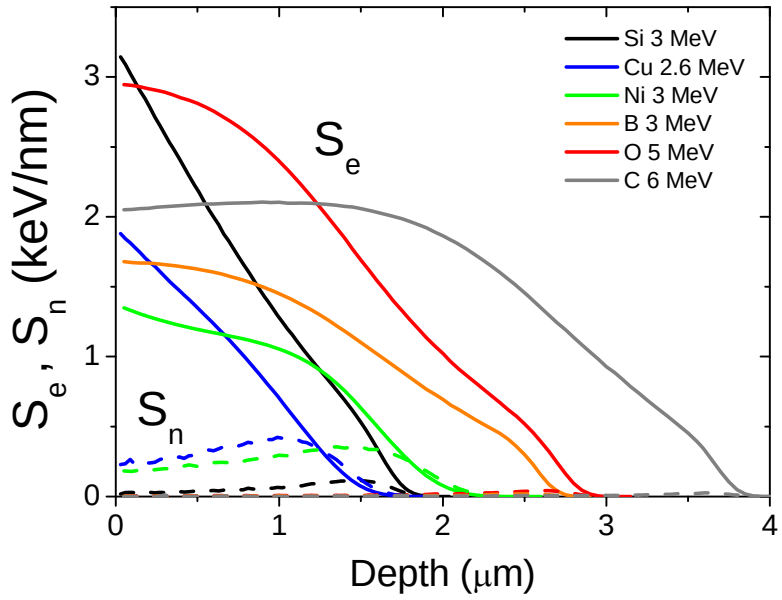

Fig. 28. Distributions of electronic (solid lines) and nuclear (dashed lines) energy loss of ions and energies listed in the leyend into $LiNbO_3$ crystals calculated by SRIM 2008 [6].

implantation is one of the most effective techniques to guide structures within them [357, 358]. $LiNbO_3$ waveguides produced by the implantation of light and heavy (medium-mass) ion beams have been realized for many years and exhibit attractive properties for various photonic applications.

3.1.1.2 Swift ion irradiation.

For the purpose of optical waveguide fabrication, ions with energies as great as 1 MeV/amu have been used, in the case they have energies greater than that value, they are usually called "*swift*" ions; in some cases of material modification, the minimum threshold value is ~ 5-6 KeV/nm, corresponding to ~ 0.1 MeV/amu for the projectile energy, like in the case of $LiNbO_3$ [167]. There is an increasing demand for such high energetic ion beams for physics as well as material science, particularly in the case of heavy ions. In these cases, the electronic damage created by the irradiation is dominant over the nuclear damage along the trajectory of the incident ions [41, 42, 103, 104, 109, 122, 348, 349, 359, 360]. **Figure 29** shows the distribution of the electronic and nuclear energy deposition of 46 MeV Cl ions into $LiNbO_3$ crystals. Each incoming ion creates an amorphous latent track with a diameter of a few nanometers along the ion trajectory. At ultralow doses (~10^{12} ions/cm^2 or even lower), these tracks do not overlap [348, 360], while in the case of higher fluences, the nanotracks may have a homogenous superposition, forming a strongly damaged layer buried at some depth beneath the sample surface [103, 122].

Swift heavy ion irradiation on $LiNbO_3$ crystals was first performed by Canut *et al*. [42] at GANIL using Sn, Gd, and U ions in the energy range of GeV to modify a crystal surface. At nearly the same time, Ramos *et al.* [41] observed diffusion enhancement of Eu ions for GeV Ni-ionirradiated $LiNbO_3$ samples. Although in those cases, the doses of these heavy ions were very low (typically 10^{11} - 10^{12} ions/cm^2), significant lattice disorders were induced in the $LiNbO_3$ crystals due to electronic excitation [42]. Recently, swift heavy ions such as F [103], Si [109, 122], Cl [348, 349, 360], or Cu [349] at energies of tens of MeV have been used to irradiate $LiNbO_3$ samples for theoretical and practical investigations. Various nanostructures and optical waveguides have been formed using this method under different irradiation conditions. For example, Garcia-Navarro *et al.* [349]applied 50 MeV Cu ion irradiation (at a dose of ~ 10^{11}-10^{13} ions/cm^2) to bombard *z*-cut $LiNbO_3$ crystals, forming hillocks with a radius of several nanometers, and, following chemical etching, created nanopores on the top of the sample surface. In addition, electronic damage layers induced by swift heavy ion irradiation were also observed in same samples. It was found that the in-depth position of the amorphous layer could be tuned by selecting suitable ion species and energies, and the thickness of the layers increases with the ion dose [104, 167]. The irradiated damage layer can be used as a "thick" barrier that can confine light propagation to the surface (i.e., air).

3.1.1.3 Ion beam-enhanced etching.

The technique known as "ion beam-enhanced etching" (IBEE) is a combination of ion implantation and chemical wet etching [175, 176, 211, 212, 216, 361, 362]. The mechanism is somewhat similar to the wet-etching-related crystal ion slicing (CIS) technique.

Considerably large numbers of defects are induced by the ion irradiation due to energy transfer to the crystal lattices, forming highly damaged or even amorphized regions. This energy transfer may be due to nuclear energy deposition (in low energy cases) [176, 211], electronic damage (in the case of swift heavy ion irradiation) [218, 361], or a synergy of both effects in moderate energy regimes [175, 212, 216]. One of the direct consequences of the highly

damaged regions is that chemical resistance is considerably reduced; as a result, the irradiated regions can be removed by wet chemical etching. The key factor in IBEE is the generation of a damaged layer in selected regions. For $LiNbO_3$ wafers, many ion species, e.g., He (E = 40 keV), Ar (E = 60-600 keV), O (E=0.5 and 5 MeV), Ti (E = 12.5 MeV), Si (E = 3.6 MeV), have been

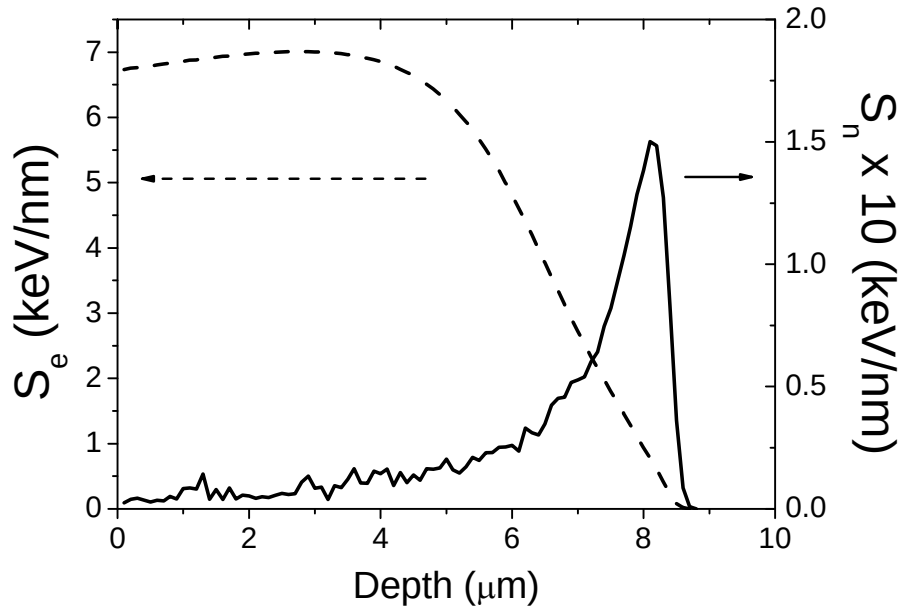

Fig. 29. Distribution of electronic (dashed line) and nuclear (solid line) energy deposition distribution of 46 MeV Cl ions into the $LiNbO_3$ crystals calculated by SRIM 2008 [6].

used for the first step of ion irradiation by different groups [175, 176, 211, 212, 216, 361, 362]. The bombardment of these ions creates damaged layers in $LiNbO_3$ to some extent, and the addition of liquids such as HF or HNO_3 will preferably etch the irradiated regions.

Normally, the etching rate is mainly determined by the damage density and the crystallographic orientation. In addition, it has been shown that the irradiation temperature is another parameter that influences the etching rate of $LiNbO_3$ [176]. High-temperature irradiation brings out partial lattice recrystallization through annealing effects, which requires ion irradiation at higher fluences for the same level of damage achieved by ion bombardment at low temperature [362].

3.1.2 Chemical etching.

It is worth noting that, although this issue will be more fully developed later, herein we will briefly show wide variety of chemical scenarios combined with different techniques of micro-structuration of LN that exist reported in the literature. All this understood as an advance of a more detailed study carried in two ways: on one hand, based on the differential chemical behaviour shown by the different facets (crystallographic orientations) of the LN substrate, and another one focused on the chemical development of nanostrutures produced after ionic irradiation, and the subsequent optimization of the process through the modification of different variables (chemical echants, ratios between them, physical variables – liquid/vapour mixture,

temperature, etc…, as well as the processes related to the irradiation parameters: ion´s energy, stopping power (S_e), ion range, ... etc.

We have to say that chemical wet etching of $LiNbO_3$ has been mainly investigated in the context of ion beam processing or periodic domain poling, so that it is used to reveal volumes whose external face presents a different etchability, mainly as a result of lattice changes such as amorphization or different optical axis orientation. The main etching agents used so far in $LiNbO_3$ are: $HF:H_2O$ mixtures in different concentrations [212, 215], $HF:HNO_3$ in mainly (1:2) mixture [80, 345, 349, 363], and $HF:H_2SO_4$ in (1:2) mixtures [364]. The ***+c***-face normally presents a much higher resistance to HF solutions than the ***–c***-face. Enhancements of the etching process have been reported by means of low-temperature (175-275 ºC) annealing after processing with ion beams [215], or by ultrasonic baths and/or heating during the wet etching process [364].

3.1.3 New synthesis techniques of nano-structured $LiNbO_3$.

3.1.3.1 Nanotechnology.

It is nowadays well known that properties of materials on the nanoscale can be quite different from their macroscopic counterparts. One reason for that is the increasing surface to volume ratio which enhances the influence of surface properties. Also, as one approaches the molecular scale, the particle nature of matter becomes relevant in physical processes, for example as the dimensions of electronic devices approach the electron mean free path length, or those of ionic devices reach the distances between ions in solution.

Nanotechnology is a rapidly developing field with great potential for applications in many areas, in particular in electronics and information technology [365]. The construction of small nanodevices is technologically very difficult and no unique solution has been found so far. Often, lithographic or self-assembly methods are applied to construct these nanodevices.

Heavy ion tracks in dielectric films offer unique possibilities for the realization of nanometer-sized structures. In combination with lithography they open up new ways for biofluidic, electric, magnetic and optic device fabrication. Heavy ions produce along their path a nanometer channel of modified material with track diameter between 1 and 10 nm, adjustable by the chosen ion and its kinetic energy. The latent tracks created in irradiated materials may be used directly, e.g., creating conducting and magnetic nanowires in insulating matrices or they may be selectively etched into pores and then used for nanobiofluidic applications or as templates for growing micro/nanostructures. Commercial irradiation can produce ion track filters with pore density ranging from single pore to 10^8 pores/ cm^2.s. Ion track technology offers a broad variety of scientific challenges. Heavy ion tracks can be used as a tool kit for fabrication of nanodevices. The scientific innovation is in the short time-scale especially on the ion track enabling of optical lithography. In the long time-scale, the use of heavy ion material modification in latent ion tracks has enormous potential in creating novel nanomaterials.

3.1.3.2 The case of Lithium Niobate.

As it has been explained above, $LiNbO_3$ is one of the most versatile optical materials due to its adequate combination of non-linear and ferroelectric properties, which has led to a deep investigation of its properties over more than 40 years. All along this introductory Part, references have been given referring to bulk sample devices, however, it is worth mentioning some alternative synthesis approaches which have been recently explored in the context of nanostructure material research.

During the last decade considerable interest has been given to the fundamental application of the $LiNbO_3$ properties into nano-structured materials such as photonic crystals and other nanostructures, due to their potential application in nano-photonic devices. The interest relies on the fact that an enhanced behaviour relative to their bulk counterparts is expected, emerging from the dimensional confinement of light interactions in the media.

As it has been shown, most of the fabrication techniques rely on the growth of samples and subsequent micro-structuring approaches for obtaining thin films or micro-structured devices from them. To avoid further processing of $LiNbO_3$ to achieve nanoscale dimensions, some new approaches have recently been addressed which could allow the synthesis of crystalline nanosized or nanoporous $LiNbO_3$ crystals.

Lately, a great effort has been made by researchers, trying to go to smaller and smaller dimensions, structuring lithium niobate surfaces. For optical waveguide applications smooth side walls and surfaces are needed to keep optical losses as small as possible. These are then used to tailor ridge waveguides, T-junctions, V-grooves and other features. Structures with micrometric and even submicrometric scales in $LiNbO_3$ with high aspect ratios (*A.R.*, defined like: diameter of a structure/depth or height) have been reported. The highest aspect ratios in $LiNbO_3$ (~5) were produced either by ion beam enhanced etching (IBEE) [241], focused ion beam (FIB) milling combined with subsequent reactive ion etching [151], electric-field-assisted proton exchange [366], and differential etched inverted ferroelectric domains on electric field periodically poled lithium niobate (PPLN) [367]. Among these techniques the first named is most promising, because it has high selectivity, independence of the crystal symmetry and short production times. Multiple implantations with different energies and fluences can be used to obtain deep structures with smooth bottoms and vertical walls. Thus, the achievement of nanometric structures in $LiNbO_3$ is a challenging problem, because the material is very resistant to standard etching technologies. However, the fabrication of nanostructures by ion beam modification of materials (IBMM) has become a rather common technique [32].

As mentioned, ion irradiation modifies the physical and chemical properties of $LiNbO_3$ such as the refractive index, the etching behaviour, the chemical stability and the density due to radiation damage generating defects, which can be caused by both nuclear and electronic energy loss of the impinging ions [111, 171-182]. Thereby it is utilized, that the defects formed due to ion irradiation reduce the chemical resistance of the crystal. Thus the irradiated regions can easily be removed by means of wet chemical etching solution. However, in order to apply IBEE successfully, the alteration of the etching rate with the damage formation depending on the irradiation conditions and with the etching parameters must be understood and controlled.

One of the strongest motivation for this research work is to find new features to be used in waveguides concerning the fabrication of chemically etched single ion tracks (nanopores) that

may enhance nonlinear optical effects or plasmons when refilling these nanostructures with metals (e.g. Au, Ag, Pt, Cu, etc.).

Recent achievements include the optimization of pores sizes in $LiNbO_3$ with tailored structural properties, which could prove useful for photonic applications and waveguide sensors, and, in addition, the subsequent growth of $LiNbO_3$ crystalline nanoparticles, showing control over the growth length along the polar axis.

In any case, in order to apply IBEE successfully for all these possible applications it is crucial to have a fundamental understanding of the etching process; besides, a systematically study must be carried out to control the damage formation, which depends on the irradiation conditions and the etching parameters.

3.2 Refractive index tailoring.

As it has been studied in a previously Section, $LiNbO_3$ is a negative birefringent crystal, with a difference between the extraordinary and ordinary index $\Delta n = n_e - n_o \approx -0.08$ (in the congruent composition) at a wavelength of 632.8 nm. In this Section, several types of refractive index profiles of lithium niobate waveguides generated using different ion beam techniques will be briefly presented.

3.2.1 "Barrier"- type index profiles.

The optical barrier refers to low refractive index layers buried inside the substrate generated by nuclear damage through energy transfer from implanted ions (particularly light ions, e.g., He or H) to the target matrix [183, 184]. These elastic collisions between the incident ions and target nuclei mainly occur at the end of the ion range, forming a disordered layer accompanied by a reduction in the physical density of the substrate and resulting in a decrease in the refractive index. Meanwhile, within most regions along the incident ions' trajectory inside the target, the nuclear damage is quite small; therefore, there is almost no change (or only slight changes) in the refractive index. In this way, the regions between the surface of the substrate (i.e., air) and the optical barrier are surrounded by low-index regions, which act as waveguides [183]. These barrier-confined refractive index profiles are quite typical for ion-implanted waveguides in various materials, and are particularly common for those related to light ion implantation [183, 184].

Fig. 30 (a) shows a typical barrier-type profile of the ordinary index (n_o) of $LiNbO_3$ waveguides produced by the implantation of protons or He. The n_o value in the waveguide regions only slightly decreases after implantation (typically $\Delta n_o \sim$ -0.1 % to - 0.5%), while in the barrier regions a large reduction in n_o is found, ranging from -1% to -5% depending on the ion dose [177, 183, 184, 286]. In this case, the low index barrier is the only confinement for the waveguide, which normally results in relatively strong light leakage through the barrier into the substrate regions due to optical *tunneling* effects [183]. This phenomenon is obvious for all barrier-confined waveguides, particularly when the barrier layers are very thin [183]. Nevertheless, by broadening the barrier (through multiple-energy ion implantations, see **Fig. 30 (a)**, the tunneling effect can be considerably reduced, resulting in a better confinement of the

light modes. It should be stressed that for normal barrier distributions, the index value does not decrease significantly in the waveguide regions, just as in the case of n_o for light ion-implanted $LiNbO_3$ waveguides.

However, for heavier ions such as O, Si, or P, implantation at energies of several MeV will induce large reductions (typically from ~ -2% to -3%) in the waveguide regions [207], while a larger n_o decrease (typically ~ -5%) occurs at the end of the ion track (**Fig. 30 (b)**). This

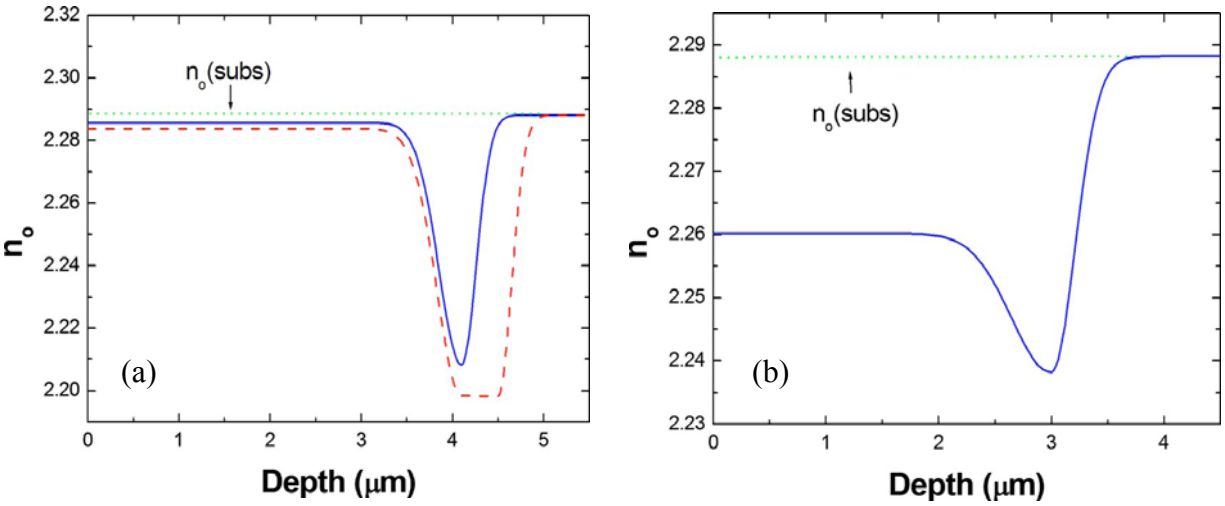

Fig. 30. Typical barrier-confined n_o profile of (a) light ion-implanted $LiNbO_3$ waveguide. The solid and dashed lines represent the single and multiple-energy implants configurations, respectively. (b) after heavy ion implantation in $LiNbO_3$.(from Ref. [185]).

non-typical barrier-type index profile theoretically makes the confined structures act as waveguides; however, more leakage of light into the substrate will occur due to the smaller index difference between the waveguide and the barrier, as well as the poor transmission properties. Therefore, in this a configuration, waveguides are not adequate for practical applications due to very high propagation losses. In practice, almost no transmission lines for guided light have been observed for these waveguides in $LiNbO_3$, even for samples produced with long-time annealing at sufficiently high temperatures.

3.2.2 "Enhanced-well + barrier-type" index profiles.

The mechanism for modification of the extraordinary refractive index (n_e) is much more complicated. The implantation of light ions (He or H) will cause positive changes in n_e (for example, Δn_e ~ +0.5 %) in the near-surface regions, resulting in an enhanced index well. At the end of the ion track, a negative index barrier, just as in the case of n_o profiles, is built up due to nuclear energy deposition (nuclear damage) [183]. This profile is called a typical "enhanced well + barrier" distribution (**Fig. 31 (a)**). On the other hand, for the implantation of heavy (medium-mass) ions (with energies of several MeV) such as C, O, or Si, a larger increase in n_e (up to ~ 2 %) will occur in the near-surface region, while a negative index barrier might be constructed at the end of the ion range inside the crystal (**Fig. 31 (a)**).

As a representative example of the manufactured waveguides described by increasing the extraordinary refractive index, n_e, it is shown in **Figure 31 (b)** (from reference [101]) the n_e profile of 5 MeV at $1x10^{14}$ at/cm^2 implanted $LiNbO_3$ optical waveguide. Note how an increasing value of the index appears at the surface, with $\Delta n_e \approx 0.03$. Moreover, it also created a low index value to the depth where the ions are slowed down completely (≈ 2.6 μm), i.e., where the collisions of incident ions with the lattice atoms happens, responsible for the nuclear stopping (see **Figure 28**).

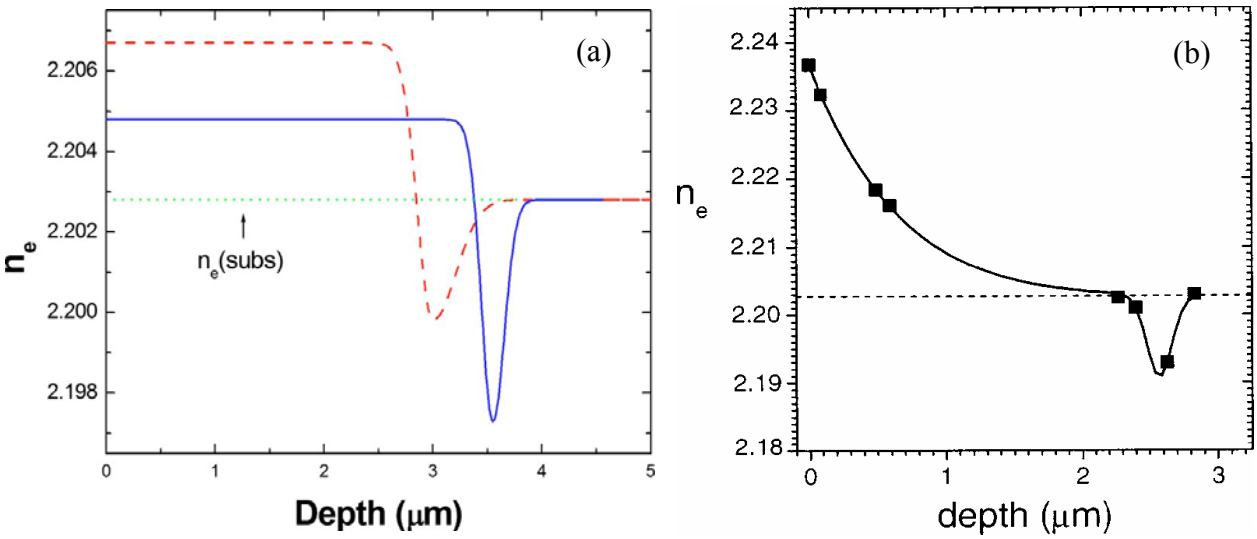

Fig. 31. (a) "Enhanced well+barrier" confined n_e profile of $LiNbO_3$ waveguide formed by light (solid line) and heavy (dashed line) ion implantation. (from Ref. [185]). (b) Extraordinary index (n_e) profile (solid line) of 5 MeV, $1x10^{14}$ O/cm^2 implanted $LiNbO_3$ The dashed line represents the bulk value (from Ref. [101])

For H- or He-implanted $LiNbO_3$ waveguides, the light confinement is achieved by the combination of an enhanced well and a negative barrier, although theoretically, the enhanced well is sufficient for a fairly good restriction of light propagation [183, 184]. As for heavy-ion-implanted $LiNbO_3$ waveguides, the large positive index well is mainly responsible for the light confinement, through which the light inside the waveguide can propagate in a non-leaky manner [184].

Respect to the mechanism by which such a n_e profile is produced, we have to say that it has not been well characterized, and none of the potential explanations have reached the wide level of acceptance of the barrier model. Barriers with reduced refractive indices are constructed at the end of the ion range, i.e., in the nuclear damage regions, in which the elastic energy deposition caused by the collisions of incident ions with target atoms is dominant over the electronic damage. Therefore, it is reasonable to conclude that the n_e barrier comes from the same source as the n_o one. The key problem, which is still under debate to some extent, lies in the mechanism of positive n_e well formation. Nevertheless, one may assume that the n_e increase is somehow related to electronic-energy-deposition-induced effects on the $LiNbO_3$ cell matrix since it happens in the electronic damage region (i.e., in the guiding layer).

In any case, since the $LiNbO_3$ crystal lattice has a network of oxygen octahedrons (BO_6) and since most of the optical properties of oxygen-octahedron ferroelectrics depend on the presence of BO_6 octahedron building blocks [368], it seems reasonable to study the changes in refractive index of ion-implanted $LiNbO_3$ waveguides by invoking the lattice damage in these cells induced by the ion implantation process. Jiang *et al.* [369] have proposed a theoretical model based on these "lattice damage" effects.

3.2.3 Swift heavy ion-irradiated waveguides.

Recently, swift ion irradiation in $LiNbO_3$ has received considerable attention due to its novel modification of structures and refractive indices of the crystal [80, 103, 104, 109, 122, 167, 348, 349, 359, 360]. In these cases, the electronic energy deposition is dominant over the nuclear one, and the refractive index changes are mainly due to the electronic-damage-related structural modifications. In this sense, it is worthy to remark the research carried out by Olivares *et al.* [167], who studied swift heavy ion-irradiated $LiNbO_3$ waveguides and related physical mechanisms. They found that the electronic stopping power (S_e) of the incident ions is a key parameter that affects the structures and refractive indices of the $LiNbO_3$ substrate. Unlike the ion implantation normally used for $LiNbO_3$ waveguide formation, which has a low S_e value, the swift heavy ions usually possess considerably high electronic stopping powers. As it has been discussed throughout this introductory Part, there is an *intrinsic* threshold value S_{th}, which strongly influences the formation of nanometer-sized amorphous tracks occurring during the irradiation process. For $LiNbO_3$, $S_{th} \approx 5$ keV/nm. [104, 167].

3.2.3.1 "Buried amorphous layer" confined waveguides. Swift ion irradiation at low fluence: high index jump waveguides.

If ions have S_e values lower than S_{th}, the tracks with partial damage occur along the trajectory of the incident ions. When the dose is sufficiently high (for $LiNbO_3$, $\sim 10^{14}$ - 10^{15} ion/cm^2), the tracks overlap due to damage accumulation even in low energy cases, forming homogenous amorphous layers [103]. This may be due to a so-called "*preamorphization*" step [104, 122], in which the amorphization occurs even for $S_e < S_{th}$, and the amorphous layer thickness increases with the ion dose. If we recall the work of Bentini *et al.*, [111] the near-surface damage of O-ion-implanted $LiNbO_3$ occurs when $S_e > 2.2$ keV/nm, which may be classified as such a process. **Figure 32 (b)** shows the n_e and n_o profiles of 22 MeV F-ion-irradiated $LiNbO_3$ waveguides. As it is indicated, the profile has a "*steplike*" distribution with sharp boundaries. Both n_e and n_o have the same value, i.e., ~ 2.10, in the amorphous region, while the surface indices for both n_e and n_o are only slightly modified. In this way, the waveguide layer is therefore confined in the region surrounded by the surface (air) and the buried amorphous layer.

3.2.3.2 Swift ion irradiation at ultra-low fluences: nanostrutured gradient index waveguides.

On the other hand, when ions with $S_e > S_{th}$ are used for irradiation of $LiNbO_3$ crystals, amorphous tracks with dimensions of a few nanometers will be created [80, 349], and at ultralow fluences (10^{12} ions/cm^2), [360] effective waveguides can be formed with buried damage layer confined refractive index profiles. In this case, each nanometer-sized latent amorphous track creates a single ion impact with an isotropic refractive index ($n_o = n_e$ =2.1). The radius of each track increases monotonically with S_e, forming a depth-shaped distribution [360]. In this way, the refractive index of the irradiated regions will follow the electronic

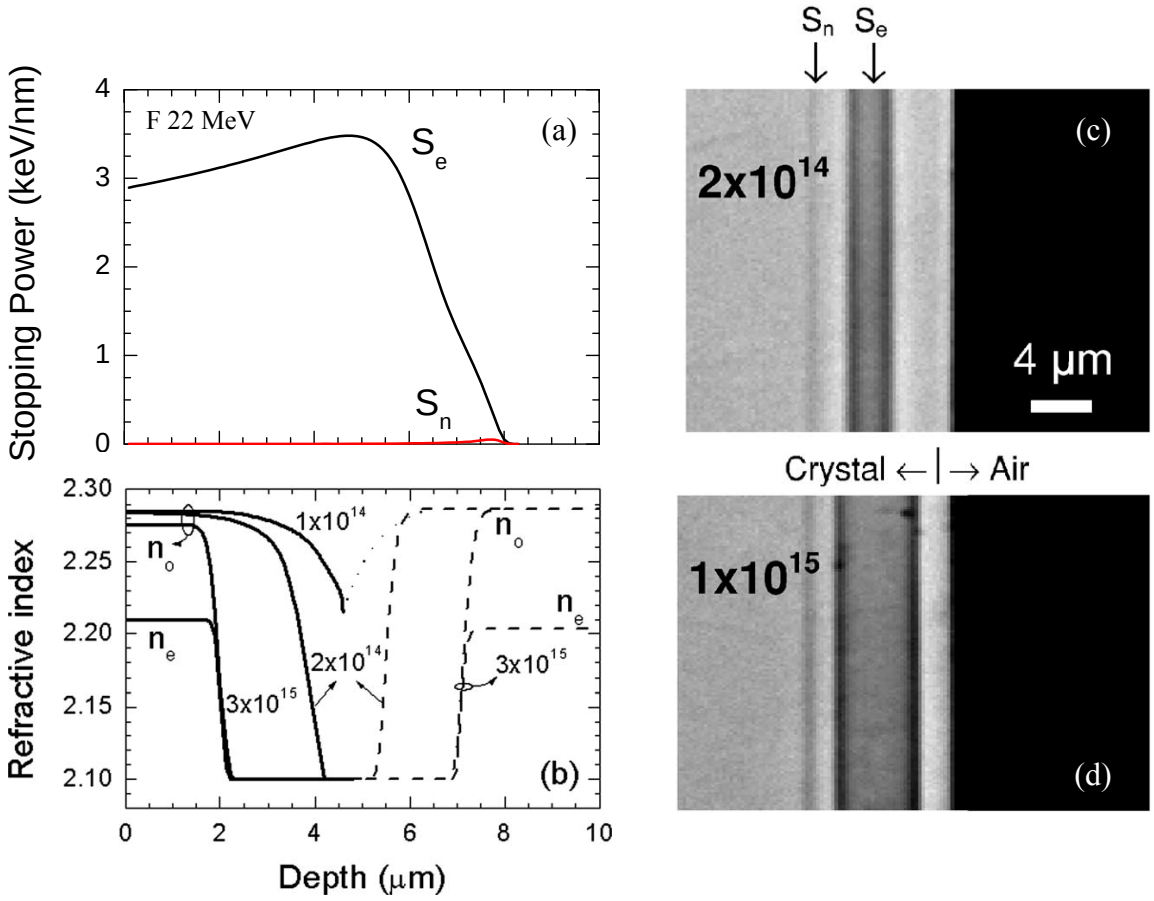

Fig. 32. (a) The electronic stopping power for F^{4+} at 22 MeV in $LiNbO_3$ [103] versus the crystal depth, (b) The refractive index profiles (n_o and n_e) of *z*-cut samples with this irradiation at different ion fluences (at/cm^2) [103], (c) and (d) Optical microphotographs of a polished *y*-cut cross section for samples irradiated with F^{4+} at fluences of 2 × 10^{14} (c), and 1 × 10^{15} (d). The depths of the maximum electronic stopping power, (S_e) and nuclear stopping power (S_n) are indicated with arrows [370].

damage (S_e) behaviour. **Figure 33 (c, d)** shows the refractive index profiles of 46 MeV Cl-irradiated $LiNbO_3$ waveguides in $LiNbO_3$ at a fluence of ~ 10^{12} ions/cm^2. It should be also noted that both n_e and n_o are strongly related to the ion fluence, and before they reach the amorphous value (~ 2.10), the higher doses create a larger index decrease in the damage layer.

In addition, it is possible to use a much higher energy for ion irradiation, e.g., several GeV, to form "thick" waveguides (tens of microns) for applications in the infrared wavelength bands, like can be found in one of our last publication [188]. In this way, since $S_e >> S_{th}$, a lower dose is required for waveguide formation in $LiNbO_3$.

Specifically, heavy mass ions, Kr and Xe, having energies in the ~10 MeV/amu range have been used to produce thick planar optical waveguides at the surface of lithium niobate. The waveguides have a thickness of 40-50 micrometers, depending on ion energy and fluence, smooth profiles and refractive index jumps up to 0.04 (λ = 633 nm). They propagate ordinary and extraordinary modes with low losses keeping a high nonlinear optical response (SHG) that makes them useful for many applications. It implies the generation of a buried low-index layer (acting as optical barrier), made up of amorphous nano-tracks embedded into the crystalline lithium niobate crystal. This would allow the fabrication of much thicker waveguides (up to tens

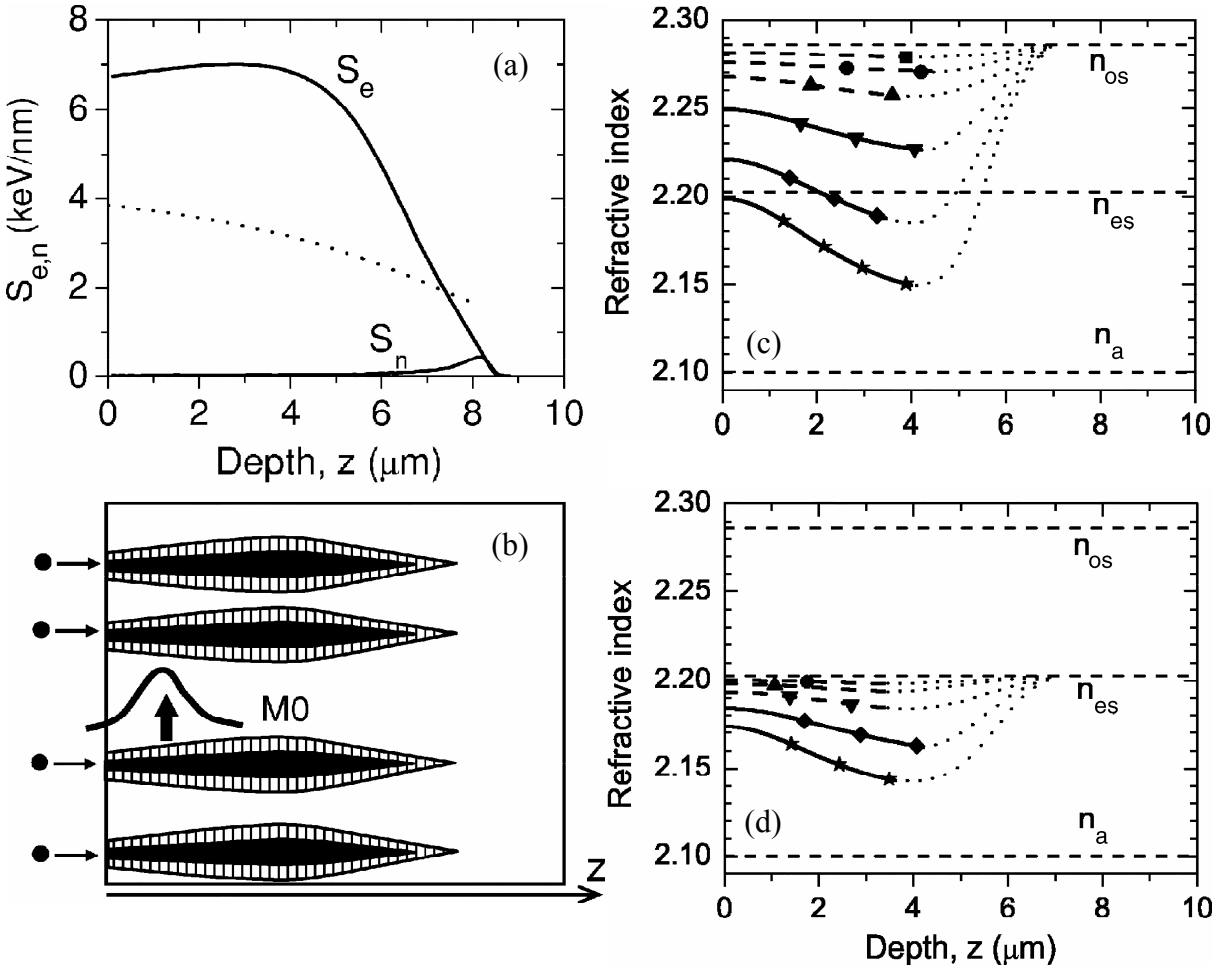

Fig. 33. (a) Electronic, S_e, and nuclear, S_n, stopping power curves for Cl 45.8 MeV in $LiNbO_3$ calculated with SRIM 2008. The dotted line shows the corresponding "amorphization" threshold curve from the data collected in Ref. [31]. (b) Schematic depth morphology of the tracks, showing the core (black) and the surrounding halo (dashed). (MO) stands for a probable light profile behaviour in this waveguide. (c) ordinary and (d) extraordinary refractive index profiles of samples irradiated with Cl 45.8 MeV at different fluences (at./cm^2) of 5 x 10^{11} (squares), 1 x 10^{12} (circles), 2 x 10^{12} (up triangles), 4 x 10^{12} (inverted triangles), 8 x 10^{12} (diamonds), and 1 x 10^{13} (stars). Horizontal dashed lines show the refractive index values for the crystal (n_{os} and n_{es}) and

amorphous (n_a) regions. A guess of the expected refractive index profiles behind the minimum is also plotted with a dotted line. (All these results have been taken from reference [102]).

of microns) with ultralow fluences (< 10^{12} cm^{-2}). Such thick optical barriers may be useful in the mid-IR e.g. for astrophysical applications (or "Astrophotonics") [189, 190]. Moreover, in this energy range ion trajectories are more straight that would allow for better resolved waveguides patterns.

As a summary we can say that, swift heavy ion irradiation presents a novel way to fabricate waveguides in $LiNbO_3$ [167, 371]. In this case of heavy ions, the electronic damage is the main cause of the index change. This technique overcomes some of the disadvantages of light ion implantation, such as the large fluence of ions required (10^{16} - 10^{17} cm^2) and the contamination of the material with the irradiated ions in the optical barrier. Irradiation parameters such as ion species, energy, and dose must be chosen by carefully considering the S_e

Ion beam techniques	Typically used ion species	Typical ion energies	Typical ion fluences (at/cm^2)	Typical postannealing conditions
Light ion implantation	H and He	100 keV - 3 MeV	~ 10^{16} - 10^{17}	200 - 450 ºC, Δt = 30 min.- several hours in air.
Heavy (medium-mass) ion implantation	C, N, O, F, Si, P, Cu, Ni, etc.	2 - 7 MeV	~ 1 x 10^{14} - 2 x 10^{15}	200 - 350 ºC, Δt = 30 min.- several hours in air.
Swift heavy (medium-mass) ion irradiation	O, Si, Cl, Cu, etc.	12 - 50 MeV	~ 10^{12} - 10^{14}	200 - 350 ºC, Δt = 30 min.- several hours in air.

Table IX. Summary of typical parameters of methods that have been used for 1D waveguides in $LiNbO_3$ by ion beam techniques.

values of the ions in $LiNbO_3$ crystals.

On one hand, when the incident ions have $S_e < S_{th}$, tracks with partial damage will be created along the ion trajectory, and at sufficiently high doses (10^{14} - 10^{15} ions/cm^2), a homogenously amorphous layer of damage accumulation will be generated within the crystal. This amorphous layer is related to electronic energy deposition, and its thickness can be tuned by choosing suitable ion fluences. Moreover, the profile index shapes obtained with this new technique are sharper, the index change is higher, and the barrier can be thicker.

On the other one, when the energy increases further, i.e., the ions become faster, $S_e > S_{th}$, the fluence required for waveguide formation is remarkably reduced to ~10^{12} ions/cm^2 or even less. The advantage of this over threshold irradiation is the avoidance of overlapping nanotracks, which requires ultralow doses. Subsequent annealing treatments at ~ 200-350 °C will improve the swift heavy ion-irradiated waveguide quality [167, 371].

Part I. References.

[1]C. Lehman, *"Interaction of radiation with solids and elementary defect production"*, Vol., (Ed.), North-Holland Publishing Company, 1977.

[2]J.F. Ziegler, J. P. Biersack and U. Littmark, (Ed.), *The Stopping and Ranges of Ions in Solids*, Pergamon Press, New York, 1985.

[3]G.H. Kinchin, and R. S. Pease, *"The displacement of atoms in solids by radiation"*, Rep. Prog. Phys. 18 (1955) 1.

[4]J.P. Biersack, and L. G. Haggmark, Nucl. Instr. and Meth. B 174 (1980) 257.

[5]R.L. Fleischer, P. B. Price, and R. M. Walker, *"Nuclear Tracks in Solids: Principles and Applications"*, Vol., (Ed.), University of California Press, Berkeley, CA, 1975.

[6]J. Ziegler, computer code SRIM version 2008, (http://www.srim.org).

[7]R. Katz, K. S. Loh, L. Daling and G. R. Huang, *"An analytic representation of the radial distribution of dose from energetic heavy ions in water, Si, LiF, NaI and SiO_2"*, Rad. Eff. and Defect in solids 114 (1990) 15-20.

[8]B. Gervais, and S. Bouffard *"Simulation of the primary stage of the interaction of swift heavy ions with condensed matter"*, Nucl. Instr. and Meth. B 88 (1994) 355-364.

[9]M.P.R. Waligorski, R.N. Hamm and R. Katz, *"The radial distribution of dose around the path of a heavy ion in liquid water"*, Nucl. Tracks Radiat. Meas. 11 (1986) 309-319.

[10]H. Bethe, Handbuch der Physik 14 (1933) 491.

[11]J.F. Ziegler, *"Stopping of energetic light ions in elemental matter"*, J. App. Phys. 85 (1999) 1249-1272.

[12]L.C. Northcliffe, *"Energy loss and effective charge of heavy ions in aluminum"*, Phys. Rev. 120 (1960) 1744-1757.

[13]J.F. Ziegler, and J. M. Manoyan, *"The stopping of ions in compounds"*, Nucl. Instr. and Meth. B 35 (1988) 215-228.

[14]J. Lindhard, M. Scharff, and H. E. Schiott, *"Range concepts and heavy ion ranges"*, Mat. Fys. Medd. Dan. Vid. Selsk 33 (1963) 14.

[15]L.G. Glazov, and P. Sigmund, *"Nuclear stopping in transmission experiments"*, Nucl. Instr. and Meth. B 207 (2003) 240-256.

[16]F. Agulló-López, *"Técnicas nucleares aplicadas a problemas de estado sólido (II)"*, Energía Nuclear 34 (1965) 119-136.

[17]F. Agulló-López, R. C. Catlow and P. D. Townsend, *"Point Defects in Materials"*, Vol., (Ed.), Academic Press, London, 1984.

[18]D.O. Boerma, Lecture notes: *Atomic collisions in solids*, 2001.

[19]F. Seitz, and J. S. Koehler, *"Displacement of atoms during irradiation"*, Solid State Phys., Vol. 2, pp. 305, F. Seitz, and D. Turnbull (Ed.), Academic Press, Inc., New York, 1956

[20]J.A. Brinkman, *"Production of atomic displacements by high-energy particles"*, Am. J. Phys. 24 (1956) 246-267.

[21]J.C. Pivin, in: *"Ion Beam Nanostructuring of Materials"*. A. Vaseashta, et al., (Ed.), *Nanostructured and Advanced Materials*, Springer & Verlag, Netherlands, 2005, pp. 155-188.

[22]D.A. Thompson, *"High density cascade effects"*, Rad. Eff. and Defect in solids 56 (1981) 105-150.

[23]R.L. Fleischer, P. B. Price, and R. M. Walker, *"Ion Explosion Spike Mechanism for Formation of Charged-Particle Tracks in Solids"*, J. Appl. Phys 36 (1965) 3645.

[24]K. Izui, *"Fission fragment damage in semiconductors and ionic crystals"*, J. Phys. Soc. Japan 20 (1965) 915-932.

[25]M. Toulemonde, C. Dufour and E. Paumier *"Transient thermal process after a high-energy heavy-ion irradiation of amorphous metals and semiconductors"*, Phys. Rev. B 46 (1992) 14362-14369.

[26]M. Toulemonde, Ch. Dufour, A. Meftah, and E. Paumier, *"Transient thermal processes in heavy ion irradiation of crystalline inorganic insulators"*, Nucl. Instr. Meth. B 166-167 (2000) 903-912.

[27]C. Dufour, A. Audouard, F. Beuneu, J. Dural, J.P. Girard, A. Hairie, M. Levalois, E. Paumier and M. Toulemonde, *"A high-resistivity phase induced by swift heavy-ion irradiation of Bi: a probe for thermal spike damage?"*, J. Phys.: Condens. Matter 5 (1993) 4573.

[28]Z.G. Wang, Ch. Dufour, E. Paumier and M. Toulemonde, *"The S_e sensitivity of metals under swift-heavy-ion irradiation: a transient thermal process"*, J. Phys.: Condens. Matter 6 (1994) 6733.

[29]Thermal spike code for insulators, jean-paul.stoquert@phase.c-strasbourg.fr and marcel.toulemonde@ganil.fr.

[30]R. Spohr, in: *"Ion Tracks and Microtechnology: Basic Principles and Applications"*. K. Bethge, (Ed.), Vieweg, Braunchsweig, 1990.

[31]A. Meftah, J.M. Constantini, N. Khalfaoui, S. Boudjadar, J.P. Stoquert, F. Studer and M. Toulemonde, *"Experimental determination of track cross-section in $Gd_3Ga_5O_{12}$ and comparison to the inelastic thermal spike model applied to several materials"*, Nucl. Instrum. Methods B 237 (2005) 563-574.

[32]M. Toulemonde, C. Trautmann, E. Balanzat, K. Horjt, A. Weidinger, *"Track formation and fabrication of nanostructures with MeV-ion beams"*, Nucl. Instr. Meth. B 216 (2004) 1-8.

[33]J.H. Zollondz, and A. Weidinger, *"Towards new applications of ion tracks"*, Nucl. Instr. Meth. B 225 (2004) 178-183.

[34]E.C.H. Silk, and R.S. Barnes, *"Examination of fission fragment tracks with an electron microscope"*, Philos. Mag. 4 (1959) 970 - 972.

[35]R.L. Fleischer, in: *"Tracks to innovation, Nuclear tracks in science and technology"*, Springer, New York, 1998.

[36]T.A. Tombrello, *"Track damage and erosion of insulators by ion-induced electronic processes"*, Nucl. Instr. and Meth. B 2 (1984) 555-563.

[37]D. Albrecht, P. Armbruster, R. Spohr, M. Roth, K. Schaupert, H. Stuhrmann, *"Investigation of heavy ion produced defect structures in insulators by small angle scattering"*, Appl. Phys. A: Mater. Sci. Process. 37 (1985) 37-46.

[38]M. Toulemonde, and F. Studer, *"Comparison of the radii of latent tracks induced by high-energy heavy ions in $Y_3Fe_5O_{12}$ by HREM, channelling Rutherford backscattering and Mössbauer spectrometry"*, Phil. Mag. A 58 (1988) 799-808.

[39]A. Meftah, F. Brisard, J. M. Constantini, M. Hage-Ali, J. P. Stoquert, F. Studer and M. Toulemonde, *"Swift heavy ions in magnetic insulators: A damage-cross-section velocity effect"*, Phys. Rev. B 48 (1993) 920-925.

[40]A. Meftah, F. Brisard, J. M. Costantini, E. Dooryhee, M. Hage-Ali, M. Hervieu, J. P. Stoquert, F. Studer and M. Toulemonde, *"Track formation in SiO_2 quartz and the thermal-spike mechanism"*, Phys. Rev. B 49 (1994) 12457–12463.

[41]S.M.M. Ramos, B. Canut, M. Ambri, C. Clement, E. Dooryhee, M. Pitavale, P. Thévenard and M. Toulemonde *"Europium diffusion enhancement in $LiNbO_3$ irradiated with GeV nickel ions: influence of the damage morphology"*, Nucl. Instr. and Meth. B 107 (1996) 254-258

[42]B. Canut, S.M.M. Ramos, R. Brenier, P. Thevenard, J.L. Loubet, M. Toulemonde, *"Surface modification of $LiNbO_3$ single crystals by swift heavy ions"*, Nucl. Instrum. Methods B 107 (1996) 194 -198

[43]B. Canut, S. M. M. Ramos, N. Bonardi, J. Chaumont, H. Bernas and E. Cottereau, *"Defect creation by MeV clusters in $LiNbO_3$ "*, Nucl. Instr. and Meth. B 122 (1997) 335-338.

[44]B. Canut, A. Benyagoub, G. Marest, A. Meftah, N. Moncoffre, S. M. M. Ramos, F. Studer, P. Thevenard and M. Toulemonde, *"Swift-uranium-ion-induced damage in sapphire"*, Phys. Rev. B 51 (1995) 12194 –12201.

[45]C. Müller, M. Cranney, A. S. El-Said, N. Ishikawa, A. Iwase, M. Lang and R. Neumann, *"Ion tracks on LiF and CaF_2 single crystals characterized by scanning force microscopy"*, Nucl. Instr. and Meth. B 191 (2002) 246-250

[46]T. Wiss, Hj. Matzke, C. Trautmann, M. Toulemonde and S. Klaumünzer *"Radiation damage in UO_2 by swift heavy ions"*, Nucl. Instr. and Meth. B 122 (1997) 583-588.

[47]C. Trautmann, M. Toulemonde, J. M. Costantini, J. J. Grob and K. Schwartz, *"Swelling effects in lithium fluoride induced by swift heavy ions"*, Phys. Rev. B 62 (2000) 13-16.

[48]M. Boccanfuso, A. Benyagoub, K. Schwartz, C. Trautmann and M. Toulemonde *"Study of the damage produced in CaF_2 by swift heavy ion irradiation"*, Nucl. Instr. and Meth. B 191 (2002) 301-305.

[49]A. Benyagoub, F. Levesque, F. Couvreur, C. Gibert-Mougel, C. Dufour and E. Paumier, *"Evidence of a phase transition induced in zirconia by high energy heavy ions"*, Appl. Phys. Lett. 77 (2000) 3197.

[50]J. Vetter, R. Scholz, D. Dobrev and L. Nistor, *"HREM investigation of latent tracks in GeS and mica induced by high energy ions"*, Nucl. Instr. and Meth. B 141 (1998) 747-752.

[51]B. Canut, N. Bonardi, S. M. M. Ramos and S. Della-Negra, *"Latent tracks formation in silicon single crystals irradiated with fullerenes in the electronic regime"*, Nucl. Instr. and Meth. B 146 (1998) 296-301.

[52]A. Colder, O. Marty, B. Canut, M. Levalois, P. Marie, X. Portier, S. M. M. Ramos and M. Toulemonde, *"Latent track formation in germanium irradiated with 20, 30 and 40 MeV fullerenes in the electronic regime"*, Nucl. Instr. and Meth. B 174 (2001) 491-498.

[53]M. Levalois, P. Bogdanski and M. Toulemonde, *"Induced damage by high energy heavy ion irradiation at the GANIL accelerator in semiconductor materials"*, Nucl. Instr. and Meth. B 63 (1992) 14-20.

[54]P.I. Gaiduk, A. Nylansted-Larsen, C. Trautmann and M. Toulemonde, *"Discontinuous tracks in arsenic-doped crystalline $Si_{0.5}Ge_{0.5}$ alloy layers"*, Phys. Rev. B 66 (2002) 045316.

[55]P.I. Gaiduk, F. F. Komarov and W. Wesch, *"Damage evolution in crystalline InP during irradiation with swift Xe ions"*, Nucl. Instr. and Meth. B 164–165 (2000) 377-383.

[56]G. Szenes, Z. E. Horvath, B. Pecz, F. Paszti and L. Toth, *"Tracks induced by swift heavy ions in semiconductors"*, Phys. Rev. B 65 (2002) 045206.

[57]H. Dammak, A. Barbu, A. Dunlop, D. Lesueur and N. Lorenzelli, *"$\alpha \rightarrow \omega$ phase transformation induced in titanium during ion irradiations in the electronic slowing-down regime"*, Philos. Mag. Lett. 67 (1993) 253-259.

[58]S. Klaumünzer, M. D. Hou and G. Schumacher, *"Coulomb explosions in a metallic glass due to the passage of fast heavy ions?"*, Phys. Rev. Lett. 57 (1986) 850-853.

[59]A. Audouard, E. Balanzat, G. Fuchs, J. C. Jousset, D. Lesueur and L. Thomé, *"High-energy heavy-ion irradiations of Fe // 8 // 5B // 1 // 5 amorphous alloy: Evidence for electronic energy loss effect"*, Europhys. Lett. 3 (1987) 327-331.

[60]A. Dunlop, D. Lesueur, J. Morillo, J. Dural, R. Spohr and J. Vetter, *"High electronic excitations and damage production in GeV-ion-irradiated metals"*, Nucl. Instr. and Meth. B 48 (1990) 419-424.

[61]A.D. Marwick, L. Civale, L. Krusin-Elbaum, R. Wheeler, J. R. Thompson, T. K. Worthington, M. A. Kirk, Y. R. Sun, H. R. Kerchner and F. Holtzberg, *"Processing high -Tc superconductors with GeV heavy ions"*, Nucl. Instr. and Meth. B 80-81 (1993) 1143.

[62]J. Jensen, A. Dunlop and S. Della Negra, *"Tracks induced in CaF_2 by MeV cluster irradiation"*, Nucl. Instr. and Meth. B 141 (1998) 753-762.

[63]A. Dunlop, H. Dammak and D. Lesueur, *"Track formation in metals by electronic processes using atomic and cluster ions"*, Nucl. Instr. and Meth. B 112 (1996) 23-25.

[64]H. Dammak, A. Dunlop and D. Lesueur, *"Phase transformation induced by swift heavy ion irradiation of pure metals"*, Nucl. Instr. Meth. B 107 (1996) 204-211.

[65]C. Trautmann, M. Toulemonde, C. Dufour and E. Paumier *"Effect of radial energy distribution on ion track etching in amorphous metallic $Fe_{81}B_{13.5}Si_{3.5}C_2$"*, Nucl. Instr. and Meth. B 108 (1996) 94-98.

[66]A. Gutzmann, S. Klaumünzer and P. Meier, *"Ion-Beam-Induced Surface Instability of Glassy $Fe_{40}Ni_{40}B_{20}$"*, Phys. Rev. Lett. 74 (1995) 2256–2259.

[67]S. Klaumünzer, C. L. Li, S. Löffler, M. Rammensee, G. Schumacher and H. C. Neitzert, *"Ion-Beam-Induced plastic deformation: A universal behavior of amorphous solids"*, Radiat. Eff. Def. Sol. 108 (1989) 131-135.

[68]M.D. Hou, S. Klaumünzer and G. Schumacher, *"Dimensional changes of metallic glasses during bombardment with fast heavy ions"*, Phys. Rev. B 41 (1990) 1144-1157.

[69]M. Waiblinger, Ch. Sommerhalter, B. Pietzak, J. Krauser, B. Mertesacker, M. Ch. Lux-Steiner, A. Weidinger, C. Ronning and H. Hofsäs *"Electrically conducting ion tracks in diamond-like carbon films for field emission"*, Appl. Phys. A 69 (1999) 239–240.

[70]B. Gervais, S. Bouffard, *"Simulation of the primary stage of the interaction of swift heavy ions with condensed matter"*, Nucl. Instr. Meth. B 88 (1994) 355-364.

[71]B. Canut, R. Brenier, A. Meftah, P. Moretti, S. Ould Salem, S.M.M. Ramos, P. Thevenard and M. Toulemonde, *"Damage induced in $LiNbO_3$ single crystals by GeV gadolinium ions"*, Nucl. Instr. Meth. B 91 (1994) 312.

[72]B. Canut, R. Brenier, A. Meftah, P. Moretti, S. Ould Salem, M. Pitaval, S.M.M. Ramos, P. Thevenard and M. Toulemonde, *"Latent track formation in $LiNbO_3$ single crystals irradiated by GeV Uranium ions"*, Rad. Eff. and Defect in solids 136 (1995) 307-310.

[73]N. Bonardi, PhD. Dissertation, University C. Bernard, Lyon, France, 1998.

[74]C. Houpert, F. Studer, D. Groult and M. Toulemonde, *"Transition from localized defects to continuous latent tracks in magnetic insulators irradiated by high energy heavy ions: A HREM investigation"*, Nucl. Instr. and Meth. B 39 (1989) 720-723.

[75]M. Toulemonde, N. Enault, J. Y. Fan and F. Studer, *"Does continuous trail of damage appear at the change in the electronic stopping power damage rate?"*, J. App. Phys. 68 (1990) 1545.

[76]A. Audouard, R. Mamy, M. Toulemonde, G. Szenes and L. Thomé, *"Impacts of GeV heavy ions in amorphous metallic alloys investigated by near-field scanning microscopy"*, Europhys. Lett. 40 (1997) 527.

[77]D. Fink, P.S. Alegaonkar, A.V. Petrov, M. Wilhelm, P. Szimkowiak, M. Behar, D. Sinha, W.R. Fahrner, K. Hoppe and L.T. Chadderton, *"High energy ion beam irradiation of polymers for electronic applications"*, Nucl. Instr. Meth. B 236 (2005) 11-20.

[78]Z. Siwy, P. Apel, D. Baur, D.D. Dobrev, Y.E. Korchev, R. Neumann, R. Spohr, C. Trautmann and K.-O. Voss, *"Preparation of synthetic nanopores with transport properties analogous to biological channels"*, Surf. Sci. 532-535 (2003) 1061-1066.

[79]R. Sanz, J. Jensen, A. Johansson, M. Skupinski, G. Possnert, M. Boman, M. Hernández-Vélez, M. Vázquez and K. Hjort, *"Well-ordered nanopore arrays in rutile TiO_2 single crystals by swift heavy ion-beam lithography"*, Nanotechnology 18 (2007) 305303

[80]M.L. Crespillo, M. Otto, A. Muñoz-Martín, J. Olivares, F. Agulló-López, M. Seibt, M. Toulemonde and C. Trautmann, *"Optimization of nanopores obtained by chemical etching on swift-ion irradiated lithium niobate"*, Nucl. Instr. Meth. B 267 (2009) 1035-1038.

[81]D. Kanjilal, *"Swift heavy ion-induced modification and track formation in materials"*, Current Science 80 (2001) 1560-1566.

[82]D. Fink, P.S. Alegaonkar, A.V. Petrov, A.S. Berdinsky, V. Rao, M.Müller, K.K. Dwivedi and L.T. Chadderton, *"The emergence of new ion track applications"*, Radiation Meas. 36 (2003) 605-609.

[83]C. Trautmann, *"Modifications induced by swift heavy ions"*, Bull. Mater. Sci. 22 (1999) 679-686.

[84]A. Berthelot, S. Hémon, F. Gourbilleau, C. Dufour, B. Domengès and E. Paumier, *"Behaviour of a nanometric SnO_2 powder under swift heavy-ion irradiation: from sputtering to splitting"*, Phil Mag A 80 (2000) 2257-2281.

[85]N. Khalfaoui, C. C. Rotaru, S. Bouffard, M. Toulemonde, J. P. Stoquert, F. Haas, C. Trautmann, J. Jensen and A. Dunlop, *"Characterization of swift heavy ion tracks in CaF_2 by scanning force and transmission electron microscopy"*, Nucl. Instr. and Meth. B 240 (2005) 819-829.

[86]J. Vetter, R. Scholz, N. Angert, *"Investigation of latent tracks from heavy ions in GeS crystals by high resolution TEM"*, Nucl. Instr. Meth. B 91 (1994) 129-133.

[87]J. Wiesner, C. Traeholt, J. G. Wen, H. W. Zandbergen, G. Wirth and H. Fuess, *"High resolution electron microscopy of heavy-ion defects in superconducting Bi-2212 thin films in relation to their effect on J_c"*, Physica C 268 (1996) 161-172.

[88]E. Ferain, and R. Legras, *"Pore shape control in nanoporous particle track etched membrane"*, Nucl. Instr. Meth. B 174 (2001) 116-122.

[89]N. Itoh, D. M. Duffy, S. Khakshouri and A. M. Stoneham, *"Making tracks: electronic excitation roles in forming swift heavy ion tracks"*, J. Phys.: Condens. Matter 21 (2009) 474205.

[90]N. Itoh, and A. M. Stoneham, *"Materials Modification by Electronic Excitation"*, Vol., (Ed.), Cambridge University Press, 2001.

[91]G. Schiwietz, K. Czerski, M. Roth, F. Staufenbiel and P.L. Grande, *"Femtosecond dynamics - snapshots of the early ion-track evolution"*, Nucl. Instr. and Meth. B 226 (2004) 683-704.

[92]D. Lesueur, and Dunlop, A., *"Damage creation via electronic excitations in metallic targets part II: A theoretical model"*, Rad. Eff. and Defect in solids 126 (1993) 163-172.

[93]A. Dunlop, P. Legrand, D. Lesueur, N. Lorenzelli, J. Morillo, A. Barbu and S. Bouffard, *"Phonon Soft Modes and Damage Production by High Electronic Excitations in Pure Metals"*, Europhys. Lett. 15 (1991) 765-770.

[94]A. Dunlop, and D. Lesueur., *"Damage creation via electronic excitations in metallic targets part I: Experimental results"*, Radiat. Eff. Def. Sol. 126 (1993) 123-128.

[95]F. Dessauer, *"Über einige Wirkungen von Strahlen. I"*, Zeitschrift für Physik A Hadrons and Nuclei 12 (1923) 38-47.

[96]G. Szenes, *"Thermal spike model of amorphous track formation in insulators irradiated by swift heavy ions"*, Nucl. Instr. and Meth. B 116 (1996) 141-144.

[97]G. Szenes, F. Pászti, A. Péter and A. I. Popov, *"Tracks induced in TeO_2 by heavy ions at low velocities"*, Nucl. Instr. and Meth. B 166-167 (2000) 949.

[98]A.M. Prokhorov, and Yu. S. Kuz'minov, *"Physics and chemistry of cristaline lithium niobate"*, Vol., (Ed.), Adam Hilger. Series of Optics and Optoelectronics, Bristol, 1990.

[99]I.A. Baranov, Yu. V. Martynenko, S. O. Tsepelevich, Y. N. Yavlinskii, *"Inelastic sputtering of solids by ions"*, Sov. Phys. Usp. 31 (1988) 1015.

[100]M. Toulemonde, A. Meftah, J. M. Costantini, K. Schwartz and C. Trautmann, *"Out-of-plane swelling of gadolinium gallium garnet induced by swift heavy ions"*, Nucl. Instr. and Meth. B 146 (1998) 426-430.

[101]G.G. Bentini, M. Bianconi, M. Chiarini, L. Correra, C. Sada, P. Mazzoldi, N. Argiolas, M. Bazzan and R. Guzzi, *"Effect of low dose high energy O^{3+} implantation on refractive index and linear electro-optic properties in X-cut $LiNbO_3$:Planar optical waveguide formation and characterization"*, J. Appl. Phys 92 (2002) 6477.

[102]J. Olivares, A. García-Navarro, G. García, A. Méndez and F. Agulló-López, *"Optical determination of three-dimensional nanotrack profiles generated by single swift-heavy ion impacts in lithium niobate"*, Appl. Phys. Lett. 89 (2006) 071923.

[103]J. Olivares, G. García, A. García-Navarro, F. Agulló-López, O. Caballero and A. García-Cabañes, *"Generation of high-confinement step-like optical waveguides in $LiNbO_3$ by swift heavy ion-beam irradiation"*, Appl. Phys. Lett. 86 (2005) 183501.

[104]F. Agulló-López, G. García and J. Olivares, *"Lattice preamorphization by ion irradiation: Fluence dependence of the electronic stopping power threshold for amorphization"*, J. Appl. Phys 97 (2005) 093514.

[105]G. García, F. Agulló-López, J. Olivares and A. García-Navarro, *"Monte Carlo simulation of damage and amorphization induced by swift-ion irradiation in $LiNbO_3$"*, J. Appl. Phys. 99 (2006) 053504.

[106]G. Szenes, *"General features of latent track formation in magnetic insulators irradiated with swift heavy ions"*, Phys. Rev. B 51 (1995) 8026-8029.

[107]G. Szenes, *"Amorphous tracks in insulators induced by monoatomic and cluster ions"*, Phys. Rev. B 60 (1999) 3140–3147.

[108]G. Szenes, *"A possible mechanism of formation of radiation defects in amorphous metals"*, Mater. Sci. Forum 97-99 (1992) 647-652.
[109]J. Olivares, G. García, F. Agulló-López, F. Agulló-Rueda, A. Kling, J.C. Soares, *"Generation of amorphous surface layers in $LiNbO_3$ by ion-beam irradiation: thresholding and boundary propagation"*, Appl. Phys. A 81 (2005) 1465-1469.
[110]J. Olivares, G. García, F. Agulló-López, F. Agulló-Rueda, J.C. Soares and A. Kling, *"Optical investigation of the propagation of the amorphous–crystalline boundary in ion-beam irradiated $LiNbO_3$"*, Nucl. Instr. Meth. B 242 (2006) 534-537.
[111]G.G. Bentini, M. Bianconi, L. Correra, M. Chiarini, P. Mazzoldi, C. Sada, N. Argiolas, M. Bazzan and R. Guzzi, *"Damage effects produced in the near-surface region of x-cut $LiNbO_3$ by low dose, high energy implantation of nitrogen, oxygen, and fluorine ions"*, J. Appl. Phys 96 (2004) 242.
[112]G. Szenes, *"Amorphous track formation in SiO_2"*, Nucl. Instr. and Meth. B 122 (1997) 530-533.
[113]K.K. Wong, (Ed.), *Properties of Lithium Niobate*, EMIS Data Review Series, INSPEC Exeter, 2002.
[114]J. Frenkel, *"Kinetic Theory of Liquids"*, Vol., (Ed.), Dover, New York, 1955.
[115]T. van Dillen, A. Polman, W. Fukarek and A. van Blaaderen, *"Energy-dependent anisotropic deformation of colloidal silica particles under MeV Au irradiation"*, Appl. Phys. Lett. 78 (2001) 910.
[116]J. Frantz, J. Tarus, K. Nordlund and J. Keinonen, *"Mechanism of electron-irradiation-induced recrystallization in Si"*, Phys. Rev. B 64 (2001) 125313.
[117]K.S. Song, and R. T. Williams, *"Self Trapped Excitons"*, Vol., (Ed.), Springer, Berlin, 1993.
[118]N. Itoh, *"Self-trapped exciton model of heavy-ion track registration"*, Nucl. Instr. and Meth. B 116 (1996) 33-36.
[119]N. Itoh, and A. M. Stoneham, *"Excitonic model of track registration of energetic heavy ions in insulators"*, Nucl. Instr. and Meth. B 146 (1998) 362-366.
[120]Y.M. Annenkov, and A. M. Pritulov, Sov. Phys. Solid State 23 (1981) 616.
[121]N. Itoh, *"Subthreshold radiation-induced processes in the bulk and on surfaces and interfaces of solids"*, Nucl. Instr. and Meth. B 135 (1998) 175-183.
[122]F. Agulló-López, A. Méndez, G. García, J. Olivares and J. M. Cabrera, *"Synergy between thermal spike and exciton decay mechanisms for ion damage and amorphization by electronic excitation"*, Phys. Rev. B 74 (2006) 174109.
[123]F. Agulló-López, G. García and J. Olivares, *"Theoretical modeling of swift-ion-beam amorphization: Application to $LiNbO_3$"*, Nucl. Instr. Meth. B 249 (2006) 118–121.
[124]A. Rivera, A. Méndez, G. García, J. Olivares, J.M. Cabrera and F. Agulló-López, *"Ion-beam damage and non-radiative exciton decay in $LiNbO_3$"*, Journal of Luminescence 128 (2008) 703-707.
[125]A. Rivera, J. Olivares, G. García, J.M. Cabrera, F. Agulló-Rueda and F. Agulló-López, *"Giant enhancement of material damage associated to electronic excitation during ion irradiation: The case of $LiNbO_3$"*, Phys. Status Solidi A 206 (2009) 1109-1116.
[126]F. Agulló-López, and P. D. Townsend, *"On the temperature dependence of the F-coloring efficiency in KCl"*, Solid St. Commun. 33 (1980) 449-452.
[127]P.D. Townsend, and F. Agulló-López, J. Phys. (Paris), Colloq. C6 41 (1980) 279.

[128]A. Rivera, M. L. Crespillo, J. Olivares, R. Sanz, J. Jensen and F. Agulló-López *"On the exciton model for ion-beam damage: The example of TiO_2"*, Nucl. Instr. Meth. B 268 (2010) 3122-3126.
[129]E.M. Bringa, and R. E. Johnson, *"Coulomb Explosion and Thermal Spikes"*, Phys. Rev. Lett. 88 (2002) 165501.
[130]E.M. Bringa, R. E. Johnson and M. Jakas, *"Molecular-dynamics simulations of electronic sputtering"*, Phys. Rev. B 60 (1999) 15107-15116.
[131]M.M. Jakas, E. M. Bringa and R. E. Johnson *"Fluid dynamics calculation of sputtering from a cylindrical thermal spike"*, Phys. Rev. B 65 (2002) 165425
[132]S.S. Mao, F. Queré, S. Guizard, X. Mao, R. E. Russo, G. Petite and P. Martin, *"Dynamics of femtosecond laser interactions with dielectrics"*, Appl. Phys. A 79 (2004) 1695-1709.
[133]R.T. Williams, and K. S. Song *"Self-trapped Excitons"*, Vol., (Ed.), Second edition, Springer-Verlag, Berlin, 1996.
[134]M. Fox, *"Optical properties of solids"*, Oxford Master Series in Physics, Vol., (Ed.), Oxford University Press, 2001.
[135]V. Mürk, *"Exciton Relaxation in wide-gap complex oxides"*, Materials Science Forum 239-241 (1997) 537-542.
[136]G. García, J. Olivares, F. Agulló-López, A. García-Navarro, F. Agulló-Rueda, A. García- Cabañes and M. Carrascosa, *"Effect of local rotations on the optical response of $LiNbO_3$: Application to ion-beam damage"*, Europhys. Lett. 76 (2006) 1123-1129.
[137]F. Agulló-López, (Ed.), *Insulating materials for optoelectronics: New developments*, World Scientific, Singapore, 1995.
[138]P.W. Haycock, and P. D. Townsend, *"Exciton luminescence from pure $LiNbO_3$"*, J. Phys. C: Solid State Phys. 20 (1987) 319.
[139]P. Herth, D. Schaniel, Th. Woike, T. Granzow, M. Inlau and E. Krätzig, *"Polarons generated by laser pulses in doped $LiNbO_3$"*, Phys. Rev. B 71 (2005) 125128.
[140]C. Merschjann, D. Berben, M. Imlau and M. Wöhlecke, *"Evidence for Two-Path Recombination of Photoinduced Small Polarons in Reduced $LiNbO_3$"*, Phys. Rev. Lett. 96 (2006) 186404.
[141]P. Herth, T. Granzow, D. Schaniel, Th. Woike, M. Imlau and E. Krätzig, *"Evidence for Light-Induced Hole Polarons in $LiNbO_3$"*, Phys. Rev. Lett. 95 (2005) 067404.
[142]P.W. Haycock, and P.D. Townsend, *"Ion beam induced luminescence spectra of $LiNbO_3$"*, Radiat. Eff. 98 (1986) 243-248.
[143]A. García-Cabañes, J. A. Sanz-García, J. M. Cabrera, F. Agulló-López, C. Zaldo, R. Pareja, K. Polgár, K. Raksányi and I. Földvàri, *"Influence of stoichiometry on defect-related phenomena in $LiNbO_3$"*, Phys. Rev. B 37 (1988) 6085-6091.
[144]E.R. Hodgson, and F. Agulló-López, *"Oxygen vacancy centres induced by electron irradiation in $LiNbO_3$"*, Solid State Commun. 64 (1987) 965-968.
[145]B. Andreas, K. Peithmann, K. Buse and K. Maier, *"Modification of the refractive index of lithium niobate crystals by transmission of high-energy $^4He^{2+}$ and D^+ particles"*, Appl. Phys. Lett. 84 (2004) 3813.
[146]H.J. Fecht, *"Defect-induced melting and solid-state amorphization"*, Nature 356 (1992) 133.
[147]B.T. Matthias, and J. P. Remeika, *"Ferroelectricity in the ilmenite structure"*, Phys. Rev. 76 (1949) 1886.
[148]V.V. Atuchin, *"Causes of refractive indices changes in He-implanted $LiNbO_3$ and $LiTaO_3$ waveguides"*, Nucl. Instr. Meth. B 168 (2000) 498-502.

[149]G.G. Bentini, M. Bianconi, A. Cerutti, Chiarini, G. Pennestrì, C. Sada, N. Argiolas, M. Bazzan and P. Mazzoldi, *"Integrated Mach-Zehnder micro-interferometer on $LiNbO_3$"*, Optics and Lasers in Engineering 45 (2007) 368-372.

[150]O. Caballero-Calero, *"Nonlinear Optical Waveguides in $LiNbO_3$ and Periodically Poled $LiNbO_3$"*, PhD. Dissertation, Departamento de Física de Materiales, Universidad Autónoma de Madrid, Madrid, 2007.

[151]F. Lacour, N. Courjal, M.B. Bernal, A. Sabac. C. Bainier and M. Spajer *"Nanostructuring lithium niobate substrates by focused ion beam milling"*, Opt. Mat. 27 (2005) 1421-1425.

[152]X. Liu, K. Kitamura, K. Terabe, H. Hatano and N. Ohashi, *"Photocatalytic nanoparticle deposition on $LiNbO_3$ nanodomain patterns via photovoltaic effect"*, Appl. Phys. Lett. 91 (2007) 044101.

[153]A. García-Navarro, *"Irradiación con iones pesados de alta energía en dieléctricos para aplicaciones fotónicas: Guías de onda en $LiNbO_3$"*, PhD. Dissertation, Departamento de Física de Materiales, Universidad Autónoma de Madrid (UAM), Madrid, July 2007.

[154]Photox Optical Systems Ltd. Lithium Niobate Crystal ($LiNbO_3$) Properties.http://www. photox.co.uk/linbo3.htm, 2008.

[155]C. Restoin, S. Massy, C. Darraud-Taupiac and A. Barthelemy, *"Fabrication of 1D and 2D structures at submicrometer scale on lithium niobate by electron beam bombardment"*, Optical Materials 22 (2003) 193-199.

[156]V. Foglietti, E. Cianci, D. Pezzetta, C. Sibilia, M. Marangoni, R. Osellame and R. Ramponi, *"Fabrication of band-gap structures in planar nonlinear waveguides for second harmonic generation"*, Microelectron. Eng. 742 (2003) 67-68.

[157]R.-C. Twu, C.-C. Huang and W.-S. Wang, *"Zn indiffusion waveguide polarizer on a Y-cut $LiNbO_3$ at 1.32-μm wavelength"*, Photonics Technology Letters, IEEE 12 (2000) 161-163.

[158]E. Wooten, K. Kissa, A. Yi-Yan, E. Murphy, D. Lafaw, P. Hallemeier, D. Maack, D. Attanasio, D. Fritz, G. McBrien and D. Bossi, *"A review of lithium niobate modulators for fiber-optic communications systems. Selected Topics in Quantum Electronics"*, Journal of IEEE 6 (2000) 69-82.

[159]R. Müller, M. T. Santos, L. Arizmendi and J. M. Cabrera, *"A narrowband interference filter with photorefractive $LiNbO_3$"*, J. Phys. D: Applied Physics 27 (1994) 241-246.

[160]S. Breer, and K. Buse, *"Wavelength demultiplexing with volume phase holograms in photorefractive lithium niobate"*, Appl. Phys. B 66 (1998) 339-345.

[161]J. Lee, M. P. Singh and J. Zucker, *"Suppression of higher harmonic generations of SAW in $LiNbO_3$"*, Appl. Phys. Lett. 36 (1980) 896-898.

[162]C. Ruppel, L. Reindl and R. Weigel, *"SAW devices and their wireless communications applications"*, Microwave Magazine, IEEE 3 (2002) 65-71.

[163]D.E. Allen, P. P.-L. Kwan and D. P. Stumbo, *"Saw filter device for radio tranceiver utilizing different coupling coefficient ratios"*, Patent (International Classification H03H 972) 5726610 Motorola Inc. (1997).

[164]K.J. Richter, M. A. Pugel and J. S. Stewart, *"Saw filter for a tuner of a digital satellite receiver"*, Patent (International Classification H04N 544) 5898900 Thomson Consumer Electronics, Inc. (1997).

[165]I. Baumann, R. Brinkmann, M. Dinand, W. Sohler and S. Westenhofer, *"Ti:Er:$LiNbO_3$ waveguide laser of optimized efficiency"*, J. Quantum. Elect., IEEE 32 (1996) 1695-1706.

[166]L. Arizmendi, *"Photonic applications of lithium niobate crystals"*, Phys. Stat. Sol. A 201 (2004) 253-283.

[167]J. Olivares, A. García-Navarro, A. Méndez, F. Agulló-López, G. García, A. García-Cabañes and M. Carrascosa, *"Novel optical waveguides by in-depth controlled electronic damage with swift ions"*, Nucl. Instr. Meth. B 257 (2007) 765-770.

[168]J. Manzano, J. Olivares, F. Agulló-López, M. L. Crespillo, A. Moroño and E. Hodgson, *"Optical waveguides obtained by swift-ion irradiation on silica (a-SiO_2)"*, Nucl. Instr. and Meth. B 268 (2010) 3147-3150.

[169]A. García-Navarro, J. Olivares, G. García, F. Agulló-López, S. García-Blanco, C. Merchant and J. Stewart Aitchison, *"Fabrication of optical waveguides in KGW by swift heavy ion beam irradiation"*, Nucl. Instr. and Meth. B 249 (2006) 177-180.

[170]C.A. Merchant, P. Scrutton, S. García-Blanco, C. Hnatovsky, R. S. Taylor, A. García-Navarro, G. García, F. Agulló-López, J. Olivares, A. S. Helmy and J. S. Aitchison, *"High Resolution refractive index and micro-raman spectroscopy of planar waveguides in $KGd(WO_4)_2$ formed by swift heavy ion irradiation"*, IEEE J. Quantum Electronics 45 (2009) 373-379.

[171]M. Kawabe, M. Kubota, K. Masuda and S. Namba, *"Microfabrication in $LiNbO_3$ by ion-bombardment-enhanced etching"*, J. Vac. Sci. Technol. 15 (1978) 1096-1098.

[172]G. Götz, and H. Karge, *"Ion implantation into $LiNbO_3$"*, Nucl. Instr. Meth. B 209-210 (1983) 1079.

[173]C.I.H. Ashby, G.W. Arnold and P.J. Brannon, *"Ion-bombardment-enhanced etching of $LiNbO_3$ using damage profile tailoring"*, J. Appl. Phys. 65 (1989) 93.

[174]T.H. Shao, X.Y. Jiang, W. Shang and X.Q. Feng, *"Effects of ion implantation on surface composition and enhanced etching in $LiNbO_3$"*, Mater. Sci. Eng. B 10 (1991) 19-24.

[175]D.M. Gill, D. Jacobson, C.A. White, C.D.W. Jones, Y. Shi, W.J. Minford and A. Harris, *"Ridged $LiNbO_3$ modulators fabricated by a novel oxygen-ion implant/wet-etch technique"*, J. Lightwave Technol. 22 (2004) 887.

[176]F. Schrempel, T. Gischkat, H. Hartung, E.-B. Kley and W. Wesch *"Ion beam enhanced etching of $LiNbO_3$"*, Nucl. Instr. Meth. B 250 (2006) 164-168.

[177]G.L. Destefanis, P.D. Townsend and J.P. Gailliard, *"Optical waveguides in $LiNbO_3$ formed by ion implantation of helium"*, Appl. Phys. Lett. 32 (1978) 293.

[178]S. Wei, X.-Y. Jiang and X.-Q. Feng, *"Annealing of ion induced damage and alteration of composition in the near-surface of ion-implanted $LiNbO_3$"*, Vacuum 39 (1989) 287-288.

[179]P.D. Townsend, *"An overview of ion-implanted optical waveguide profiles"*, Nucl. Instr. Meth. B 46 (1990) 18-25.

[180]B.-R. Shi, K.-M. Wang, Z.-L. Wang, X.-D. Liu, T.-B. Xu, P.-R. Zhu, *"Radiation damage behaviour of $LiNbO_3$ crystal by MeV F ion implantation"*, J. App. Phys. 74 (1993) 1625.

[181]A. Kling, M.F. da Silva, J.C. Soares, P.F.P. Fichtner, L. Amaral and F. Zawislak, *"Defect evolution and characterization in He-implanted $LiNbO_3$"*, Nucl. Instr. Meth. B 175-177 (2001) 394-397.

[182]A. Meldrum, L. A. Boatner, W. J. Weber and R. C. Ewing, *"Amorphization and recrystallization of the ABO_3 oxides"*, J. Nucl. Mater. 300 (2002) 242-254.

[183]P.D. Townsend, P. J. Chandler and L. Zhang, *"Optical Effects of Ion Implantation"*, Vol., (Ed.), Cambridge University Press, Cambridge, 1994.

[184]F. Chen, X. -L. Wang and K. -M. Wang, *"Development of ion-implanted optical waveguides in optical materials: A review"*, Opt. Mater. 29 (2007) 1523-1542.
[185]F. Chen, *"Photonic guiding structures in lithium niobate crystals produced by energetic ion beams"*, J. Appl. Phys. 106 (2009) 081101.
[186]P.D. Townsend, *"Optical effects of ion implantation"*, Rep. Prog. Phys. 50 (1987) 501.
[187]J. Rams, J. Olivares, P. J. Chandler and P. D. Townsend, *"Mode gaps in the refractive index properties of low-dose ion-implanted $LiNbO_3$ waveguides"*, J. Appl. Phys. 87 (2000) 3199.
[188]J. Olivares, M.L. Crespillo, O. Caballero-Calero, M.D. Ynsa, A. García-Cabañes, M. Toulemonde, C. Trautmann and F. Agulló-López, *"Thick optical waveguides in lithium niobate induced by swift heavy ions (~10 MeV/amu) at ultralow fluences"*, Optics Express 17 (2009) 24175-24182.
[189]J. Bland-Hawthorn, and P. Kern, *"Astrophotonics: a new era for astronomical instruments"*, Opt. Express 17 (2009) 1880-1884.
[190]L. Labadie, and O. Wallner, *"Mid-infrared guided optics: a perspective for astronomical instruments"*, Opt. Express 17 (2009) 1947-1962.
[191]*"lithium niobate or $LiNbO_3$"*, See for example published works with the words "lithium niobate or $LiNbO_3$" in the title, in the Web of Science database of ISI Web of Knowledge, published by Thomson Reuters.
[192]A. Räuber, in: *"Chemistry and physics of lithium niobate "*. E. Kaldis, (Ed.), *Current Topics in Materials Science, Vol. 1*, North-Holland Publishing Company, Amsterdam, 1978, pp. 481-601.
[193]W.H. Zachariasen, Skr. Norske Vid.-Ada, Oslo, Mat. Naturv. 4 (1928).
[194]S.A. Fedulov, Z. I. Saphiro and P. B. Ladyzhin, *"Growth of crystals of $LiNbO_3$, $LiTaO_3$ and $NaNbO_3$ by Czochralski method"*, Sov. Phys. Crystallogr. 10 (1965) 218.
[195]A.A. Ballman, *"Growth of piezoelectric and ferroelectric materials by the Czochralski technique"*, J. Am. Ceram. Soc. 48 (1965) 112.
[196]K. Nassau, H. J. Levinstein and G. M. Loiacono, *"Ferroelectric lithium niobate. 1. Growth, domain structure, dislocations and etching"*, J. Phys. Chem. Solids 27 (1966) 983.
[197]K. Nassau, H. J. Levinstein and G. M. Loiacono, *"Ferroelectric lithium niobate. 2. Preparation of single domain crystals"*, J. Phys. Chem. Solids 27 (1966) 989.
[198]S.C. Abrahams, J. M. Reddy and J. L. Bernstein, *"Ferroelectric lithium niobate. 3. Single crystal X-ray diffraction study at 24ºC"*, J. Phys. Chem. Solids 27 (1966) 997.
[199]S.C. Abrahams, J. M. Reddy and J. L. Bernstein, *"Ferroelectric lithium niobate. 4. Single crystal neutron diffraction study at 24ºC"*, J. Phys. Chem. Solids 27 (1966) 1013.
[200]S.C. Abrahams, J. M. Reddy and J. L. Bernstein, *"Ferroelectric lithium niobate. 5. Polycrystal X-ray diffraction study between 24ºC and 1200ºC"*, J. Phys. Chem. Solids 27 (1966) 1019.
[201]T. Volk, and M. Wöhlecke, *"Lithium Niobate. Defects, Photorefraction and Ferroelectric Switching"*, Vol., (Ed.), Springer-Verlag, Berlin, Heidelberg, 2008.
[202]B.-R. Shi, K. M. Wang, Z. L. Wang, X. D. Liu, T. B. Xu and P.R. Zhu, *"Lattice disorder in $LiNbO_3$ crystals induced by MeV Cu^+ implantation"*, J. Appl. Phys. 72 (1992) 899.

[203]B.-R. Shi, and N. Cue, *"The study of damage profiles in MeV Si^+-implanted $LiNbO_3$ crystals by Rutherford backscattering and oxygen resonance scattering"*, J. Phys. D: Appl. Phys. 29 (1996) 419.

[204]S.M.M. Ramos, B. Canut, M. Ambri, N. Bonardi, M. Pitaval, H. Bernas and J. Chaumont, *"Defect creation in $LiNbO_3$ irradiated by medium masses ions in the electronic stopping power regime"*, Radiat. Eff. Defects Solid 143 (1998) 299-309.

[205]A. Garcia-Navarro, F. Agulló-López, M. Bianconi, J. Olivares and G. García, *"Kinetics of ion-beam damage in lithium niobate"*, J. Appl. Phys. 101 (2007) 083506.

[206]H. Hu, F. Lu, F. Chen, B. -R. Shi, K. -M. Wang and D. -Y. Shen, *"Monomode optical waveguide in lithium niobate formed by MeV Si^+ ion implantation"*, J. Appl. Phys. 89 (2001) 5224.

[207]F. Chen, H. Hu, J. H. Zhang, F. Lu, B. R. Shi, K. M. Wang, D. Y. Shen and C. Q. Wang, *"Optical waveguide in x-cut $LiNbO_3$ crystals by MeV P^+ ion implantation with low dose"*, Phys. Stat. Sol. A 187 (2001) 543-548.

[208]G. Fu, K. M. Wang, F. Chen, X. L. Wang, S. L. Li, D. Yu Shen, H. J. Ma and R. Nie *"Extraordinary refractive-index increase in MeV B^{3+} ion-implanted $LiNbO_3$ waveguide"*, Nucl. Instr. and Meth. B 211 (2003) 346-350.

[209]S.L. Li, K. M. Wang, F. Chen, X. L. Wang, G. Fu, D. Y. Shen, H. J. Ma and R. Nie, *"Monomode optical waveguide excited at 1540 nm in $LiNbO_3$ formed by MeV carbon ion implantation at low doses"*, Opt. Express 12 (2004) 747-752.

[210]F. Chen, H. Hu, X. L. Wang, F. Lu and K. M. Wang, *"Property investigation of C^+-ion-implanted $LiNbO_3$ planar optical waveguides"*, J. Appl. Phys. 98 (2005) 044507.

[211]J. Reinisch, F. Schrempel, T. Gischkat and W. Wesch, *"Etching of Ion Irradiated $LiNbO_3$ in Aqueous Hydrofluoric Solutions"*, J. Electrochem. Soc. 155 (2008) D298-D301.

[212]M. Bianconi, F. Bergamini, G.G. Bentini, A. Cerutti, M. Chiarini, P. De Nicola and G. Pennestri, *"Modification of the etching properties of x-cut Lithium Niobate by ion implantation"*, Nucl. Instr. Meth. B 266 (2008) 1238-1241.

[213]M. Levy, R.M. Osgood Jr., R. Liu, E. Gross, G.S. Cargill III, A. Kumar and H. Bakhru, *"Fabrication of single-crystal lithium niobate films by crystal ion slicing"*, Appl. Phys. Lett. 73 (1998) 2293.

[214]P. Rabiei, and P. Günter, *"Optical and electro-optical properties of submicrometer lithium niobate slab waveguides prepared by crystal ion slicing and wafer bonding"*, Appl. Phys. Lett. 85 (2004) 4603.

[215]A. Ofan, O. Gaathon, L. Vanamurthy, S. Bakhru, H. Bakhru, K. Evans-Lutterodt and R. M. Osgood Jr., *"Origin of highly spatially selective etching in deeply implanted complex oxides"*, Appl. Phys. Lett. 93 (2008) 181906.

[216]L. Wang, K. M. Wang, X. L. Wang, F. Chen, Y. Jiang, C. L. Jia, Y. Jiao, F. Lu, D. Y. Shen, H. J. Ma and R. Nie, *"Selective etching in $LiNbO_3$ combined of MeV O and Si ion implantation with wet-etch technique"*, Surf. Coat. Technol. 201 (2007) 5081-5084.

[217]H. Hartung, E. -B. Kley, A. Tünnermann, T. Gischkat, F. Schrempel and W. Wesch, *"Fabrication of ridge waveguides in zinc-substituted lithium niobate by means of ion-beam enhanced etching"*, Opt. Lett. 33 (2008) 2320-2322.

[218]F. Nesprías, M. Venturino, M.E. Debray, J. Davidson, M. Davidson, A.J. Kreiner, D. Minsky, M. Fischer and A. Lamagna *"Heavy ion beam micromachining on $LiNbO_3$"*, Nucl. Instr. and Meth. B 267 (2009) 69-73.

[219]P.D. Townsend, J. Phys. E: Sci. Instrum. 10 (1977) 197.
[220]C. Buchal, D. Fluck and P. Günter, J. Electroceram. 3 (1999) 179-193.
[221]P.F. Bordui, R. G. Norwood, C. D. Bird and G. D. Calvert, *"Compositional uniformity in growth and poling of large-diameter lithium niobate crystals"*, J. Crystal Growth 113 (1991) 61-68.
[222]J.G. Bergman, A. Ashkin, A. A. Ballman, J. M. Dziedzic, H. V. Levinstein and R. G. Smith, *"Curie temperature, birrefringence and phase-matching temperature variations in $LiNbO_3$ as a function of melt stoichiometry"*, Appl. Phys. Lett. 12 (1968) 92-94.
[223]S.C. Abrahams, and P. Marsh, *"Defect structure dependence on composition in lithium niobate"*, Acta Cryst. B42 (1986) 61-68.
[224]I. Baumann, P. Rudolph, D. Krabe and R. Schalge, *"Orthoscopic investigation of the axial optical and compositional homogeneity of Czochralski grown $LiNbO_3$ crystals"*, J. Cryst. Growth 128 (1993) 903-908.
[225]S.C. Abrahams, W. C. Hamilton and J. M. Reddy, J. Chem. Phys. Solids 27 (1966) 1013.
[226]S.C. Abrahams, H. J. Levinstein and J. M. Reddy, J. Chem. Phys. Solids 27 (1966) 1019.
[227]R.S. Weis, and T.K. Gaylord *"Lithium niobate: Summary of physical properties and crystal structure"*, Applied Physics A 37 (1985) 191-203.
[228]T. Bartholomäus, K. Buse, C. Deuper and E. Krätzig, *"Pyroelectric coefficients of $LiNbO_3$ crystals of different compositions"*, Physica Status Solidi A 142 (1994) K55-K57.
[229]O. Beyer, D. Maxein, K. Buse, B. Sturman, H. T. Hsieh and D. Psaltis, *"Investigation of nonlinear absorption processes with femtosecond light pulses in lithium niobate crystals"*, Phys. Rev. E 71 (2005) 056603.
[230]S.C. Abrahams, E. Buehler, W.C. Hamilton and S. J. Laplaca, J. Chem. Phys. Solids 34 (1973) 521-532.
[231]H.D. Megaw, *"A note on the structure of lithium niobate, $LiNbO_3$"*, Acta Cryst. A24 (1968) 583-588.
[232]M.E. Lines, and A. M. Glass, *"Principles and applications of ferroelectrics and related materials"*, Vol., (Ed.), Clarendon Press, Oxford, 1977.
[233]L. Rebouta, M. F. da Silva, J. C. Soares, J. A. Sanz-García, E. Diéguez and F. Agulló-López, *"$^{7}Li(p, \alpha)\ ^{4}He$, PIXE and RBS/channeling studies of the lattice site location of impurities in $LiNbO_3$ and $LiNbO_3$ co-doped with magnesium"*, Nucl. Instr. Meth. B 64 (1992) 189-192.
[234]J.C. Soares, *"Microscopic characterization of materials by ion beam and hyperfine interaction analysis"*, Nucl. Instr. Meth. B 64 (1992) 215-220.
[235]A. Kling, L. Rebouta, J. G. Marques, J. G. Correia, M. F. da Silva, E. Diéguez, F. Agulló-López and J.C. Soares, *"Ion beam channeling and hyperfine interaction analysis for the characterization of stoichiometry and anti-site population in $LiNbO_3$"*, Nucl. Instr. Meth. B 118 (1996) 622-625.
[236]L. Rebouta, P. J. M. Smulders, D. O. Boerma, F. Agulló-López, M. F. da Silva and J. C. Soares, *"Ion-beam channeling yields of host and impurity atoms in $LiNbO_3$: Computer simulations"*, Phys. Rev. B 48 (1993) 3600-3610.
[237]S. Sanna, and W. G. Schmidt, *"Lithium niobate X-cut, Y-cut, and Z-cut surfaces from ab initio theory"*, Phys. Rev. B 81 (2010) 214116.
[238]J.R. Tesmer, and M. Nastasi, *"Handbook of Modern Ion Beam Materials Analysis"*, Vol., (Ed.), MRS, Pittsburg, Pennsilvania (USA), 1995.

[239]C. Trautmann, J. M. Costantini, A. Meftah, K. Schwartz, J. P. Stoquert and M. Toulemonde, in: *"Atomistic Mechanisms in Beam Synthesis and Irradiation of Materials "*. J.C. Barbour, S. Roorda, D. Ila, and M. Tsujioka, (Ed.), Materials Research Society (MRS Symposia Proceedings), vol. 504, Pittsburgh, 1999, pp. 123.

[240]R. Brenier, B. Canut, S. M. M. Ramos and P. Thevenard, *"Surface swelling of sapphire induced by MeV and GeV heavy ions"*, Nucl. Instr. Meth. B 90 (1994) 339-343.

[241]F. Schrempel, T. Gischkat, H. Hartung, E.-B. Kley, W. Wesch and A. Tünnermann, *"High aspect ratio microstructures in $LiNbO_3$ produced by Ion Beam Enhanced Etching"*, Mater. Res. Soc. Symp. Proc. 908E (2006).

[242]J.R. Carruthers, G. E. Peterson, M. Grasso and P. M. Bridenbaugh, *"Nonstoichiometry and crystal growth of lithium niobate"*, J. Appl. Phys. 42 (1971) 1846-1851.

[243]J. Kushibiki, H. Takahashi, T. Kobayashi and N. Chubachi, *"Characterization of $LiNbO_3$ crystals by line-focus-beam acoustic microscopy"*, Appl. Phys. Lett. 58 (1991) 2622-2624.

[244]L. Kovacs, and K. Polgar, *"Properties of Lithium Niobate"*, Vol., (Ed.), EMIS Datareviews Series. INSPEC, 1989.

[245]P. Lerner, C. Legras and J. P. Dumas, *"Stoechiométrie des monocristaux de métaniobate de lithium"*, J. Cryst. Growth 3 (1968) 231-235.

[246]H.M. O'Bryan, P. K. Gallagher and C. D. Brandle *"Congruent composition and Li-rich phase boundary of $LiNbO_3$"*, J. Am. Ceram. Soc. 68 (1985) 493-496.

[247]K. Chow, H. G. McKnight and L. R. Rothrock, *"The congruently melting composition of $LiNbO_3$"*, Mat. Res. Bull. 9 (1974) 1067.

[248]CrystalMaker Software (Free version for Windows), http://www.crystalmaker.com.

[249]F.C. Philips, *"An introduction to crystallography"*, Vol., (Ed.), Oliver & Boyd, Edinburgh, 1971.

[250]J. Czochralski, *"Ein neues verfahren zur messung der kristallisationsgeschwindigheit der metalle"*, Z. Phys. Chemie 92 (1918) 219-221.

[251]G. Malovichko, and V. Grachev, *"Evolution of conception of intrinsic and extrinsic defects in lithium niobate"*, in Fourth Annual Meeting of the COST Action P2 "Applications of nonlinear optical Phenomena" and Workshop on $LiNbO_3$, Budapest, 2001.

[252]L.O. Svaasand, M. Eriksrud, G. Nakken and A. P. Grande, *"Solid solution range of $LiNbO_3$"*, J. Cryst. Growth 22 (1974) 230.

[253]L.O. Svaasand, M. Eriksrud, A. P. Grande and F. Mo, *"Crystal growth and properties of $LiNb_3O_8$"*, J. Cryst. Growth 18 (1973) 179-184.

[254]M.D. Serrano, V. Bermúdez, L. Arizmendi and E. Diéguez, *"Determination of the Li/Nb ratio in $LiNbO_3$ crystals grown by the Czochralski method with K_2O added to the melt"*, J. Cryst. Growth 210 (2000) 670 - 676.

[255]M.D. Serrano, V. Bermúdez, L. Arizmendi and E. Diéguez, *"'"Determination of the Li/Nb ratio in $LiNbO_3$ crystals grown by the Czochralki method with K_2O added to the melt"*, J. Cryst. Growth 210 (2000) 670-676.

[256]S. Erdei, and F. W. Ainger, *"Trends in the growth of stoichiometric single crystals"*, J. Crystal Growth 174 (1997) 293-300.

[257]G.I. Malovichko, V. G. Grachev, L. P. Yurchenko, V. Y. Proshko, E. P. Kokanyan and V. T. Gabrielyan, *"Improvement of $LiNbO_3$ microstructure by crystal growth with potassium"*, Phys. Stat. Solidi 133 (1992) K29-K32.

[258]G.I. Malovichko, V. G. Grachev and O. F. Schirmer, *"The effect of iron ions on the defect structure of lithium niobate crystals grown from K_2O containing melts"*, Sol. State Commun. 89 (1994) 195-198.

[259]K. Kitamura, J. K. Yamamoto, N. Iyi, S. Kimura and T. Hayashi, *"Stoichiometric $LiNbO_3$ single crystal growth by double crucible Czochralski method using automatic powder supply system"*, J. Cryst. Growth 116 (1992) 327-332.

[260]P.F. Bordui, R. G. Norwood, D. H. Jundt and M. M. Fejer, *"Preparation and characterization of off-congruent lithium niobate crystals"*, J. Appl. Phys. 71 (1992) 875-879.

[261]D.H. Jundt, M. M. Fejer and R. L. Beyer, *"Optical properties of lithium-rich lithium niobate fabricated by vapor transport equilibration"*, IEEE J. Quantum Electron. 26 (1990) 135-138.

[262]T. Fukuda, and H. Hirano, *"Growth and characteristics of $LiNbO_3$ plate crystals"*, Mater. Res. Bull. 10 (1975) 801-806.

[263]A.V. Stepanov, Zh. Tekhn. Fiz. 29 (1959) 381.

[264]A.L. Shakh-Bugadov, and A. V. Stepanov, Zh. Tekhn. Fiz. 2 (1959) 394.

[265]A.R. Betts, and C. W. Pitt, *"Growth of thin-film lithium niobate by molecular beam epitaxy"*, Electron. Lett. 21 (1985) 960-962.

[266]A.A. Wernberg, H. J. Gysling, A. J. Filo and T. N. Blanton, *"Epitaxial growth of lithium niobate thin films from a single-source organometallic precursor using metalorganic chemical vapour deposition"*, Appl. Phys. Lett. 62 (1993) 946-950.

[267]A. Yamada, H. Tamada and M. Saitoh, *"$LiNbO_3$ thin-film optical waveguide grown by liquid phase epitaxy using Li_2O-B_2O_3 flux"*, Appl. Phys. Lett. 61 (1992) 2848-2851.

[268]M. Shimizu, Y. Furushima, T. Nishida and T. Shiosaki, *"Preparation and optical waveguide properties of $LiNbO_3$ thin films by RF magnetron sputtering"*, Jap. J. Appl. Phys. 32 (1993) 4111.

[269]R.I. Tomov, T. K. Kabadjova, P. A. Atanasov, S. Tonchev, M. Kaneva, A. Zherikhin and R. W. Eason, *"$LiNbO_3$ optical waveguides deposited on sapphire by electric-field-assisted pulsed laser deposition"*, Vacuum 58 (2000) 396-403.

[270]G. Balestrino, S. Martellucci, P. G. Medaglia, A. Paoletti et al., *"Epitaxial $LiNbO_3$ thin films grown by pulsed laser deposition for optical waveguides"*, Appl. Phys. Lett. 78 (2001) 1204-1206.

[271]S. Yin, *"Lithium niobate fibers and waveguides: Fabrication and applications"*, Proc. IEEE 87 (1999) 1962-1974

[272]H. Zhong, Y. Hou, N. Quan, X. Chen and R. Wang, *"Growth of lithium niobate single crystal fiber by an edge-defined, film-fed growth method"*, Cryst. Res. & Tech. 26 (1991) 395-399.

[273]G.E. Peterson, and A. Carnevale, *"^{93}Nb NMR linewidths in nonstoichiometric lithium niobate"*, J. Chem. Phys. 56 (1972) 4848.

[274]K.L. Sweeney, and L. E. Halliburton, *"Oxygen vacancies in lithium niobate"*, Appl. Phys. Lett. 43 (1983) 336-338.

[275]H. Donnerberg, S. M. Tomlinson, C. R. A. Catlow and O. F. Schirmer, *"Computer-simulation studies of intrinsic defects in $LiNbO_3$"*, Phys. Rev. B 40 (1989) 11909-11916.

[276]J. Blümel, E. Born and Th. Metzger, *"Solid state NMR study supporting the lithium vacancy model in congruent lithium niobate"*, J. Phys. Chem. Solids 55 (1994) 589-593.

[277]N. Zotov, H. Boysen, F. Frey, T. Metzger and E. Born, *"Cation substitution models of congruent $LiNbO_3$ investigated by x-ray and neutron powder diffraction"*, J. Phys. Chem. Solids 55 (1994) 145-152.

[278]X.H. Zhen, L. C. Zhao and Y. H. Xu, *"Defect structure and optical damage resistance of Zn:Fe:$LiNbO_3$ crystals"*, Appl. Phys. B 76 (2003) 655-659.

[279]F. Jaque, T. P. J. Hana and G. Lifante *"Comparative study of the singularity in the optical properties of congruent doped $LiNbO_3$ crystals"*, J. Luminiscence 102 (2003) 248-252.

[280]J.M. Cabrera, J. Olivares, M. Carrascosa, J. Rams, R. Müller and E. Diéguez, *"Hydrogen in lithium niobate"*, Adv. in Phys. 45 (1996) 349-392.

[281]X. Feng, T. Shao and J. Zhang, *"An infrared absorption band caused by H^+ implantation in $LiNbO_3$ crystals"*, J. Phys. Condens. Matter 3 (1991) 4145-4150.

[282]J.L. Jackel, C. E. Rice and J. J. Veselka, *"Proton exchange for high index waveguides in $LiNbO_3$"*, Appl. Phys. Lett. 41 (1982) 607-608.

[283]C. Canali, A. Carnera, G. D. Mea, P. Mazzoldi, S. M. Al Shukri, A. C. G. Nutt and R. M. de la Rue, *"Structural characterization of proton exchanged $LiNbO_3$ optical waveguides"*, J. Appl. Phys. 59 (1986) 2643-2649.

[284]Y.N. Korkishko, and V. A. Fedorov, *"Structural phase diagram of $H_xLi_{1-x}NbO_3$ waveguides: The correlation between optical and structural properties"*, J. Select. Topics in Quant. Electr. 2 (1996) 187-196.

[285]C.E. Rice, *"The structure and properties of $Li_{1-x}H_xNbO_3$"*, J. Sol. State Chem. 64 (1986) 188-199.

[286]H. Hu, F. Lu, F. Chen, F. -X. Wang, J. -H. Zhang, X. -D. Liu, K. -M. Wang and B. -R. Shi, *"Optical waveguide formation by MeV H^+ implanted into $LiNbO_3$ crystal"*, Optics Commun. 177 (2000) 189-193.

[287]W.K. Burns, P. H. Klein, E. J. West and L. E. Plew, *"Ti diffusion in Ti:$LiNbO_3$ planar and channel waveguides"*, J. Appl. Phys. 50 (1979) 6175.

[288]G.J. Griffiths, and R. J. Esdaile, *"Analysis of titanium diffused planar optical waveguides in lithium niobate"*, IEEE J. Quantum Electron. QE-20 (1984) 149.

[289]W.M. Young, M. M. Frejer, M. J. F. Digonnet, A. F. Marshall and R. S. Feigelson, *"Fabrication, characterization and index profile modeling of high damage resistance Zn-diffused waveguides in congruent and MgO:$LiNbO_3$"*, J. Lightwave Technol. 10 (1992) 1238.

[290]G.D. Boyd, R. C. Miller, K. Nassau, W. L. Bond and A. Savage, *"$LiNbO_3$: An efficient phase matchable nonlinear optical material"*, Appl. Phys. Lett. 5 (1964) 234.

[291]M. DiDomenico, and S. H. Wemple, *"Oxygen-octaedra ferroelectrics. I. Theory of electro-optical and nonlinear optical effects"*, J. Appl. Phys. 46 (1969) 720-734.

[292]L. Hafid, and F. M. Michel-Calendini, *"Electronic structure of $LiNbO_3$: Densities of states, optical anisotropy and spontaneous polarisation calculated from the $X\alpha$ molecular orbital method"*, J. Phys. C: Solid State Phys 19 (1986) 2907-2917.

[293]K. Bärner, R. Braunstein and H. A. Weakliem, *"The optical properties of $LiNbO_3$"*, Phys. Stat. Sol. (b) 68 (1975) 525-531.

[294]D. Redfield, and W. J. Burke, *"Optical absorption edge of $LiNbO_3$"*, J. Appl. Phys. 45 (1974) 4566.

[295]L. Kovacs, G. Ruschhaupt, K. Polgár, G. Corradi and M. Wöhlecke, *"Composition dependence of the ultraviolet absorption edge in lithium niobate"*, Appl. Phys. Lett. 70 (1997) 2801-2803.

[296]E. Wiesendanger, and G. Güntherodt, *"Optical anisotropy of $LiNbO_3$ and $KNbO_3$ in the interband transition region"*, Solid Stat. Comm. 14 (1974) 303

[297]A.S. Barker, and R. Loudon, *"Dielectric properties and optical phonons in $LiNbO_3$ "*, Phys. Rev. 158 (1967) 433-445.

[298]J.D. Axe, and D. F. O'Kane, *"Infrared dielectric dispersion of $LiNbO_3$"*, Appl. Phys. Lett. 9 (1966) 58.

[299]U. Schlarb, S. Klauer, M. Wesselmann, K. Betzler and M. Wöhlecke, *"Determination of the Li/Nb ratio in lithium niobate by means of birefringence and raman measurements"*, Appl. Phys. A 56 (1993) 311-315.

[300]U. Schlarb, and K. Betzler, *"Refractive indices of lithium niobate as a function of temperature, wavelength and composition: A generalized fit"*, Phys. Rev. B 48 (1993) 15613.

[301]A.M. Mamedov, *"Optical properties (V-UV region) of $LiNbO_3$"*, Opt. Spectrosc. (USRR) 56 (1984) 645-649.

[302]R.W. Boyd, *"Nonlinear Optics"*, Vol., (Ed.), Academic Press, California, USA, 1992.

[303]B.E.A. Saleh, and M. C. Teich, *"Fundamentals of Photonics"*, Vol., (Ed.), Wiley Series in Pure and Applied Optics. Wiley Interscience, USA, 1991.

[304]R.C. Eckardt, H. Masuda, Y. X. Fan and R. L. Byer, *"Absolute and relative nonlinear optical coefficients of KDP, MgLN and KTP measured by phase-matched second-harmonic generation"*, IEEE J. Quant. Electr. 26 (1990) 922

[305]B. Kim, B. K. Rhee and M. Cha, *"Simple measurement of space-charge field in a $LiNbO_3$ crystal doped with 0.65 mol% MgO using second harmonic generation"*, Optics Communications 173 (2000) 377-380.

[306]M.M. Fejer, G. A. Magel, D. H. Jundt and R. L. Byer, *"Quasi-phasematched second harmonic generation: Tuning and tolerances"*, J. Quant. Electr. 28 (1992) 2631-2654.

[307]D.H. Jundt, G. A. Magel, M. M. Fejer and R. L. Byer, *"Periodically poled $LiNbO_3$ for high-efficiency second-harmonic generation"*, Appl. Phys. Lett. 59 (1991) 2657-2659.

[308]Y.L. Chen, J. J. Xu, X. Z. Zhang, Y. F. Kong, X. J. Chen and G. Y. Zhang, *"Ferroelectric domain inversion in near stoichiometric lithium niobate for high efficiency blue light generation"*, Appl. Phys. A 74 (2002) 187-190.

[309]F. Agulló-López, J. M. Cabrera and F. Agulló-Rueda, *"Electrooptics. Phenomena, Materials and Applications."*, Vol., (Ed.), Academic Press Inc., San Diego, California (USA), 1994.

[310]R.C. Alferness, in: *"Titanium diffused $LiNbO_3$ waveguides devices"*. T. Tamir, (Ed.), *Guided wave optoelectronic*, Springer-Verlag., New York, 1990.

[311]R. Chen, and C. S. Tsai, *"Thermally annealed single-mode proton-exchanged channel-waveguide cutoff modulator"*, Optics Lett. 11 (1986) 546-548.

[312]P. Mollier, H. Porte and J. P. Goedgebuer, *"Proton exchanged imbalanced Ti:$LiNbO_3$ Mach-Zehnder modulator"*, Appl. Phys. Lett. 60 (1992) 274.

[313]R. Chen, *"Electro-optic depolarization switch on y-cut $LiNbO_3$ proton-exchanged channel waveguides"*, Appl. Phys. Lett. 54 (1989) 2628.

[314]J.A. de Toro, M. D. Serrano, A. García-Cabañes and J. M. Cabrera, *"Accurate interferometric measurement of electro-optic coefficients: Application to quasi-stoichiometric $LiNbO_3$"*, Opt. Comm. 154 (1998) 23-27.

[315]A.M. Glass, D. Van der Linde and T. J. Negran, *"High voltage bulk photovoltaic effect and the photorefractive process in $LiNbO_3$"*, Appl. Phys. Lett. 25 (1974) 233-235.

[316]V.M. Fridkin, *"Photoferroelectrics"*, Vol., (Ed.), Springer-Verlag, New York, 1979.

[317]M. Carrascosa, and F. Agulló-López, *"Optimization of the developing for fixed gratings in $LiNbO_3$"*, Opt. Comm. 126 (1996) 240.

[318]M. Carrascosa, and F. Agulló-López, *"Kinetics for optical erasure of sinusoidal holographic gratings in photorefractive materials"*, IEEE J. Quantum Electron. 22 (1986) 1369-1375.

[319]A. Ashkin, G. D. Boyd, J. M. Dziedzic, R. G. Smith, A. A. Ballman, J. J. Levinstein and K. Nassau, *"Optically-induced refractive index inhomogeneities in $LiNbO_3$ and $LiTaO_3$"*, Appl. Phys. Lett. 9 (1966) 72.

[320]P. Günter, *"Nonlinear optical effects and materials"*, Vol., (Ed.), Springer, Berlin, 2000.

[321]D.L. Staebler, and J. J. Amodei, *"Thermally fixed holograms in $LiNbO_3$"*, Ferroelectrics 3 (1972) 107-113.

[322]B.C. Grabmaier, W. Wersing and W. Koestler, *"Properties of undoped and MgO-doped $LiNbO_3$: correlation to the defect structure"*, J. Cryst. Growth 110 (1991) 339-347.

[323]K. Nakamura, and H. Shimizu, *"Hysteresis-free piezoelectric actuators using $LiNbO_3$ plates with a ferroelectric inversion layer"*, Ferroelectrics 93 (1989) 211-216.

[324]L.B. Schein, P. J. Cressman and L. E. Cross, *"Electrostatic measurements of unusually large secondary pyroelectricity in partially clamped $LiNbO_3$"*, Ferroelectrics 22 (1979) 937-943.

[325]D. Kip, B. Gather, H. Bendig and E. Krätzig, *"Concentration and refractive index profiles of titanium- and iron-diffused planar $LiNbO_3$ waveguides"*, Phys. Status Solidi A 139 (1993) 241-248.

[326]Y. Avrahami, and E. Zolotoyabko, *"Diffusion and structural modification of Ti:$LiNbO_3$ studied by high-resolution x-ray diffraction"*, J. Appl. Phys. 85 (1999) 6447.

[327]M.L. Bortz, and M. M. Fejer, *"Annealed proton-exchanged $LiNbO_3$ waveguides"*, Opt. Lett. 16 (1991) 1844-1846.

[328]W.-Y. Hsu, G. Braunstein, V. Gopalan, C. S. Willand and M. C. Gupta, *"Correlation between structural and optical properties in proton-exchanged $LiNbO_3$"*, Appl. Phys. Lett. 61 (1992) 3083.

[329]D.-W. Kim, S. -H. Lee and T. W. Noh, *"Structural and nonlinear optical properties of epitaxial $LiNbO_3$ films grown by pulsed laser deposition"*, Mater. Sci. Eng. B 56 (1998) 251-255.

[330]J.-W. Son, S. S. Orlov, B. Phillips and L. Hesselink, *"Pulsed laser deposition of single phase $LiNbO_3$ thin film waveguides"*, J. Electroceram. 17 (2006) 591-595.

[331]T. Kawaguchi, K. Mizuuchi, T. Yoshino, M. Imaeda, K. Yamamoto and T. Fukuda, *"Liquid-phase epitaxial growth of Zn-doped $LiNbO_3$ thin films and optical damage resistance for second-harmonic generation"*, J. Cryst. Growth 203 (1999) 173-178.

[332]S. Mailis, C. Riziotis, I. T. Wellington, P. G. R. Smith, C. B. E. Gawith and R. W. Eason Opt. Lett. 28, 1433, *"Direct ultraviolet writing of channel waveguides in congruent lithium niobate single crystals"*, Opt. Lett. 28 (2003) 1433-1435.

[333]M. Levy, and A. M. Radojevic, in: *"Wafer bonding: Applications and Technology"*. M. Alexe, and U. Gosele, (Ed.), Springer-Verlag, Berlin, Heidelberg, 2004.

[334]R.R. Thomson, S. Campbell, I. J. Blewett, A. K. Kar and D. T. Reid, *"Optical waveguide fabrication in z-cut lithium niobate ($LiNbO_3$) using femtosecond pulses in the low repetition rate regime"*, Appl. Phys. Lett. 88 (2006) 111109.

[335]P. Zhang, Y. Ma, J. Zhao, D. Yang, and H. Xu, *"One-dimensional spatial dark soliton-induced channel waveguides in lithium niobate crystal"*, Appl. Opt. 45 (2006) 2273-2278.

[336]C.W. Choi, Y. U. Kwon and J. Lee, J. Korean Phys. Soc. 32 (1998) S1417.

[337]Y. Tan, F. Chen, X. L. Wang, L. Wang, V. M. Shandarov and D. Kip, *"Formation of reconfigurable optical channel waveguides and beam splitters on top of proton-implanted lithium niobate crystals using spatial dark soliton-like structures"*, J. Phys. D 41 (2008) 102001.

[338]W. Sohler, H. Hu, R. Ricken, V. Quiring, C. Vannahme, H. Herrmann, D. Büchter, S. Reza, W. Grundkötter, S. Orlov, H. Suche, R. Nouroozi and Y.H. Min, *"Integrated optical devices in lithium niobate"*, Opt. Photonics News 19 (2008) 24-31.

[339]T. Suhara, H. Tazaki and H. Nishihara, *"Measurement of reduction in SHG coefficient of $LINbO_3$ by proton exchanging"*, Electron. Lett. 25 (1989) 1326-1328.

[340]G.G. Bentini, M. Bianconi, A. Cerutti, M. Chiarini, G. Pennestri, C. Sada, N. Argiolas, M. Bazzan, P. Mazzoldi and R. Guzzi, *"Structural and compositional characterization of X-cut $LiNbO_3$ crystals implanted with high energy oxygen and carbon ions"*, Nucl. Instr. Meth. B 240 (2005) 174-177.

[341]M.H.F. Chu, and W. C. Shui, *"Theoretical studies of AlGaAs-GaAs multiple-quantum-well single-channel waveguide defined by ion-implantation-induced intermixing"*, Proc. SPIE 3944 (2000) 149.

[342]L. Mutter, M. Jazbinsek, Ch. Herzog and P. Günter, *"Electro-optic and nonlinear optical properties of ion implanted waveguides in organic crystals"*, Opt. Express 16 (2008) 731-739.

[343]K. Balasubramanian, P. J. Heard and M. J. Cryan, *"Focused ion beam fabrication of two dimensional photonic crystals in silicon-on-insulator"*, J. Vac. Sci. Technol. B 24 (2006) 2533.

[344]S.S. Sarkisov, M. J. Curley, E. K. Williams, D. Ila, V. L. Svetchnikov, H. W. Zandbergen, G. A. Zykov, C. Banks, J. -C. Wang, D. B. Poker and D. K. Hensley, *"Nonlinear optical waveguides produced by MeV ion implantation in $LiNbO_3$"*, Nucl. Instr. Meth. B 166-167 (2000) 750-757.

[345]H. Hu, R. Ricken, W. Sohler and R. B. Wehrspohn, *"Lithium niobate ridge waveguides fabricated by wet etching"*, IEEE Photonics Tech. Lett. 19 (2007) 417-419.

[346]D.W. Ward, E. R. Statz, K. A. Nelson, R. M. Roth and R. M. Osgood, *"Terahertz wave generation and propagation in thin-film lithium niobate produced by crystal ion slicing"*, Appl. Phys. Lett. 86 (2005) 022908.

[347]M. Bianconi, G. G. Bentini, M. Chiarini, P. De Nicola, G. B. Montanari, A. Nubile and S. Sugliani, *"Defect engineering and micromachining of Lithium Niobate by ion implantation"*, Nucl. Instr. and Meth. B 267 (2009) 2839-2845.

[348]T. Ruiz, A. Méndez, M. Carrascosa, J. Carnicero, A. García-Cabañez, J. Olivares, F. Agulló-López, A. García-Navarro and G. García, *"Tailoring of refractive*

index profiles in $LiNbO_3$ optical waveguides by low-fluence swift-ion irradiation", J. Phys. D: Appl. Phys. 40 (2007) 4454-4459.

[349]A. García-Navarro, A. Méndez, J. Olivares, G. García, F. Agulló-López, M. Zayat, D. Levy and L. Vazquez, *"Morphology of ion tracks and nanopores in $LiNbO_3$ produced by swift-ion-beam irradiation"*, Nucl. Instr. Meth. B 249 (2006) 172-176.

[350]J.F. Ziegler, *"Handbook of ion implantation technology"*, Vol., (Ed.), North-Holland, Amsterdam, 1992.

[351]J.S. Williams, and J. M. Poate, *"Ion implantation and beam processing"*, Vol., (Ed.), Academic, Orlando, 1984.

[352]M. Bianconi, N. Argiolas, M. Bazzan, G. G. Bentini, M. Chiarini, A. Cerutti, P. Mazzoldi, G. Pennestri and C. Sada, *"Nuclear and electronic energy loss synergy in the process of damage growth in ion implanted $LiNbO_3$"*, Nucl. Instr. Meth. B 249 (2006) 122-125.

[353]H. Hu, F. Lu, F. Chen, B. -R. Shi, K. -M. Wang and D. -Y. Shen, *"Extraordinary refractive-index increase in lithium niobate caused by low-dose ion implantation"*, Appl. Opt. 40 (2001) 3759-3761.

[354]F. Lu, T. Zhang, X. Wang, S. Li, K. Wang, D. Shen and H. Ma, *"Formation of waveguides by implantation of 3.0 MeV Ni^{2+}"*, J. Appl. Phys. 96 (2004) 3463.

[355]F. Schrempel, T. Steinbach, Th. Gischkat and W. Wesch., *"Channeling irradiation of $LiNbO_3$"*, Nucl. Instr. Meth. B 266 (2008) 2958-2961.

[356]T. Steinbach, F. Schrempel, Th. Gischkat and W. Wesch, *"Influence of ion energy and ion species on ion channeling in $LiNbO_3$"*, Phys. Rev. B 78 (2008) 184106.

[357]K.E. Youden, S. W. James, R. W. Eason, P. J. Chandler, L. Zhang and P. D. Townsend, *"Photorefractive planar waveguides in $BaTiO_3$ fabricated by ion-beam implantation"*, Opt. Lett. 17 (1992) 1509-1511.

[358]G. Vázquez, J. Rickards, G. Lifante, M. Domenech and E. Cantelar, *"Low dose carbon implanted waveguides in Nd:YAG"*, Opt. Express 11 (2003) 1291-1296.

[359]D.K. Avasthi, *"Nanostructuring by energetic ion beams"*, Hyperfine Interact. 160 (2005) 95-106.

[360]J. Olivares, A. García-Navarro, G. García, A. Méndez, F. Agulló-López, A. García-Cabañes, M. Carrascosa and O. Caballero, *"Nonlinear optical waveguides generated in lithium niobate by swift-ion irradiation at ultralow fluences"*, Optics Letters 32 (2007) 2587-2589.

[361]T. Gischkat, H. Hartung, F. Schrempel, E. B. Kley, A. Tünnermann and W. Wesch, *"Patterning of $LiNbO_3$ by means of ion irradiation using the electronic energy deposition and wet etching"*, Microelectron. Eng. 86 (2009) 910-912.

[362]T. Gischkat, F. Schrempel, Th. Höche and W. Wesch, *"Annealing behavior of lithium niobate irradiated with He-ions at 100 K"*, Nucl. Instr. Meth. B 267 (2009) 1492-1495.

[363]F. Laurell, J. Webjorn, G. Arvidsson and J. Holmberg, *"Wet etching of proton-exchanged lithium niobate-a novel processing technique"*, J. Lightwave Technol. 10 (1992) 1606.

[364]Z.D. Gao, Q. J. Wang, Y. Zhang and S. N. Zhu Opt. Mat., *"Etching study of poled lithium tantalate crystal using wet etching technique with ultrasonic assistance"*, Opt. Mat. 30 (2008) 847-850.

[365]R. Waser, (Ed.), *Nanoelectronics and Information Technology*, Wiley-VCH, Weinheim, 2003.

[366]T.-J. Wang, C.-F. Huang, W.-S. Wang and K.-K. Wei *"A Novel Wet-Etching Method Using Electric-Field-Assisted Proton Exchange in $LiNbO_3$"*, J. Lightwave Tech. 22 (2004) 1764-1771.

[367]C.L. Sones, S. Mailis, W. S. Brocklesby, R. W. Eason and J. R. Owen, *"Differential etch rates in z-cut $LiNbO_3$ for variable HF/HNO_3 concentrations"*, J. Mat. Chem. 12 (2002) 295-298.

[368]S.H. Wemple, M. DiDomenico and I. Camlibel, *"Relationship between linear and quadratic electro-optic coefficients in $LiNbO_3$, $LiTaO_3$, and other oxygen-octahedra ferroelectrics based on direct measurement of spontaneous polarization"*, Appl. Phys. Lett. 12 (1968) 209.

[369]Y. Jiang, K. M. Wang, X. -L. Wang, F. Chen, C. -L. Jia, Y. Jiao, L. Wang and Y. Jiao, *"Model of refractive-index changes in lithium niobate waveguides fabricated by ion implantation"*, Phys. Rev. B 75 (2007) 195101.

[370]J. Olivares, A. García-Navarro, G. García, F. Agulló-López, F. Agulló-Rueda, A. García-Cabañes and M. Carrascosa, *"Buried amorphous layers by electronic excitation in ion-beam irradiated lithium niobate: structure and kinetics"*, J. Appl. Phys 101 (2007) 033512.

[371]J. Olivares, M. L. Crespillo, O. Caballero, F. Agulló-López and M. Carrascosa, *"Novel optical waveguides by means of using electronic damage of swift heavy ions"*, Proceedings of the 16th International Conference of Ion Beam Modifications of Materials (IBMM2008), Dresden (Germany), 2008 (unpublished).

Part II.

Experimental Methods.

This Part comprises the different experimental techniques used in this Thesis work. Firstly, the different irradiation setups, fabrication methods, necessary to carry out the experiments, will be shown. Then, several analytical techniques used to characterize the samples studied in this work, with the aim of obtaining information from the ion beam modification of material, will be described.

In this sense, the submission refers, in first place, the description of heavy ion accelerators with which the irradiations were carried out. Here, a brief description of the Facilities used will take place. Here, it is necessary to comment that, the ion beam accelerator is used as a double tool: for analysis of samples and for the modification of properties of the irradiated materials. Then, the following paragraphs are devoted to the characterization techniques used, mainly, Rutherford Backscattering Spectroscopy in channelling configuration (RBS/C) and Atomic Force Microscopy (AFM). Finally, additional characterization methods, like, transmission electron microscopy (TEM) and profilometry, will be reported too.

Chapter 4

Ion Beam Techniques.

4.1. Ion beam modification of materials. Irradiation Facilities.
4.2. Ion beam analysis. Characterization by ion channelling. RBS.

4.1. Ion beam modification of materials. Irradiation Facilities.

Irradiations of samples were performed at three different facilities: GANIL (Caen, France), GSI (Darmstadt, Germany) and CMAM (UAM Madrid), although most of the experiments, both irradiations and characterization, were carried out in the latter. It should be noted that the irradiations in the foreign centers were accomplished in collaboration with Dr. Marcel Toulemonde (GANIL - *Grand National d'Ions Lourds Accélérateur Lourds*-) and Dr. Christina Trautmann (GSI - *Gesellschaft für Schwerionenforschung*-), respectively. The following paragraphs present the main features of the heavy ion accelerator used and the most important parameters of irradiation experiments. There will be a further explanation in the case of the CMAM accelerator, explaining its work and the different parts of that, however, with the aim of obtaining a more detailed study, it is recommended to see Ref. [1].

4.1.1. Tandem accelerator at CMAM. (Centro de Microanálisis de Materiales).

The processing of the most of the samples studied in this Thesis work was carried out in the ion accelerator installed at the Centro de Microanálisis de Materiales at the Campus of the University Autonoma de Madrid (CMAM-UAM)) [2-4], which was officially opened in 2003. This is a linear electrostatic tandem accelerator of 5 MV terminal voltage, designed and installed by the company High Voltage Engineering (HVE) [5]. **Figure 1** shows a panoramic view of the accelerator and beam lines at CMAM.

This accelerator consists of two acceleration stages: in the first one, negative ions are accelerated, while in the second one, they are positive. The transition from negative to positive ions is performed by a charge exchange element called "*stripper*".

The operation of such accelerators is based on the original idea of J. Cockroft and E. Walton in 1932 to create a potential difference of the order of MV, which the ions produced by the source are accelerated. Originally, they were able to accelerate protons to energies between 100 and 500 KeV using a voltage multiplier based on a transformer-rectifier-capacitor unit

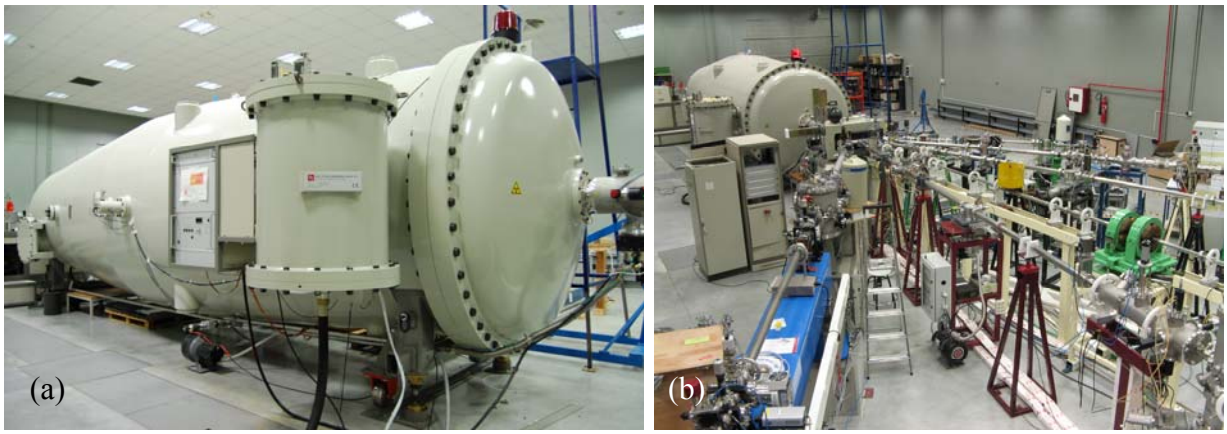

Fig. 1. (a) The Accelerator tank, seen from the high energy side, installed at CMAM, **(b)** General view of the beam lines. The switching magnet is after high energy side of the accelerator tank.

capacitor [6]. The solution for producing high voltages implemented by Cockcroft and Walton in their accelerator consisted on a, conceptually simple, electrical circuit formed by capacitors and switches (in current designs, the switches can be implemented by diodes or transistors and radio-frequency voltage supplies are used). Basically, the high voltage is produced by charging a bank of capacitors in parallel and then connecting them in series, thereby adding up their separate voltages.

The Cockcroft-Walton solution posses, nowadays, the advantage of being entirely based on solid state circuits, not depending on any moving part for the voltage generation -in contrast to the Van de Graaff generators- and thus achieving very good stability and very low ripple in the terminal voltage, which translates into a more precise and stable beam.

Independently from the voltage generation system, the availability of reliable negative ion sources since the 1950's, opened the door to a new class of accelerators that provided more energetic beams for a given terminal voltage by applying it twice to the particle. In the so-called *tandem* accelerators - as opposite to traditional *single ended* machines -, the positively charged terminal is positioned *in front* of the ion source, and the negatively charged ions are accelerated towards it (see **Fig. 2**). Precisely when the ions pass through the terminal, they enter a gas-filled region where they get stripped from electrons, thus becoming positive ions. These positive ions are now repelled by the positive terminal, receiving extra acceleration.

Let us review, briefly, the different parts of the accelerator and how they work. As mentioned above, additional details of the whole system can be found in Ref. [1].

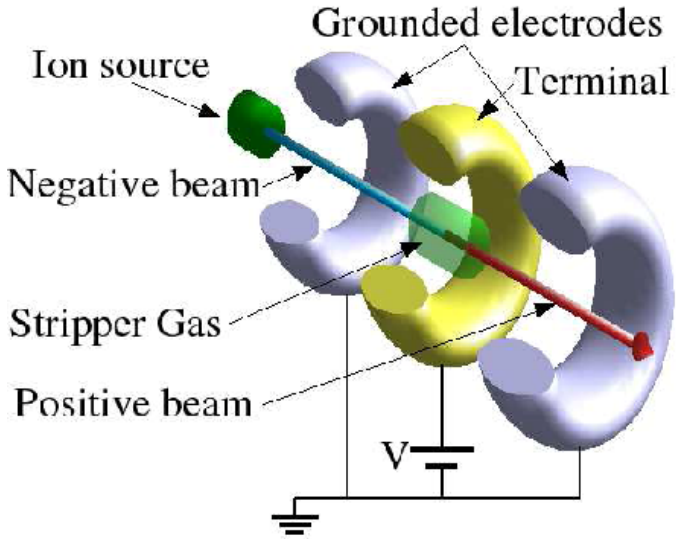

Fig. 2. Schematic diagram of a tandem accelerator.

4.1.1.1. Ion sources.

The accelerator has two commercial ion sources: a source of gas, called *Duoplasmatron*, and a negative sputtering ion source, which make it possible to obtain (negative) ion beams for, practically, any element in the periodic table.

Duoplasmatron source.

Duoplasmatron source (Model HVE-358) is essentially used for ion beam of gaseous species, especially He^+ and H^-.

In the case of He, the source is mainly used to produce He^- ions, since these cannot be produced by the sputtering source. Due to the difficulty of producing He^- directly in sufficient number, the source is operated in "positive mode", i.e., He^+ ions are produced, then being inserted into a Lithium charge exchange canal to obtain the final negative beam (He^-). **Fig. 3** shows a scheme of the Duoplasmatron source.

The ions are generated in two discharge stages. The first discharge is fed by termo-ionic emission from a filament and occurs between the filament an the intermediate electrode (**Fig 3**). The ions are extracted through an aperture in the intermediate electrode to the second discharge region, located between this electrode and an anode. These discharges occur with voltage differences of ~ +150 V and the anode is polarized at ~ +20 kV with respect to the ground (the extraction electrode). The plasma is heavily confined by a magnetic field, increasing its density. The ions flow through an aperture in the anode to the extraction region, where they accelerate towards the ground potential. An Einzel lens, immediately after the source, is responsible of focusing the beam into the Li charge exchange canal, where exchange ions with the atoms, yielding a beam of He- ions.

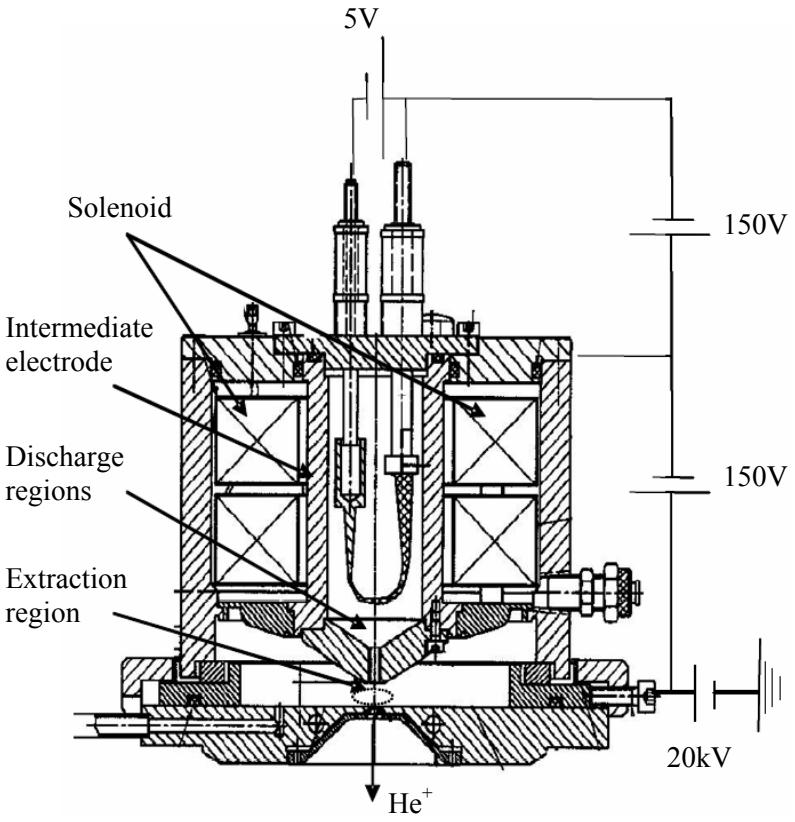

Fig. 3. Schematic diagram of a Duoplasmatron ion source.

Negative sputtering ion source.

The negative sputtering ion source (model HVE-860) is able to produce negative ion beams from atoms present in solid targets[1] (most of the species with the notable exception of He).

The ions are produced by bombardment - with Cesium (Cs^+) ions- of a Cesium-covered surface of a target. Cs^+ ions come from a reservoir that is heated to a temperature of about 100°C. The evaporated Cs is ionized by passing through an ionizer (*thermocoax* resistance being passing through a large current ~ 19 A). The atoms of the target that are sputtered, pass through the Cs surface layer and interchange electrons, increasing the fraction of negative ions (**Fig. 4**).

A fraction of the Cesium vapor provided by a heated Cs reservoir, condensates on the surface of the cooled target, which is mounted on a cylindrical cupper cathode polarized to ~ -10 kV. Some other fraction of the Cs is ionized and, hence, it accelerates towards the cathode where it sputters the target material, as mentioned before. The negative target ions produced after the charge exchange in the Cs layer are repelled towards the extraction region, while the secondary electrons are eliminated from the negative ion beam by means of a magnetic field produced by permanent magnets. (For more information, see, e.g., Ref. [7]).

[1] While nearly all the ions can be generated, it should be noted that some of them are more prolific than others, for example, O, Si and all the halides (F, Cl, ...).

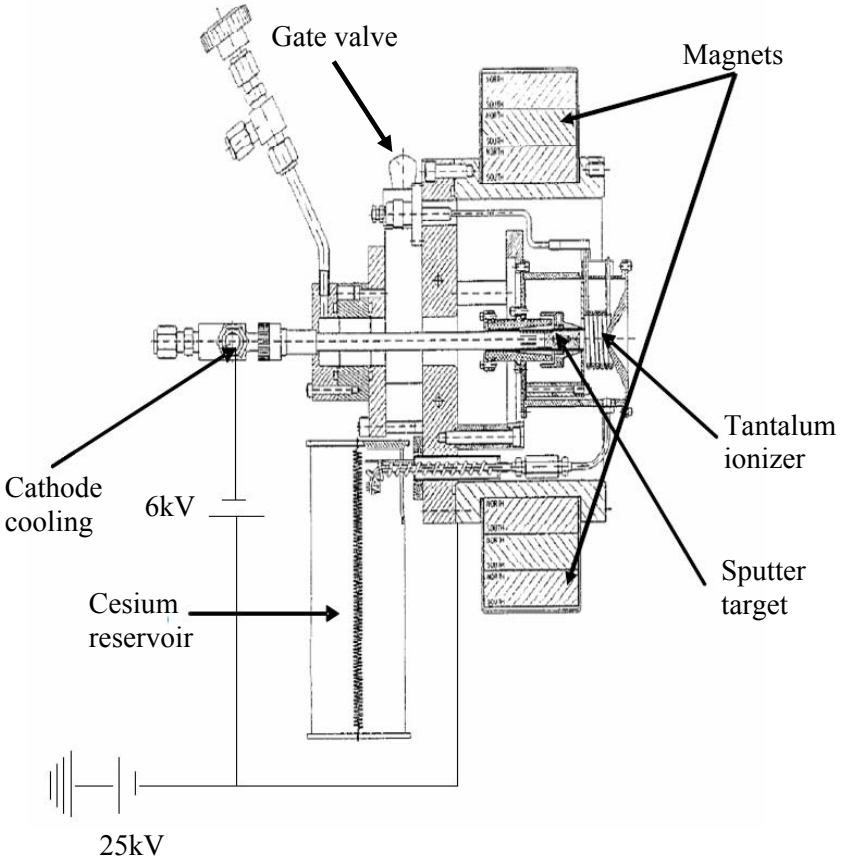

Fig. 4. Schematic diagram of a negative sputtering ion source.

4.1.1.2. Acceleration tube.

Upon exiting the source, the ion beam, with negative charge state, is led to acceleration tube through several focusing Einzel lens and passes through a magnet (*low energy magnet*), which acts as a mass selector of all the species that make up the beam at this point.

Subsequently, the acceleration of ions is carried out gradually until reaching the terminal voltage with the maximum voltage applied, in the case of the accelerator installed at CMAM, can reach 5 MV. This progressive increase of the the electrostatic potential is achieved by conducting the beam through segmented tubes in which each segment is at a slightly higher potential than the preceding one. The electric field is uniform inside each segment and the acceleration is produced in the insulating gaps between them. The field lines in these gaps, have also a focusing effect on the beam. The acceleration from the grounded low energy side to the terminal voltage at the center of the accelerator is done in 50 steps (therefore, in the case of maximum terminal voltage of 5MV, the voltage drop at each segment is 100kV).

The terminal, located approximately half-way in the accelerator tube, and where it reaches its maximum voltage, is an equipotential region in which Nitrogen gas is circulated by a turbo-molecular pump. The gas pressure is maintained in the regime where the charge-exchange processes between the accelerated ions and the N_2 molecules are favoured (*stripper*), producing a considerable fraction of positive ions in the beam. The charge distribution of these depends, among other things, the gas pressure. Thanks to a differential vacuum system ensures that the

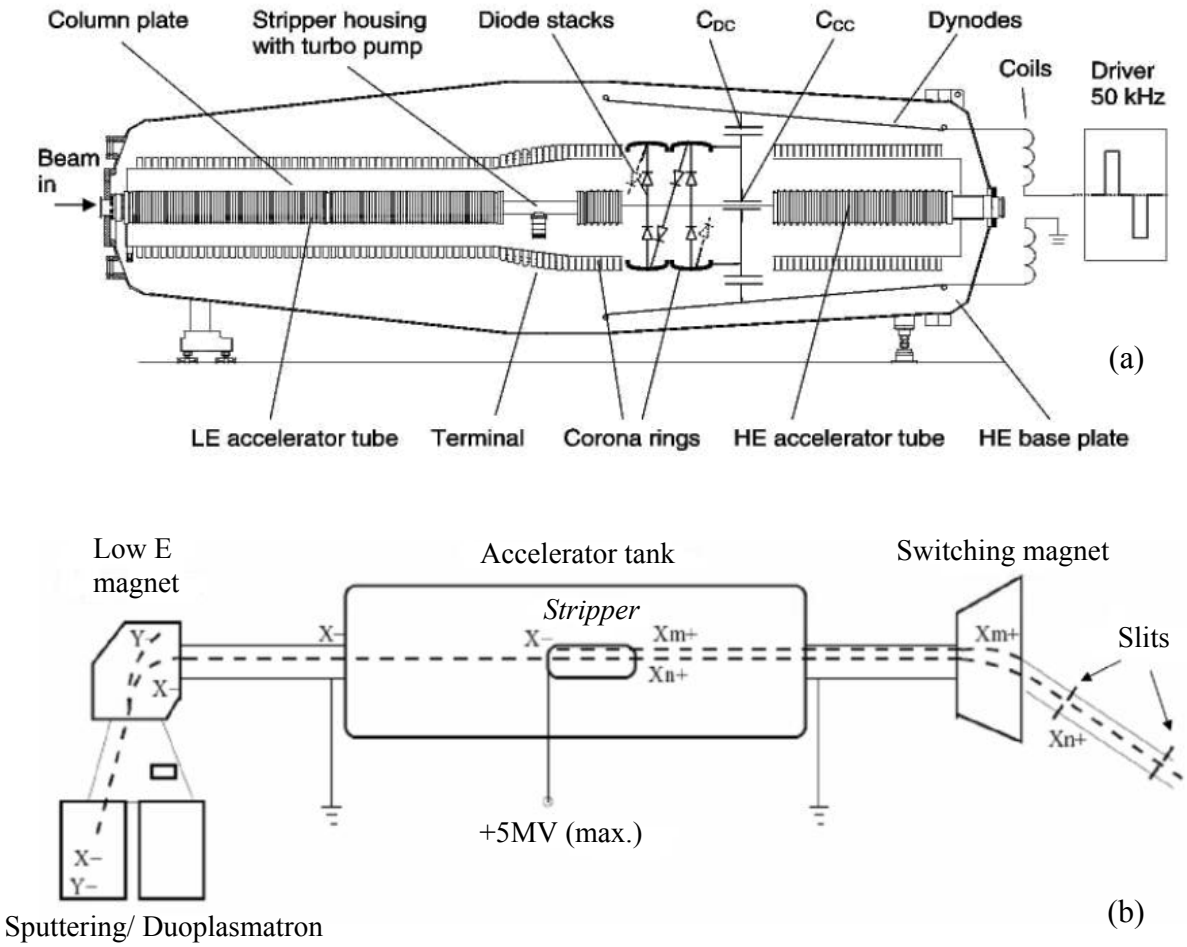

Fig. 5. (a). Internal layout of the 5 MV Tandetron (reproduced from [4], courtesy of HVE). **(b)** General diagram of the acceleration system. Schematic of negative ion sources, switching magnets and acceleration tube (with neutral housing and maximum positive voltage in the center of the tube).

gas exchange region is located mainly in the maximum terminal voltage. Thus, negative ions arriving become positive, being repelled by the same potential, and are again accelerated towards the other end of the accelerator tube. That is, these now-positive ions are accelerated in a tube similar to the one described but with opposite polarity voltage differences. **Figure 5** shows the internal schematic of the accelerator tank indicating each of its parts and a general diagram of the ion sources, switching magnets and acceleration tube.

The energy attainable by a tandem accelerator depends on the charge state of the particle after being stripped of electrons (q). and it is given by **Eq. (1),** where V is the applied potential in the acceleration tube. In the first acceleration stage, the ion charge is $-e$, i.e., the electron charge (only single-charged negative ions can be produced efficiently). After passing through the gas, the charge state, q, for each given ion of the beam will be in the range $(-e,+Ze)$, where Z is the atomic number of the ion. Note that, in general, the charge of the ions emerging from the stripper is not unique but a distribution which depends on the electronic configuration of the beam species, the beam energy and the amount of gas in the stripper. Consequently, the resulting beam at the exit of the accelerator tube will have a discrete energy

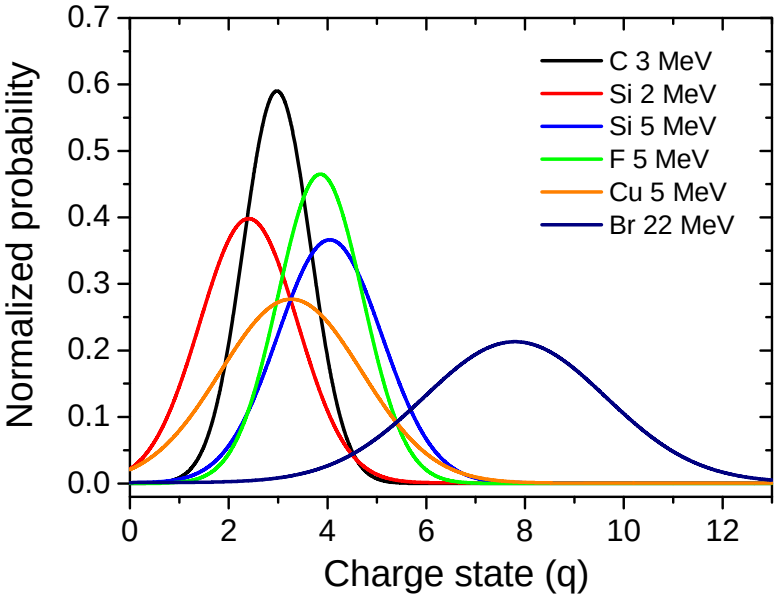

Fig. 6. Normalized probability distribution of charge states for ions and energies (which the ions reach the *stripper*) indicated in the figure

spectrum, i.e. the exact probability of each charge state will described by a distribution of charge states, as shown in **Figure 6**. The maximum energy for a terminal voltage, V, is then:

$$E\,(\text{MeV}) = (q+1)\text{e} \times V\,(\text{MV}) \qquad (1)$$

Moreover, each "monoenergetic" component will, necessarily, have a certain spread as a result of two main causes: on the one hand, the terminal voltage ripple and, on the other hand the energy straggling in the stripper and residual gas of the tubes [8]. In the case of our accelerator, the ripple is maintained at a very low fraction due to the absence of moving parts in the Cockroft-Walton voltage generation [1], while the residual gas is minimized by the pumping efficiency due to large section of the accelerator tubes. Hence, the main contribution to the beam energy spread comes, generally, from the stripper gas, specially for heavier ion beams.

Compared to single-ended accelerators - for which the maximum energy is qeV - the enhancement results especially important for light ions, for which the maximum q is low. For example, in the case of H^+, the energy is doubled with respect to that of a single-ended machine (this is very important, since the price of the accelerators increases more than linearly with energy). A side effect which is also advantageous is that, by separating the terminal from the ion source, the latter can be placed outside of the accelerator tank and, therefore, more easily serviced.

Distributions of charge states in equilibrium can be calculated using phenomenological formulas, and are found to favor the higher charge states the higher the energy with which the ion reaches the *stripper*. Overall, the most favored charge states are between +2 to +5, however, are obtained routinely charge states up to +8 and +9, with the loss in population, but gain in energy. For example, in the case of Si ions (quite prolific ions) is passed over currents I = 100 nA for Si^{4+} ions at 20-30 MeV to currents around I =10 nA for Si^{8+} ions at 45 MeV.

It is worthy to notice that, in order to minimize the radiation, power consumption and damage produced by the acceleration of secondary electrons (specially those produced in the

stripper), a set of permanent magnets located around the tube creates a spiralled magnetic field which drives the secondary electrons towards the walls of the tube *before* they are significantly accelerated.

Once the beam leaves the acceleration tube is again focused by a set of three electrostatic quadrupoles and, finally, another magnet (*switching magnet*), which selects the ions with the proper charge and determines the energy which ions are accelerated, leads them to the corresponding experimental line.

4.1.1.3. Multi-purpose beam line.

At CMAM are currently available four experimental beamlines offering a wide range of different techniques to explore and understand the properties of the physical systems [9]. Throughout this work it was used the beamline called *multi-purpose* or *Standard Beam line*, (*STD*) (**Fig. 7 (I)**) [2], due to it was used for both, the processing and damage characterization of the irradiated samples by Rutherford Backscattering Spectroscopy in channeling configuration (*RBS/c*). Moreover, it is equipped with a fixed and a movable particle detectors, as well as X-Ray and *gamma*-ray detectors, allowing us to perform many different kinds of experiments, when they are needed. Precise sample orientation - *e.g.,* for channeling experiments - is possible with a 3-axis goniometer. Attending to its relevance, we will proceed to describe its main features.

The multi-purpose line (STD) is attached to the 30º port of the high *E* magnet (switching magnet); two sets of slits are used for the collimation of the beam allowing to control the beam size till reaches the vacuum chamber[2]. The beam line and the experimental chamber are under high-vacuum conditions (~10^{-6} mbar) using a turbo-molecular pump assisted by a rotatory pump, in order to avoid the beam losses and the contamination of the samples with the residual gas.

Figure 7 (II) shows a picture of the STD chamber (inside), with several elements to control the experimental conditions. Three detectors are installed in the chamber: two Si barrier particle detectors (*Ortec* BU-012-50-500) for RBS and one reverse-electrode Ge detector (*Canberra* GR3520) for gamma-ray detection. One of the Si detectors is fixed at 170.4º respect to the incident beam direction, and the other is movable, allowing to vary the detection angle from 0º to 170º with estimated precision of 0.5º, and has a carrousel of six different absorber foils and/or slits for making additional measurements. Both detectors have a nominal resolution of 12 keV. The beam induced current in the sample is fed into a current meter and integrator, from HVE which integrates it, therefore giving a measure of the beam fluence. This device provides control signals which allow to start and stop acquisition based on accumulated charge criteria. In order to control the total dose, the sample is positively biased to suppress the effect of secondary electrons leaving the sample. The STD chamber incorporates a cable to apply +180 V bias for this purpose.

The center of the STD chamber at CMAM is occupied by a 3-axes goniometer (*Panmure Instruments* [10],), where the sample holder is mounted. The accuracy of the

[2] The combination of the slits allows a collimated beam spot of 1 mm^2 on the surface of the sample, with a divergence of ~ 0.1º.

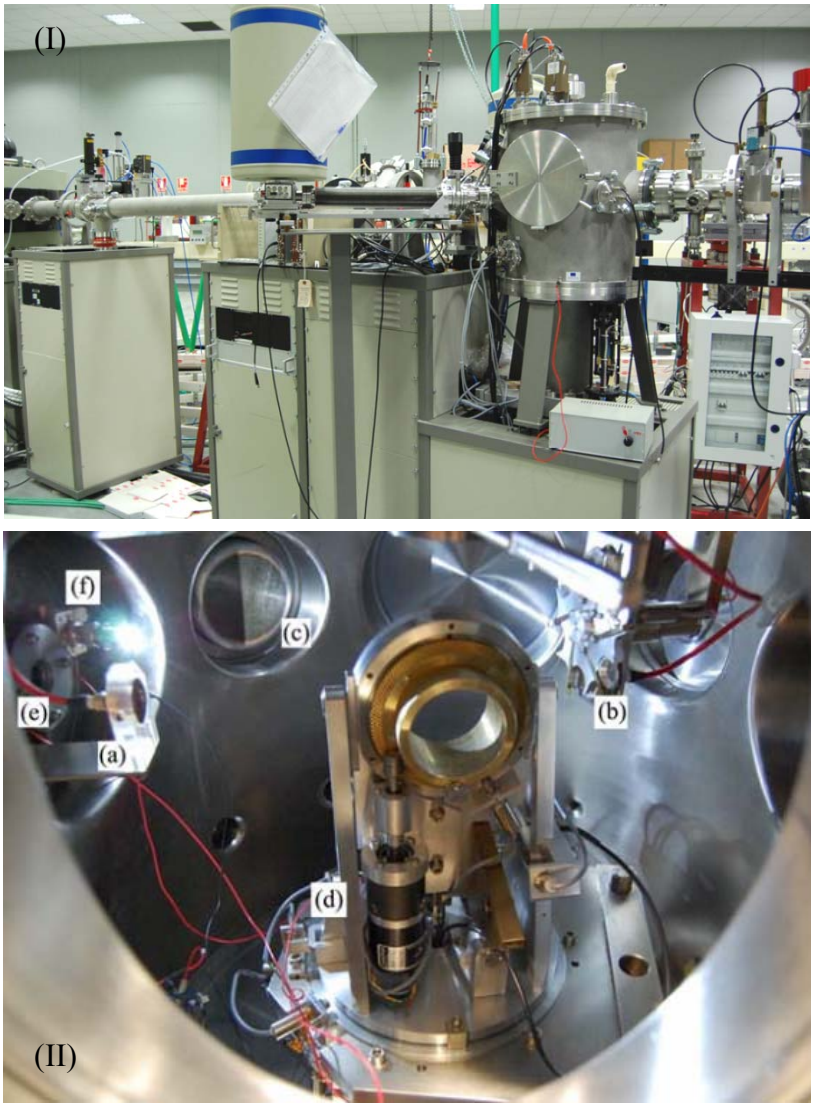

Fig. 7. (I) General view of the Standard beam line (STD) and the vacuum chamber. **(II)** Picture of the experimental chamber in the STD beam line (CMAM). Several elements are visible: **(a)** RBS fixed detector, **(b)** RBS movable detector with the foils carousel, **(c)** gamma detector **(d)** 3-axes goniometer, **(e)** beam entrance and **(f)** light

movement in the 3 axes is ±0.01º, although the range is different for each degree of freedom. For *X-axis* (phi angle, φ) and *Y-axis* (theta angle, θ), the range is 360º, while for the *Z-axis* (tilt angle, χ) it is only ±30º (see **Figure 8 (a)**). Additionally, the whole goniometer is mounted on a translation table which allows the change in the vertical direction (*lift*) and then, the possibility of measuring in different points (movements up to 22 mm with 0.1 mm accuracy). All the movements are driven by stepping motors, being the intersection of all three axes within a 0.05 mm diameter sphere. The sample holder is placed in the center of the goniometer, so the zero position of both elements (holder and goniometer) is shared.

The beam hits the sample-holder in a point situated in the vertical axis of the chamber and, therefore, the goniometer *X* rotation combined with the vertical translation can be used to select the point of the sample to be measured. And turns around the *Y* and *Z*- axes make possible to choose the angle of the beam with the normal direction of sample-holder.

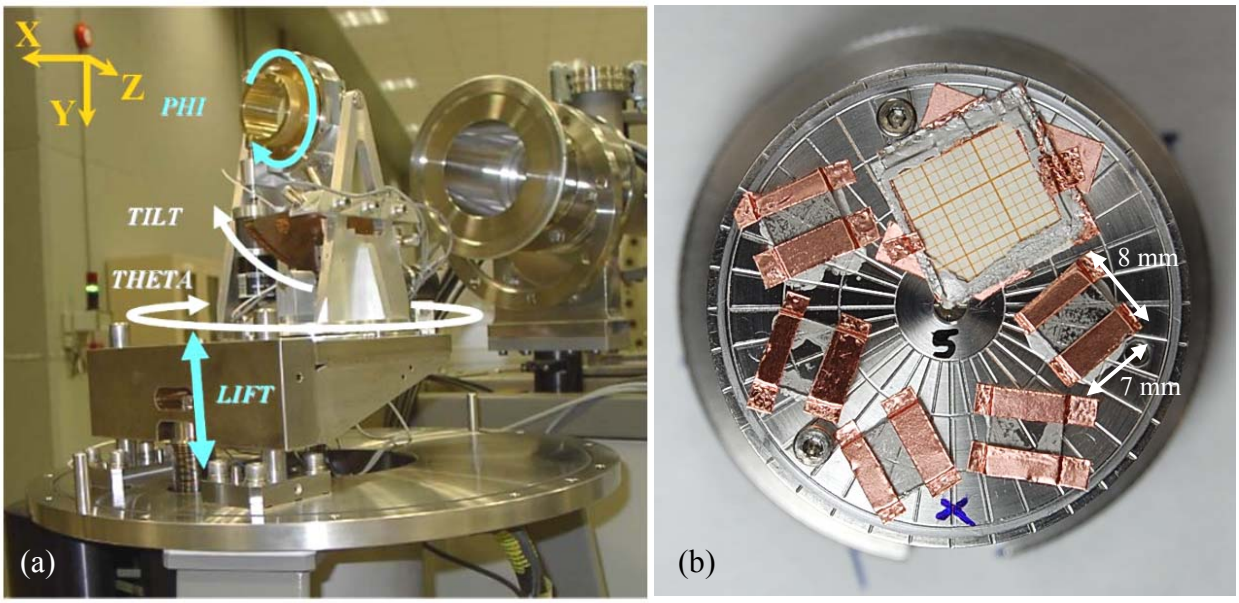

Fig. 8. (a) Picture of the 3-axis goniometer of STD beamline chamber. Arrows define the rotation movements of the goniometer (from Panmure documentation). **(b)** Picture of a typical sample holder with various $LiNbO_3$ crystals, glued with silver paint to its surface, to be irradiated. Double-side Cu tape masks cover part of the sample in order to avoid the irradiation (virgin area). In the upper part, a silica cover slip scintillator (1 mm thickness) on a millimeter paper sheet is shown too.

4.1.2. Irradiation conditions at CMAM.

Almost all of the irradiation experiments presented throughout this Thesis work were performed using the accelerator installed at CMAM facility, and, in particular, the *multi-purpose* or *Standard Beam line*, (*STD*) (**Fig. 7**) [2], described in the previous **Section 4.1.1.3**.

All the samples, were irradiated at room temperature and under high vacuum conditions (~ 10^{-6} torr.). The crystals were mounted on a three-axis goniometer head from Panmure Instruments installed in the center of the chamber of the STD beamline, and the irradiations were carried out under a few degrees (goniometer is rotated about ~ 7 ° around *Z* and *Y* axes) out of normal incidence to avoid channelling effects, defining this direction a random configuration. The procedure consists in defocalizing the ion beam (see **Figure 11**), and adjust its size by two sets of tantalum slits, resulting in a square shaped irradiation area into the sample. A typical spot size of 6 x 6 mm^2 homogeneous area is obtained.

The homogeneity of the ion beam must be accurately checked just before the irradiation takes place. In this sense, in addition to the beam profile meter, placed directly before the irradiation chamber, a CCD-camera (Kappa camera, Model DX 20N) with high sensitivity and color range (12 bits) is used. By this way, the ionoluminiscence from an amorphous silica reference plate (scintillator) placed on the sample holder while the over-focusing of the beam via the quadrupole-triplet of the line takes place, allows us to get the experimental conditions to guarantee the homogeneity. **Figure 12** shows an example of images taken *in situ* to adjust the parameters of the accelerator, giving a better than 10% homogeneity.

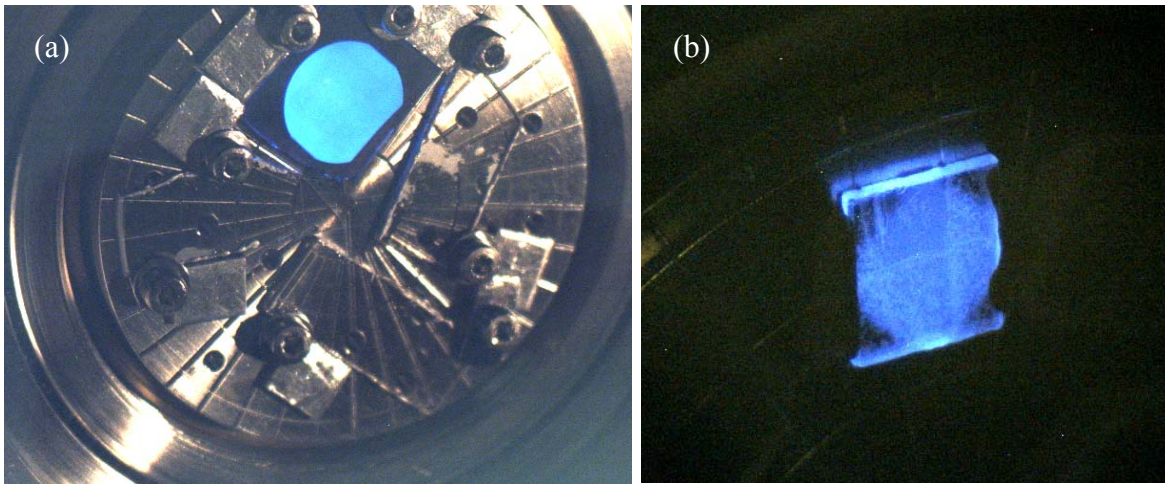

Fig. 12. Picture of the ionoluminiscence induced by the ion beam (F 20 MeV) **(a)** from an amorphous silica scintillator placed on the sample holder with slits entirely opened (12 mm, 12 mm); **(b)** from X-cut LN sample during irradiation with typical slits aperture (6 mm, 6 mm). Blue region indicates the irradiated area.

Another very important point to take into account is related to the effect of the temperature reached by the sample during the irradiation, trying to avoid modification of the material by ion beam induced-annealing. In this sense, we have to remark that, while this effect is not appreciable for the irradiations in the single track regime (ultra low fluences, usually with Br 45 MeV ions), due to the low fluxes and irradiation time required; however, in the case of long term irradiations with F 20 MeV ions, specific care must be taken in mind.

In this way, in order to have an accurate control of the temperature of the sample, a high precision infrared camera (VarioCAM high resolution, Jenoptic Laser, Optik, Systeme GmbH) mounted on a ZnSe viewport (transparent for the IR spectra) on the irradiation chamber is used. With the adequate parameters configuration of the IR-camera we can state that, with the beam currents and fluxes used, in any case, the temperature of the samples under irradiation never reached temperatures higher than 100 ºC. As we will see later, this temperature does not cause any annealing during the irradiation. By the other way, this effect is not appreciable for the irradiation with Br 45 MeV ions at ultra low fluences. Nevertheless, the measured temperature on the sample was around 40-50 ºC due to the heat transmission from the engines of the three-axis goniometer to the sample holder. **Figure 13** shows the typical setup with the distinct cameras mounted on viewports of the STD chamber during the irradiation experiments.

Throughout this work we used crystals of $LiNbO_3$, congruent composition, obtained from commercial wafers (Casix and Photox Ltd.) 1 mm thick and 3 inches in diameter. No difference was found between samples of both commercial companies, which, hereinafter, the origin is not specified. *X*, *Y* and *Z*-cut named crystals were used, indicating the axis of the $LiNbO_3$ crystal structure perpendicular to the surface of the wafer. The commercial wafers had to be cut to smaller size samples before the irradiation process is carried out. This was made with a with a diamond cut-off wheel cutting machine (*Ata Gmbh Brilliant 250 diamond saw*) installed at CMAM. Several appropriate sizes were chosen, according to the characterization experiments they were to be practiced, but always in rectangles side between 4 to 20 mm (4 x 8 mm for AFM pores characterization, 8 x 7 for RBS/C damage characterization and 20 x 7 mm

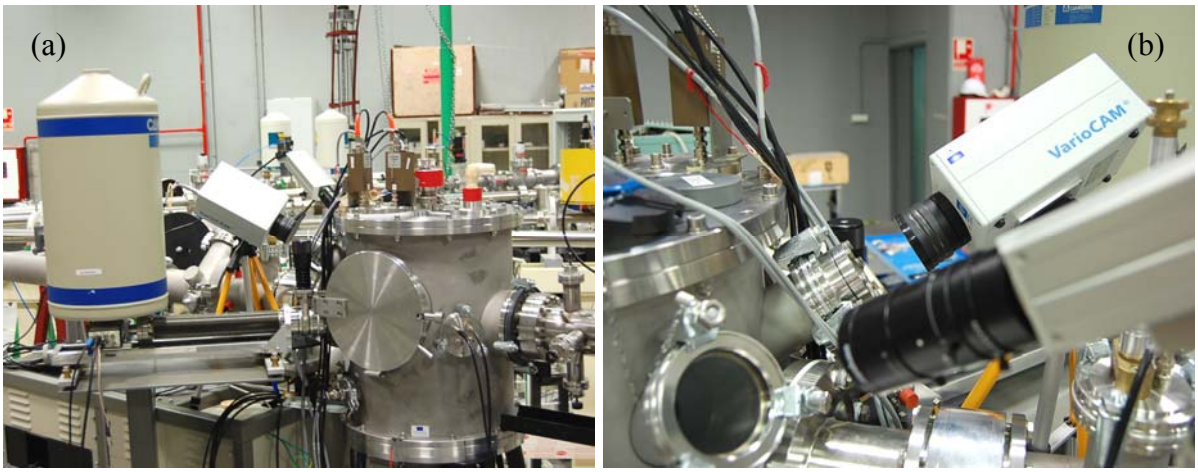

Fig. 13. (a) General view of the cameras setup on the STD beam line with the vacuum chamber for monitoring during the irradiation the sample temperature and the homogeneity of the ion beam. **(b)** Both cameras, the infrared (VarioCam) mounted on a ZnSe DN 40 CF viewport and the CCD camera on silica one are shown in detail.

for waveguides obtention and Dark Modes characterization technique). Subsequently, the samples are mounted in the sample holder shown in **Figure 8 (b)**, and this, in turn, on the goniometer.

The samples designed to measure waveguide propagation must be sufficient large to allow the guiding light at a distance farther than the usual 36 mm^2 covered by the beam. Therefore, in order to get the maximum irradiated area on the sample, the irradiation experiment is performed with the both slits totally opened (12 mm, 12 mm) obtaining a covered area of about ~ 85 mm^2, but with half part of the beam with rounded borders due to the projected shadow of the electron suppressor ring (*bias ring* allocated previous to the STD chamber) avoiding the entirely beam passes through it. Thus samples were processed up to around ~ 1.5 cm in length (**Figure 12 (a**)).

Determining the number of ions per unit area (fluence) that affect the sample is performed through the current induced in it by the beam. This current is measured and the charge is integrated using a current meter and integrator of HVE company [5], connected to the sample holder. Ideally, all the charge arriving to the sample is taken to the integrator, which, knowing the charge state of the ions and the irradiated area, one gets the total number of ions per unit area reaching the sample, that is, the fluence. However, this behavior, in fact, deviates from the ideal for several reasons. For example, secondary electrons emission from the sample changes the charge measurement. In order to control the total dose, as mentioned the sample is positively biased to suppress that effect, thus the STD chamber incorporates a cable to apply +180 V bias to the sample holder for this purpose. Another possibility is that the ion beam is accompanied by a halo of low-energy electrons. With the aim of preventing these electrons impinge on the sample holder and distort the charge measurement there is an electron suppressor ring (*bias ring*) biased at - 60 V at the entrance of the vacuum chamber. On the other hand, when the sample is not a good conductor it can be charged to subsequently produce a quick discharge that the current meter is not able to detect. To avoid this it is necessary to maintain the beam current density to values < 120 nA/cm^2 (for the case of irradiations with F 20

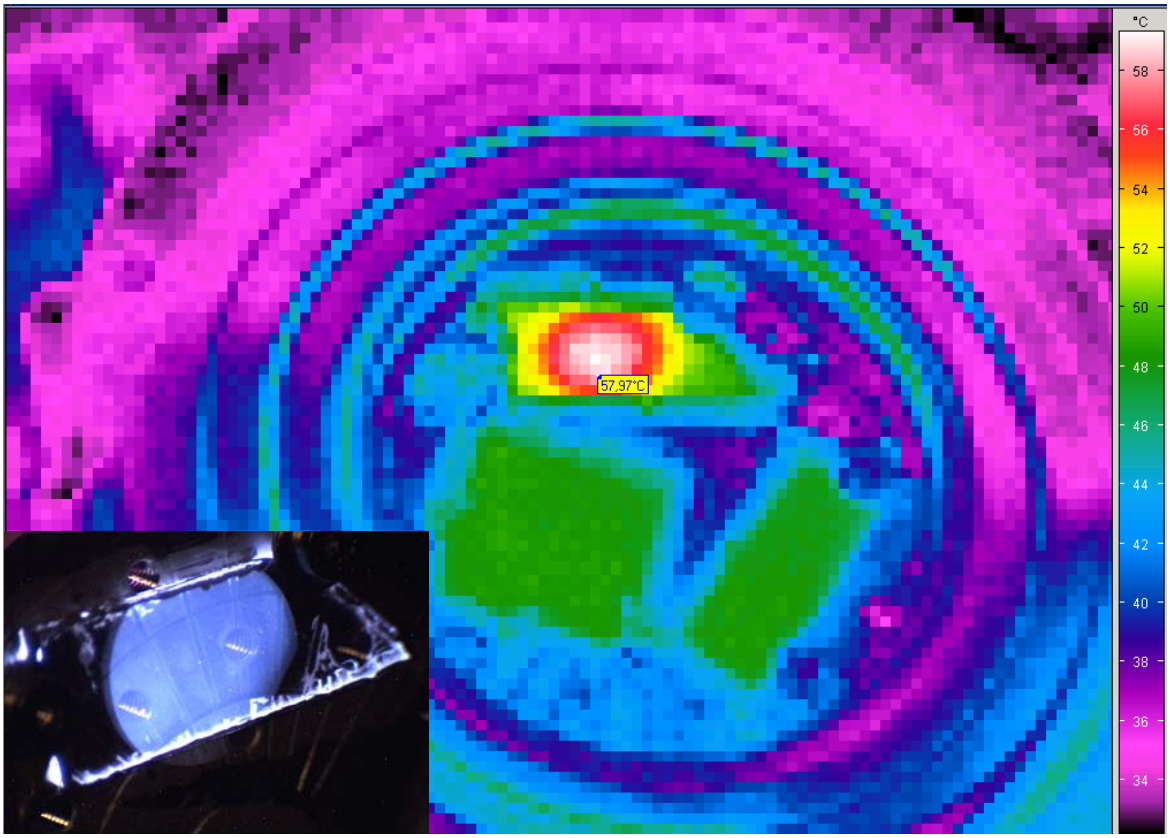

Fig. 14. Infrared picture of the sample holder during the irradiation of *X*-cut LN sample with a beam of F 20 MeV ions (slits opened (12 mm, 12 mm), spot size ~ 84 mm^2, beam current measured on the sample holder ~ 100 nA, beam current density ~ 120 nA/cm^2). The temperature color-scale appears on the right part, and the target temperature on the beam spot is marked in the picture. The visible image captured by CCD camera of the irradiated sample showing the induced ionoluminiscence is shown as inset.

MeV ions) (see **Fig. 14**). In addition, using current density values not too high avoid possible damage (cracks) of the sample as well as distortions in the *RBS/C* spectra due to "*pile up*" phenomenon (see following **Section 4.7.1.3.**). Also, to improve the conductivity of the sample, the sample surface is hold with metal hooks to enhance the discharge to the metallic sample holder. Other strategies such as painting the samples edges with silver paint are carried out. Another important point is to keep the entire the ion beam impinges the surface of the sample holder, since if part of it is gone away, this fraction of ions will not be measured, thus underestimating the fluence.

In the particular case of the irradiations series with Br 22 and 45 MeV ions for the study of the amorphization kinetics, they were carried out with beam currents, measured on the sample holder of around 10 nA and fluxes of ~ 1.6 e 10 at/cm^2 s. Moreover, in this case, part of each sample was masked by a thick double-sided Cu tape to stop the incident ions and keep virgin part of samples. The mask covers the middle area of the sample, leaving the rest of the sample as irradiated area (similar to **Fig. 8 (b)**). The purpose of this configuration is two-fold; on one hand, by this way we can carry out out-of-plane swelling measurements between virgin and irradiated areas by means of the surface profiling technique and to study the evolution versus the irradiation fluence; and on the other one, with the aim of assisting the alignment

procedure during the process of finding the channelling configuration by RBS in the non-irradiated zone.

The irradiations with Br 45 MeV ions to investigate the thermal stability of amorphous tracks (**Chapter 7**) were carried out with the following selected parameters: fluences: 3 e11 at/cm^2, 5 e11 at/cm^2 and 1 e12 at/cm^2; charge state: + 8; spot size: 49 mm^2; beam currents (measured on the sample holder): ~ 10 nA; flux: ~ 1.6 e 10 at/cm^2 s; beam current density: ~ 30 nA/cm^2. Again, part of each sample was masked by a thick double-sided Cu tape to stop the incident ions and keep virgin part of samples. The mask covers the opposite sides of the sample, leaving the central part as irradiated area. The same purpose described above for the series of Br 22 and 45 MeV is pursued.

For the case of amorphous buried layers, the irradiation conditions for the F 20 MeV ions, were: fluence: 4 e14 at/cm^2; charge state: + 5; spot size: 77 mm^2; beam currents (measured on the sample holder): ~ 100 nA; flux: ~ 1.5 e 11 at/cm^2 s; beam current density: < 120 nA/cm^2.

On the other hand, for the case of irradiations at ultra low fluences (*isolated track regime*), the beam currents, measured on the sample holder and checked in the Faraday Cup just before the irradiation chamber, were in the order of ~ 10 - 500 pA, the ion beam flux ~ 5 e7 at/cm^2.s, and the irradiation fluences were in the range of: 1 e8- 1 e9 at/cm^2 in order to get avoid the overlapping of neighboring tracks, that's to say, ensuring the isolated track regime irradiation.

In this sense, decreasing the beam current is the first necessary step to enable the possibility of ultra low fuences ≤ 1 e9 at/cm^2, which are needed to avoid perpendicular stress between the nanotracks. Moreover, a high accurate extra setup will be taken into account to ensure the extreme irradiation conditions for single track irradiation through the precise control of ultra low irradiation currents.

4.1.2.1. Realization of Ultra-Low Fluence irradiations.

As mentioned, the induced beam current arriving at the sample was usually fed into a nano-amperimeter from HVEE Company. The integrated current gives a measure of the charge deposited on the sample, and therefore, of the irradiation fluence. To reduce the effect on the charge measurement due to secondary electrons leaving the sample, the sample holder can be biased with +180 V by a set of batteries. The current measurement was limited to minimal currents of 1 nA. Furthermore, the device does not provide control signals which allow to start and stop an irradiation using criteria based on the accumulated charge. Thus, irradiation times had to be estimated and controlled manually and the fluence could not be monitored in real time.

To achieve ultra low fluences of ~1 e8 at/cm^2, with accurate control, via opening and closing one of the Faraday Cups automatically, the *program STANDARD* developed by M. Otto, was developed in the scope of this work to handle the accelerator control. To establish the technical requirements, the beam current had to be decreased to a few picoamperes, which then resulted in feasible times accounting for reaction times of the Faraday Cups. For comparison, a practical example of Br 46 MeV, is showed:

The fluence (ϕ, at/cm^2) accumulated by the sample during irradiation with ions of the charge state Z = 8+, in an area: A = 6 × 6 mm^2, during time Δt = 1 s, at a beam current I = 1 nA, is:

$$Q(C) = I(A) \cdot \Delta t(s) = \phi(at/cm^2) \cdot A(cm^2) \cdot Z \cdot q_e(C), \quad (2)$$

$$\phi(at/cm^2) = \frac{I(A) \cdot \Delta t(s)}{A(cm^2) \cdot Z \cdot q_e(C)} \approx 2 \text{ e10 at/cm}^2. \quad (3)$$

where q_e, is the electron charge (q_e = 1.6 e-19 C). In consequence, a commercial Kithley Model 6485 picoamperimeter, which can measure currents of 0.01 pA-20 mA, with 0.01 pA sensitivity in the pA-range (in the following, PAM), is connected to the exit of the Faraday Cup 2, (FC2), localized in the Standard Beam Line, prior the irradiation chamber at CMAM. Moreover, the current must be significantly reduced by closing the slits on the low energy system, prior to the acceleration tube.

Due to the picoamperimeter signals were not compatible with the accelerator operating system provided by HVEE accelerator, the *Software PICO-Control* developed by M. Otto, was used. By this way the main accelerator system STANDARD SOFTWARE, is capable of managing irradiation procedures. Thereby, opening and closing Faraday Cups, the beam is passed to the sample or stopped, respectively.

It is remarkably to comment the major problems that appear in the *picoA* range measured from the sample holder during the irradiation with this setup. For non-conductive samples, that obviously falsifies a current measurement in the *picoA* range, and all kinds of electronics cross-talk (e.g. goniometer engine currents etc.), the connection cable between the sample holder and the signal feedthrough had to be screened to reduce this effect. Irradiations with ultra low fluences have been made opening and closing the Faraday Cup (FC) manually, and using one picoamperimeter connected to FC to measure accurately the beam current (pA), and another one adequately connected to the sample holder to check, only for read out, the sample current. Maybe, this configuration could be improved if the entire irradiation chamber could turn into itself in a big Faraday Cup, disconnecting the power supplies wires of the goniometers engines; by this way, the current measured from the sample holder should be real in the pA range.

Anyway, it is necessary to comment that on samples that were irradiated at ultra low fluences, the observed number of impacts was usually higher than nominal, which is probably due to the manual control of short irradiation times (~ few seconds).

4.1.3. Swift heavy ion irradiations. GANIL and GSI.

4.1.3.1. SME line at GANIL (Grand Accélérateur National d'Ions Lourds).

The Grand Accélérateur National d'Ions Lourds (GANIL), Caen (France) has *ECR* sources (*Electron Cyclotron Resonance*), capable of producing charged ions or completely bare of charge from ^{12}C a ^{238}U. The first part consists of two ions injectors (**C01** and **C02**), which produce multi-charged ions from a gas source (Xe, Ar, Kr) or solid one (Pb, Sn).

The ions thus produced can be used in the **IRRSUD** beam line at energies around 1 MeV/u, or be injected into a first cyclotron **CSS1** being accelerated to energies of several MeV/u. After these two accelerations, the ions pass through a stripper to increase their charge state. Thus, after three accelerations can reach energies of 90 MeV/u for lighter ions (as C) or 24 MeV/u for heavier (as U). Ions with lower charge states are oriented toward the beam line **SME** (*Sortie Moyenne Energie* - Low and Medium Energy) with the help of magnetic elements (dipoles, quadrupoles, switches,…). Ions with higher charge states are sent to a second cyclotron (**CSS2**) and are oriented to the beamline **HE** (*Haute Energie* - High Energy).

Depending on the needs of the experiment, the ion beam is sent to an experimental room. One of them, called **D1** for *high energy* and **SME** for the production of *medium energy*, is dedicated specifically to the non-nuclear physics experiments.

We have used the **SME** beamline. The remaining rooms, are dedicated to specific applications to nuclear physics. Thus, the ions can be collected after two accelerations (**SME**) or three accelerations (**HE**). The ion beam is directed to three experimental sites.

- a beam line for atomic physics at **SME**,
- a beam line for irradiation of materials at **SME** (**IRASME**),
- a beam line for irradiation of materials at low-temperature 4 K (**IRABAT**), and with the aim of having higher energy and radioactive ion beams.

The **IRASME** beam line used for this study includes a samples irradiation system. This device consists of a set of horizontal and vertical sweeps, a flux measurement system *in line* and slits mounted on the line to modify and control the beam area on the sample. Available energies range from 14 MeV/u for C and 4 MeV/u for U. The samples are placed on sample holder plates that can be rotated to produce the irradiation at different incident angles. In our case, the irradiations were carried out during three days at GANIL with $^{78}Kr^{31+}$ (10.4 MeV/u) ions with a double purpose. For the irradiations at low fluence regime (1 e7 - 1 e8 at. cm^{-2}) the ion beam flux was maintained in the order of 1 e5 - 1 e6 at. cm^{-2} s^{-1}. On the other hand, for the case of high fluences (5 e10 - 8 e11 at. cm^{-2}), the flux was in the order of 1 - 5 e8 at. cm^{-2} s^{-1}, i.e., at least two orders in magnitude lower than the required final fluence. In both cases, the irradiations were carried out at room temperature and the ion beam was scanned over the target surface in order to ensure a homogeneous irradiation.

4.1.3.2. UNILAC accelerator at GSI (Gesellschaft für SchwerIonenforschung).

The UNILAC accelerator of G.S.I. (Gesellschaft für Schwerionenforschung) in Darmstadt (Germany) [11-13]. The beam line used in the research is devoted to the study of ion-matter interaction, and consists of an injector which provides several types of ions (up to uranium) with different charge states. The low energy section of the accelerator (injector) is followed by a linear accelerator section, then, this line continues to the experimental areas, where ions have energies up to 11.4 MeV/u. The beam line in which the irradiations were carried out is the line **X0**.

In our case the irradiations were carried out with two types of ions and for different purposes. On the one hand, irradiations were carried out with de $^{208}Pb^{55+}$ (11.1 MeV/u) ions at low fluence regime (1 e8 - 1 e9 at. cm^{-2}), being the ion beam flux in the order of 1 e5 - 1 e6 at. cm^{-2} s^{-1}. On the other hand, for the case of high fluences (1 e11 - 4 e11 at. cm^{-2}), ^{129}Xe (11.1 MeV/u) ions were selected. In the latter case, the ion beam flux was in the order of ~ 1 e8 at. cm^{-2} s^{-1}. Both kinds of irradiations were carried out at room temperature.

In the case of the irradiations at GSI, the samples were irradiated with 11.1 MeV/u. At the beginning, the beam of Xe/ Pb ions has an initial energy of 11.4 MeV/u, however, a 3-foil detector (3 x 1 μm thick Al foils) is used in front of the samples in order to have an on-line fluence control, thus, this reduces the energy of the ions when entering the sample surface to about 11.1 MeV/u. The foils belong to the SEETRAM detector monitoring the beam.

In the case of the ^{208}Pb irradiations, initially the ions enter into the beam line being 26+ charged and after passing through the Al foils they are stripped to their equilibrium charge state (~ 55+, in this case). This, of course leads to a broad charge distribution impinging on the sample. Energy- and angular-straggling are negligible at these high velocities. As the ion slows down inside the target, the equilibrium charge state is always adjusted along the trajectory.

Moreover, it is worthy to notice that this accelerator is a pulsed machine, (in contrast to cyclotrons or smaller facilities), with a rather low frequency. The ions arrive within a pulse length of 1-4 ms, then, there is a break (according to the frequency) until the next pulse. Specifically, for the case of ^{129}Xe irradiations, we have a flux[3] in the order of ~1 e8 at. cm^{-2} s^{-1}, pulse length 1.2 ms and pulse frequency 4 Hz.

[3] It must be understood as a mean value averaged over time. Thus, if one compares to a quasi-continuous ion beam, one has in principle to calculate the beam current within the short pulse, yielding, of course, a much higher pulse flux. However, its influence has been tried to test by Dr Christina Trautmann at GSI, but never has been discovered an obvious effect, not even in polymers if they limit the flux to 1-2 e8 at. cm^{-2} s^{-1} for the heavy projectiles. Thermal degradation effects do not appear at these irradiation conditions.

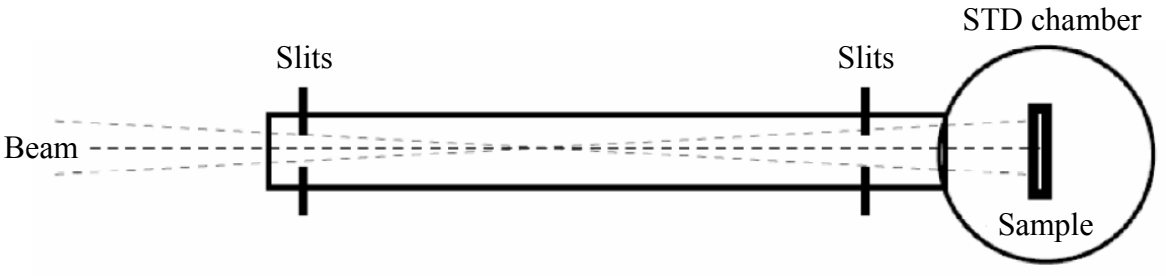

Fig. 11. Schematic of the de-focusing and consequent expansion of the ion beam on the sample at STD beam line.

4.2. Ion beam analysis. Characterization by ion channelling. RBS.

The following sections will be devoted to briefly describe the techniques used to characterize the samples studied in this Thesis work, with the aim of obtaining information on the ion beam-induced modification of the irradiated materials.

4.2.1. Introduction.

The Rutherford Backscattering Spectrometry (RBS) was the first Ion Beam Analysis (IBA) technique developed and is still the most frequently used. RBS is a well-established [14, 15] powerful technique for the compositional characterization of materials [16]. In this technique, the beam ions that have been backscattered from the sample are detected and analyzed as a function of their energy. The backscattering spectrometry provides information about sample composition with depth sensitivity, the stoichiometry of the material, the distribution of impurities, etc…, for any species except for Hydrogen.

Essentially, the idea behind RBS is similar to that developed by Geiger and Marsden in 1909 [14]: a beam of energetic particles is launched toward a target (sample) and the scattered projectiles are detected at a certain angle. When the beam reaches the sample, a small portion of the incoming ions suffer close encounters with the target nuclei and, due to the Coulomb interaction, are backscattered. Such elastic processes can be treated within the classical mechanics framework since the involved velocities are not high (2 MeV He beam has a velocity of 0.033c). As an additional simplification, only binary collisions between the projectile and the atom can be considered, so the problem can be solved exactly assuming a two-body model [16]. Imposing conservation laws for the energy and the momentum, the velocity and scattering angle of the projectiles can be obtained as a function of the initial parameters of the incoming ion [16].

Hence, it is conceptually simple in the sense that it can be adequately explained in terms of classical mechanics making use of few non-complicated concepts, and, at the same time, it is a flexible technique because many parameters can be optimized to fit special experimental requirements[4]. Moreover, the special variant, which takes place in channeling configuration (RBS/C), provides information on the existing order-disorder ratio in the atomic structure of

[4] A note about naming convention should be done: Along this Thesis, the acronym RBS - which stands for Rutherford Backscattering Spectrometry - and RBS/C, for the case of - Rutherford Backscattering Spectrometry in channelling configuration - are usually used. This is done for the sake of simplicity.

material under study. This method will be used throughout this work as a main characterization technique.

Three main aspects have to be considered during RBS experiments: the mass resolution, the sensitivity limits for the compositional analysis and the depth resolution. The accuracy of an RBS analysis depends essentially on these factors.

In the following, these relevant aspects of the backscattering spectrometry are discussed. Much more comprehensive information on this technique can be found in [16].

4.2.2. Kinematics of a backscattering experiment.

In general, a backscattering experiment consists on probing a sample with a mono-energetic light ion beam (H, He) - energies are in the order of $E_0 \sim 1$ MeV/u - and detecting the energy spectrum of those ions that have been backscattered by collisions with the atomic nucleus of the sample, i.e., measuring the ratio of all the incident ions that are backscattered and the energy E_1 at the target output. **Fig. 18** introduces the geometry of a typical backscattering experiment.

Mass sensitivity: kinematic factor.

In first place, RBS can provide mass-resolved information of the elements belonging to the specimen. This fact is a consequence of the mass-dependence of the energy loss during the collision with the atom, i.e., the output energy E_1 will depend on the mass of the target atom.

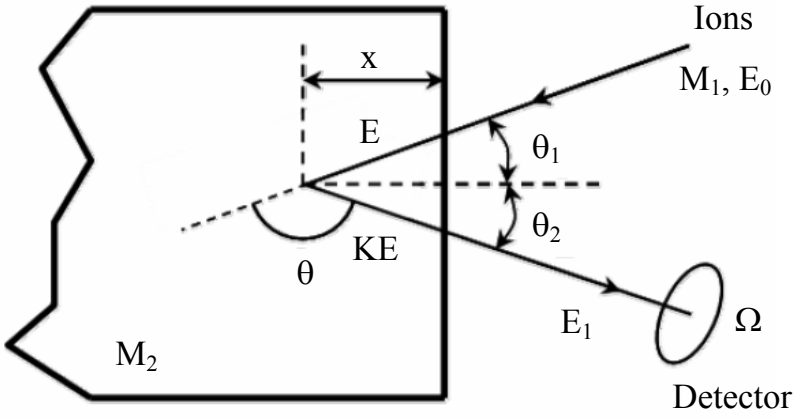

Fig. 18. Schematic diagram of a typical Rutherford backscattering experiment showing the geometric parameters.

Actually, due to the elastic behaviour of the collision, the ratio between the final and the initial energies of the ion, known as the *kinematic factor* (K), obtained from the application of conservation of energy and momentum in an elastic collision of two isolated bodies, will be lower than 1. If M_1 and M_2 are the masses of the projectile and the target atom and θ is the scattering angle (**Fig. 18**), then it can be proved that [16]:

$$K = \left(\frac{(M_1/M_2)\cos\theta + \sqrt{1-(M_1/M_2)^2 \sin^2\theta}}{1+(M_1/M_2)} \right)^2 \quad (\mathbf{10})$$

Therefore, the energy of the backscattered ions arising from the surface of the sample is: $E_1 = K \cdot E_0$, being, E_0 the energy of the incident ions, as can be seen in **Fig. 18**. Alike, assuming that the collision takes place only at the surface, the mass of the element can be measured only by the reduction of the energy of the projectile *(ΔE=E-KE)*. Thus, the mass resolution is a function of *K* (actually proportional to $(\partial K/\partial M_2)^{-1}$) [16]. If the difference in the kinematic factor is high, the resolution is high too; whereas similar values of *K* lead to a difficult separation of the elements.

From **Eq. 10** some conclusions can be obtained: The largest separation between elements takes place at 180º, indicating that this position corresponds to the best mass resolution. Actually, this is the reason to place the detectors in backscattering geometry in the experimental chambers. Moreover, *K* is almost constant in a wide range close to 180º, which allows an increase in the solid angle of the detector without changing significantly the depth resolution. The variation of *K* with the scattering angle is almost indistinguishable for every particle-atom couple, especially between 135º-180º. Heavy atoms will scatter the impinging ions with higher energies than light atoms, which means that they will appear at higher energies in the spectrum too. However, even more remarkable, heavy elements are worse resolved in mass than light elements in RBS. This is evidenced by the asymptotic behaviour obtained for large mass ratios. Hence, the measurement of heavy elements with a small difference ΔK might require special conditions in the experiment to separate the signals in the spectrum (e.g., when the energy resolution is lower than the detector resolution).

Quantification of the composition: cross sections.

Once the identification of the individual elements of the target is known, the second aspect to consider in RBS is how to quantify their concentration. Of course, the number of detected backscattered particles (yield) will be proportional to the number of target atoms per unit area (concentration), but also to other factors such as the number of incident particles or dose (*Q*) and the solid angle of the detector (*Ω*). All of these factors can be known experimentally. Nevertheless, there is another important variable to consider when calculating the concentration: the scattering probability. Atoms with different masses have different scattering probabilities because the Coulomb potential depends on the atomic number and, therefore, the repulsing force will be higher for heavy elements than for light ones.

The physical quantity representing the scattering probability is the differential cross section ($d\sigma/d\Omega$) [15], and it is the essential parameter to consider for the calculation of the concentration. The physical meaning of the cross section is the effective area of each nucleus presented to the beam of incident particles. The calculation $d\sigma/d\Omega$ was first derived by Rutherford for the Coulomb potential [15] and, in the laboratory frame of reference, it can be expressed as [16]:

$$\frac{d\sigma}{d\Omega} = \left(\frac{Z_1 Z_2 e^2}{16\pi\varepsilon_0 E}\right)^2 \frac{4}{\sin^4\theta} \frac{\left(\sqrt{1-\left[(M_1/M_2)\sin\theta\right]^2} + \cos\theta\right)^2}{\sqrt{1-\left[(M_1/M_2)\sin\theta\right]^2}} \quad (\mathbf{11})$$

where E is the energy of the ion and Z_1 and Z_2 are the atomic numbers of the ion and the target atom, respectively.

From the quadratic dependence with Z_2, it can be deduced that heavy atoms are more efficient scatterers than light atoms, i.e., RBS is much more sensitive to them. This is also true for the impinging ions: the yield obtained with a He ($Z_1 = 2$) beam is four times as large as the obtained with a proton beam ($Z_1 = 1$). Indeed, this is one of the reasons to prefer He instead of H as probing particles in RBS. However, the use of heavier ions than He results in the deterioration of the energy resolution of the detectors, so they are not suitable for RBS, except for very specific configurations.

Following **Eq. 11**, the cross section has its lowest value for angles close to 180º, which means that backscattering events at such angles are very rare. Unfortunately, those angles provide normally the best conditions to enhance the mass separation, although the constant value of the kinematic factor at ~180º makes possible the use of large detectors (high Ω) without the loss of mass resolution. Additionally, the statistics of the experiment can be increased using high doses too.

But probably the most relevant consequence of **Eq. 11** is the energy dependence of the scattering probability. The cross section is proportional to $1/E^2$, what means that backscattering yield will increase very rapidly with decreasing projectile energy before the collision event. This point explains the conventional 1-2 MeV energies used in RBS experiments and the typical rising yield in the low energy region of the spectra (see, for example, **Figure 20**).

Deviations from the Rutherford expression occur either at low or at high energies and are often expressed as scalings of the Rutherford value at the same energy. The low energy

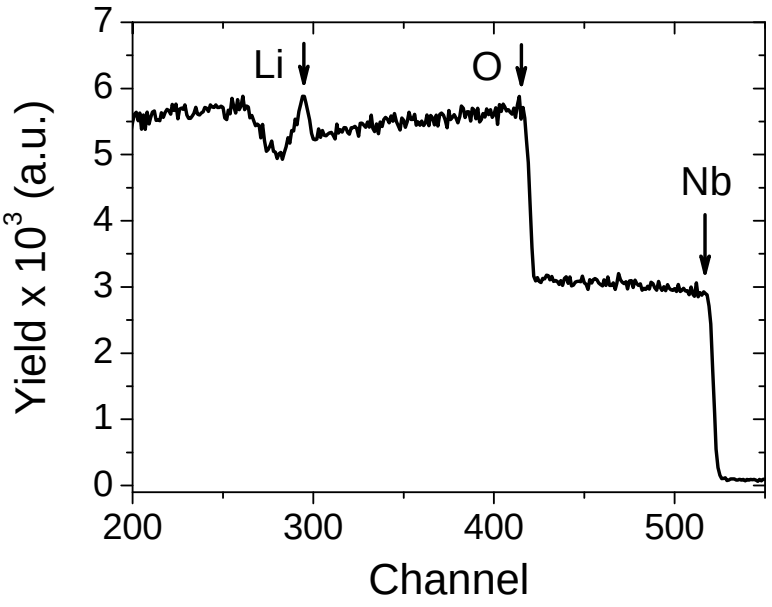

Fig. 19. RBS spectrum for *Z*-cut virgin sample of $LiNbO_3$. The Nb surface peak is located around energy channel 525. Analysis condition: 3-MeV H^+, dose = 4 μC.

departure is due to the screening of the nuclear charges by the electronic shells of both the target and the ion, and can be calculated approximately with semi-empirical expressions. In the case of high energies, and especially for light elements, severe deviations to the Rutherford scattering cross section exist. These deviations appear because, at high energies, the two nuclei may reach distances at which the nuclear forces dominate over electrostatic ones and, hence, the average differential cross section also departs from Rutherford values [16]. Therefore, nuclear resonances can affect the RBS spectrum when measuring at high energies. No simple general model is available that accurately predicts the non-Rutherford cross sections at high energies, and experimentally measured values are used.

Although the non-Rutherford cross sections have to be tabulated [17], they should not be considered always as an inconvenient. On the contrary, the nuclear resonances become a great help for the enhanced detection of light elements, which are more difficult to detect in RBS experiments. The resonances take place for specific energies and usually for specific scattering angles too.

Once the cross section is known, the quantification of the composition can be developed as a function of Ω, Q and the experimental backscattering yield (Y). In the simplest case of RBS on a thin film under normal incidence, the areal density (number of atoms per unit area) can be calculated as $N_A = Y/Q\sigma\Omega$, where σ is the average cross section (coinciding with the $d\sigma/d\Omega$ for small Ω). However, this formula is only a surface approximation, where a constant energy of the particles is assumed. When the beam enters into the target, the ions slow down and lose energy. To take this effect into account the stopping power must be considered.

In our case, plotting the number of ions measured for each energy value E_1 we obtain a typical spectrum shown in **Figure 19**, corresponding to a *RBS* experiment performed on a *Z*-cut $LiNbO_3$ crystalline sample. In the spectrum, the number of backscattered ions (counts, RBS yield) is plotted versus the channel number of the detector, which has a linear dependence with

the energy E_1. We note that three marked steps corresponding to each element present in the material take place in the spectrum. The greater the mass of the target atom, the more energy of the scattered ions at the output, and therefore, the greater the value of the channel associated to the step that appears in the spectrum. Thus, in the spectrum of $LiNbO_3$ shown in **Figure 19**, the step of Nb appears on energy channel 525 approx. Moving in the channel spectrum to lower values, to the step of Nb is overlapped first, the step associated to O, and then, the one correspond to Li specie. Once we past the step of Li, at lower channel values, the spectrum has a shape different from the smooth flat step because in this energy region, the scattering cross section has a complicated dependence on incident ion energy.

Depth profiling: stopping power and energy straggling.

As the particles travel into the sample, the interaction with the surrounding atoms makes decrease their energy. The fact that occur steps at RBS spectra (not peaks as obtained with an infinitesimally thin film) is caused by the energy loss of the incident ions as they penetrate into the material, i.e., due to electronic stopping power (Se = dE/dx)[5]. The greater the depth, at which the collision occurs that causes ion backscattering, x, the lower energy, E_1, which with it will arrive to the detector.

The stopping force is the physical link between energy and depth and, therefore, it is the mechanism providing depth resolution to RBS. Thus, the total energy loss by an ion can be divided in three steps. First the ion travels from the surface towards the target atom, feeling the stopping force of the surrounding electrons of the material. Then, the ion interacts with the atom in a two-body collision, losing energy proportionally to the kinematic factor. Finally, the backscattered ion leaves the sample losing more energy, again, due to the stopping power. Consequently, if the same ion-atom collision is considered but occurring at the surface and in-depth, the backscattered ion will be found at very different energies for each case, because in the first situation it does not lose energy inside the target, whereas in the second case it does. This is the key feature of RBS allowing depth concentration profiling.

To carry out the correlation between the energy of the backscattered particle and the depth in the sample at which the scattering took place we have to take into account that the latter depends on the energy loss suffered by the incident ion passing through the sample, the kinematic factor (**Eq. 10**) and the orientation of the normal to the sample with respect to the incident beam and the direction of the detector. The difference in energy between a particle scattered at the surface and other scattered at a depth x, measured perpendicular to the sample surface, i.e., the quantification of energy loss ΔE at a depth x, responds to the equation [16]:

$$\Delta E = \left[K\left(\frac{dE}{dx}\right)_{in} \frac{1}{\cos\theta_1} + \left(\frac{dE}{dx}\right)_{out} \frac{1}{\cos\theta_2} \right] \cdot x \qquad \textbf{(12.a)}$$

Assuming the surface energy approximation (constant stopping power):

[5] The definition of the stopping power is not completely convenient for RBS calculations, because it depends on the thickness of the target and not on the atomic areal density. A more practical magnitude is the stopping cross section ($\varepsilon = Se/N$), i.e., the energy loss normalized by the atomic density of the material.

$$\Delta E = S \cdot x \cdot \left[\frac{K}{\cos\theta_1} + \frac{1}{\cos\theta_2} \right] \qquad \textbf{(12.b)}$$

where K is defined in (**Eq. 10**), (dE/dx) is the stopping power of incident ions and the scattered ones out of the sample, and θ_1 and θ_2 are the incident and exit angles (with respect to the surface normal) described in **Figure 18**. From **Eq. 12** we can derive the parameters governing the depth resolution achievable in the measurement. The difference in minimum resolved depth, δx, is related to the minimum detectable difference in energy, δE, by

$$\delta x = \frac{\delta E}{\left[K\left(\frac{dE}{dx}\right)_{in} \frac{1}{\cos\theta_1} + \left(\frac{dE}{dx}\right)_{out} \frac{1}{\cos\theta_2} \right]} \qquad \textbf{(13)}$$

Apart from the stopping power, the statistical behavior of the close encounters also provokes the energy loss. In particular, this fact makes identical energetic particles not to have exactly the same energy after passing through a thickness of a homogeneous medium. Therefore, the energy loss is also subjected to fluctuations, a phenomenon known as *energy straggling*. The principal factor contributing to the straggling is the interaction of the beam with the electrons. As the beam penetrates deeper into the sample, the straggling becomes more important, so it establishes a limit for the depth resolution of RBS.

From **Eq. 13** we conclude that we can improve the depth resolution of the experiment by increasing the stopping power of the proving ions, for example, increasing the atomic number, Z, of the projectile, or improving the energy resolution, in which some parameters have an important influence like the detector resolution, the dispersion in energies of the incident beam and statistical fluctuations (*straggling*)[6].

Figure 20 shows the general scheme of an RBS experiment and the interpretation of the spectrum for the simple case of a bilayer (with two elements $M_1 > M_2$), taking into account the kinematic factor, the cross section and the stopping power. Note that heavier atoms (M_1) appear at higher energies and exhibit higher yields. The concentration of the elements is proportional to the yield. Since M_2 belongs to two layers, the spectrum shows two regions. The first one (higher energies) corresponds to the shallower layer with a concentration of 50 % and, hence, the signal is approximately the half of the second one (substrate, 100 %). The thickness of the layer is measured through the energy loss ΔE.

4.2.3. Basic concepts of ion channelling (RBS/C).

As was mentioned previously, RBS measurements that appear throughout this work were performed in channeling configuration (RBS/C).

When measuring crystalline materials, RBS can be carried out with the beam aligned along a major crystallographic direction (RBS/C). This particular geometry allows the appearance of a physical phenomenon called channeling [18], i.e., ions entering inside the crystal are steered by the atomic rows and, consequently, there is a reduction of the measured backscattering events.

[6] The energy straggling introduces an imprecision in the energy which increases -approximately linearly - with the square root of the analyzed depth.

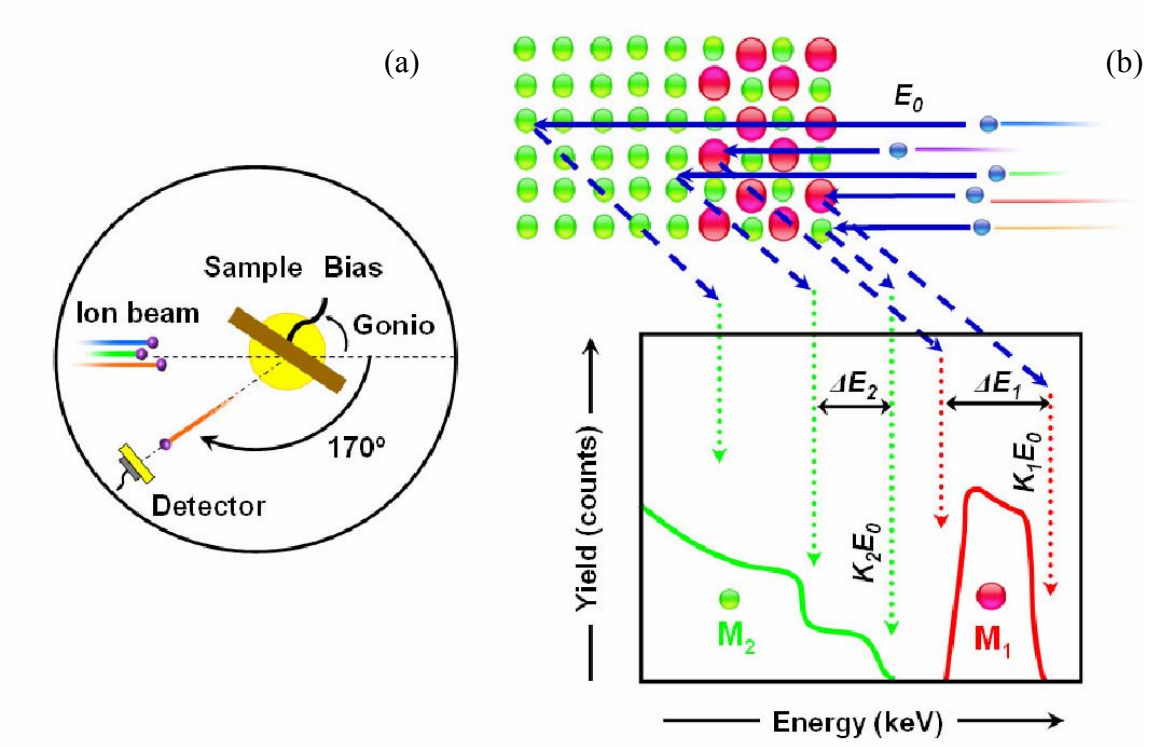

Fig. 20. (a) Sketch of a RBS experimental system. **(b)** Representation of an RBS spectrum for the simple case of two layers ($M_1 > M_2$).

If a well-collimated beam incides on a crystalline sample along one of its major crystalline axes or planes - i.e., low Miller index direction - the sample appears to the ion as a set of rows (or planes) formed by the atoms, separated by "empty" space, commonly named channels. **Figure 21** illustrates the three prototypical situations when inciding on a crystalline sample. If the ions incides with an angle very close to that of a channel, chances are high that they will enter the channel, where they will interact weakly with the surrounding atoms and will tend to stay close to the center of the channel, where the potential is minimum. As a result, channeled ions do not approach the rows of atoms beyond the edges of the cut-off distance, and the probability of being back scattered decreases with respect to unchannelized ions.

In an ideal channeling condition, the surface atoms produce a "shadow" in beam terms, making the beam almost insensitive to large angle deflections - i.e., short range collisions - with the inner atoms. Hence, the scattering cross section is greatly diminished except for a few surface atomic layers. Moreover, the stopping forces are also diminished, due to the larger average distance between the ion and the atoms of the sample. This decrement allows the beam to penetrate deeper in the sample.

An important characteristic of channeled beams is that, they are very sensitive to any imperfection of the crystal. In a non-ideal crystal - e.g., with substitutional defects or atoms oscillating around their equilibrium position due to temperature -, the channeled ions have a relatively higher probability of interaction with any atom that may "interrupt" the channel, i.e., there is an enhancement in the scattering cross section by the imperfections.

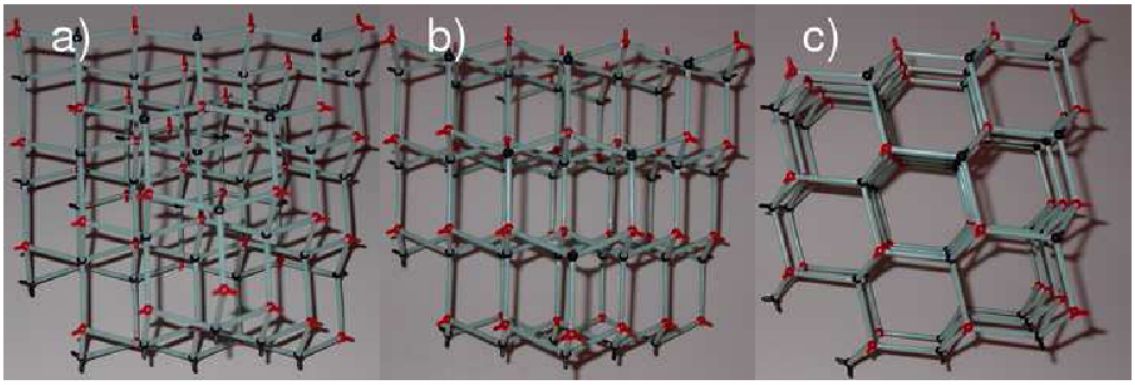

Fig. 21. Illustration of the channeling phenomenon in a diamond-like lattice model: **(a)** random, **(b)** planar and **(c)** axial directions. (Model courtesy of Dr. Angel Muñoz Martín.

Figure 22 shows the reduction in the number of RBS yield (counts) suffered by the spectrum acquired in a direction aligned with a crystal axis or plane (*aligned* or *channeled* spectrum), in comparison to the spectrum taken in a random direction (*random* spectrum). Similarly, any disturbance in the crystal lattice will lead to an increase in *yield* of the spectrum, this will allow us to detect the depth and the distortion ratio respect to the crystalline structure suffered by the ion beam damaged substrate.

The main feature of channeling, reduction of the measured backscattering events, is characterized by a pronounced dip of the RBS yield when making an angular scan. As mentioned, when a sample is channeled, the rows of atoms in the lattice are aligned parallel to the incident ion beam. The bombarding H/He ions will backscatter from the first few monolayers of material at the same rate as a non-aligned sample, but backscattering from buried atoms in the lattice will be drastically reduced since these atoms are shielded from the incident H/He atoms by the atoms in the surface layers. Taking advantage of this effect, a depth-resolved structural analysis can be carried out [19].

The theoretical modeling of ion channelling phenomena is complex and often requires Monte Carlo simulations; in any case, the complexities of this field are totally out of the scope of this work, and the reader is referred to [16, 19-21] for a more extensive and rigorous description.

4.2.4. Description of the RBS/C experiments and subsequent analysis.

The RBS/C measurements shown throughout this Thesis work were all performed at the Centro de Microanálisis de Materiales (CMAM), using the accelerator and the STD beam line previously described in **Section 4.1.1**. The Si barrier particle detectors (Ortec BU-012-50-500) used to measure the backscattered ions are installed in the chamber. One of the Si detectors is fixed at 170.4º respect to the incident beam direction, and the other is movable, allowing to vary the detection angle from 0º to 170º with estimated precision of 0.5º (typically fixed at 165.0º). Detectors are a diode-type silicon implanted barrier, with a nominal resolution of 12 keV. These detectors, also known as solid state detectors, work producing charge pulses proportional to the the energy of the incident particle.

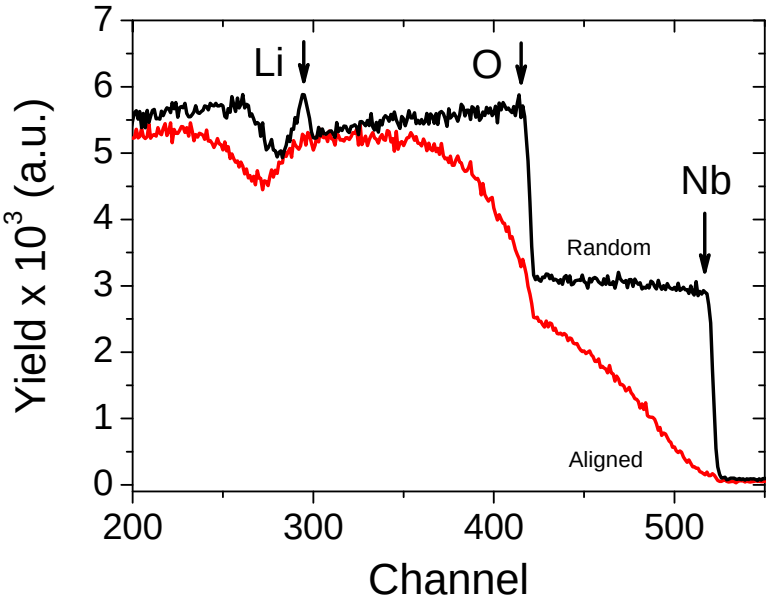

Fig. 22. RBS spectra in random (black solid line) and channelling (red solid line) configuration for *Z*-cut virgin sample of $LiNbO_3$. Analysis condition: 3-MeV H^+ ions, dose = 4 μC.

As mentioned in **Section 4.2**, while acquiring the RBS/C spectra, it should maintain the current values in the order of a few nA, due to currents too high can cause distortion of measurement because of the dead time of the detector is too high or the overlapping effect (*pile-up*) takes place. The latter is caused when two ions arrive simultaneously to the detector, and they are measured as a single ion with energy equal to the sum of both.

Subsequently, this pulse passes through a preamplifier, which converts the charge pulse into a voltage pulse, and a signal amplifier, which transforms it into a Gaussian shape and amplifies it to the range of volts. Finally the signal passes to an analog-digital converter, which measures the height of each pulse and sends the output digitized to a multichannel analyzer, where the arriving pulses which each amplitude are counted, i.e, for each energy, and will be assigned and added in each channel. The univocal and linear correspondence, mentioned before, existing between each channel and energy, is calculated known the *kinematic factor* (**Eq. 10**), from the value of the channel in which backscattered ions are detected at the surface. In **Figure 19** are marked the channels for ions backscattered from Nb and O nuclei at the sample surface.

Once the energy-channel correspondence has been performed, it is necessary to do the same with the channel-depth correspondence. This one was carried out using the software SIMNRA [22], by which the RBS spectra of $LiNbO_3$ samples of different thicknesses were simulated, and hence, being found the correlation. In this way, the RBS spectra can be represented as a histogram giving the number of particles measured for each energy, or for each depth. In this sense, it is worthy to notice that the determination of channel-depth correspondence is a delicate matter because, according to the described procedure, first, spectra acquired in random configuration are simulated, and secondly, it is necessary to transform the units from at/cm^2 to nm, which involves the knowledge of the atomic density of the material. However, when we have layers of amorphous material due to damage induced by irradiation, the density of these layers is not exactly the same as those of virgin material, neither is slightly

lower; introducing a small error in estimating the depth scale (energy channel-depth calibration). All of which brings us to consider the depth scale as an indicative measure, but not exact.

One frequent problem in RBS analysis is the acquisition of an accurate random spectrum, i.e., a spectrum which does not privilege any certain direction of the sample (equivalent to an amorphous layer). In samples with good crystal quality, the deviation of the measured yield from the one given by the simulation can be high. This difference arises from the fortuity alignment of the beam with a crystallographic direction, which produces the channeling of the ions thought the lattice (RBS/C) and reduces the backscattering events. Therefore, an accurate random spectrum without directional effects is needed, thus, this point has to be taken into account when performing the experiments.

One conventional way of acquiring a random spectrum is evading the crystallographic position tilting the sample some degrees (~7 º) in θ and χ off of the channeling axis. However, depending on the sample structure, some channeling may be still present. Another approach is the rotation of the sample during the measurements to average all directions. This is a better solution but the rotation of φ can only be performed for one single sample (in the center of the sample holder).

In the first measurements carried out spectra in random configuration were taken by setting χ = -9 º and scanning $\theta \in$ (-10, -5), or even at fixed point (θ, χ) = (-7, -9). In both cases we are clearly out of channeled configuration, however, is not strictly a measurement independent of the orientation of the sample, which can cause an error, not more than 10 %. If we compare the random spectrum obtained from both methods, the first one, obtained from fixing a position out of the axis, and the second one, by the batch method, the relative error between them is inside the statistical uncertainty, showing that both measurements cannot be distinguished.

In order to take advantage of the other two axes of the goniometer, an accurate method to acquire the random spectrum was used in this work. This procedure is based on a batch of 200 spectra of low dose (~20 nC), thus, yielding a total dose Q = 4 μC, recorded during the combined movement of θ and χ angles (within a short range of ~2º around the origin (0, 0)). Both θ and χ are moved describing a circumference around the center of the axis. This movement can be easily parameterized with only one variable (the angular step t, related with the number of acquisition points), following the equation: (θ, χ) = ($\theta_0 \cos t$, $\chi_0 \sin t$).

Consequently, using the batch, a random spectrum of the sample can be generated by the sum of all the individual spectra, obtaining a measurement independent of the orientation of the sample (**Fig. 19**). As it will be shown later, this kind of scan has a very important additional advantage when used to perform channeling experiments.

To make possible the circular scan in θ-χ, a Visual Basic program called *AngScan* developed by Dr. Ángel Muñoz-Martín was used. The program creates automatically the θ - χ batch, but it also allows single angular scans in φ, θ and χ with a selected step and dose for each point.

Set-up and special considerations for RBS/C.

There are several special considerations that have to be taken into account when performing RBS/C experiments [23]. Firstly, due to the directional principle of channeling, a good collimated beam is required. Secondly, an accurate measurement of the dose is needed since the comparison between aligned and random spectra depends on it. The slits and the bias in the STD beam line allow a good control of both parameters, as it was already discussed.

In addition, to avoid double-alignment geometries (both incident and exit beams aligned with crystallographic directions) in RBS/C, a large generous solid angle is needed. Since the fixed detector of the system at CMAM is placed at 170º with a solid angle of 4.75 msr, it fulfills the required conditions. On the other hand, the most crucial part of the system for RBS/C is the goniometer, since it is the tool for the alignment of the crystals, and the accuracy of the angular scans is limited by the good control of the position provided by the stepping motors. The center of the goniometer coincides with the center of the sample holder.

As was mentioned before, the acquisition of a precise random spectrum is as important as the acquisition of the aligned one. Actually, it can be understood that finding a good random spectrum is more difficult than finding a good aligned one: there is only one way of getting the aligned spectrum but there are infinite ways to collect a random spectrum. Therefore, for channeling experiments the θ-χ batch described above was used to find a reliable random spectrum. Simultaneously to the acquisition of the spectra in the θ-χ mixed scan, the different crystallographic planes of the crystal are crossed, so the position of the axis can be also determined by the intersection of all of these planes. Therefore, the program *AngScan* can be used to find the aligned position searched for channeling. Since the program allows single scans in the three axes, the obtained position can be corrected to enhance the accuracy.

The calculation of the dips requires the integration of the yield in some energy windows of the spectra. To make this, a new program called *DIP* was used. It allows the definition of three energy windows for both detectors (fixed and movable). The program reads the spectra and integrates them in the selected windows. Then, we will proceed to add the number of counts obtained for each individual spectrum in the corresponding channels near to the step edge associated to Nb signal (**Figure 19**), range where the spectrum efficiency decreases more in the case of spectra taken in channeling configuration with an axis of the crystal (**Figure 22**). Representing the obtained result (see **Figure 23** and **Figure 24**) allows us to find the points (*dip*) which produces a decrease in the number of accounts, and correspond to any of the crystallographic planes of $LiNbO_3$. That is, the identification of each dip determines the (θ_i, χ_i) pairs in the circumference, and the intersection of such pairs gives the center of the axis.

By this way, from the intersection of two or three planes obtained we get the point corresponding to the orientation aligned with the $LiNbO_3$ channel, as observed in **Figure 25**. Finally, for the sake of greater precision in determining the channel, additional scans around the point found are performed, to find the exact value of (θ, χ) that make minimum the spectrum efficiency in channeled configuration.

As a demonstration of the application of the batch scan, **Figure 23** shows the result of the integration with *DIP* program in two different axes of a *Z*-cut Lithium niobate crystal. The solid circumference is the experimental points acquired with *AngScan* program. The RBS

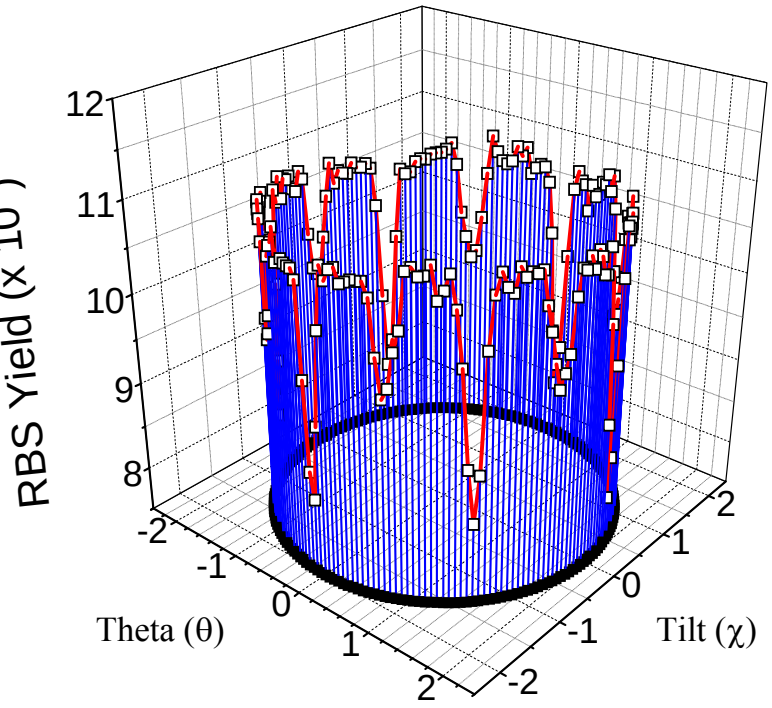

Fig. 23. Plot of the number of counts obtained in the corresponding channels to the signal of Nb for the spectra acquired in (θ, χ) orientations. Angular scans around <0001> axis in a LN virgin crystal. Six crossing planes are visible.

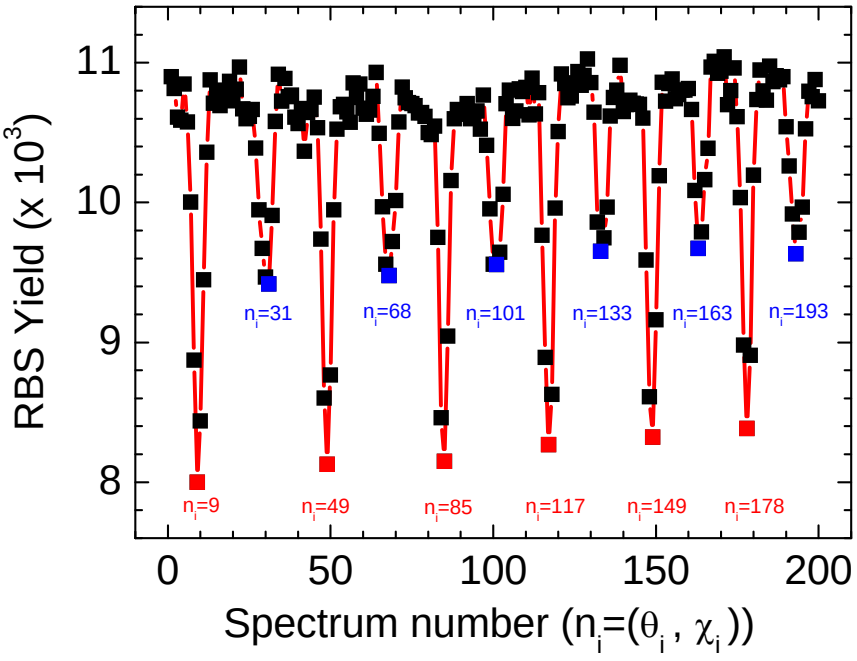

Fig. 24. Detail of the number of counts obtained for the each spectrum acquired in (θ_i, χ_i) orientations. Each number of spectrum (n_i) associated to an orientation in which there is a decrease of the efficiency has been identified.

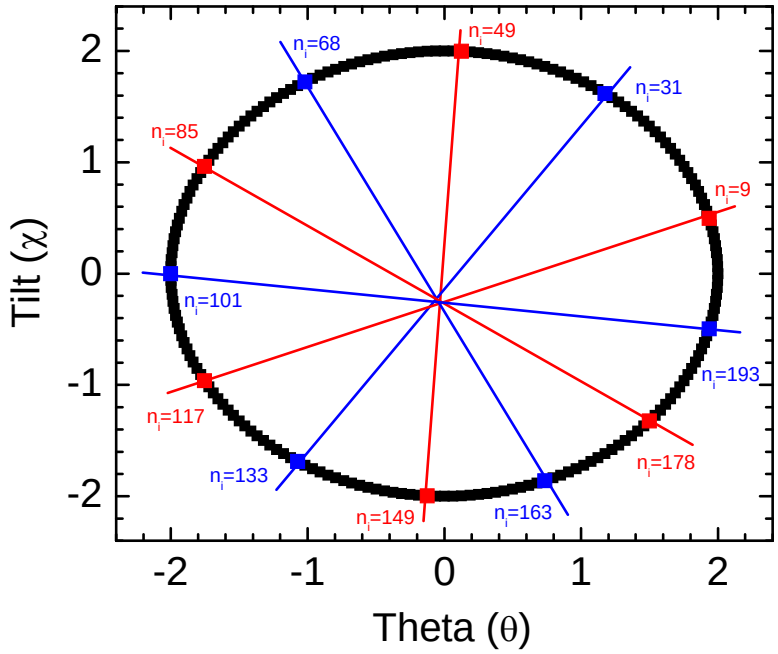

Fig. 25. Identification of each dip (n_i), previously marked in **Figure 24**, determining the (θ_i, χ_i) pairs in the circumference. The intersection of such pairs gives the orientation aligned with the channel of a *Z*-cut LN virgin crystal.

experiment was carried out using 2 MeV H^+ ions and total of 200 points was used in the θ - χ batch within a radius of 2º around the origin (0, 0). On the other hand, with the aim of obtaining high enough statistics, a total dose of Q = 20 μC was divided in the 200 spectra, having each one an individual dose of 0.1 μC/spectrum.

For the <0001> axis, twelve dips are recognized (6 crossing planes). The intersection of all the dips coincides with the position of the axis, where the most pronounced dip is found (**Figure 23**).

In order to carry out the determination of the disorder induced in crystals by irradiation, first, the acquisition of a RBS spectrum *in channeling* and *random* configuration are performed in a virgin sample. They will be used as a reference. Also, a spectrum in channeling configuration of the sample under study will be acquired and, subsequently, compared with the two previous spectra. The ion beam induced damage of the sample at the surface can be obtained direct and reliably from the measurement described above. However, when you want to do an analysis of the induced damage at depth, a number of assumptions will be required.

4.2.5. Dechanneling.

An imperfect crystal contains defects. These defects, together with the combination of multiple scattering by electrons and thermally displaced atoms, lead to an increase with depth of χ_{min}.

It is worthy to notice that, from a theoretical point of view and according to the Lindhard's continuum model [18], the *minimum yield* (χ_{min}) is exactly describing the fraction of

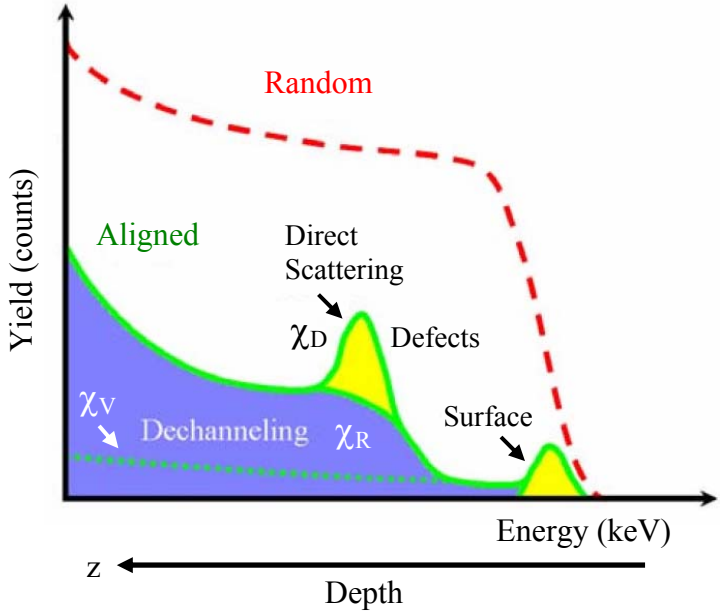

Fig. 26. Main features in an aligned RBS spectrum (RBS/C) of a crystal with defects. Scheme of the change in RBS yield when a buried disordered layer is traversed, giving rise to dechanneling effect and direct scattering of the incident ions. The dechanneled fraction (χ_D) of the beam in a damaged crystal is greater than the fraction (χ_R) of the beam that has become dechanneled down to a depth *z*, where the crystal is disordered.

the channel area which is forbidden by the vibrating strings of atoms. On the other hand, from the experimental point of view, the determination of χ_{min} requires only two spectra, one in a random configuration and one aligned. Therefore, the crystal quality of a material can be measured by RBS/C using the ratio between the aligned and the random yields.

For experimental considerations, dechanneling can be defined as the rate at which the normalized yield is changing with depth ($d\chi/dz$) [19]. The magnitude of dechanneling processes depends on the nature and concentration of defects. The intrinsic sources of dechanneling (electron scattering and thermal vibrations) are normally playing a minor role. However, the presence of point or extended defects can be strongly marked in the aligned spectrum, provoking an intense peak of dechanneling when they are located inside a narrow depth region. All these features are summarized in **Figure 26**.

Dechanneling is an essential parameter to quantify the density of defects and the crystal disorder of a material. For interstitial atoms, stacking faults and grain or twin boundaries, dechanneling is proportional to the defect concentration, $n_d(z)$ [24]. However, the estimation of the dechanneled fraction requires the deconvolution of direct scattering events from random scattering in the crystal. This fraction (χ_D) is interpreted as the areal fraction that becomes disordered by the irradiation at the depth where the channeling yield has been measured. The analysis is developed within the framework of the two-beam formulation [19, 25] and states that the dechanneled fraction of ions (χ_D) is the sum of the random scattered component (χ_R) and the contribution from the direct scattering by defects (χ_S). Thus, it assumes that the RBS yield $\chi_D(z)$ for the considered axial (or planar) direction is given by:

$$\chi_D(z) = \chi_R(z) + \chi_S(z) = \chi_R(z) + [1 - \chi_R(z)]\frac{f \cdot n_d(z)}{N} \quad \textbf{(14)}$$

where $n_d(z)$ is the concentration of defects; f is the direct scattering probability; N is the atomic density (hence, $n_d(z)/N$ is the normalized defect concentration to the total atomic concentration N); $\chi_R(z)$ is the fraction of the beam that has become de-channeled down to a depth z; and χ_D is the dechanneled fraction of the beam in a damaged crystal obtained from the ratio of RBS yield in aligned and random configuration, thus, being an amount that is obtained experimentally. More specific comments must been done respect to f factor: f is the scattering factor of the defect that measures the direct scattering probability of each defect, and depends on its geometry. That is, f accounts for any difference between the number of defects and the effective number of scattering centers by defect. For example, for defects that consist of single atoms displaced f takes the value 1. However, for small distortions of the lattice as dislocations, the value of f can be close to 0, so that, the presence of such distortion is detected in the dechanneling process of the beam, rather than by direct scattering. In practice, most of the analysis consider one of the limit cases ($f = 1$ or $f = 0$).

Note that **Eq. 14** can be inverted to find the defect concentration as a function of χ_D and χ_R. Unfortunately, despite of χ_D is experimentally known, χ_R is not a direct measurable quantity. However, the probability rate for random dechanneling per unit depth is proportional to the defect density via a cross section σ_d (theoretically estimated) [19]. Thus, χ_R is given by [19]:

$$\chi_R(z) = 1 - [1 - \chi_V(z)]\exp\left(-\int_0^z \sigma_d n_d(z')dz'\right) \quad \textbf{(15.a)}$$

or, using a series expansion,

$$\chi_R(z) = \chi_V(z) + [1 - \chi_V(z)]\int_0^z \sigma_d n_d(z')dz' \quad \textbf{(15.b)}$$

where χ_V is the random fraction for a defect-free (virgin) crystal, i.e., the dechanneled fraction of the beam in a virgin crystal obtained from the ratio of RBS yield in aligned and random configuration, and thus, an amount that is obtained experimentally. The expression (**15**) can be approximated to a linear expression for small defect concentrations, and therefore, it can be calculated from the RBS spectra, channel by channel.

Overall, we can say that the number of collisions of channeled ions, which give rise to backscattering, is a differential measurement of disorder at that depth, while the collisions of dechanneled ions represent an integral measurement of disorder from the surface to that considered depth. Therefore, the resulting spectrum is a result of both contributions, which is not a direct indication of the amount of disorder at each depth. Hence, an iterative analysis of data will be required, performed under several approximations, since, the type of defects present after irradiations are not known. (see **Figure 26**).

Chapter 5

Characterization Techniques.

5.1. Scanning Force Microscopy.
5.2. Optical characterization methods.
5.3. Transmission electron microscopy.
5.4. Profilometry.

5.1. Scanning Force Microscopy.

5.1.1. Introduction.

Since G. Binnig and H. Rohrer developed the scanning tunneling microscope (STM) in 1982 [26] scanning probe microscopy (SPM) has become a significant tool for observation and characterization in surface science technology, i.e. for surfaces, interfaces and structures on the nanometric and atomic scale. The STM is a surface probe capable of atomic spatial resolution which measures tunneling current as a function of position on the surface of electrically conductive material. The atomic force microscope (AFM) was created by G. Binnig, C. Quate and C. Gerber in 1986 as a method to image insulators, in addition to conductors, on an atomic scale [27, 28]. Nowadays SPM is a characterization standard in all kinds of branches in industry, research and development and fundamental research. Due to the fact of measuring forces that occur between the sample and the tip one can focus on the best interaction to achieve a very high accuracy, depending on the properties in which one is interested. The tip is then scanned over the sample[7], and with a computer the topography of its surface can be reproduced. Although the original function of AFM was to measure surface topography, it has extended to a variety of other surface force probing techniques including electrostatic force microscopy (EFM) [29-32], piezoresponse force microscopy (PFM) [33-35] and scanning Kelvin probe microscopy (SKPM) [36], among others.

In this Section, SPM technique employed for this dissertation is introduced and described. SPM is the focus of numerous books [37-42], therefore, an extensive review is not given here and only the basics of the technique are discussed. First, an overview of AFM is given followed by an explanation of each of its primary imaging modes: contact, non-contact and tapping. These three modes of imaging are the basis for all other scanning surface force probing techniques. Finally, sources of experimental error in the SPM technique are discussed.

5.1.2. The idea.

In the case of the STM, a voltage is applied between scanning probe and sample and the tunnelling current is measured. Via this voltage, the tunnel barrier between sample and tip is shifted. Thus, the tunneling effect is promoted and then exploited to measure a small current resulting from electrons tunneling from the examined surface into the tip (or vice versa). For sufficiently small distances the dependence of this current is even exponential which leads to an excellent resolution (in *z*-direction, i.e. perpendicular to the sample surface).

The scanning force microscopy (SFM) was the first extension of the STM. In this case, the metallic tip is replaced by a force sensor, so-called cantilever, to measure the interaction forces acting between probe and sample, thus, instead of measuring a current, the idea was to observe a force to map the surface. The concept is to scan a tip over a sample surface, just like in an STM or, generally speaking, in scanning probe microscopy (SPM), but to measure a surface of constant force. That is, the interaction between tip and sample leads to a movement of

[7] In many cases the sample is attached to the scanner and moves relative to the tip, yielding the same result.

a small cantilever which then can be measured as a variation of this force. The first question to the developers was the feasibility of such a force measurement. These forces are usually in the range of nN to μN and, though atomic resolution can be achieved, typical lateral resolution ranges between 5 nm and 20 nm depending on the sharpness of the probe. Vertical distances can be measured with an accuracy of less than 1nm. Therefore, to attain this, the probe has to be displaced over the analyzed sample in a sufficiently small distance which is implemented using piezoelectric crystals. Besides surface topography, the probe-sample interactions also reveal information about lattice symmetry, adhesion, friction, elasticity, wear, etc… with unprecedented spatial resolution.

The success of the SFM technique mainly arises from the possibility to image surfaces independent of their conductivity properties, a severe limitation of the STM technique. But SPM in general and SFM in particular, offer much more than just imaging. Some alternative and outstanding applications of SPM in the field of material science have recently been collected in [43].

5.1.3. Overview.

An AFM has three basic components: a force sensor, a scanner and a device to detect the motion of the cantilever, which are all connected to an electronic controller and a computer. Variations of these components are the foundation for all SPMs. The controller generates the electronic signals necessary to move the components of the AFM and also converts data so that it can be displayed by the computer. Specially designed computer software acquires and displays data in the form of an AFM image, which is a map of surface topography. **Fig. 27** shows a typical AFM setup.

The AFM measurements presented in this research work (*Chapter 6*) have been carried out at CMAM, using commercial equipment from Nanotec Electronica S. L. [44], capable of operating in *contac*t and *tapping mode*. Stands out the use of the measurement mode "*PLL-Tapping mode*", without which there would not have been possible to characterize the structures revealed by chemical etching in the irradiated samples, due to strong tip-sample interaction (for more details see *Chapter 6*). Moreover, it is worthy to notice that, an optical microscope is coupled to AFM that allows viewing tip-sample position in order to place the tip on a particular area of the sample.

The AFM force sensor consists of a microfabricated rectangular or triangular cantilever with a small tip, or probe, at one end. The probe can be conical or pyramidal in shape. The geometries and properties of the SPM probes and cantilevers used in this research will be listed later (*Section 4.7.2.8.2.* **Fig. 36** and **Table IV**). Microfabricated cantilevers are most commonly made of Si_3N_4 or Si. The backside of the cantilever (the side without the tip) is sometimes coated with a metal such as Al to increase reflectivity.

Movement of the tip over the surface and the tip-sample distance are controlled by the scanner which is made of a piezoelectric ceramic, such as PZT (lead zirconate titanate). As discussed in **Chapter 2.** *(Section 2.7.1)* of this dissertation, piezoelectric materials expand or contract when a voltage is applied. This fact is known as the *inverse piezoelectric effect*, found by the Curie brothers in 1880. It is traced back to the fact that electric charges occur on surfaces

of mechanically deformed crystals and accordingly finds a wide range of applications. Since the applied voltage is proportional to the mechanical motion of the material, the scanner has precise

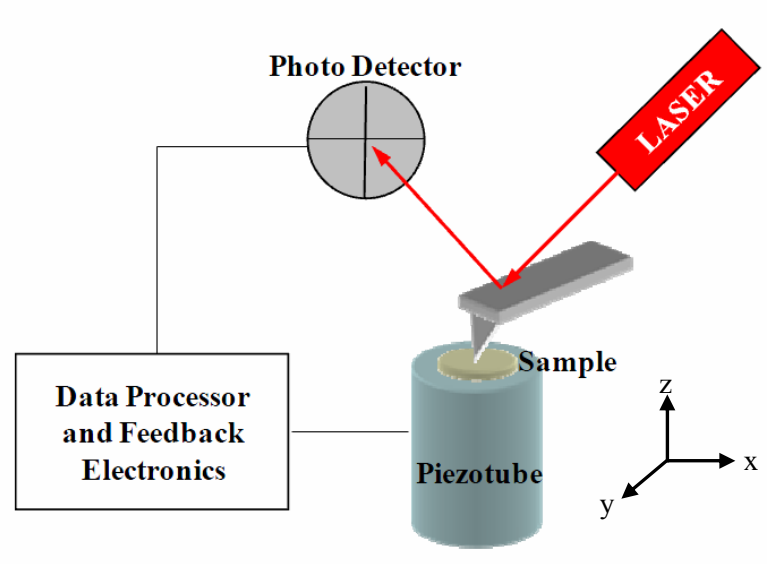

Fig. 27. Schematic view of the components of an AFM measuring system. A piezoelectric scanner controls the movement of the sample and tip-sample distance. A laser beam is reflected from the back side of the cantilever to a photodetector which records the deflection of the cantilever as it moves across the sample. The data processor and feedback electronics convert the signals and generate an image of the sample surface.

control over lateral and vertical movements. The scanner can have two different configurations; either the tip moves and the sample is stationary or the sample is rastered and the tip is fixed. Our AFM equipment is a sample-scanning instrument.

There are various methods to detect the motion of the cantilever as it scans across the surface of a sample such as tunneling detection, capacitance detection, and optical interferometry. The Nanotec AFM use laser beam deflection ("beam bounce" deflection). The displacement of the cantilever is measured by detecting the deflection of the laser beam from the back side of the cantilever as it rasters across the sample surface. The detector in this case is a position-sensitive photodetector (PSPD) composed of four photodiodes. When the laser beam hits a photodiode, a current is generated, and a difference in intensity can be measured between the quadrants. The difference in intensity is referred to as the "error signal".

5.1.4. Components of the SFM: Our experimental setup.

In our setup, a so-called *piezoelectric tube* was used to implement all lateral movements of the tip relative to the sample, as well as to assure an adequate distance control.

A brief overview of the measuring sequence shall be given and the most important components of the AFM will be explained, for which the just mentioned piezoelectric elements only play a role for the scanner unit.

The tip is fixed to a flat-spring, the so-called *cantilever*. Nowadays, the tips are grown directly on their cantilevers, and scan the surface line by line. Due to the forces of the surface atoms acting on the tip, the cantilever is bent. This deflection is then measured and the piezoelements are steered by a controller in such a way, that the force between tip and surface is kept constant.

From the obtained data which was processed by a computer, and with the corresponding software a 3-dimensional image of the surface can be reconstructed, or other evaluations can be carried out. This process is sketched in **Figure 27**. Independent of the kind of interaction that is used to visualize the surface topography, every SPM consists of the five following integrated mechanisms, which compose the system.

5.1.4.1. The force sensor. The probe.

The probe is a critical component of a scanning probe microscope because different probes can measure different properties of the sample. Also the probe determines the force applied to the sample and the ultimate resolution of the system. The most common probes in scanning probe microscopy are the cantilevers. These cantilevered probes are highly suited to measure the topography of a sample. Using different coating on the cantilevers different properties of the sample can be measured, like magnetic (MFM), electrostatic (EFM), capacitance (SCM) etc.

Strictly speaking, the SFM does not measure forces but the bending and torsion of a lever (also called *cantilever*), induced by the forces acting on a nanometer-sized tip attached to one of the lever ends. Atomic force microscopes require not only sharp tips, but also cantilevers with optimized spring constants. Therefore, this cantilever has to be as soft as possible to be able to detect forces down to the pN. Ideally, the stiffness should be below interatomic spring constants, which are typically in the range of 10 - 20 N/m. To achieve this and additionally prevent the transmission of external vibrations to the cantilever, its effective mass has to be as small as possible. The spring constant of the cantilever depends on its shape, its dimensions, and the material from which it is fabricated. Thicker and shorter cantilevers tend to be stiffer and have higher resonant frequencies. The spring constants of commercially available cantilevers range over four orders of magnitude, from thousandths of a Newton per meter to tens of Newton's per meter. Resonant frequencies range from a few kilohertz to hundreds of kilohertz providing high - speed response and allowing for non-contact AFM operation.

Today, such cantilevers with integrated tips are commercially produced by standard microfabrication techniques, mostly from silicon or silicon nitride and manufactured using photolithographic techniques. The later use of a coating layer allows producing tips with different surface properties (conductive, magnetic…). The two most used cantilever geometries are the rectangular and the V-shaped cantilever. Typical dimensions are: length of 100 - 300 μm, width of 10 - 30 μm, thickness of 0.3 - 5 μm, tip height of 3 - 15 μm and tip radius of 10-100 nm, which yield typical spring constants ranging from 1 N/m for *contact mode* to 60 N/m for *tapping mode*[8] measurements. The corresponding typical resonance frequencies extend from 20 to 350 kHz, respectively.

[8] Operational modes will be explained in a latter Section.

The working principle is schematically depicted in **Figure 28**: normal forces acting on the tip (perpendicular to the cantilever plane) produce a vertical deflection of the cantilever (Δz), while lateral forces perpendicular to the long axis cause the torsion of the cantilever (Δx).

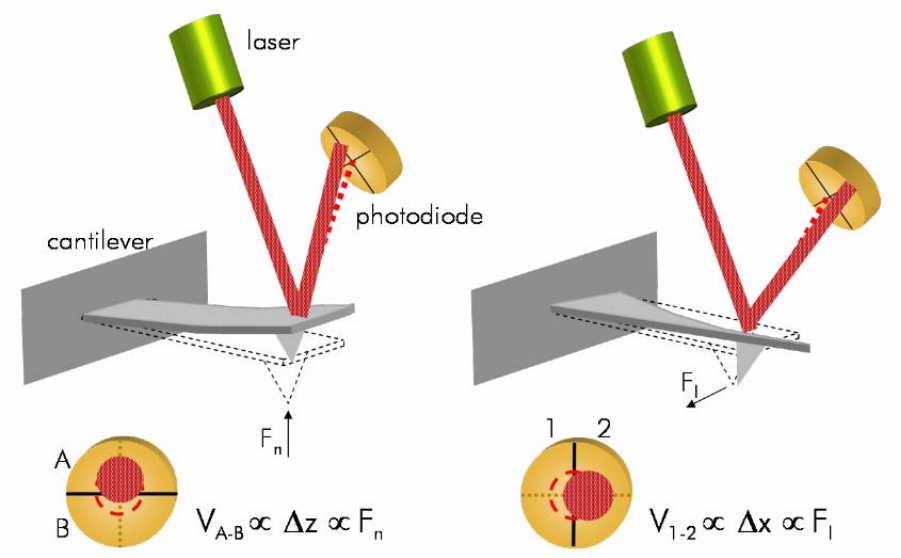

Fig. 28. Schematic representations showing the optical detection method used to measure the cantilever displacement produced by **(a)** normal and **(b)** lateral forces. Dashed cantilever and laser path represent their respective position in the absence of forces. At this position $\mathbf{V_{A-B}}$ and $\mathbf{V_{1-2}}$ are adjusted to zero. Normal forces are proportional to the $\mathbf{V_{A-B}}$ signal whereas lateral forces, to the $\mathbf{V_{1-2}}$ signal.

Generally, the cantilever response is approximated by a spring in each direction, and the relation between the forces and the corresponding displacements is straightforward derived from the Hook's law:

$$F_n = k_Z . \Delta z \quad (\mathbf{16})$$

$$F_l = k^T . \Delta x \quad (\mathbf{17})$$

with k_Z and k^T the spring constants for normal deflection and lateral torsion, respectively.

In this work, different types of cantilevers, from μ-masch™, Nanosensors™ and Veeco Probes, have been employed. Rectangular-shaped cantilevers with a nominal force constant k_Z = 42. N/m (*tapping mode*) have been mainly used for the structural characterization, though in some experiments we have employed cantilevers with spring constant k_Z = 3.5 N/m for contact *mode* measurements.

5.1.4.2. The Deflection sensor.

The next important AFM component is the measuring unit to determine the deflection of the cantilever. Different techniques have been proposed to detect the small bending of the cantilever due to tip-sample forces [39]. Though in the first SFM setup, this deflection was measured with an STM tip (the backside of the cantilever was metalized, and the tunnelling tip was brought close to it, to measure the normal deflection [27]), subsequent designs simplified

the original by using optical (interferometer, beam reflection) or electrical methods (piezoresistive, piezoelectric).

Our systems employ the optical beam deflection method, proposed in [45, 46] and found nowadays in most of the microscopes. Within this method, a laser beam is focused on the rear metalized side of the cantilever via mirrors and lenses and the reflected beam is collected by a segmented position-sensitive photodiode (PSPD). Each sector of the photodiode generates a voltage proportional to the intensity received. If the photodiode is segmented in four quadrants (as in our systems), the normal bending and the torsion of the cantilever can be separated and quantified [47]. Since we are normally operating in *dynamic mode*, which will be explained more in detail later, the sensor records the cantilever oscillation amplitude signal. A schematic drawing of our setup is shown in **Figure 28**. Another, equivalent measurement, is the interferometric method, which also works by laser light. The benefit of these optical methods is that the radiation pressure of the light beam on the cantilever is completely negligible and has no effect on the actual force measurement at all.

In the absence of forces the laser spot is centred, i.e. equal signals are measured in each of the four sectors. When a force acts on the tip, the lever is deflected and the reflected spot is displaced. As depicted in (a), normal forces produce a vertical bending of the cantilever that is proportional to the signal difference between the upper and lower halves of the detector ($\Delta z \propto V_{A-B}$). Similarly, the main effect of lateral forces is the torsion of the cantilever (b), which is proportional to the signal difference between the right and left halves of the photodiode ($\Delta x \propto V_{1-2}$).

For every cantilever used, a calibration of the photodiode response is required to obtain the conversion from the measured signals, V_{A-B} and V_{1-2}, to the cantilever displacements, Δz and Δx:

$$\Delta z = S_Z V_{A-B} \quad (\mathbf{18})$$

$$\Delta x = S_X V_{1-2} \quad (\mathbf{19})$$

where S_Z and S_X are the calibration factors for the bending in the vertical and lateral directions, respectively.

5.1.4.3. The Scanning System.

The scanning probe needs to be extremely fine moved and positioned over the sample. This is usually achieved by attaching either the tip or the sample (this latter is the configuration used in this work) to piezoelectric actuators. These generally consist of lead-zirconate-titanate (PZT) ceramic materials placed between two metal electrodes. When a potential difference is applied across the electrodes, the piezoelectric ceramic expand or contract in a direction that is perpendicular to the applied electric field. The motion of the ceramic is controlled by the polarity and magnitude of the applied voltage.

The tube shaped piezoelectric actuator of **Figure 29** is the most frequently used in SFM. It is a hollow cylinder that has one electrode on the inner surface and four equally spaced electrodes on the outer surface. Biasing the inner electrode controls the tube's motion in the $\pm z$ direction. This change will be referred to as the piezo displacement (Δz) from now on (though

we use the same symbol, it can differ from the vertical cantilever displacement). Biasing two opposite outer electrodes moves the tube in the ±x and ±y directions. This provides the scan area (Δx, Δy) on the surface plane of a typical SPM image. The particular vertical and lateral displacements depend upon the geometrical and physical characteristics of the piezoelectric tube:

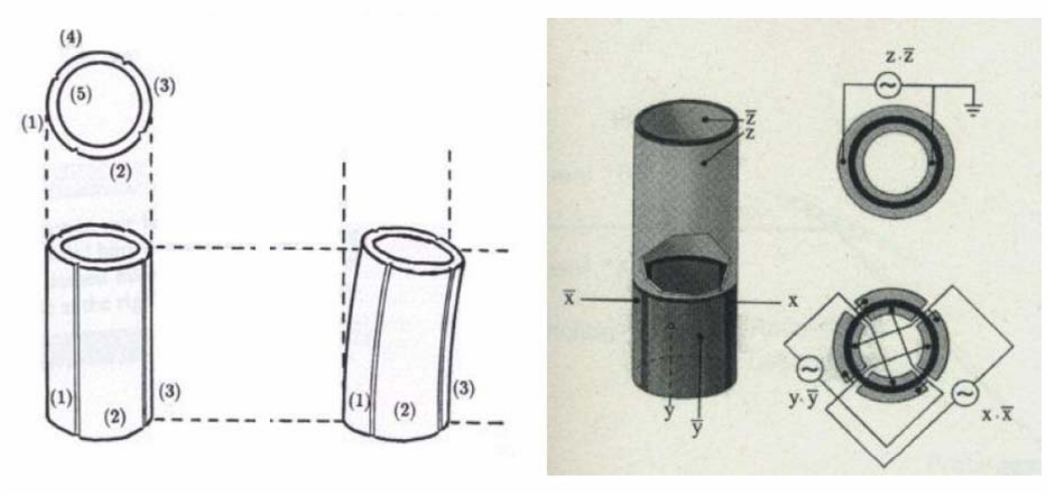

(a) (b) (c)

Fig. 29. (a) Cross-section of a piezoelectric tube (top) with its four outer electrodes (1-4) and one inner counter electrode (5), in neutral position (bottom). **(b)** Schematic representation of the response of a tube-shaped piezo actuator to an applied voltage between the two opposite external sectors: a voltage +U is applied between (1) and (5), as well as a voltage −U between (3) and (5). c) Schematic view of the actually used tube in our setup without segmented electrodes in the upper division, including circuit diagram.

$$\Delta z = V \cdot L \frac{d_{31}}{t} \tag{20}$$

$$\Delta x(\Delta y) = 2\sqrt{2} \cdot V \cdot d_{31} \frac{L^2}{\pi D t} \tag{21}$$

where L is the length, t is the wall thickness, D is the outer diameter and $d_{31}$is the piezoelectric constant of the particular ceramics from which it is fabricated. We have used a piezo scanner whose nm/V ratios are - 17 nm/V for the vertical displacement and 49 nm/V for the lateral movement. This yield a maximum horizontal and vertical scan ranges of 10 μm and 5 μm respectively, which allows measuring samples with enough accuracy from completely flat to rough surfaces.

The above equations serve as estimation but, in SPM, to avoid undesired uncertainties (intrinsic non-linearity, manufacturing differences, aging effects…) the piezos are usually in-situ calibrated to obtain an accurate conversion between the applied voltage and the displacement. Due to the non-linearity in the piezo movement, we have employed different calibration gratings to obtain nm/V ratios for large and small scan areas.

In this sense, it is worthy to notice that, the test grating TGX1 [48] was scanned to evaluate lateral distortions. **Figure 30** shows an image acquired from the commercial calibration grating. The grating structure is formed on a Si wafer top surface and consists of a chessboard-like array of square pillars with sharp undercut edges in a 3.00 ± 0.05 µm period. The edges have curvature radii of 10 nm on the sides and are about 1.2 × 1.2 μm^2 wide, thereby not touching each other. This way one can see how good the tip resolves the interspaces between diagonal pillars and the angles on ascending edges assumably are the tip's half con angle. The total pillar height is ≈ 600 nm, which is deeper than any examined etched pore. The AFM

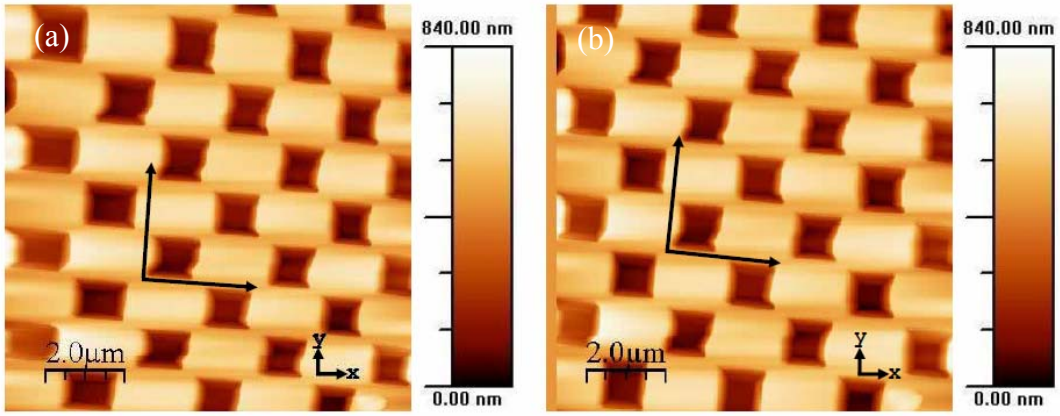

Fig. 30. SFM image (10 x 10 μm^2) showing a forward scan of the test grating TGX1 used to calibrate the piezo scanner. The nominal step heights and periodicity are provided by the manufacturer. **(a)** Raw measured data. **(b)** Structure resulting from the application of the nonlinear correction to the measured data (a). The scan axis *X* and *Y* are indicated in the lower right corner.

measurements were used to calculate a nonlinear correction matrix. The nonlinear filter with the correction matrix was then run over the image data. The original measurement (**Figure 30 (a)**) can be compared to the result of the correction **Fig. 30 (b)**. The unlabeled arrows indicate lengths of 3 µm each. Even though the square pillars have really the same size, they appear stretched at the beginning of the trace and reduced at the end (forward scan), whereas in *Y* direction they are contracted. After applying the nonlinear correction there are still a lot of distortions visible, some of which are due to the tip shape. The vertical stripe on the left is due to a contraction of the image points.

On the other hand, in order to perform the vertical calibration of the piezo scanner a commercial grating TGZ1 [49] was used. It presents a 1-D arrays of rectangular SiO_2 steps on a Si wafer which nominal height is 18.5 ± 1 nm and the distance between steps 3.00 ± 0.05 µm. In this case, the vertical step height measured was only 4 % higher. However, the piezo was calibrated by the provider for smallest heights and is even more accurate on smaller steps.

5.1.4.4. The Feedback Control Unit.

A high voltage unit connected to a digital signal processor (DSP) inside a PC basically completes our experimental setups. The DSP board is mainly in charge of collecting the signal coming from the photodiode and controlling the movement of the piezo. Due to the limited

voltage range of the DSP (± 3 V) and the high voltages required by the piezo to work (up to 300 V), the signal is amplified and supplied to the microscope through a high voltage unit. The amplification gain is selected by the user depending on the vertical and lateral scales of the sample under study: lower gains imply smaller scanned area but increased resolution.

The DSP is also in charge of the so-called *feedback loop*, a way to control the vertical distance between tip and sample by maintaining a selected magnitude fixed to a preset value during the scanning. The controller regulates the lateral movements in *x*- and *y*-direction of the sample, steers the *z*-piezo segment, gives the excitation frequency (EF) signal to the cantilever in the *dynamic mode*, and processes the data acquired by the detector. Furthermore the feedback-loop is mostly governed by two important parameters: (1) proportional gain (P) and (2) integral gain (I). During part of this work the magnitude used has been the normal deflection of the cantilever, i.e. the normal force. By means of the feedback loop, this deflection and the preset set point are continually compared at each point of the image. If they are not equal, a voltage is applied to the scanner in order to move the sample closer to or further from the probe, to maintain constant the normal force. This applied voltage is the signal used for generating the SFM image. On the other hand, the feedback can be done on more than one magnitude, e.g. instead of adjusting force or distance, one can correct for amplitude or phase like in *dynamic mode*.

The program used for data acquisition and image processing is Nanotec WSxM software [50], being a very powerful and complex program,

5.1.4.5. Vibration isolation.

The construction of the tip holder, sample holder and piezo scanner should be as rigid as possible in order to increase the mechanical resonance frequency of the system. Moreover, to achieve sub-nanometre sensitivity, the whole setup should be well isolated and protected from external perturbations, in this sense, typical vibrations in buildings coming from elevators, stepping on the floor or motion of the entire building itself (frequency range between 0.1 and 2 Hz) and acoustic noise (frequency range of 10 to 20 Hz) must be eliminated. In order to accomplish it, one can mount the SFM on a rigid granite plate, being the whole system suspended with four bungee cords that act as springs. The resonance frequency of the system is ~1Hz and filters out higher mechanical vibrations. Another possibility consists in placing the SFM and the granite plate supported by four damping legs (that act as a low resonant frequency support) in a suitable rack at the ground floor of the building (**Fig. 31**). The idea of place the entire setup on top of a soft rubber damper filtering fast oscillations could be useful too. In any case the system should be placed on one or multiple heavy plates to filter for longer wavelengths. Combinations can improve isolation against vibrations [51]. Finally, in any of the above cases, a hood covers the scanning force microscope head (tip, sample, detection system and piezo actuator) which provides further acoustic isolation and allows controlling the relative humidity of the working atmosphere.

5.1.5. Operation modes in SFM.

Several forces typically contribute to the deflection of an AFM cantilever. The interaction potential between the tip and surface can be modeled by the *Lennard-Jones potential*, where, mainly *Van-der-Waals* and *dipole-dipole interactions* are considered. The dependence of the model of the potential energy of the interaction upon the distance between the tip and the sample is shown in **Figure 32**. Two distance regimes are labeled: 1) the *contact regime*; and 2) the *non-contact regime*. In the *contact regime*, the cantilever is held less than a few angstroms from the sample surface, and the interatomic force between the cantilever and the sample is repulsive. In the *non-contact regime*, the cantilever is held on the order of tens to hundreds of angstroms from the sample surface, and the interatomic force between the

Fig. 31. The SFM system used in this research supported by four damping legs, acting as a low resonant frequency support, placed in a suitable rack at the ground floor of the building. The SFM head is covered by a hood providing further acoustic isolation and allowing to work under controlled relative humidity. Additionally, the feedback electronics and computer appear on another table next to the SFM. Behind the AFM head an optical microscope with the external light source is shown too.

cantilever and sample is attractive (largely a result of the long-range van der Waals interactions).

By this way, through the rich variety of interactions detected in SFM a wide variety of operation modes has been made possible. In the so-called *contact mode*, where the tip and the sample are in direct mechanical contact, by measuring the change in the vertical deflection of the cantilever (due to repulsive forces) as the tip scans the sample surface, topographic images are obtained. Simultaneously to the surface topography, maps of friction or conductivity, which also imply direct contact, can be measured. Another kind of operation modes are the so-called *dynamic modes* where the cantilever is oscillated near its resonance frequency at a given distance from the sample surface. Depending on the amplitude of oscillation, compared to the tip-sample distance, the tip may either not contact the sample (small amplitude) or intermittently contact the sample surface (large amplitude). By measuring changes in amplitude, phase or

frequency of the oscillating cantilever in response to the existing tip-sample interactions, one can obtain not only topographic images of the surface but also dissipation, magnetic or electrostatic maps.

Though further details are given on those modes employed throughout this work, a complete description of all of them can be found in general SFM books as [52].

5.1.5.1. Contact mode.

In contact mode (c-AFM), the probe is in contact with the sample surface. A map of the sample topography is created by keeping either the force between the probe and sample constant or the probe height constant. All contact mode images in this dissertation were taken in *constant force mode*, wherein the force is maintained by means of a feedback loop (via the controller)

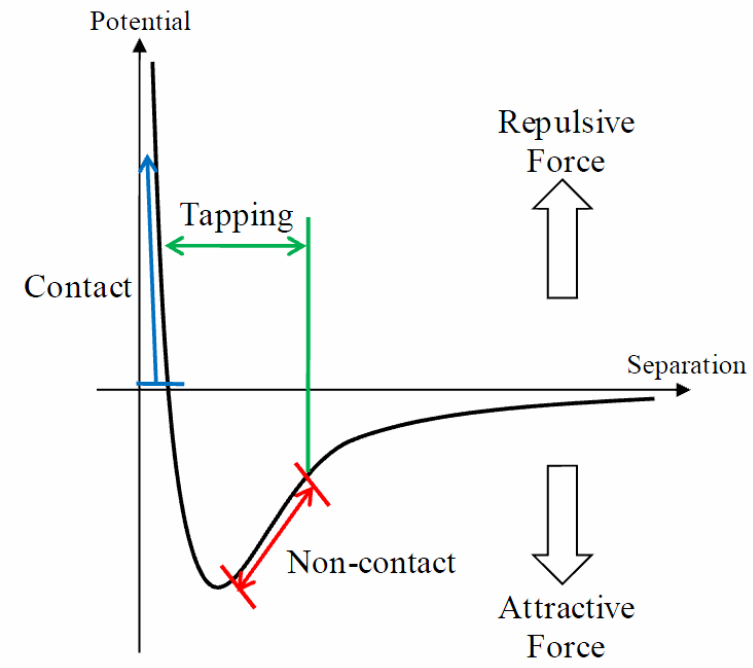

Fig. 32. Lennard-Jones model of the potential energy of the tip-surface interaction as a function of the distance between them. As the distance between the tip and surface decreases, the tip first experiences attractive, long-range van der Waals forces and then strong, short-range forces due to the Pauli exclusion principle as it comes in "contact" with the surface.

that applies a voltage to the piezoelectric scanner which subsequently adjusts the height of the tip/sample. Therefore, a topographic image is obtained by recording the applied voltage (in the *z* direction), not by measuring the cantilever deflection as in constant height mode.

The image is generated by plotting, at each point of the scanned area, the vertical piezo movement needed to keep the cantilever normal deflection constant. In contact mode, the variation of this deflection is mainly due to changes in surface topography (care has to be taken when measuring heterogeneous sample with areas of different elastic constant), and therefore a topographic image of the sample surface is generated.

The information collected during a scan of the surface is quantitative in three dimensions, two specifying the lateral position and the third specifying the height at that position. When presented as a topographic image, the elevation of each point in the picture is encoded according to a grey scale or a false colour scale. The general agreement is that higher (lower) features appear brighter (darker) in the top view image. Profiles or cross-sections through the surface can be plotted and quantitative horizontal and vertical distances measured.

To highlight topographic features such as steps or grain boundaries, error or derivative images are commonly presented. These images are generated by plotting the difference between the measured cantilever deflection and the setpoint value, at each point of the image.

Since the tip is within a few angstroms of the sample surface, it is acting in the repulsive force regime, as shown in **Fig. 32**, primarily under strong, short-range forces due to the Pauli exclusion principle. As mentioned, the interaction potential between the tip and surface can be modeled by the Lennard-Jones potential,

$$V_I(r) = 4V_0\left[\left(\frac{\sigma}{r}\right)^{12} - \left(\frac{\sigma}{r}\right)^{6}\right]\cdot = \frac{B}{r^{12}} - \frac{A}{r^{6}} \qquad (22)$$

with $A = 4V_0\sigma^6$ and $A = 4V_0\sigma^{12}$, which describes the interaction between two atoms. The atom separation is denoted by r and σ is a parameter that can be determined experimentally [53]. The interaction force between the tip and surface is given by $F_I(r) = -\left(\frac{\partial V}{\partial r}\right)$.

In addition to the tip-sample interaction force, there are two other forces between the probe and surface in c-AFM: forces exerted by the tip and capillary forces. The force exerted on the surface by the tip is like the force of a compressed spring, thus, it can be found using Hooke's Law,

$$F = -kd \qquad (23)$$

where k is the force (spring) constant of the cantilever and d is the amount of tip deflection. The spring constant of the cantilever should be as low as possible so that its deflection is maximized and small forces can be detected. There is a thin layer of liquid (usually composed of water) present on surfaces in an ambient environment, sometimes referred to as a "double layer", that gives rise to a capillary force [54, 55]. The capillary force, which is a strong, attractive force that tends to hold the tip in contact, is dependent on the distance of the tip from the surface.

Due to the strong repulsive forces present in contact mode, there is a possibility for larger force gradients and greater cantilever deflection than in other imaging modes. This results in images with higher resolution. The disadvantage of contact mode is that the tip and sample are in contact, thus both the tip and sample are at a higher risk of being easily damaged. Because the tip is essentially being dragged across the surface, it is vulnerable to lateral (shear) forces. If the tip is in contact with a very hard surface, it can become dull quickly which leads to poor image quality and the need to change tips frequently. If the sample is soft, the tip can scratch the surface, as well as pick up contaminants that will create artifacts in the image data. On the other hand, in the case of insulating materials there is the danger of electrostatically charging the surface from which unwanted coulomb forces arise, that again, negatively influence the measuring process and falsify topographic data.

5.1.5.2. Non-contact mode.

In non-contact mode AFM (NC-AFM), as the name suggests, the probe is not in contact with the sample. Instead, the probe is vibrated at a frequency between 100 and 500 kHz above the surface of the sample at a distance of tens to hundreds of Å [56]. Then, it detects changes in the resonant frequency or vibration amplitude as the tip comes near the sample surface. At this distance, the tip is acting in the attractive force regime under force gradients from long-range van der Waals (VDW) and electrostatic forces between the tip and sample (see Fig. 32). In order to keep the frequency of vibration constant, the tip-sample separation is maintained by means of a feedback loop as the oscillating cantilever is rastered across the surface; hence, a voltage is applied to the piezoelectric scanner in response to changes in the cantilever vibration and the

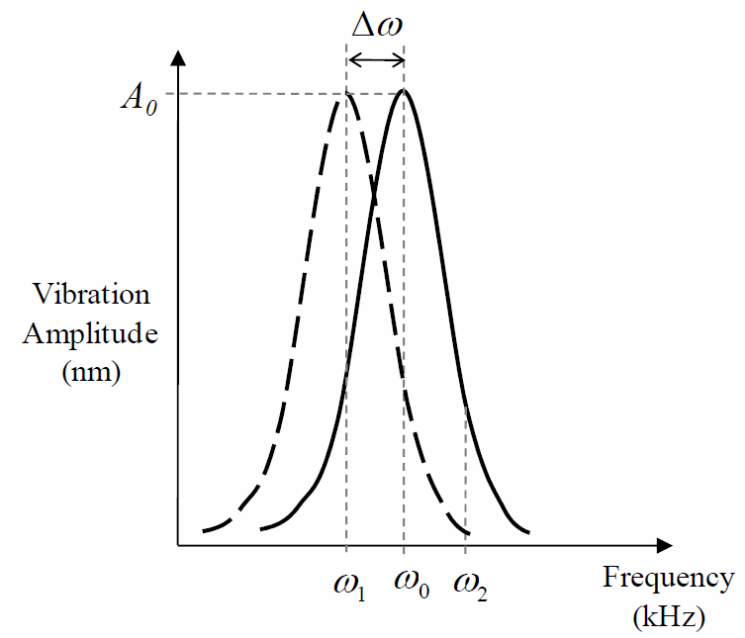

Fig. 33. Example of an amplitude versus frequency curve for an oscillating force sensor (cantilever). The resonant frequency, ω_0, of the cantilever is located at the peak of the curve where the amplitude is a maximum. In NC-AFM, the cantilever is oscillated at frequency ω_2; whereas in TM-AFM, the cantilever is oscillated at frequency ω_1.

tip/sample height is adjusted accordingly. In this manner, a topographic image is generated from the feedback data of the scanner.

Although the Lennard-Jones potential only applies to the interaction between two atoms, a macroscopic form of the potential can be approximated by integrating the interaction across microscopic bodies. In the case of NC-AFM, a sphere is chosen to represent the tip and a plane to represent the sample surface.

Therefore, taking into account the attractive and repulsive components we obtain the *total interaction potential*, $V_I(z)$. From it, the *interaction force* can be found by taking the derivative of with respect to z, $F_I(z)$, and taking the derivative again yields the *force gradient*, $F_I'(z)$.

The presence of a *force gradient* causes the effective force constant of the cantilever to change as follows,

$$k_{eff} = k - F_I' \quad (24)$$

Here, k is the force constant of the cantilever in the absence of an interaction force. If the force constant changes, then the resonant frequency of the cantilever must also change as displayed in **Fig. 33**. From Hooke's law for simple harmonic motion, the resonant frequency, ω_0, is known to be

$$\omega_0 = \left(\frac{k}{m}\right)^{1/2} \quad (25)$$

where m is the effective mass of the cantilever and tip. Thus, when the tip is subject to a force gradient $F_I'(z)$, the resonant frequency becomes

$$\omega_1 = \omega_0\left(1 - \frac{F_I'}{k}\right)^{1/2} \quad (26)$$

For large values of z where the effect of the sample on the tip is negligible, the vibration amplitude of the tip, A, as a function of the frequency is a Lorentzian of the following form:

$$A = \frac{A_0(\omega_0/\omega)}{\sqrt{1 + Q^2(\omega/\omega_0 - \omega_0/\omega)^2}} \quad (27)$$

where A_0 is the amplitude at resonance and Q is the quality factor (Q >> 1) [57]. **Fig. 33**, an example of an A vs ω curve, shows that there is a large peak in the vibration amplitude at the resonant frequency. As can be seen from **Eq. 24**, an attractive force ($F_I'(z) > 0$) will cause a decrease in the spring constant which, in turn, causes a decrease in the resonant frequency. Thus, changes in the resonant frequency of the cantilever can be used as a measure of changes in the force gradient, which reflect changes in the tip-to sample spacing, or sample topography. In order to maximize the cantilever deflection and detect small force gradients, the vibration frequency of the cantilever should be chosen at the steepest part (greatest slope) of the A vs ω curve. By this way, as mentioned, in NC-AFM mode, the system monitors the resonant frequency or vibrational amplitude of the cantilever and keeps it constant with the aid of a feedback system that moves the scanner up and down. By keeping the resonant frequency or amplitude constant, the system also keeps the average tip-to-sample distance constant. As with contact AFM (in constant-force mode), the motion of the scanner is used to generate the data set.

In NC-AFM, the vibration of the cantilever is driven at a frequency just to the right of the resonant peak maximum (at the off-resonant frequency ω_2 in **Fig. 33**) by a piezoelectric actuator, called a "dithering piezo." All dynamic modes need a further piezoelectric crystal, the dither piezo, to excite cantilever and tip to oscillations with the excitation frequency (ω_e). The cantilever is oscillated slightly below its resonance frequency (ω_0), which has the advantage of being able to tell what direction changes have occurred. E.g. if the resonance frequency is shifted the amplitude will change. On top of the resonance curve, where the amplitude has its maximum, it would always be reduced. A stiff cantilever (a cantilever with a high force

constant) is usually chosen to reduce the tendency of the cantilever to be pulled down to the surface. Since the spring constant is high, the amplitude of the oscillation is typically small (on the order of tens to hundreds of Å) so as to keep the motion of the tip in the attractive force regime [37].

The dynamic mode is much more sensitive to structural changes and has some more advantages, but also a few drawbacks compared to c-AFM. The tip for instance does not easily engage or break, nor picks up dust particles and drags them around. Hence, the surface will not be modified, nor additionally, electrostatically charged, which is important since we try to measure insulating materials, where local charges only very slowly disappear.

NC-AFM is a very favourable technique for imaging "soft" samples that can be easily damaged, such as biological materials or molecules that are poorly adhered, because the tip does not come in contact with the surface. Unfortunately, attractive VDW forces are significantly weaker than contact mode forces and there is only a small range above the surface where they exist. Under ambient conditions, all or a portion of their range may be occupied by the thin layer of adsorbates (mostly water) that is present, which is not seen in contact mode, where the tip would easily pass through conserving the intrinsic sample topography. Consequently, it is difficult to maintain the tip-sample separation necessary for NC-AFM since the cantilever can easily slip into contact with the surface due to stronger repulsive forces and capillary forces.

In general, the resolution in dynamic mode is higher than in c-AFM and via changes in amplitude and phase (frequency modulation mode, FM-AFM) one can obtain atomic resolution [58].

5.1.5.3. Tapping mode.

In intermittent contact AFM, or tapping mode (TM-AFM) as it is commonly called, the tip is oscillated in and out of contact with the surface of the sample. Hence, it is acting through both the attractive and repulsive force regimes. Similar to NC-AFM, the amplitude of the operating frequency of vibration, the "set point" amplitude, is held constant and the scanner adjusts the tip/sample separation via a feedback loop to maintain the frequency, which is typically between 100 and 500 kHz. As with c-AFM and NC-AFM, a topographic image is generated from the feedback data of the scanner.

To account for damping that occurs as the tip approaches the surface, the vibration of the cantilever is driven at a frequency just to the left of the resonant peak maximum (at the off-resonant frequency ω_1 in **Fig. 33**) by a dithering piezo. In general, a stiff cantilever with a high Q factor (~ 100 to 1000) is used for TM-AFM and it is oscillated with a large amplitude (on the order of tens to hundreds of nanometers) [59]. This guarantees the tip has enough energy to overcome attractive forces, such as capillary forces, and is able to tap in and out of the contaminant layer on the sample surface. Vibrating a stiff, high Q factor cantilever with a large amplitude also ensures that the energy of the probe oscillation is much higher than the energy that is lost when the tip strikes the surface.

As stated earlier, the force exerted by the tip on the sample when it strikes the surface is given by Hooke's law,

$$F = k\Delta A \qquad (\mathbf{28})$$

where k is the force constant of the cantilever and ΔA is the amplitude change in one cycle of oscillation. The change in amplitude during one cycle of oscillation can be approximated with the formula

$$\Delta A = \frac{(A_0 - A_S)}{Q} \quad (29)$$

where A_0 and A_S are the free amplitude and the set point amplitude, respectively.

Tapping mode has many advantages over contact and non-contact mode AFM. Frictional shear forces are avoided and the force exerted by the tip on the sample can be up to three orders of magnitude lower than in contact mode; thus, the risk of damage to the tip and sample surface that is prevalent in c-AFM is greatly reduced in TM-AFM. This makes tapping mode ideal for imaging soft samples. The cantilever in tapping mode operates in a larger range (with a larger amplitude of oscillation) above the sample surface and with greater energy than in NC-AFM. High resolution images can be obtained since the cantilever is able to tap in and out of the water layer on the surface.

5.1.5.4. Phase-Locked Loop (PLL).

With excitation frequency (ω_e, EF), amplitude, and thus phase, more parameters come into play that need to be adjusted, and can be used in a second *feedback loop*. The main feedback loop is on the amplitude. But in the presence of strong interactions (attractive or repulsive) the resonance frequency (ω_0) changes significantly. This leads to a stronger beating with the excitation frequency, thus a phase detuning, and finally, to a critical loss of amplitude signal. Thanks to these effects, the PLL feedback makes our method very sensitive to the smallest superficial changes and thus to the most suitable to detect nanometric holes on a sample´s surface.

The phase-locked loop (PLL) is basically a closed loop frequency control system, whose functioning is based on the detection of phase difference between the input and output signals of the voltage controlled oscillator (VCO). The cantilever oscillates with the frequency ω and is continuously compared to the excitation frequency ω_e. If the phase shifts this is adjusted by a shift in excitation frequency.

5.1.6. Tip simulation and correction of the pores depth for short etching times.

In the beginning of our measurements, we were not sure if we could just not reveal pores for short etching times because they were simply too small for the AFM, or rather the tips used for scanning were too big, or even, the pores were simply nonexistent. Thus, to estimate an approximate penetration depth for suspected nanopores the tip was modeled by a simple mathematical function combining the typical tip features guaranteed by the providers. Basically it considers the tip cone angle and curvature radius to calculate a quick look-up-profile.

In this Section we briefly describe the equations that characterize the structures created by etching. As we mentioned in **Section 4.4.** *Controlled etching of single ion tracks.*

Fabrication of track-etched nanopores and geometry of the tracks. The geometry of a track, subject to chemical attack, in the simplest case is dictated by the simultaneous action of two processes: chemical dissolution along the track with a rate (v_t), and general chemical attack on the non-damaged surfaces and the inner surface of the track, characterized by a rate, v_b. **Figure 16** showed this process, which creates a cone which one axis is oriented along the direction of irradiation (track direction). It is assumed that: (1) v_t is constant throughout the track, and (2) v_b is constant and isotropic. As etching rate is higher in the irradiated than in the virgin area, the corresponding track area will be preferentially attacked. This means we can assume that etching starts on a region with a diameter (D_0) equal to that track core. We define with n_i the different levels of the surface for each etching time t_i (see **Figure 34**).

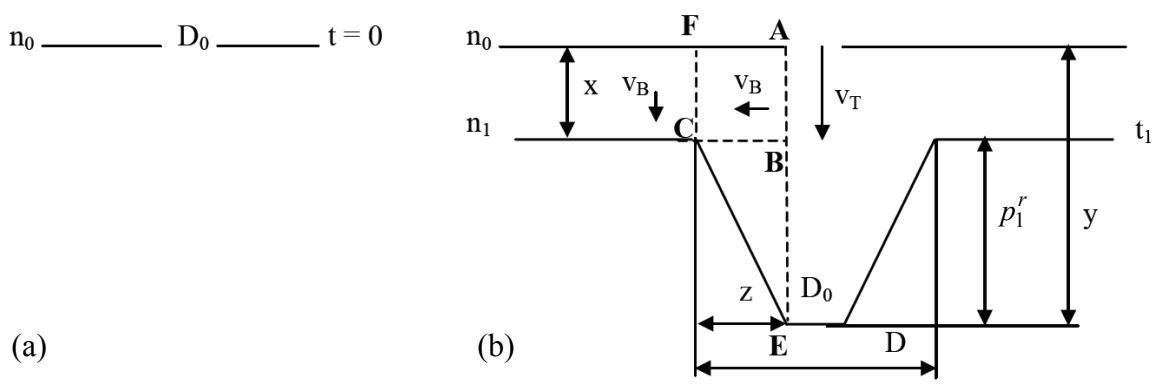

Fig. 34. Evolution of the surface and the shape of the hole with etching time. **(a)** shows the beginning of etching process (D_0 is the diameter of the track on which the etching starts, $t = 0$), **(b)** shows a frame of the track shape for the time $t_1 > 0$.

In light of the fact that the etching rate is higher in the track than in the non-irradiated material the acid follows as far as possible in the irradiated area. For when the acid solution reaches the point ***C*** (end of hole after etching) the process is as follows: the track is attacked on the vertical direction x in time t_a (distance $AB = x$), then, the virgin material is attacked on the horizontal direction (distance $BC = z$) in a time t_b. On the vertical direction the attack is performed in the time $t = t_a + t_b$: in the track (distance $AE = y$) and in the non-irradiated area (distance $FC = x$).

The *diameter at the surface* (for all the etching process) evolves according to **Eq. (30)** (see **Fig. 34**).

$$\left.\begin{array}{l} t = t_a + t_b \\ x = v_b \,.\, t \\ x = v_t \,.\, t_a \\ z = v_b \,.\, t_b \\ D = D_0 + 2 \,.\, z \end{array}\right\} \quad \Rightarrow \quad D = D_0 + 2 \cdot v_b \cdot t\left(1 - \frac{v_b}{v_t}\right) \tag{30}$$

The *depth of the holes* evolves from the relationship **Eq. 31** according to **Fig. 34**.

$$\left.\begin{array}{l} y = v_t \,.\, t \\ x = v_b \,.\, t \end{array}\right\} \quad \Rightarrow \quad p_1^r = y - x = \left(v_t - v_b\right) \cdot t \tag{31}$$

The hole depth was estimated from cross-sectional profiles measured by AFM as the difference between the lowest level (bottom of hole) and the highest one (p_1^r), which corresponds to the virgin area.

However, as mentioned in the beginning, it is worthy to notice that, the depth of the holes is affected by the size of the measuring tip in the case of short etching times, while for the long etching times determining the depth does not depend on the size of the tip AFM. By this way, we present a method for determining the depth of the holes in the case of short etching times. For this we have eliminated the effect of the tip by a geometric correction, which does not take into account the interaction forces between the tip and the sample surface.

Assuming the hypothesis that the etching process takes place homogeneously, thus, theoretically, the created holes have the form shown in **Figure 35**. The lowest part of the holes is represented by the track diameter, D_0. The tip is described by its curvature radius, R. As the size of the hole is comparable to the tip size, the latter can not describe the shape of the hole.

We take a coordinate system (x, y) whose origin is the intersection of the walls of the hole (O). The lowest point that the AFM tip can describe is the point B (which represents the extreme edge of the assumed parabolic shape tip[9]). This means that the deep holes will be underestimated by a value between point B and the lowest part of the hole (A). We will note that distance with BA, where A indicates the middle of the diameter at the bottom. The tangent (intersection) point between the parabola and the wall is noted $T\ (x_T,\ y_T)$. We will write equations of the parabola, which represents the AFM tip, and the straight line equation which describes the hole wall.

$$y_p = a \cdot x^2 + c = \frac{1}{2R} x^2 + c \qquad \text{(tip)} \qquad \textbf{(32)}$$

$$y_t = b \cdot x = \frac{v_t}{v_b} x \qquad \text{(hole wall)} \qquad \textbf{(33)}$$

Correction stages.

1. Condition of equality of the coordinates of point $T\ (x_T,\ y_T)$ for both curves, i.e.,: both functions pass through that point:

$$\left.\begin{aligned} y_T = y_p^T = y_p(x_T) &= \frac{(x_T)^2}{2R} + c \\ y_T = y_t^T = b \cdot x_T &= \frac{v_t}{v_b} \cdot x_T \end{aligned}\right\} \Rightarrow \quad \frac{(x_T)^2}{2R} + c = \frac{v_t}{v_b} x_T \qquad \textbf{(34)}$$

[9] A parabolic tip can be characterized by its radius of curvature, R. This tip shape is often used to approximate a real tip, because generally smooth surfaces can be approximated, for mathematical reasons with parabolic surfaces [60]. Note that what we fit by a parabola is the apex of the tip. The parameter "a", characteristic of a parabolic function, is related to the radius of curvature (R) of the parabola by the relationship: $a = 1/(2R)$.

2. Condition of equality of the derivative in the point $T\ (x_T,\ y_T)$ for both curves, i.e.,: both functions have the same slope at that point:

$$\frac{x_T}{R} = \frac{v_t}{v_b} \quad \Rightarrow \quad x_T = R \cdot \frac{v_t}{v_b} \tag{35}$$

3. Calculation y_T:

$$y_T = R \cdot \left(\frac{v_t}{v_b}\right)^2 \tag{36}$$

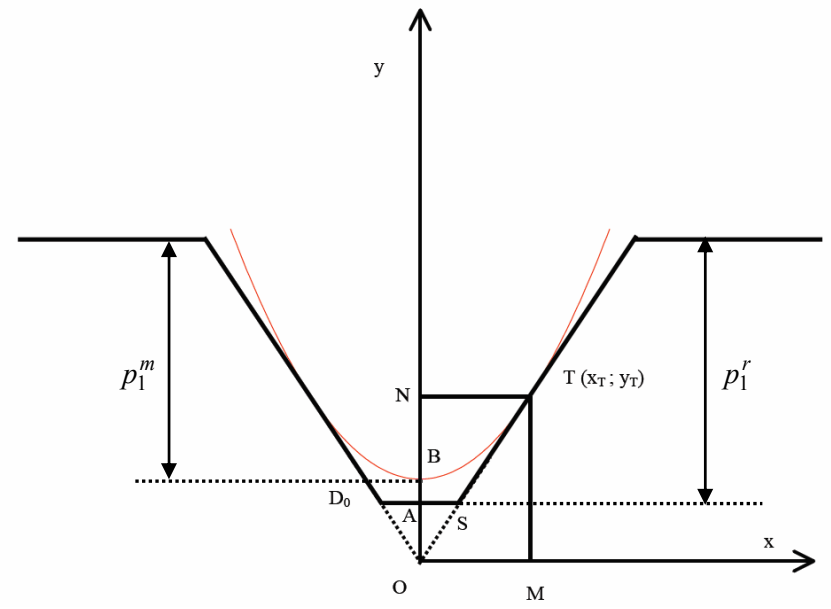

Fig. 35. Correction of the pore depth by geometrical considerations.

4. Calculation c:

$$c = R \cdot \left(\frac{v_t}{v_b}\right)^2 - \frac{R}{2}\left(\frac{v_t}{v_b}\right)^2 = \frac{R}{2}\left(\frac{v_t}{v_b}\right)^2 \tag{37}$$

5. Calculation of coordinates of point $S\ (x_S,\ y_S)$ - the intersection of the wall with the diameter at the bottom.

$$\left.\begin{aligned} x_S &= \frac{D_0}{2} \\ y_S &= \frac{D_0}{2} \cdot \frac{v_t}{v_b} \end{aligned}\right\} \tag{38}$$

6. Calculation of AB (correcting value):

$$AB = OB - OA = c - y_S = \frac{R}{2}\left(\frac{v_t}{v_b}\right)^2 - \frac{D_0}{2} \cdot \frac{v_t}{v_b} \tag{39}$$

This means that the depths of the holes corresponding to short etching times are underestimated. Thus, the *measured values* for the depths and the *true values* are linked by the relationship:

$$p_1^r = p_1^m + AB = p_1^m + \frac{R}{2}\left(\frac{v_t}{v_b}\right)^2 - \frac{D_0}{2}\cdot\frac{v_t}{v_b}, \text{ and} \qquad \textbf{(40.a)}$$

$$p_1^m = p_1^r - \frac{R}{2}\left(\frac{v_t}{v_b}\right)^2 + \frac{D_0}{2}\cdot\frac{v_t}{v_b}, \qquad \textbf{(40.b)}$$

And finally, the depths measured by AFM can be calculated, using **Eq. (31),** with the expression:

$$p_1^m = \left(v_t - v_b\right)\cdot t - \frac{R}{2}\left(\frac{v_t}{v_b}\right)^2 + \frac{D_0}{2}\cdot\frac{v_t}{v_b}, \qquad \textbf{(41)}$$

where p_1^m is the *value measured* by AFM and p_1^r is the *real value* of the depth.

5.1.7. Sources of error.

As with all experimental measurements, there are several sources of possible error in scanning probe microscopy. The most common errors, or image artifacts, are due problems with the tip. Images measured with a SPM are the result of the interaction between tip geometry (radius of curvature and sidewall angles) and surface topography. This implies the shape of a tip directly influences what a topographic image will look like; hence, it is important to choose an appropriate tip for the application. If the radius of curvature of the tip is much larger than the features on the surface being measured, the lateral resolution is reduced. A protrusion on the surface, such as a nanoparticle, will appear larger and a depression will appear smaller than its true size. Likewise, if a feature has a steeper slope than the sidewall angle of the tip, the image will reflect the sidewall angle of the tip rather than the actual profile of the feature.

As a tip scans across a surface, there is a possibility for loose debris to accumulate on the tip or for the tip to become worn or even chip, especially in contact mode. Any modification of the tip can result in image distortion. One example of such distortion is tip imaging, wherein it is actually the shape of the tip that is being imaged. The most obvious sign of tip imaging is if many of the features in an image appear exhibit structures that resemble each other. Another example is double or multiple tip imaging in which the tip has more than one point in contact with the surface. If tip imaging occurs, the tip should be replaced. Loose debris on the surface can also produce skips and streaking in images; although, there is a chance the debris can be swept out of the scan area after a few scans and the tip does not have to be replaced.

In addition to the tip, the scanner is also a source of error. Scanner artifacts, which include bow, drift and edge overshoot, are due to piezoelectric properties of the scanner material (PZT). The end of the scanner that contains the tip or sample is free to move while the other end is attached. As a result, the motion of the scanner is nonlinear (in the *z*-direction) and the image appears bowed. Bow, which increases with scan size, can be removed from an image with image processing software. Large changes in *x* and *y* offsets and external temperature changes

cause creep in the piezoelectric scanner. Creep produces drift in images that causes features to appear curved or elongated. Hysteresis in the scanner (in the *z*-direction) can lead to edge overshoot. Edge overshoot is most often observed in line profiles at the leading and trailing edges of a feature such as a step. Creep and hysteresis can be sufficiently controlled with proper calibration of the scanner.

Forces between the tip and sample are another source of image artifacts, especially when imaging in non-contact mode. For example, if a sample possesses a large electric field, such as lithium niobate, it is possible for the electrostatic interaction between the tip and sample to dominate in a NC-AFM image (rather than attractive VDW forces). This is usually evidenced through the several scanning force microscopy (SPM)-based techniques - *piezoresponse force microscopy* (PFM) [61] by which the piezoelectric properties which provide information about domain structure can be measured; *electrostatic force microscopy* (EFM) [62] and *scanning Kelvin probe microscopy* (SKPM) [36], to generate an image with information about the ferroelectric domains - developed and employed for the characterization of ferroelectric domains, in which the domain measurement is independent of the surface topography. In this sense, sometimes the domain boundaries appear to be raised from the surface, where there is no difference in height between domains and domain boundaries when the same area is imaged in contact mode. On the other hand, NC-AFM images may also reflect the surface of the adsorbate layer instead of the actual surface of the material.

5.1.8. Sample analysis by our experimental setup.

The most of experiments has been performed using a Nanotec^{TM} Cervantes AFM System [63] installed at the CMAM. All corresponding components are provided by Nanotec Electronica S.L., including the Dulcinea Electronics control system [64]. The dynamic force board for NC-Mode (dynamic mode) was also upgraded, allowing measurements with an additional phase-locked loop feedback (PLL-NC). The images were recorded and analyzed with the WSxM software [50], which is distributed freely by Nanotec.

As mentioned in **Section 4.7.2.4.3.** *The Scanning System*, the voltage applied to the piezos has to be transformed into the corresponding distance/height. A fixed parameter set is the basis for this Conversion. The actual piezo scanner expansion is measured to be 49 nm/V in *x*- and *y*-directions, and -17 nm/V in *z*-direction, being calibrated by the company. Thus, the total maximal lateral image size is limited to 10 μm and the feasible vertical extension of the piezo tube is ± 2.5 μm. In the image representation, in general, lighter colours always correspond to higher values.

5.1.8.1. Feedback parameters and operational mode.

All AFM measurements were performed applying two independent feedback loops simultaneously. The main feedback channel is the amplitude of the cantilever oscillation. The system keeps the amplitude constant by adjusting the tip sample distance. Hence, the set point value defines this distance, and accordingly the interaction strength between the tip and the sample. The piezo tube, and thus the height, is steered such that the amplitude matches the set point voltage at all times, and thus the topography image really is a surface of constant

amplitude. The distance regulation is accomplished via the parameters *P* and *I* (proportional and integral gains).

The second feedback circuit adjusts the excitation frequency (ω_e, *EF*) in such a way, the phase between ω_e and the resonance frequency, ω_r, of the cantilever (incoming signal) is matched to zero. This is also done by means of a set of gain values (P_{PLL}, I_{PLL}). The variation of the resonance frequency of the cantilever oscillating in the force potential of the sample, and hence the phase shift, is even a lot more sensitive to changes of the interaction strength than the amplitude; e.g. one can see a clear difference if the material changes, but the topography remains the same.

It is worthy to mention that, usually the interactions between the tip and the surface for LN samples were so strong that convenient set point parameters exceeded the adjustment range of the system. Thus, the almost entire characterization experiments were carried out on *x*-cut LN samples where the strength of the interaction was less intense.

5.1.8.2. The tips.

Four different types of tips have been used throughout this work. This is important for a verification of the data. It was outlined that a convolution could falsify the measured image. Thus, we used tips of different materials, sizes and properties, as listed in **Table IV** to try to eliminate this doubt. SEM images of the tip shapes as given by the providers are shown in **Fig. 36**. The data images obtained by different tips are compared in a following Section.

Our measurements have basically all been done with tips of the NSC18 type. If a presented image was captured with a different tip type this will be explicitly mentioned.

5.1.8.3. Scanning resolution.

The scanning resolution depends on many parameters. Besides the actual tip size, which is the governing parameter, the tip-sample distance and the vertical resolution influence the lateral one [65]. Larger tips tend to have a flattening effect on the topographic image due to poorer access to lower spots on the surface.

On the other hand, the digital image resolution is determined by the scanning parameters such as image size, scanning speed, the *x*-, *y*-, and *z*-gain, which delimit the sampling resolution, and the smallest possible stepping distance of the piezo drive. Our typical image sizes range from 500 x 500 nm^2 to 10 x 10 μm^2. The fast axis scan speed (image *x*-axis) was usually $\nu \approx 1$ Hz, collecting 512 points/line. Hence, the digital resolution scales with the image size from around 1 - 20 nm/pixel, respectively. When using faster scan frequencies the feedback is not capable anymore to render the surface topography and the tip shows significantly higher wear out. Lower frequencies neither improve the resolution because of *drift effects* become more important for longer acquisition times. If the tip size is well larger than the digital resolution the overall lateral resolution is a bit worse.

The *P* and *I gains* of both feedback loops also clearly influence the image quality. For tips with high quality factors (*Q*), the parameters may take higher values without provoking an overreaction of the feedback loop. The *z*-gain restricts the total vertical range and sets the

vertical sampling distance, thus affecting the resolution. Again, nonlinearities play a role as well. At last, the theoretical lateral resolution in dynamic mode lies below the tip diameter, scaling roughly with its square root:

$$\Delta x = \sqrt{2 \cdot R \cdot \Delta x}\ , \qquad \textbf{(42)}$$

where R is the radius of curvature and Δz the vertical resolution. The latter is supposed to be in the sub-nanometer range (≈ 0.4 nm). Consequently, a tip with R = 10 nm could theoretically resolve structures of ≈ 3 nm. In PLL mode, the EF image usually possesses an even higher lateral resolution than the topography. In conclusion, the lateral resolution normally matches the

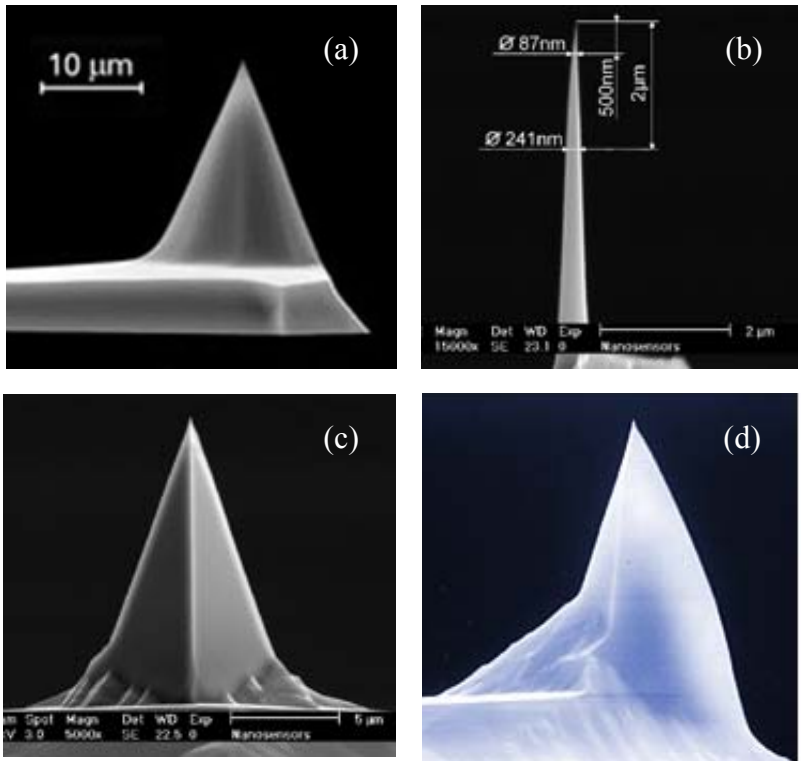

Fig. 36. SEM images showing the geometries of the AFM tips used in this research work, as given by themanufacturers. (a) NSC18, (b) AR5-NCHR, (c) PPP-NCHR, (d) TESP.

Tip Type	Shape	Material	Tip Radius Curvature (nm)	Half Tip Cone Angle (º)	Manufacturer
NSC18	Tetrahedral	n-type Si (P doped)	< 10	< 20	MikroMasch
AR5-NCHR	A.R. > 5:1	highly doped Si	< 15	< 5	NanoSensors
PPP-NCHR	Tetrahedral	highly doped Si	< 7	< 25	NanoSensors
TESP	Anisotropic	n-type Si (Sb doped)	< 10	< 25	Veeco

Cantilever	Length (µm)	Width (µm)	Thickness (µm)	Resonant Frequency (kHz)	Force Constant (N/m)
NSC18	230 ± 5	40 ± 3	3 ± 0.5	75 ± 15	3.5 ± 1.5
AR5-NCHR	125 ± 10	30 - 45	4 ± 1	330 ± 67	42 (10 - 130)
PPP-NCHR	125 ± 10	30 ± 7.5	4 ± 1	330 ± 67	42 (10 - 130)
TESP	125 ± 15	40 ± 10	4 ± 0.75	320 ± 90	42 (20 - 80)

Table IV. Specifications of the used AFM tips and cantilevers. The parameters are taken from the corresponding datasheets. (MikroMasch [66], NanoSensors [67, 68] and Veeco [69]).

digital resolution in large images; for smaller scan sizes it is limited by the tip dimensions if the nonlinearities are not more intense.

5.1.9. Additional remarks and concerns on the AFM measurements.

In a following Chapter (**Chapter 6**), the results of all experiments as described in previous sections will be presented, analyzed, and discussed. During the first part the successful achievement of the desired nanometric structures, as well as the feasibility of morphological variation under the different conditions will be described, and problems of the methods and systematical errors will be addressed.

As has been mentioned, the AFM technique has been introduced as one of the main characterization tools. It has also been stated that, when the sizes of both nanopores and tips are of the same order of magnitude, the possibilities of the AFM method are limited. This, in combination with the fact that the nanostructures lies inside a piezoelectric substrate, $LiNbO_3$, really makes the analysis by AFM some kind of a *state of the art* measurement. Anyhow, a very great expertise it is necessary to acquire realistic AFM images, avoiding typical aberrations due to the tip-surface interactions.

At this moment, it is necessary to state that, the measurements carried out when the subject to be measured and quantified its features, are pores with nanometric sizes, that means, structures limited on all bidimesional sides and with defined nanometric depth, the topic to face out is one of the most difficult ones. Moreover, due to the very strong interactions with *z*-cut samples and resulting difficulties, it was only possible to measure very few of the fabricated samples. Either the tip was forcibly repelled making it impossible to reach an adequate position, or it crashed directly during the approach procedure. The excitation frequency (EF), added in the Tapping + Phase Locked Loop (PLL + Tapping) acquisition mode, changed rapidly in this case, jumping out of range, and thus could not be regulated by the PLL mechanism. Subsequently the amplitude and the tip-sample distance went straight to zero, while the piezo completely contracted. This definitely indicates a crash of the tip on the surface. It is remarkable that, in some cases it was even challenging to attain approaches on *x*-cut surfaces.

The results that will be presented in this Thesis work were investigated on *x*-cut samples if not indicated otherwise. Besides LN and SiO_2 was also used as a substrate material in order to compare the revealed nanostructures.

5.1.9.1. Excitation Frequency Criterion.

It is worthy, before to introduce the features of the different nanostructures revealed after several etching process under studied, to pay attention on the important criterion used to define the limits of the pores sizes. Really, the first difficulty which we have to face off is related to know exactly where to begin or end the measurement of the diameter of a nanopore, if the corresponding profile is smoothed due to a worn out tip or a similar reason. Sometimes it is not even evident if a little swale or a bigger crack-like well has been formed due to an etched ion track, or it has been originated from defects of another kind. In these cases, but also in general, a clear definition is necessary to decide precisely if a nanostructure qualities as a nanopore or not.

If the topographical data does not provide the necessary information, the excitation frequency (EF) image can be consulted. Concerning to the EF data a lot of complicated physics is involved and to get a clean interpretation is once more very difficult, but it was noticed that a certain EF pattern is underlying every pore structure. When entering or exiting a nanopore, the interactions between tip and sample surface change strongly and the corresponding change in excitation frequency (EFc) is quite abrupt. The EFc can amount more than 2 kHz in some cases, which is extremely high. The reaction is more extensive than elsewhere and not known from any other kind of sample, as was confirmed by Nanotec Ltd.. The EF reaches a local extreme at the point, where the tip slightly loses its "contact" - i.e. momentarily, the working distance between tip and surface increases and thus, the discrepancy of amplitude and the set point value grows. These points, in correlation with the corresponding height information facilitate the compliance of pore identification. By this way, the reproducibility of the pore diameter in the direction of the profile is enhanced, and thus differently etched pores can be compared more easily. An example of the excitation frequency criterion (EFC) is given in **Fig. 37**. It shows a well faceted nanopore from a Br 46 MeV irradiated *x*-cut LN sample after etching process carried out with aqueous HF 40% acid at 55 Cº during 30 min. The pore shapes in terms of the EF always look like this or similar. A high increase denotes the beginning of the pore. The stronger interaction keeps hold on the tip which lets the cantilever appear harder (resonance frequency of the cantilever, ω_r, is shifted to higher frequencies). Then, the EF sways more or less forcibly around a broad peak function having a minimum at the core site and again decays to the surface-level EF value. The minimum, which usually lies below the surface EF level, indicates a "disengaged" tip that can oscillate freely. Another benefit of using the EF image is that the location of the inner pore can be clearly estimated. The small step up from the bottom of the inner pore (at x ≈ 240 nm) the EF value jumps more than 0.5 kHz. The strongest EFc indicates this edge.

On the other hand, in principle, the number of pores has to coincide "statistically" with the fluence (at/cm^2), i.e. the number of tracks per unit area. A higher number of impacts makes an identification easier, but then the superficial stress, perpendicular to the tracks, could influence into the pore creation, due to the damaged-stressed crystal shows less resistance to be etched. Additionally, the pores would overlap earlier than in case of lower fluences. Thus, 1 e8 at/cm^2 was our nominal fluence in most of cases. This implies that statistical significance is not given from all measurements. To receive an impression on the pore shapes and later on the etching behaviour, the corresponding pore quantities are considerably trustworthy.

The pore dimension values have been obtained by measuring various pores if available, in order to get enough statistics. Apparently, this was not possible where the structure only appears once as e.g. a pore in a TEM image. In such cases the same dimension was measured various times over the same structure to obtain an average value. However, in most of the cases in AFM images, the EFc is successful and the values can be reproduced.

Finally, if not announced otherwise, the indicated errors are the corresponding standard deviations; the errors of magnitudes that depend on different erroneous variables are ascertained by obeying the common rules of weighted averages and error propagation.

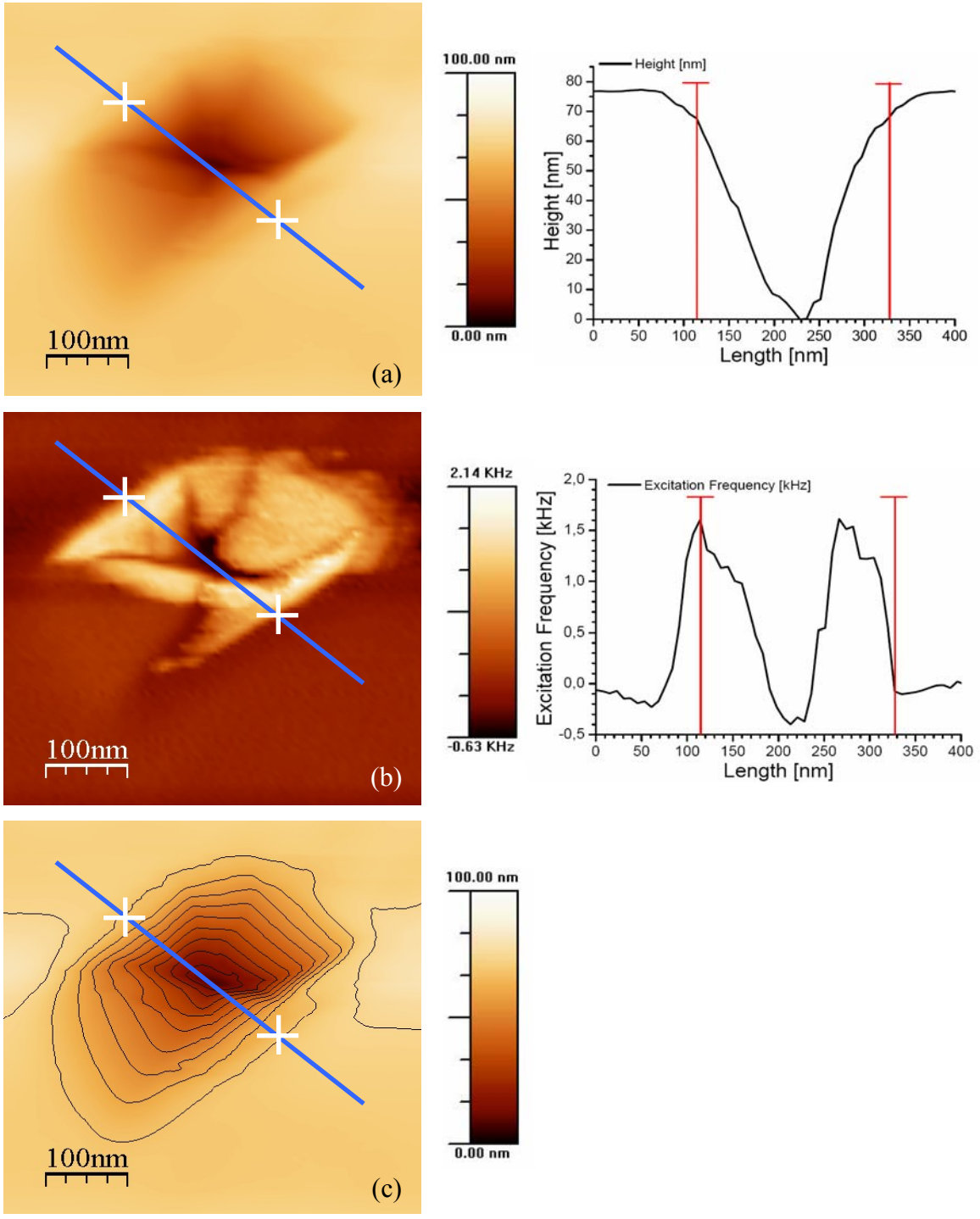

Fig. 37 (a, b, c). Application of the Excitation Frequency Criterion. **(a)** Topography Image and Profile, **(b)** EF Image and Profile and **(c)** Contour Topography plot. The markers indicate the diameter of the pore's short axis. Both intersect the topography profile plot at the same height. The shown profile is drawn as the short pore axis is usually measured. The long pore axis measured in a correspondingly orthogonal profile. Both profiles have to intersect at the lowest point inside the pore. z-scales and EF-scales appear as a bar scales next to the AFM images.

5.1.9.2. Comparison of measurements with different AFM tips.

The performance of our AFM system was tested using different tips. A few images that were captured with distinct tips and tip types will be shown here and in **Chapter 6**. Now, the question of a possible convolution of the tip and sample morphologies shall be addressed, and to what extent the data may be falsified. Since all the trapezoidal pore shapes look quite similar in the various measurements, one has to ask himself if really the physical pore was observed, or if the pyramidal form of the tip is repeatedly imaged by smaller, eventually even circular pores. In order to eliminate this doubt as far as possible, a specific experiment with SiO_2 samples with pore dimensions similar to the investigated lithium niobate pores was designed.

Silica samples were irradiated with Br 46 MeV ions under the exact same conditions like the LN samples. From the literature it is well known that such tracks are most effectively etched by exposing them to HF vapour [70-72]. Pores with high aspect ratios are obtained if the irradiated samples have a temperature of a few degrees centigrade higher than the acid solution. Most important to test the influence of tip convolution to the pore morphology was the well known superficial circular pore shape in SiO_2. We exposed the reference sample to 40% HF vapour for 1 min at RT, without controlling the temperature of the sample. In that case the nanopores are proposed to be conical. The pores were then measured with the three available tip types at the CMAM (NCS 18, PPP and - high aspect ratio: AR 5). The measurements taken with the dissimilar tips are shown in **Fig. 38**. The depth profiles shown on the right correspond each to the line drawn in the measurement image. The profile direction from left to right is carried out in the same direction on the AFM image. The insets are zooms into the EF images, which show the frequency changes over single pores, respectively. The measured fluences coincide perfectly with the nominal value of 1 e9 at/cm^2, which confirms that the ion energy was well above the suggested stopping power threshold of $S_e \approx 2$ keV/nm [73]. With the used stopping power for Br 46 MeV ions into SiO_2 ($S_e \approx 8.7$ keV/nm), it is certain that continuous tracks were formed.

A) The NSC18 probe.

Tips of the NSC18 series were used as a standard in all measurements. If not indicated otherwise, the presented images were acquired with tips of this kind. **Image 38 (a)** and the corresponding profile show the result gained with this kind of tip. Obviously the sample surface was contaminated by rests of paper tissue because the pores appear covered to different extents and the sample was cleaned by an acetone soaked paper tissue. The contamination in the measured area is so high that almost all the pores are covered. Thus, the profile is taken from the cleanest pore. Furthermore, only this pore profile has the particular shape of visible core and halo regions.

Musket et al. [71] propose that on the bottom of each cone there was an inner pore of ≈ 50 nm diameter. The samples in the publication were etched under very similar conditions. The core diameter from our measurement measures 45 nm, which is in excellent agreement, considering that our acid concentration was 40% vol., whereas Musket et al used 48 wt% HF vapour. Furthermore, they report a half cone angle of 40º. We see mean half cone angles of 64º ± 5º, which is probably due to the blocking contamination. Other reasons could be a worn tip

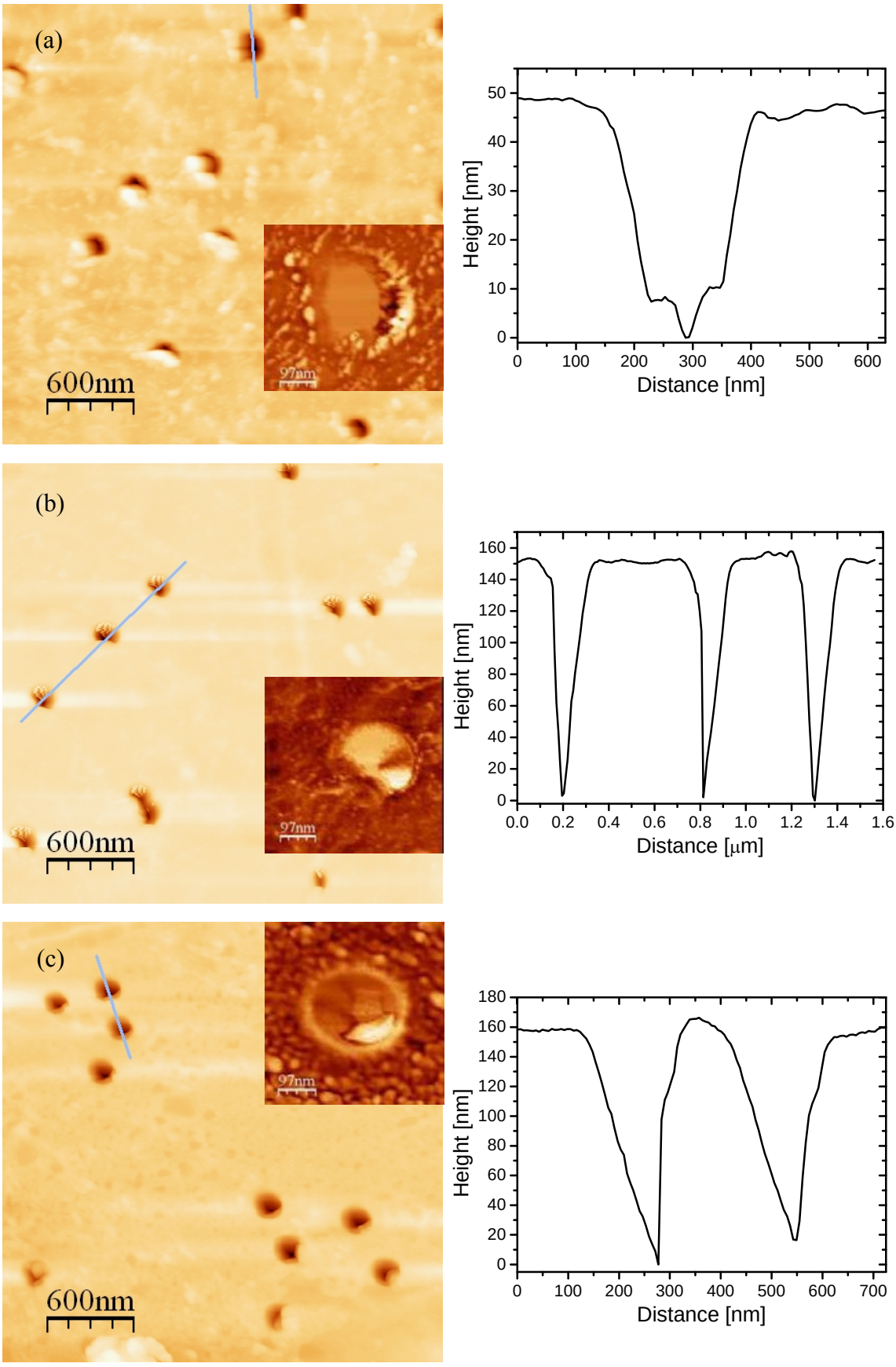
(a)
600nm
97nm
Height [nm]
Distance [nm]
(b)
600nm
97nm
Height [nm]
Distance [μm]
(c)
600nm
97nm
Height [nm]
Distance [nm]

Fig. 38 (a, b, c). 3 x 3 μm^2 AFM images of vapor etched tracks in SiO_2 exposed to 40% HF vapour for 1 min at RT measured with different probes in order to investigate the possible tip convolution in the revealed nanostructures. The corresponding depth profiles drawn on the AFM images appear on the right positions. A pore's zoom in the excitation frequency image (EF) recorded by PLL mode is shown as inset for each case. **(a)** Tip: NSC 18. AFM image z-scale: 70 nm, **(b)** Tip: AR 5. AFM image z-scale: 225 nm, **(c)** Tip: PPP. AFM image z-scale: 225 nm.

and the measuring parameters, which were presumably not forced to the possible limits. The mapped pores have mean depths of 43.5 ± 7 nm and are 216 ± 23 nm wide. These values are not very reliable, since the contamination did not permit to measure an entire circumference nor diameter and impeded the tip from entering the pore correctly. The EF image is also influenced significantly by the contamination, which resulted in a blocking of signal over a broad area in the pores. The EF is scaled to 530 Hz, total (dark to bright).

Finally, we have to say that measurements with much higher image quality were obtained with other tips of this series. It seems that this tip in particular was not fulfilling the requirements given by the provider anymore. On the other hand, of course that it is possible that the tip has been damaged during the approach or the mounting process.

B) The High Aspect Ratio probe - AR5.

The best mean pore depth was yielded by the AR 5 tip measurement, shown in **image 38 (b)**. Even though the pores are also partly covered in the examined area, the tip entered more than three times as deep as in the previous measurement where the NSC 18 probe was used. The total depth amounts to 152 ± 16 nm, meanwhile the diameter with 187 ± 13 nm is even smaller, resulting in a better aspect ratio. The tip is especially designed to obtain AR´s as good as 5 and higher, here, yielding an AR of ~ 0.8. This is the highest overall AR observed throughout our AFM measurements. The pore depth of Br 46 MeV irradiated LN samples though could not be improved by scanning with an AR5 probe, compared to one from the NSC 18 series. The profile is drawn such that the elevated regions affected by the flatten filter, i.e. bright stripes beside pores in scanning direction, are avoided. The result shows the accurately levelled surface including three uniform pore shapes. The half cone angle is 35º ± 2º, which is also higher than in the previous case. Certainly, the feedback values were immoderately high, causing the known image perturbations, mostly on the upper pore side. In the EF image again the modulations inside the pore well are homogeneous. This time, the cone shape can be distinguished even though there a certain contamination is present.

Altogether, the gained image quality is better for this tip type, even though the larger radius of curvature of the tip is a drawback compared to the other ones. Much smaller and more superficial pores should better be resolved with tips of the NSC 18 or PPP series.

C) The PPP probe.

It is worthy to state, that, the main objective of the investigation on nanopores in silica was to verify that the undoubtedly present tip convolution is not the cause for the pyramidal pore shape obtained in most of the cases of Br 46 MeV and Br 22 MeV irradiated LN samples

revealed under adequate etching conditions; thus, being real features of the nanostructures. Thus, to finally verify this presumption a LN sample was measured (see **Fig. 3 (d)**, *Chapter 6*). Directly, after this and under the exact same conditions with this very tip, the silica sample was examined, exhibiting the pores presented in **Fig. 38 (c)**. Finally, we measure again the LN sample physically rotated 90º on the plane, yielding nanopores with similar sizes and shapes.

When measuring the silica, luckily a very clean spot was found (or this tip was the only one that was not contaminated like both probes discussed above). Almost no pores were covered by tissue paper. The much higher Q-factor of the tip enables high sensitivity measurements. The depth profile shows the cross sections of two ordinary pores. Their mean dimensions lie between the previously determined ones. The diameter amounts to 207 ± 9 nm, and all pore depths average 147 ± 9 nm. The measured half cone angle is 44º ± 2º. In general, very good and high quality images were obtained with this tip. The sensitivity is excellent.

As a final consideration, there has been enough clear that, the measured dimensions can only be given as a worst case approximation, meaning hopefully that the nanopores in reality have higher aspect ratios than observed. It is evident, that the measured pore dimensions depend on the tip conditions and properties. The higher Q-factors of the AR 5 and PPP series strongly improve the image quality. The highest feedback values are possible in case of the PPP probe.

According to this knowledge, selecting NSC 18 type probes as the standard ones seems implausible, but the decision was taken without having the presented data at disposal from the beginning of the study; moreover, being the most reliable ones, taking into account the difficult scenario in which the AFM measurements were carried out due to the strong interactive behaviour revealed by the surface after the etching treatment. This fact with the mentioned extreme difficulties, were well known, during previous investigations published by García-Navarro et al. in [74] and [75]. Thus, a great number of AFM tips were destroyed since the beginning and during the measurements.

On the other hand, special attention must be taking into account related to the texture and contamination of the sample surface, having special care during the cleaning after the etching treatment, and the removal of the rests, to obtain acceptable results.

Finally, it is interesting to mention that this reference measurement with the NSC 18 tip is a bad case compared to the good images that have been captured with other tips of this series. Thus, the aim to prove the reliability of our AFM data in general, could clearly be accomplished. The comparison of pores in SiO_2 assisted by previously published and complimentarily investigated ones strikingly demonstrated that the obtained morphology is a physical property of the sample. The astonishingly equal appearing pores presented by Musket *et al.* were measured by means of SEM. Minor convolutions are also apparent, but do not lead to distortions that make the structures unrecognizable.

Without any kind of doubts, a great expertise in AFM measurements is required to carry out this kind of experiments on such kind reactive surface, moreover its piezoelectric behaviour, due to the features of the revealed structures. It has been a challenge from the beginning, and although the process was full of difficulties during all the time, the results derived from the study are well worthy.

5.1.9.3. Comparison of different operational modes and AFM equipments.

Basically all measurements were performed in Dynamic Mode applying the Phase - Locked – Loop feedback (NC-PLL) even though simple Contact and Non-Contact modes were also available. The main purpose for using the first mode is due to the better lateral and depth resolution in order to get high accurate measurements of the revealed nanostructures.

However, it is worthy to mention that, some few AFM measurements were carried out with the Digital Instruments Nanoscope IIIA MultiMode scanning probe microscope located at the IV. Physikalisches Institut of the University of Göttingen (Germany). The instrument provides the Tapping Mode (TM). A commercial tip of the TESP (tip curvature radii smaller than 10 nm and an opening angle of ≈ 50º) series by Veeco Instruments was available for scanning.

The sample under study was a Br 12 MeV irradiated LN sample, etched in a 1:2 blend of HF and HNO_3 acids for a total of 31 min at RT. The emerged nanopores were clearly visible, and their shapes look the same and appear again as square pyramidal holes. Firstly, the same sample was performed at CMAM by NC-PLL over the exact same surface and using a NSC 18 tip.

Now, assuming that the tips were both of approximately equally sized, when looking at the pore dimensions one can study the differences which then have to be due to the operational mode. The diameters of both measurements are coherent and reliable, but indicate that the NSC 18 probe was larger than the TESP probe. However, we have to mention that, in an early etching stage of the same sample (after 11 min. of etching), no pores were visible when we scanned the sample without applying the PLL feedback loop and in contact mode. The sensitivity of the modes is crucially lower than in PLL or TM-AFM.

Moreover, in order to check the real trapezoidal shapes shown by pores revealed under same specific etching conditions, we seized the opportunity to scan one of our most spectacular nanostructured samples with another AFM equipment, the AIST-NT- Scanning Probe Microscope. The sample studied was: Br 46 MeV irradiated LN at a fluence of 1 e 8 at/cm^2, etched in 40% HF aqueous solution (L) at 55 ºC during 30 min (see **Fig. 3 (d),** *Chapter 6*). The measurements were carried out using a standard commercial probe and in Non-Contact Mode. Really, no more details can be given in, due to the measurements was performed in a formal technical session during a visit to CMAM; in any case, the main goal was to have another proof of the well nanofaceted nanopores. The shapes and sizes were checked that were similar to them obtained by our AFM equipment (see **Fig. 39**).

5.2. Optical characterization methods.

5.2.1. Waveguides optical characterization: refractive index profiles.

Firstly, we have to remark that we introduce in **Chapter 3** the basic concepts of optical waveguides, from now we will present some necessary concepts in order to understand the procedure used to characterize the waveguides obtained after irradiation. The measurements related to this topic presented in this work were performed by Dr. Olga Caballero-Calero at

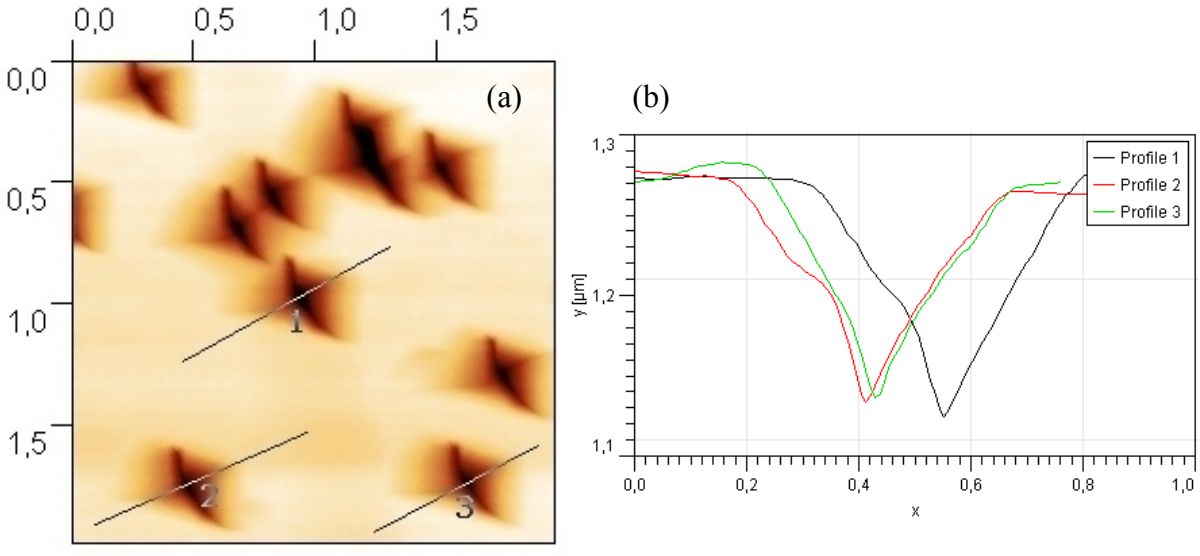

Fig. 39 (a, b). (a) 2 x 2 µm^2 AFM image of etched tracks on *x*-LN after irradiation with Br 46 MeV and etched during 30 min. in HF 40% at 55 ºC measured with AIST-NT- Scanning Probe Microscope in order to investigate the real well faceted shape of the revealed pores. **(b)** The corresponding depth profiles (1, 2, 3) drawn on the AFM image. z-scale: 200 nm.

Non-Linear Optics Laboratory belonging to Materials Physics Department at Universidad Autónoma de Madrid.

The characterization carried on the waveguides inquires into their optical properties, that is, refractive index profile, optical losses, etc. The optical characterization of waveguides processed throughout this work was carried out using the prism-coupling technique for measuring the effective indexes of dark modes. These measurements allow us to determine the refractive index profile of the waveguide.

5.2.1.1. Waveguides modes.

As was mentioned, the confinement dimensions will be considered of the order of microns, (i.e., of photonic applications). In this case the propagation of light along the waveguide is not simply explained by multiple reflections. Only those electromagnetic waves

that after two reflections in the boundaries reproduce themselves, can be propagated along the waveguide. This is called the *constructive interaction condition*, and the waves that fulfill it, are the *modes of the waveguide*. These are characterized by the maintenance of their transverse distribution and polarization along their propagation in the waveguide. The accurate study of these modes has to be done with the aid of the electromagnetic theory.

A thorough theoretical analysis of optical waveguides can be found in most optics books [76, 77], but there are also more simple ways to have a quite correct and intuitive idea of the phenomena without going into too many details. With ray optics and a very elementary waveguide structure, the main properties of a waveguide can be presented. In **Figure 26** *of Chapter 3* there has been presented a planar waveguide with a film width of *d* and refractive indexes for the substrate, cover and guide n_s, n_c, n_g, respectively. For the above mentioned condition of constructive interaction to be fulfilled, the phase change after two reflections for a waveguide mode has to be multiple of 2π.

The phase change of a ray travelling a distance *d* with a bounce angle, θ, is

$$\phi = k \cdot d \cdot \cos\theta = k_0 \cdot n_g \cdot d \cdot \cos\theta \qquad (43)$$

being *k* and k_0 the waveguide vector in the guiding medium and in vacuum ($k = \frac{2\pi}{\lambda}$), respectively. In addition, two other phase changes take place in the boudaries, $2\phi_c$ (guide-cover interface) and $2\phi_s$ (guide-substrate interface), which depend on the polarization of the light. If all these contributions are taken into account, the *self-consistency equation* is obtained:

$$k_0 \cdot n_g \cdot d \cdot \cos\theta_m + \phi_s(\theta_m) + \phi_c(\theta_m) = m\pi \qquad (44)$$

where *m* is an integer called the *mode order*. This equation must be satisfied by all θ_m angles corresponding to guided modes. Other relevant magnitudes of waveguides are:

$\beta_m = k \cdot \sin\theta_m \Rightarrow$ Propagation constant.

$N_m = n_g \cdot \sin\theta_m \Rightarrow$ Effective refractive index.

The number of modes is finite, because the angles θ_m of these modes must be higher than the critical angle for total internal reflection for both boundaries. That means,

$$\theta_m > \arcsin\frac{n_{c,s}}{n_g} \Leftrightarrow n_{c,s} < N_m < n_g \Leftrightarrow k_{c,s} < \beta_m < k_g \qquad (45)$$

Therefore, in the most general case, a finite number of modes propagate along the waveguide. From these, the one with *m = 0* is referred to as the *fundamental mode*. There are also waveguides where there is only one possible mode, which are called *monomode waveguides*.

5.2.1.2. Index profile characterization.

The calculation of the index profile is important in the characterization of any waveguide. It includes two steps. First, the effective refractive indexes for the different

propagation modes (N_m) have to be obtained from experimental data. The most commonly used method to determine them is the *m-lines spectroscopy*. Then, the refractive index profile can be inferred by means of numerical calculations.

5.2.1.2.1. Effective refractive indexes determination. Dark modes.

The *dark modes technique*, also called *m-line spectroscopy*, was implemented in the Non Linear Optics (NLO) laboratory of Materials Physics Department at UAM by Dr. J. Olivares [78]. Given that the dark modes technique has been extensively treated in many other thesis works of ONL group [79, 80], an abridged explanation of the setup will be given here. A brief scheme of the experimental setup can be seen in **Figure 40.**

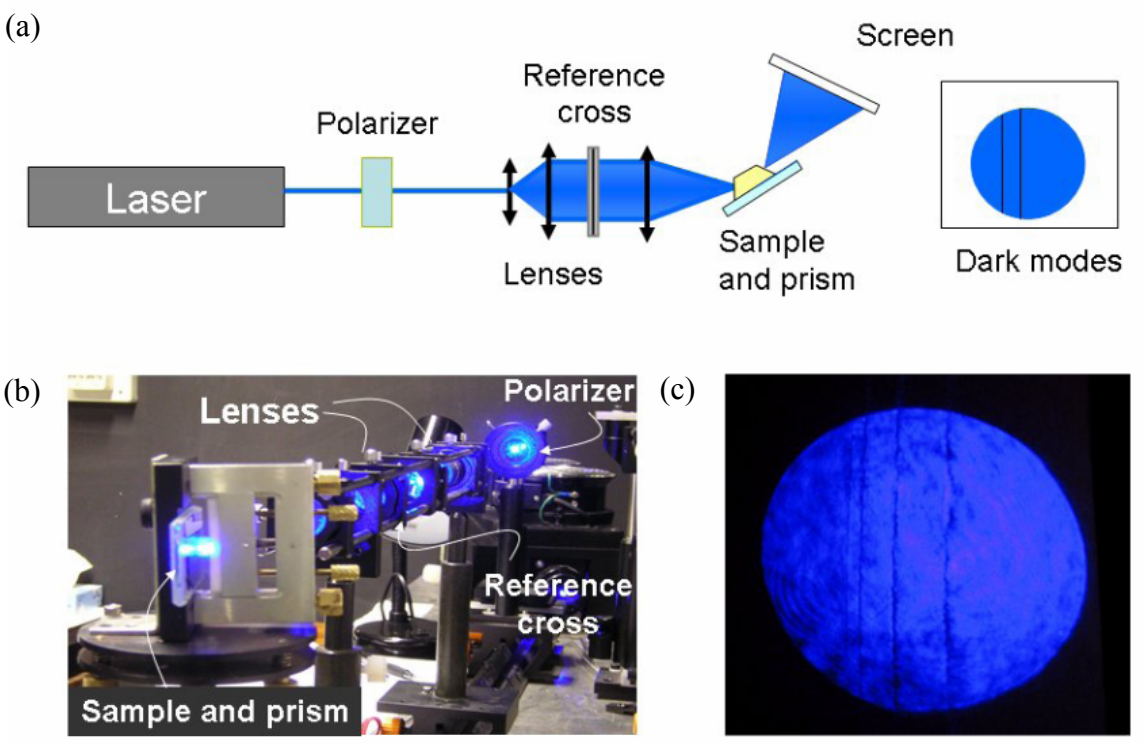

Fig. 40. (a) Layout of the experimental setup necessary for the characterization of the index profile with the *dark modes technique*. **(b)** Photograph of the actual setup. **(c)** Photograph of the dark modes as they appear on the screen.

As mentioned, only the light attached to certain discrete values of angles which satisfy the condition (**Eq. 44**) will be guided by an optical waveguide. The continuous light source used was a He-Ne laser (Uniphase, mod 1125, λ = 632.8nm). After passing through a polarizer, the beam is expanded with a microscope objective (40x) and collimated with a spherical lens. Then, to have a wide range of $\vec{k}$ vectors reaching the waveguide, light is focused on the sample with another lens. A rutile (TiO_2) biprism with refractive index, n_p (n_o = 2.5831, n_e = 2.8650), greater than the waveguide, n_g [81, 82] is used to couple light into the waveguide. To assess a good optical contact between the prism and the guide, they are pressed against each other until it reduces the thickness of the layer of air between it and the guide, so that the evanescent wave

that escapes from the prism penetrates within the optical waveguide. The holder we use can be seen in **Figure 41**, where even the optical contact can be distinguished.

To ensure that the propagation of light within the waveguide takes place the effective index in the prism must be equal to the effective index of a propagating mode. From this condition and using simple trigonometric expressions is easy to get to the expressions (**Eq. 46**) from which one can extract the effective indexes based on the experimentally measured coupling angle, $\phi_{exp} = \phi_1 + \phi_2$, known the prism angles α_1 and α_2 (see **Figure 42**).

$$N_{eff} = n_p \cdot \sin\left[\alpha_1 - \arcsin\left(\frac{1}{n_p} \cdot \sin(\alpha_1 - \phi_1)\right)\right] \quad \textbf{(46.a)}$$

$$N_{eff} = n_p \cdot \sin\left[\alpha_2 - \arcsin\left(\frac{1}{n_p} \cdot \sin(\alpha_2 - \phi_2)\right)\right] \quad \textbf{(46.b)}$$

To carry out the measure of angle ϕ_{exp}, in the dark modes technique, a previously expanded beam is focused on the prism base at the point where the optical contact has occurred, as seen in **Figure 40**. This will cover a range of coupling angles simultaneously. This rutile biprism also decouples most of the incoming light, except from the light matching the angles which fulfil the *self-consistency equation* (**Eq. 44**). For these angles, light is guided in the waveguide and reflected from the base of the prism, producing dark lines in the image corresponding to the outcoupled light, as shown in **Figure 40 (c)**. The angles (ϕ_{exp}) corresponding to each mode of the waveguide, which satisfy the guiding condition, can be measured with an accuracy of ~ 0.001º, thanks to a cross placed in the optical path between the two lenses, and to a circular precision rotation stage, with stepper motor and optical encoder, which holds the sample. Once these external $\phi_{exp,m}$ angles are determined, and given that the geometry (see **Figure 42**) and refractive indexes of the prisms and substrate are known, from the measured values of $\phi_{exp,m}$ the effective index for each mode can be obtained. Having in mind the possible error sources such as those present in the measurement of the angles of the used prism, we estimate measurement accuracy in N_{eff} in the order of $\sim 10^{-4}$. To minimize systematic errors in all steps, the entire measurements of this work has been performed with the same prism.

Once the angles at which the light is guided have been measured, and providing that the angles and refractive indexes of the rutile prism and $LiNbO_3$ are known, the effective refractive

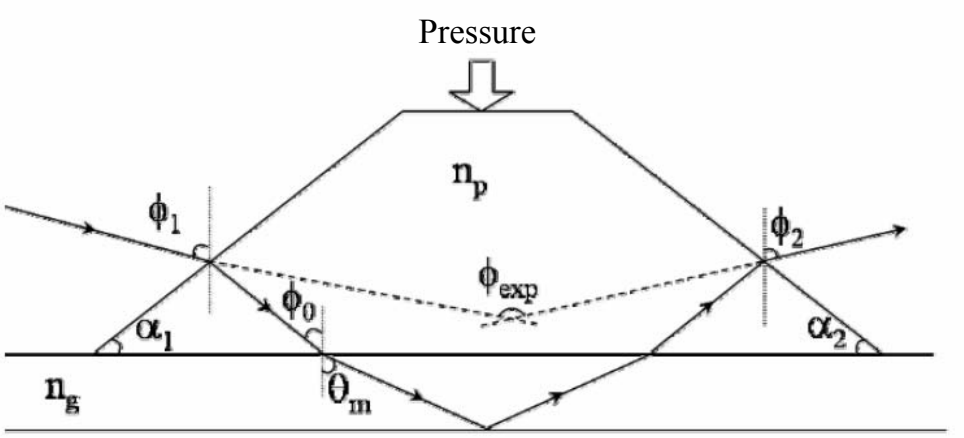

Fig. 42. Scheme of the prism-waveguide coupling from the ray-model point of view.

indexes can be obtained. There are different calculation methods, such as *WKB* or *reflection calculation method*, that with the aid of several computer programs gives us the index profile of the waveguide [78]. In most cases, the profiles so obtained have enough precision. Nevertheless, if the number of modes was not enough or a more accurate profile was needed, a more sophisticated calculation method based on the exact resolution of the wave equation in an analytic index profile was used[10] which supplies a much better profile, based on the minimization of the differences between the experimental modes and the calculated ones.

5.2.1.2.2. Refractive index profile calculation.

The calculation of the refractive index profile is not an easy task. Once the propagation modes are known, there is a range of refractive index profiles mathematically compatible with the same set of values for the effective index, thus, one has to infer the actual index profile function that originates those modes. Normally the largest gap occurs in the surface. The answer is not unique, because different profiles could give the same modes. Therefore, it is necessary to assume some approximations to obtain index profiles. However, considering only physically possible profiles, the uncertainty is less than about 20% of the difference between effective indexes of the first two modes (m = 0, 1) [83].

There are indications that give us some clues about which type of profile is present in every case. Hence, it is necessary to have a former idea of the kind of profile expected in each case. By this way, knowing the mechanism of fabrication of the waveguide, one can predict the approximate shape of the profile, whether it will be abrupt or smooth. Furthermore, representing the values of the effective refractive indexes squared versus $(m+1)^2$ get a line in the case of step-like profiles, and will be deviating from linearity as the profile will smoothing. Guided by these indications we can use the most appropriate approach in each case. Let us review the two approaches considered throughout this work.

[10] The program used was made by Prof. J. M. Cabrera.

Step index profiles approximation.

For step index profiles, the *reflection calculation method* can be used. This method consists on the extrapolation of the *self-consistency equation* (**Eq. 44**) to calculate the refractive index of the waveguide (n_g). Then, an approximate idea of the depth of the waveguide is obtained. If the waveguide is not exactly a step one, the obtained effective depth will be different for each mode, giving a rough idea of the actual depth corresponding to each of them.

IWKB approximation.

On the other hand, in the case of the index profile shape is a rather smooth one (i.e., for metal in-diffused waveguides, soft proton exchanged and others), the self-consistency equation with smooth boundary conditions takes the form of:

$$\int_{x_A}^{x_B} \sqrt{n^2(x) - N_m^2}\, dx = \left(m + \frac{1}{2}\right)\frac{\lambda}{2} \qquad (47)$$

which has to be numerically solved. To cope with it, one can take advantage of the analogy between this problem and another similar one in quantum mechanics. That is, the modes are the roots of the system comprising guide, substrate and cover (the *wave equation*) and the boundary conditions of this system are analogous to that of quantum wells. Besides, the wave equation is equivalent to the *Schrödinger equation*, where the roots are discrete energy levels associated with a wave function. In this analogy, the potential becomes the refraction index profile and the field distribution is changed into the wave function. As a result, the energy levels are changed to *effective refractive indexes* with discrete values, lower than the guiding layer but higher than the surrounding media.

Given that analogy, a variation of the WKB method (Wentzel, Kramers and Brillouin) [84, 85] used to solve the Schrödinger equation, called the *inverse WKB method* [83, 86-88] is used. Its use is limited to small refractive index variations, in the order of a wavelength, which is not always fulfilled, but the errors in the calculation are ~10^{-4} for smooth profiles (for step profiles it is not recommended, because the errors are much higher).

5.2.2. Optical losses.

One relevant parameter for photonic applications includes light propagation losses. Information about propagation losses was obtained by the light scattering technique [89, 90] on samples ~20 mm long[11]. The technique consists in measuring the exponential decay of the scattered light out of the guide, assuming that the intensity of the scattered light is proportional to the guided light.

For this purpose a laser beam is coupled into the guide with the prism technique, in the same manner and with the same experimental device that was mentioned in the previous **Section 4.7.3.1.;** then, the scattered light intensity out of the waveguide of a guided mode is

[11] Prior to this measurement, the samples were annealed in oxygen atmosphere (1 h, at 150 ºC) to remove absorption introduced by the ion irradiation. The refractive index profiles and the damage fraction measured by RBS/C remained unchanged after this annealing process.

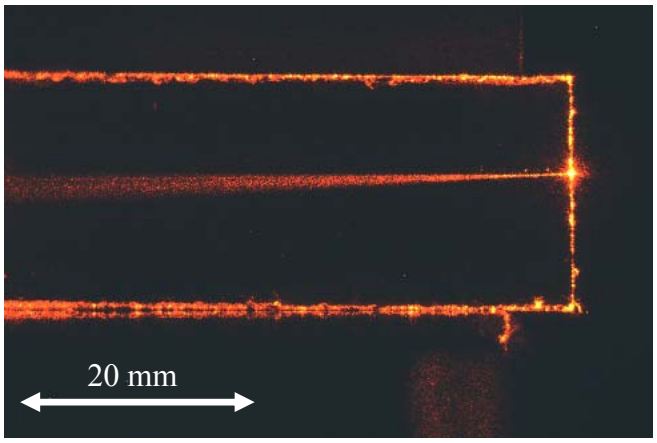

Fig. 43. Image used for the measurement of propagation losses of the waveguide with the scattering light technique.

monitored with a CCD camera. A CCD (Charged Coupled Device)-camera (Kappa camera, Model DX 20N) with high sensitivity and color range (12 bits) was used. Previously, a study of the linearity in the measurement of the intensity acquired by the device was performed, and the effective dynamic range was found. Although only the scattered light at 90º can be detected, this is expected to be proportional to the intensity scattered inside the waveguide at the same point. Then, the decay of scattered light along the waveguide can be mapped from the image of the propagated mode captured with the camera. **Figure 43** shows one of these images, from which we extract the intensity versus the propagation distance.

The corresponding intensity for each point follows **Eq. 48**.

$$I = I_0 \cdot \exp(-\alpha \cdot L) \tag{48}$$

where I is the intensity of scattered light at a propagation length L, I_0 the intensity at the beginning of the propagation and α the loss coefficient. From the representation of the light intensity on a logarithmic scale versus distance, we are able to obtain the value of the losses from the slope of the linear fit, following the definition of decibels per unit length (**Eq. 49**).

$$dB = -10 \cdot \log\left(\frac{I}{I_0}\right) \Rightarrow dB = 10 \cdot \log(e) \cdot \alpha \cdot L \tag{49}$$

As example **Figure 43** shows the image for measuring propagation losses of the waveguide in the case of 1-mm thick *Z*-cut $LiNbO_3$ samples irradiated with ^{129}Xe 1432 MeV ions of fluence $2x10^{11}$ cm^{-2} (see **Chapter 8**)[12], where the light was in coupled with a rutile prism, and then propagated along the waveguide for around 20 mm. Once the image has been recorded, with appropriate software[13], the light intensity at different propagation lengths is extracted and plotted (**Figure 44**)[14]. The value of α is obtained from the fit of these data.

[12] Most reliable data for Xe-irradiated samples yield attenuation values in the range 2.6 to 4.5 dB/cm.
[13] Different software applications have been used; in this sense, special acknowledgements must been given to Dr. V. Joco for the development of several software versions to analyse the raw data.
[14] This graphic must be understood only from a qualitative point of view in order to illustrate the typical behaviour followed by the propagation losses. This plot does not correspond to the case shown in **Fig. 43**.

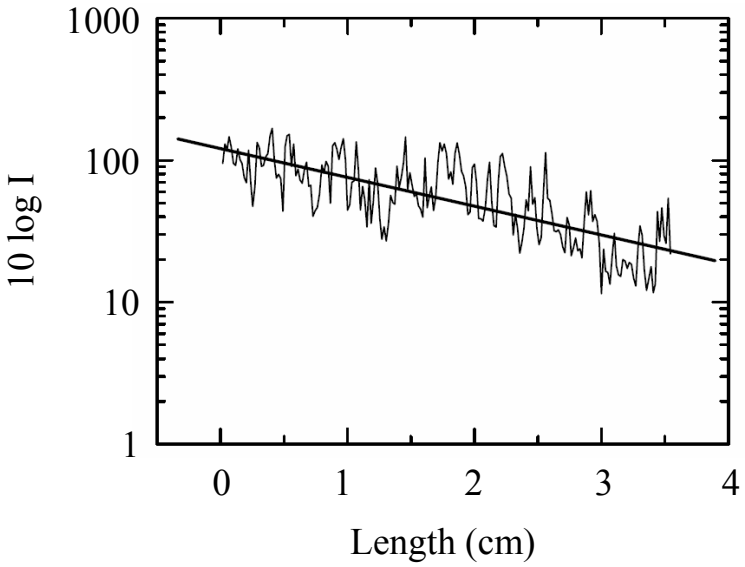

Fig. 44. Plotting of the logarithm of the scattered light intensity out of the waveguide compared to the propagation distance.

5.3. Transmission electron microscopy (TEM).

Transmission electron microscopy[15] is a very reliable and precise method for structural analysis. In high resolution transmission electron microscopy (HRTEM) lateral resolutions up to a few Å can be achieved. This versatile method can be applied to a very large class of materials including insulators. One of the restrictive factors to sample requirements is the fact that the methods can only be applied under high vacuum conditions, thus no outgassing samples can be introduced into the chamber. The exact measurement processes are very complicated and contain even more difficulties than ones presented above for scanning probe microscopy. A very comprehensive introduction on diffraction, imaging and spectrometry is given in [92].

Electrons, once generated, are accelerated with several hundreds of kilovolts onto the sample, passing different lenses and filters. Subsequently, when arriving at the sample, the electrons get backscattered (scanning electron microscope, SEM), may provoke secondary- or Auger-electrons, photons (cathodoluminescence), and X-rays (electron dispersive x-ray spectrometry, EDX), which can be used for sample analysis. Many methods and operational modes are possible. If the sample is thinned to less than 100 nm the electron energy (typically 200 keV) is sufficient to traverse the thin target. Some of the transmitted electrons (TEM) get (multiply) scattered elastically and inelastically (electron energy loss spectroscopy, EELS).

For further structural characterization of the nanopores revealed after etching (see **Chapter 6**) the Philips CM200-FEG-UT [93] transmission electron microscope located at the IV. Physikalisches Institut of the Faculty for Physics at the Georg-August-Universität of Göttingen (Germany) was used. The apparatus combines a field emission gun (FEG) for electron generation with an ultra high resolution objective lens, ultra twin (UT). Electrons were

[15] For his fundamental work in electron-optics, and for the design of the first electron microscope E. Ruska obtained the other half of the Nobel Prize in 1986, together with Binning and Rohrer [91].

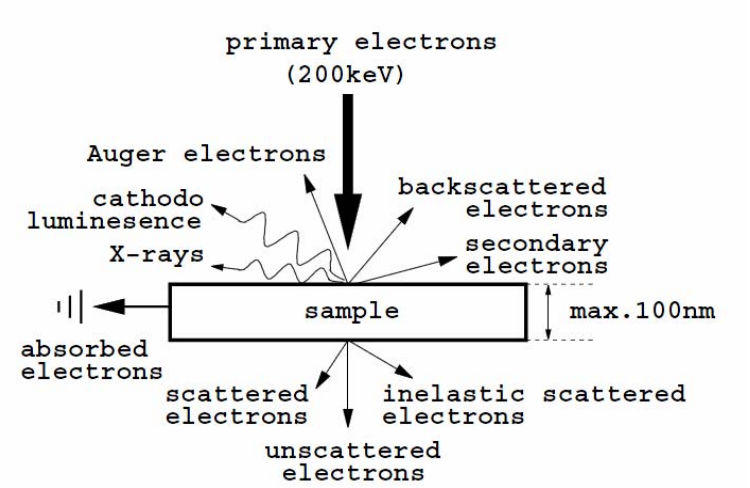

Fig. 45. The different interactions of transmission and scanning electron microscopy occurring during a measurement.

accelerated with 200 kV and guided by a set of condenser lenses onto the target, which was located in the center of the objective lens. After passing the sample and a second set of focusing lenses, the beam arrived on a CCD photo detector. In high resolution mode (HRTEM), where up to 560 kV were applied, the microscope can achieve a maximal lateral resolution of 0.11 nm. For insulating samples this resolution is a little worse, but in our case the structures of interest are at least two orders of magnitude larger than this limit.

Besides TEM measurements the instrument is also capable of scanning a strongly focused, and thus very small electron beam across the sample, enabling scanning TEM (STEM), and highly space resolved element analysis (1-2 nm) by energy-dispersive X-ray spectrometry (EDX). This ultra high resolution demands very low magnetic fields (< nT), acoustic noise lower than 22 dB including building vibrations, and very stable temperatures of 0.1 K/h. All this is implemented in an extra laboratory building, constructed especially for this reason.

Samples preparation. Focused Ion Beam (FIB).

Samples were prepared with the focused ion beam (FIB) at the Materialphysikalisches Institut. The Nova 600 NanoLab [94] provides a DualBeamTM SEM/FIB system for nanoscale characterization and manipulation. Material can be sputtered via a *keV* Ga-ion beam. For sample preparation a gold film of ~200 nm thickness was vapour deposited on the Lithium Niobate surface. This is necessary to prevent the sample from charging when looking at it with the SEM or during ion bombardment. Then, a region of 12 × 1 μm was selected and a thin platinum layer was electron beam deposited. A thicker protection layer of 2 μm height was then deposited via the Ga beam. Two markers indicated where the region was located. This allowed the machine to automatically sputter the material around the region of interest to a depth of ≈ 6 μm. The new transverse sample layer was then welded to a TEM-grid. Subsequently, it was thinned to ≈50 nm at the surface, until the Pt protection layers and the Au film were almost vanished. This leaves measurable lamella width of a few microns. TEM measurements were performed with the parameters given in **Chapter 6.** *6.3.3. Pores morphology and latent tracks from Transmission Electron Microscopy (TEM)*, where the data are presented.

5.4. Profilometry.

Profilometry is a standard, widely used technique to measure film thickness and roughness. Similar to the AFM a much bigger tip (typically r ≈12 μm) is scanned over the surface, applying tracing a 1-dimensional long distance[16] profile of the samples surface. Hence, it is a mechanical method in which a stylus is placed in contact with the sample's surface and then gently dragged along it, measuring the vertical deflections. This can be used to obtain height values too big for measuring via atomic force microscopy provided that a step is present in the sample e.g., produced by chemically etching a homogeneously damaged region (spot of irradiation). Under certain conditions the vertical resolution of the method is claimed to be as low as 0.1 nm [95]. Routine measurements are easily done with 10 nm precision, or less.

Latent ion tracks start to influence each other (halo overlap) approximately in the range of fluences of 10^{11}-10^{12} cm^{-2}. Even though the track cores are not yet overlapping [75] a significant proportion of material is being damaged[17]. Thus, two effects can be measured by profilometry:

i) surface swelling

ii) etching rates of damaged bulk material.

The latter was examined with the Veeco Dektak 150 Profilometer. The set of Cu 51 MeV irradiated samples with fluences of 10^{12} cm^{-2} in channeling and random directions, respectively, were available for bulk etching investigation.

On the other hand, surface swelling studies were done on Br 12, 22 MeV and Cu 51 MeV irradiated samples with fluences of 10^{9} cm^{-2} but neither significant surface swelling nor etch pit depths in the spot area could be denoted as was expected for these ultra low fluences.

For profilometry measurements a sample preparation was not necessary. The scans were carried out with a 12.5 μm radius needle applying a force of 3 mg, and had typical lengths of a few mm to cover the whole sample width. The vertical resolution was restricted by leveling of the gained data and amounted approximately a few nm. It is neither exactly clear how big the systematic error was that is caused by the sample surface's divergence. It was estimated to be a few ten nanometer.

[16] Measurement ranges up to 55 mm laterally and 524 μm vertically are covered.
[17] Cores overlap at fluences higher than 10^{14} cm^{-2} [73].

Chapter 6

Additional experimental techniques of samples processing.

6.1. Nanostructures revealing by chemical etching.
6.2. Annealing treatments.

6.1. Nanostructures revealing by chemical etching.

6.1.1. Chemical etching behaviour of Lithium Niobate.

As a first step to discuss the generation of nanopores after etching of the irradiated samples we present this Section concerning to the wet chemical etching behaviour of the unirradiated samples.

Even though lithium niobate (LN) has been thoroughly investigated for more than five decades, detailed information on the chemical etch processes is still quite scarce. For instance, since the early days, when wet etching of LN was first employed, the method of using a hydrofluoric and nitric acid (HF/HNO_3) solution in a 1:2 ratio as the mixture of choice has widely been adopted as the mixture of choice for revealing domain inverted regions. More recently etching studies have been undertaken on both periodic structures, and microdomains, using respectively the 1:2 ratio and HF alone, but none of these works offers any systematic concerning etch rates as a function of etch chemistry, or the mechanism behind differential etching. Even until the year 2002 it was more or less unclear why, if ever, that was the best mixture to obtain cleanly etched structures. Sones et al. [96] report higher etching rates as well as smoother surfaces (with roughness of the order of the optical grade polished virgin samples, ~2 nm rms), and feature walls for pure HF acid than for any mixture containing HNO_3.

The wet chemical etching behaviour of $LiNbO_3$ shows high resistivity against most acids and different etching rates for various crystal cuts. There is an extremely large difference between the etch rates for $+z$ and $-z$ crystal faces. The $+z$ face is the strongest orientation, resisting even pure 48% HF acid (all concentrations are expressed in vol. % throughout this work) up to 95 ºC for extremely prolonged etching times without being significantly attacked (The material only gets etched at defects and dislocations). After 600 h in a HF/HNO_3 (1:2) mixture (The HF acid in this case was a 48% solution in water, whereas the HNO_3 solution contained 78% of pure acid.) at 60 ºC the $+z$ face shows no sign of etching [97]. In contrast, the $-z$ face is etchable with rates depending on the temperature, going from ~ 0.8 - 1 μm/h at room temperature (RT) to 30 μm/h at 95 ºC. The etching rates for each of the two $\pm y$-faces, as well as for the x-faces are assumed to be more or less equal and lower than the one measured on the $-z$ side (see **Table I**).

Etching rate, v (nm/min)	$-z >$	$\pm y \geq$	$\pm x >$	$+z$
Crystalline	≈ 15	n/a	≈ 0.1	≈ 0
Amorphous	n/a	n/a	80 - 130	n/a

Table I. Relative etching rates for the different crystal directions. The crystalline - z-face is etched roughly more than 150 times faster than the x-faces, whereas the etching rate increases by about a factor of 1000 for amorphous material of a x-cut substrate.

For ion beam enhanced etching, as carried out for this work, the etching of the amorphous material is an even more interesting parameter. As soon as the crystal is completely

amorphized the etching rate is enhanced such that the original etch rate of the crystal becomes negligible [98]. Due to its high selectivity, the method is considered very promising and aspect ratios greater than 2 have been fabricated on the submicrometric scale [97]. This number does not seem to be very high, but technical processing is quite complicated, and yet, there are no methods yielding much higher aspect ratios. It shall be emphasized here, that such structures still have almost micrometric dimensions that cannot be diminished to truly nanometric size.

6.1.1.1. Reaction parameters.

The chemical reaction process depends on different parameters that have to be understood and controlled in order to apply etching successfully. Besides the very sensitive, intrinsic etching conditions as acid concentration, etching time and temperature, the etching rate

Etching Parameter	Etch Rate Dependence	Tendency
HF Concentation, c	superlinear	$c_{HF} / (c_{H_2O} - c_{HF})$
Etching Time, t	linear	$t_1 < t_2 \Rightarrow v(t_1) < v(t_2)$
Etch Temperature, T_e	linear (above RT)	$T_1 < T_2 \Rightarrow v(T_1) < v(T_2)$

Table II. Etch rate dependence on the etching parameters as reported by Schrempel [97, 98] and Sones [96].

also depends on the structure of the damage, and hence, on the irradiation conditions. The defect creation is mainly determined by the ion energy and species, the stopping power, fluence, beam flux and irradiation temperature, yielding the corresponding defect concentration. The irradiation temperature was not controlled, but should be preferably as low as possible to freeze in-situ annealing effects [99]. The most important parameters and their dependencies are listed in **Table II**. The tendencies are shown to outline what behaviour is expected if the corresponding parameter is changed. Extrinsic defects introduced by ion bombardment, as has been discussed, enhance the etching rate by a factor of almost 1000 if complete amorphization is achieved (see **Table I**). This extremely high selectivity should, in principal, allow selective etching of amorphous latent nanotracks, as it is known from many polymers. For tracks with radii larger than 3 nm [100, 101], chemical etching becomes very sufficient whatever the material [102].

6.1.1.2. A brief description of the etching mechanism.

When trying to describe the etching process, two questions have to be answered: Which molecules are present in the acidic solution and how do they participate in the etching reaction?

Thus, at first a basic understanding of the dissociation of HF in aqueous solutions needs to be achieved in order to describe the relationship between the total HF concentration and the existing composition of the solution. The dissociation behaviour of HF in aqueous solutions has been examined by many authors using different methods of measurement [103-108]. However

there are substantial disagreements in the interpretation of the results e.g. regarding the existence of the dimer $(HF)_2$, the complex formation of H_2O with HF and the formation of higher fluoride ions of the type with $n > 1$.

Concerning the HF etching of $LiNbO_3$ there is only one description of the dependence of the etching rate on the HF concentration for domain inverted $LiNbO_3$ [96]. The authors refer to a study of HF etching of SiO_2 [109] justified by the likewise hydroxide-terminated surface and successfully describes their results after slight modification of the reaction model.

Looking at the full variety of mechanisms set up for HF etching of SiO_2 [109-114], a number of similarities can be denoted. Mostly a two-step reaction scheme is used, containing both the dissolution of the oxygen atoms by adsorption of H^+ - atoms at the surface (*activation step*) and the dissolution of silicon atoms by fluoride species (*substitution step*). Besides of the existing diversity concerning the models of dissociation referred to, the etching mechanisms considerably differ also concerning the function of the protonation process and the type of fluoride species being active in substitution. These differences in the mechanism also cause differences in the rate laws. HF, HF_2^- or the dimer $(HF)_2$ are regarded as the reactive fluoride species, some authors also consider parallel reaction paths with different reactants [109-111, 114].

To obtain further information on the chemical processes, the model of dissociation of HF in aqueous solutions and the kinetic models set up for HF etching of SiO_2, both briefly introduced above, were applied to $LiNbO_3$ [115]. It was presumed that the etching rate is dominated by the same molecular reaction steps for the full range of concentration considered (0 to 14%). That way only two reaction models are found to describe the experimental dependence of the etching rate on the HF concentration appropriately. In both cases it is described as a catalytic reaction with H^+ acting as a catalyst in the activation of the process. The substitution step can be assigned to an attack of either HF or HF_2^- molecules.

Interpreting the rate laws obtained, the surface interactions can be described similarly to the ones set up for HF etching of SiO_2: At first the negatively charged free bonds of oxygen atoms at the surface are saturated with H^+-ions very rapidly by electrostatic attraction. Now the oxygen can desorbs from the surface in the shape of an OH^--molecule or as H_2O after a further complex formation by another H^+-ion. These two alternative reaction paths cause the additive ansatz of the catalytic reaction. In a second step the metallic (Li and Nb) atoms can be removed by an attack from either HF or HF_2^-, leaving behind free oxygen bonds at the new surface.

Contrary the exceptional increase of the etching rate for a total concentration of 40.8% cannot be described appropriately by the catalytic model. But even if other rate laws may be attempted, it will not be possible to find a reliable description in this range of concentration, because the validity of the model of dissociation is limited to 14%. Nevertheless it shall be announced that the same exceptional increase of the etching rate has also been measured for concentrations above 20% for HF etching of domain inverted $LiNbO_3$ [96].

6.1.1.3. Chemistry of HF/HNO_3 etching and differential etching behaviour.

There will be described briefly the mechanisms behind the HF/HNO_3 etch behaviour, with particular attention to the differential etch behaviour for the + *z* and - *z* crystal faces [96].

The variation of the etch rate with HF concentration in water shows that the etch rate increases superlinearly with the HF concentration. In the apparent absence of previous quantitative reports on this etching reaction we refer to a recent study of HF etching of SiO_2, which has a hydroxide-terminated surface similar to what is expected in the present case. As it has been commented above, Knotter [109] concluded that the etching of SiO_2 in HF solutions was controlled by fluoride substitution of the surface hydroxide. The accelerating effect of a low pH was attributed to the greater extent of surface protonation, leading to hydroxide removal as a precursor to fluoridation by HF_2^-, or H_2F_2 at very low pH.

The highly plausible notion that etching is initiated by surface protonation immediately explains two qualitative observations:

(1) Faster etching on the negative *z*-face is due to easier absorption of the positively-charged proton, and such enhanced dehydroxilation.

(2) The etch rate increases with increasing concentration of acidic protons.

6.1.1.3.1. HF solutions.

The rapid increase as the HF concentration approaches 48% does not correlate with the acid proton concentration computed from the thermodynamic data presented by Knotter [109]. Of many attempted correlations, the one which had the most successful fit and the most plausible physical explanation, is that which takes into an account the ratio $c_{HF}/(c_{H_2O} - c_{HF})$ where c_{H_2O} and c_{HF} are the total molar concentrations of water and HF in the mixture.

It is suggested by [96] that the inverse correlation with $(c_{H_2O} - c_{HF})$ is due to the reduction of the thermodynamic activity of water at high HF concentrations. It is known that water is complexed by HF to form H_3OF [116] so that only the residual, uncomplexed water would be active in the dehydroxylation equilibrium (**4**):

$$MOH_s + H^+ \equiv M_s^+ + H_2O_{free} \qquad (4)$$

where MOH_s and M_s represent normal (residual group), and dehydroxylated surface groups. (From their computations show that H_2F_2 is the majority fluorine-containing species in the system).

The linear dependence of rate on c_{HF} can be explained by assuming that fluoridation of the surface occurs by an electrostatically - enhanced attack of M_s^+ by HF_2^-, Eq. (**5**):

$$M_s^+ + HF_2^- \rightarrow MF + HF \qquad (5)$$

The reaction details are a lot more complicated than this, and can be found in [96] for differential etching of *z*-cut material, and in [115] for amorphous regions in crystalline *x*-cut

samples, i.e. for the IBEE method. As it has been commented, due to the acid solution, H_3OF molecules are formed among others [116]. For this reason it is assumed that the thermodynamic activity of water decreases at high HF concentrations. Between 20% and 30% a threshold-like behaviour of the etching rate was observed which seems to be inversely proportional to the content of free water $(c_{H_2O} - c_{HF})$. Concentrations above this threshold seem to yield much higher etching rates. For low HF concentrations the rate dependence shows linear behaviour on the same. For pure HF in water solutions is (**6**):

$$v_{etch} \approx \frac{c_{HF}}{(c_{H_2O} - c_{HF})} \qquad (\mathbf{6})$$

6.1.1.3.2. HF/HNO_3 solutions.

Data for the etch solutions containing HNO_3 show a simple relation where the etch rate is simply proportional to the HF concentration. The model in this case assumes that nitric acid is probably strong enough to saturate the negatively charged surface with protons, dehydroxylate completely and then cover the M_s^+ surface with nitrate, Eq. (**7**):

$$MOH_s + H^+ \rightarrow M_s^+ + MNO_3 \qquad (7)$$

The subsequent reaction is determined by the rate of fluoride substitution at the surface. Here there is no electrostatic enhancement of HF_2^- attack, so that the more abundant H_2F_2 is more effective than HF_2^- in this case, Eq. (**8**).

$$MNO_3 + H_2F_2 \rightarrow MF + HNO_3 + HF \qquad (\mathbf{8})$$

The proposed model also explains the observation that the etching is much faster on the - *z* crystal face, since a negative surface charge would favour protonation. Also, the short metal-oxygen bond on the positively charged surface should be more stable, and therefore less reactive, than the long bond on the negative surface.

6.1.2. Controlled etching of single ion tracks. Fabrication of track-etched nanopores and geometry of the tracks.

Nanopores are little nanometric pit-like structures on the surface of a substrate. In case of this work, they are produced by single swift heavy ion impact, and subsequent chemical etching of the latent nanotracks. As mentioned, the objective of this investigation is to show the possibility of fabricating reproducible nanopores of different shapes and sizes, and the morphological characterization of their features. Thus, through this Section, the experimental details which led to the generation of our results will be given in. A general sketch of the nanopores fabrication process steps is illustrated in **Fig. 15**.

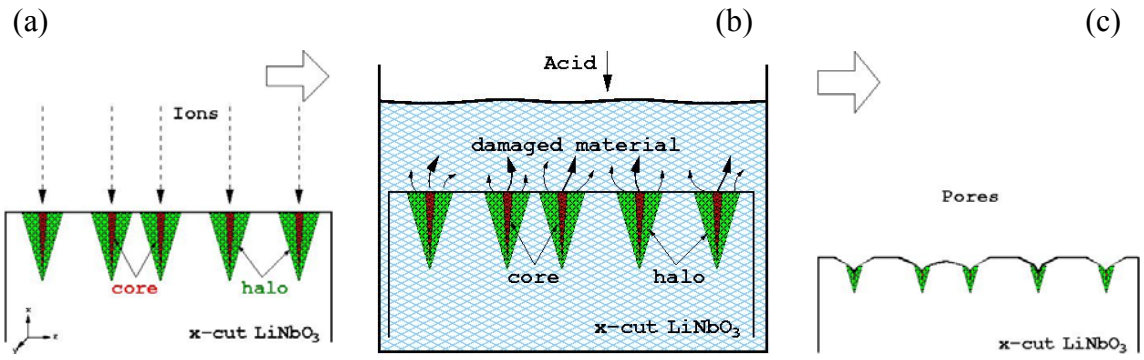

Fig. 15. This scheme shows the basic nanopores fabrication steps: **(a)** sample irradiation, **(b)** etching of the damaged regions and **(c)** resulting nanopores.

After etching, the samples were rinsed in de-ionized water and dried with dry nitrogen gas. Further details on the processing of the pores are given in the following Section. The main characterization technique used for the examination of surface morphology was an AFM commercial instrument from Nanotec Electrónica S.L. under ambient condictions; a phase-locked loop (PLL) feedback was added to the dynamic or tapping mode which allowed us to realize accurate measurements. On the other hand TEM observations were performed at 200 kV in cross-section specimens prepared by ion milling. Mean values of the etched-pore diameter D and half- cone angle φ, averaged over 50-100 tracks for each specific irradiation, were obtained from AFM images. Cone features extracted from cross-section TEM images are, in principle, more accurate than those extracted from AFM images, which may be distorted by the finite size of the probe tip.

In the following, the term fabrication means the irradiation and etching procedures the sample undergoes to fabricate the desired nanopores, whereas preparation will include further sample treatments, such as the FIB preparation, etc.

It is important to comment that, before any treatment of the optical-grade 3´´ wafers of congruent $LiNbO_3$, purchased from Photox Inc. [117], had to be cut into adequate pieces of 3 × 4 mm^2, or in some cases (7 × 8 mm^2). As mentioned, this was carried out with a cutting machine via a slowly rotating (~ 10 rpm) diamond blade. The crystal cannot be broken clean and easily as may be known from silicon (through the cleavage plane), or SiO_2. For that reason the wafers were glued with wax to a glass plate to prevent them from breaking during sawing. When melting the wax, and during cool down, one has to be careful with the heating ramps. If the crystal is exposed to high temperature gradients, it cracks due to its high pyroelectric coefficients. The z-cut is the most sensitive to this effect.

Ion track etching is governed by the selective removal of the latent ion track compared with the pristine material. The final shape of the etched pores depends on how much faster the track is etched in comparison to the bulk material, which is removed isotropically during the etching process. Successful track etching requires that the etching rate v_t along the track is greater than the etching rate v_b of the non- irradiated bulk material. The ratio of the two etching rates v_b / v_t determines the geometry of the etched pores.

The geometry of a track, subject to chemical attack, in the simplest case is dictated by the simultaneous action of two processes: chemical dissolution along the track with a rate (v_t), and general chemical attack on the non damaged surfaces and the inner surface of the track, characterized by a rate, v_b. **Figure 16** shows this process, which creates a cone which one axis is oriented along the direction of irradiation (track direction). It is assumed that: (1) v_t is constant throughout the track, and (2) v_b is constant and isotropic.

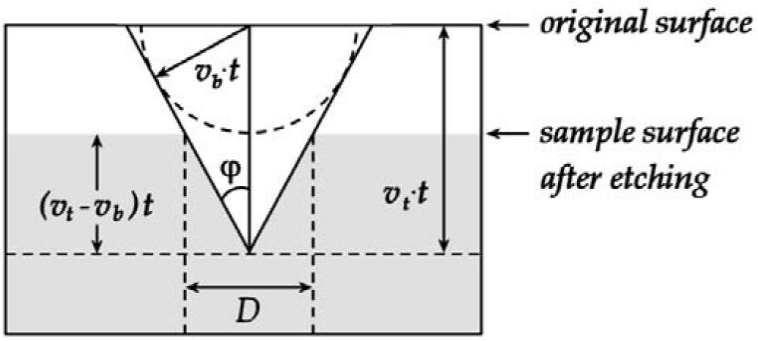

Fig. 16. Schematic of an etched ion track. The opening angle φ is determined by the ratio of track etch rate v_t and bulk etch rate v_b. D is the final pore diameter.

If the irradiation was made at normal incidence, the track is perpendicular to the surface sample. **Figure 16** shows that the surface material is removed together chemical attack of the track occurs. Thus, the two quantities, D (diameter of the hole surface) and $h = (v_t - v_b).t$ (depth of the track), are the result of competition between the effects of v_b and v_t. Really, the situation is not so simple: v_t is not constant throughout the track, and v_b is not isotropic depending on the crystal faces.

While the bulk-etch velocity v_b (etch rate of undamaged material) and the track-etch velocity v_t (etch rate along the track) both depend on the etching conditions, v_t is also influenced by the energy loss of the incoming ion. It increases with increasing the stopping power (dE/dx), due to the higher damage along the ion track.

In general, the bulk etching rate (v_b) remains constant for a given material and for a given etchant applied under a specific set of etching conditions such as concentration and temperature. In addition to the factors mentioned, the track etching rate (v_t) depends on the density of damage in the track and hence on the energy and on the energy loss of the track-forming ion.

The etching process is shown schematically in **Fig. 16**. The opening angle φ of the resulting pore is determined by the ratio v_t and v_b. The higher the track-etch velocity v_t is compared to the bulk-etch velocity v_b, the more cylindrical the pores become.

Over short distances, the cone half-angle φ depends on the track etch ratio, which is defined as the ratio of the track etch rate v_t and the bulk etch rate and v_b according to Eq. (**9**). The cone half-angle φ can be increased either by increasing v_b or by decreasing v_t.

$$\varphi = \arcsin\left(\frac{v_b}{v_t}\right) \qquad (\mathbf{9})$$

For most samples, the number of pores revealed corresponded to the applied ion fluence. In contrast to polymers, where an extremely small v_b / v_t ratio leads to almost cylindrical pore geometry, etched tracks in the investigated $LiNbO_3$ yielded conical pits with an opening angle φ of around 55 º - 60 º. The shallow and wide-angled conical holes observed show that the etching velocity in the track v_t is near the bulk etching velocity v_b. This geometry corresponded to an etching ratio of v_b/v_t = 1:0.85 and an Aspect Ratio (A.R.) as better as ≈ 0.35. Although it could be thought that is a signature of a low density of defects along the track [118, 119], the most of irradiations were carried out above the S_e *threshold* at the surface, therefore the complex chemical behaviour of the $LiNbO_3$ plays a crucial role for the revealing of nanostructures. One possible hypothesis is that a residual phase of the chemical reaction between the chemical agent and the damaged surface can be deposited in the deeper part of the nanopore blocking the chemical process. [At this point we can introduce a new parameter for the characterization of the nanostructured pores: Aspect Ratio (*A.R.*), the ratio between the depth of the pore ($h = (v_t - v_b).t$), and the diameter chemically revealed (D) of the pore, both quantities physically measured: $A.R. = (h/D)$].

6.1.3. Track etching procedures.

The chemical treatment of all samples was carried out under the conditions defined below. We tried to vary different intrinsic etching parameters to detect and isolate dependencies in the nanopore development process and later compare the influence of variation in the various sets. Besides the ion energy and irradiation fluence were investigated, in order to introduce

Wet Etching Parameters	Typical values
Pure Acids: HF , HNO_3 (c_{HF} : c_{HNO_3})	40 %, 78 %
Blend: HF , HNO_3	1:1, 1:2
(c_{HF} : c_{HNO_3})	40 %, 78 %
Concentrations, c_{HF}	5 %, 40 %
Etching Time, t	0.5 - 180 min.
Etch Temperature, T_e	19 ºC - 55 ºC
Annealing Temperature, T_a	150 ºC - 300 ºC

Table III. An overview of the typical etching parameters used throughout nanopores fabrication.

further irradiation parameters that may influence in the revealed nanostructures by chemical etching. As a reference, all etching parameters are listed in detail in **Table III**.

6.1.3.1. Aqueous solutions.

Chemical wet etching of the damaged sample regions was performed by exposing the irradiated samples to various aqueous acid solutions. Etchings were performed in pure HF with concentrations of 5% and 40%, and in blends of the latter with 70% HNO_3 in a 1 : 1 and a 1 : 2 ratios. The etching bath temperature was varied from 19 to 55ºC for a few experiments. In most cases room temperature (RT) was used (~25 ºC). The setup used is illustrated in **Fig. 17 (a)**. The sample is placed face up into a little teflon (which is chemically inert to the used acids) basket with many little holes for good washing-round of acid to the sample. To control the etch temperature, the acid container was placed into a water bath on top of a heat plate which was continuously adjustable from RT to > 200 ºC. The given temperatures are averaged and were measured every 5 min (2 min for short etching times of 10 min total) with a thermopar in the water bath close to the acid container. For good temperature homogeneity the water was continuously stirred by a small magnetic rod. After thermalization of at least 10 minutes the samples were immersed into the solution and withdrawn after the desired etching time (0.5 - 180 min). Moreover, one sample was etched with the support of an ultra-sonic bath.

After every etching, the samples were first put in de-ionized water from a micro filtering system in our lab (electronic conductance ~13 μS/cm), and from there into an Eppendorff- container with ultra-pure water (1.0 μS/cm) from Panreac Ltd. to rinse them from any remaining acid. They were dried on ultra clean optical tissue in a laminar-air-flow-box. In some cases we cleaned the surface with the tissue dipped in acetone. Just before being scanned with the AFM, they were dried with dry nitrogen gas, in order to get a clean surface without powder or dirty.

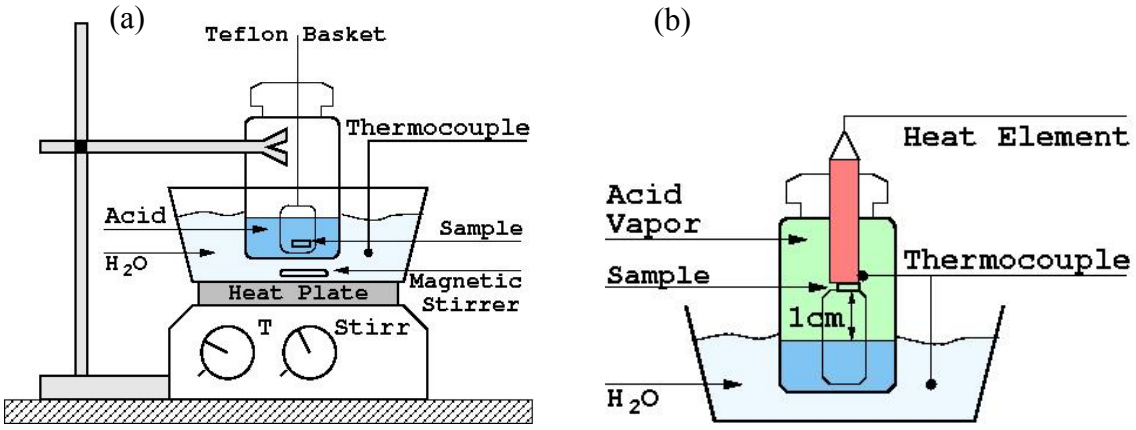

Fig. 17 (a, b). Schematic of the typical setups used for etching experiments. **(a)** Wet etching, **(b)** Vapour etching.

6.1.3.2. Vapour etching.

$LiNbO_3$ - samples were etched in the vapour of hydrofluoric acid of the 40% solution for comparable times as in liquid (30 and 60 min). The acid had either room temperature (RT) or was heated to 55 ºC. The sample was placed 1 cm above acid level, facing downwards (see **Fig. 17 (b)**). Two teflon baskets forming a container with a hole on top, served as a spacer. The

majority of our vapour etching experiments was done without any control of the sample temperature. Later, we tried to heat the sample with a heat element, as shown in the **Figure 17 (b)**. It is reported for vapour etching in SiO_2 that the best aspect ratios are obtained if the sample temperature is slightly higher than that of the acid vapour [70, 71]. The sample temperature was measured by a second thermopar that was wrapped in teflon together with the heat element.

As a reference sample, a SiO_2 substrate was fabricated. It was irradiated with Br 46 MeV ions. The corresponding pore shape is known to be circular. The etching time had to be a lot shorter (60 s), due to the much higher etching rates. Also, some SiO_2 samples were prepared, where the temperature was higher than the one of the acid vapour.

6.2. Annealing treatments.

For the case of the study of the recrystallization properties of amorphous tracks and layers generated by swift-ion beam irradiation (see **Chapter 7**), annealing treatments were performed with two different set-ups in air atmosphere. For the annealing of thick uniform layers (irradiations with F 20 MeV ions) the sample was kept at a fixed temperature of 350 ºC (from 30 minutes to several hours ~ 10 h) in a standard tubular Carbolite furnace with an integrated Eurotherm temperature controller assuring thermal uniformity and stability better than 1 ºC. Nevertheless, the transitory time till the set up temperature is reached by the sample has been studied with a thermocouple located in a protected position very close together the sample inside the work-tube. It was checked that it usually takes about 50 seconds till the fixed temperature of 350 ºC is reached; what means an error of 1.3 % in the first stage of annealing (1 hour), thus, for the rest of thermal stages (4-10 hours) it should be considered negligible.

On the other hand, for tracks (low fluences of Br 45 MeV) thermal annealing treatments were carried out at different temperatures in the range of 250 ºC - 350 ºC and for different time scales, from very short till long times. A specific annealing setup has been designed for this purpose trying to be reliable and minimizing the transitory till the sample reaches the fixed temperature.

In this sense, we built a system that consisted of an aluminum solid block with a flat horizontal surface with a cylindrical cartridge heating element inside and a thermocouple located just under the position of the sample. By this way, these elements form and integral part of the heating element to ensure excellent thermal uniformity. The thermocouple is located in a protected position between the outside, where the sample will be, and heating element, allowing a rapid and trusty measurement of the temperature. The temperature of the aluminum holder was controlled by an external Eurotherm controller. The aluminum block is heated at the desired temperature and then the sample was placed quickly on the horizontal hot surface after a few seconds of pre-heating the sample by holding it close to the hot surface. With the infrared camera it was checked that the final rise time for the temperature on the sample (surface) was in all cases below 3 s, which is considered acceptable. Note that this set-up was convenient for some of the short annealings performed at the highest temperatures (for example, 30 sec at 350 ºC).

6.2.1. Thermal annealings before chemical etching.

Thermal treatments after irradiation may anneal out some of the defects generated in and around the track and thus influence the subsequent etching rates and pore morphologies. After previous ion irradiation with Br at 46 MeV ions, a few samples were annealed for one hour in air at temperatures of 150 ºC, 175 ºC, 200 ºC, and 300 ºC, respectively. On the other hand, Br 22 MeV ions irradiated samples have been annealed at 150 ºC and 300 ºC.

For the thermal annealings of the irradiated samples, a tubular furnace Carbolite with an integrated Eurotherm temperature controller at a fixed temperature is used. Subsequently, all samples were etched in 40% HF aqueous solution at RT.

Part II. References.

[1]C. Pascual, *"Experimental determination of stopping forces for ions in matter"*, PhD. Dissertation, Departamento de Física Aplicada, Universidad Autónoma de Madrid (UAM), Madrid, 2004.

[2]A. Climent-Font, F. Pászti, G. García, M.T. Fernández-Jiménez and F. Agulló-López, *"First measurements with the Madrid 5 MV tandem accelerator"*, Nucl. Instr. and Meth. B 219-220 (2004) 400-404.

[3]D.J.W. Mous, A. Gottdang, R. G. Haitsma, G. García López, A. Climent-Font, F. Agulló-López and D. O. Boerma, *Proceedings CAARI*, 2002.

[4]A. Gottdang, D. J. W. Mous and R. G. Haitsma, *"The novel HVEE 5 MV Tandetron™"*, Nucl. Instr. and Meth. B 190 (2002) 177.

[5]High Voltage Engineering. (URL: http://www.highvolteng.com/).

[6]J. Miranda, *"Técnicas analíticas de origen nuclear: Un curso introductorio"*, Vol., (Ed.), Instituto de Física, UNAM. Cap. 1, Mexico, 2000.

[7]W.T. Diamond, Y. Imahori, J. W McKay, J. S. C. Wills and H. Schmeing, *"Efficient negative-ion sources for tandem injection"*, Rev. of Scientific Instruments 67 (1996) 1404-1409.

[8]B. Hartmann, S. Kalbitzer and Ch. Klatt, *"Energy spread of ion beams passing a gas stripper"*, Nucl. Instr. and Meth. B (1997) 490-499.

[9]Centro de Microanálisis de Materiales. (http://www.cmam.uam.es).

[10]Panmure Instruments Ltd. (URL: http://www.panmurescientific.com).

[11]W. Barth, et al., *"Development of the UNILAC Towards a Megawatt Beam Injector"*, Proc. of *22nd International LINAC Conference*, Luebeck, Germany, 2004, pp. 204.

[12]W. Barth, et al., "UNILAC Status and Developments" (GSI Report), 2003.

[13]http://www.gsi.de/portrait/index.html.

[14]H. Geiger, and E. Marsden, *"On the diffuse reflection of the α-particles"*, Proc. Roy. Soc. London 82 A (1909) 495-500.

[15]E. Rutherford, *"The scattering of α and β particles by matter and the structure of the atom"*, Phil. Mag. 21 (1911) 669-688.

[16]W.K. Chu, J. W. Mayer and M. A. Nicolet, *"Backscattering Spectrometry"*, Vol., (Ed.), Academic Press, New York, 1978.

[17]A.F. Gurbich, "*Ion Beam Analysis Nuclear Data Library*". http://www-nds.iaea.org/ibandl/, 2003.

[18]J. Lindhard, *"Influence of crystal lattice on motion of energetic charged particles"*, K. Dan. Vidensk. Selsk. Mat. Fys. Medd. 34 (1965) 14.

[19]L.C. Feldman, J. W. Mayer and S. T. Picraux *"Materials Analysis by Ion Channeling"*, Vol., (Ed.), Academic Press, New York, 1982.

[20]D.S. Gemmell, *"Channeling and related effects in the motion of charged particles through crystals"*, Rev. Mod. Phys. 46 (1974) 129-227.

[21]J.R. Tesner, M. Nastasi, J. C. Barbour, C. J. Maggiore and J. W. Mayer, (Ed.), *Handbook of Modern Ion Beam Materials Analysis*, Materials Research Society, 1995.

[22]M. Mayer, SIMNRA, Version 6.04, Max-Plank-Institut für Plasmaphysik. Matej.Mayer@ipp.mpg.de. http://www.rzg.mpg.de/~mam/.

[23]J.R. Tesmer, and M. Nastasi, *"Handbook of Modern Ion Beam Materials Analysis"*, Vol., (Ed.), MRS, Pittsburg, Pennsilvania (USA), 1995.

[24]R.C. Bird, and J. S. Williams, *"Ion beams for materials analysis"*, Vol., (Ed.), Academic Press, London, 1989.

[25]E. Albertazzi, M. Bianconi, G. Lulli, R. Nipoti and M. Cantiano, *"Different methods for the determination of damage profiles in Si from RBS-channeling spectra: a comparison"*, Nucl. Instr. and Meth. B 118 (1996) 128-132.
[26]G. Binnig, and H. Rohrer, *"Scanning tunneling microscopy"*, Helv. Phys. Acta 55 (1982) 726.
[27]G. Binnig, C. F. Quate and C. H. Gerber, *"Atomic force microscope"*, Phys. Rev. Lett. 56 (1986) 930-933.
[28]T.R. Albrecht, and C. F. Quate, *"Atomic resolution imaging of a nonconductor by atomic force microscopy"*, J. Appl. Phys. 62 (1987) 2599.
[29]J.W. Hong, D. D. Kahng, J. C. Shin, H. J. Kim and Z. G. Khim, *"Detection and control of ferroelectric domains by an electrostatic force microscope"*, J. Vac. Sci. Technol. B 16 (1998) 2942.
[30]J.W. Hong, S. Park and Z. G. Khim, *"Measurement of hardness, surface potential, and charge distribution with dynamic contact mode electrostatic force microscope"*, Rev. Sci. Instrum. 70 (1999) 1735.
[31]F. Saurenbach, and B. D. Terris, *"Imaging of ferroelectric domain walls by force microscopy"*, Appl. Phys. Lett. 56 (1990) 1703.
[32]B.D. Terris, J. E. Stern, D. Rugar and H. J. Mamin, *"Contact electrification using force microscopy"*, Phys. Rev. Lett. 63 (1989) 2669-2672.
[33]A. Gruverman, O. Auciello and H. Tokumoto, *"Scanning Force Microscopy for the Study of Domain Structure in Ferroelectric Thin Films"*, J. Vac. Sci. Technol. B 14 (1996) 602-605.
[34]A. Gruverman, O. Auciello and H. Tokumoto, *"Scanning Force Microscopy: Application to Nanoscale Studies of Ferroelectric Domains"*, Integr. Ferroelectrics 19 (1998) 49-83.
[35]O. Kolosov, A. Gruverman, J. Hatano, K. Takahashi and H. Tokumoto, *"Nanoscale Visualization and Control of Ferroelectric Domains by Atomic Force Microscopy"*, Phys. Rev. Lett. 74 (1995) 4309-4312.
[36]M. Nonnenmacher, M. P. O'Boyle and H. K. Wickramasinghe, *"Kelvin probe force microscopy"*, Appl. Phys. Lett. 58 (1991) 2921.
[37]R. Howland, and L. Benatar, *"A Practical Guide to Scanning Force Microscopy"*, Vol., (Ed.), Park Scientific Instruments, 1993.
[38]R. Wiesendanger, *"Scanning Probe Microscopy and Spectroscopy: Methods and Applications"*, Vol., (Ed.), Cambridge University Press, Cambridge, 1994.
[39]D. Sarid, *"Scanning Force Microscopy with Applications to Electric, Magnetic and Atomic Forces"*, Vol., (Ed.), Oxford University Press, New York, 1994.
[40]T. Sakurai, and Y. Wantanabe, *"Advances in Scanning Probe Microscopy"*, Vol., (Ed.), Springer, New York, 2000.
[41]P. West, *"Introduction to Atomic Force Microscopy"*, Vol., (Ed.), Pacific Nanotechnology, 2006.
[42]S. Morita, *"Roadmap of Scanning Probe Microscopy"*, Vol., (Ed.), Springer, New York, 2007.
[43]J. Loos, *"The art of SPM: Scanning Probe Microscopy in Material Science"*, Adv. Mater. 17 (2005) 1821.
[44]Nanotec TM Electrónica. www.nanotec.es.
[45]S. Alexander, L. Hellemans, O. Marti, J. Schneir, V. Elings, P. K. Hansma, M. Longmire and J. Gurley, *"An atomic-resolution atomic-force microscope implemented using an optical lever"*, J. Appl. Phys. 65 (1989) 164.
[46]G. Meyer, and N. M. Amer, *"Optical-beam-deflection atomic force microscopy: The NaCl (001) surface"*, Appl. Phys. Lett. 56 (1990) 2100.

[47]G. Meyer, and N. M. Amer, *"Simultaneous measurement of lateral and normal forces with an optical-beam-deflection atomic force microscope"*, Appl. Phys. Lett. 57 (1990) 2089.
[48]NT-MDT. Calibration Grating TGX1. http://www.ntmdt-tips.com/catalog/gratings/afm_cal/products/TGX1.html.
[49]NT-MDT. Calibration Grating TGZ1. http://www.ntmdt-tips.com/catalog/gratings/afm_cal/products/TGZ1.html.
[50]I. Horcas, R. Fernández, J. M. Gómez-Rodríguez, J. Colchero, J. Gómez-Herrero and A. M. Baro, *"WSxM: A software for scanning probe microscopy and a tool for nanotechnology"*, Rev. Sci. Instrum. 78 (2007) 013705.
[51]C. Bai, *"Scanning Tunneling Microscopy and Its Application"*, Springer Series in Surface Science, Vol., (Ed.), Springer Verlag, Berlin, 1999.
[52]E. Meyer, H. J. Hug and R. Bennewitz, *"Scanning Probe Microscopy. The lab on a tip"*, Vol., (Ed.), Spring-Verlag, Berlin, 2004.
[53]C. Kittel, *"Introduction to Solid State Physics"*, Vol., (Ed.), Wiley, New York, 1996.
[54]A. Torii, M. Sasaki, K. Hane and S. Okuma, *"Adhesion of Microstructures Investigated by Atomic Force Microscope"*, Sens. Actuators A. 40 (1994) 71.
[55]T. Stifter, O. Marti and B. Bhushan, *"Theoretical investigation of the distance dependence of capillary and van der Waals forces in scanning probe microscopy"*, Phys. Rev. B 62 (2000) 13667-13673.
[56]M. Di Ventra, S. Evoy and J. R. Heflin, *"Introduction to Nanoscale Science and Technology"*, Vol., (Ed.), Springer, New York, 2004.
[57]Y. Martin, C. C. Williams and H. K. Wickramasinghe, *"Atomic force microscope-force mapping and profiling on a sub 100-Å scale"*, J. Appl. Phys. 61 (1987) 4723.
[58]J. Polesel-Maris, and S. Gauthier, *"A virtual dynamic atomic force microscope for image calculations"*, J. Appl. Phys. 97 (2005) 044902.
[59]Q. Zhong, D. Inniss, K. Kjoller and V. B. Elings, *"Fractured polymer/silica fiber surface studied by tapping mode atomic force microscopy"*, Surf. Sci. Lett. 290 (1993) L688-L692.
[60]C. Odin, J. P. Aimé, Z. El kaakour and T. Bouhacine, *"Tip's finite size effects on atomic force microscopy in the contact mode: simple geometrical considerations for rapid estimation of apex radius and tip angle based on the study of polystyrene latex balls"*, Surface Science 317 (1994) 321-340.
[61]A. Gruverman, O.Auciello and H.Tokumoto, *"Imaging and Control of Domain Structures in Ferroelectric Thin Films via Scanning Force Microscopy"*, Ann. Rev. of Mat. Sci. 28 (1998) 101-124.
[62]Y. Leng, and C. C. Williams, *"Electrostatic characterization of biological and polymeric surfaces by electrostatic force microscopy"*, Coll. Surf. A 93 (1994) 335-341.
[63]Nanotec Electronica S.L. Cervantes AFM System. http://www.nanotec.es/products/cervantes.php.
[64]Nanotec Electronica S.L. Technical specifications: Nanotec Scanning Probe Microscope Control System (Electronics). http://www.nanotec.es/products/dulcinea.php.
[65]S. Morita, Y. Sugawara, K. Yokoyama and T. Uchihashi, in: *"Atomic Scale Origins of Force Interaction"*. B. Bhushan, (Ed.), *Fundamentals of Tribology and Bridging the Gap Between the Macro- and Micro/Nanoscales*, Springer, 2001, pp. 103-120.

[66]MikroMasch. Datasheet NSC18/Al BS. http://www.spmtips.com/nsc/18/si3n4.
[67]Nanosensors. Datasheet AR5-NCHR. http://www.nanoandmore.com/AFM-Probe-AR5-NCHR.html.
[68]Nanosensors. Datasheet PPP-NCHR. http://www.nanosensors.com/PPP-NCHR.htm.
[69]Veeco Instruments. TESP - Premium Line Metrology Probes. http://www.brukerafmprobes.com/p-3394-tesp.aspx.
[70]F. Bergamini, M. Bianconi and S. Cristiani, *"Wet and vapor etching of tracks produced in SiO_2 by Ti ion irradiation"*, Nucl. Instr. Meth. B 257 (2007) 593-596.
[71]R.G. Musket, J.M. Yoshiyam, R.J. Contolinic and J.D. Porter, *"Vapor etching of ion tracks in fused silica"*, J. Appl. Phys. 91 (2002) 5760-5764.
[72]M. Skupinski, J. Jensen, A. Johansson, G. Possnert, M. Boman, K. Hjort and A. Razpet, *"Nanopattern transfer to SiO_2 by ion track lithography and highly selective HF vapor etching"*, J. Vac. Sci. Technol. B 25 (2007) 862-867.
[73]M. Toulemonde, C. Trautmann, E. Balanzat, K. Horjt, A. Weidinger, *"Track formation and fabrication of nanostructures with MeV-ion beams"*, Nucl. Instr. Meth. B 216 (2004) 1-8.
[74]A. García-Navarro, A. Méndez, J. Olivares, G. García, F. Agulló-López, M. Zayat, D. Levy and L. Vazquez, *"Morphology of ion tracks and nanopores in $LiNbO_3$ produced by swift-ion-beam irradiation"*, Nucl. Instr. Meth. B 249 (2006) 172-176.
[75]A. García-Navarro, *"Irradiación con iones pesados de alta energía en dieléctricos para aplicaciones fotónicas: Guías de onda en $LiNbO_3$"*, PhD. Dissertation, Departamento de Física de Materiales, Universidad Autónoma de Madrid (UAM), Madrid, July 2007.
[76]J.M. Cabrera, F. Agulló-López and F. J. López, *"Óptica Electromagnética II: Materiales y Aplicaciones"*, Vol. 2, (Ed.), Addison-Wesley/Universidad Autónoma de Madrid, 2000.
[77]B.E.A. Saleh, and M. C. Teich, *"Fundamentals of Photonics"*, Vol., (Ed.), Wiley Series in Pure and Applied Optics. Wiley Interscience, USA, 1991.
[78]J. Olivares, *"Guías de onda planares en $LiNbO_3$ por intercambio protónico"*, PhD. Dissertation, Departamento de Física de Materiales, Univ. Autónoma de Madrid, Madrid, 1994.
[79]A. Alcázar de Velasco, *"Daño óptico en guías de onda PE:$LiNbO_3$"*, PhD. Dissertation, Departamento de Física de Materiales, Universidad Autónoma de Madrid, Madrid, 2004.
[80]G. de la Paliza, *"Guías de onda PE:$LiNbO_3$ para aplicaciones fotorrefractivas"*, PhD. Dissertation, Dpto. Fisica de Materiales, Univ. Autónoma de Madrid (UAM), Madrid, 2004.
[81]P.K. Tien, R. Ulrich, and R. J. Martin, *"Modes of propagating light waves in thin deposited semiconductor films"*, Appl. Phys. Lett. 14 (1969) 291.
[82]P.K. Tien, and R. Ulrich, *"Theory of Prism-Film Coupler and Thin-Film Light Guides"*, J. Opt. Soc. Am. 60 (1970) 1325-1337.
[83]P. Hertel, and H. P. Menzler, *"Improved inverse WKB method procedure to reconstruct refractive index profiles of dielectric planar waveguides"*, Appl. Phys. B 44 (1987) 75-80.
[84]J.P. Gordon, *"Optics of general guilding media"*, The Bell System Technical Journal 45 (1966) 321-332.

[85]A. Gedeon, *"Comparison between rigorous theory and WKB-analysis of modes in graded-index waveguides"*, Opt. Comm. 12 (1974) 329-332.
[86]J.M. White, and P. F. Heidrich, *"Optical waveguide refractive index profiles determined from measurement of mode indices: A simple analysis"*, Appl. Opt. 15 (1976) 151-155.
[87]K.S. Chiang, *"Construction of refractive-index profiles of planar dielectric waveguides from the distribution of effective indexes"*, J. Lightwave Technology 3 (1985) 385-391.
[88]P. Mathey, and P. Jullien, *"Numerical analysis of a WKB inverse method in view of index profile reconstruction in diffused waveguides"*, Optics Comm. 122 (1996) 127-134.
[89]B.M. Foley, P. Melman and K. T. Vo, *"Novel loss measurement technique for optical waveguides by imaging of scattered light"*, Electr. Lett. 28 (1992) 584-585.
[90]Y. Okamura, S. Yoshinaka and S. Yamamoto, *"Measuring mode propagation losses of integrated optical waveguides: a simple method"*, Appl. Opt. 22 (1983) 3892-3894.
[91]The Nobel Prize in Physics. (http:www.nobelprize.org/nobel_prizes/physics/laureates/1986/), 1986.
[92]D. Williams, and C. Carter, *"Transmission Electron Microscopy: A Textbook for Materials Science"*, Vol., (Ed.), Plemum Press, New York, 1996.
[93]I. P. I. Halbleiterphysik. CM200-FEG-UT. http://www.ph4.physik.uni-goettingen.de/ulbrich/seibt/cm200.html, (09.11.2007).
[94]FEI Company. Nova 600 NanoLab. http://www.fei.com/, (05.06.2006).
[95]Veeco Instruments Inc., *Dektak 150 Surface Profiler.*, Veeco Instruments Inc., www.veeco.com, Jun. 2007.
[96]C.L. Sones, S. Mailis, W. S. Brocklesby, R. W. Eason and J. R. Owen, *"Differential etch rates in z-cut $LiNbO_3$ for variable HF/HNO_3 concentrations"*, J. Mat. Chem. 12 (2002) 295-298.
[97]F. Schrempel, T. Gischkat, H. Hartung, E.-B. Kley, W. Wesch and A. Tünnermann, *"High aspect ratio microstructures in $LiNbO_3$ produced by Ion Beam Enhanced Etching"*, Mater. Res. Soc. Symp. Proc. 908E (2005).
[98]F. Schrempel, T. Gischkat, H. Hartung, E.-B. Kley and W. Wesch *"Ion beam enhanced etching of $LiNbO_3$"*, Nucl. Instr. Meth. B 250 (2006) 164-168.
[99]T. Gischkat, F. Schrempel, Th. Höche and W. Wesch, *"Annealing behavior of lithium niobate irradiated with He-ions at 100 K"*, Nucl. Instr. Meth. B 267 (2009) 1492-1495.
[100]M. Toulemonde, N. Enault, J. Fan and F. Studer, *"Does continuous trail of damage appear at the change in the electronic stopping power damage rate?"*, J. App. Phys. 68 (1990) 1545.
[101]C. Trautmann, S. Bouffard and R. Spohr, *"Etching threshold for ion tracks in polyimide"*, Nucl. Instr. Meth. B 116 (1996) 429-433.
[102]C. Trautmann, C. Dafour, E. Paumier, R. Spohr and M. Toulemomde, *"Track etching in amorphous metallic $Fe_{81}B_{13.5}Si_{3.5}C_2$"*, Nucl. Instr. Meth. B 107 (1996) 397-402.
[103]R. Braddy, P. T. McTigue and B. Verity, *"Equilibria in moderately concentrated aqueous hydrogen fluoride solutions"*, J. Fluorine Chem. 66 (1994) 63-67.
[104]H.H. Broene, and T. DeVries, *"The Thermodynamics of Aqueous Hydrofluoric Acid Solutions"*, J. Am. Chem. Soc. 69 (1947) 1644-1646.

[105]P. McTigue, Th. A. O'Donnell and B. Verity, *"The determination of fluoride-ion activities in moderately concentrated aqueous hydrogen-fluoride"*, Aust. J. Chem. 38 (1985) 1797-1807.
[106]J. Khorami, R. Beaudoin and H. Menard, *"Study of water-HF mixtures by Fourier transform infrared spectroscopy"*, Can. J. Chem. 65 (1987) 817-820.
[107]P.A. Giguère, and S. Turell, *"The nature of hydrofluoric acid. A spectroscopic study of the proton-transfer complex $H3O^{+}F^{-}$."*, J. Am. Chem. Soc. 102 (1980) 5473-5477.
[108]L.J. Warren, *"The measurement of pH in acid fluoride solutions and evidence for the existence of $(HF)_2$"*, Anal. Chim. Acta 53 (1971) 199.
[109]D.M. Knotter, *"Etching Mechanism of Vitreous Silicon Dioxide in HF-Based Solutions"*, J. Am. Chem. Soc. 122 (2000) 4345–4351.
[110]K. Osseo-Asare, *"Etching Kinetics of Silicon Dioxide in Aqueous Fluoride Solutions: A Surface Complexation Model"*, J. Electrochem. Soc. 143 (1996) 1339-1347.
[111]M. Prokopowicz-Prigogine, Glastech. Ber. 62 (1989) 249.
[112]H.S. Fogler, K. Lund and C. C. McCune, *"Acidization III-The kinetics of the dissolution of sodium and potassium feldspar in HF/HCl acid mixtures"*, Chem. Eng. Sci. 30 (1975) 1325-1332.
[113]S. Verhaverbeke, I. Teerlinck, C. Vinckier, G. Stevens, R. Cartuyvels and M. M. Heyns, *"The etching mechanisms of SiO_2 in hydrofluoric acid"*, J. Electrochem. Soc. 141 (1994) 2852-2857.
[114]J.S. Judge, *"A study of the dissolution of SiO_2 in acidic fluoride solutions"*, J. Electrochem. Soc. 118 (1971) 1772-1775.
[115]J. Reinisch, F. Schrempel, T. Gischkat and W. Wesch, *"Etching of Ion Irradiated $LiNbO_3$ in Aqueous Hydrofluoric Solutions"*, J. Electrochem. Soc. 155 (2008) D298-D301.
[116]F.A. Cotton, and G. Wilkinson, *"Advanced Inorganic Chemistry"*, Vol. 5th edition, pp. 104, (Ed.), Wiley, New York, 1988.
[117]Photox Optical Systems Ltd. Lithium Niobate Crystal ($LiNbO_3$) Properties. http://www.photox.co.uk/linbo3.htm, 2008.
[118]R. Spohr, in: *"Ion Tracks and Microtechnology: Basic Principles and Applications"*. K. Bethge, (Ed.), Vieweg, Braunchsweig, 1990.
[119]R.L. Fleischer, P.B. Price, and R.M. Walker, *"Nuclear Tracks in Solids: Principles and Applications"*, Vol., (Ed.), University of California Press, Berkeley, Calif., 1975.

Part III.

Results.

Chapter 7

Kinetics of amorphization induced by swift ion beams in lithium niobate: The role of defective preamorphous areas (halos).

7.1. Introduction.

In this Chapter we will focus our attention on the study of the structure of the damage on Lithium Niobate induced by dense electronic excitation following the slowing down of high energetic ion beams, that is, in the electronic regime, where the situation is poorly understood. The purpose is to critically discuss the main features about ion-beam amorphization of dielectric crystals, emphasizing the competition between the nuclear collision and electronic excitation routes.

In order to get a deeper understanding the amorphization induced by the transfer of energy left by the swift heavy ions on the target electrons to the atomic network, one has to consider the results in various conditions of irradiations exhibiting a wide palette of physical properties. Thus, we will face this challenge from a double perspective. From one side, selecting experimental conditions with the aim of studying the kinetic of evolution of the damage induced by ion bombardment with stopping power below and above the amorphization threshold; on the other one, a theoretical strategy is developed. Respect to the first part, we will introduce some new experimental results obtained on $LiNbO_3$ from RBS-C techniques, which are not consistent with the mostly used *thermal spike* scheme and offer new clues for analysis. These results will be, subsequently, discussed within a recent damage approach model developed for $LiNbO_3$, in which amorphization results from the accumulation of the defects generated by the irradiation (*cumulative model*) through non-radiative decay of localized excitons. This approximation relies on the synergy between the thermal spike generated by electron-phonon interaction and the non-radiative decay of localized "self-trapped" excitons. This new scenario offers a better perspective for a comparative analysis of the two types of damage processes.

A main piece of information concerning ion-beam damage and amorphization is the kinetics of the process, i.e., the evolution with irradiation fluence of the disordered (damaged) area f_a (or amorphized fraction) up to the amorphization stage, $f_a = 1$. By using a recently reported MonteCarlo code [1] it will be shown that the kinetic data in a broad range of stopping powers can be adequately explained within such a model. Calculations have been carried out to describe the effect of single impact as well as multiple impact "high fluence" irradiations. In this sense, a MonteCarlo approach is necessary to simulate the evolution of the damage morphology with irradiation fluence from the single track regime to the overlapping track regime. A detailed comparison between the morphologies found for sub-threshold and above threshold irradiations is presented. Moreover, a good representation of the Avrami's type kinetics for amorphization has been achieved and it is in fair accordance with experiment. So far, a microscopic physical analysis of such behaviour has not been, yet, offered although it is a clear indication that the process is cumulative. It is expected that a proper understanding of the kinetic laws should throw some light on the amorphization and damage mechanisms. Consequently, our work provides strong support for the excitonic model and yields a formalism to understand amorphization as the cumulation of point defects. Moreover, it yiels the physical clues to understand the role of defective preamorphous areas around the ion path trajectory inside the crystal. The main differences with the nuclear collision route will be emphasized.

Finally, it is worthy to notice that in this framework of the study on the structure and the evolution of the damage in the electronic excitation regime, the information revealed from the latent amorphous tracks and the defective halo, should be very useful to understand the nature of

electronic damage and its operative mechanisms, which are still not sufficiently known, existing a great controversy. This is, at variance with nuclear collision damage, more extensively investigated [2, 3], where advanced simulation codes are available and provide a satisfactory quantitative description of the amount and morphology of the damaged regions.

7.2. Assessment of swift-ion damage by RBS-C: determination of the amorphization threshold.

In this section a theoretical strategy has been developed to quantitatively assess the ion-beam damage as measured by Rutherford-backscattering spectrometry under channeling conditions (RBS-C) in $LiNbO_3$ crystals. The approach is based on a recent exciton decay model to calculate the concentration of defects generated by the incoming ions as a function of their stopping power. To describe the channeled RBS yield the model takes into account the amorphous (core) as well as the defective halo contributions to the defect tracks caused by the ion impacts. It is concluded that the halo may significantly influence the assessed damage.

It has been stated earlier that, heavy damage and amorphization can be produced in dielectric crystals by bombarding with swift ions through electronic excitation mechanisms [4-11]. In fact, for ions having specific energies ≥ 0.1 MeV/amu, the electronic stopping power S_e is dominant over the nuclear stopping power S_n along most of the trajectory. The electronic excitation damage presents remarkable differential features in comparison to that induced by elastic nuclear collisions and implantation. For $LiNbO_3$ (as well as for other amorphizable dielectrics) the key feature is the occurrence of a well-defined threshold (S_{th}) in the electronic stopping power needed to induce amorphization (*thresholding*). In fact, every single ion generates a well-defined amorphous track of nanometer diameter whenever its stopping power is above a threshold value ($S_e > S_{th}$). These tracks have been observed and investigated by a variety of techniques (TEM [12, 13], STM, AFM [14, 15], small angle X-ray [16], neutron diffraction [17], RBS/C [8-10, 18-20] and optical methods [10, 11, 21, 22], among others).

We have to point out that the precise determination of the threshold, S_{th}, is essential to understand the mechanisms of electronic damage and test possible physical models. Such a determination relies on the measurement of the area of the damage track, σ, (often called damage cross-section) as a function of S_e and its extrapolation to zero radius. In practice, this is accomplished by measuring the disordered areal fraction at low enough fluences where tracks are not overlapped and a linear slope can be assumed. Most experiments have used RBS/channeling techniques to assess the damage area as a function of irradiation. The results of such measurements include two contributions, namely, a central amorphous *core* surrounded by an extensive *halo* containing point-like and extended defects [13, 23, 24]. Therefore, one expects that the outcome of any damage measurement should be strongly dependent on the sensitivity of the method to either the core or the halo. A very clear illustration of this assertion is provided by the data [24] on the complex structure of tracks in LiF combining three different measuring techniques: optical absorption, chemical etching and small-angle X-ray spectroscopy (SAXS). In particular the structure included a small core of 1-2 nm surrounded by a large halo (20-30 nm) containing F-centers.

The purpose of this section is to apply a recent theoretical scheme to discuss the RBS-C method for damage assessment and elucidate the relative role played by *core* and *halo*. The

work focuses on $LiNbO_3$ for which a substantial amount of ion-beam irradiation data is available. We propose an approach based on an exciton decay model [25] that allows one to calculate the concentration of point defects generated by every single ion impact. We are not aware of any other alternative model to deal with the core/halo problem. An overall back-scattering factor is introduced to quantify the de-channeled ion-beam fraction caused by the defects induced by irradiation (including both, core and halo). It is assumed that such a factor is a constant up to a threshold concentration where the relative backscattering yield rises abruptly to 1 (full random fraction). One should remark that the analysis presented here exclusively refers to the method of measurement and has nothing to do with real differences in measured values that arise when ions with different masses (velocities) are used [5, 6] in the irradiation experiments (*velocity effect*).

7.2.1. Profile of point defect concentration at a track: amorphous core and halo.

One of the most important results obtained from the theoretical model for electronic damage, **Non-radiative excitonic-decay model (**described in **Chapter 1)**, is the radial profile of the point defect concentration,

$$n(z,r) = \int_0^\infty dt \nu_0 N_X(z,r,t) \exp\left(-\frac{\varepsilon}{kT(z,r,t)}\right), \qquad (1)$$

where $N_X(z,r,t)$ has to be obtained from a full solution of **Eq. (2)**; which, using cylindrical coordinates (r, z) with the ion trajectory along the z axis, describes the rate equation for the decay of the local exciton concentration N_X generated by the impact,

$$\frac{dN_X(z,r,t)}{dt} = -N_X(z,r,t)\left\{\nu_0 \exp\left(-\frac{\varepsilon}{kT(z,r,t)}\right) + \frac{1}{\tau}\right\}, \qquad (2)$$

ν_0 being a frequency factor, τ the radiative lifetime and T (z, r, t) the evolution of the temperature profile in the spike.

Eq. (1) predicts a strongly superlinear dependence of n on stopping power but without any definite threshold. Finally, it is assumed that when the local concentration $n(z, r)$ reaches a threshold value, n_{th}, corresponding to S_{th}, the crystal lattice collapses (*defect driven transition* [26]) and becomes amorphous. As an illustration, the results obtained from **Eq. (1)** are shown in **Fig. 1** for two different values of S_e. The threshold concentration level for amorphization, n_{th}, is marked on the figure and corresponds to S_{th} = 6 keV/nm (discussion in **Section 5.2.3**). For S_e = 3 keV/nm, below threshold, no amorphization is induced and the track only contains point defects (halo). For S_e = 7 keV/nm, above threshold, a circular amorphous area (core) is generated, as illustrated in the figure. Outside the core, the existing point defects (halo) are also expected to contribute to observable effects on physical properties. Formally speaking one could define a radius for the halo, R_H, as that where the defect concentration around the ion trajectory decreases down to a value characteristic of the material (e.g. 10^{-5} ppm). A more instrumental definition of the halo will be described in the next section on ion-beam channeling.

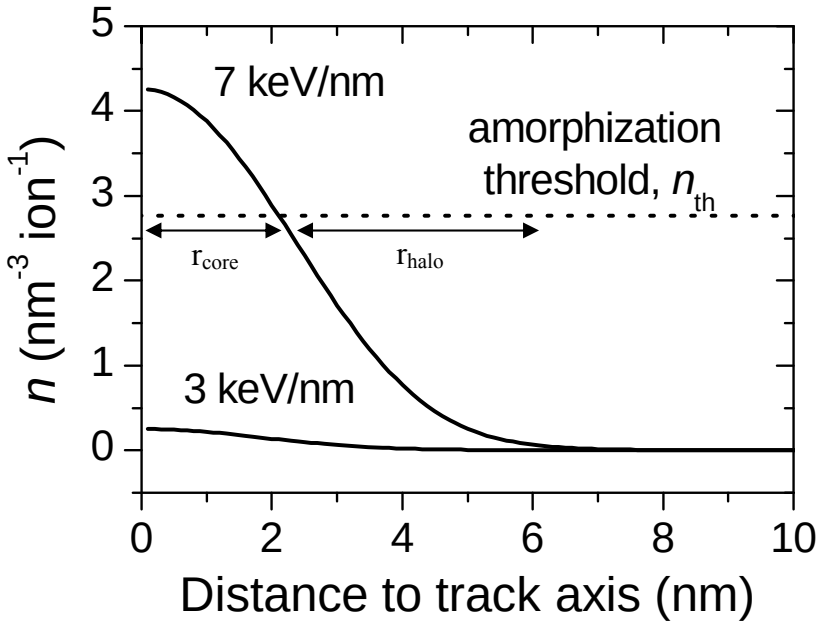

Fig. 1. Theoretical defect concentration profiles obtained from the excitonic model for ions with S_e = 3 keV/nm and 7 keV/nm impinging on a $LiNbO_3$ crystal. The amorphization threshold (n_{th}) is indicated and corresponds to the defect concentration generated at the surface by an ion with S_e = 6 keV/nm.

7.2.2. Experimental determination of halo and track radius by (RBS-C).

In the RBS-C experiments, mostly used by researchers, one uses an ion beam incident along a given channeling (crystallographic) direction and measures the fraction $\chi(z)$ of the beam that becomes de-channeled and presents a random yield after a very low irradiation fluence (*linear response region*). This fraction is interpreted as the areal fraction that becomes disordered by the irradiation at the depth where the channeling yield has been measured. The analysis is developed within the framework of the two-beam formulation [27, 28]. It assumes that the RBS yield $\chi(z)$ for the considered axial (or planar) direction is given by

$$\chi(z) = \chi_R(z) + \{1 - \chi_R(z)\}\Sigma^*(z) \qquad (3)$$

where $\chi_R(z)$ is the fraction of the beam that has become de-channeled down to a depth z and $\Sigma^*(z)$ is the relative area contributing to the backscattering yield. At the sample surface, ($z = 0$ and $\chi_R = 0$), but correcting for the surface peak, **Eq. (3)** simplifies to $\chi(0) = \Sigma^*(0)$. The damage cross section per ion impact writes $\sigma = \Sigma^*(0) / \phi$, where ϕ is the ion fluence.

In order to apply our model to the prediction of the RBS-C yield one has relate the effective concentration of backscattering centers, n^*, to the true concentration of defects generated by irradiation, n, through the backscattering factor $f = n^*/n$. It represents the enhancement/reduction factor in the scattering cross-section for each individual point defect in comparison to the area of the atomic cell. For low enough concentrations, i.e. at the halo, it is expected that the distortions associated to the different defects are uncoupled and thus, f is nearly independent of the defect concentration [29]. Therefore, we assume that the "filter" function $n^*(n)$ is (see **Fig. 2**)

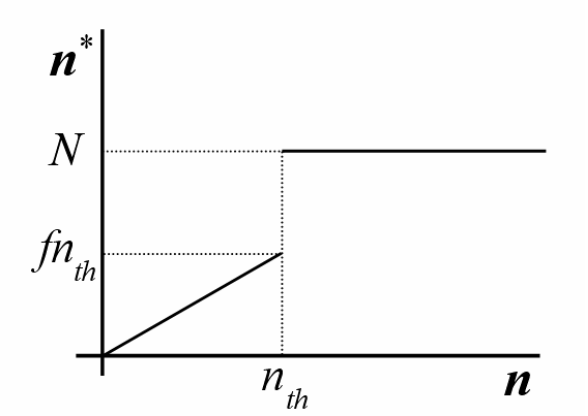

Fig. 2. Proposed "filter" function for the relation between the effective concentration of backscattering centers (n*) and the concentration of defects generated by irradiation (n).

$$n^* = f\,n \qquad \text{for} \quad n < n_{th}$$
$$n^* = N \qquad \text{for} \quad n \geq n_{th}, \qquad (\mathbf{4})$$

where N is the density of atoms in the sublattice mostly contributing to RBS-C, i.e., 18.9 Nb atoms nm^{-3} for experiments on $LiNbO_3$. The last relation indicates that when $n > n_{th}$, the whole volume becomes amorphized and contributes to random scattering.

Using the "filter" function ((**Eq. 4**)), we get from the model the value of σ that RBS-C experiments would provide for different values of f, $\sigma = \frac{1}{N}\int_0^\infty 2\pi r n^*(z,r)dr$.

7.2.3. Threshold determination: comparison to experiments.

Irradiation experiments at RT were performed on commercial congruent $LiNbO_3$ samples using F (5 MeV), O (5 MeV), Mg (29 MeV), Si (5, 7.5 MeV), Cl (11, 30, 46 MeV) and Cu (18, 50 MeV) ions in the 5 MV tandem accelerator at CMAM. These ions and energies cover an electronic stopping range from around 2.9 to 12 keV/nm. The damage at the surface of the samples was assessed by measuring the backscattering yield under axial (*Z*) channeling conditions for H irradiation (3 MeV) at sufficiently low fluences (10^{11} - 10^{14} cm^{-2}). (For more details on experiments, see [4, 20, 21]).

In **Fig. 3 (a, b)**, the experimental σ is plotted as a function of S_e for ion irradiations in $LiNbO_3$. In addition, the curves represent σ obtained from the model for several values of f. The parameters used for modeling were optimized in [25]. Calculations were done varying S_{th}. The best results, shown in **Fig. 3 (a, b)**, were obtained for S_{th} = 6 keV/nm. This corresponds to a threshold concentration n_{th} = 2.8 nm^{-3} (= 0.15 N). The curves fairly fit the experimental points for f in the range 0.5-1.0 (e.g. 0.9). This value is in rough accordance with [29]. In addition, one observes in RBS-C experiments (not shown) that the de-channeling yield abruptly increases to 1 (random value) when $\Sigma^*(0) \sim 0.13$. This corresponds to the threshold concentration $n_{th} = 0.15\,N$, giving $f \sim 0.9$ in agreement with **Fig. 3 (a, b).** Such a value for f shows that the defects generated in the excitation electronic regime have atomic-size dimensions. Several choices for this parameter have been tried for comparison.

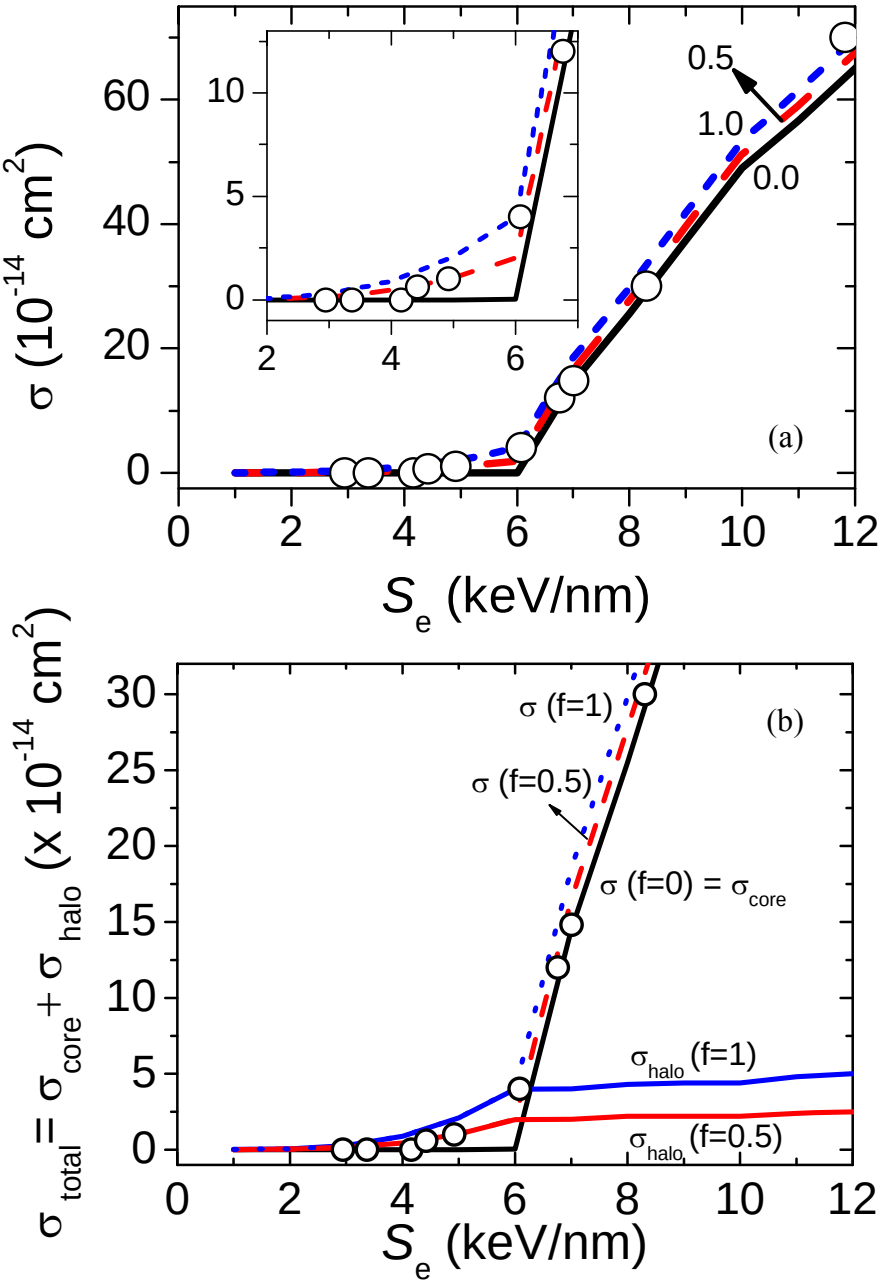

Fig. 3 (a, b). (a) Experimental damage cross section symbols obtained for several ions at a fluence of 1×10^{12} cm^{-2}. The curves are the damage cross sections obtained from the model for different values of the backscattering factor f (indicated with labels) and with S_{th}=6 keV/nm. The inset shows the sub-threshold behavior in detail. (b) The core-plus-halo cross-section (σ (f > 0)), and the contribution of the core (σ (f = 0), and the halo for different values of the de-channeling factor (f > 0) is explicitly shown (solid lines).

For f = 0, there is no halo contribution and the theoretical curve shows an abrupt threshold at S_{th} (solid line). For S_e above S_{th} the core-plus-halo cross-section (f > 0) is significantly enhanced with respect to the previous curve (f = 0) and presents two clear branches corresponding, respectively, to low and high stopping powers. The enhancement markedly decreases on moving to higher S_e. For $S_e < S_{th}$, where no amorphization is induced (there is no core) the contribution of the halo is still quite significant. In **Fig. 3 (b)** appears explicitly the contribution of the halo for different values of the de-channeling factor (f > 0). Moreover, the

role of halo is particularly relevant for stopping powers near or below threshold. One should note that for very high stopping powers [12] a relevant elastic strain distribution may contribute to the halo and it has not been considered here.

From extrapolation of the high-S_e branch in **Fig. 3 (a, b)** one can derive the threshold stopping power that leads to lattice amorphization. It is concluded that the determined threshold becomes underestimated when the contribution of the halo to de-channeling is not taken into account. This is particularly clear for stopping powers below threshold that still show significant damage (although no amorphization) and thus can be erroneously considered to be above threshold.

Optical methods have also been systematically applied to determine the amorphization threshold. They are powerful because the refractive index of the bombarded layer changes dramatically when amorphization occurs. In fact, $LiNbO_3$ crystals are initially birrefringent (n_o = 2.28 and n_e = 2.20) and become isotropic after irradiation (n = 2.10) [10]. On the other hand, the irradiated regions that do not undergo amorphization, experience only small changes in refractive index [30]. Although details are beyond the scope of this Chapter, we should highlight that S_{th} obtained from optical methods is in the range 5-6 keV/nm, in agreement with the value found solely by means of RBS-C data properly analyzed with our model.

7.2.4. Summary and conclusions.

As main conclusions obtained in this section we can state that, the amount of disorder that is assessed by RBS-C in $LiNbO_3$ has been analyzed using a recently proposed model to calculate the defect profile generated by every ion impact. The analysis describes the de-channeling caused at the surface by using a "filter" function $n^*(n)$. It is concluded that the amorphized area (core) of the track is markedly overestimated for stopping powers near the threshold value. The proposed scheme to describe the formation of the halo and predict its diameter represents, just, a first attempt for a quantitative analysis of the problem. Other alternative models have been invoked such as elastic strains or viscoelastic deformations [31, 32], but, so far, a quantitative analysis has not been carried out. Moreover, there is some evidence that at low stopping powers tracks may be discontinuous possibly due to statistical fluctuations in the energy transfer to the crystal. This feature should be also taken into account for a more rigorous and complete analysis [6, 33-35].

7.3. Experimental data on the amorphization kinetics induced by electronic excitation on $LiNbO_3$: summary of experiments.

For $LiNbO_3$ there is abundant experimental information on the effects of swift ion-beam damage. Above a certain stopping power threshold of around $S_{th} \approx 6$ keV/nm an amorphous track is generated by every ion impact in accordance with TEM measurements and less direct chemical etching and optical data. The threshold value depends slightly on ion and energy (*velocity effect*) but this effect will not be considered in this work. For increasing fluences the amorphous tracks overlap and eventually give rise to a homogeneous amorphous layer. This information is in accordance with the predictions of the thermal spike model mostly used by researchers. However, the amorphization kinetics measured for $LiNbO_3$ by RBS-C and optical

Ion	Crystallographic orientation LN substrates	Energy (MeV)	Fluences (10^{13} at/cm^2)	Stopping Power (S_e) (keV/nm)	RBS/C
O	X	5.0	20, 40, 60	3.1	H 2.2 MeV
F	X	5.1	0.1, 0.5, 1, 2, 4, 10, 20, 40, 100, 300	3.4	H 3 MeV
Si	Z	5.0	0.2, 0.4, 1, 2, 4, 10, 20, 40, 80, 200	4.2	H 3 MeV
Si	Z	7.5	0.1, 0.2, 0.4, 0.8, 1, 2, 4, 10, 20, 40, 80	5.3	H 3 MeV
Si	X	41	0.1, 0.2, 0.4, 1, 1.5, 2, 2.5, 3, 3.5, 4, 4.5, 5	5.2	H 3.8 MeV
Cl	X	11	0.08, 0.1, 0.2, 0.4, 0.8, 1, 2, 4, 20	6.1	H 2.2 MeV
Cl	X	46	0.2, 0.4, 0.8, 1	6.8	H 3 MeV
Br	Z	22	0.008, 0.016, 0.032, 0.064, 0.13, 0.16, 0.24, 0.32	8.7	He 3 MeV
Br	X, Z	45	0.005, 0.03, 0.05, 0.1, 0.15, 0.2, 0.25, 0.3	11.9	He 3 MeV

Table I. Parameters for the irradiations and RBS/C analyses.

methods show that amorphization can be induced both, *above and below the threshold value*. The available experimental information for the damage fraction at the sample surface is illustrated in **Fig. 6 (a-i)** for a number of stopping powers covering a wide range around the threshold [20]. Moreover this set of experimental data with stopping powers below and above threshold (S_{th}), we incorporate new experimental ones corresponding to series of samples irradiated with bromine 22 and 45 MeV ions.

The irradiation parameters are summarized in **Table I**. The performed irradiations, sweeping wide fluences ranges, have allowed us to study the evolution of the damage from the case of isolated defects tracks, to the overlapping regime resulting in the formation of an amorphous layer whose thickness increases with the fluence.

The electronic stopping power curves for all cases, derived from the SRIM code [36, 37], are shown in **Fig. 4**. Note that, with such irradiations, the region of stopping powers around the amorphization threshold value has been covered ($S_{th} \approx 5$ keV/nm): irradiations bellow the threshold (O 5 MeV and F 5.1 MeV ions), irradiations around the threshold (Si ions at various energies), that ones slightly above the threshold (Cl 11 and 45.8 MeV), and finally, experiments with stopping powers well above the amorphization threshold (Br 22 and 45 MeV ions). By this way, we are able to cover in this study different regimes of ion damage.

The characterization of the created disorder and the damage evolution of the irradiated samples was studied by RBS/C spectra taken along the *c*-axis using H and He ion beams with energies listed in **Table I**. The alignment procedure was performed on the virgin part of the crystal, covered by masks during the irradiation, in order to restrict any additional damage due

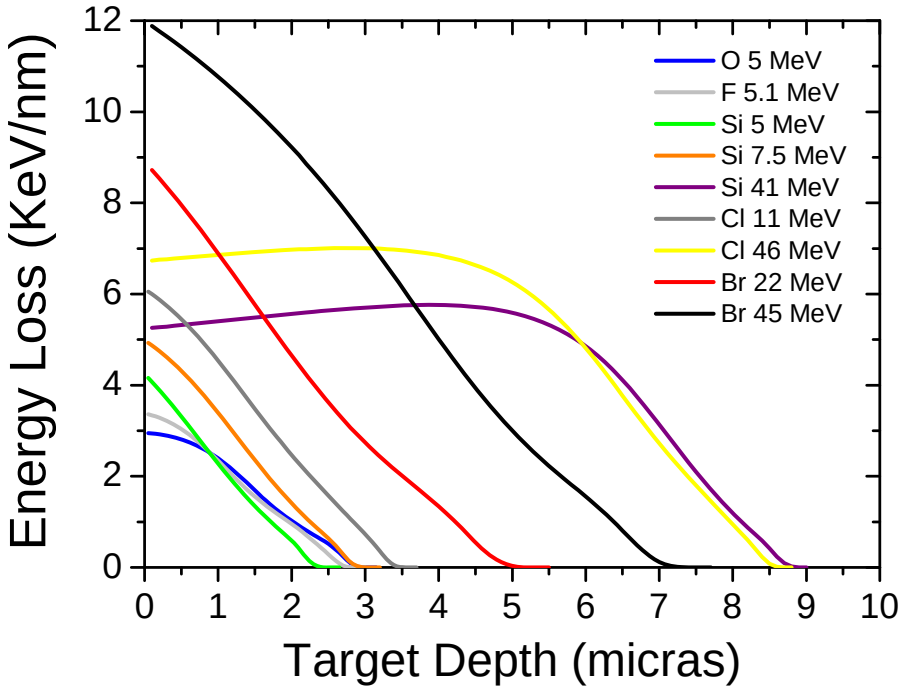

Fig. 4. Electronic energy loss curves for ions and energies indicated in the labels as a function of penetration depth in $LiNbO_3$ obtained with the SRIM-2003 code [36].

to the analyzing He beam itself; and, on the other hand, being easier and negligible the experimental error during the process of finding the channeling configuration in the non-irradiated zone. Then, the channeling spectrum was recorded after translating the sample holder so that the beam particles collide the Br-irradiated zone. Through the selected ion beams, a complete analysis of the damage fraction f_a generated at the surface, as a function of electronic stopping power (S_e) and ion fluence (ϕ), can be carried out.

As an example, **Fig. 5** illustrates the RBS/C spectra obtained from a 3-MeV $^4He^+$ analysis of irradiated (x, z -cut) $LiNbO_3$ samples with Br 45 and 22 MeV ions. The labelled spectra have been recorded in channeling conditions corresponding to the several irradiation fluences (see the chart legend). The aligned and random spectra obtained on a virgin crystal are also presented for comparison[1].

Before irradiation, a minimum yield $\chi_v = 2.7$ % was measured at the low-energy side of Nb surface peak. This low value, typical in single alignment geometry, gives evidence of the high-crystalline quality of the $LiNbO_3$ substrates. The increase of the backscattering yield observed for the irradiated samples is related to the damage induced by the ion bombardment. This indicates a defect creation process in both oxygen and niobium sublattices. The sensitivity of $LiNbO_3$ to such kind of irradiations, characterized by high electronic stopping powers, has been reported by Canut et al. [38]. Due to the lack in RBS sensitivity for detecting low atomic masess, the disorder calculations have been carried out only from the niobium signal. Assuming

[1] It is worthy to notice that, in following Chapter of this Thesis work (**Chapter 7**), we will address the study of the recrystallization properties of the amorphous tracks and layers submitted to annealing treatments. In the case of tracks, the selected irradiations were performed with Br 45 MeV ions on z-cut LN samples; for that reason we present here the RBS/C spectra for that case.

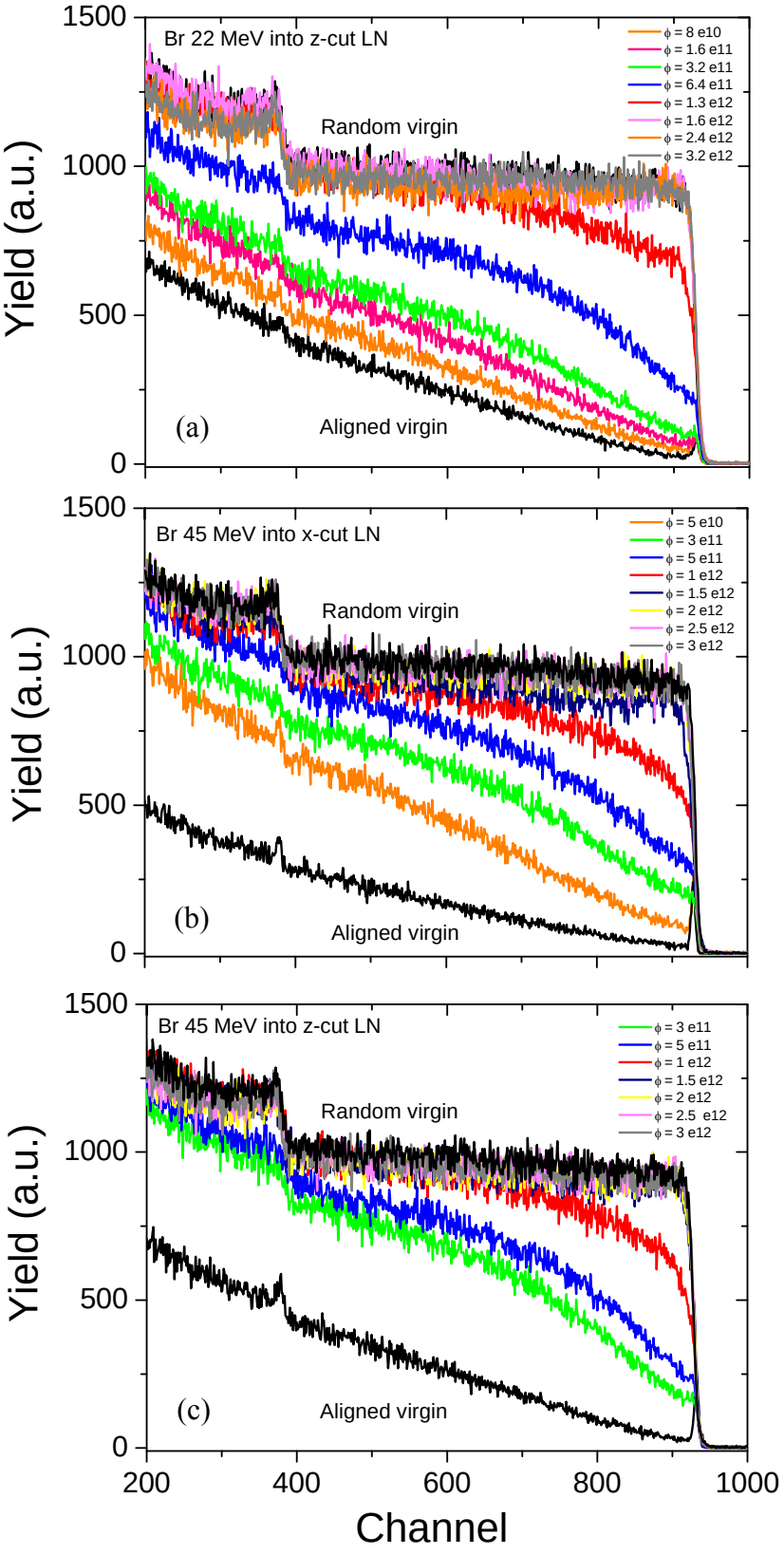

Fig. 5 (a-c). RBS/C spectra for *x*, *z* -cut samples of $LiNbO_3$ irradiated with Br ions at 45 and 22 MeV incident energy at different fluences (at/cm^2), indicated in the labels. The aligned and random spectra obtained on the virgin samples are presented for comparison. The Nb surface peak is located around energy channel 925. Analysis condition: 3-MeV $^4He^+$, detection angle = 170º.

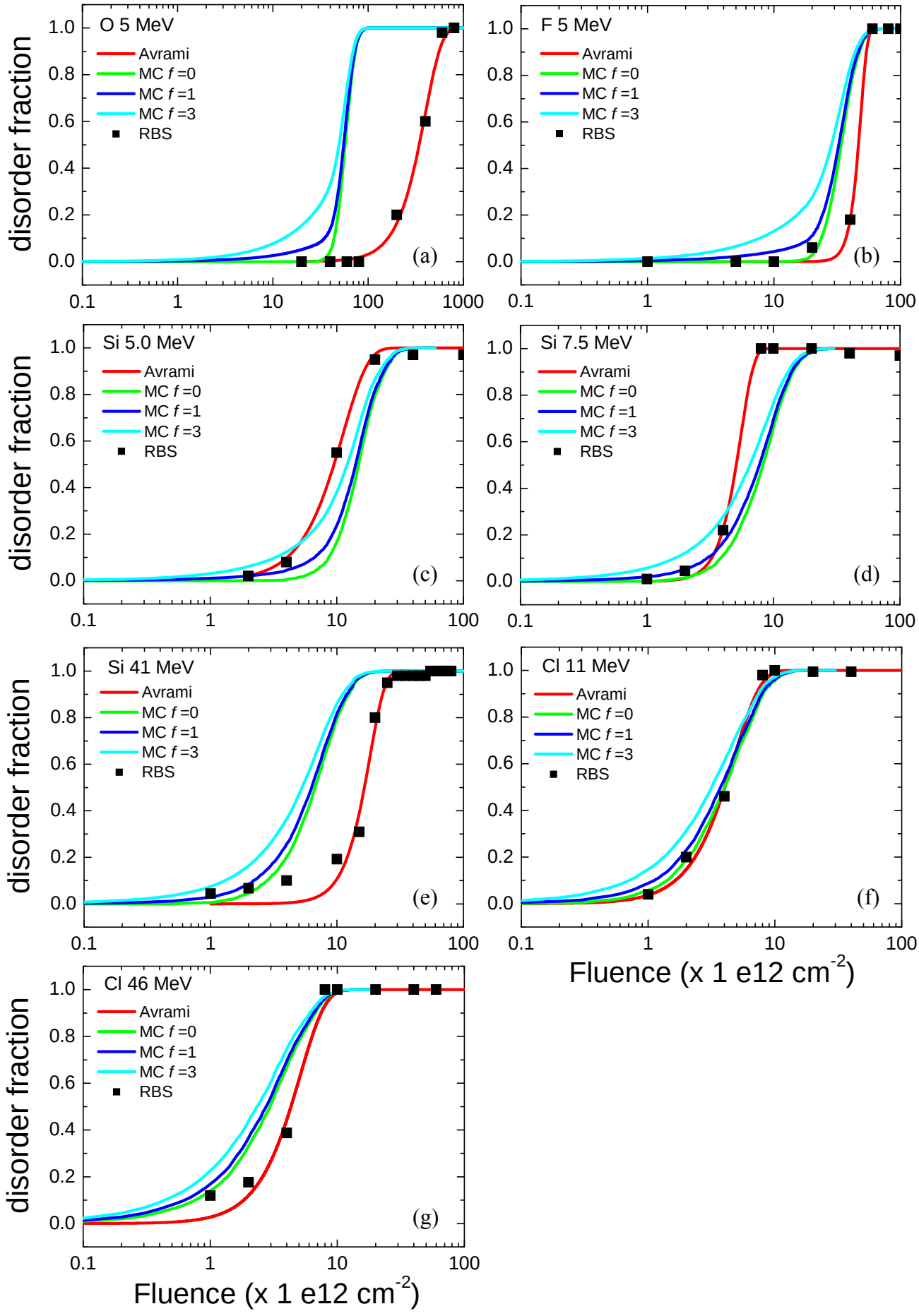
O 5 MeV
F 5 MeV
Si 5.0 MeV
Si 7.5 MeV
Si 41 MeV
Cl 11 MeV
Cl 46 MeV
Avrami
MC f =0
MC f =1
MC f =3
RBS
disorder fraction
Fluence (x 1 e12 cm-2)
(a)
(b)
(c)
(d)
(e)
(f)
(g)

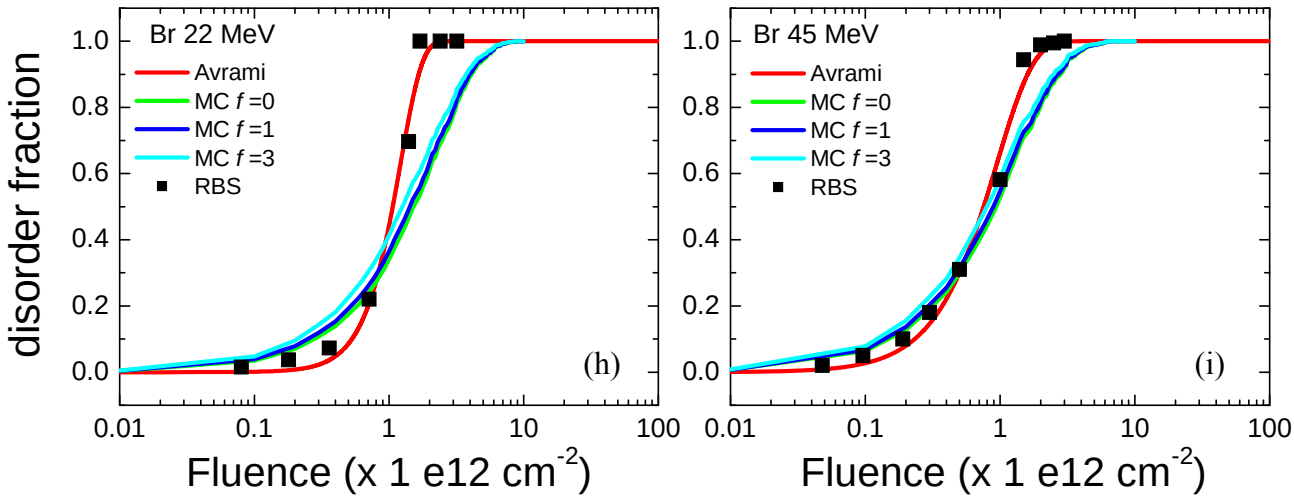

Fig. 6 (a-i). Evolution of the disorder fraction (f_a) measured at the sample surface vs the irradiation fluence ϕ, fluence for all investigated cases. Avrami´s fits (red solid lines) and MonteCarlo fits for different de-channeling factors (f) are specified in the labels.

the same ratio of displacements for lithium, oxygen and niobium atoms, the relative disorder fraction f_a for the irradiated samples at the LN surface will be given by the classical formulas [39]:

$$f_a = \frac{\chi_i - \chi_v}{\chi_r - \chi_v} \qquad (5)$$

where the dechanneling yield χ_i of the irradiated sample was measured at the low energy edge of the Nb surface peak. By taking into account the minimum yield χ_v corresponding to virgin crystal in channeling conditions, and the χ_r, the yield of the randomly-oriented crystal.

Fig. 6 (a-i) and **Fig. 7** represents the evolution of the disorder fraction f_a measured at the surface versus the irradiation fluence ϕ, for the several cases under study.

Experimental results [9, 11, 20, 40] on $LiNbO_3$ show clear evidence of the cumulative behaviour through the observation of an Avrami-like (sigmoidal) kinetics, $f_a = 1 - \exp\{-(\phi/\phi_0)^n\}$, for the growth of the normalized disordered area f_a as a function of fluence, for irradiation conditions below as well as above threshold. For irradiations well above threshold the measured Avrami curves correspond to the Poisson limit *(n = 1)*, whereas for conditions below threshold, the Avrami curves present parameters n and ϕ_0 , that steadily increase on decreasing electronic stopping power. The experimental data as collected in a recent paper [40] are shown in **Fig. 8**.

More specifically, we can extract the following main conclusions as follows:

a) Above the stopping power threshold the amorphization kinetics roughly obeys a Poisson-type law, although some clear deviations appear (see below). They are more significant as the stopping power decreases to approach the threshold value. In fact, a pure Poisson behaviour ($n = 1$) is only obtained for stopping powers higher than twice the threshold value as apparent in **Table II** and **Fig. 9**, as it has been recently remarked

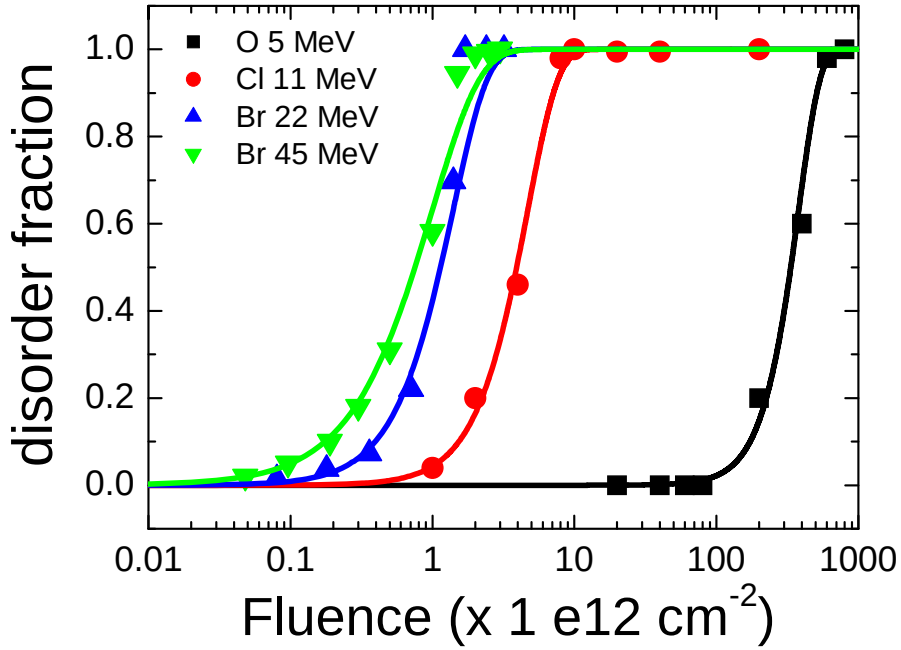

Fig. 7. Comparison of the disorder fraction (f_a), as derived from RBS-C experiments, on $LiNbO_3$ samples irradiated with O at 5 MeV (S_e = 3.1 keV/nm) (full squares), Cl at 11 MeV (S_e = 6.1 keV/nm) (full circles), Br at 22 MeV (S_e = 8.7 keV/nm) (full upright triangles) and Br at 45 MeV (S_e = 11.9 keV/nm) (full inverted triangles). The best fit obtained with Avrami curves (solid lines) is shown for comparison.

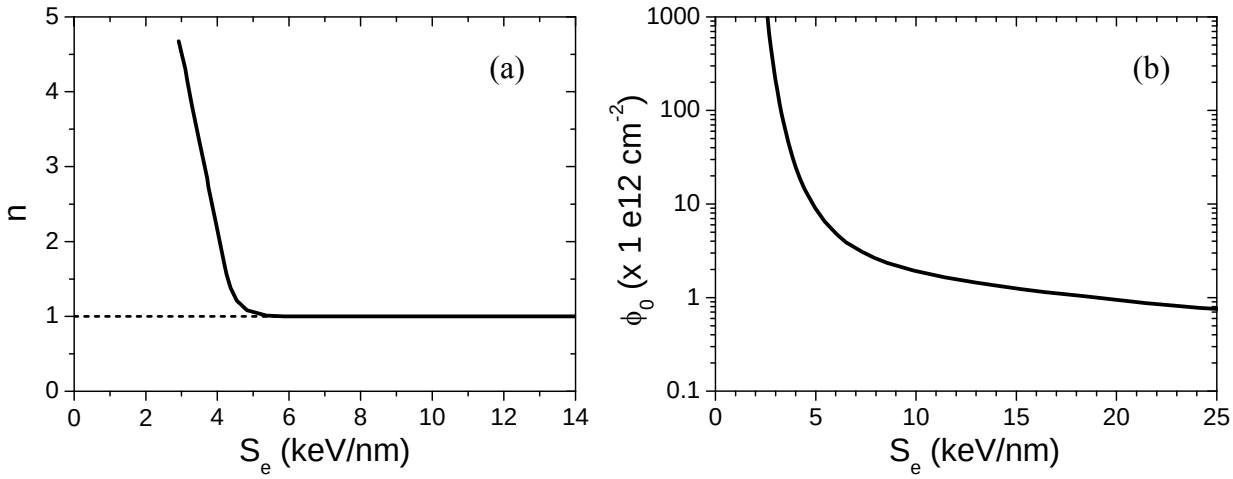

Fig. 8. Avrami parameters ϕ_0 and n, as determined from a fit to experimental data, shown as a function of the stopping power S_e of the incident ion (extracted from Ref. [20, 40]). $f_a = 1 - \exp\{-(\phi/\phi_0)^n\}$

by Italian workers [40]. This is the situation achieved in most experiments of the French and German groups at GANIL and GSI.

b) Below the stopping power threshold the kinetics departs from the Poisson law and follows a sigmoidal-type dependence so that a certain incubation fluence is needed before significant amorphization is produced. The process appears quite similar to that caused by *mechanism II of nuclear collisions* (cascade-overlap model) in many

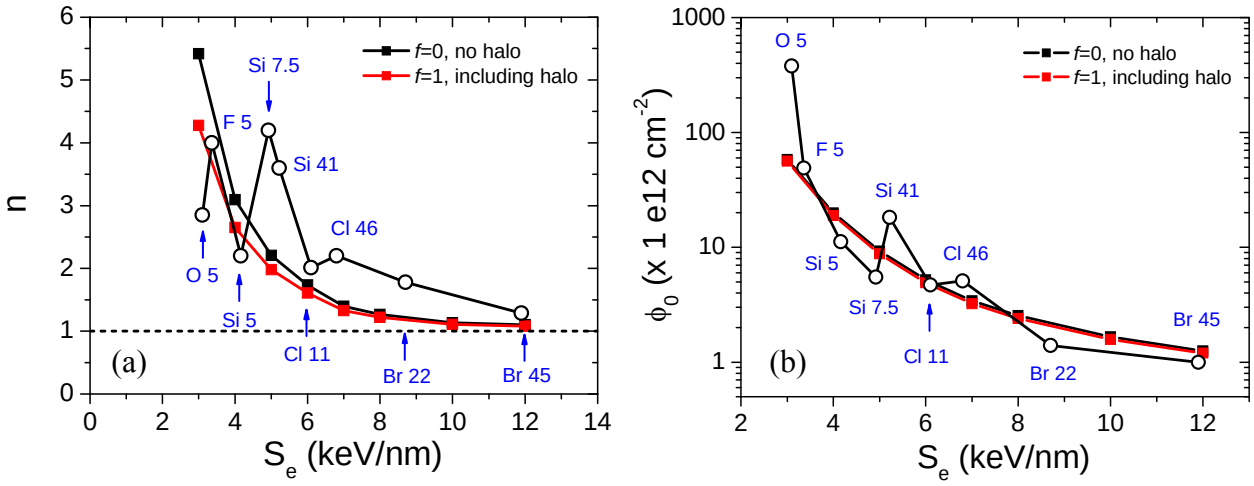

Fig. 9. Avrami parameters ϕ_0 and n, as determined from a fit to experimental data detailed in **Table I**, shown as a function of the stopping power S_e of the incident ion. In addition, the Avrami parameters corresponding to the Monte Carlo fits for different de-channlieng factors (f) is presented (discussed later), being specified in the labels.

Ion	Energy (MeV)	Stopping Power (S_e) (keV/nm)	ϕ_0 (1 e12 at/cm^2)	n
O	5.0	3.1	380	2.85
F	5.1	3.4	49	4
Si	5.0	4.2	11.2	2.2
Si	7.5	5.3	5.5	4.2
Si	41	5.2	18.2	3.6
Cl	11	6.1	4.7	2.01
Cl	46	6.8	5.1	2.2
Br	22	8.7	1.4	1.78
Br	45	11.9	1	1.29

Table II. Values of the curve parameters ϕ_0, n, derived from Avrami's fit to the damage kinetics yielding the best description of the experimental data as shown in **Fig. 6 (a-i)**. The electronic stopping power and the ion energies are also included.

ceramics [2, 41]. In previous works such behaviour has been described by an Avrami´s dependence [20], whose exponent n and ϕ_0 strongly depend on the stopping power (S_e). The dependence is shown in **Fig. 9**, where, in fact, the exponent, n, changes from around 4 for S_e = 4 keV/nm to ≈1 for S_e = 12 keV/nm. Moreover, the Avrami parameters corresponding to the MonteCarlo fits for different de-channling factors (f) show the same behaviour (explained later).

Although the Avrami kinetics is generally assumed by most workers we have tested the accuracy of the fitting by using either a minimum square root algorithm of: - $Ln\ (1\text{-}f_a)$ versus ϕ

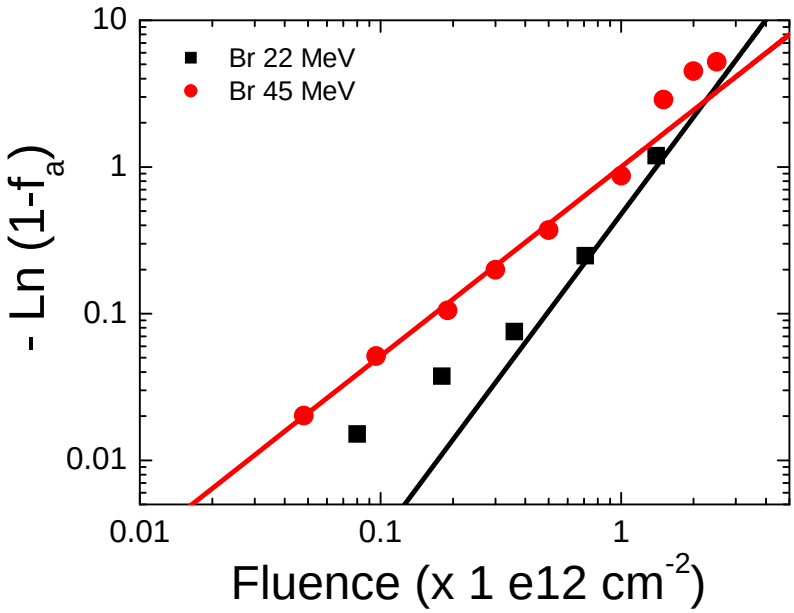

Fig. 10. Plot of the - *Ln (1-f_a)* versus ϕ in a log scale for the case of Br 45 and 22 MeV irradiations. The plot should be linear with slope *n* and $\phi_0 = k^{-1/n}$. The RBS/C experimental data of disorder fraction (f_a) and the avrami´s fittings (solid lines) from the corresponding cases are shown as a function of the stopping power S_e of the incident ion.

in a log scale. The plot should be linear with slope *n* and $\phi_0 = k^{-1/n}$, where *log k* is the point in which the linear curve passes through *y*-axis. Results for two irradiation conditions (Br 22 MeV and Br at 45 MeV) clearly show some divergences in the appropriate parameters to get a good fit as displayed in **Fig. 10**. In particular it comes out from the log plot that the parameters of the fit change with fluence. In fact, one should remark that for stopping powers above threshold the Avrami law could not apply since it yields slope zero and one should more properly talk of a modified-Poisson kinetics. This analysis suggests that one should use some caution with the Avrami´s fits used for many authors and particularly on the curve parameters. Independently of the accurate shape of the kinetics we will illustrate in this Chapter the key role of the surrounding defect halo on the kinetic behaviour and its departure from Avrami-Poisson curves.

7.4. MonteCarlo simulations based on the non-radiative exciton decay.

According to the Thermal Spike Model the amorphization is *only possible* above threshold and its kinetics should obey a Poisson law. The data in **Fig. 6 (a-i)** and **Fig. 7** as well as some other data clearly demonstrate that amorphization does, indeed, occur *both above and below* the amorphization threshold measured for single tracks. The observed behaviour and its similarity with the results for amorphization in the nuclear regime suggests that possibly an *accumulative model* should apply for ion-beam damage in the two stopping power regimes. Recently, a non-radiative exciton-decay model has been put forward for $LiNbO_3$ that may possibly apply to other oxides (and even semiconductors) [25, 42]. The model is mostly phenomenological, although quantitative (provides the defect concentration). It takes into account the fraction of energy deposited as heat (*thermal spike*) as well as the fraction of energy

deposited in the form of potential energy in electron-hole pairs, which in many cases readily get localized forming self-trapped excitons (*exciton spike*). The latter is often ignored despite it can be as high as 50% of the total energy. The model relies on the synergy between both spikes generated upon ion impact. A key parameter of the model is the energy barrier that separates bound and unbound regions of the excited state of the localized exciton. A myriad of experiments show that electronic excitation is far more complex and in contrast with the nuclear collision regime far less understood. The main novel idea is that point defects are, indeed, produced around the ion trajectory *whatever the electronic stopping power*. Specifically, it has been proposed that these defects are produced as a consequence of the non-radiative decay of localized (or self-trapped) excitons.

It is worthy to notice that, the basic formula yielding the concentration of defects as a function of stopping power is **Eq. (1)**, where $N_X(r, z, 0)$ obeys condition (**6**), providing a superlinear growth rate with stopping power. One may note that, for the purpose of this Chapter, this specific excitonic mechanism is not critical.

$$\int_0^\infty 2\pi r N_X(r,z,0)dr = \frac{S_e(z)}{I}, \qquad (\mathbf{6})$$

On the other hand, a second assumption of the model is that there is a critical defect concentration that triggers a transition to an amorphous phase (not necessarily melting). The transition may be understood as a *defect-driven phase transition* as discussed by Fecht [26]. The analysis of a variety of experimental results on $LiNbO_3$ indicates that this critical concentration is around 7%. For a single impact irradiation formula (**Eq. 1**) determines the radial profile of the defect concentration around the trajectory axis. By comparing this profile with the threshold concentration level for amorphization, **Fig. 1**, one obtains the structure of the track consisting of an *amorphous core* and a *surrounding halo*, which could be clearly illustrated in a two-dimensional colour map. This geometry has significant implications on the amorphization kinetics above threshold in comparison with the Poisson behaviour predicted by the standard Thermal Spike Model. In order to deal with the amorphization kinetics associated to track overlapping, analytical formulae are not adequate due to the random nature of impact distribution. Then, one has to rely on MonteCarlo computer simulations, such as recently reported [1].

7.4.1. MonteCarlo approach. A numerical recipe description.

As it was described in the previous section, the excitonic model provides the defect concentration $n(r, z)$ originated by a single ion (**Eq. 1**). In order to account for the damage evolution in a multiple track scenario we have developed a MonteCarlo algorithm that operates as follows (**Fig. 11** is a schematic illustration):

- The sample is divided in thin slabs, typically 50-100 nm thick, parallel to the surface. Each slab starts at a depth z from the surface.
- Each slab consists of a grid of 100 × 100 cells. Each cell has an area (parallel to the surface) of 1 nm^2.

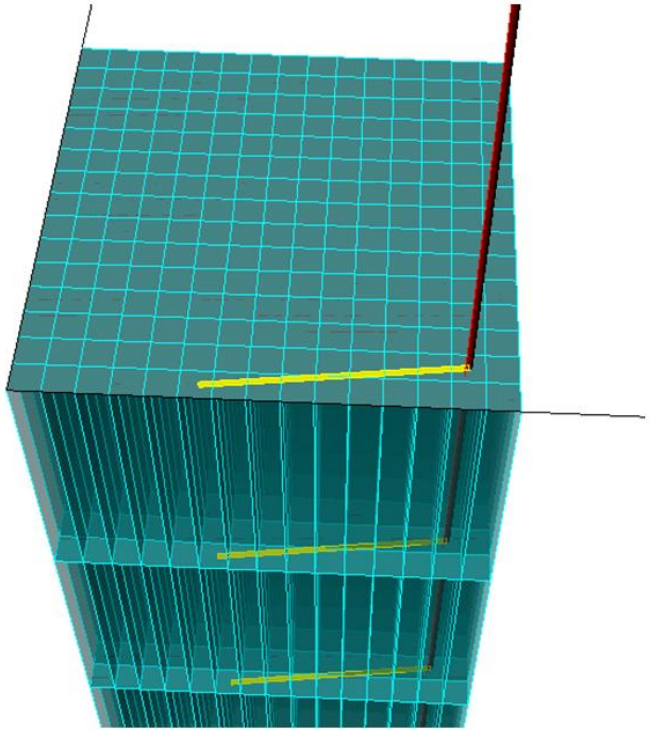

Fig. 11. Schematic illustration of the structure employed for the MonteCarlo algorithm. Note that the sample is divided in slabs parallel to the surface and each slab contains 10.000 identical cells whose area parallel to the surface is 1 nm^2. The red line represents an ion trajectory. In order to consider the damage generated by every ion in every cell, the distance to the ion trajectory axis is calculated as it is indicated with the yellow lines for every cell.

- Ions are assumed to hit the sample perpendicular to the surface at a random position X, Y ($0 < X, Y < 100$ nm), see red line in **Fig. 11**.
- Each ion impinging the sample corresponds to a fluence of 10^{-4} $nm^{-2} = 10^{10}$ cm^{-2}.
- The distance from the center of every cell to the track axis is evaluated in every slab as indicated by the yellow lines in **Fig. 11**.
- The effect of the ion passage to every cell of the sample is given by the defect concentration, $n(r, z)$, calculated by the Excitonic Model (**Fig. 1**). Now r, represents the distance of every cell to the track axis. Since the electronic damage is cumulative, the damage generated by the incoming ion in every cell is added up to the damage generated by previous ions.
- If the critical defect concentration n_{th} is exceeded, we assume that the cell becomes amorphous and thus, its defect concentration equals the molecular density of the sample (N). The critical defect concentration, n_{th}, corresponds to the damage concentration generated at the surface by a single ion with stopping power S_{th}.

This procedure provides the defect concentration at any given cell as a function of ion fluence. In addition, it predicts the appearance of amorphous regions not only as an effect of an ion passage with $S_e > S_{th}$ but as an effect of damage accumulation produced by several ions.

7.4.2. Evolution of damage morphology with stopping power and ion fluence.

The MonteCarlo approach allows us to build two-dimensional maps where the local damage level and the morphology of amorphized areas at a given depth from the crystal surface are easily visualized. With regard to stopping power one can consider two cases:

7.4.2.1. Stopping power at the map plane is above threshold.

As an example, defect concentration maps of the surface of a $LiNbO_3$ crystal irradiated with Cl ions at 45.8 MeV (S_e = 6.8 keV/nm at the surface) are given in **Fig. 12** (left) for different fluences. Based on previous works [43] we take as threshold stopping power S_{th} = 6 keV/nm. For the lowest fluence only one impact (corresponding to a fluence of 10^{10} cm^{-2}) is registered. Since $S_e > S_{th}$, the ion impact produces a single amorphous track (white area) that is surrounded by a colored halo containing point defects whose concentration is below the critical value n_{th}. On increasing fluence more tracks appear and the extension and morphology of the amorphous region is markedly modified. At low fluences the amorphous regions present a cylindrical symmetry surrounded by a defective region (colored area) because they stem from one single ion impact. As the fluence increases, track overlapping takes place and the regular cylindrical shape of the amorphous regions becomes more blurry. Note that the overlap of regions with certain concentration of defects leads to amorphization. This clearly illustrates the cumulative character of the electronic damage. The resulting amorphous fraction for the surface layer is 0.1%, 15.4% and 80.2% for the fluences 10^{10}, 10^{12} and 5×10^{12} cm^{-2}, respectively. The MonteCarlo simulations also predict the depth of the amorphous tracks, **Fig. 12 (right)**. At a fluence of 1×10^{12} cm^{-2} the amorphous tracks reach a depth of around 6 μm. In overlapping track regime (5×10^{12} cm^{-2}), one observes that the amorphous depth increases approaching 7 μm. It is the cumulative character of the electronic damage that makes both the amorphous depth (**right**) and the amorphous area (**left**) increase with fluence.

7.4.2.2. Stopping power below threshold.

Fig. 13 (left) illustrates defect concentration maps at the surface of a $LiNbO_3$ crystal irradiated with Si ions at 5 MeV (S_e = 4.2 keV/nm at the surface). In this case, single ions do not form amorphous tracks but only defective spots, as observed in **Fig. 13 (a)** corresponding to a fluence of 10^{10} cm^{-2} (only one impact). The amorphous regions appear as a consequence of defect accumulation after every ion passage. At a fluence of 5×10^{12} cm^{-2}, some amorphous regions start to develop. They do not present cylindrical symmetry because they occur as a result of multiple track overlapping. This is more evident at higher fluence. At 10^{13} cm^{-2}, the amorphous fraction amounts to 20.6% and the shape of amorphous regions do not resemble a set of single ion tracks at all. One sees from the sequence **13 (a) → 13 (b) → 13 (c)**, that for $S_e < S_{th}$ a certain minimum fluence is needed before amorphization starts (incubation fluence). Note that the amorphous depth (**right**) is now very small (< 300 nm). The role of defect generation is important in this case. On the other hand, when $S_e > S_{th}$, every impinging ion generates an amorphous track. Then, the role of the amorphous core of the track is dominant from the point

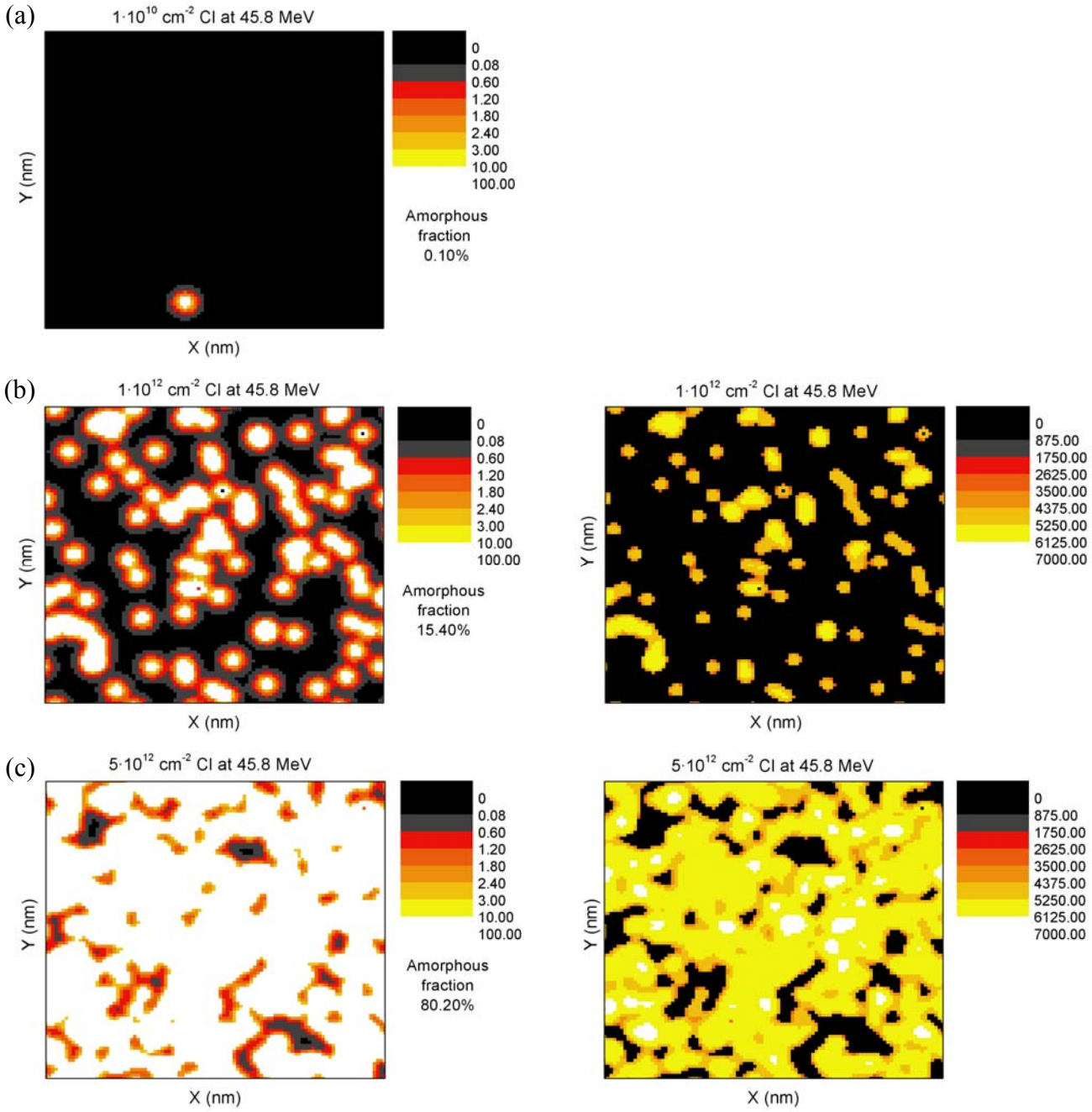

Fig. 12. (**Left**) defect concentration maps at the surface of a $LiNbO_3$ crystal irradiated with Cl ions at 45.8 MeV (Se = 6.8 keV/nm at the surface). The color scale indicates defects/nm^3. (**Right**) Maximum amorphized depth below the surface at any (x, y) position. The color scale is given in nm. Ion fluence equals 10^{10} cm^{-2} (**a**), 10^{12} cm^{-2} (**b**) and 5×10^{12} cm^{-2} (**c**).

of view of sample properties or defect analysis, while the surrounding defective regions play a minor role, as will be discussed below.

Appropriate experiments to observe the morphology patterns predicted by our MonteCarlo approach are a difficult task. A possibility would be to use high resolution SNOM that would distinguish the crystalline and amorphous regions of the pattern due to the very

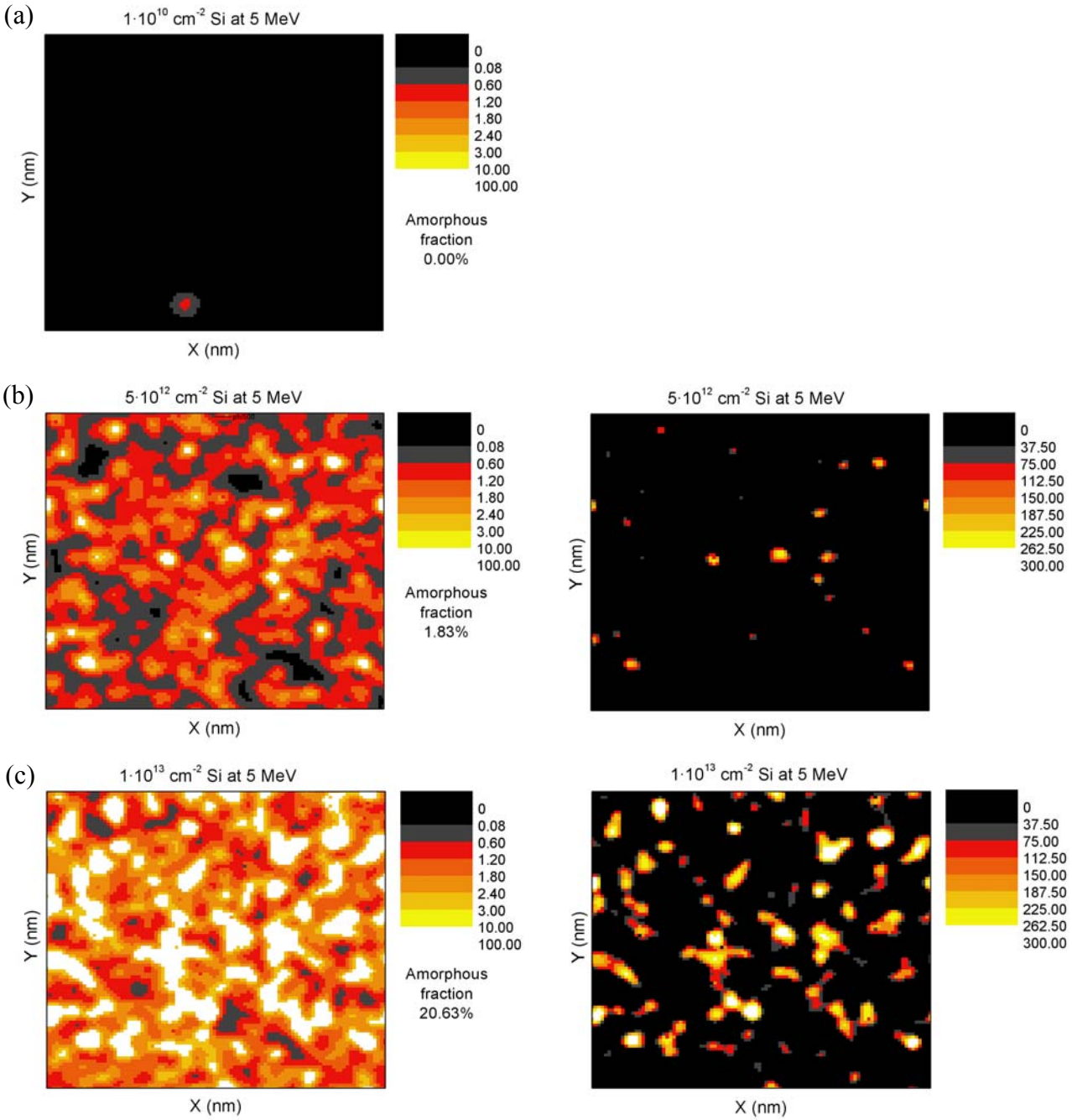

Fig. 13. (**Left**) defect concentration maps at the surface of $LiNbO_3$ crystal irradiated with Si ions at 5 MeV (Se = 4.2 keV/nm at the surface). The color scale indicates defects/nm^3. (**Right**) Maximum amorphized depth below the surface at any (*x*, *y*) position. The color scale is given in nm. Ion fluence equals 10^{10} cm^{-2} (**a**), 5×10^{12} cm^{-2} (**b**) and 10^{13} cm^{-2} (**c**).

different refractive indices (n_a = 2.10 for the amorphous phase, and n_o = 2.28 and n_e = 2.20 for the crystalline phase). However, the attainable resolution (~ 50 nm) is still insufficient for adequate observation. Alternatively, one may appreciate that the patterns resemble those achieved after suitable selective chemical etching treatments [44] that excavate the amorphous regions of the surface while leaving essentially undisturbed the crystalline zones. Although the comparison is suggestive, the etching is an aggressive technique that strongly modifies and broadens the features initially present in the irradiated surface.

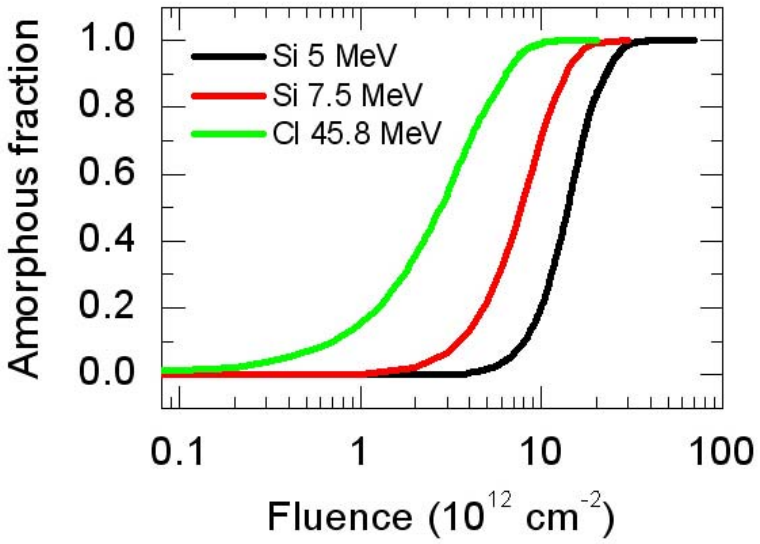

Fig. 14. Amorphous fraction at the surface of a $LiNbO_3$ crystal irradiated with 5 MeV Si ions (Se = 4.2 keV/nm), 7.5 MeV Si ions (Se = 4.9 keV/nm) and 45.8 MeV Cl ions (Se = 6.8 keV/nm). The amorphous fraction is obtained from the MonteCarlo algorithm and given as a function of the ion irradiation fluence.

However, one can focus on a particular relevant feature of the simulations. For irradiations below threshold and low enough fluences, amorphous spots are not generated as observed in **Fig. 13 (a)**. A certain *incubation* fluence is needed to make them appear as a consequence of track overlapping. This incubation fluence to induce amorphization has been, indeed, confirmed [20] by data of damage kinetics obtained by means of RBS-C. A detailed discussion of this point will be addressed in the next section.

7.4.3. Simulation of the disordered and amorphization kinetics.

The described MonteCarlo approach is suitable to obtain the kinetics for the two components of damage, namely amorphized and disordered (non amorphous) regions. These two cases will be now discussed.

7.4.3.1. Kinetics of amorphization.

From the defect concentration maps one can plot the quantitative evolution of the amorphous fraction for every slab as a function of fluence for a given incident ion. **Fig. 14** shows the amorphous fraction of the surface layer of a $LiNbO_3$ crystal as a function of fluence for several ions calculated from the model. They present an S-shape typical of Avrami-type kinetics. Note that the higher the stopping power the lower the fluence required for full amorphization. In addition, it is very interesting to note that the shape of the curve corresponding to irradiations with 45.8 MeV Cl ions differs with respect to the other two curves. The reason is that the latter curves correspond to irradiations in sub-threshold conditions, i.e., an incubation fluence is needed to produce amorphous phases. In contrast, when irradiations are performed with 45.8 MeV Cl ions every single ion is able to produce an amorphous track. In other words, every single ion contributes directly to increase the amorphous fraction. The

features observed in **Fig. 14** are essentially in agreement with the results of detailed RBS-C experiments. However, one has to be aware that this technique measures disorder and not only amorphization. Therefore, for a meaningful comparison between theory and experiment one has to carefully discuss the information gathered in the RBS-C experiments.

7.4.3.2. Kinetics of disorder: RBS-C experiments.

Most data on the evolution of damage with ion-beam fluence are derived from RBS-C experiments. In them, samples are probed with a hydrogen or helium beam aligned along a crystallographic axis or planar direction, and the reduction in RBS yield in comparison to that obtained under random incidence is measured. The problem with the technique is that it does not distinguish between fully amorphous or defective areas, so it yields information on the disorder. In order to properly analyze the data one should introduce a filter function as it was explained in a previous section (and see Ref. [45]). A suitable filter function would require a detailed knowledge of the back-scattering yield of each of the point defects generated by irradiation. As it has been commented, this problem is not simple. A reasonable and useful approximation for $LiNbO_3$ considers that the yield corresponds to an atomic (Nb) size cross-section, i.e., a filter function must be introduced which behavior has been described in **Eq. (4)**, and its plot has been shown in **Fig. 2** of a previous section. The use of the filter function allows one to compare the experimental de-channeled fraction obtained by RBS-C with the results of our model. For every possible value of f, we can get the de-channeled fraction that RBS-C would provide as n^*/N.

Fig. 15 shows disordered areal fractions obtained by RBS-C and by the exciton model for different values of the backscattering factor, f. The results obtained by the model reproduce well the experimental values. Note that phenomena like the so-called "velocity effect" [18, 46] are not included in the model and may play an important role. The curves obtained for $f = 0$ are identical to those presented in **Fig. 14** because $f = 0$ implies that only amorphization is considered and the defective regions produced by irradiation are neglected. From **Fig. 15 (a)** and **15 (b)** it is clear that neglecting the defective regions leads to a bad agreement with the experimental results. On the other hand, the curves obtained from the model for various values of f in the case of 45.8 MeV Cl irradiation (**Fig. 15 (c)**) are very close to each other. The reason is that such an irradiation leads to the production of single amorphous tracks by every single ion, which becomes dominant over the defective halos. This fact evidences that in the presence of amorphous regions the surrounding defective regions play a minor role.

7.5. Application of the model to determine the kinetic laws.

A MonteCarlo approach based on the Excitonic Model has been described above. At variance with the analytical approaches, it can be used at very low fluences where the randomness of ion impacts and damage fluctuations plays a decisive role. We have used here such MonteCarlo code to simulate the amorphization kinetics for a number of stopping powers (S_e) and assess the role of the surrounding halo of point defects. The kinetics of amorphization for various stopping powers below and above the threshold value as predicted by our model is illustrated in **Fig. 16**. The general behaviour, that is in accordance with experiment (**Fig. 6 (a-i)** and **7**), is as follows: below threshold one observes a sigmoidal behaviour whereas above

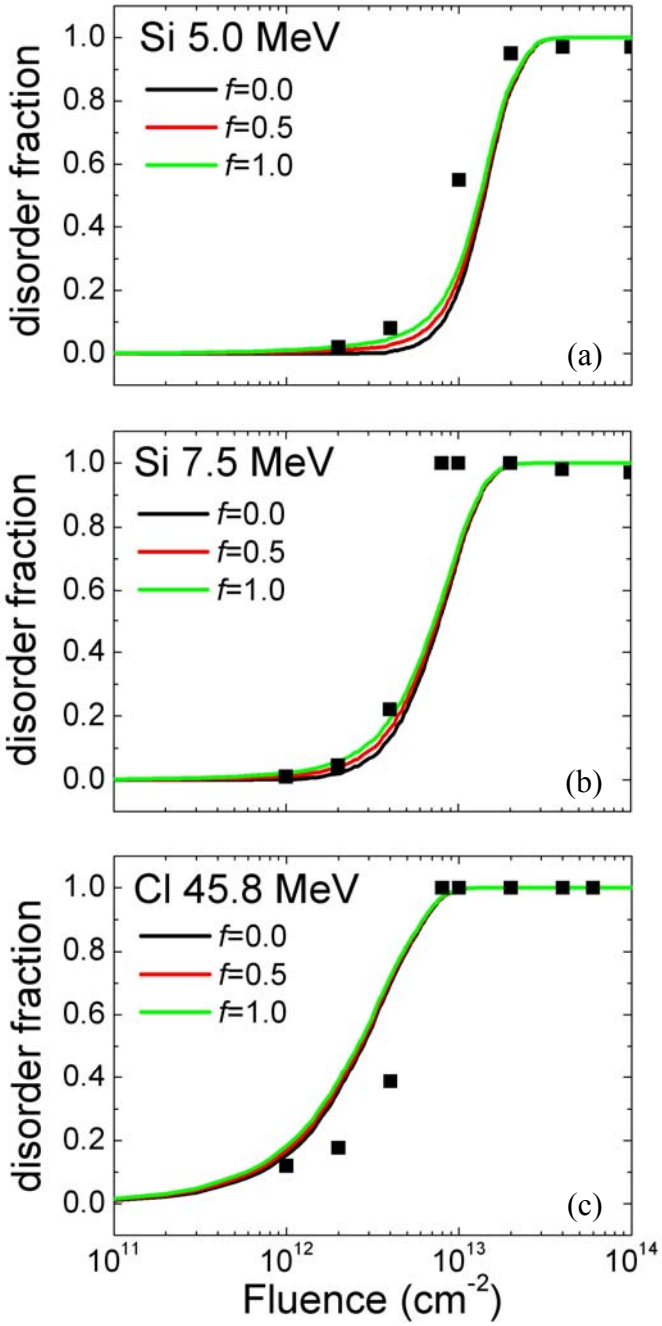

Fig. 15. Disordered surface fraction obtained from RBS-C as calculated from the model for different values of the backscattering factor, *f*. $LiNbO_3$ has been irradiated with (**a**) 5 MeV Si ions, (**b**) with 7.5 MeV Si ions and (**c**) with 45.8 MeV Cl ions.

threshold one obtains Poisson or nearly Poisson kinetics. This feature is a clear consequence of the cumulative character of the ion-beam damage. In order to evaluate more accurately the type of kinetics we have now plotted the above curves, as for the experimental ones, according to a log [-Ln (1-f_a)] vs log ϕ [2] (**Fig. 17**). For Avrami kinetics (including the Poisson case) one should obtain a straight line with slope *n*. As for the experimental curves this is not the case suggesting that the observed departures are not due to experimental errors but have an intrinsic character.

[2] Specifically, log [-Ln (1-f_a)] = log k + nlog ϕ, being $\phi_0 = k^{-1/n}$.

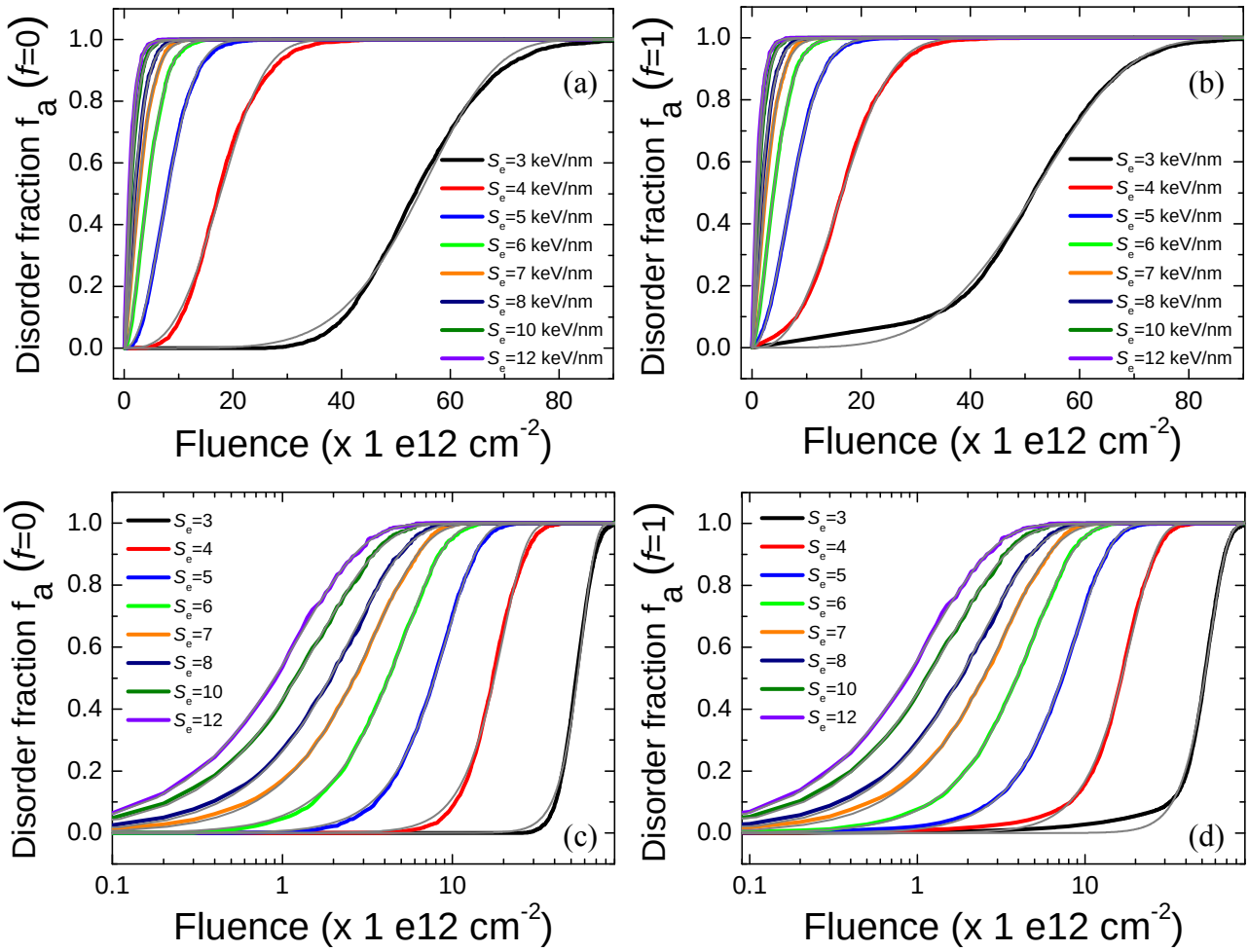

Fig. 16 (a-d). (**a**, **b**) Evolution of the simulated disorder fraction (f_a) from the MonteCarlo code for different de-channeling factors (*f=0, 1*) vs fluence ϕ, for different stopping powers (S_e), specified in the labels. Avrami´s fits (gray solid lines) for all the curves to calculate the characteristic parameters *n* and ϕ_0 are shown too.

Anyhow the discrepancies have more a fundamental than practical relevance and so we will perform our analysis using approximate (average) Avrami parameters.

The dependence of exponent *n* and ϕ_0 as a function of stopping power that one derives from the MonteCarlo simulations is illustrated in **Fig. 9 (a, b)**. It is clear that *n* decreases from around a value of 4 for stopping powers quite below threshold to around 1 for stoppings above twice the threshold value. The model very satisfactorily explains the experimental results obtained in several laboratories as in Madrid [20] and Bologna [40] and provides physical support to the empirical analysis recently reported. The agreement provides a nice experimental proof of the generation of point defects whatever the stopping power and the cumulative character of such damage. One should note that for stoppings above, but not far from threshold, one does not obtain a Poisson type kinetics but an Avrami-related curve with an exponent *n* between 1 and 2. The reason for this behaviour clearly departing from the predictions of the Thermal Spike Model is the existence of an halo of surrounding point defects.

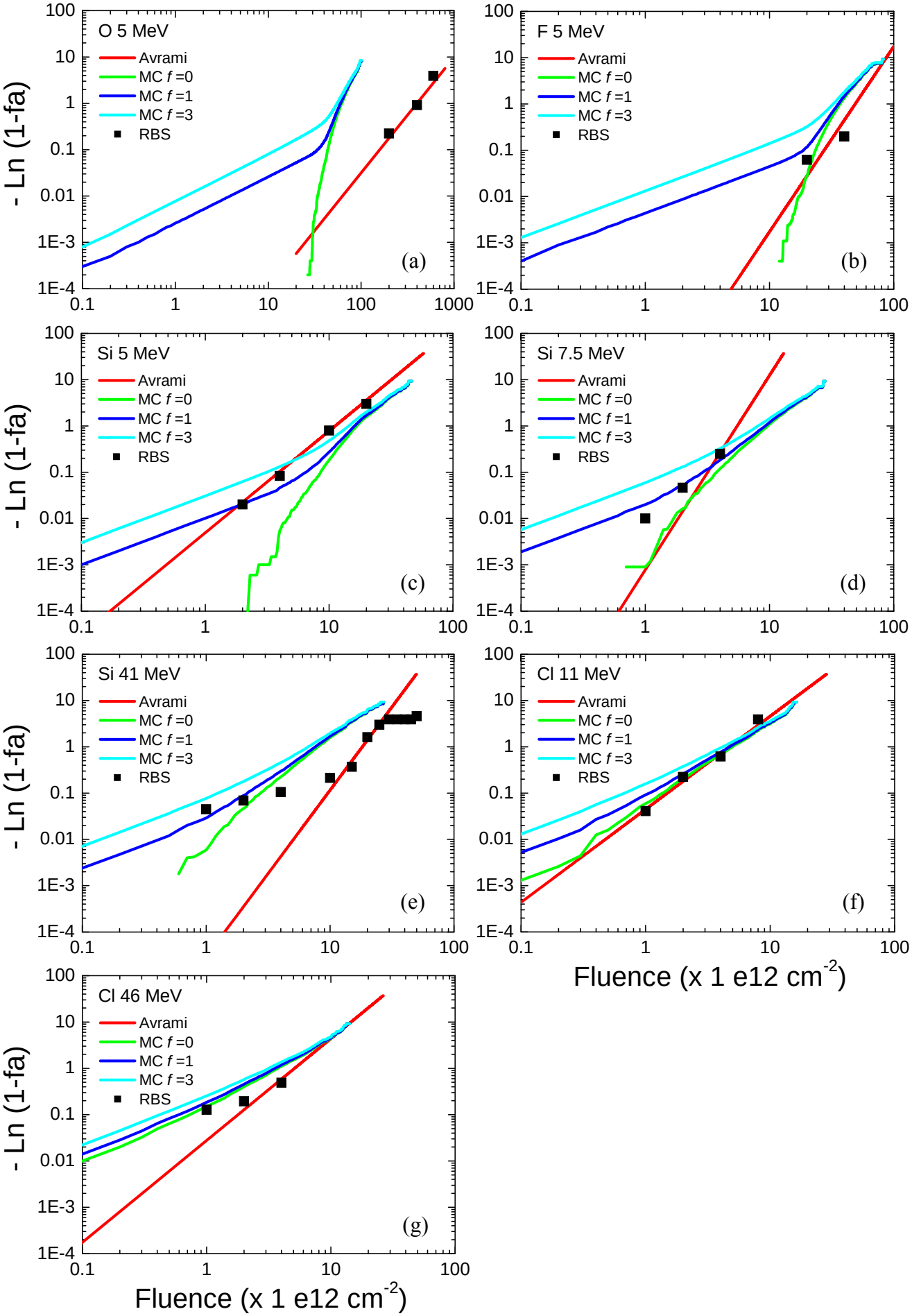
O 5 MeV
F 5 MeV
Si 5 MeV
Si 7.5 MeV
Si 41 MeV
Cl 11 MeV
Cl 46 MeV
Avrami
MC f =0
MC f =1
MC f =3
RBS
(a)
(b)
(c)
(d)
(e)
(f)
(g)
- Ln (1-fa)
Fluence (x 1 e12 cm-2)

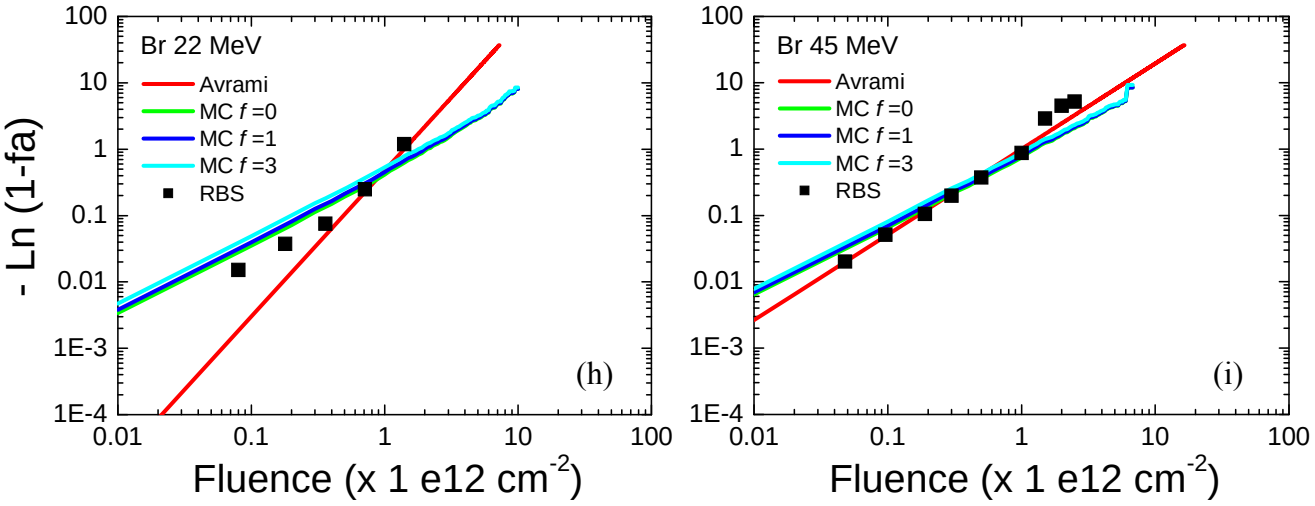

Fig. 17 (a-i). Evolution of the disorder fraction expressed as [-Ln (1-f_a)] vs ϕ vs the irradiation fluence ϕ, in a double log scale for all investigated cases (see **Fig. 6**). Avrami´s fits (red solid lines) and Monte Carlo fits for different de-channeling factors (f) are specified in the labels.

7.6. Role of surrounding halo on the amorphization kinetics.

The simulations of the previous section clearly reveal that the amorphization kinetics requires a cumulative model producing point defects that add to achieve a critical level leading to lattice amorphization. In particular, the data above threshold confirm the existence of a surrounding halo of point defects that account for the departure of the kinetics from the Poisson behaviour. The role of halo can be clearly illustrated by comparing the true model predictions considering core plus halo with those eliminating the halo. The results are illustrated in **Fig. 9 (a, b)** for several stopping powers. Note that the experimental results using RBS-C can be interpreted as the results of introducing a certain efficiency factor, f (normally between zero and one), and consequently would yield curves intermediate between those shown in **Fig. 9 (a, b)**. These results suggest that one should be very careful when obtaining damage cross-sections or track radii from the initial slope of the kinetic curves (non-poissonian).

7.7. Generation of uniform amorphous layers: Some statistical features.

Our MonteCarlo model predicts full (100%) amorphization of a surface for stopping powers above threshold and high enough fluences (see saturation stage in **Fig. 14** and **Fig. 15**). Moreover, all slabs of the crystal subjected to those conditions become amorphous so that, an homogeneous amorphous layer is produced by the irradiation. To deal with this situation an analytical formulation of the exciton model that ignores statistical aspects is appropriate and has been developed in [25]. The model predicts that the thickness of the homogeneous amorphous layer increases appreciably with fluence i.e. the crystalline-amorphous interface propagates into the crystal. The amorphous thickness as a function of fluence was satisfactorily described within the analytical model for the case of $LiNbO_3$. In fact, the tailoring of these layers provides a useful technique to fabricate optical waveguides as an advantageous alternative to the standard ion implantation technique [21]. Then, which are the advantages of a MonteCarlo vs. an

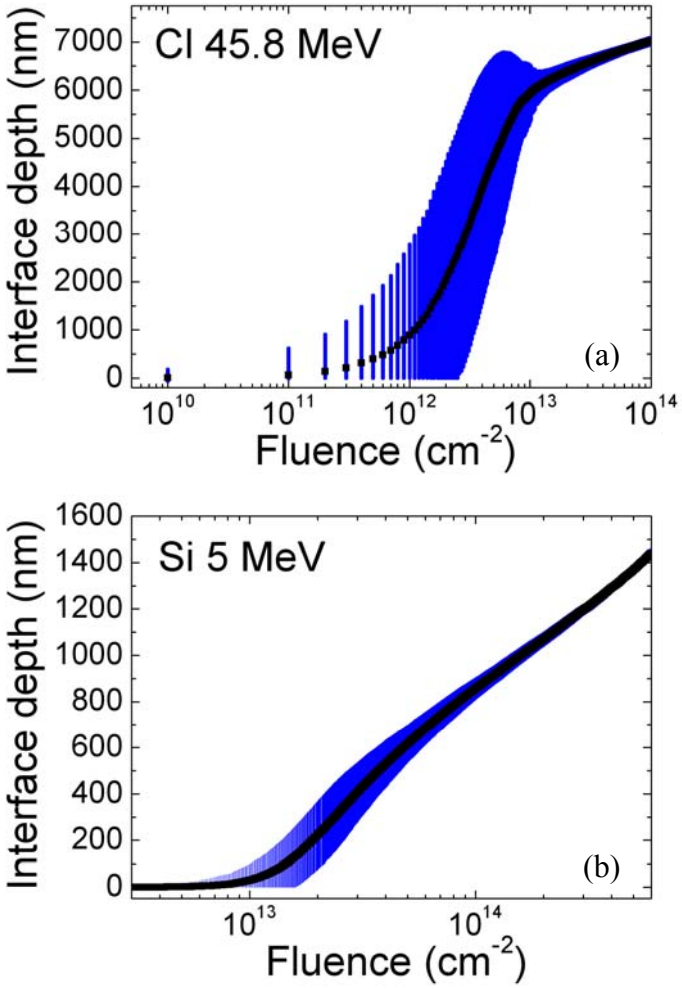

Fig. 18. Average amorphous depth (nm) as a function of fluence. This value gives an idea about the evolution of the amorphous region as a function of fluence. The error bars represent the standard deviation and they are an estimation of the amorphous-crystalline interface roughness. (**a**) The crystal is irradiated with Cl at 45.8 MeV, (**b**) The crystal is irradiated with Si at 5 MeV.

analytical approach in relation to those amorphous thick layers?. The MonteCarlo approach is the only suitable tool to deal with several relevant features that are associated to the statistical nature of the ion-matter interaction. There is one particular aspect that may play a relevant role for photonic (waveguide) applications, namely the definition (boundary) of the amorphous-crystalline interface. In fact, the MonteCarlo method provides a unique way to simulate the microstructure of the interface i.e. its roughness and abruptness. Let us compare the situation for irradiations with Si at 5 MeV and Cl at 45.8 MeV. From the MonteCarlo results we can extract the local amorphous depth at any (x, y) position for every fluence as shown in the right side of **Figs. 12** and **13**. Averaging the local amorphous depth to all the (x, y) positions (10.000 cells), we get the average amorphous depth together with its standard deviation. In **Fig. 18** we plot the average amorphous depth for the two considered irradiation cases as a function of fluence using the standard deviation as error bars. Note that the homogeneous amorphous depth obtained from the analytical model gives the thickness of fully amorphous uniform layers. The average amorphous depth calculated now with the MonteCarlo formalism does not consider whether a fully amorphous layer is formed or not, it simply gives an idea about the depth evolution of the

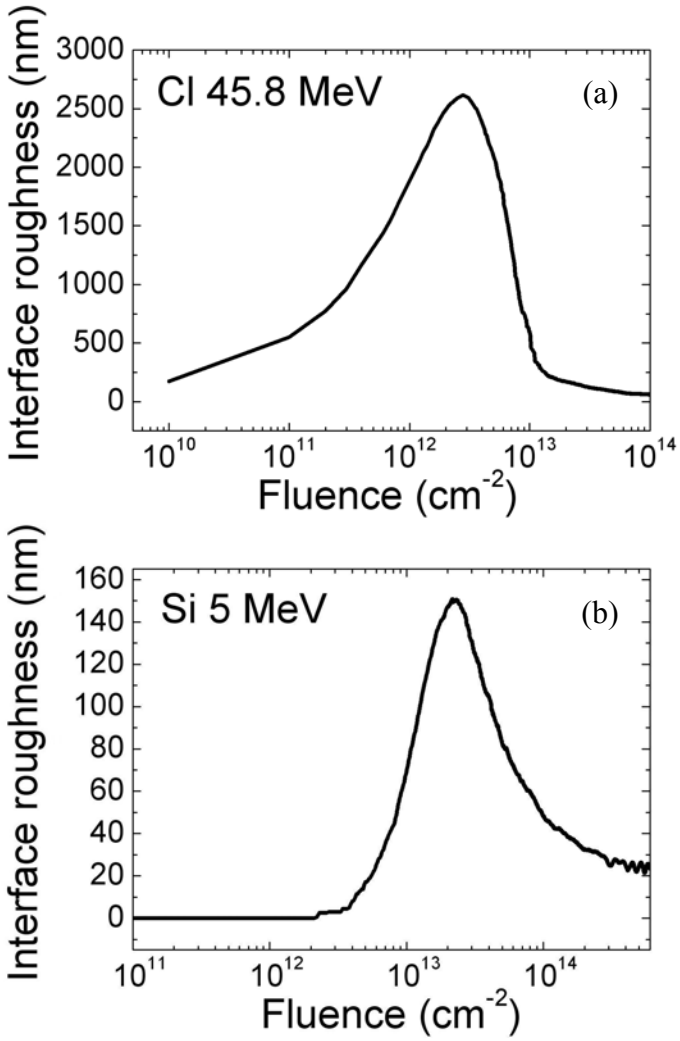

Fig. 19. Roughness of the crystalline-amorphous interface as a function of fluence for irradiations with (**a**) Cl ions at 45.8 MeV, (**b**) Si ions at 5 MeV.

amorphous-crystalline interface as a function of depth. Moreover, one can use the standard deviation of the average amorphous depth as a parameter of roughness. In other words, it is an useful estimation of the width of the crystalline-amorphous boundary. In **Fig. 19** it is plotted for irradiations with both ions. One should note that the coexistence of crystalline regions within the amorphous layer has been confirmed by micro-Raman spectroscopy [10, 21]. As expected, one sees that the boundary is much better defined for high fluences and that the definition is bad for low fluences where the layer is not yet truly amorphous. It is worthy to notice the importance of these results for the optimization of waveguide performance, in which energy losses during the propagation appears very relevant.

7.8. Summary and general conclusions.

As to the kinetics of amorphization for a given material the situation appears quite different. Although ion energy plays a role on such kinetics for the nuclear damage it shows drastic differences for electronic amorphization. Recent experiments on many dielectric and semiconductor crystals have conclusively shown that the structural damage induced on dielectric materials by swift ions, in which the electronic stopping power is dominant, has some peculiar features such as thresholding and cumulative character. The existence of a stopping power threshold to cause lattice amorphization has been satisfactorily explained by the thermal spike model as a melting-resolidification process around the ion trajectory (latent track formation). On the other hand, the cumulative (additive) damage behaviour under successive irradiation is not consistent with such model. In other words, there is a clear transition from a Poisson-like amorphization kinetics behaviour for stopping powers above threshold (typical of a direct process, *direct impact model,* as a result of track overlapping) to a sigmoidal evolution below threshold, where no amorphization should be induced. The existence of a critical ion energy that changes from a Poisson to an Avrami behaviour may be a good method to distinguish the two, electronic and nuclear, mechanisms.

Here we present experimental results on $LiNbO_3$ that show clear evidence of the cumulative behaviour through the observation of an Avrami-like (sigmoidal) kinetics, $f_a = 1 - \exp\{-(\phi/\phi_0)^n\}$, for the growth of the normalized disordered area f_a as a function of fluence, for irradiation conditions below as well as above threshold. For irradiations well above threshold the measured Avrami curves correspond to the Poisson limit *(n = 1),* whereas for conditions below threshold, the Avrami curves present parameters n and ϕ_0 , that steadily increase on decreasing electronic stopping power.

The amount of disorder that is assessed by RBS-C in $LiNbO_3$ has been analyzed using a recently proposed model - non-radiative exciton-decay model- to calculate the defect profile generated by every ion impact. The analysis describes the de-channeling caused at the surface by using a "filter" function. It is concluded that the amorphized area (core) of the track is markedly overestimated for stopping powers near the threshold value. The proposed scheme to describe the formation of the halo and predict its diameter represents, just, a first attempt for a quantitative analysis of the problem.

Within those cumulative models every ion impact is expected to produce an inner amorphous core surrounded by a defective halo when the electronic stopping power overcomes a certain threshold that generates such critical defect concentration. Below threshold only a halo (defective region) should be produced without causing amorphization. Anyhow, the complex structure of the track should play a key role in determining the kinetics for amorphization through track overlapping. Therefore, a suitable cumulative model can offer a useful proof for the track structure and a relevant test for the theoretical modelling of the damage process.

In this sense, a MonteCarlo approach to the non-radiative exciton-decay model has been developed. It takes into account the statistical spatial distribution of the ion impacts at any depth in the sample (in particular, at the sample surface). At variance with the previous analytical formulation, the new method is able to describe adequately the range of low irradiation fluences where overlapping is still poor and statistical divergences of the true amorphized area with

regard to the average values are quite significant. A good representation of the Avrami's and Poisson´s -type kinetics for amorphization has been achieved. On the other hand, the thickness of the layers having a mixed amorphous-crystalline composition has been obtained as a function of fluence.

We consider that the MonteCarlo approach will be a useful tool to deal with other pending ion-beam damage problems such as the coupling between the disorders caused by nuclear elastic collisions and electronic excitations. On the other hand, it is worthy to notice that, an important parameter that has not yet been investigated for the electronic amorphization is the sample temperature during irradiation.

7.9. References.

[1] A. Rivera, M. L. Crespillo, J. Olivares, G. García and F. Agulló-López, *"Effect of defect accumulation on ion-beam damage morphology by electronic excitation in lithium niobate: A MonteCarlo approach"*, Nucl. Instr. Meth. B 268 (2010) 2249–2256.

[2] W. J. Weber, R. C. Ewing, C. R. A. Catlow, T. Diaz de la Rubia, L. W. Hobbs, C. Kinoshita, Hj. Matzke, A. T. Motta, M. Nastasi, E. K. H. Salje, E. R., Vance and S.J. Zinkle, *"Radiation effects in crystalline ceramics for the immobilization of high-level nuclear waste and plutonium"*, J. Mater. Res. 13 (1998) 1434-1484.

[3] I. Farnan, H. Cho and W. J. Weber, *"Quantification of actinide a-radiation damage in minerals and ceramics"*, Nature 445 (2007) 190.

[4] B. Canut, S. M. M. Ramos, R. Brenier, P. Thevenard, J.L. Loubet, M. Toulemonde, *"Surface modification of $LiNbO_3$ single crystals by swift heavy ions"*, Nucl. Instrum. Methods B 107 (1996) 194 -198.

[5] A. Meftah, J. M. Constantini, N. Khalfaoui, S. Boudjadar, J. P. Stoquert, F. Studer and M. Toulemonde, *"Experimental determination of track cross-section in $Gd_3Ga_5O_{12}$ and comparison to the inelastic thermal spike model applied to several materials"*, Nucl. Instrum. Methods B 237 (2005) 563-574.

[6] M. Toulemonde, W. Assman, C. Dufour, A. Meftah, F. Studer, and C. Trautmann, in: *"Ion Beam Science: Solved and Unsolved Problems"*. P. Sigmund, (Ed.), *The Royal Danish Academy of Sciences and Letters*, Copenhagen, 2006, pp. 263.

[7] G. Szenes, *"General features of latent track formation in magnetic insulators irradiated with swift heavy ions"*, Phys. Rev. B 51 (1995) 8026-8029.

[8] G. G. Bentini, M. Bianconi, M. Chiarini, L. Correra, C. Sada, P. Mazzoldi, N. Argiolas, M. Bazzan and R. Guzzi, *"Effect of low dose high energy O^{3+} implantation on refractive index and linear electro-optic properties in X-cut $LiNbO_3$:Planar optical waveguide formation and characterization"*, J. Appl. Phys 92 (2002) 6477.

[9] G. G. Bentini, M. Bianconi, L. Correra, M. Chiarini, P. Mazzoldi, C. Sada, N. Argiolas, M. Bazzan and R. Guzzi, *"Damage effects produced in the near-surface region of x-cut $LiNbO_3$ by low dose, high energy implantation of nitrogen, oxygen, and fluorine ions"*, J. Appl. Phys 96 (2004) 242.

[10] J. Olivares, G. García, F. Agulló-López, F. Agulló-Rueda, A. Kling, J.C. Soares, *"Generation of amorphous surface layers in $LiNbO_3$ by ion-beam irradiation: thresholding and boundary propagation"*, Appl. Phys. A 81 (2005) 1465-1469.

[11] F. Agulló-López, G. García and J. Olivares, *"Lattice preamorphization by ion irradiation: Fluence dependence of the electronic stopping power threshold for amorphization"*, J. Appl. Phys 97 (2005) 093514.

[12] S. M. M. Ramos, R. Brenier, B. Canut, G. Fuchs, P. Thevenard, M. Trilleux, A. Meftah, M. Toulemonde, *"Europium diffusion enhancement in lithium niobate by GeV gadolinium ion irradiations"*, J. Appl. Phys. 77 (1995) 2952.

[13] J. Vetter, R. Scholz, N. Angert, *"Investigation of latent tracks from heavy ions in GeS crystals by high resolution TEM"*, Nucl. Instr. Meth. B 91 (1994) 129-133.

[14] F. Thibaud, J. Cousty, E. Balanzat, S. Bouffard, *"Atomic-force-microscopy observations of tracks induced by swift Kr ions in mica"*, Phys. Rev. Lett. 67 (1991) 1582-1585.

[15] J. Ackermann, N. Angert, R. Neumann, C. Trautmann, M. Dischner, T. Hagen, M. Sedlacek, *"Ion track diameters in mica studied with scanning force microscopy"*, Nucl. Instr. Meth. B 107 (1996) 181-184.

[16] S. Abu Saleh, and Y. Eyal, *"Porous tracks along wakes of swift uranium ions in polyimide"*, Appl. Phys. Lett. 85 (2004) 2529.

[17] D. Albrecht, P. Armbruster, R. Spohr, M. Roth, K. Schaupert, H. Stuhrmann, *"Investigation of heavy ion produced defect structures in insulators by small angle scattering"*, Appl. Phys. A: Mater. Sci. Process. 37 (1985) 37-46.

[18] A. Meftah, F. Brisard, J. M. Constantini, M. Hage-Ali, J. P. Stoquert, F. Studer and M. Toulemonde, *"Swift heavy ions in magnetic insulators: A damage-cross-section velocity effect"*, Phys. Rev. B 48 (1993) 920-925.

[19] M. Bianconi, N. Argiolas, M. Bazzan, G. G. Bentini, M. Chiarini, A. Cerutti, P. Mazzoldi, G. Pennestri and C. Sada, *"On the dynamics of the damage growth in 5 MeV oxygen-implanted lithium niobate"*, Appl. Phys. Lett. 87 (2005) 072901.

[20] A. Garcia-Navarro, F. Agulló-López, M. Bianconi, J. Olivares and G. García, *"Kinetics of ion-beam damage in lithium niobate"*, J. Appl. Phys. 101 (2007) 083506.

[21] J. Olivares, A. García-Navarro, G. García, F. Agulló-López, F. Agulló-Rueda, A. García-Cabañes and M. Carrascosa, *"Buried amorphous layers by electronic excitation in ion-beam irradiated lithium niobate: structure and kinetics"*, J. Appl. Phys 101 (2007) 033512.

[22] J. Olivares, A. García-Navarro, G. García, A. Méndez and F. Agulló-López, *"Optical determination of three-dimensional nanotrack profiles generated by single swift-heavy ion impacts in lithium niobate"*, Appl. Phys. Lett. 89 (2006) 071923.

[23] M. Enculescu, K. Schwartz, C. Trautmann and M. Toulemonde, *"Heavy ion induced damage in NaCl and KCl crystals"*, Nucl. Instr. Meth. B 229 (2005) 397-405.

[24] C. Trautmann, K. Schwartz, J. M. Constantini, T. Steckenreiter and M. Toulemonde, *"Radiation defects in lithium fluoride induced by heavy ions"*, Nucl. Instr. Meth. B 146 (1998) 367-378.

[25] A. Rivera, A. Méndez, G. García, J. Olivares, J. M. Cabrera and F. Agulló-López, *"Ion-beam damage and non-radiative exciton decay in $LiNbO_3$"*, Journal of Luminescence 128 (2008) 703-707.

[26] H. J. Fecht, *"Defect-induced melting and solid-state amorphization"*, Nature 356 (1992) 133.

[27] L. C. Feldman, J. W. Mayer and S. T. Picraux *"Materials Analysis by Ion Channeling"*, Vol., (Ed.), Academic Press, New York, 1982.

[28] E. Albertazzi, M. Bianconi, G. Lulli, R. Nipoti and M. Cantiano, *"Different methods for the determination of damage profiles in Si from RBS-channeling spectra: a comparison"*, Nucl. Instr. and Meth. B 118 (1996) 128-132.

[29] M. Bianconi, E. Albertazzi, S. Balboni, L. Colombo, G. Lulli and A. Satta, *"Channeling characterization of defects in silicon: an atomistic approach"*, Nucl. Instr. and Meth. B 230 (2005) 185-192.

[30] G. García, J. Olivares, F. Agulló-López, A. García-Navarro, F. Agulló-Rueda, A. García-Cabañes and M. Carrascosa, *"Effect of local rotations on the optical response of $LiNbO_3$: Application to ion-beam damage"*, Europhys. Lett. 76 (2006) 1123-1129.

[31] C. Trautmann, S. Klaumünzer and H. Trinkaus, *"Effect of Stress on Track Formation in Amorphous Iron Boron Alloy: Ion Tracks as Elastic Inclusions"*, Phys. Rev. Lett. 85 (2000) 3648–3651.

[32] H. Trinkaus, *"Dynamics of viscoelastic flow in ion tracks: origin of plastic deformation of amorphous materials"*, Nucl. Instr. and Meth. B 146 (1998) 204-216.

[33] F. Villa, M. Grivet, M. Rebetez, C. Dubois, A. Chambaudet, A. Chevarier, P. Martin, F. Brossard, G. Blondiaux, T. Sauvage and M. Toulemonde, *"Damage morphology of Kr ion tracks in apatite: dependence on dE/dX"*, Radiat. Meas. 31 (1999) 65-70.

[34] P. I. Gaiduk, A. Nylandsted Larsen, C. Trautmann and M. Toulemonde, *"Discontinuous tracks in arsenic-doped crystalline $Si_{0.5}Ge_{0.5}$ alloy layers"*, Phys. Rev. B 66 (2002) 045316.

[35] M. Lang, U. A. Glasmacher, B. Moine, R. Neumann and C. A. Wagner, *"Etch-pit morphology of tracks caused by swift heavy ions in natural dark mica"*, Nucl. Instr. and Meth. B 218 (2004) 466-471.

[36] J. Ziegler, computer code SRIM version 2008, (http://www.srim.org).

[37] J. F. Ziegler, J. P. Biersack and U. Littmark, (Ed.), *The Stopping and Ranges of Ions in Solids*, Pergamon Press, New York, 1985.

[38] B. Canut, R. Brenier, A. Meftah, P. Moretti, S. Ould Salem, M. Pitaval, S.M.M. Ramos, P. Thevenard and M. Toulemonde, *"Latent track formation in $LiNbO_3$ single crystals irradiated by GeV Uranium ions"*, Rad. Eff. and Defect in solids 136 (1995) 307-310.

[39] W. K. Chu, J. W. Mayer and M. A. Nicolet, *"Backscattering Spectrometry"*, Vol., (Ed.), Academic Press, New York, 1978.

[40] M. Bianconi, G. G. Bentini, M. Chiarini, P. De Nicola, G. B. Montanari, A. Nubile and S. Sugliani, *"Defect engineering and micromachining of Lithium Niobate by ion implantation"*, Nucl. Instr. and Meth. B 267 (2009) 2839-2845.

[41] W. J. Weber, *"Models and mechanisms of irradiation-induced amorphization in ceramics"*, Nucl. Instr. Meth. B 166-167 (2000) 98.

[42] A. Rivera, M. L. Crespillo, J. Olivares, R. Sanz, J. Jensen and F. Agulló-López *"On the exciton model for ion-beam damage: The example of TiO_2"*, Nucl. Instr. Meth. B 268 (2010) 3122-3126.

[43] A. Rivera, J. Olivares, G. García, J.M. Cabrera, F. Agulló-Rueda and F. Agulló-López, *"Giant enhancement of material damage associated to electronic excitation during ion irradiation: The case of $LiNbO_3$"*, Phys. Status Solidi A 206 (2009) 1109-1116.

[44] A. García-Navarro, A. Méndez, J. Olivares, G. García, F. Agulló-López, M. Zayat, D. Levy and L. Vazquez, *"Morphology of ion tracks and nanopores in $LiNbO_3$ produced by swift-ion-beam irradiation"*, Nucl. Instr. Meth. B 249 (2006) 172-176.

[45] A. Rivera, J. Olivares, M. L. Crespillo, G. García, M. Bianconi and F. Agulló-López, *"Assessment of swift-ion damage by RBS/C: Determination of the amorphization threshold"*, Nucl. Instr. Meth. B 267 (2009) 1460-1463.

[46] G. Szenes, *"Ion-velocity-dependent track formation in yttrium iron garnet: A thermal-spike analysis"*, Phys. Rev. B 52 (1995) 6154–6157.

Chapter 8

Nanopores obtained by chemical etching on ion irradiated lithium niobate.

8.1. Introduction.

Nanometer-diameter amorphous tracks are generated by irradiation with swift ions on a variety of dielectric crystals and minerals whenever the electronic stopping power is above a certain threshold value [1-3] (i.e., $S_{th} \sim 5$ keV/nm for the case of $LiNbO_3$). It is well known that the ion damaged material presents an etching rate higher than the non-irradiated one, due to the induced defective areas after irradiation, so that, the *ion beam enhanced etching* (IBEE) turns into a valuable tool to develop nanostructures by differential chemical etching. Thus, these ion-tracks can be chemically etched to produce nanopores and a number of applications [1, 4, 5] have been tested or suggested including fission-fragment dosimetry, molecular sieves, magnetic storage, field-emission displays,... For most applications the morphology of these nanopores has to be carefully controlled and optimized, that means, it is necessary to have an accurate control of the morphology of the revealed nanopores.

So far, latent tracks in $LiNbO_3$, as relevant photonic material [6], have been produced and characterized by RBS-C and optical methods [7, 8]. The kinetics of chemical etching has also been studied by SEM [9-12] and the etching rate measured by profilometry in experiments where the role of nuclear processes is significant. On the other hand, very scarce information is available on the detailed morphology of single etched tracks [13], what is the relevant point for nanopatterning applications. To our knowledge no systematic investigation on this topic is available in the literature, although a few data have been reported [7, 14].

In this sense, this Chapter appears devoted to investigate a powerful tool that may allow us to obtain tailored-size nanostructured pores in an interesting material for optical applications like Lithium Niobate. This study is interesting both from the fundamental point of view and with the aim of optimizing and tailoring various technological applications like nanostructuring induced by ion beams, optical waveguides, etc. Therefore, in order to get a deeper insight into the formation of nanostructured pores generated by chemical etching after ion irradiation on Lithium Niobate, a systematically study under different etching parameters is carried out along this Chapter.

On the other hand, in the framework of the study on the structure of the damage produced in the electronic excitation regime by swift-heavy ions, the information revealed after chemical etching of latent tracks should be useful to understand the damage mechanisms. Thus, this Chapter presents investigations on nanostructured Lithium Niobate by IBEE. A morphological characterization of the revealed nanopores, mostly by scanning force microscopy, and their fabrication process by ion irradiation is presented in detail.

Hence, with the aim of obtaining a further understanding into the etched ion track formation process, and to ascertain the role of irradiation conditions (ion energy, ion stopping power), as well as, etching parameters on the morphology of etched tracks; ions with input stopping powers from 3.4 keV/nm (F at 5 MeV) up to 35 keV/nm (Pb at 2300 MeV) have been used. By this way, a correlation of the track etching velocity with the ion stopping power/energy, so that the effects of electronic damage can be easily discriminated from those due to nuclear collisions, can be performed. The role of thermal annealing after irradiation on the track morphology has been also investigated, moreover, both aqueous and vapour etchings in different chemical solutions were systematically investigated.

8.2. Experimental procedure: ion-beam irradiations, etchings and AFM.

X-cut oriented congruent $LiNbO_3$ single optical grade crystals from Photox Optical Systems Ltd. of 8 x 7 mm^2 and 1 mm thickness with optical polished surfaces were irradiated with swift heavy ions at room temperature. The irradiations were performed at normal incidence in the 5 MV Tandem accelerator installed at CMAM-UAM facility (Madrid, Spain) with Br, F and Cu ions; in GANIL (Caen, France) with Kr ions, and in GSI (Darmstadt, Germany) with Pb ions. The energies, stopping powers (S_e) at the surface, and projected ranges (R_P), of the ions species used in this study are listed in **Table I**. Irradiation fluences were in the range of: 1 e7- 1 e9 at/cm^2 in order to get latent isolated tracks. The evolution of the electronic energy loss (S_e), calculated with the SRIM-2003 code [15] as a function of penetration depth is shown in Fig. **1 (a, b)**. In the energy domain explored here, the nuclear stopping power (S_n) is negligible over the major part of the of the ion trajectory and consequently at the surface. It is clearly seen that, whatever the irradiation conditions, the slowing down of the studied ions is mainly governed by electronic processes up to a depth of a few microns (see **Fig.1** and **Table I**).

Ion	Energy (MeV)	Energy (MeV/amu)	S_e surface (keV/nm)	S_n max (keV/nm)	R_p (μm)
$^{19}F^{3+}$	5	0.3	3.4	0.1	2.8
$^{79}Br^{5+}$	12	0.2	6.0	0.5	3.8
$^{79}Br^{5+}$	22	0.3	8.7	0.5	5.0
$^{79}Br^{8+}$	46	0.6	11.9	0.5	7.2
$^{63}Cu^{9+}$	51	0.8	11.9	0.4	8.0
$^{78}Kr^{31+}$	809	10.4	12.3	0.5	62
$^{208}Pb^{55+}$	2300	11.1	35	1.7	72.8

Table I. Irradiation parameters including the electronic energy loss (S_e) at the sample surface, the maximum nuclear energy loss (S_n) and the projected ion range (R_p) according to the SRIM-2003 code [15].

For all the cases under study, the maximum value of the energy loss (S_e) is reached at the surface; this value is clearly above the expected *amorphization threshold* for lithium niobate (S_{th} ~ 4 - 6 keV/nm) [7], thus, producing latent tracks along the ions trajectories from the crystal surface. Except for the case of F 5 MeV ions, where we are below the stopping power threshold during all the ion range, no amorphous track will be created along the path, neither defective halo of damage crystal. On the other hand, for the case of ions from GANIL and GSI, the S_e at the surface is well above the threshold and it is approximately constant along all the ion range till reach the Bragg peak, which is localized buried far away (~ 50 μm) from the surface of the crystal.

Chemical etchings were performed in aqueous solutions and vapor, at room temperature and hot echants in pure HF with concentrations of 5 % and 40 %, and blends of HF (40%) with

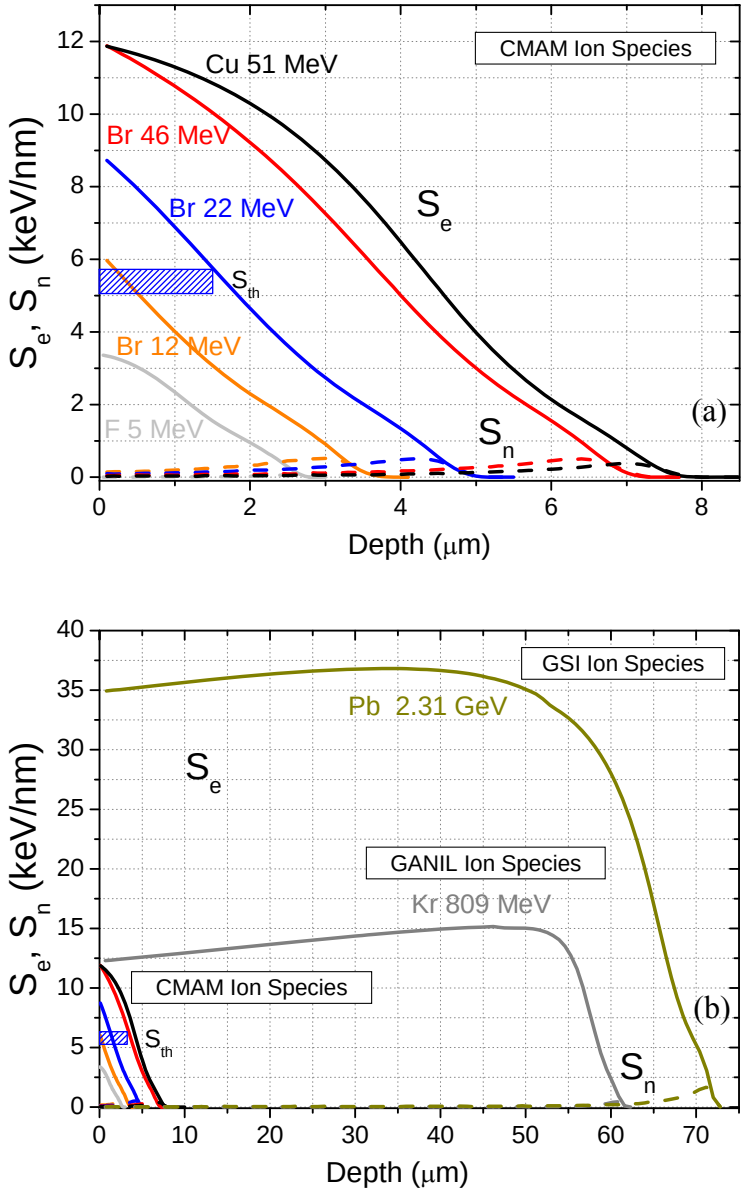

Fig. 1 (a, b). Electronic (S_e, solid lines) and nuclear (S_n, dashed lines) energy loss of CMAM ion species (F 5 MeV, Br 12, 22, 46 MeV, Cu 51 MeV) **(a)** and Facilities (GANIL, Kr 809 MeV and GSI, Pb 2.31 GeV) **(b)** as a function of penetration depth in $LiNbO_3$ obtained with the SRIM-2003 code [15]. In **(b)** all the stopping powers curves are shown to be compared the different magnitude order of the ions from different facilities. For comparison, the electronic stopping power for the *amorphization threshold* (S_{th}) is also shown.

HNO_3 (70%) in 1:1 and 1:2 ratio; anyhow, each case will be properly explained and discussed with more details in the following sections.

The main characterization technique used for the examination of surface morphology was an AFM commercial instrument from Nanotec Electrónica S.L. with phase-locked loop (PLL) feedback added to the dynamic or tapping mode which allowed us to realize accurate measurements. It resulted extremely necessary due to the presence of very strong interactions (attractive/repulsive) between the probe and the sample. This technique allowed us to carry out

high accurate measurements, providing high enough sensitivity to detect the smallest superficial changes on nanometric scale. AFM investigations were performed on X-cut samples to avoid the strong tip-surface interaction typically observed through the experience for Z-cut samples (piezoelectric behavior of $LiNbO_3$).

For further structural characterization of the nanopores the Philips CM200-FEG-UT transmission electron microscope (TEM) was used. Samples were prepared with the focused ion beam (FIB) and a gold film of 200 nm thickness was deposited on the surface. All images were recorded in bright field mode. Some complementary experiments using a Veeco Dektak 150 profilometer were performed.

8.3. Morphology of Nanopores in Lithium Niobate.

The morphology of the etched nanopores in swift heavy ion irradiated *x*-cut LN will be discussed throughout this section. Crystallographic facets are developed as the pore seems to open up at the sample surface during etching. Furthermore, the pore shape changes when certain parameters are modified.

8.3.1. Effect of irradiation on nanopores morphology.

In this study, the known behaviour earlier reported in the literature about changes in the pores shape, that is, pores emerging from Cu 51 MeV irradiated material are strongly anisotropic [13], whereas they are only slightly anisotropic in the case of Br 12 MeV irradiations, is confirmed.

AFM pictures are shown in **Fig. 2 (a-f)**, corresponding to ions and energies indicated on the images. For stopping powers close to the threshold value (5 keV/nm), as for F at 5 MeV (**Fig. 2 (a))**, the shape of the nanopores exhibits axial symmetry and is approximately circular. The same shape is also observed for larger stopping powers at low enough etching times (≤ 10 min) and weaker acid concentration (HF 5% and blends). On increasing stopping power and standard etching times (20-60 minutes at RT) the pores clearly develop a pyramidal structure with well-defined facets, as illustrated by the irradiations with Br at 46 MeV (**Fig. 2 (d)**). At even higher stopping powers, i.e. for irradiations with Kr at 809 MeV (**Fig. 2 (e)**) and Pb at 2300 MeV (**Fig. 2 (f)**), the faceting turns into a rather smooth and elongated profile. The long axis lies at 33º from the *z* crystallographic axis (see **Fig. 2 (d)**) and so approximately coincides with the easy cleavage plane [6]. Track etch pit has a double-shape well that was also observed in our previous work [13]. It has been checked that the above morphological trend is independent of the AFM tips used for the observations and the scanning direction. Hence, we can state that, the track morphology after etching markedly depends on the irradiation conditions: ion and energy.

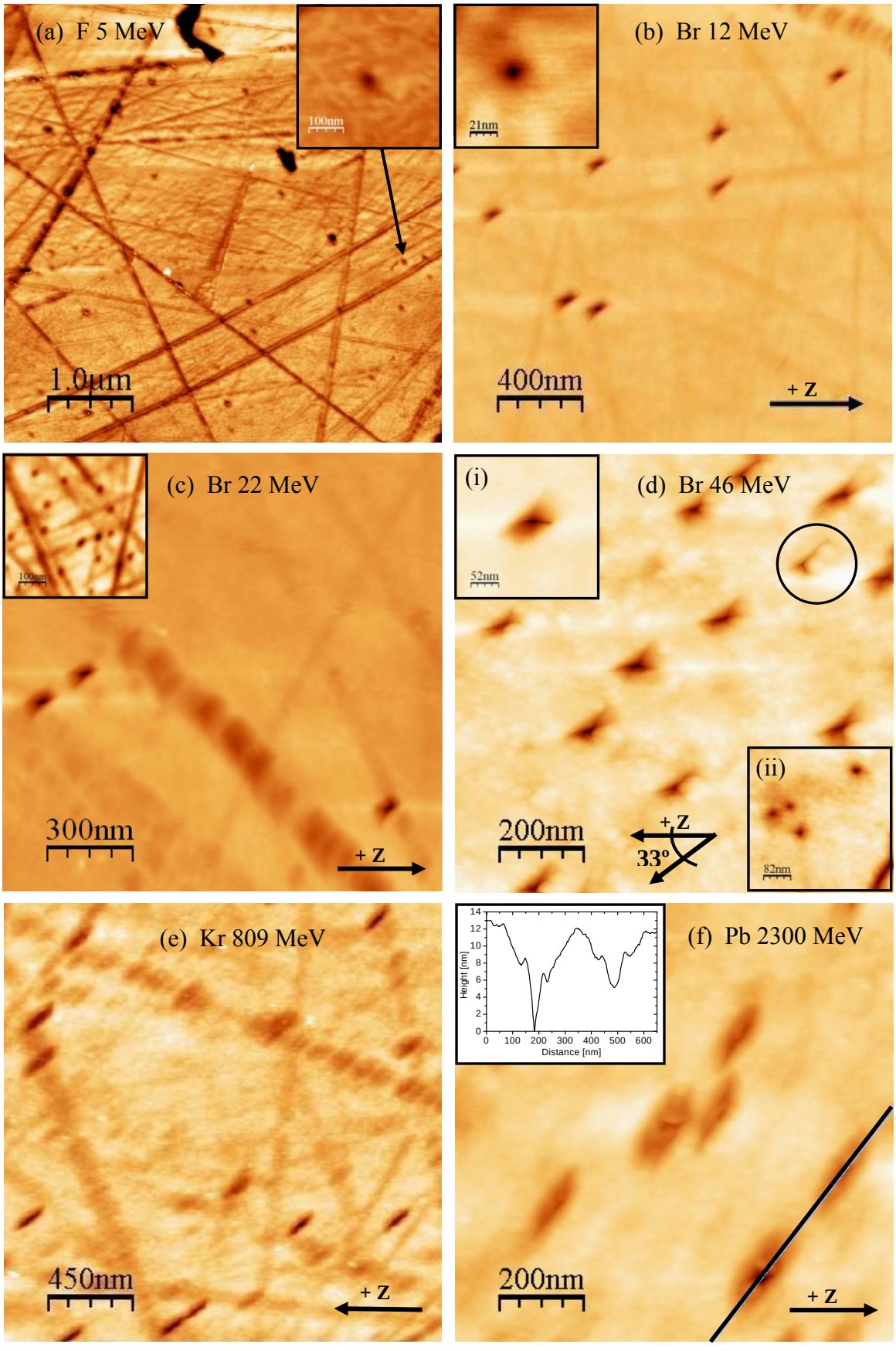
(a) F 5 MeV
100nm
1.0µm
(b) Br 12 MeV
21nm
400nm
+ Z
(c) Br 22 MeV
100nm
300nm
+ Z
(i)
52nm
(d) Br 46 MeV
200nm
+ Z
33°
(ii)
82nm
(e) Kr 809 MeV
450nm
+ Z
Height [nm]
Distance [nm]
(f) Pb 2300 MeV
200nm
+ Z

Fig. 2 (a-f). This overview illustrates diverse pore morphologies. AFM images of different etch pit morphologies obtained after etching tracks (HF 40% at RT for different times) produced with different kind of ions and energies: **(a)** F 5 MeV, after 60 min, z-scale: 8 nm; **(b)** Br 12 MeV, after 60 min, z-scale: 30 nm; **(c)** Br 22 MeV, after 60 min, z-scale: 30 nm; **(d)** Br 46 MeV, after 60 min, z-scale: 30 nm; **(e)** Kr 809 MeV, after 10 min, z-scale: 10 nm and **(f)** Pb 2300 MeV, after 10 min, z-scale: 16 nm. Different AFM image sizes and depth-scales have been used. The inset in **(f)** shows the depth profile recorded along the line across the long axis of the two elongated pores. The lines are the polishing scratches revealed after etching process in **(a)**.

8.3.1.1. Nanopores revealed from subthreshold irradiations. F 5 MeV irradiated LN.

After the irradiation with the low energy, F 5 MeV ions, pores could just be revealed only after etching for 60 min in 40% HF at RT (in the following referred to as our *standard conditions*). At earlier stages there are no pores visible. It is surprising to actually see pores at all, because the stopping power at the surface was only S_e = 3.4 keV/nm. This is below the known amorphization threshold of about ~ 4-6 keV/nm. Of course, damage is done nevertheless, and so the material is punctually weakened where single ion impacts have occurred. It is also proposed that the threshold for damage creation in LN and other insulating materials depends on the energy of the incident ion beam, the so called "velocity effect" [3]. The lower the ion energy, the lower is the damage creation threshold, which may be as low as ~ 1.3 keV/nm in case of 1.3 MeV Xe ion beam (at this energy (E= 0.01 MeV/amu, S_n is already greater than S_e). According to Meftah et al, this dependence accounts for the higher energy density deposited on the electrons, and thus to the lattice atoms, and may be counted to the velocity effect.

In **image 2 (a)**, only the really small dark spots are pores. Their number is slightly lower than the used fluence, but still coincides very well with the nominal value of 1 e8 at/cm^2 in the range of the experimental error. It is expected that not every ion creates an etchable track [4]. The inset in the upper right corner shows a zoom into the pore indicated by the arrow. Looking closely, one can already suspect the slight anisotropy, even in this case of very low energy. However, although one may take this as a first sign that the pore could be anisotropic, which could be attributed to the crystals' etching behaviour and more or less independent of the energy of the ion that created the nanotrack, we have to consider the shape of the nanopores exhibits axial symmetry and is approximately circular. In this stage the evidence is still poor, considering that drift during the image acquisition could also cause the pores to be elongated. The image has been captured with a tip of the AR5 series (high aspect ratio tips).

We have to remark that, although more attempts with different etching times and etching conditions were carried out: HF 40%, L(liquid), RT, 60 min; and very aggressive etching conditions: HF 40%, L(liquid), 55 ºC, 30 min, trying to reveal some kind of nanostructures, in any case, we never obtain better results, inclusive with set ups for the AFM acquisition image extremely forced and using very high aspect ratio probes (AR 5). The usual identified nanopores features were about: diameter ~100 nm, and depth ~2.5 nm. Moreover, although the etching conditions were modified substantially, the sizes of the pores never develop to deeper pores.

8.3.1.2. Nanopores revealed from Bromine ions irradiations.

8.3.1.2.1. Case of Br 12 MeV.

For the various bromine irradiations a couple of different pore shapes were found. **Image 2 (b)** shows a sample surface irradiated with Br 12 MeV, which was subsequently etched in 40% HF for 60 min at RT. The pores here are already much deeper (≈18 nm) than in case of F 5 MeV, and one can clearly see anisotropy. The image is very clear, showing an absolutely clean surface. The scratches seem to have almost vanished and appear less deep. Here, the same colour range corresponds to a total depth three times as deep as in the previous one. The arrow in the lower right corner assigns the +z direction of the crystal. The image and inset are both zoomed into larger scans of $3 \times 3\ \mu m^2$. The inset represents a sample which was irradiated alike, but immersed in the acid mixture of HF:HNO_3 in a 1:1 ratio for 3 min at RT. At this stage the pores are still perfectly circular. The height z-scale in the inset extends to 2 nm total.

It is necessary to comment that, firstly, we etched the samples step by step, attacking them for the missing time to reach the next etching stage (0.5-30 min), but in the early stages it is very hard to see any differences in pore size or depth. Basically all pores look equally small, which is in these very early stages due to the limits of our method to reveal them. In case of the inset, the pores only have diameters of about 25 nm and the tip entered 1.3 nm deep. For that reason it is really not sure if it penetrated correctly into the pore or not. According to the calculated tip shape from tip simulation section the probe should have entered ≈ 16 nm into a 25 nm wide pore. In many cases the pores looked the same after different etching times (up to 10 min), even in very clear images, which could be caused by eventually discontinuous tracks in the low velocity regime. In *Section 6.3.3*, TEM investigations show that in case of Br 46 MeV and Cu 51 MeV, tracks are homogeneously damaged according to the image contrast (see **Section** *TEM results*).

In order to exclude a possible doubt that a reaction salt from the etching of the substrate that could cover the etched pores after the first etching steps, and thereby retarding a further attack, we immersed the samples only once to reach the desired stage. Following this procedure, a set of more reproducible results were obtained. Such etching behaviour is not known to be common according other research groups, which are mostly stepwise etching bulk material. In case of very tiny nanopores capillary effects or similar may occur.

8.3.1.2.2. Case of Br 22 MeV.

The first pores, which were revealed with our AFM equipment, are shown in the inset of **Image 2 (c)**. The image was captured directly in Dynamic Mode (inset, z-scale: 3 nm). In this early phase, after only 3 min of etching in the 1:2 blend of HF:HNO_3 at RT, the pores look similar to the almost circular ones from the fluorine irradiation but are smaller due to the shorter etching time.

The large image shows pores that arose after etching in 40% HF for 60 min at RT. A starting more defined trapezoidal feature of the revealed pores than in the later case of Br 12

MeV is observed[1]. An equivalent pore features is reached when immersing the sample directly in the acid for shorter times. The initial appearing facets, which were observed in a similar form in other crystals (e.g. LiF [16]) will be discussed more in detail in the following sections.

8.3.1.2.3. Case of Br 46 MeV.

The sample investigated in **Figure 2 (d)** was irradiated with Br ions at 46 MeV[2]. The sample was etched in 40% HF for 60 min at RT. It is evident that not all pores look exactly the same, which, in general, is always a good quality indicator for the measurement (if the image quality does not change and the tip was not evidently modified during the capture).

Looking closely at the biggest pore in the center (**Figure 2 (d)**), one realizes that the orientation of the triangular shape is not consistent with the other ones. This is most likely due to the drying or cleaning procedure. After the sample was etched it was wiped with a paper soaked in acetone that may have covered the pores on one side. If this is the case, the paper was wiped from the upper left towards the lower right corner, because all tissue remains, that partly cover the pores, stick on the lower right side. An obvious case is the encircled pore, which is almost completely occluded. All other nanopores are also covered to some extent, which may influence the observed pore shape, and thus turn the direction of pore orientation[3]. A clean sample measured with AR5 tip in this etching stage is presented in the upper inset **(i)** (nevertheless, it will mentioned more detailed in a following section). Another possibility how the contamination could be explained is that the tip may have picked up a dust-particle. Then, the dust particle as the larger structure would convolute with the surface leaving its shape in every position like an indenter would leave its print. This would also explain the dirt covering the pores always on the lower right side. However, it is worthy mentioned that the same pores features have been observed for other samples measured with different tips under the same etching conditions.

The arrow again indicates the +z-direction of the crystal. The angle, which is enclosed by the longer pore axis and the crystallographic one, is ≈ 33º ± 5º, as is marked in the picture. For the pores of all other irradiations and etching experiments, the angle is the same within the uncertainties of the measurement. The angle of 32.75º with respect to the +z-direction is known to be a plane of cleavage. This direction is reported to be chemically weak [6], which could be the reason that the pores are "stretched" in this direction. Of course the combination of the etch rates in the ± *y* and ± *z* contribute to the final pore shape. Other crystallographic axis may also contribute.

For shorter etching times and/or weaker acid concentration, the pores look more circular, as shown in the inset on the bottom right **(ii)**. This image was taken after immersing an identically irradiated sample into the 5% HF solution for 60 min at RT. (z-scale: 7 nm).

---

[1] The bright stripes next to the pores in *fast scan direction* are due to a mathematical data correction. Via the applied flatten filter by software a line average is subtracted to eliminate offset adjustments during the measurement.

[2] Because the implementation for ultra-low fluences was not yet installed to the time of fabrication, the lowest possible fluence was 1 e9 at/cm^2.

[3] The surface is a quite dirty, showing little bright bumps. These nano-dust-particles were probably also left by the paper tissue. Because of this and other types of surface contaminations, cleaning methods were studied extensively. This was quite time consuming because the results were in most cases not very clear.

It is worthy to mention that, for sample cleaning after etching, it is recommended to not use paper tissue, neither when soaked in acetone since the paper may get stuck in the pores and can cover them up. Acetone baths did not leave residuals on the surface in most cases but some samples were still found to be disturbingly dirty, which could also be due to tip contamination. After cleaning with acetone, the surface was mostly harder to approach by the tip, especially when wiped with a soaked paper tissue. The solvent may have left charges on the surface, which dissipate only very slowly in the dielectric substrate and the sample can not be examined for long times. The most effective cleaning treatment was found to be rinsing the sample in de-ionized water in two steps and to subsequently dry it in the clean environment of a laminar air flow box providing filtered air and. Just before being scanned with the AFM, they were dried with dry nitrogen gas, in order to get a clean surface without powder or dirty.

8.3.1.3. Nanopores obtained after irradiations with Kr 809 MeV and Pb 2300 MeV ions.

When the ion energy is very high, the pores appear more elongated. A sample irradiated at GANIL with Kr 809 ions is shown in **Fig. 2 (e)**. It was etched for 10 min under *standard conditions* (40% HF, at RT). The Kr-pores are about twice as large as the Br 46 MeV-pores for the same etching conditions and the same time, evidencing stronger anisotropic. Thus, giving rise to the assumption that nanopore anisotropy increases with increasing energy.

An even more striking pore shape is found after irradiation with Pb ions at 2300 MeV at GSI. The pores shown in **Fig. 2 (f)** arose after etching the sample for 10 min under *standard conditions*. These pores are the biggest ones at this etching stage, which can be explained by the high stopping power of the impinging ions of 35 keV/nm and the accordingly higher defect creation. As mentioned in **Chapter 4. (Section 4.1.3)**, the samples were irradiated with Pb ions of a broad charge distribution and this could possibly be the cause for the different pore sizes at the same etching stage. However, even though the ions are stripped to an equilibrium charge state before entering the target, this equilibrium might be slightly different in $LiNbO_3$ than in Al. The energy deposition, and thereby the defect creation at the very surface should be inappreciably higher or lower from case to case. So far, it is scarcely understood how this process takes place exactly, but it is widely accepted that the effective ion charge has an effect. The big craters might have their origin in relation to the nanohills creation, which was not subject of this Chapter. Canut et. al. report nanohills of about 50 nm radius on swift heavy ion irradiated $LiNbO_3$, which represents a drastic lateral expansion of about one order of magnitude compared to the track diameter calculated from the i-TS [7]. This behaviour can not be explained by the Thermal Spike model and it is still subject-matter of active investigations. Thermal and mechanical effects are proposed to be the cause of the lateral expansion of the nanohills. Furthermore, it is reported that the swelling of a sample surface after irradiation is related to the projected ion range and depends on the deposited fluence [17]. These phenomena could well play a role in pore fabrication, but a clear dependency is not obvious.

The depth profile, in the inset, reveals the anisotropic well with a deeper pore inside. It was proposed before [13] that the impact corresponds to the amorphous nanotrack core, whereas the defective halo develops into the bigger crater. In the study by García-Navarro et al the *inner cores* were circular. Very interesting is that those *inner pores* (dark spots) are not located

exactly in the center of the surrounding wells (bright spots). Here, the effect is especially good visible in the smaller pores, those are not yet as evolved.

The etching rates of entirely amorphous material have to be totally equal in all directions and hence, the corresponding pores would be isotropic and circular. Obviously, this is not the case. It looks like the material is etched anisotropically in analogy to the predicted relations mentioned in a previous Section (**Chapter 4. Section 4.3** *Chemical etching behaviour of Lithium Niobate.* **Table I**). Due to the different etching rates in the different crystal directions, the pores grow faster in -*z* than in +*z*-direction. The fastest etch rate seems to be the one along the cleavage plane, which lets them appear stretched out in this direction. Furthermore, the inner pore tends to be closer to the diagonal edge on the +z side of the surrounding pore. It was proposed that the etch rate along -*y* is slightly higher than along +*y*. Thus, this axis should point to the bottom of the image, which was also expected because we irradiated the +*x* face of the crystal. The average depth of the halo is ≈ 4.5 nm in case of this sample, which was immersed in HF 40% at RT for 10 min. For comparison, García-Navarro declared that the etched Cu 51 MeV tracks had an approximate halo depth of 8 nm after 30 min in a 1:2 mixture of 40% HF and 70% HNO_3 [13, 18]. One has to keep in mind that pure hydrofluoric acid may attack more aggressively than the blend [10]. Due to the good image quality and because of the fact that the pores are not appear all exactly equally shaped, it is believed that the revealed nanopore shapes on both swift heavy ion irradiated samples are most probably real and include only small tip convolution.

8.3.1.4. Special morphology of nanopores revealed under other etching conditions.

Till now all the nanostructures shown have been revealed after the same etchings conditions, called *standard conditions* (40% HF, aqueous solution (L), at RT), after different times: 60 min. for F and Br series, and 10 min. for the swift heavy ions, Kr and Pb. However, remarkable structures with accurate morphologies can be obtained after adequate selection of the etching parameters. Specifically, from the use of acids in vapour estate (V) and, in aqueous solution (L) at high temperature (55 ºC), appropriated well defined nano-faceted structures can be developed. In the following pictures appear some of them; in particular we will pay attention in the shapes of pores revealed after irradiations with Br 22 MeV and Br 46 MeV. These AFM images have been recorded from different samples and using different kinds of probes. All the information appears in the figures and in the caption below. This demonstrate that the singular features developed after etching can be considered real and reproducible, independent on the AFM probes used; moreover, although some kind of convolution effect with the used tip must appear, this well-tailored nanofaceted structures, depends mainly on the differential etching behaviour presented by the crystallographic orientations of the crystal.

The overview showed in **Fig. 3 (a-f)** illustrates diverse pore morphologies emerged from etching samples under the conditions explained in the text. The AFM images show different etch pit morphologies obtained after etching tracks produced with different ions and energies. Different AFM image sizes and depth-scales have been used. Due to the changed etching and irradiation parameters the measurements can not be compared directly in most cases. However, **Figures 3 (a)** and **3 (f)** can be compared in order to see differences in the

Series Br 22 MeV

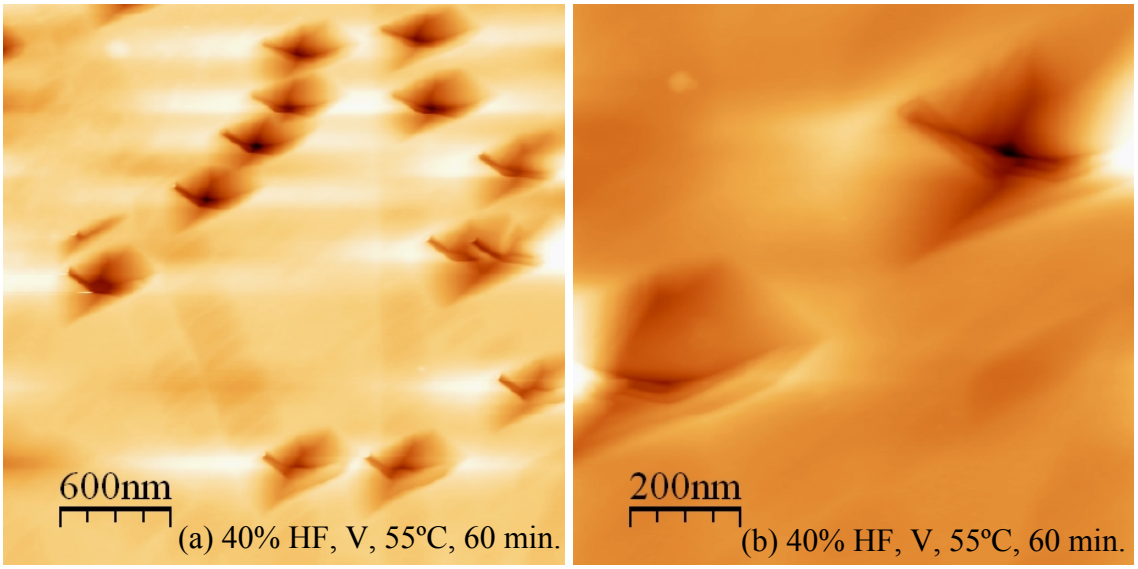

Fig. 3 (a, b). Series Br 22 MeV, Etching conditions: 40 % HF, Vapour (V) at 55 ºC, 60 min. **(a)** 3 x 3µm^2 AFM image of *x*-cut LN irradiated with Br 22 MeV at a fluence $\phi \approx$ 1.5 e9 at/cm^2, z-scale = 180 nm, **(b)** 1 x 1 µm^2 AFM zoom image showing the well defined facet pores revealed after etching, z-scale = 130 nm.

Series Br 46 MeV

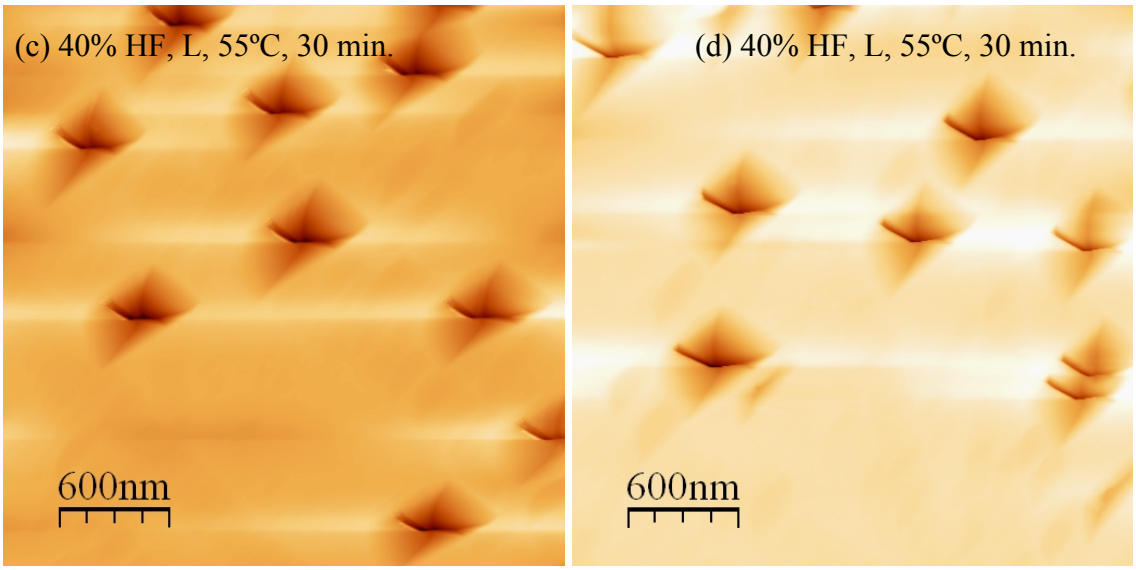

Fig. 3 (c, d). Series Br 46 MeV, Etching conditions: 40 % HF, Liquid (L) at 55 ºC, 30 min. **(c)** 3 x 3µm^2 AFM image of *x*-cut LN irradiated with Br 46 MeV at a fluence $\phi \approx$ 1 e8 at/cm^2, z-scale = 260 nm, recorded using a commercial NSC18 tip, **(d)** 3 x 3 µm^2 AFM image showing the well defined facet pores revealed after etching, z-scale = 260 nm. This image has been acquired with a PPP AFM probe.

nanostructures revealed after the same etching conditions for Br 22 MeV and Br 46 MeV irradiated samples. Moreover, in **Fig. 3 (e)** and **3 (f)** a time evolution of the pores morphology under the same conditions (40% HF, V, 55ºC) for 30 and 60 min., shows an increase of pores sizes and depths.

Series Br 46 MeV

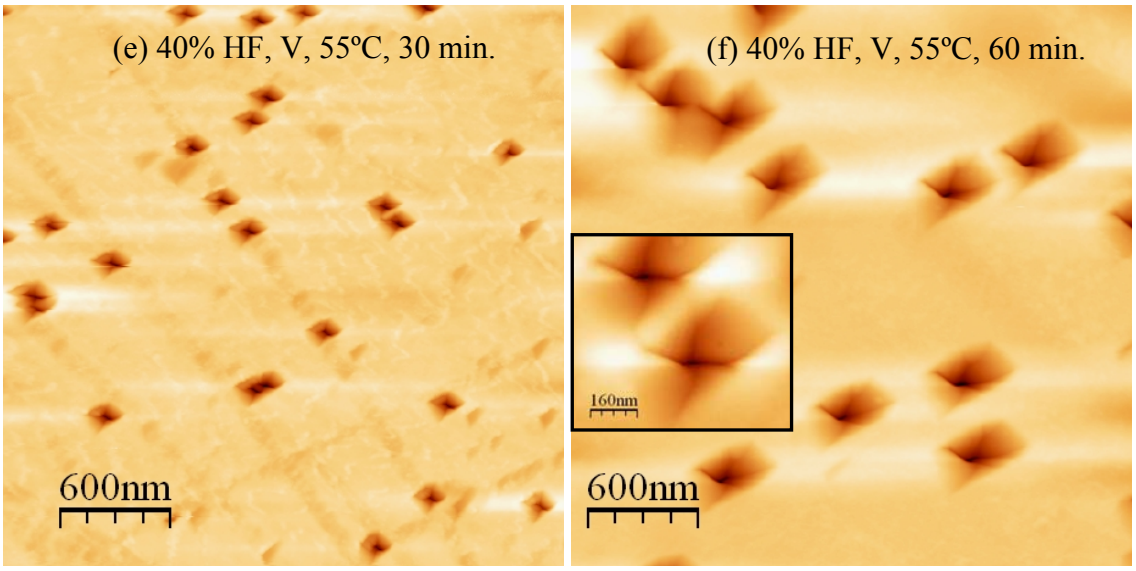

Fig. 3 (e, f). Series Br 46 MeV time evolution. Etching conditions: 40 % HF, Vapour (V) at 55ºC, **(e)** 3 x 3μm^2 AFM image of *x*-cut LN irradiated with Br 46 MeV at a fluence ϕ≈ 2 e9 at/cm^2, Etching time: 30 min., z-scale = 70 nm, recorded using a commercial NSC18 tip, **(f)** 3 x 3 μm^2 AFM image of *x*-cut LN irradiated at a fluence ϕ ≈ 1 e9 at/cm^2, Etching time: 60 min., z-scale = 170 nm, recorded using a commercial High Aspect Ratio AR 5 tip. The inset shows with more details the well defined revealed faceted nanopores, z-scale = 120 nm.

The effect of the vapour etching at high temperature can be studied through the comparison of the pores revealed in **Fig 2 (c-d)** for Br 22 and 46 MeV (after 40% HF, L, for 60 min at RT), and **Fig 3 (a, f)** were the etching were carried out in vapour conditions (40% HF, V, 55 ºC, 60 min.); in the latter case, the pores features exhibit better defined inverted pyramidal facets. Perhaps, the chemical behaviour manifested by the different crystallographic faces of the damaged crystal has been enhanced in the vapour conditions of the etching process.

Additional comments can be made through the examination, as example, of the case showed in **Fig 3 (a)**, Br 22 MeV irradiated sample etched in the vapour that came from 40% HF at 55 ºC during 60 min. The image shows pores arose from vapour etching over hot acid. The bath temperature averaged 55ºC. The prominent trapezoidal forms at the surface with the almost pyramidal inner facets are significant for a "late" phase in the etching procedure. Even though the sample was only attacked for 60 min. the pore diameter is quite large because the elevated temperature promoted the attack rate. An equivalent pore size is reached when immersing the sample directly in the acid for shorter times or lower temperatures. As it has been comment in a previous Section, when we described the pores features revealed in the case of Br 22 MeV in aqueous solutions, the appearing facets have been observed in a similar form in other crystals (e.g. LiF [16]).

Inside the liquid solution the etching rate is higher than in the vapour, which after 60 min at the high temperature (55 ºC) leads to a total overlap of pores being, then, unrecognizable. As mentioned, the bright stripes next to the pores in *fast scan direction* are due to a mathematical data correction. Via the applied *flatten filter*, as a mathematical tool, a line average is subtracted to eliminate offset adjustments during the measurement. This leads to a mean elevation on the pore sides, but is needed to eliminate piezo voltage offset adjustments

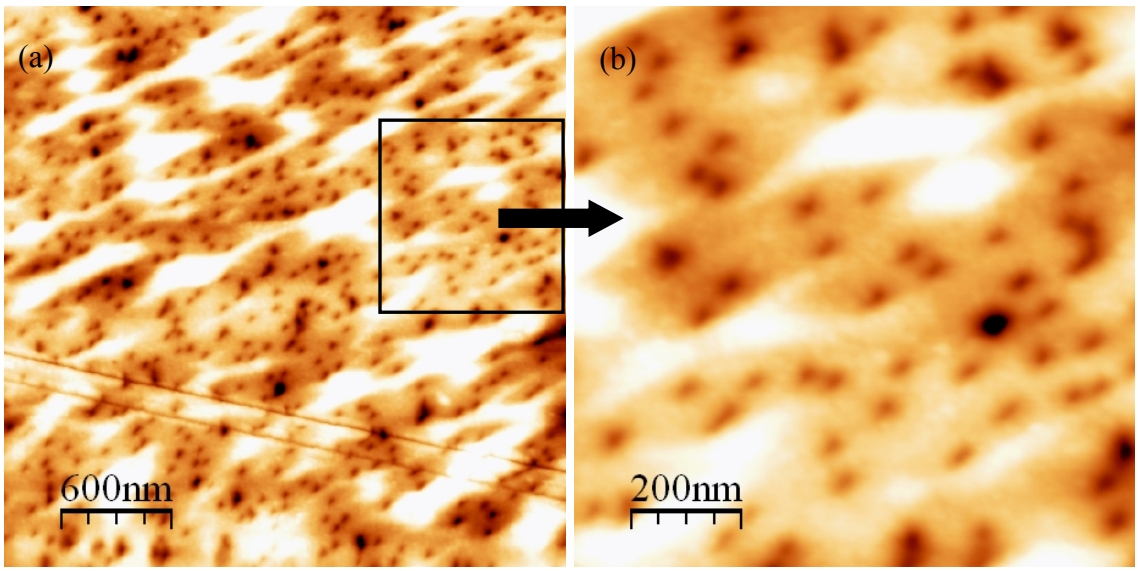

Fig. 4 (a, b). Samples irradiated at higher fluences were investigated by means of Tapping Mode - Phase Lock Loop (PLL) AFM **(a)** 3 x 3 μm^2 AFM image of *x*-cut LN irradiated with Br 46 MeV at fluence $\phi \approx$ 1 e10 at/cm^2. Etching conditions: 40% HF, L, at RT, (*standard conditions*) time: 30 min., z-scale optimized to remark the nanostructures = 6.5 - 22.2 nm, rms roughness = 3.6 nm. **(b)** 1 x 1 μm^2 AFM image zoom from drawn rectangle in **(a)**, z-scale optimized = 6.5 – 21 nm, rms roughness = 2.75 nm.

during the measurement which are necessary to prevent the tip from crashing. The phenomenon appears in most of the images and is more pronounced when the pores are deeper. It amounts up to 30% of the intrinsic height of the structure step size (depth). In some cases the much better *path flatten filter* could be used where a line average along a certain manually selected equipotential path is subtracted. This method does not produce the image elevation. Moreover, vertical hysteresis and creep of the piezo tube may also influence the image in this sense, but should only appear in scanning direction, i.e. behind the pore. Hence, the line elevation would only appear to the right of the pores because all presented images are forward scans.

8.3.1.5. Ion fluence as a parameter for tailoring optical applications.

It is worthy to comment that, for this work ultra low irradiation fluences were used preferably. The main purpose was to benefit from the large mean distances between nanopores, in order to avoid pore overlapping in later etching stages and to prevent a possible halo overlap and eventual influences of tensions perpendicular to the ion tracks. However, for waveguide fabrication usually higher swift heavy ion fluences (~1 e12 at/cm^2) are necessary, and to use desired etched nanopores structures in optical devices, fluences of 1 e10 at/cm^2 are recommendable. Hence, a study of the fluence as a fabrication parameter is necessary to be carried out.

Figure 4 (a, b) shows an AFM image captured from a sample irradiated with Br 46 MeV at a fluence of 1 e10 at/cm^2. The sample was immersed for 30 min in 40% HF (L) at RT. The evolving pores surprisingly have a similar shape to the ones irradiated with high energy ions (Kr and Pb) shown in **Fig. 2 (e, f)**. Apparently the surrounding halo wells already overlap,

leaving an astonishingly flat surface behind which is very suitable for optical applications. A few higher regions remained indicating the initial two-step morphology of a large surrounding halo with an inner pore. Applying the right etching parameters these walls can be removed to tailor an optical grade surface with pores that could then be used as a detector. As was denoted above, the inner pores are considered to be the ion impact sites, which again are located closer to the +z-side of the halo pores. We have to remark that the scanning AFM tip used to acquire this image was obviously very accurate, as it possessed a higher quality factor (Q-factor ≈ 500) than other probes (≈ 300).

Dealing with the lower fluences, as used throughout the rest of the research work, no major changes can be denoted, e.g. when comparing samples irradiated with 1 e8 and 1 e9 at/cm^2. Here, due to the pore overlapping the dimensions can only be measured vaguely. The mean halo is about 96 ± 18 nm x 311 ± 28 nm wide and the sidewall are 9.1 ± 2 nm high. Considering the slightly higher etching rate of 40% HF compared to the blend that was used in the previous work, these values are in good accordance to the ones published by A. García-Navarro et al [13]. The inner pores appear to be circular with a diameter of less than 76 ± 18 nm and a minimal depth of at least 5.4 ± 2.1 nm. The number of pores is slightly lower than nominal counting 6 e9 at/cm^2. This could be due to a dislocated measurement on the irradiated surface, not being carried out in the center of the irradiated spot. Thus, when measuring on the border of the spot, the observed fluence may be lower than nominal, but due to the over-focussed ion beam a certain beam halo still provides a large number of impacts.

8.3.1.6. Pore elongation and surface aspect ratio.

In almost all AFM images, the observed pores appear anisotropically. As mentioned above, this is already conjecturable in very early stages or for low energies. Since the samples were all irradiated under the same tilting angles for avoiding channelling conditions, the question came up if this could cause the pore elongation. It is worthy to remark that specific experiments were carried out to determine or exclude this possible dependency.

Some samples were irradiated under different tilting angles ranging all the possibilities: for low angles (θ, tilt): (0,0), (0, 9º), (9º, 0) and (9º, 9º). The irradiations were performed with Cu 51 MeV ions at fluences of 1 e9 at/cm^2. After irradiation, a systematic study was carried out to see the evolution of the nanostructures revealed after etching at RT in the 1:1 mixture of HF:HNO_3. For the investigation, different etching stages were analyzed with the AFM using NSC 18-type tips.

The main result is that, the evolved pores on the different samples always had comparable sizes and showed the same orientations in equivalent etching stages. Moreover, in order to also exclude that the two-fold symmetry and elongation was caused by a tip convolution, the samples were physically turned by 90º around the normal axis and measured again under the same conditions. This test was repeated from time to time and under different angles as other samples were examined, always yielding the result that the pore morphology is reliable and tip independent. By this experiment it was demonstrated that, pore elongation is not related to the irradiation conditions, concerning the inclination angles during track fabrication. Moreover, it brought evidence that the elongation is most likely not caused by tip convolution.

All together, this is a further indication that the evolving pore shape is depending on the crystal structure.

Due to the strong anisotropy of the pores especially in later etching stages, it is suggestive to define an appropriate parameter that accounts for it, the *surface aspect ratio* (SAR). The SAR shall be defined as the ratio of the longer pore axis divided by the shorter one. Thereby, the pore anisotropy can be described in a quantitative way and a comparison between pore SAR´s of different etching stages becomes possible.

8.3.1.7. Chiral pores on positive and negative x-cut crystal faces.

In order to get a better understanding on the origin of the pore asymmetry, we have investigated the effect of Br irradiation at 46 MeV on +*x* and -*x* crystals faces on the pore morphology. The results are displayed in **Fig. 5 (a, b)** showing a chiral behaviour, i. e., the two pore images are mirror images to each other.

Lithium Niobate *x*-cut crystals were irradiated on either side (±*x*-faces) in order to investigate a possible influence on the pore morphology. Both samples shown in **Fig. 5 (a, b)** were irradiated with Br 46 MeV ions and subsequently etched under *standard conditions* (40% HF, L, at RT, for 60 min.). Both samples have been measured with the same tip to avoid the influence of its shape. In order to get enough accurate resolution, a high aspect ratio AFM probe (AR5 series), was used to carry out the measurements. The height scales (z-scales) are also adjusted and the lateral dimensions of both images are 250 × 250 nm^2. The arrows indicate the +*z*-direction, both pointing to the same side. Nevertheless, the two pores are obviously not congruent. In **image 5 (a)**, the +*x*-face was irradiated, whereas in **5 (b)** -*x*-face was facing to the beam. The longer side of the trapezoidal nanopore is the +*z*-edge. This, again, supports the assumption that the impact lies closer to this back wall of the pore. In this manner, it is also explained why the back wall has the longest edge on the surface. The pore seems to open faster towards -*z* and along the 33º direction, which coincides with the plane of cleavage.

Irradiating the sample from the other side, results in chiral pores which can only be transformed one into another by mirroring the image. That the pore images are not congruent becomes more apparent watching the core region and the insets showing the EF (Excitation Frequency) images, respectively. In the topography image the brighter points are due to an operational fault of the feedback circuit and indicate that the tip could not enter deeper into the well. As a advanced technical comments, we have to point out that the feedback gain parameters, (Proportional and Integral parameters) *P* and *I*, have to be as high as possible to have enough reliability to follow the structure shape, and thus, the structure to be reproduced as good as possible. If *P* and *I* are selected a bit too high, as it is the case here, upon elevation the tip will be withdrawn further than necessary, which causes the height errors.[4] However, these step features in both pores are oriented oppositely.

The EF images showed as insets give an account of the interaction strength. The EF image reveals more details than are visible from the topography. The signal changes are quite apparent along the step. The chiral pore shape is evident once more, since an alignment of all

[4] The malfunction is more sensitive to the integral than to the proportional part, and only occurs where the tip is scanned close the step-like wall inside the nanopore. These features will be discussed in a following section.

Chiral Nanopores

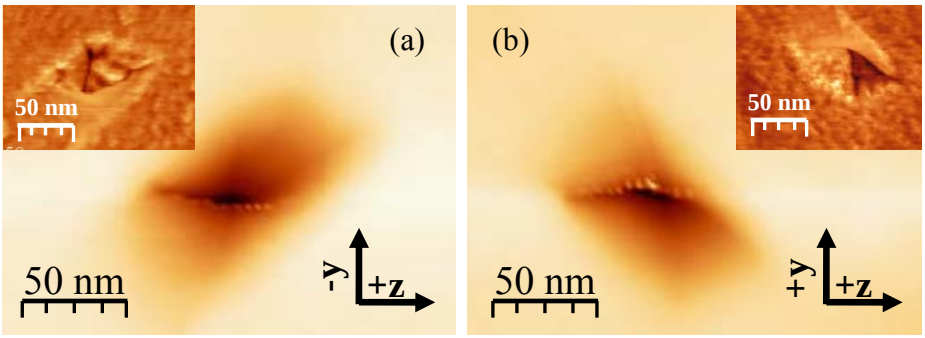

Fig. 5 (a, b). 250 x 250 nm^2 AFM images of etched tracks on the *+ x*-face **(a)** vs the *- x*-face **(b)** of lithium niobate after irradiation with Br 46 MeV and etched during 60 min in HF 40% at RT. Revealed facets appear clearly in the excitation frequency image recorded by PLL mode shown as inset in each case. Depth-scale: 30 nm.

pore features can only be obtained by flipping the image by 180º around the *z*-axis (arrow), i.e. irradiating the other side of the sample in the first place.

8.3.1.8. Further details in the study of the well defined faceted pores in Lithium Niobate.

After the study undertaken in **Fig. 3 (d)**, *x*-cut LN irradiated with Br 46 MeV at fluence $\phi \approx 1$ e8 at/cm^2, recorded using a PPP commercial tip, we can state some conclusions. The pore shape is very complex and not yet understood in every detail. For proposing a more precise assignation of the single facets, it would have been very useful to have information about the pore structures on *z* and *y*-cut single crystal surfaces in comparable etching stages, whose data are unavailable. *Y*-cut material was not available at all, whereas *z*-cut samples could not be examined in most cases due to great interaction between AFM probe and surface, as it has been previously commented. Furthermore, the pore shape is affected to a certain extent by the tip and even somewhat by the scanning direction. Better feedback conditions also yield higher image quality. The diameters are always the same and do not depend on the scan direction or tips. In case of the NSC 18 tip the depth were worse and the EF changes higher. The latter could be caused by different doping of the tip material. The etched pore structure seems to be mostly caused by intrinsic crystal properties (mainly the crystal structure and etching rates of minor damaged regions are considered to be influential parameters), where the ion track acts as a seed.

On the other hand, that the observed groove looks V-like at the bottom of the pore is certainly due to the measurement. When entering the pore, the tip does not forge ahead as fast as it is withdrawn which causes this shape. The groove forms an angle around 45º with the *z* and the *y*-axis, pointing towards both negative directions. In earlier stages it seemed that a curb-like structure was pointing directly towards the negative *z*-direction. As it has been mentioned above, the lowest point is suspected to be the impact site, which again lies a bit closer to the longer pore edge than to any other. The groove could originate from the impact, considering the direction which coincides with the highest etching rates of bulk material: *-z* and *-y*. Since reliable values for the etching rates of crystalline bulk material under our conditions have

neither been measured nor are available, it is not possible to quantitatively prove this assumption.

The facets are sharply separated, having different angles one to another forming the very complex and strongly anisotropic pore structure. Considerably the configuration can be ascribed to the crystal properties and is evolving partly from etching damaged regions, but mainly by the removal of crystalline material. The two facets on the bottom side are less inclined than the others and should be resolved correctly by the probes. It is unlikely that all used tips have the same defect which always leads to the same convolution. The distinct gradients of the facets could emerge from the different etching rates. It is not understood why the *fingerprint* lines are moderately curved. The effect could have its origin in image distortions, but should then be shaped differently from pore to pore which in principle is not the case. Thus, stress perpendicular to the ion track may cause twist.

The fact that the EF image contains kind of a two-dimensional representation of three-dimensional topography data could be another reason. In all EF images, the EF is maximal on the long pore edge (+*z* side), which appears brighter for that reason. As example, when measuring with the standard NSC 18 tips (see EF image in **Fig. 37. Chapter 4**), the effect is a lot more pronounced and also visible on the opposing edge. Since the edge usually lies in scanning direction, a shorter distance to the sample surface may lead to an increase of the *excitation frequency* (ω_e). More than for topographical reasons the effect could also be evoked by charges that are accumulated on these edges. Electric field lines arising through the piezoelectric structure should preferably end on these sites.

Additionally to the enormous interactions and the corresponding EF changes, they may have been amplified by a hardware error that was present through all our measurements. We discovered that the setup applied a bias voltage of ≈ 14 mV even though the control program indicated zero in the corresponding control box. This raised the question if this voltage could be high enough to induce a domain flip since it was applied on a very small distance, but such an electric field is too weak to penetrate the sample. Even if the consideration could be applied, the electric field may have been at most 14 kV/mm (on the nm-scale) which still is below the poling threshold of 28 kV/mm (on a macroscopic scale) in *z*-cut LN. It is very unlikely that the small voltage has modified our *x*-cut samples, but it may have influenced the interaction strength in terms of a maximal EF change, and, hence, must be commented here.

8.3.2. Influence of thermal annealings.

Thermal treatments after irradiation may anneal out some of the defects generated in and around the ion track leading to a damage recovery; moreover, they can influence the subsequent etching rates and pores morphologies.

It is well established that high temperature annealing of single ion tracks in irradiated $LiNbO_3$ leads to damage reduction. The track halo can recrystallize if the sample is annealed for proper times (~30 min), whereas the core only heals up at much higher temperatures [18], e.g. the propagation losses of optical waveguides can be significantly reduced by this method [19, 20]. Hence, a study of the influence of annealing temperature as a parameter in pore fabrication it is demanded.

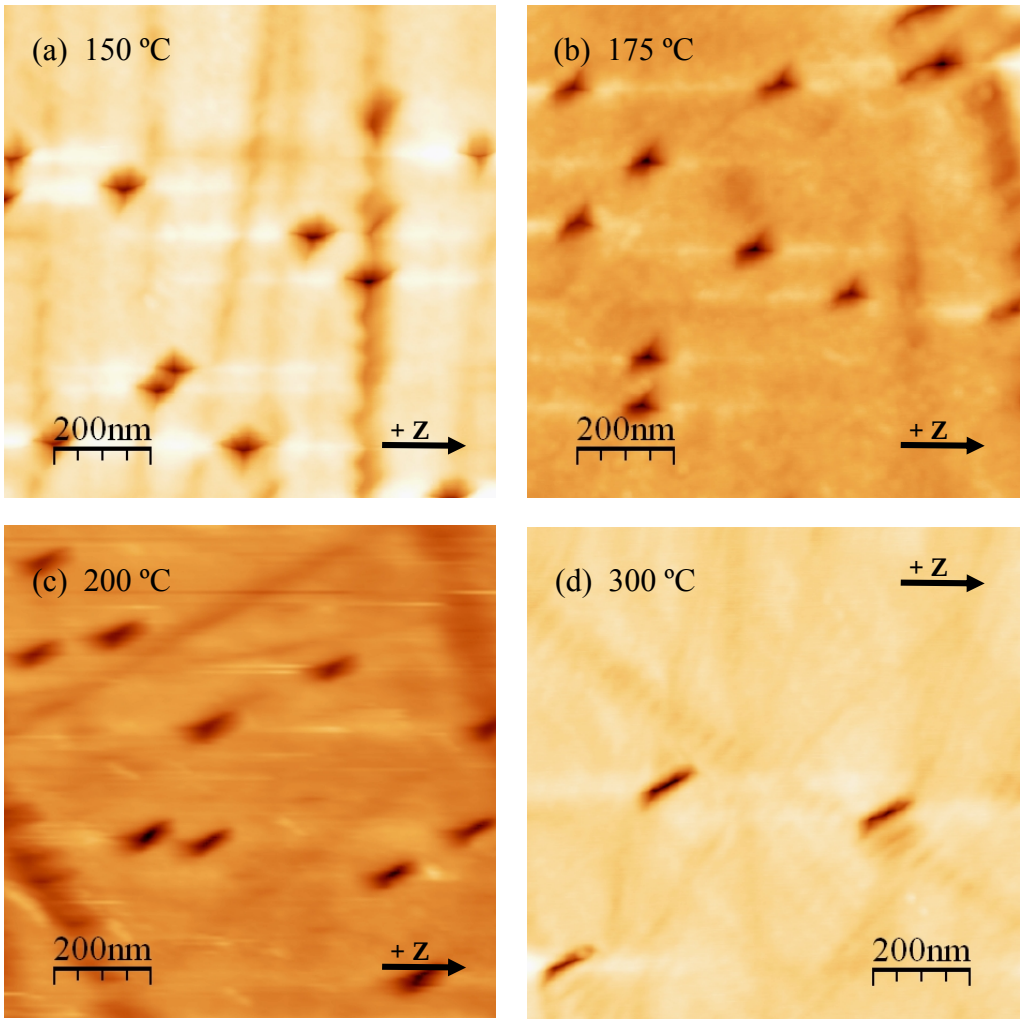

Fig. 6 (a-d). 1 x 1 μm^2 AFM images of pore morphologies obtained for samples irradiated with Br ions of 46 MeV ions and subjected to annealing in air for 1 hour at different temperatures (see labels), prior to the *standard etching process* (HF 40%, L, at RT) for 1 hour. **(a-c)** Correspond to irradiations with fluences of (ϕ = 1 e 9 at/cm^2) and depth-scale: 33 nm, **(d)** Fluence of ϕ = 1 e 8 at/cm^2, depth-scale: 20 nm, in order to optimize the image contrast. +z-cut direction is showed on the drawn arrow.

The results are illustrated in **Fig. 6**, AFM images corresponding to the irradiation with Br ions of 46 MeV, followed by, thermal annealing in air for 60 minutes at various temperatures as marked on the AFM images (ranged from 150 ºC to 300 ºC), and finally etched under *standard conditions* (HF 40%, aqueous solutions (L), at RT) for 60 minutes. As a technical question, for measuring the samples, tips of the NSC 18 series were used[5].

One observes that the annealing treatment does not remove entirely the latent tracks, moreover, remarkably after the annealing at higher temperature (300 ºC for 1 hour), pores structures have been revealed in similar sizes than the obtained after irradiation without any thermal treatment. From this important fact, it is easy to deduce that not all the damaged area is recovered after the thermal annealing undertaken, due to the differential etching behaviour

[5] It is worthy to comment that, the annealed samples corresponding to 150 ºC and 300 ºC were scanned with the same tip.

revealing pores as – *damage fingerprints*. (This result will be interesting to remember when we study the recrystallization of amorphous tracks after different thermal treatments, in the **Chapter 7** of this Thesis work). Furthermore, it induces a clear elongation of the pore shape and gives rise to higher surface aspect ratios. Br 22 MeV irradiated and annealed samples were also investigated showing similar manners. A quantitative evaluation of the images will be presented in a following section.

8.3.3. Pores morphology and latent ion tracks from Transmission Electron Microscopy (TEM).

In order to continue with the discussion on the revealed pores morphologies, some TEM data will be presented. Moreover, throughout this section some features of the latent tracks underneath the pores can be observed. The method is so valuable because it is totally independent from any AFM results and provides complementary structural information. All the TEM measurements were performed by PD Dr. Michael Seibt of the IV. Physikalisches Institut of the University of Göttingen, Germany. From preparing a transversal view lamella, it was hoped to gain some insights to the sample properties underneath the surface. The question if tracks are really continuous, or, if the pores may be a lot deeper than observed in AFM, can be addressed. Furthermore, it is possible to investigate the problematic *z*-cut for AFM measurements. For that reason three samples, two *x*-cut and one *z*-cut, were investigated by means of transmission electron microscopy (TEM), yielding the results as described in the following (see **Table II**: Samples descriptions).

Sample	Crystal cut	Irradiation parameters (Ion, Energy, Fluence)	Wet Etching parameters: Blend 1:1, HF:HNO_3 RT. Etching time.
A	x-cut	Br 46 MeV, 1 e9 at/cm^2	30 min.
B	x-cut	Br 46 MeV, 1 e9 at/cm^2	60 min.
C	z-cut	Cu 51 MeV, 1 e10 at/cm^2	30 min.

Table II. A brief description of the samples used for the TEM study with information related to the crystallographic oriented substrate used, irradiation parameters and the etching features.

Before the description of the results, it is remarkable to note that the elaborate sample preparation with the focused ion beam (FIB) is crucial for obtaining reliable results, and it is worthy to comment some technical aspects related to the preparation. However, to be able to cut out and to thin the desired lamella via ion bombardment, the sample has to be covered by a set of protection films, as was explained in **Chapter 4.** *Section 4.7.3.3*. Because of $LiNbO_3$ is an insulator it would accumulate charges that deflect the ion and electron beams. Hence, it would not have been possible to measure the surface nor to manipulate it with the available scanning electron microscope (SEM) and focused ion beam (FIB), respectively. Therefore, a gold film was deposited before mounting the sample to the system to ensure sufficient charge dissipation

and enable precise ion bombardment. The major problem of this method was that the pores could not be located below the Au layer. In case of the Cu irradiated sample, the used fluence of 1 e10 at/cm^2 provided an adequate track density, whereas the probability to catch a nanopore in case of the Br irradiations, which were carried out with 1 e9 at/cm^2 was significantly reduced. This also implies that, if later a pore appeared in the lamella, it was not clear where exactly it was cut. For instance, it is possible that the contrast is high enough to identify a pore, even though half of the lamella may still consist of substrate material. This is the case for the pores captured from the samples irradiated with Br ions, shown in **Fig. 7**.

Another problem that may occur is sample inclination. The samples were fabricated via exposing them to high energetic ion irradiation (Br 46 MeV and Cu 51 MeV ions) under the tilting angles and conditions given below. Now, if the lamella is not cut out of the sample having the same inclination, the tracks may just pierce or scratch the lamella, and thus the possibility of observing the track correctly in transversal view is not given. Since only one pore could be found in each of the Br irradiated samples, it is not possible to make a real statistical statement about the pore dimensions. Thus, length measurements were performed several times on the same structure to obtain the errors.

Both *x*-cut samples, called *A* and *B*, were fabricated under the same conditions. After the irradiation with Br 46 MeV ions they were etched in the 1:1 blend of HF: HNO_3 at RT for 30 and 60 min, respectively. The *z*-cut sample was irradiated with Cu 51 MeV and etched in the same solution for 30 min at RT. The bold white arrows in the images indicate the +*z*-directions[6]. The four bright field images were captured with acceleration voltages of 22, 100, 22, and 60 kV, respectively, which enabled the different resolutions, zooms and rotations (see figure captions).

8.3.3.1. Sample A: *x*-cut LN irradiated with Br 46 MeV etched for 30 min.

In general, the image contrast is due to the different effects that were mentioned rather short in **Chapter 4.** *Section 4.7.3.3*. The regions where electrons can penetrate the sample easier are brighter, whereas regions where more electrons get absorbed or scattered appear darker. Beginning from the top in **Fig. 7 (a)**, the "grainy" looking grey matter are remains of the electron beam deposited platinum protection film, which has been removed above the region of interest. Below that, covering the whole surface, lies the Au layer. Owing to its high conductance, the gold film appears quite dark. More electrons are absorbed in this layer, which was connected to ground via the copper TEM grid. The layer has vertical gaps, which could be explained plausibly by the well known Stranski-Krastanov growth. One can see that a few monolayers cover the whole surface. After a few nanometers island growth started. The gaps appear preferably above pores, hence another possibility could be that the material entered into the pores and is therefore missing in the Au layer. The comparatively smooth looking, single crystalline Lithium Niobate substrate begins directly below the gold film. The strong change in contrast closely underneath the surface is due to a thickness step along the sample. The last

[6] In this sense, it is worthy to mention that, the direction is not necessarily exactly the +*z*-axis because the lamella is cut out of the sample having a certain inclination with respect to the axis and can also be inclined in the TEM during measuring.

TEM Images of Br 46 MeV Irradiated $LiNbO_3$

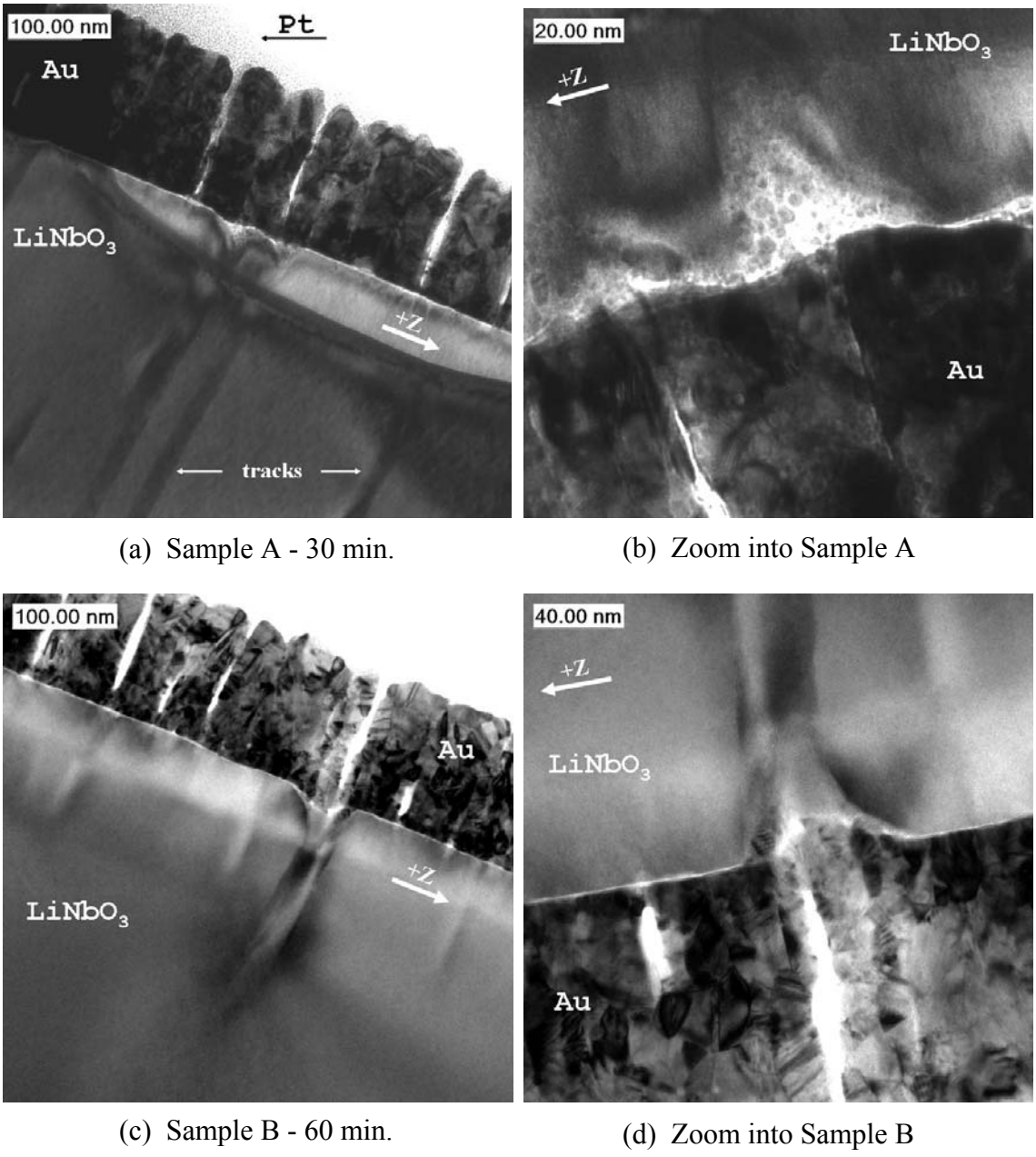

(a) Sample A - 30 min.

(b) Zoom into Sample A

(c) Sample B - 60 min.

(d) Zoom into Sample B

Fig. 7 (a-d). Bright field TEM images of Br 46 MeV irradiated *x*-cut $LiNbO_3$ samples and subsequently etched for **(a)** 30 min. and **(c)** 60 min. in the 1:1 acid blend of HF and HNO_3 at RT. **(b)** and **(d)** represent zooms into their corresponding **(a)** and **(c)** TEM images. The images were captured with different acceleration voltages: **(a, c)** 22 kV, **(b)** 100 kV and **(d)** 60 kV, which enabled the different resolutions, zooms and rotations. The bold white arrows in the images indicate the *+z* directions.

thinning step was not completed correctly, leaving a quite thick lamella behind, which was hard to penetrate with the electron beam.

One can see the ion tracks very clearly, and from the surface, at the site of the double impact, two pores have formed close to each other. The second track, counting from left to right, seems to only scratch the lamella. Thus, the focus is put on the first track. The third track,

further to the right, enters the lamella below the surface, which is the reason why no pore is visible at its top. On the left side of the image, two more tracks are visible. The lower one enters the field of view at the bottom like track three, and the one penetrating from the surface, neither seems to have developed a pore, but a small indentation is visible. The sample thickness does not allow furthering examination of this structure.

A closer snapshot, applying an acceleration voltage of 100 kV, was taken from the larger pore, and the image is shown in **Fig. 7 (b)**. The view is rotated because of the TEM lens system[7]. The border of the pore looks bright, which is probably due to the reduced sample thickness. The small dark spots are, doubtless, nanometric gold clusters, according to a subsequent chemical analysis performed by means of EDX (Electron Dispersive X-ray Spectrometry) in STEM (Scanning TEM) mode. The gold clusters are either remains of the gold refilled pore, or may have arrived there during FIB preparation. The diameter of the latent track has been measured in both images. The average amounts to 25.1 nm. This is a rather large value, which is not in accordance to the predictions of the i-TS model [3]. From latter, through **Fig. 7** in **Chapter 1**, for these irradiations in particular (Br 46 MeV, S_e = 11.9 keV/nm), one would expect a track radius of ~ 3.2 nm. The large discrepancy could be due to aberrations such as the image contrast, that might be falsified due to additional scattering and energy loss of the imaging electrons inside the thick lamella.

The pore diameter is 59.5 ± 3.2 nm in both TEM images, calculated as the weighted mean value. This pore diameter is in very good accordance to the AFM data, where, despite of the dirty surface, mean diameters of 61.3 and 83 nm have been measured on the short and the long axis, respectively. Both, the TEM and the AFM short axis value lie inside the other error range, respectively. In the TEM images, the pore depth is not easy to interpret and seems to depend on the used acceleration voltage that implies distinct contrasts in the images **Fig. 7 (a)** and **(b)**. The same pore appears to be 42.5 and 66.7 nm deep, respectively. The weighted average is 54.4 nm. The value is by more than a factor of three larger than the depth obtained from the AFM measurements, where the mean pore depth amounts only 15.2 ± 1.0 nm. The overall pore dimensions in TEM correspond to an AR ~ 1, which is more than three times as high as the proposed mean AFM AR ~ 0.25. However, it is possible that besides pure chemical etching, the pore depth may have been enlarged during FIB preparation. On the other hand one has to keep in mind that the sample surfaces were very dirty, and the covered pores could not be penetrated by the AFM tip all the way to the bottom.

8.3.3.2. Sample B: *x*-cut LN irradiated with Br 46 MeV etched for 60 min.

The lower images, **Fig. 7 (c)** and **(d)**, show an identically fabricated sample. The only difference is that, it was immersed twice as long in the acid blend. The thinning in FIB preparation was more successful, and the lamella is thin enough for good observation. The polycrystalline gold structure is outstanding in both images, where the growth may have lead to the confinement of bubbles. Due to problems while transferring the lamella from the sample to

[7] We have to keep in mind that, when changing the acceleration voltage, the electron optics needs to be adjusted in order to keep the sample inside the plane of focus.

the TEM grid[8], it was thinned under a different inclination angle, so that tracks only pierce the lamella. Structures or patterns that arise during FIB-preparation of the sample are usually visible uniformly along all layers including the Pt and Au protection layers, which are then called *curtain effect*. A slight curtain effect influence can not be excluded here because the tracks are inclined by 7 ± 2º with respect to the surface normal, but there are also curb-structures that are aligned to the surface normal spreading from −4º to 3º. It is possible that the last thinning step, that is foreseen to remove material from the lamella which was amorphized (or damaged) during FIB preparation, has sputtered the damaged material around the latent ion tracks and/or below slots between islands in the gold structure -e.g. below the LN tag. It looks like the focused ion beam engaged and sputtered easily removable material on the surface side end of the ion tracks. This may lead to deeper looking pores.

The average pore depth, measured from both images, is 71.6 ± 10 nm. In AFM 22.7 ± 8 nm were obtained, which is again more than a factor three smaller. The same influencing factors, as discussed above, have to be considered. Here, the diameters of both methods are in very good accordance. The TEM pore is 85.6 ± 2.7 nm wide, and lies between the widths of 77.4 ± 5.7 and 125 ± 13 nm that were determined by AFM for the short and long pore diameter, respectively. The AR´s, like the depth, are almost three times higher in TEM (0.84) than in AFM (0.29). It is also apparent that the pore opened faster toward the -*z*-direction, and a small angle face has evolved, which appeared at the same position and under the same angle as in the sample shown above (see image **Fig. 7 (b)**).

When comparing the inner pores measured from TEM and AFM, the TEM provides more consistent and more reliable results, just as one would expect. In AFM it is not possible to measure the inner pores correctly since the tip does apparently not enter all the way into the pore and the tip-pore convolution most likely distorts this region. Nevertheless, the inner pore structure can be seen astonishingly well in AFM (compare **Fig. 37** *Chapter 4*), even though the determined dimensions are not correct. All obtained values were compared and the ratios of TEM to AFM have been calculated. The results are summarized in **Table III**. The diameter ratio of 0.98 denotes that the coherence of both methods is excellent, which is not the case for the inner pore. The TEM values are 2.5 times bigger than the AFM ones, meanwhile the depth values are consistently too small by a factor of three - in the inner pore even up to a factor of ten. The overall AR´s comport just like the depth, whereas the AFM inner pore AR´s seem not to be reliable at all. However, tip convolution is most probably the influencing factor here.

The TEM measurements evidently show again, that especially the depth values obtained by means of AFM are worst case values. One can see that the pores open up at the surface more and more with higher etching times, whereas the inner pore structure remains the same. The craters seem to develop at two different etching rates. The deeper inner pore is penetrating into the damaged track, while a larger diameter is observed at the surface. Again, it is obvious that the larger pore is slightly displaced toward -*z*-direction, which also confirms the observations made in the AFM measurements. The funnel-like profile forms different angles with respect to the surface. The pore shapes look in some way similar to the ones observed by AFM, but since it is not clear where the pores were cut, it is not possible to identify and assign the features. Furthermore, the image quality of the corresponding AFM measurements was not good enough

[8] during the lift-up process of the lamella, it slipped from the transfer needle several times and was slightly inclined when mounting it to the TEM grid.

Sample/ Etching Time		Overall (nm)			Inner Pore (nm)		
		Diameter	Depth	Aspect Ratio	Diameter	Depth	Aspect Ratio
A, x-cut	TEM	59.5	54.4	0.91	37.8	29.3	0.78
30 min.	AFM	61.3	15.2	0.25	11.9	2.1	0.18
B, x-cut	TEM	85.6	71.6	0.84	45.7	36.2	0.79
60 min.	AFM	77.4	22.7	0.29	23.6	5.2	0.22
C, z-cut	TEM	30.9	3.4	0.11			
30 min.	AFM	36.2	1.1	0.03			
Ratio	TEM/AFM	0.98	3.3	3.7	2.56	10.46	3.99

Table III. Comparison of the pores dimensions as mean values determined from TEM and AFM measurements. The ratios are calculated as mean values of all performed measurements.

to reveal the different funnels in detail. The AFM image of the surface etched for 60 min is shown in **Fig. 2 (d)**. It is worthy to note that when comparing the determined TEM dimension a linear evolution over time seems reasonable if the lower depth value of the 30 min pore is taken into account. The evolution of the pore dimensions over time will be discussed in the following section. Due to the possibly present *curtain effect* and the unknown exact pore location on the lamella, the TEM neither allows a definite statement about the pore depth and a direct comparison is complicated. Moreover, a comparison is meaningful only if the measured magnitudes are reliable from both methods which are not the case for the distinct pore depths from the 30 min sample.

However, despite of these uncertainties, it is believed that the depth obtained from the present cross-sections is more reliable. At least, it seems clear that the pores are deeper than seen in AFM. The measured TEM diameters are slightly smaller than the short axis pore diameters from the AFM measurements. Finally, to conclude we can say from the results that the measurements from AFM and TEM are complimentary and coherent.

8.3.3.3. Sample C: z-cut LN irradiated with Cu 51 MeV etched for 30 min.

Further TEM investigation of latent tracks and pores were performed on a *z*-cut sample irradiated with 1 e10 at/cm^2 of Cu 51 MeV ions, which was subsequently etched in the acid blend 1:1 of HF:HNO_3 for 30 min at RT (i.e., equivalent to sample *A*, irradiated with Br 46 MeV ions described above.

A TEM image captured with 40 kV is shown in **Fig. 8 (a)**. Just as the two previous ones, the sample has been prepared in the FIB, yielding a thin lamella with a slim gold layer on

TEM Images of Cu 51 MeV Irradiated $LiNbO_3$

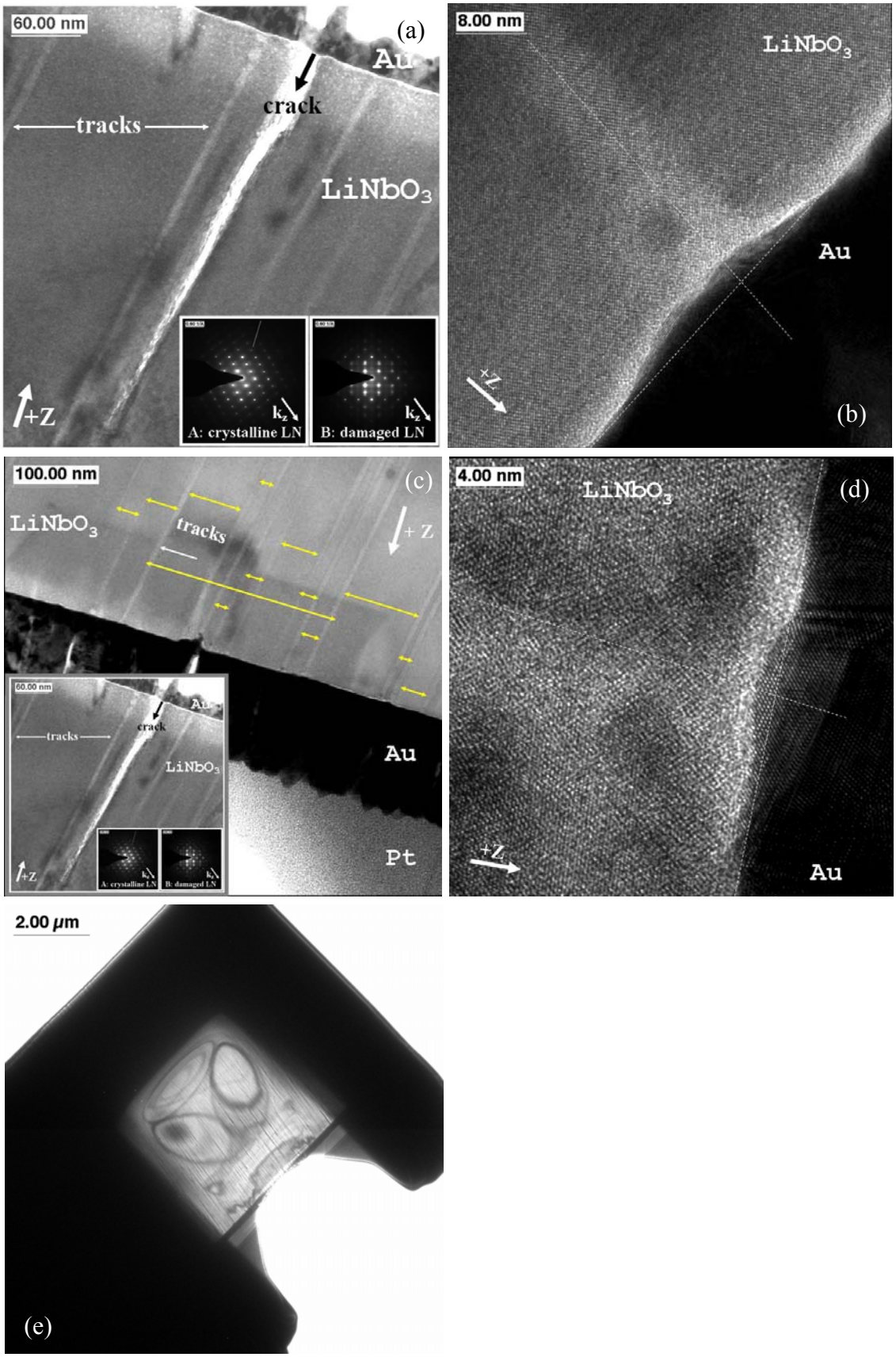

Fig. 8 (a-e). Bright field TEM images of Cu 51 MeV irradiated *z*-cut $LiNbO_3$. The bold white arrows in the images indicate the *+z*-direction. **(a)** The light stripes indicate the unetched tracks induced by ion bombardment; insets show the diffraction patterns recorded from a HRTEM measurement with an acceleration voltage of 300 kV. A crack of ~18.3 nm width and ~ 306 nm depth was observed. The inclination of 8º corresponds to the tilting angle during irradiation. Acceleration voltage: 40 kV; **(b)** HRTEM image captured at 300 kV showing etched nanopore at the surface and the ion track inside the crystal, in cross-sectional view; **(c)** TEM image with less magnification showing a great number of ion tracks with yellow arrows. Acceleration voltage: 22 kV, as inset appears **(a)**; **(d)** HRTEM image captured at 560 kV showing with more detail the latent track underneath another etched nanopore in cross-sectional view, revealing again the asymmetric axis; **(e)** Sample holder with lamella details showing the latent tracks tilted respect the surface. Acceleration voltage: 1.3 kV.

top of the surface. The image shows a crack of ≈ 18.3 nm width, that reaches ≈ 306 nm deep into the sample. Presumably the high fluence and/or the flux are to blame for this additional damage between the tracks. The dark regions in between the crack and the tracks are seemingly due to further tensions rectangular to the tracks in the crystal. The crack starts orthogonally into the surface, but at a depth of approximately 70 nm it makes a step-like turn and continues under an angle of about ≈ 8.5º, almost in parallel with the track direction. The mean track inclination of 8º ± 2º with respect to the surface normal is in exact accordance to the sample tilting during irradiation. It is worthy to comment that, for this sample, any artefacts like *curtain effects* are observed. The deposited gold did not enter into the crack. We expected that a pore refill would be easily possible, which presumably was accomplished for the Br irradiated samples above. Apparently this is not the case for this narrower and much deeper crack. It is worthy mentioned that, the deposition conditions have neither been very preferably. The gold has been deposited under medium vacuum conditions onto the sample at RT.

The contrast is high enough to reveal the latent tracks. At first glance, the tracks seem to be continuous and have average diameters of ≈ 8.4 nm, which is significantly closer to the expectation, but still higher than the proposed value in the literature [3], from one would expect a track radius of ~ 3.2 nm for this case (Cu 51 MeV, S_e = 11.9 keV/nm, at the surface). On the other hand, the lamella was cut out under a more suitable angle, so that the tracks can be observed over the whole range of sight.

In the *insets A* and *B*, two different diffraction patterns are shown. They correspond to zones located aside (crystalline region) and inside the ion track (damaged region), respectively, and they were recorded from a HRTEM (High Resolution Transmission Electron Microscopy) measurement with an acceleration voltage of 300 kV similar to the track shown in **Fig. 8 (b)**. As in all images so far, the bold white arrows indicate the +*z*-direction. The arrows in the insets illustrate the k_z wave vector of the diffraction patterns. One notices the marked disorder apparent in the *inset B*. In *inset A*, much more reflections are present than in *B*, which indicates that the crystal structure changed and some kind of a phase transition has taken place. The spots in *A* also have higher intensities[9]. The background noise of the patterns contains information about the general lattice disorder, which is good visible in both spectra. The effect is most probable due to intrinsic crystal defects. The overall background noise (brightness) is higher in spectrum

[9] It must be mentioned that, the window of sight has only been shifted by a few nm via the piezo controlled stage. All other parameters were left constant.

B (damaged area). The pattern was recorded while the objective lens was situated directly over an ion track, but of course the image also included some crystalline material. The underlying structure though is completely distinct from that in pattern, - i.e. the penetrating ion significantly damaged the crystal structure through its path[10]. Presumably, the ion energy was high enough to break the single crystalline structure of the $LiNbO_3$ crystal of the volume inside the track cylinder. Since some form of crystallinity remains, it is believed possible, that minor crystal units, eventually the oxygen octahedra, remain intact [21]. The contrast is high enough to reveal the latent tracks, but the partial crystallinity leaves some doubt about the amorphization ability of the used single ions, although we are greater than the amorphization threshold for LN (S_{th} = 4-6 keV/nm). The track volume is seemingly not completely amorphous. This would be a very plausible explanation why the track volume is not emptied by the acid with the expected rate and contrast proposed in **Section 4.3.** *Chemical etching behaviour of Lithium Niobate* (**Chapter 4**).

Figure 8 (b) shows a HRTEM image captured at 300 kV. The dashed lines indicate the surface and the symmetry axis of the ion track and enclose an angle of 98º. The track is ≈ 9.2 nm wide in diameter and evidently becomes broader at the surface. The origin of the strange circular inclusion closely underneath the surface is quite mysterious. It makes the track look T-bone-like. The eye appears in nearly all the tracks along the lamella. Moreover, those spots seem to be crystalline and are always located in this position below the surface and on the -*y* side of the track. The pore, which is the only one captured with sufficient resolution to measure its dimensions is ≈ 30.9 nm wide in diameter. It is very interesting that the asymmetric nanopore appears clearly shifted in relation to that for the latent ion track. Assumingly the shift is most likely due to the directional etching rate difference in *y*-direction, which seems to be almost strong as the differential etching rates in *z*-direction in *x*-cut samples. Even though the sample was also etched for 30 min, the nanopore is only ≈ 3.4 nm deep. Above, the *x*-cut pores had mean depth of ≈ 54.4 nm after the same etching time. This shows the great chemical stability of the *z*-cut face. Even though the material is supposedly hardly damaged, its chemical resistance is still remarkable. It was proposed that on both, *x* and *z*-cut, the same etching rates are observed for amorphous material, even though the *x*-cut samples exhibited much higher damage response in terms of defect concentration [22]. It was argued that the higher defect concentration observed in RBS measurements could be due to a better "visibility" of Nb atoms on preferred vacant octahedral sites that are located close to the watched channel. Specifically, it is commented that, the defect concentration measured for a given ion fluence is much higher in *x*-cut $LiNbO_3$ compared to *z*-cut samples [21, 23]. This fact is explained by a preferential rearrangement of the displaced Nb-atoms to vacant octahedral sites, which are situated close to the middle of the channel. These positions lead to a large "visibility" of the Nb atoms by the analyzing He-beam, i.e., a high backscattering yield is measured. In contrast, for the *z*-cut the rearranged of Nb-atoms are shielded by Nb-atoms on regular lattice sites, which reduces the RBS-yield. However, here, in this case, where only single ion tracks and the correspondingly emerging pores are examined, it seems possible that the induced damage on the *z*-face may really be lower than for the *x*-face. On the other hand, one has to consider the chemical

[10] However we have to take into account that since these HRTEM measurements are cross-sections some signal may come from the crystalline material surrounding the track. Further investigations taking plan view measurements (i.e. along the track) must be carried out.

resistance of the crystalline *z*-face, which is extremely high [10] compared to the proposed rates of crystalline *x*-cut material.

From the AFM measurements of the etched *z*-cut surface[11], thanks to the great sensitivity of the phase-locked loop (PLL) measuring mode, it was possible to interpret the data unambiguously. In the EF image the pores were visible as little pits of almost circular shape. The frequency ranges from -200 to 100 Hz, which was an very small EF change for a *z*-surface. The appearing polishing scratches have depths ~ 2 nm, which is the given roughness of the optical grade polished wafers. It is worthy to comment that, measuring the pore dimensions without the EFC (*Excitation Frequency Criterion*) would not have yielded any reproducible result, as the pores are very washed out in the topography image. In both images, EF and topography, distances have been measured simultaneously. In some cases the pore was hardly recognizable in the topography image, whereas the EF window clearly showed a dark circular spot. The mean pore depth was ~ 1.1 nm and the average diameter amounted ~ 36.2 nm. Again, the depth is measured to be less than a third of the value gained from TEM; the diameter is only slightly larger. The off-center location of the impact site inside the pore, as observed from TEM measurements, can not be denoted by AFM. A more detailed analysis of the pore morphology is not possible.

In conclusion, the TEM measurements are very valuable, especially considering the desired pore depth information, which could be gained. It seems clear that as *a rule of thumb* the real pore depth is about three times the one determined by AFM. This discrepancy can be explained by the used operational mode (Tapping + PLL). The maximal depth that can be seen is strongly limited by the tip dimensions, as was stated in a previous Section. The diameters were slightly larger than the pores observed in TEM but appear to be in very good accordance in all three cases. The good lateral resolution of the tapping + phase-locked loop (Tapping + PLL) is gained at the expense of the observed maximal depth. On the other hand, some morphological pore features could also be confirmed, such as the opening of the pores at the *x*-cut surface and thus, that the pores evolve in two different etching stages: a fast initial development of the inner pore followed by a slower stage forming a halo-like funnel.

8.4. Etching Kinetics of latent ion tracks. Nanopores tailoring in lithium niobate.

It has been shown that single ion tracks in $LiNbO_3$ are etchable and develop into nanopores with the discussed characteristics. Measurement images have been presented and methods to evaluate the data were discussed. Throughout this Section, the results on data of the whole acquired range will be analyzed. The principal aim is to report the found tendencies and to quantitatively analyze the etching behaviour as far as possible that depends on the different parameters which were independently changed and investigated.

[11] The topography is not shown because it is fairly blurry and of rather poor quality.

8.4.1. Effect of etching time on the development of pores features in HF acid aqueous solution.

In order to carry out a quantitative study on the behaviour of the features pores revealed after etching, systematic etching steps were performed being characterized for each case the dimensions of the nanostructures.

Samples irradiated with bromine ions at 12, 22, and 46 MeV were etched in pure 40% HF aqueous solution at RT. The behaviour of pore evolution with time under slight variations of the irradiation conditions was investigated. The data are shown in **Fig. 9**. Clear rising tendencies are obvious. From the literature it is well known that the etching rate is usually constant over time. Hence, the data can be linearly fitted. The linear fits plotted in **Fig. 9 (a)** depict the pore diameters of the long axis (solid lines) and the short axis (dashed lines). The inner pore diameters are also shown (dotted lines). On the other hand, even though the depth of the depth data does not approximate the early data points very well, the assumed linearity seems reasonable. The discrepancy may be due to slight differences of the etching temperature, which will be examined in a following Section. Since the measurement images were all very clear, a falsification due to the tip convolution does not appear plausible. From a comparison of the diameters of the distinct irradiation conditions during the first hour of attack time, no big differences are apparent. The resulting diameters from all three irradiations with different ion's energies are of the same order of magnitude. This, once more time, supports the assumption that the pore is opening due to crystal etching, which is rather independent of slight ion energy variations. The material at a lateral distance of about 200 nm (pore radius) from the track is definitely not amorphous. The mean etching rate of all three fits is ~ 1.89 nm/min in direction of the long pore axis. The short axis diameter increases with ~ 0.97 nm/min. It is worthy to notice that after 3 hours, the Br 22 MeV irradiated sample was measured with two tips of the NSC18 series, but the image quality was fairly poor in either case, resulting in a quite large diameter. Hence, some kind of tip influence may, of course, be present in the presented data plots.

From the linear fits we can obtain the corresponding etching rates for the different pore features (long and short axis, inner pore diameter, and depths), being able to make a comparison with the different ion energies. Although, a deep analysis will be carried out in a following Section, in which a wider study will take place with the swift heavy ions (Kr and Pb) features evolution with etching time, we can now outguess it and draw some conclusions from this preliminary stage in this short range of energies. In this sense, in the **Fig. 11** have been presented the etchings rates corresponding to the different pores features vs. different distinctive parameters of ions species (Stopping Power at the surface, S_e; Energy/amu, and Amorphous Track Length, L, being considered the latter only for the case in which that the stopping power of the ion's pathway through the crystal is above the threshold, $S_e \geq S_{th} \approx 4$ keV/nm.), trying to observe some kind of correlations. The diameter etching rates seem to be more or less independent of the ion energy in this energy regime. In contra, one can see that the depth evolution with etching time clearly has to do with ion energy. Comparing the depth evolution with etching time associated to Br 12, 22 and 46 MeV, one can see that, there is a clear dependency with ion energy. The depths of Br 46 MeV irradiated pores are much higher than that of the 12 MeV ones (**Fig. 9 (b)**). Effectively, it is observed in **Fig. 11**, that the etching rates associated to pore depths show a more remarkable dependency than in the case of diameters

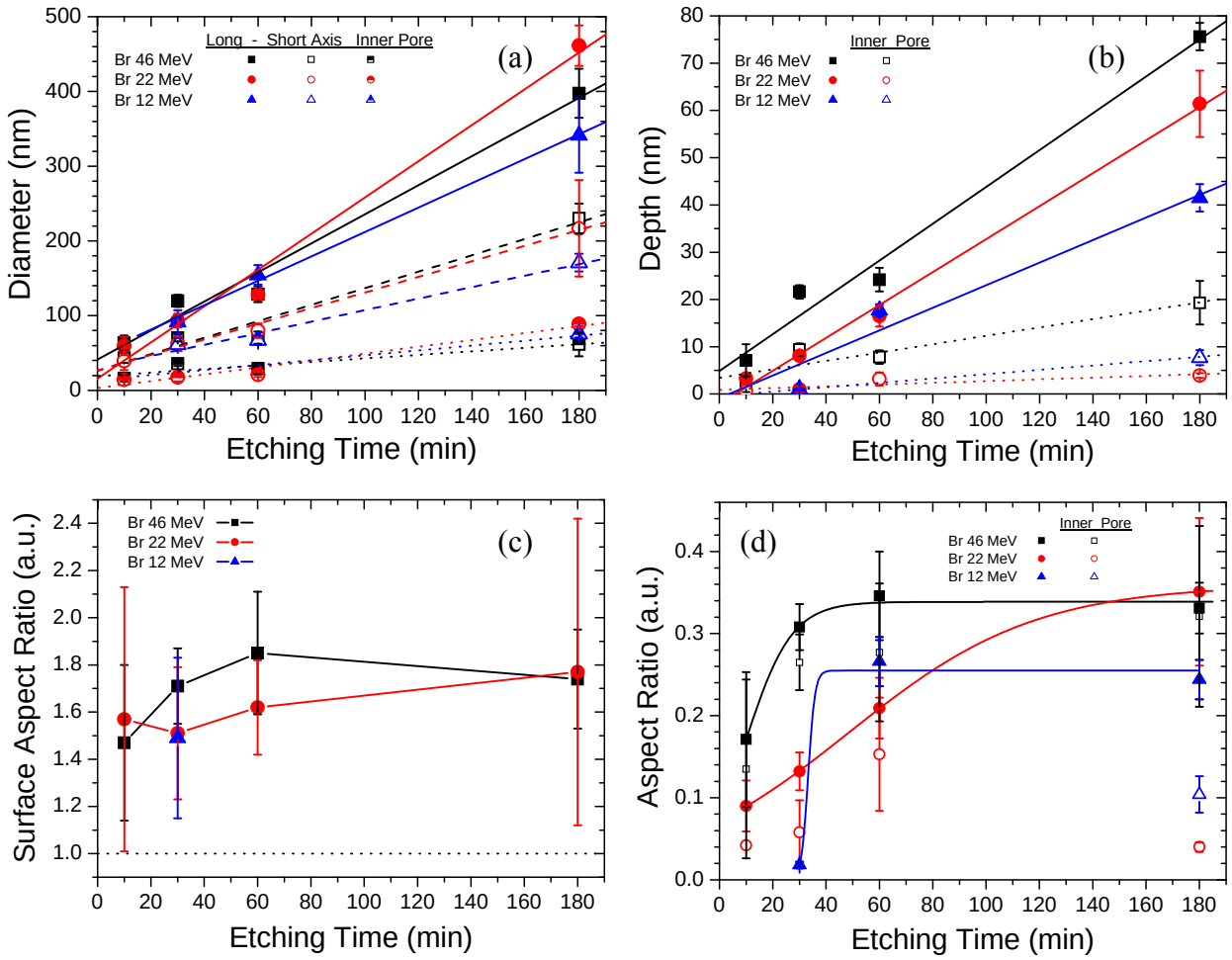

Fig. 9 (a-d). Graphs of pore dimensions versus etching time in pure HF 40% acid at RT using samples irradiated with Br ions at 12, 22 and 46 MeV.**(a)** Diameters (Long axis, short axis and inner pore), **(b)** Pore and inner pore depths, **(c)** Surface Aspect Ratio (Long axis/ Short axis) and **(d)** Aspect Ratio (Depth/ Short axis).

etching rates, with the ion specie, although we are working in a narrow energy regime. It is worthy to notice at this point that, the linear (solid and dotted lines) fits shown in the graphs correspond to a global fit in the wide energy regime, taking into account the swift heavy ions from the big facilities (Kr and Pb), and will be discussed further on; on the other hand, a satisfactory fits of the behaviour shown in this energy region have been performed by dashed lines. It seems that the defect concentration which was induced by the deposited ion energy governs the etch rate in depth. The surface aspect ratio shown in **Fig. 9 (c)** represents the long pore diameter divided by the shorter one. All points are greater than one showing the anisotropic pore shape. Although the values could look like fairly erroneous, they seem to be constant over time, which would be in agreement with the assumption that the diameter etch rates are due to the "virgin crystal" etching behaviour. The total average is ~ 1.6. In **Fig. 9 (d)** the overall ratios of depth to short diameter are plotted (Aspect Ratios, AR). The ARs show a rising tendency during the first hour of the etching time, but not clearly continued in the end. The values after 180 min were still of the same order of magnitude as the ones after 60 min within the error ranges. This could support again our hypothesis of the existence of two etching

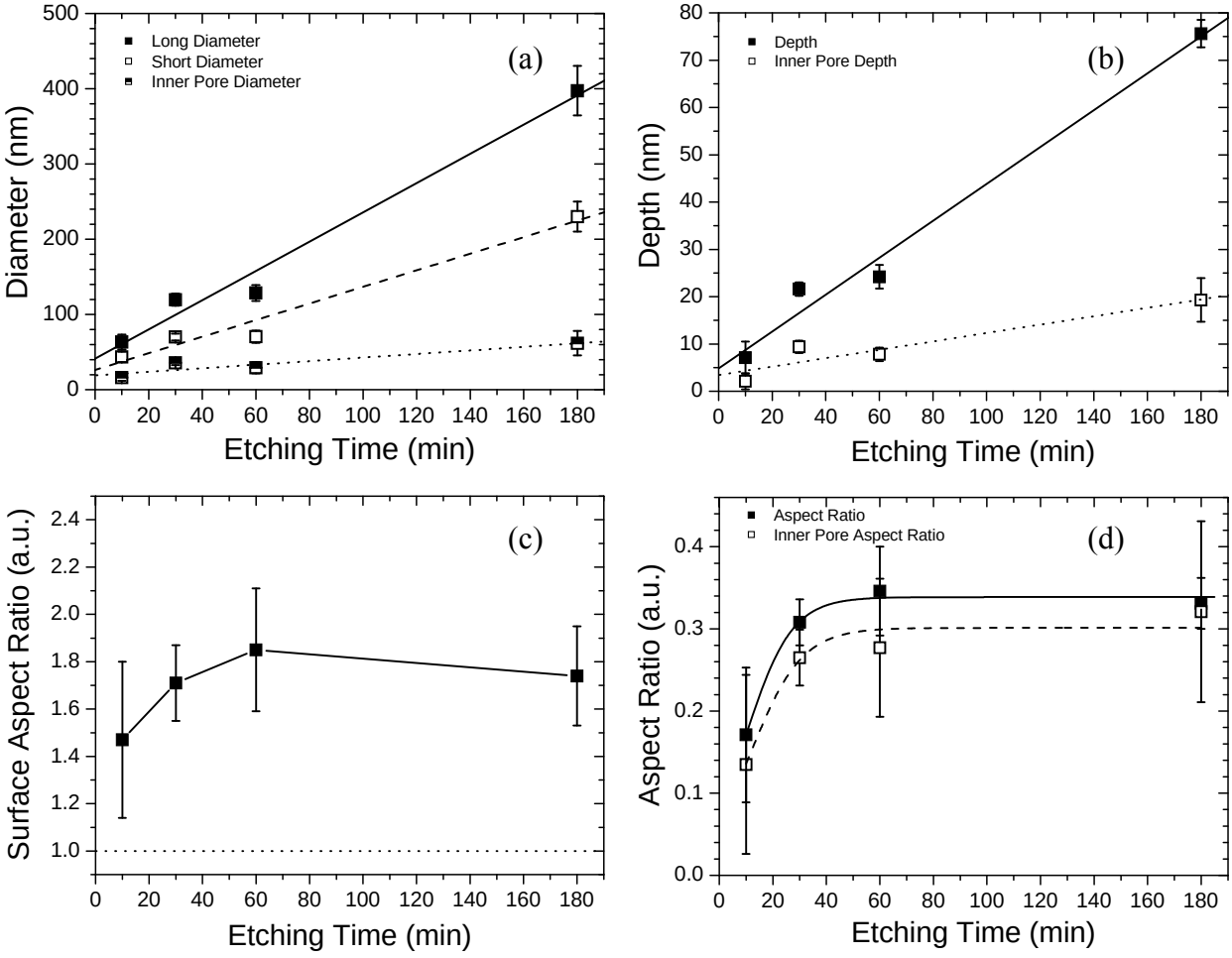

Fig. 10 (a-d). Graphs of pore dimensions versus etching time in pure HF 40% acid at RT for the case of Br 46 MeV ions irradiated samples. **(a)** Diameters (Long axis, short axis and inner pore), **(b)** Pore and inner pore depths, **(c)** Surface Aspect Ratio (Long axis/ Short axis) and **(d)** Aspect Ratio (Depth/ Short axis).

regimes: firstly, a fast etching region in the first stages of time, followed by a slower etch rate where only the crystal is affected. For the first three stages the AR increases quite abruptly, but then the pore opens up and the AR is maintained constant until it slightly decreases. This suggests that the pore structure in advanced etching stages is governed by the lattice structure and the underlying etch chemistry of crystalline material. In order to the clarify the revealed behaviour with the etching time, the case of Br 46 MeV irradiated samples, is shown in **Fig. 10 (a-d)**.

On the other hand, although a few etching treatments have been carried out supported by ultra-sound bath, they have not been included to simplify the graphs. The treatment yielded slightly smaller diameters and depths even though the bath temperature, which could not be controlled precisely, was a bit higher than for the other data points. Ultra-sound does not have a noticeable influence on the etching rate neither on pore creation, or elongation. This same behaviour has been also found for bulk material etching of amorphous *x*-cut $LiNbO_3$. Schrempel et al. report that ultrasonic support hardly influences the etching rate [22]. It seems that LN is not sensitive to the slight variations of the ion energy concerning the nanopore diameter. However, slight differences between the Br irradiations of distinct energies are only observable,

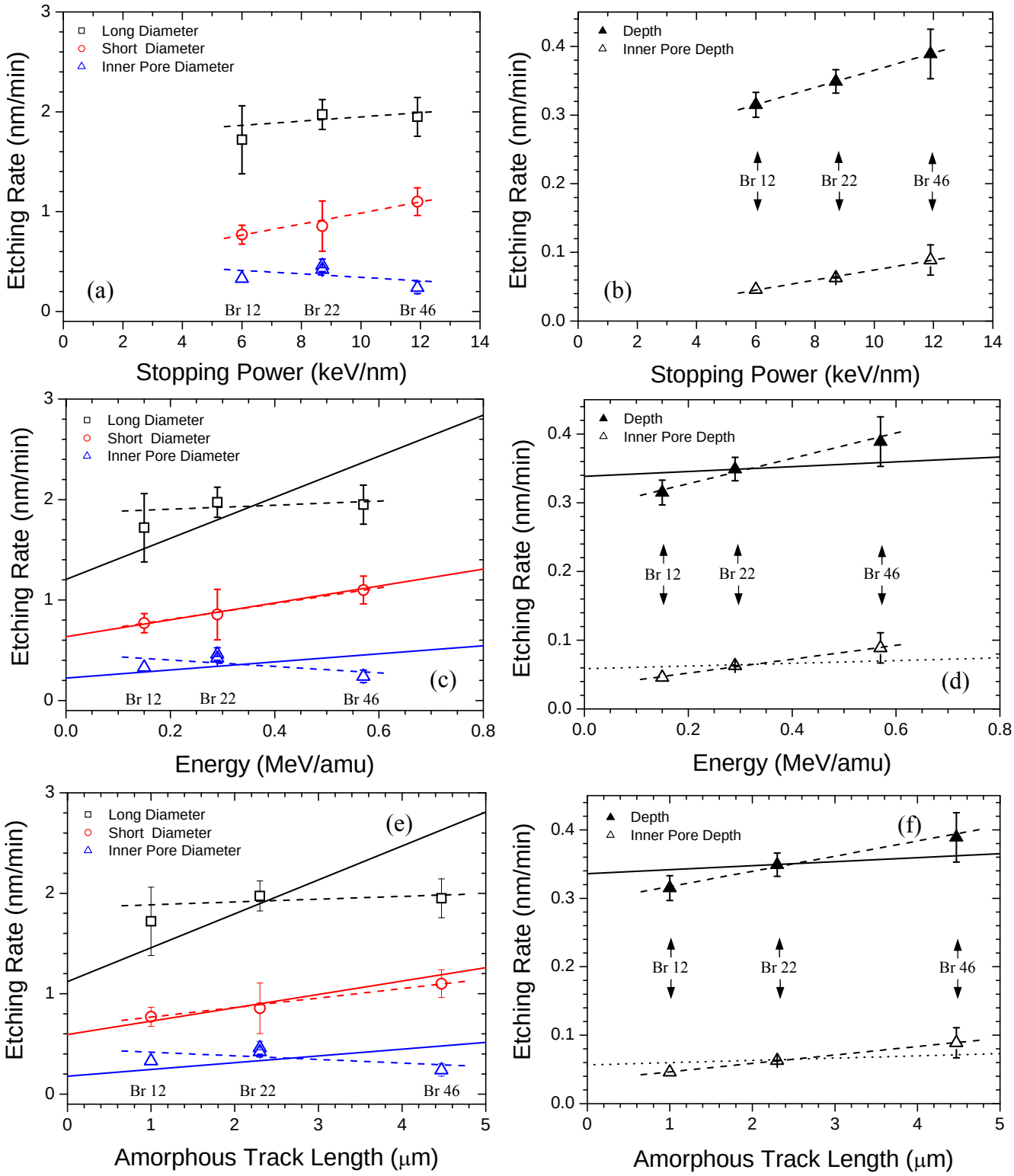

Fig. 11 (a-f). Graphs of the etching rates in pure HF 40% acid at RT for the different pores dimensions (Long - short axis, inner pore diameters and depths) versus different irradiation parameters of ions species for the case of Br 12, 22 and 46 MeV ions irradiated samples. **(a, b)** Stopping Power at the surface, S_e; **(c, d)** Energy/amu; **(e, f)** Amorphous track length, where the stopping power through the ion's pathway is above the threshold, $S_e \geq S_{th} \approx 4$ keV/nm). Dashed lines fit the behaviour in this energy region; solid and dotted lines fit the overall energy region (it will be discussed later, see **Fig. 19**).

in this energy regime, from the "questionable" depth data in the advanced etching stages. Anyhow, a linear dependence of the etched pore dimensions and, hence, a constant etching rate over time can be confirmed.

8.4.2. Effect of etching time in different acid aqueous solutions.

Samples irradiated with various ions and energies were etched in different aqueous acid solutions as was summarized in **Table III** (see **Chapter 4**. *Section 4.5.1*). However, throughout this work, we will focus on the systematic etching experiments carried out with three different kinds of acids on Br 46 MeV irradiated samples. They were treated with the acid blend in the ratio 1 : 1 from 40% HF and 70% HNO_3, pure HF acid of 40% (original), and diluted with deionized water to a concentration of 5%. The evolution of the pore diameter and pore depth with etching time at RT is respectively illustrated in **Fig. 12**. Again, a rising tendency of both, diameter and depth, are obvious in all cases. From the diameters (**Fig. 12 (a)**) it seems clear that HF 40% is the strongest acid, that's to say, it is the most efficient etching, followed by the 1 : 1 blend and diluted HF 5%, respectively. The etching rate is much larger than that obtained in a previous study with a 1:1 mixture of HF and HNO_3 [13]. This is in accordance to the proposal of Sones et al. who report increasing etching rates with decreasing HNO_3 portions in the blend, i.e. pure HF acid is yielding the highest attack rate [10]. A priori, it can not be assumed that the chemistry is the same for *x*-cut samples, because the published rates were reported on differential etch rates in *z*-cut PPLN. On the other hand, it is worthy to notice that, in some experiments (not showed here), the combination of the lowest energy (Br 22 MeV) and the lowest HF concentration ($c_{HF} \approx 13.3\%$) in the 1 : 2 blend could both be a reason for the lower etching rate.

From **Fig. 12 (b)**, corresponding to pores depth evolution, the fits show that the 1: 1 blend etched Br 46 pores are as deep as identical ion tracks after treatment with the pure 40% HF acid. Additionally it seems to be the case that the samples attacked in the acid blends were dirtier than from other etchings. The pure 40% HF acid was exchanged more often which may have helped to keep the samples clean. Just as expected, the 5% solution affects the lowest etching rate and thus the smallest pore diameters and depths are obtained. These are the most similar etching conditions to the "standard conditions" used by Schrempel et al. The research group etched $LiNbO_3$ samples in 3.7% HF acid to deduce the etch rate of crystalline *x*-cut material. The rate is given to be 0.1 nm/min [21]. Here, in the case of the 5% concentration, the observed rate is ≈ 0.22 nm/min for the damaged tracks. This shows that the nanopores etch rates determined by AFM are in the order of the one of crystalline material.

It is worthy to notice that, the linear fits in all graphs do not originate from "zero" but intersect the *y*-axis at certain heights. It is suggestive that the intercept parameter somehow reflects the mean size of the used tips. None of the diameter fit intercepts falls below the 10 nm value. Another possibility for the positive diameter in the very beginning (*fast etching regime*) could be related to the before mentioned nanohills. This would imply that pore evolution already starts with a crater that is larger than the latent nanotrack as was suggested in **Section 6.3.1.3**.

Again, a tendency of the Surface Aspect Ratio (SAR, **Fig. 12 (c)**) is not apparent. When discussing other parameters it will be shown that the SAR is mostly independent of any of them,

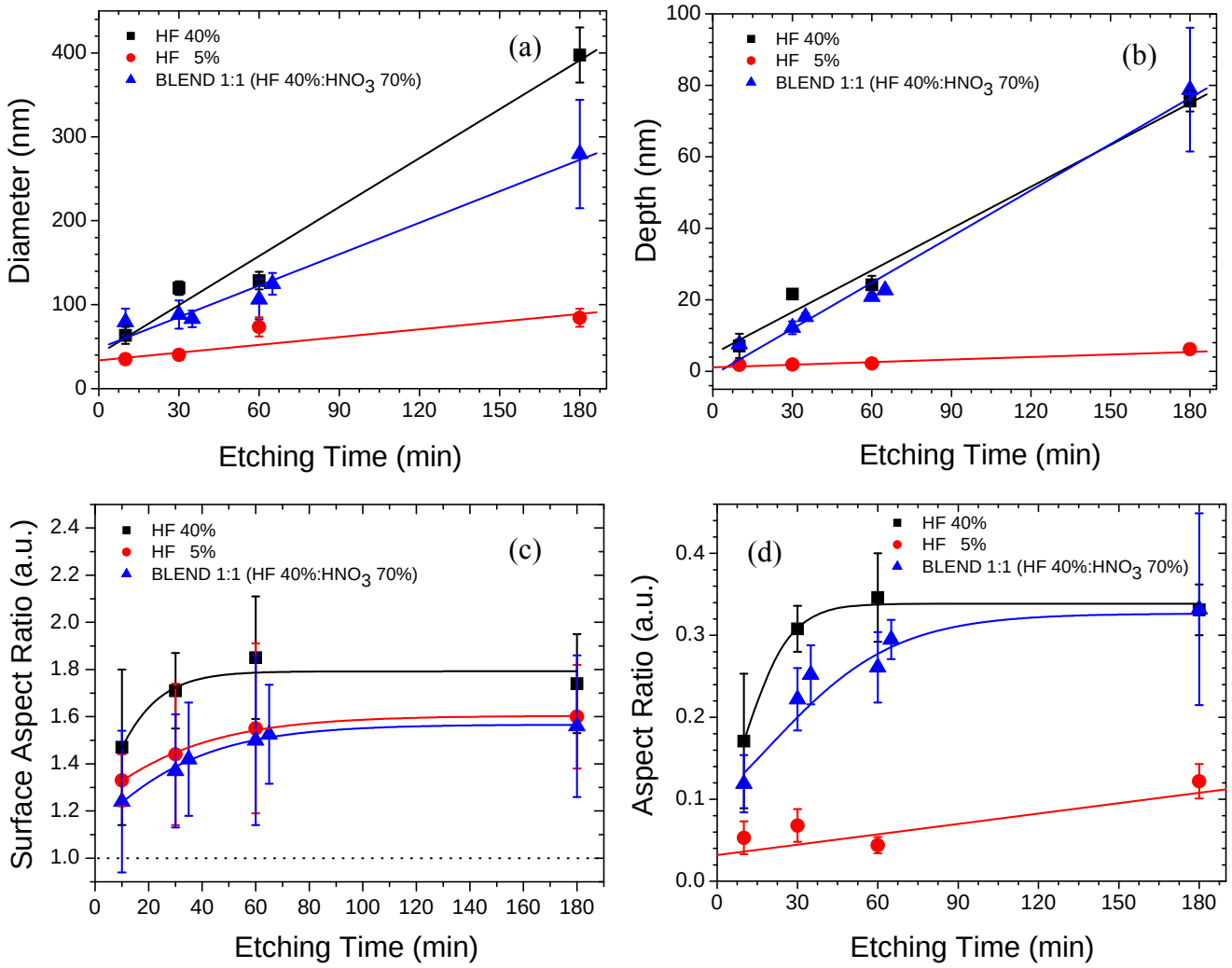

Fig. 12 (a-d). Graphs of pore dimensions versus etching time for different etching aqueous solutions at RT (HF 40 %, blend 1:1 of HF 40 % and HNO_3 70 %, and HF 5%) using samples irradiated with Br ions of 46 MeV. **(a)** Long axis diameter, **(b)** Pore depth, **(c)** Surface Aspect Ratio (Long axis/ Short axis diameter) and **(d)** Aspect Ratio (Depth/ Short axis diameter).

but it seems that after the first 30 min. of etching, some kind of steady-state is reached, where no significant changes appear, being constant the values. Again, the most efficient acid seems to be the 40% HF, producing the biggest differences in between the long and short axis etching rates. This gives reason to assume that the elongated pore shape must be due to the crystal structure since the pores turn with the sample in every performed test measurement, which excludes it as an artefact from the tip as the governing parameter to pore elongation. The Aspect Ratios (AR´s, see **Fig. 12 (d)**) show the same tendency toward longer etching times as was noted before for the SAR; here again, the biggest values for AR are reached with the strongest acid HF 40%, followed by the blend 1:1 ($c_{HF} \approx 20$ %) and the weakest 5 % diluted HF. For the latter case, an almost constant low value of AR is observed for all the range of time studied, due to perhaps, to its so high chemical weakness, being thus, the etching rate for the surface and depth extremely low. For the stronger acids, a fast increase in the beginning (first 30 min.) is evident. After one hour of etching a maximum is reached, staying approx. constant. A further

increase of the AR after longer etching times is not observed. This supports the thesis of two etching stages, fast in the beginning and slower in progression, where during the latter, only the virgin crystal is affected. The errors resulting from the discussed measurement uncertainties are fairly large and do not permit clear statements on all results.

8.4.2.1. Etch Rate Dependence on the Acid Concentration.

In bulk material the etch rate is usually defined as the increase of depth over time. Here, etching rates were defined for the depth, as well as for the diameters of the long - and short pore axis, and represent the mean increase of the structure in this direction with respect to the changing parameter during the elapsed etching time. Since the depth values may depend strongly on the AFM probes and measurement conditions the etching rate in terms of pore depth does not appear to be very meaningful. On the other hand, well defined differences between the depths of distinct ion energies were found. In **Fig. 13** the etch rates derived from the different pore dimensions are depicted versus the used HF concentration (in vol. %). It was reported by Sones et al. that pure HNO_3 acid does not attack the crystal at all [10]. Hence, it is presumed that the additional acid in the blend neither accelerates nor decelerates the reaction process, which is a rather simplistic assumption since in principal the reaction chemistry may change due to the present etchant. The increase of the etch rate with increasing HF concentration (c_{HF} (%)) in the acid blend appears to be linear. Similar behaviour was published in the study mentioned above for the investigations in undamaged *z*-cut material.

We have to say that the etching rates have been derived from the linear fits of the different pores features in **Fig. 12** for the case of Br 46 MeV irradiated samples (behaviour of long diameter and depths vs etching time for different aqueous solutions and blends). Moreover, and although there was not plotted in **Fig. 12** the case of the variation of short axis diameter with the acid concentrations in order to simplify the graphs, we have taken it into account to calculate the associated etch rate.

In the end, we have to comment too that, while our main attention has been emphasized on the systematic and whole etching study on the case of Br 46 MeV irradiations shown in previous figures (**Fig. 12**) with different concentrations (HF 40 %, HF 5% and blend 1 : 1 of HF (40 %) : HNO_3 (70 %), c_{HF} = 20 %), some extra experiments have been carried out with Cu 51 MeV and Br 22 MeV irradiated LN samples treated with two acid blends in the ratios 1 : 1 and 1 : 2, respectively. Thus, from the latter, we can deduce from the linear fits the corresponding etching rates for the different pores features associated to a c_{HF} = 13.3 %. The justification to used this etching rates belonging to Br 22 MeV is that, as we have seen in a preliminary study (**Fig. 11**) with the ion energy, only little differences appear between Br 22 and Br 46 MeV irradiated samples using the most efficient etching with that highest concentration, HF 40%, therefore, being more little ones for weaker solutions.

8.4.3. Influence of the Irradiation Energy.

In order to study the influence of the ion energy and different species on the features of the revealed nanostructures some irradiations were carried out with swift heavy ions from Big Facilities (GSI and Ganil). Through them we will be able to see if some effects are produced

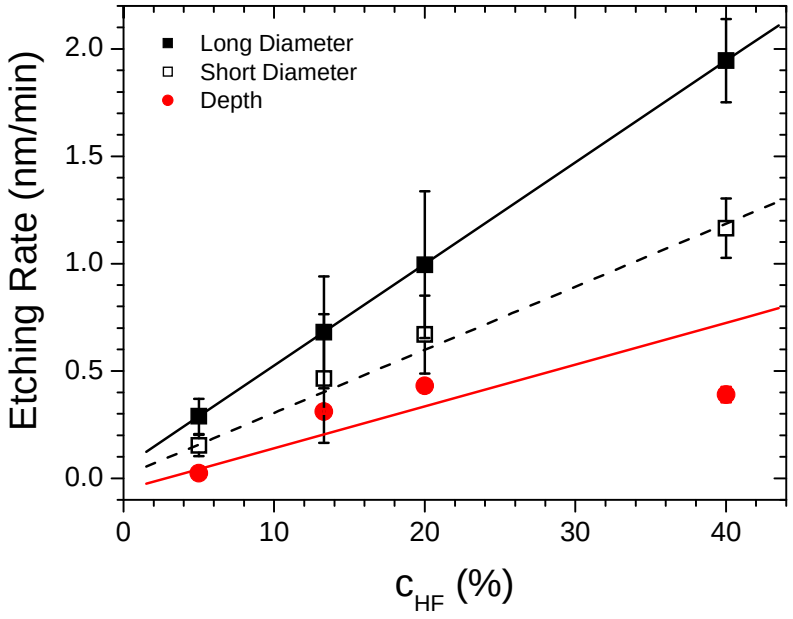

Fig. 13. Etching rates derived from the linear fits of the pores features vs the HF concentration. It is observed a well defined linear behaviour, which is in accordance to the proposed models and previously published data [10].

with the use of ions ten times greater in energy and projected range. These automatically imply variations of the stopping power, the equilibrium charge state, and the projected ion range as given in **Table I** and **Fig. 1 (a, b)**. All other irradiation parameters were supposed to be equal. It is worthy to notice that, with the aim of remarking some kind of correlation between the revealed pores dimensions (Long-short axis diameter, depths, Surface Aspect Ratios-SAR, and Aspect Ratios-AR; etchings rates) and the physical parameters of the used ions, we will perform several studies respect to those parameters (S_e, ion Energy, Amorphous Track Length- where the stopping power through the ion pathway is above the threshold, $S_e \geq S_{th} \approx 4$ keV/nm). We have to remind that a preliminary study has been shown previously for the case of Br 12-46 MeV (see **Section 6.4.1** and **Fig. 11 (a-f)**). Just before to describe the results let me to present again the *Stopping Powers curves* for the different ions and species used in this study (**Fig. 14**), and the irradiation parameters adding in a new column the values corresponding to the amorphous track length (**Table IV**). Although the amorphization threshold, S_{th}, is velocity dependent, and hence, is not a constant value through the ion path through the crystal, we will consider it only qualitatively with an approx. value, $S_{th} \sim 4$ keV (drawn in **Fig. 14**), in order to define an *amorphous track length*. It means that, for the case of very Swift Heavy Ions (Kr and Pb) from GSI and Ganil, the amorphous track length represents ~ 96 % of the ion range (R_p), while for the case of the CMAM ions: Br 46 MeV and Cu 51 MeV, it is 62.5 % of R_p; Br 22 MeV, it is 46 % of R_p and Br 12 MeV, 26.3 % of R_p.

The etchings conditions have been defined previously in **Chapter 4.** (**Section 4.5.1.** *Aqueous solutions*) and they were also fixed. All samples were immersed in 40% HF aqueous solution at RT for the indicated times. In order to observe any kind of correlation among the evolution of the pore features (diameters, depths, Aspect Ratios-AR, and Surface Aspect Ratios-SAR) and the several irradiation parameters (S_e, Energy (MeV/amu), amorphous track length,..),

Ion	Energy (MeV)	Energy (MeV/amu)	S_e surface (keV/nm)	S_e max (keV/nm)	S_n max (keV/nm)	R_p (μm)	Amorphous Track Length (μm)
$^{19}F^{3+}$	5	0.26	3.4	3.4	0.06	2.8	-
$^{79}Br^{5+}$	12	0.15	6.0	6.0	0.52	3.8	1
$^{79}Br^{5+}$	22	0.29	8.7	8.7	0.51	5.0	2.3
$^{79}Br^{8+}$	46	0.57	11.9	11.9	0.50	7.2	4.5
$^{63}Cu^{9+}$	51	0.80	11.9	11.9	0.37	8.0	5.0
$^{78}Kr^{31+}$	809	10.4	12.3	15.1	0.47	62	58.9
$^{208}Pb^{55+}$	2300	11.1	35	36.8	1.65	72.8	70.8

Table IV. Irradiation parameters including the electronic energy loss (S_e) at the sample surface and at the Bragg maximum as well as the maximum nuclear energy loss (S_n) and the projected ion range (R_p) according to the SRIM-2003 code [15]. The amorphous track length, where the stopping power through the ion pathway is above the threshold, $S_e \geq S_{th} \approx 4$ keV/nm, is shown too.

and trying to expose them clearly, they will be shown in different figures (**Figs. 15-18**) for each etching time (10 min., 30 min, 60 min, and 180 min.). Moreover, the deduced etching rates from the slopes of the linear behaviours will be plotted vs the irradiation parameters trying to find any relationships (**Fig. 19**). Finally, it is worthy to notice that, unfortunately, the only available data of pore dimensions corresponding to the swift heavy ions for the Big Facilities (Kr and Pb) come from the step etching time for 10 min. From them, moreover of plotting in the graphs for that etching time, we will have to calculate the etching rates for the pores features.

From **Fig. 15 (a)** in which the pore diameters are plotted, it is remarkable that when it is drastically increased the ion energy, obviously the pore radii become larger. More precisely, there are step-like jumps visible that seems to be related to certain amorphous track lengths, ranging from 0 nm (F) over ~ 60 nm diameter (Br 12 - 46 MeV, L= 1 - 4.5 μm) to about 230 nm (Kr and Pb, L > 55 μm). The long axis pore diameters of the large tracks after chemical attacks of 10 min are four times bigger than the diameters of the short range ions. Pores evolving from the Br irradiations would need at least 100 min to evolve to the same size, and were only about twice as large as them after 180 min. Although it has not been plotted in the graph, it is interesting to comment that pore diameters (in long, short and inner pore axis) corresponding to Pb irradiated samples after etching for 1 minute in the acid, are the same order than the associated to Br 46 MeV.

Comparing the Br 46 MeV with the Kr 809 MeV irradiations (both with approximately the same S_e at the surface), it is noticeable that the tremendous increase of the diameter is most probable due to the much higher amorphous track lengths and the great difference in energies. The Kr ions have approximately the same stopping power at the sample surface but induce a damage volume that reaches 13 times deeper into the sample. The increase of only 0.4 keV/nm is considered to be insufficient to explain the observed behaviour after the observations made

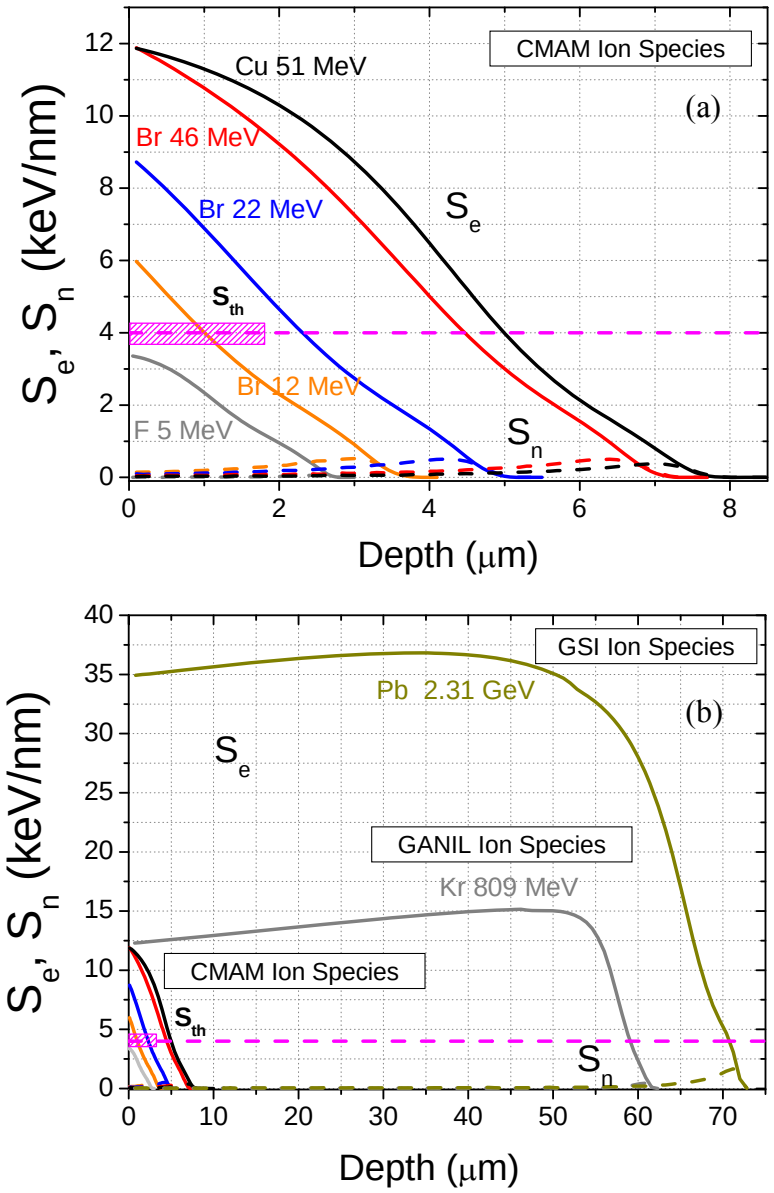

Fig. 14 (a, b). Electronic (S_e, solid lines) and nuclear (S_n, dashed lines) energy loss of CMAM ion species (F 5 MeV, Br 12-22-46 MeV, Cu 51 MeV) **(a)** and big Facilities (GANIL, Kr 809 MeV and GSI, Pb 2.31 GeV) **(b)** as a function of penetration depth in $LiNbO_3$ obtained with the SRIM-2003 code [15]. In **(b)** all the stopping powers curves are shown to be compared the different magnitude order of the ions from different Facilities. For comparison, the electronic stopping power for the *amorphization threshold* (S_{th} ~ 4 keV/nm) is also shown in order to define the amorphous track length.

above, thus we have to manage the hypothesis that the combinated effect of the amorphous track length produced by the enormous energy deposited into crystal, more that the isolated effect of the stopping power at the surface, plays an important role. From **Fig. 15 (b)** it is very interesting to observe that the pore depths (but not the depth etching rates, see **Fig. 19 (b)**) of both irradiations are equal. It might be the case that this observation is due to the limitations of the AFM depth measurements. However, since the depths are alike, the AR of the compared ion track lengths are imposed to behave reciprocally to the diameters. It is worthy to notice that, a

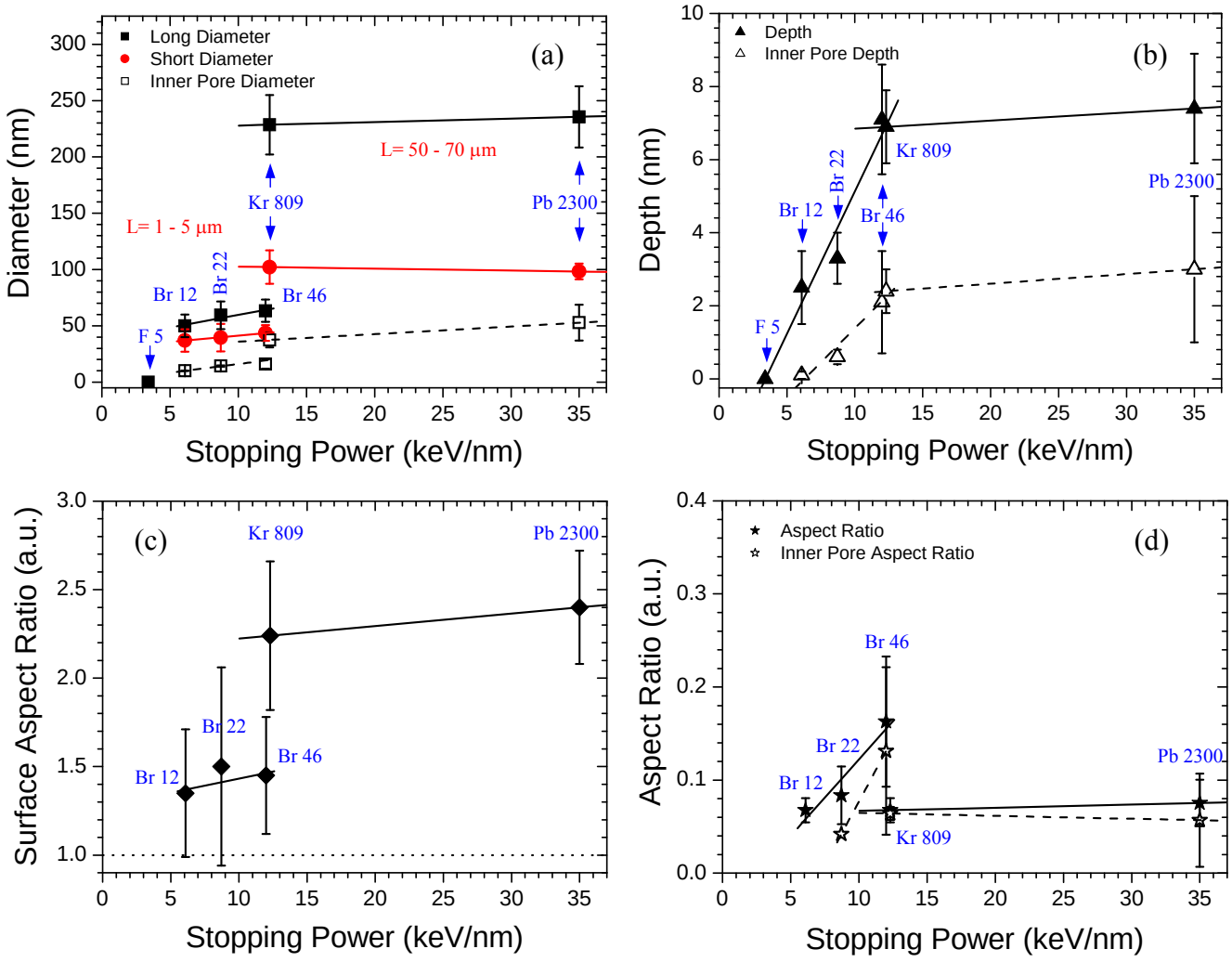

Fig. 15 (a-d). Graphs of the pores dimensions after **10 min**. of etching time in pure HF 40% acid at RT for different ion energies and species irradiated samples. **(a)** Diameters (Long axis, short axis and inner pore), **(b)** Pore and inner pore depths, **(c)** Surface Aspect Ratio (Long axis/ Short axis) and **(d)** Aspect Ratio (Depth/ Short axis). In order to remark the great different between the ion energies used in the study, the Amorphous Track length (L) is shown in the figure in each case.

more detailed study of this phenomenon is planned, including data from Xe and Au irradiations from GSI Facility, each one with energies of 11.1 MeV/u. In case of the Au ions different number of Al foils of 13 µm in thickness each one will be used to vary the projected range, meanwhile the electronic stopping power at the surface supposedly remains the same.

It is interesting to see, through the different steps of etching time, that the measured pore diameter corresponding to F 5 MeV irradiated sample directly jumped to the same diameter values as measured on the equally treated bromine irradiated ones after etching them for 60 min in 40% HF at RT (**Fig. 17 (a)**, meanwhile in the first etching stages, 10 min. and 30 min. there were no pores measurable at all (compare **Figs. 15** and **16 (a)**). Although, one could think that this equality of the pore diameters might be caused by the physical dimensions of the AFM probe, because the depth value is much lower than the pores emerging from Br irradiations, as depicted in **Fig. 17 (b)**) [notice that the pores on the F 5 MeV irradiated sample were

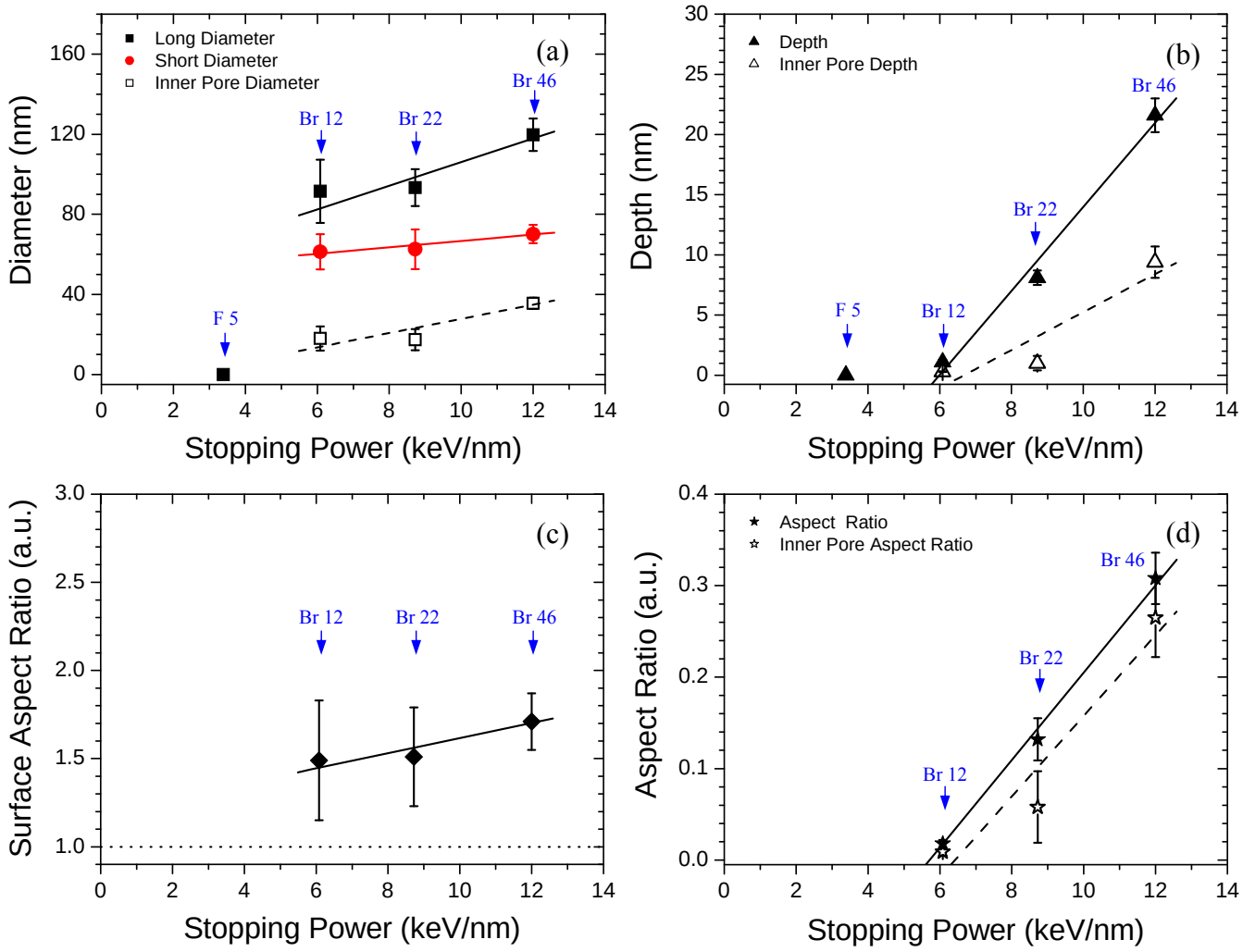

Fig. 16 (a-d). Graphs of the pores dimensions after **30 min**. of etching time in pure HF 40% acid at RT for different ion energies and species irradiated samples. **(a)** Diameters (Long axis, short axis and inner pore), **(b)** Pore and inner pore depths, **(c)** Surface Aspect Ratio (Long axis/ Short axis) and **(d)** Aspect Ratio (Depth/ Short axis).

investigated with the High Aspect Ratio tips, AR 5, that possess slightly higher tip diameters at the very front of the probe]; on the other hand, it seems more probable that the assumable low defect concentrations not high enough for proper depth etching, due to for this ion specie the S_e at the surface is below the *amorphization threshold*, and it is only in the case of extreme etching time conditions (after 60 min.) when the nanopores are revealed; moreover, the use of this high accurate tips allows us to reveal, entering well into deep crack-like structures (see the AFM images after 60 min. of etching in **Fig. 2 (a)**), the polishing scratches on the surface. Above a certain threshold, the etching depth (**Figs. 15-18**, depths at different times) seems to increase linearly with the deposited energy (see **Fig. 11** and **Fig. 19** - to compare with the etchings rates). This appears logical because it is known that the etching rate increases with higher defect density. Having said that, we have however to take in mind the old problem of the tip influence and the limitations of the acquisition technique, that very probably causes some kind of falsification of the depth data.

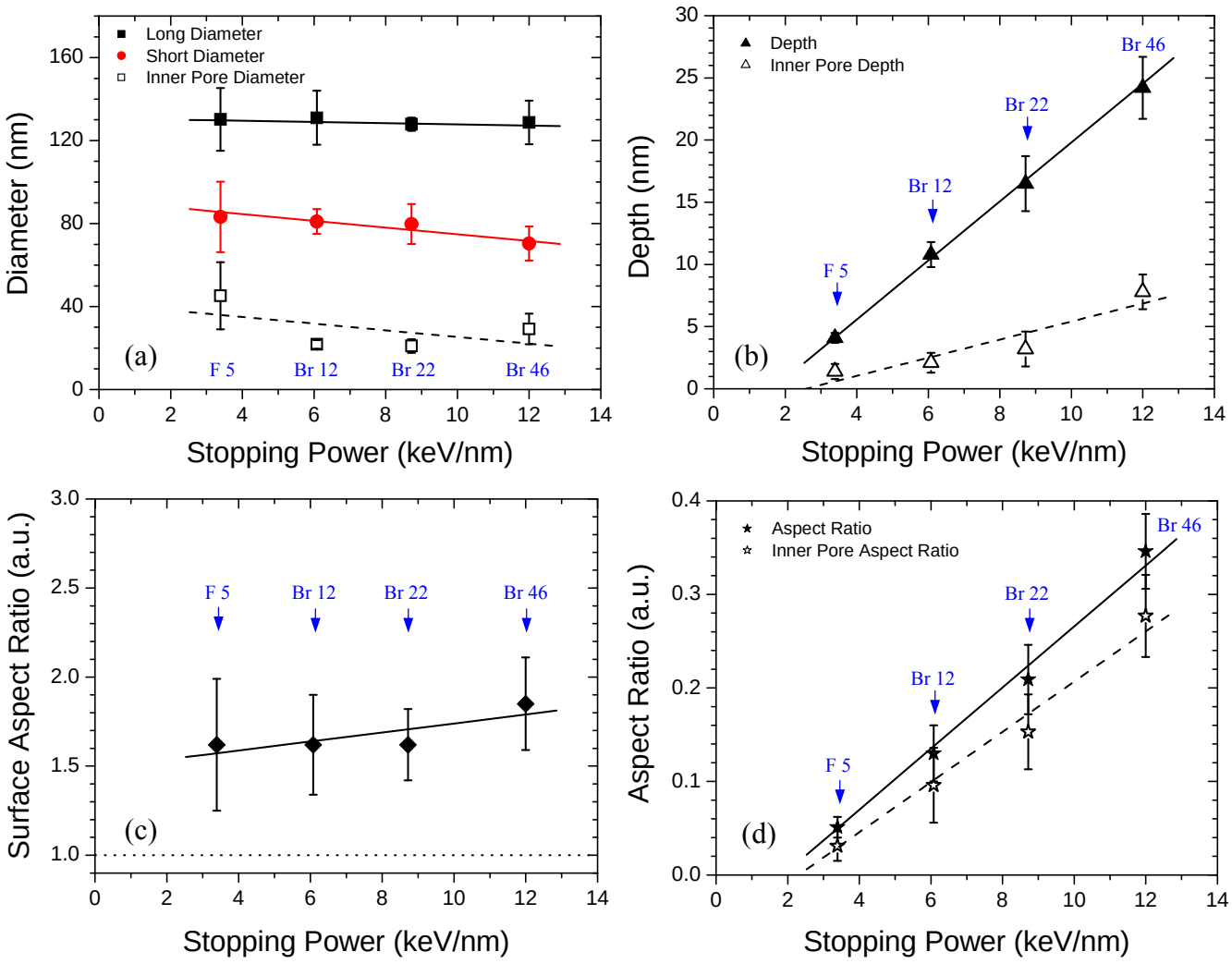

Fig. 17 (a-d). Graphs of the pores dimensions after **60 min.** of etching time in pure HF 40% acid at RT for different ion energies and species irradiated samples. **(a)** Diameters (Long axis, short axis and inner pore), **(b)** Pore and inner pore depths, **(c)** Surface Aspect Ratio (Long axis/ Short axis) and **(d)** Aspect Ratio (Depth/ Short axis).

The AR´s (**Figs. 15-18 (d)**), for the different etching times) shows a clear rising linear tendency with the stopping power up to (12 keV/nm) in all etching stages. In contra, the pores fabricated from the very long tracks of the high energy ions Kr and Pb have very low AR due to the mentioned step-like increase of the diameters and constant depths.

From the SAR (**Fig. 15 (c)**) the abrupt structural change is also visible. In the lower energy regime the SAR are constant (**Figs. 15-18 (c)**). The large axis diameter is about ~ 1.6 times as long as the shorter diameter. Then, the SAR exhibits an increase like the diameter and jumps to a value greater than ~ 2.3 (**Fig. 15 (c)**). The tendency is obvious despite of the large error bars.

Throughout this Section, we have performed an incursion into the influence of the irradiation energy, making a quantitatively "jump" in energies, stopping powers and ion ranges. This part certainly depends on a great deal of interesting physics contributing to the phenomena and needs to be studied in greater detail in a more systematic way, and inclusive with more

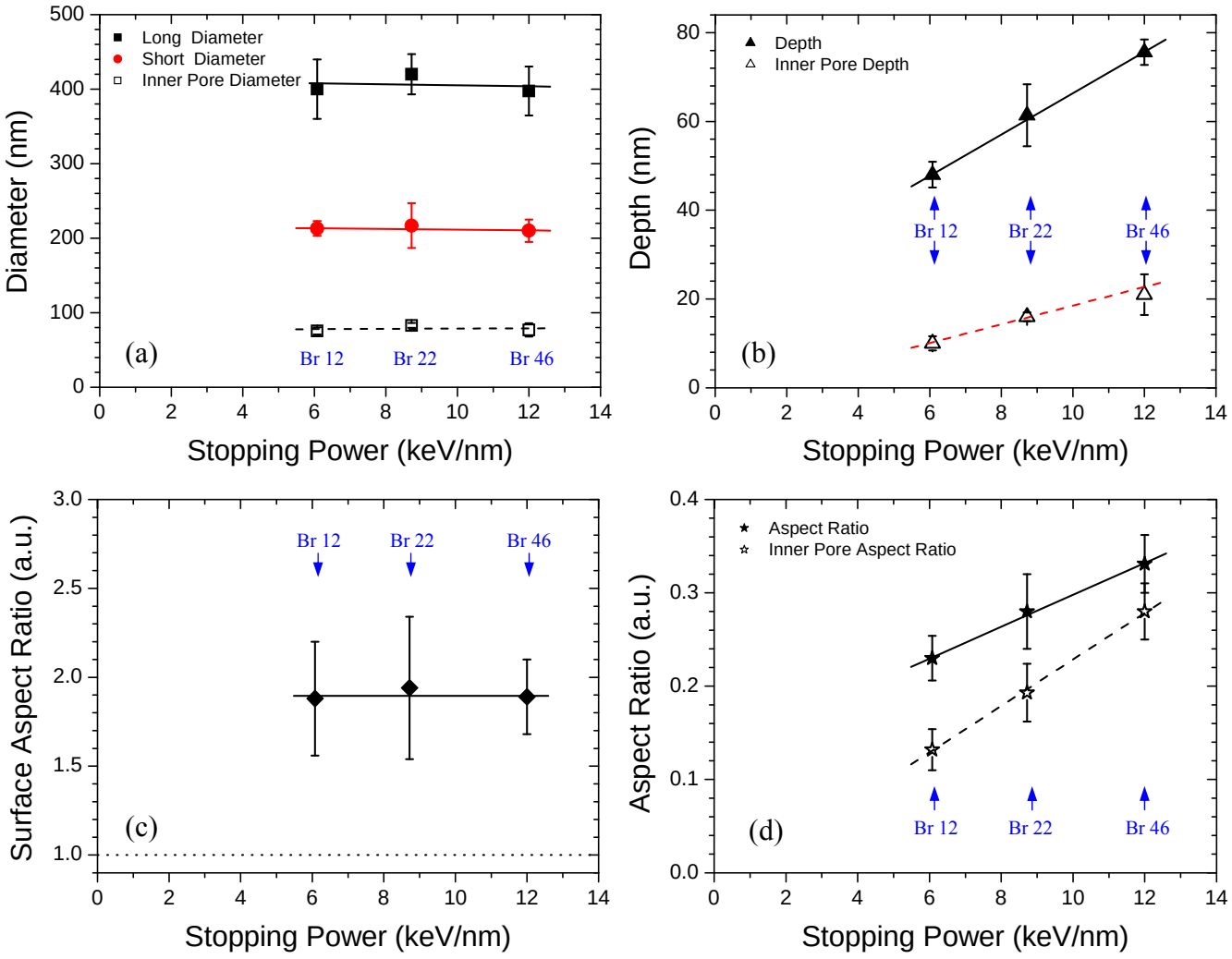

Fig. 18 (a-d). Graphs of the pores dimensions after **180 min.** of etching time in pure HF 40% acid at RT for different ion energies and species irradiated samples. **(a)** Diameters (Long axis, short axis and inner pore), **(b)** Pore and inner pore depths, **(c)** Surface Aspect Ratio (Long axis/ Short axis) and **(d)** Aspect Ratio (Depth/ Short axis).

different species, in order to gain a better understanding of the complex interaction between the swift heavy ions and the matter in the electronic excitation regime, as well as, the formation of the amorphous tracks. Nevertheless, the knowledge of the mentioned irradiation parameters in more detail, as they have been shown, it turns into by itself in a very useful tool that will very probably enable a better access to the IBEE technology in the single ion track regime.

8.4.4. Study of the Temperature dependence.

As was stated earlier, the temperature is a crucial etching parameter which has not been studied in much detail. In **Section 6.3.1.4** it was shown that an increase of the temperature makes the attack much more aggressive. A few samples were immersed in aqueous solution of 40 % HF acid at 55 ºC. The large pores were presented in **Fig. 3**. Due to, after 60 min the aggressive etching conditions lead to total pore overlapping, thus, the only available samples

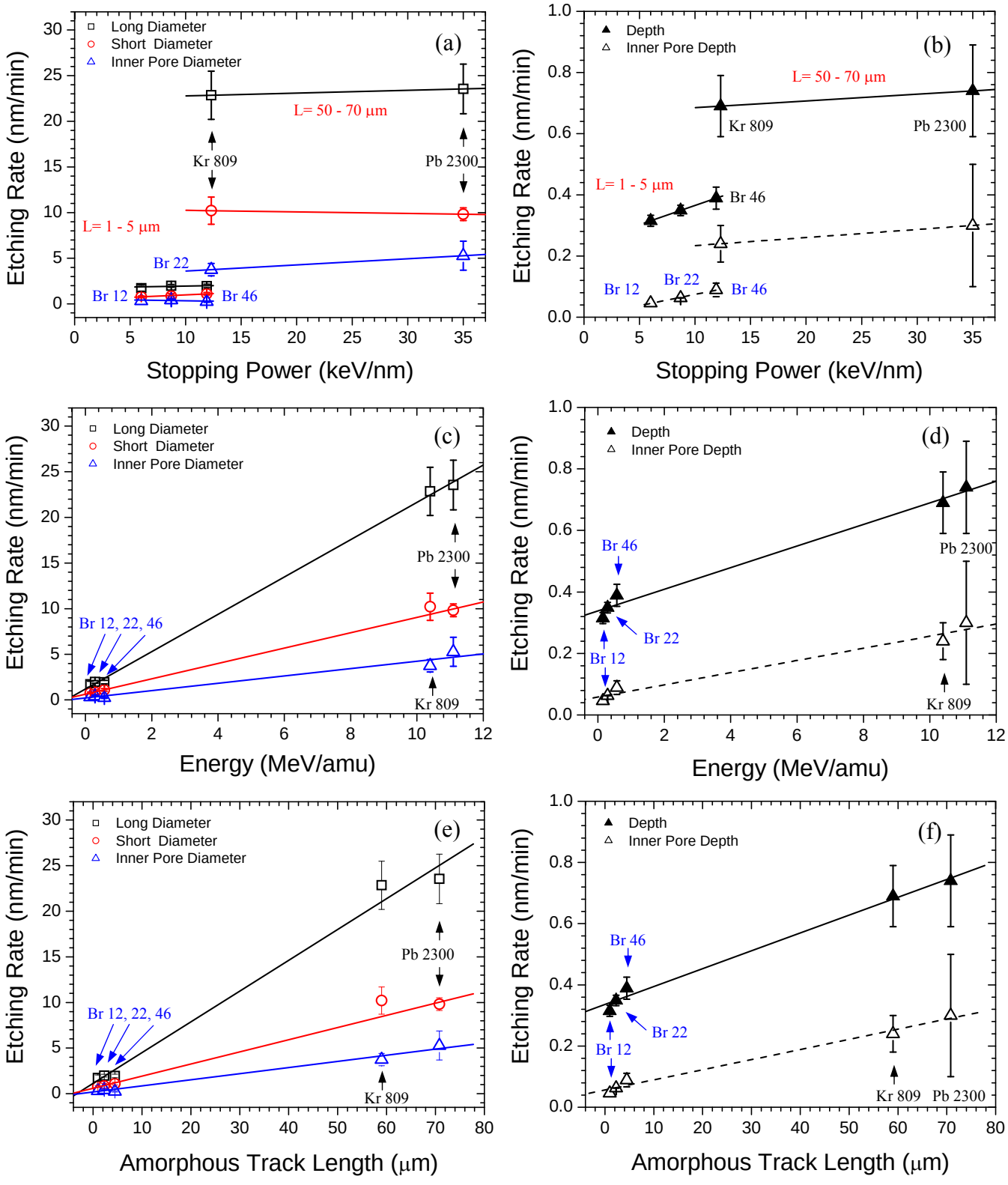

Fig. 19 (a-f). Graphs of the etching rates in pure HF 40% acid at RT for the different pores dimensions (Long - short axis, inner pore diameters and depths) versus different irradiation parameters of ions species (Br 12, 22 and 46 MeV; Kr 809 MeV and Pb 2300 MeV) irradiated samples. **(a, b)** Stopping Power at the surface, S_e; **(c, d)** Energy/amu; **(e, f)** Amorphous track length, where the stopping power through the ion pathway is above the threshold, $S_e \geq S_{th} \approx 4$ keV/nm). It is worthy notice that a zoom in these graphs has been shown in **Fig. 11 (a-f)**, where the interest was focused on the Bromine ions family.

were etched for 30 min. To be able to compare more data points of samples that were attacked for longer times, the measured pore diameters of long- and short axis as well as the depths were divided by the corresponding etching times. By this way the etching rate is obtained and can be compared with any other sample that was etched in 40% HF. In order to get more clear graphs, only the data corresponding to Br 46 MeV ions irradiated samples will be presented in **Fig. 20**, (after **30 min**. of etching time), and **Fig.21** (after **60 min.**). Moreover, a more overall insight is presented in **Fig. 22 (a, b)**, where the etching rates are presented. For better visibility, the range from 18 to 27 ºC is zoomed. At elevated temperatures the attack rate increases linearly. In contra, the deduced ratios seem to be temperature independent (**Figs. 20, 21 (c, d)** and **Fig. 22 (b)**. For the highest etching rate the long axis pore diameter evolved with ~ 21.6 nm/min. Reinisch et al. reported that the etch contrast in bulk material is constant over the investigated temperature range from 24 to 55 ºC [11]. This observation can be confirmed by our data. The AR and SAR of all measurements slightly increase at high temperature (see **Fig. 20**, (after **30 min.** of etching time), and **Fig. 21** (after **60 min.**), and both together in **Fig. 22 (b)**).

In order to get a deeper insight into the evolution of the pore dimensions (diameters, depths and Ratios) vs. the temperature of the acid aqueous solution for the two different etching times studied (**30 min.** and **60 min.**), both sets of graphs have been shown previously (**Figs. 20** and **21**); Moreover, a comparative plot of the AR and SAR with both time is plotted too (**Fig. 22 (b)**).

8.4.5. Study of Influence of thermal annealings.

As it was described in a previous **Section 6.3.2,** the damage induced by swift heavy ions in lithium niobate can be reduced by annealing the samples. Thermal treatments after irradiation may anneal out some of the defects generated in and around the track and thus influence the subsequent etching rates and pore morphologies. After previous ion irradiation with Br at 46 MeV, a few samples were annealed for one hour in air at temperatures of 150 ºC, 175 ºC, 200 ºC, and 300 ºC, respectively. On the other hand, Br 22 MeV irradiated samples have been annealed at 150 ºC and 300 ºC. Subsequently, all samples were etched in 40% HF aqueous solution at RT for 1 hour. It should be interesting to see the AFM images on the resulting pore structures after the etching treatments (**Fig. 6**).

In the charts of **Fig. 23** the measured pore dimensions are plotted versus the annealing temperature. It was expected that the diameters, as well as the depths, should decrease with lower defect concentrations. However, this behaviour is only found from the short axis diameter, which slightly narrows down after annealing the sample at 300 ºC. A clear tendency is not denoted. Similar behaviour has been found for the case of Br 22 MeV ions irradiated samples, although they have not been plotted with the aim of clarify the results; in this sense, the long axis diameter, inclusive seems to increase slightly. The resulting SAR is constant after all annealing treatments, except for the one at 300 ºC, where the ratio is higher than usual. On the other hand, the depth evolution is clearly retarded by the temperature treatments, which is also visible from the AR. Under the given fabrication conditions (annealing at a fixed Temperature and subsequent etching treatment for 1 hour at RT in aqueous solution of HF 40 %), the mean depth diminish amounts about 0.04 nm/ºC. After all temperature treatments, the reduced damage tracks were still sufficient to act as seeds that are then developing into pores as

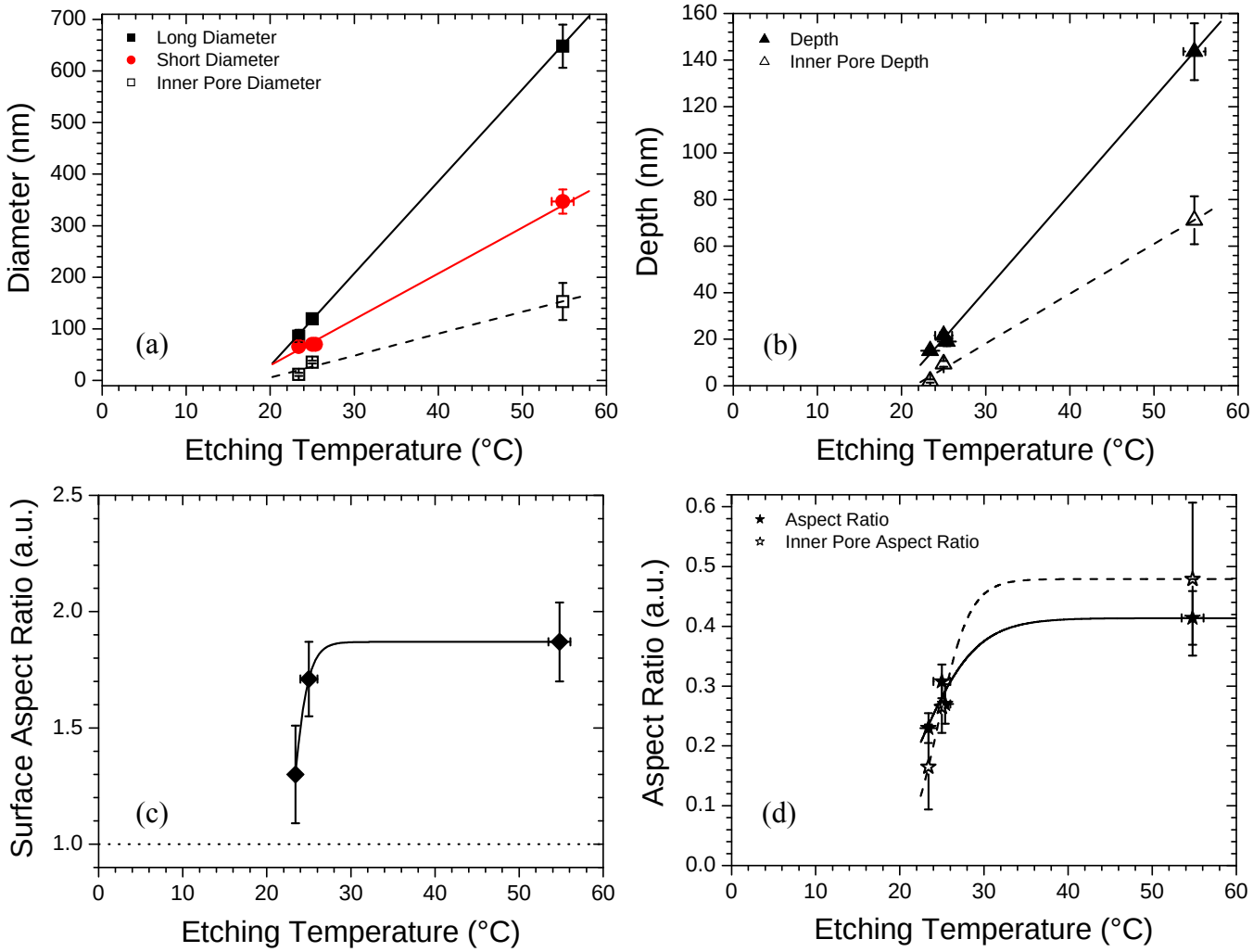

Fig. 20 (a-d). Graphs of the pores dimensions vs. the temperature of the aqueous solution after **30 min.** of etching in pure HF 40% acid for Br 46 MeV ions irradiated samples. **(a)** Diameters (Long axis, short axis and inner pore), **(b)** Pore and inner pore depths, **(c)** Surface Aspect Ratio (Long axis/ Short axis) and **(d)** Aspect Ratio (Depth/ Short axis).

the crystal opens up.

8.4.6. Etching treatments in vapour conditions.

The results from vapour etching at different temperatures are shown in the **Figure 24**. The samples were etched in 40 % HF vapour facing downwards to the acid at a distance of 1 cm approx. The same tendency showed from the liquid etching temperature observation is apparent (see **Figure 24 (a)**); with the difference that the etching rates in vapour are drastically reduced. Whereas in the liquid at 55 ºC an etching rate of ~ 22 nm/min. was effective, here the rate decreased to ~ 7 nm/min. on the long pore axis, respectively. The same factor of approximately ~ 3 times it applies also for the etching rates at RT. Hence, vapour etching is about a third as aggressive as the liquid attack.

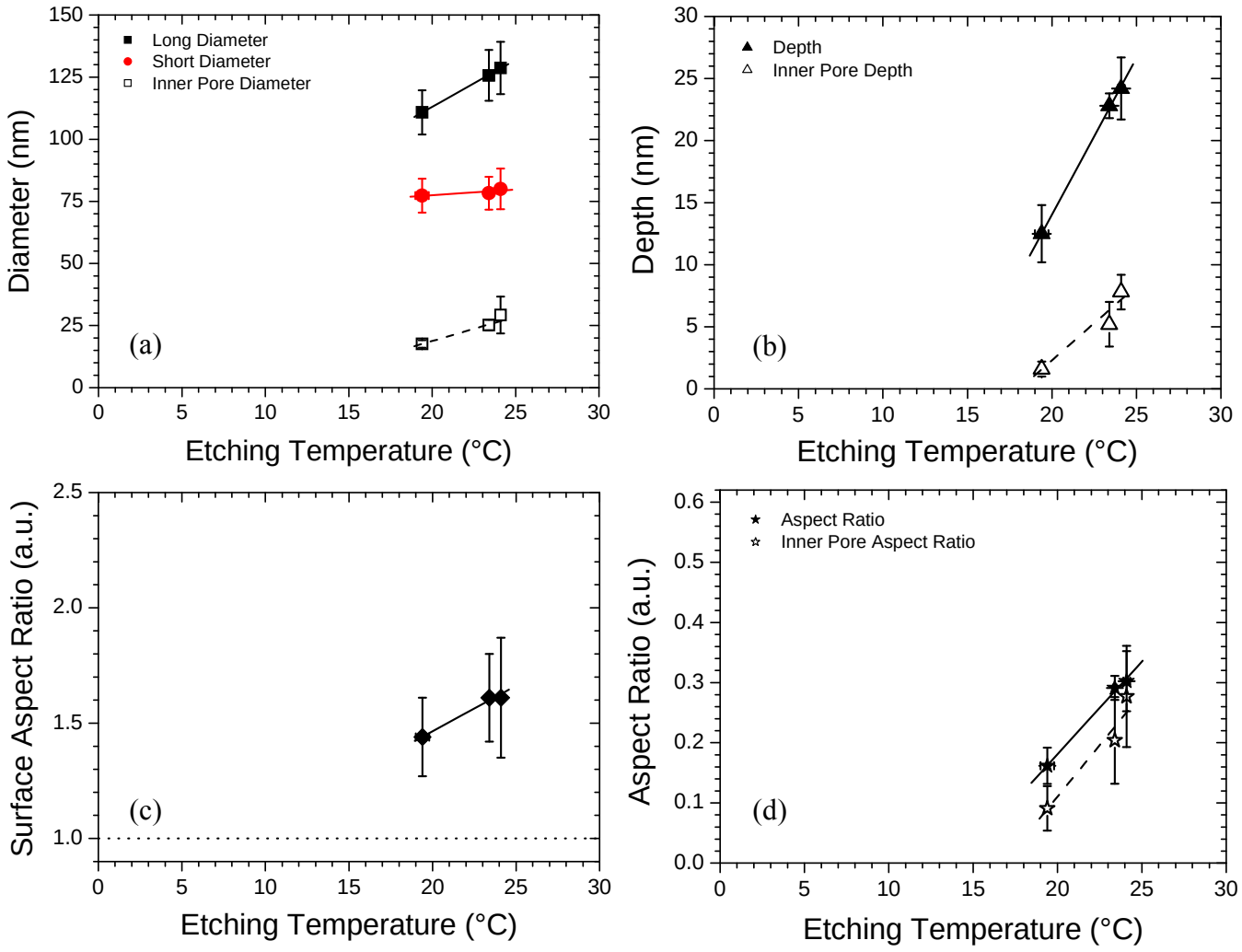

Fig. 21 (a-d). Graphs of the pores dimensions vs. the temperature of the aqueous solution after **60 min.** of etching in pure HF 40% acid for Br 46 MeV ions irradiated samples. **(a)** Diameters (Long axis, short axis and inner pore), **(b)** Pore and inner pore depths, **(c)** Surface Aspect Ratio (Long axis/ Short axis) and **(d)** Aspect Ratio (Depth/ Short axis).

In the AR graph a slight rising tendency is noticeable with increasing temperature in the presented range plotted in **Figure 24 (b)**), whereas the SAR remains constant within the error ranges (~ 1.4). Although, the main part of the systematic study was carried out from samples irradiated with Br 46 MeV ions, some specific experiments were performed with Br 22 MeV ions irradiated ones; in this sense, and although, they were not plotted in the graphs, in order to present them as clear as possible, we have to say that, again, no significantly differences between the two energies (22 and 46 MeV) of the bromine ions could be denoted. If any, the values determined from the Br 22 MeV irradiations were even slightly higher, concerning the determined diameters as well as the ratios.

When heating the sample with the heater element, the etching rate is again decreased. Firstly, we have to mention that, the measurement of the sample temperature as described in the experimental part (**Chapter 4. Section 4.5.2.** *Vapour etching*) may have a rather big systematic

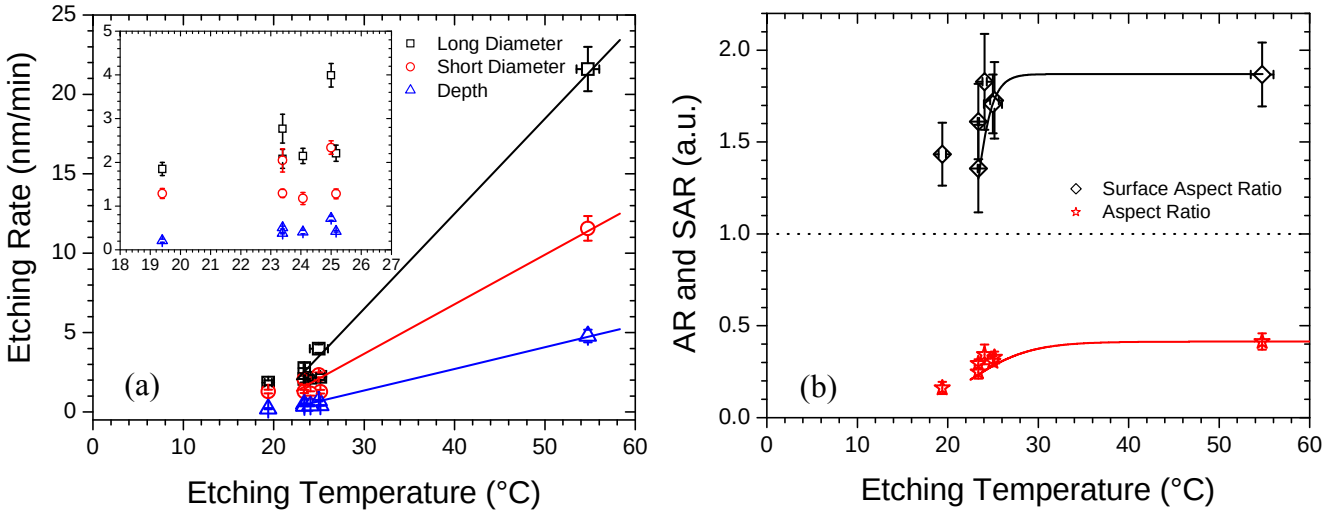

Fig. 22 (a, b). (a) Etchings rates vs. the temperature of the aqueous solution of HF 40%. The etch rates were derived from the measured pore dimensions by dividing them by the corresponding etching time. It has been taken into account the data corresponding to **30 min.** and **60 min.** A zoom in the low temperature range, is shown as an inset. **(b)** The AR and SAR remain approx. constant with the temperature. The temperature errors indicated by the diameter etch rates and SAR values are also valid for the other magnitudes.

error. The thermopar was directly attached to the side of the heat element, but bad thermal coupling to the sample and suppressed heat dissipation to the sample surfaces could have caused unknown uncertainties. Several temperature combinations were tried out. Above the acid bath at 55 ºC the samples were heated to approximately different temperatures: 65 ºC, 95 ºC, and 150 ºC. We have to say that, nanopores were only found in the two former cases. The observed pores tended to appear smaller and more circular with increasing temperature. At the highest temperature no pores were found at all.

On the other hand, one sample was heated to 95 ºC and exposed to the vapour of acid at RT. We have to say that, for this case, pores were unrecognizable. However, in SiO_2 by this method, pores with very high aspect ratios of about 17 could be fabricated [24]. It is worthy to notice that our measurement method was not capable of revealing such high aspect ratios structures, due to the pores were very small. In general, it seems that heating the sample further retards the reaction.

8.5. Ion Beam Enhanced Etching Rates of Bulk Material.

Some samples have been irradiated with higher fluences as was described in **Chapter 4.** (**Section 4.7.3.4.)** and the corresponding influence was examined by means of AFM (see **Section 6.3.1.5**). In parallel, the bulk etching rate of damaged material was determined by scanning profiles along etched surfaces of *x*-cut LN samples with the Dektak surface profilometer [25].

The samples were previously irradiated with Cu 51 MeV ions at a fluence of 1 e12 at/cm^2, and subsequently etched in the HF : HNO_3 1 : 2 blend. Samples were irradiated under

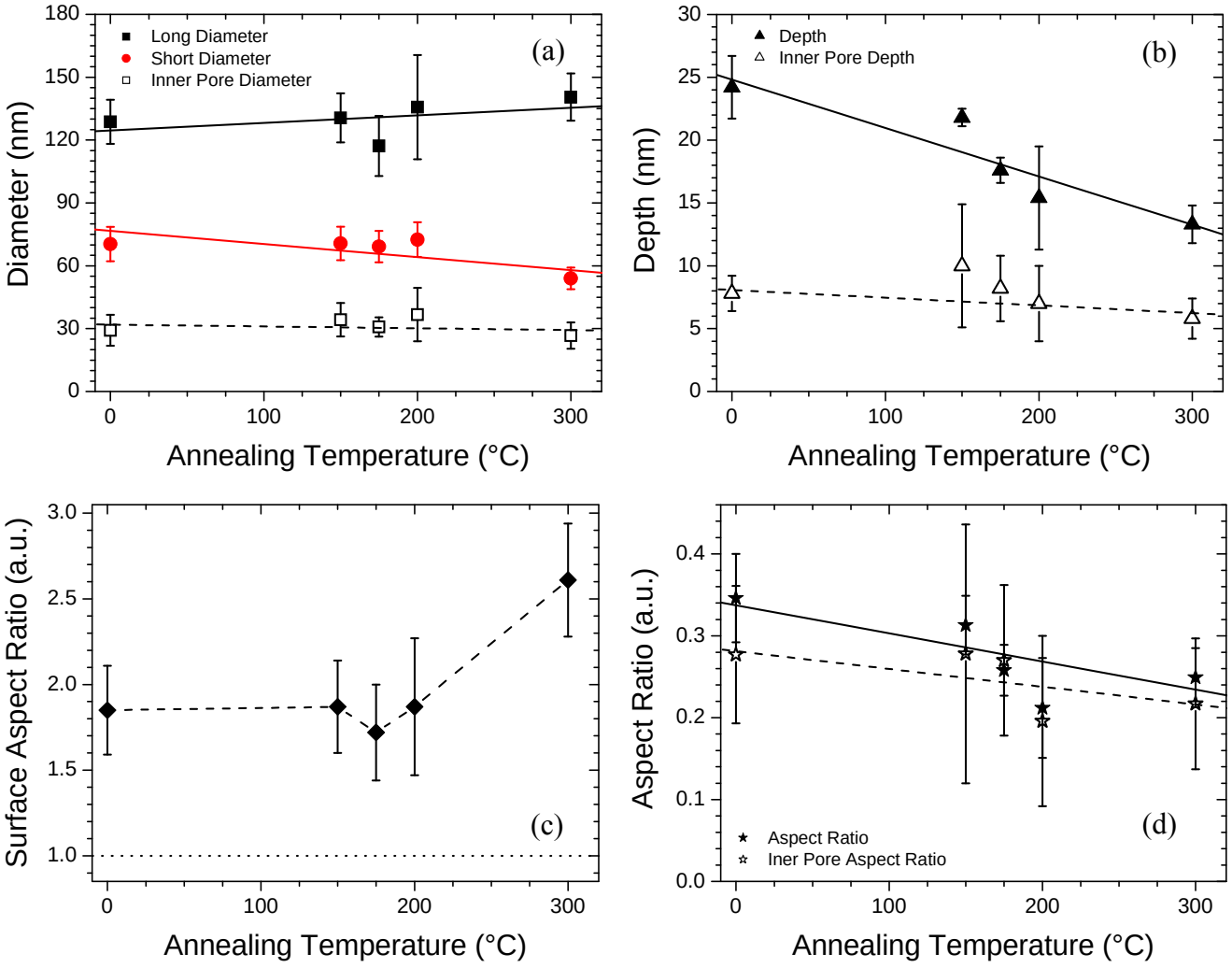

Fig. 23 (a-d). Graphs of the pores dimensions vs. the annealing temperature for 60 min. in air, as first treatment; after that, they were subjected to etching in aqueous solution in HF 40% at RT for 60 min. The pores morphologies were obtained from samples irradiated with Br 46 MeV ions. **(a)** Diameters (Long axis, short axis and inner pore), **(b)** Pore and inner pore depths, **(c)** Surface Aspect Ratio (Long axis/ Short axis) and **(d)** Aspect Ratio (Depth/ Short axis).

random conditions (7 º off axis) and channelling alignment of the beam axis with a low index crystallographic direction. The irradiation spot sizes (2 × 2 mm^2) were smaller than the dimensions of the sample (7 × 8 mm^2). In the irradiated area the etching rate is promoted, leading to mm-sized holes in the surface with depths of a few microns. After levelling the non-attacked regions of the profiles, the depths recorded after different steps of etching times (3, 10, 20, and 30 min) are plotted in the data curves shown in **Figure 25 (a)**. The extracted mean etching depth after each step, and the corresponding etching rates[12], are plotted in **Fig. 25 (b)**. The points are connected by straight lines.

It is expected that the channelling irradiation induces less damage at the surface whereas the ions penetrate deeper into the sample compared to the irradiation under random conditions.

[12] The given etching rate represents the slope between two subsequent etching stages, respectively. The mean etching rate (total depth/total time) is not shown.

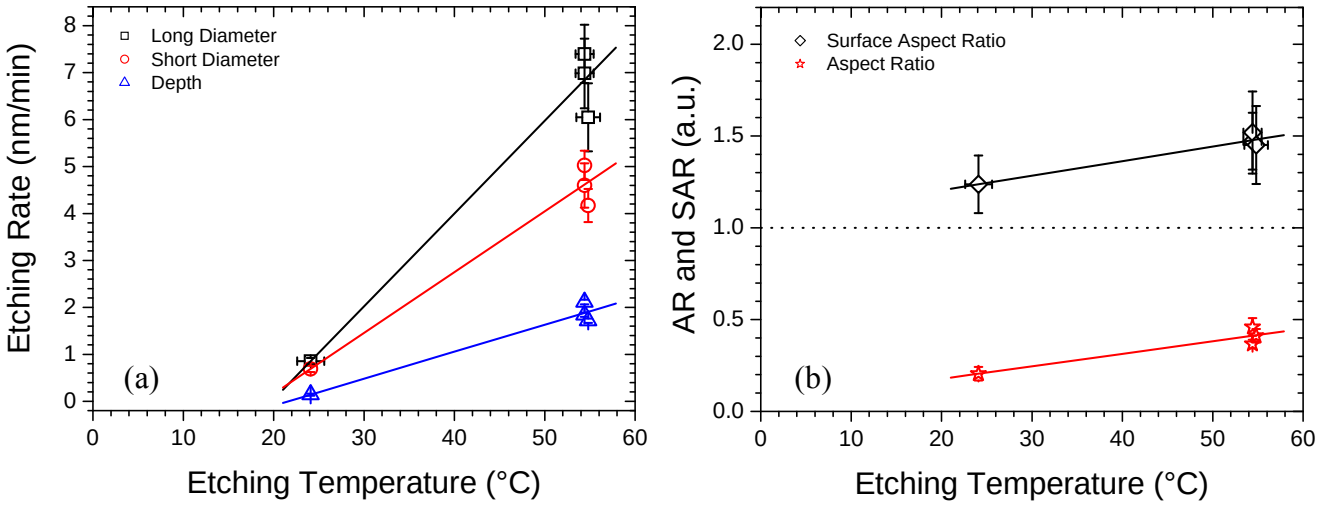

Fig. 24 (a, b). (a) Etchings rates vs. the temperature of the aqueous solution of HF 40%; to its vapour the samples were faced downwards. The etch rates were derived from the measured pore dimensions by dividing them by the corresponding etching time. It has been taken into account the data corresponding to **30 min.** and **60 min.** of exposition. **(b)** The AR and SAR remain approx. constant with the temperature.

It was proposed that this effect leads to a shift of the maximum induced damage such that deeper etch pits can be accomplished [26]. This publication is the only study available to our knowledge, concerning IBEE processing of $LiNbO_3$ using channelling irradiation. However, the data are not directly comparable to ours due to a set of different parameters such as lower ion energy[13], higher fluences and lower acid concentration (3.7 % HF). In case of our measurements both orientations, random and channelling, seem to behave fairly equal. The etching depths of both samples were not significantly distinct taking the error bars into account. However, it is worthy to mention that a slight difference was denoted, that shows the tendency of the expected effects, but due to the collective electronic excitation the induced damage seems to be rather similar and homogeneous. A slight difference is only observed in the depth for the last etching steps (20 min. and 30 min.), which was a little bit higher in case of the channelling sample. The etch rates are almost constant (~ 365 nm/min) until a mean depth of about 3.5 µm is reached for both orientations after 10 min. However, a first indication of a shifted maximal depth is noticeable after 30 min, where the error ranges of both depths values do not overlap. The difference of 320 nm amounts 7.1 % of the total depth reaching 4.35 µm and 4.67 µm for random and channelling conditions, respectively. The etching rate frustration at this depth (≈ 56 % of the total track length), is most probably affected because the electronic stopping power falls below the stopping threshold (S_{th} ≈ 4-6 keV, see **Fig. 14 (a)**), being rapidly etched the *amorphous track length*. In the first etching steps, till 10 min., a linear behaviour of the evolution of the depth is clearly observed, during that period, the mean etching rate is about 350 nm/min. However, slight differences are observed between the two etching steps studied at 3 min. and 10 min, where the etch rate changes from 420 nm/min to 315 nm/min. Since ten

[13] The induced damage used in the publication is based on nuclear stopping processes of Si 750 keV. Throughout this Thesis work the structural damage was been always caused by the electronic stopping, but the resulting etching chemical behaviour may be comparable as it is based on etching "amorphous" $LiNbO_3$.

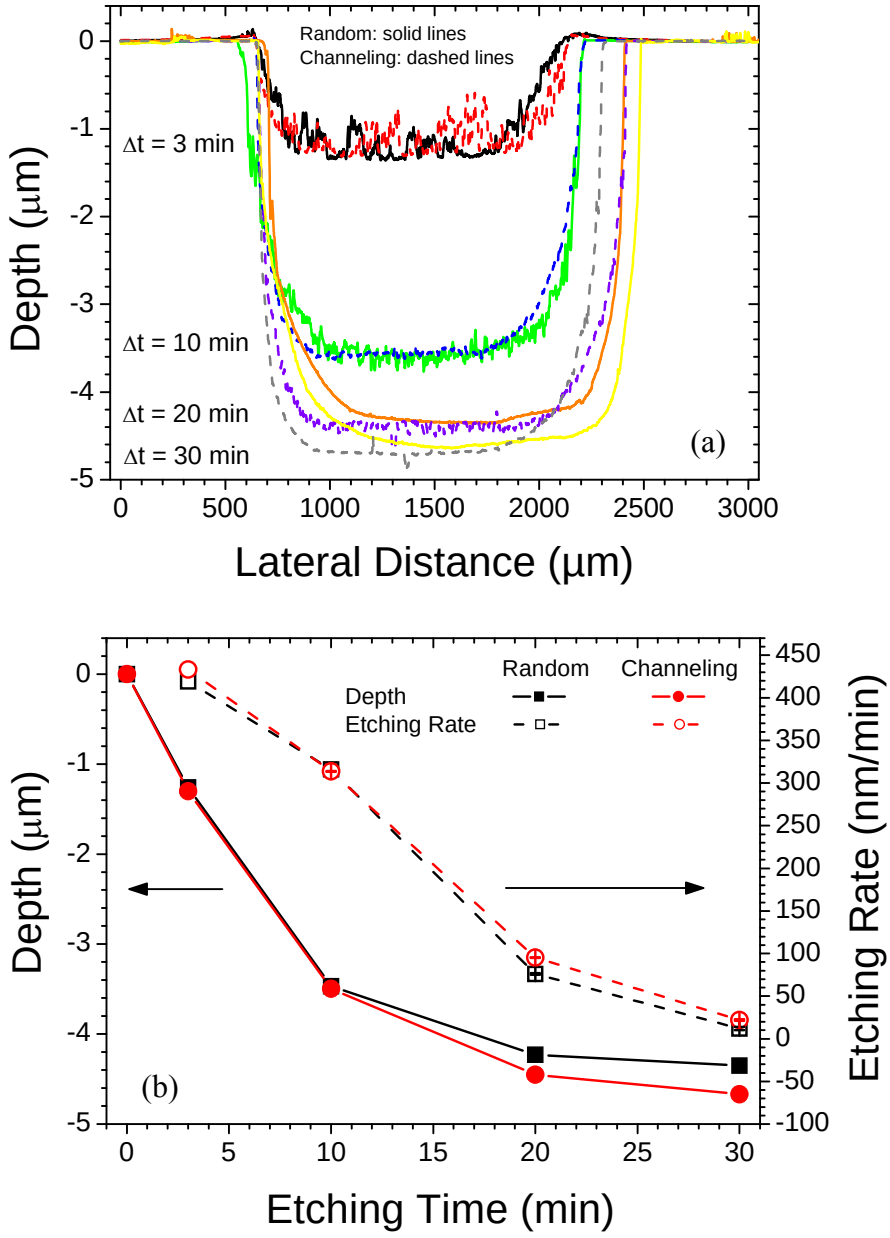

Fig. 25 (a, b). Profilometry results on irradiation spot depth. The $LiNbO_3$ sample was irradiated with Cu 51 MeV ions at a fluence of 1 e12 at/cm^2, subsequently, the bulk material was etched in the 1 : 2 solution of HF : HNO_3 for the indicated times.

minutes till 30 min. a second behaviour is observed where the etch rate decrease drastically, having a mean etching rate of 75 nm/min.

On the other hand, it is worthy to notice that, it was not possible to measure the out-of-plane swelling of the irradiated samples, because the samples had already been etched for 3 min when the profilometer was installed at our Facility. It could have slight differences in the mean etching rates on the first stages of etching, but, we have to say that no great values for the expansion will be obtained for this irradiation fluence ($\Delta h \sim 50$ nm for ϕ = 1 e12 at/cm^2 of Br 45 MeV ions), after our experience with the study of the evolution of effective out-of-plane swelling with irradiation fluence in the case of Br 45 MeV irradiated *x*-cut LN samples (not

shown in this Thesis work). Profiles recorded from samples irradiated with ~1 e9 at/cm^2 did not show significant swelling nor etch pits.

In the profile curves (**Fig. 25 (a)**) recorded after 3 min of etching the sidewall edges of the well are still a bit elevated which might be a indication of remaining surface swelling. The etch pit size increases slightly with the etching time. Due to the same axis was measured in all cases this may only be due to a beam halo impinging on the sample around the region of interest, where the fluence, and hence damage creation are lower. On the other hand, the sidewalls are quite steep and sharp defined in the questioned etching stages, whereas in the beginning the etch pit is still concave. It is worthy to notice that, after the different etching steps, a clear anisotropy in the shape of the mm-size irradiated crater was developed, yielding an elliptical etched hole with the axis (long and short) oriented in well defined crystallographic directions. Again, revealing the differential etching behaviour shown by the crystal.

On the other hand, the mean bottom micro-roughness seems to decrease with etching time. The nano-roughness, on the bottom of the etch pit determined by means of AFM, was in all etching stages about one order of magnitude higher than the micro-roughness determined from profilometry. In this sense, it is noticeable that, the tip curvature radius used in the AFM, is about three orders of magnitude smaller than the one used in profilometry, such that much smaller features can be penetrated which then leads to higher rms roughness values. In any way, we can conclude that the same behaviour shown by the evolution of the rms micro-roughness was observed for the nano-roughness by the AFM in the different etching steps. Moreover, the differences evidenced for the channelling and random irradiated samples were observed too.

Finally and, in conclusion, a significant difference of the etching rate between channelling and random irradiation can not be denoted. In this sense, the critical angle for channelling is very small, because it decreases with the square root of the incident ion energy:

$$\psi_c \approx \sqrt{\frac{2Z_1 Z_2 e^2}{4\pi\varepsilon_0 Ed}} \qquad (1)$$

ψ_c can be obtained from Rutherford Backscattering Spectroscopy (RBS) measurements and it is the half-width at half-maximum of the dip arising from the normalized channelling yield of the Nb signal in angular coordinates [27, 28]. It is important to notice that ψ_c depends mainly on the kinetic energy of the incident particle and on the charge per unit length of the string (Z_2e^2/d).

After all, the higher fluence increased the etching rate by ~ 3 orders of magnitude, which has to be taken into account when planning to use nanopores for e.g. optical applications. However, it seems that, as it has been commented in a previous **Section (6.3.1.5)**, the irradiation fluences of ~1 e12 at/cm^2 are not suitable for pore creation.

8.6. Summary and conclusions.

Nanopores were successfully created in $LiNbO_3$ in two fabrication steps. Firstly, the substrate material was irradiated with heavy swift ions in the single track regime and, then, the induced latent damaged tracks were subsequently etched in HF acid solutions. A systematically study was carried out to test and optimize the influence of some important parameters to the fabrication methods.

Distinct fabrication conditions resulted in different etching behaviour and, thus, in variations of the nanopores dimensions and/or morphology. Different ion energies and species were used for irradiating $LiNbO_3$ samples. In terms of irradiation parameters, the ion energy was varied in the wide range between 5 MeV and 2.3 GeV, implying substantial changes of the electronic stopping power, S_e, and the projected ion range, R_p[14]. Both indirectly controlled parameters have induced very interesting modifications to the etching behaviour of the ion tracks and the resulting pores. It seems that especially the projected range is responsible for a step-like increase of the pore diameters and the surface aspect ratio. A critical track length could not be determined, but the diameter was four times larger for Kr 809 MeV (L = 59 μm) ion tracks compared to Br 46 MeV (L = 4.5 μm) irradiated material, which is a considerable increase under the same etching conditions. Both ions had approximately the same stopping power at the surface. This behaviour might be related to the nanohills creation, which was not investigated in particular. The underlying mechanisms of nanohill creation are yet very scarcely understood. In contra, the depth evolution was found to depend on the ion energy and stopping power and is dependent of the amorphous track length. From our data it seems plausible to assume that the defect concentration governs the etch rate in depth, which presumably reaches a maximum around 12 keV/nm. Upon these phenomena, the pore morphology tremendously changes with larger ion track lengths and lower aspect ratios are yielded. The pore form consists of a funnel-like halo pore and a deeper inner pore. An arising difficulty is that these most influencing parameters, stopping power and projected ion range, can only be controlled indirectly over the ion energy. The surface aspect ratio increased upon the step-like rise of the projected ion range; on the other hand, adding an annealing treatment at 300 ºC previous to the etching, a rising tendency was denoted. In addition, post - irradiation annealings only led to a reduction of the pore depth, whereas the diameter was maintained. The SAR was found to be independent of any other investigated parameter. This can only be explained plausibly if the pores open up due to 'virgin crystal' etching, yielding a strongly anisotropic pore shape, which could be confirmed from several measurements.

Our extended set of etching experiments confirms that the pore morphology strongly depends on the concentration of the acid solution and etching time. Pores initially exhibit approximately axial symmetry but under extended etching they develop well defined facets that correspond to particular crystalline planes. The faceted morphology, not previously observed for $LiNbO_3$, has also been observed in other crystals [16]. On the other hand, since $LiNbO_3$ is non centro-symmetric, the morphology on the $+x$ and $-x$-faces of the sample are mirror images from one another. Finally, many facets develop and the shape rounds up but showing a very clear elongated anisotropy. The extrapolation of the data of pores shapes to “zero”-etching times ($t = 0$) indicate that the initial etching rate is quite fast up to about a (circular) pore diameter of 10 - 40 nm and a depth of a few nanometers depending on the stopping power of the ion. This fast stage could be associated to the track core (with a diameter of a few nanometers) including the highly defective surrounding halo whose diameter amounts to about 2-3 times that of the core [8]. The initial radial etch rate stage is followed by a linear slower stage (where facets develop) that reaches an average diameter of a few hundred of nanometers and a depth close to 100 nm. The slow stage has a rate of a few nm/min depending on the concentration and composition of

[14] Maybe it should be better to talk in terms of *Amorphous Track Length*, *L*.

the acid solution and should correspond to the etching of crystalline $LiNbO_3$, i.e. the etching rate should be essentially equal to that of the bulk unirradiated material.

The fluence was found to be a critical parameter which has to be delimited to fairly low values so that pore creation becomes possible. If higher fluences were accumulated, the etch rate tremendously increased, which is supposedly due to stress perpendicular to the ion tracks and the sample surface after etching became very rough. Usually the rms nano-roughness was in the order of the optical grade polish provided by the manufacturer. For using nanopores in optical applications, the critical fluence of 5·e10 at/cm^2 should not be exceeded to avoid pore halo overlapping. Thanks to the ultra low fluences, the necessary accelerator time per sample is very short. The irradiation only takes a few seconds and the etching procedures can be carried out directly afterwards. Desired pore structures can be tailored by adjusting the fabrication parameters. The overall fabrication time mainly depends on the etching time and may be regulated via the temperature, which excessively increases the attack rate. For precise control of this parameter more experiments are necessary, because of only two temperatures have been studied; however it seems that a linear behaviour is revealed in 40 % HF acid. The contrast in terms of AR and SAR is not affected. Including the blends of HF and HNO_3, the etching rate was found to be linearly increasing with the acid concentration, c_{HF}, and it is constant over time. Hence, the pores grow linearly with etching time. During chemical etching, the bulk material in between pores is also slowly depleted. In the single track regime, the IBEE contrast is just high enough for pore development which is assumable limited by insufficient damage and/or remaining minor crystal units that possess a certain chemical resistance, even though the tracks seem to be continuous in TEM measurements.

It is worthy to notice that, the majority of our results are based on investigations of *x*-cut LN. Nevertheless, one *z*-cut sample could be investigated in the AFM and the results could be confirmed by TEM measurements. The major difference that was observed between the crystallographic cuts is the extremely higher chemical resistivity of the *z*-cut surface compared to the rest of our samples. TEM measurements were not only useful but essentially necessary, providing completely complimentary structural information about the underlying ion tracks as well as for the inner pore morphology and pore depth.

To conclude, the results demonstrate the discussed difficulties and limitations of determining the nanopores dimensions by means of AFM technique as well as it showed the qualities and advantages of the NC-PLL method. The obtained depths were definitely too small in general, but on the other hand, the error was systematical, in such a way that, significant differences could be denoted for the lowest energies. Definite quantitative statements can only be made on the measured diameters, where despite of all uncertainties and difficulties of the utilized measurement techniques, the gained data from AFM and TEM are in excellent accordance. This includes the data obtained from the comparison of measurements in different operational modes and with distinct tip types, which are also coherent. On the other hand, in order to get a deeper insight into the inner pore morphology could only be investigated correctly by means of TEM. In AFM, contradictory signs of convolution were observed in some images which impede a specific conclusion of how the inner pore shape is formed. However, without any kind of doubts, we can state that the revealed nanopores in $LiNbO_3$ are evidently anisotropic.

A. García-Navarro et al. recently reported the feasibility of nanopores creation in $LiNbO_3$ [13]. The data gained in this previous work, could be vastly broadened and the mechanisms of nanopores creation are now understood in much more detail. As it has been commented, when etching for short times or after irradiations with fairly low energies, the pore shape tends to be more circular, which was also true when using low HF concentrations. From the AR one can clearly distinguish two etching stages, a fast initial stage followed by a lower constant-rate stage. The obtained pore diameters are strongly related to the corresponding track length and seem to be dependent of the ion energy. The depth depends on the stopping power, energy and on the amorphous track length. A clear different behaviour, related to the ions energies, have been shown by the structures revealed after etching from the swift heavy ions from GSI and Ganil Facilities, and the heavy ions (Bromine irradiations). These irradiation parameters are crucial to the pores fabrication and need further attention in future investigations of the subject. Without any doubt, a more systematic study must be carried out with different etchings times in order to have enough experimental data to clarify the dependency of the shown behaviour on the ion energy, S_e and amorphous track length. However, it is worthy to notice that, the reproducibility and uniformity of nanopores size and shape, accompanied by the optical grade flattened surfaces, should be suitable for future applications in optics and nanosensors.

8.7. References.

[1] R. Spohr, in: *"Ion Tracks and Microtechnology: Basic Principles and Applications"*. K. Bethge, (Ed.), Vieweg, Braunchsweig, 1990.

[2] G. Szenes, *"General features of latent track formation in magnetic insulators irradiated with swift heavy ions"*, Phys. Rev. B 51 (1995) 8026-8029.

[3] A. Meftah, J. M. Constantini, N. Khalfaoui, S. Boudjadar, J. P. Stoquert, F. Studer and M. Toulemonde, *"Experimental determination of track cross-section in $Gd_3Ga_5O_{12}$ and comparison to the inelastic thermal spike model applied to several materials"*, Nucl. Instrum. Methods B 237 (2005) 563-574.

[4] M. Toulemonde, C. Trautmann, E. Balanzat, K. Horjt, A. Weidinger, *"Track formation and fabrication of nanostructures with MeV-ion beams"*, Nucl. Instr. Meth. B 216 (2004) 1-8.

[5] J. -H. Zollondz, and A. Weidinger, *"Towards new applications of ion tracks"*, Nucl. Instr. Meth. B 225 (2004) 178-183.

[6] R. S. Weis, and T. K. Gaylord *"Lithium niobate: Summary of physical properties and crystal structure"*, Applied Physics A 37 (2004) 191-203.

[7] B. Canut, S. M. M. Ramos, R. Brenier, P. Thevenard, J. L. Loubet, M. Toulemonde, *"Surface modification of $LiNbO_3$ single crystals by swift heavy ions"*, Nucl. Instrum. Methods B 107 (1996) 194 -198

[8] J. Olivares, A. García-Navarro, G. García, A. Méndez and F. Agulló-López, *"Optical determination of three-dimensional nanotrack profiles generated by single swift-heavy ion impacts in lithium niobate"*, Appl. Phys. Lett. 89 (2006) 071923.

[9] M. Levy, R. M. Osgood Jr., R. Liu, E. Gross, G. S. Cargill III, A. Kumar and H. Bakhru, *"Fabrication of single-crystal lithium niobate films by crystal ion slicing"*, Appl. Phys. Lett. 73 (1998) 2293.

[10] C. L. Sones, S. Mailis, W. S. Brocklesby, R. W. Eason and J. R. Owen, *"Differential etch rates in z-cut $LiNbO_3$ for variable HF/HNO_3 concentrations"*, J. Mat. Chem. 12 (2002) 295-298.

[11] J. Reinisch, F. Schrempel, T. Gischkat and W. Wesch, *"Etching of Ion Irradiated $LiNbO_3$ in Aqueous Hydrofluoric Solutions"*, J. Electrochem. Soc. 155 (2008) D298-D301.

[12] M. Bianconi, F. Bergamini, G. G. Bentini, A. Cerutti, M. Chiarini, P. De Nicola and G. Pennestri, *"Modification of the etching properties of x-cut Lithium Niobate by ion implantation"*, Nucl. Instr. Meth. B 266 (2008) 1238-1241.

[13] A. García-Navarro, A. Méndez, J. Olivares, G. García, F. Agulló-López, M. Zayat, D. Levy and L. Vazquez, *"Morphology of ion tracks and nanopores in $LiNbO_3$ produced by swift-ion-beam irradiation"*, Nucl. Instr. Meth. B 249 (2006) 172-176.

[14] S. M. M. Ramos, B. Canut, M. Ambri, N. Bonardi, M. Pitaval, H. Bernas and J. Chaumont, *"Defect creation in $LiNbO_3$ irradiated by medium masses ions in the electronic stopping power regime"*, Radiat. Eff. Defects Solid 143 (1998) 299-309.

[15] J. F. Ziegler, J. P. Biersack and U. Littmark, *"Stopping Power and Ranges of Ions in Matter"*, Vol. 1, (Ed.), Pergamon Press, New York, 1985.

[16] C. Trautmann, K. Schwartz, J. M. Constantini, T. Steckenreiter and M. Toulemonde, *"Radiation defects in lithium fluoride induced by heavy ions"*, Nucl. Instr. Meth. B 146 (1998) 367-378.

[17] C. Trautmann, M. Boccanfuso, A. Benyagoub, S. Klaumünzer, K. Schwartz and M. Toulemonde, *"Swelling of insulators induced by swift heavy ions"*, Nucl. Instr. Meth. B 191 (2002) 144-148.

[18] A. García-Navarro, *"Irradiación con iones pesados de alta energía en dieléctricos para aplicaciones fotónicas: Guías de onda en $LiNbO_3$"*, PhD. Dissertation, Departamento de Física de Materiales, Universidad Autónoma de Madrid (UAM), Madrid, July 2007.

[19] J. Olivares, G. García, A. García-Navarro, F. Agulló-López, O. Caballero and A. García-Cabañes, *"Generation of high-confinement step-like optical waveguides in $LiNbO_3$ by swift heavy ion-beam irradiation"*, Appl. Phys. Lett. 86 (2005) 183501.

[20] J. Olivares, A. García-Navarro, G. García, A. Méndez, F. Agulló-López, A. García-Cabañes, M. Carrascosa and O. Caballero, *"Nonlinear optical waveguides generated in lithium niobate by swift-ion irradiation at ultralow fluences"*, Optics Letters 32 (2007) 2587-2589.

[21] F. Schrempel, T. Gischkat, H. Hartung, E. -B. Kley and W. Wesch *"Ion beam enhanced etching of $LiNbO_3$"*, Nucl. Instr. Meth. B 250 (2006) 164-168.

[22] F. Schrempel, T. Gischkat, H. Hartung, E. -B. Kley, W. Wesch and A. Tünnermann, *"High aspect ratio microstructures in $LiNbO_3$ produced by Ion Beam Enhanced Etching"*, Mater. Res. Soc. Symp. Proc. 908E (2005).

[23] G. Götz, and H. Karge, *"Ion implantation into $LiNbO_3$"*, Nucl. Instr. Meth. B 209-210 (1983) 1079.

[24] R. G. Musket, J. M. Yoshiyam, R. J. Contolinic and J. D. Porter, *"Vapor etching of ion tracks in fused silica"*, J. Appl. Phys. 91 (2002) 5760-5764.

[25] Veeco Instruments Inc., *Dektak 150 Surface Profiler*., Veeco Instruments Inc., www.veeco.com, Jun. 2007.

[26] F. Schrempel, T. Steinbach, Th. Gischkat and W. Wesch., *"Channeling irradiation of $LiNbO_3$"*, Nucl. Instr. Meth. B 266 (2008) 2958-2961.

[27] G. Braunstein, G. R. Paz-Pujalt and T. N. Blanton., *"Microstructural evolution and epitaxial alignment of thin films of lithium niobate deposited onto sapphire by metallo-organic decomposition "*, Thin Solid Films 264 (1995) 4-10.

[28] J. Lindhard, *"Influence of crystal lattice on motion of energetic charged particles"*, K. Dan. Vidensk. Selsk. Mat. Fys. Medd. 34 (1965) 14.

Chapter 9

Recrystallization of amorphous nano-tracks and uniform layers generated in Lithium Niobate by swift-ion irradiations.

9.1. Introduction.

Abundant experimental evidence is being gathered showing that defects can be also cumulatively created by every individual ion impact in the regime where the *electronic stopping power* S_e is dominant [1]. The structure of these defects is not yet clear, although some detailed data on InP [2] do not show significant differences in the atomic structure of samples amorphized by electronic excitation and elastic collisions. It has been definitely ascertained by several techniques that linear *amorphous tracks* can be generated along the ion trajectory if the electronic stopping power is above a certain *threshold* value [3-8]. These tracks have a *nanometer diameter* and are surrounded by a region of strongly defective material (*halo*). When the irradiation fluence is high enough so that individual tracks overlap a rather homogeneous amorphous layer is generated [9, 10]. For $LiNbO_3$ the final amorphous layer has a well-defined refractive index (n = 2.10 at λ = 633 nm), independently of the irradiation conditions [10], suggesting that a steady-state phase is achieved. Moreover, its amorphous character has been ascertained by Raman spectroscopy [9].

The most often used approach to describe track formation is the so-called *thermal spike* mostly developed by Toulemonde and coworkers [11-14]. However, there is evidence that electronic excitation may play a relevant role in the damaging process [15]. Along this line a non-radiative exciton-decay model has been advanced [16, 17] that explains the main features of track formation for $LiNbO_3$ and possibly other oxides. In this model point defects are generated around each ion trajectory through a synergy between the thermal spike and the associated excitation spike. Under multiple ion impacts the overall defect concentration grows by accumulation and amorphization occurs at a threshold as a defect-driven phase transition [18] that causes a lattice collapse.

The formation of amorphous tracks by electronic excitation are well aligned with beam direction and are themselves nanostructures, offering very interesting capabilities in nanotechnology [19-26]. On the other hand the formation of amorphous layers, at the surface or inside the material depending on the stopping power curve, with a lower refractive index has been advantageously used to fabricate high-confinement optical waveguides [27-29]. One main advantage of the electronic excitation method is the possibility of tailoring the thickness of the waveguide as well as of the tunneling barrier that is responsible for a substantial fraction of the optical losses. The new method has been recently used to fabricate ring resonators [30] with nanometric-size confinement of the light.

In principle, the simplest system to investigate the annealing and recrystallization of a region amorphized by swift-ion bombardment is a single amorphous track (in fact, a diluted concentration of them in a crystalline matrix). It has been well ascertained by direct TEM microscopy in lithium niobate [31, 32], other dielectric materials, such as sapphire [33] or rutile [34] and semiconductors as silicon [35], that core tracks present a roughly circular shape, regardless of the crystalline symmetry, and essentially amorphous structure. This is, indeed, consistent with the initial round dips generated by chemical etching in $LiNbO_3$ [25]. Although it is known that the amorphized fraction measured by RBS/C decreases after thermal treatments [36], the effect of annealing on individual tracks has not been directly investigated. In this work, a number of systematic isothermal annealing experiments have been performed on *z*-cut samples irradiated at RT with Br at 45 MeV and followed by monitoring the extension of the

amorphized area by RBS/C with He probing ions. The objective is to subject the crystal to irradiation with ions having a stopping power clearly above the amorphization threshold, which is around 5-6 keV at the surface (see **Fig. 1**), so that, continuous well-defined tracks are generated. Moreover, a low fluence irradiation (< 10^{12} cm^{-2}) was used to assure a small enough overlapping of the tracks. Under these conditions the damage morphology in a transversal plane is constituted by a random set of amorphous circles separated by essentially crystalline unperturbed material. In principle, the full depth amorphization profile can be measured by RBS/C. However, the method is particularly reliable to measure the extension of the amorphized area at the sample surface, where no significant lattice de-channeling occurs.

So far, most information concerning annealing of radiation damage has been performed on cases where nuclear mechanisms are dominant (*nuclear collision regime*) or there is a severe mixing of both electronic and nuclear mechanisms [37-41]. The thermal annealing of amorphous tracks of nanometer-size diameter generated in lithium niobate by Bromine ions at 45 MeV, i.e. in the electronic stopping regime, has been investigated by RBS/C spectrometry in the temperature range from 250 ºC to 350 ºC. Relatively low fluences have been used (< 10^{12} cm^{-2}) to produce isolated tracks. However, the possible effect of track overlapping has been investigated by varying the fluence between 3 x10^{11} cm^{-2} and 10^{12} cm^{-2}. The data appear consistent with a solid-phase epitaxial process that yields a constant recrystallization rate at the amorphous-crystalline boundary. HRTEM has been used to monitor the existence and the size of the annealed isolated tracks in the second stage.

On the other hand, the thermal annealing of homogeneous (buried) amorphous layers has been investigated within the same temperature range, on samples irradiated with Fluorine at 20 MeV and fluences of ~10^{14} cm^{-2}. Optical techniques are very suitable for this case and have been used to monitor the recrystallization of the layers.

Different features of the thermally activated recrystallization process have been obtained and the order of the kinetics has been determined. A universal scaling law has been found to describe the mechanisms; moreover, a model that explains the recovery behaviour of nano-tracks and thick layers is proposed and discussed in terms of local reordering and epitaxial regrowth.

Therefore, the aim of this Chapter is to study the recrystallization properties of the amorphous tracks and layers generated by swift ions in $LiNbO_3$, when the irradiated crystals are subjected to thermal annealing treatments. In this sense, the study presented has, first, a basic interest in order to get a deeper insight into the annealing behaviour of the amorphous regions generated by electronic excitation (*electronic excitation regime*). As to basic science, this information obtained should be very relevant to clarify the structure of the damage produced by high energetic ion beams on dielectrics. Second, and from the applied side, our study offers the possibility of modifying the geometry of the nano-structured photonic material produced by the low fluence swift irradiations and tuning their effective refractive index. On the other hand, the recrystallization of the amorphous buried layers offers a convenient method to tailor the performance parameters of the optical waveguides produced at the sample surface and provides an additional tool for the design of photonic components.

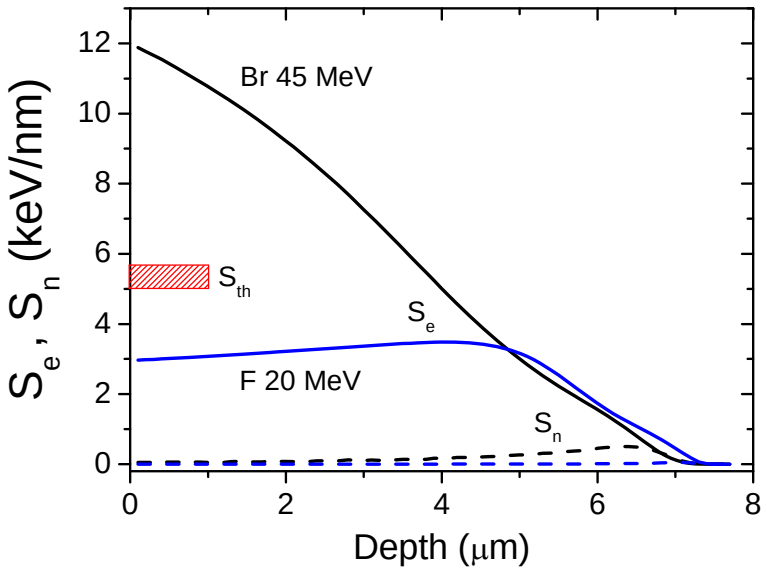

Fig. 1. Electronic (S_e, solid lines) and nuclear (S_n, dashed lines) stopping power curves for Br 45 MeV and F 20 MeV ions in $LiNbO_3$ obtained from SRIM-2008 code [42, 43]. The electronic stopping power threshold for amorphous latent track formation (S_{th}) is indicated with a short broad line indicating its approximate value (5-6 keV/nm, velocity dependent).

Ion	Energy (MeV)	Energy (MeV/amu)	S_e surface (keV/nm)	S_e max (keV/nm)	S_n max (keV/nm)	R_p (μm)	Fluences (at.cm^{-2})
$^{79}Br^{8+}$	45	0.6	11.9	11.9	0.5	7.4	(3, 5, 10) x10^{11}
$^{19}F^{5+}$	20	1.1	3.0	3.5	0.1	7.4	4 x10^{14}

Table I. Irradiation parameters including the electronic energy loss (S_e) at the sample surface and at the Bragg maximum, as well as, the maximum nuclear energy loss (S_n) and the projected ion range (R_p) according to the SRIM-2008 code [42, 43]. The irradiation fluences are shown too.

9.2. Experimental procedures.

9.2.1. Irradiation parameters.

Congruent (*z*-cut and *x*-cut) $LiNbO_3$ plates were purchased from Photox Ltd. of 8 x 7 mm^2 and 1 mm thickness with optical polished surfaces. They were irradiated in the 5 MV Tandem accelerator installed at the Centro de Microanálisis de Materiales (CMAM) [44] with Br 45 MeV ions to produce latent isolated tracks, and F 20 MeV ions at moderate fluences in order to generate buried amorphous layers. For experiments on isolated tracks, Br ions at 45 MeV and fluences below 10^{12} cm^{-2} were mostly used to avoid significant track overlapping. For the annealing of homogeneous amorphous layers irradiations were performed with F ions at 20 MeV at fluences in the order of ~10^{14} cm^{-2}. At this energy the maximum electronic stopping

power is buried in the sample. Stopping curves for the ions used in this work calculated with the SRIM-2008 code [42, 43] are shown in **Fig.1**. **Table I** lists the corresponding incident energies and ion ranges used.

The maximum value is reached at the surface for Br 45 MeV, whereas that the Bragg peak is localized at a depth of ~ 4 μm for F 20 MeV. For the case of Br 45 MeV ions, the energy loss is clearly above the expected *amorphization threshold* for lithium niobate (S_{th} ~ 4 - 6 keV/nm) [4], thus, producing latent tracks along the ions trajectories from the crystal surface. On the other hand, in the case of F 20 MeV ions, where the maximum energy loss (~ 3 keV/nm) is below the amorphization threshold, (S_{th}), the formation of the amorphous buried layer is explained by *cumulative damage mechanism* [45].

An important point to keep in mind, especially in the case of long term irradiations with F 20 MeV, is related to the temperature reached by the sample during the irradiation, trying to avoid modification of the material by ion beam induced-annealing. In this way, in order to have an accurate control of the temperature of the sample, we proceed to use a high precision infrared camera (see **Chapter 4. Section 4.2.** *Irradiation conditions at CMAM,* see **Fig. 12**). With the beam currents and fluxes used, in any case, the temperature of the samples under irradiation never reached temperatures higher than 100 ºC[1]. This effect is not appreciable for the irradiation with Br 45 MeV ions, due to the low fluxes and irradiation time used.

9.2.2. Annealing treatments.

Annealing treatments were performed with two different set-ups in air atmosphere. For the annealing of thick uniform layers the sample was kept (from 30 minutes to several hours) in a standard tubular Carbolite furnace with an integrated Eurotherm temperature controller.

On the other hand, for tracks (low fluences of Br 45 MeV) thermal annealing treatments were carried out at different temperatures in the range of 250 ºC - 350 ºC and for different time scales, from very short till long times. A specific annealing setup has been designed for this purpose trying to be reliable and minimizing the transitory till the sample reaches the fixed temperature. A complete description can be found in **Chapter 4. Section 4.6.**

9.2.3. Ion-beam damage characterization techniques.

The damage recovery evolution during the thermal annealings was characterised by Rutherford Backscattering Spectroscopy in Channeling configuration (RBS/C) for Br 45 MeV ions irradiated samples and optical measurements (Dark Guided Modes) for F 20 MeV ions irradiations.

The Br 45 MeV irradiated samples were mounted on a three-axis goniometer inside the analysis chamber and a beam of $^4He^+$ ions at 3 MeV was used as a probe. The alignment procedure was performed on the virgin part of the crystal, covered by masks during the irradiation, in order to restrict any additional damage due to the analyzing He beam itself; and, on the other hand, being easier and negligible the experimental error during the process of finding the chanelling configuration (minimum RBS yield) in the non-irradiated zone.

[1] As we will see later, this temperature does not cause any annealing during the irradiation.

In addition, high resolution transmission electron microscopy (HRTEM) was used as a complementary technique for isolated tracks in a few selected samples. Plan view samples were prepared for transmission electron microscopy (TEM) examination by dimple-grinding with a Gatan 656 dimpler followed by ion-milling with a Fischione 1010 model until an electron transparent area was obtained in the center of the sample. Transmission electron microscopy studies were done in a JEOL 2010F TEM microscope with a field-emission gun, (200 kV acceleration voltage) and with 0.27 nm of structural resolution.

For the annealing of homogeneous buried amorphous layers, an optical technique involving the determination of the propagating dark modes through the outer crystalline layer has been preferentially used [45, 46]. It is worthy to notice that, the optical (dark mode) technique, recently used for $LiNbO_3$ [46] and other crystals, is particularly suitable for homogeneous amorphous layers since the stacking of the crystalline and amorphous layer allows for the propagation of light modes that yields information on the index profiles and consequently on the damage (amorphous) profiles (see **Chapter 4. Section 4.7.3.1**). For these measurements light at λ = 633 nm from a He-Ne laser was coupled into the waveguide through a rutile prism. TE and TM polarization geometries were used to observe any possible differences that could be associated to anisotropy induced during swift ion-irradiation [47] or the subsequent annealing. Refractive index profiles were reconstructed following a standard algorithm based on the Wentzel-Kramer-Brillouin (WKB) approximation [48]. Through the thermal annealings the thickness of the buried amorphous layer will decrease, therefore, the crystalline-amorphous boundary will be shift to deeper areas and thus, the waveguide will suffer an increase in depth, being wider.

9.3. RBS-C analysis.

Rutherford backscattering experiments in channeling configuration (RBS/C) is a powerful technique to measure the damage or disorder induced near the surface (see **Chapter 4. Section 4.7.1**). With He of 3 MeV energy a thickness of around 2 μm can be probed. Basically, RBS/C data yield the damage fraction (f_d) generated at the surface as a function of electronic stopping power (S_e) and ion fluence (ϕ). This fraction is readily derived from the de-channeling yield of an incident beam placed under channeling conditions. Usually, for cylindrical amorphous tracks of radius (r), the analysis of the damage fraction versus fluence (ϕ) is performed using a Poisson law $f_d = 1 - exp(-\pi r^2 \phi)^2$ [49]; and consequently to deduce the track radius by a fit of the experimental data. Therefore, RBS/C experiments yield the track radius for any ion and energy.

Fig. 2 shows typical backscattering spectra obtained from a 3-MeV $^4He^+$ analysis of irradiated *z*-cut $LiNbO_3$ samples with Br 45 MeV ions. Spectra recorded in channelling geometry, correspond to the three fluences studied (3 e11 at/cm^2, 5 e11 at/cm^2, 1 e12 at/cm^2). The aligned and random spectra obtained on a virgin crystal are also presented for comparison.

Before irradiation, a minimum yield χ_v = 2.7 % was measured at the low-energy side of Nb surface peak. This low value, typical in single alignment geometry, gives evidence of the high-crystalline quality of the $LiNbO_3$ substrates. After irradiation, a general increase of the

[2] See extended comments made in **Chapter 5**. **Section 5.3** and at the end of this section.

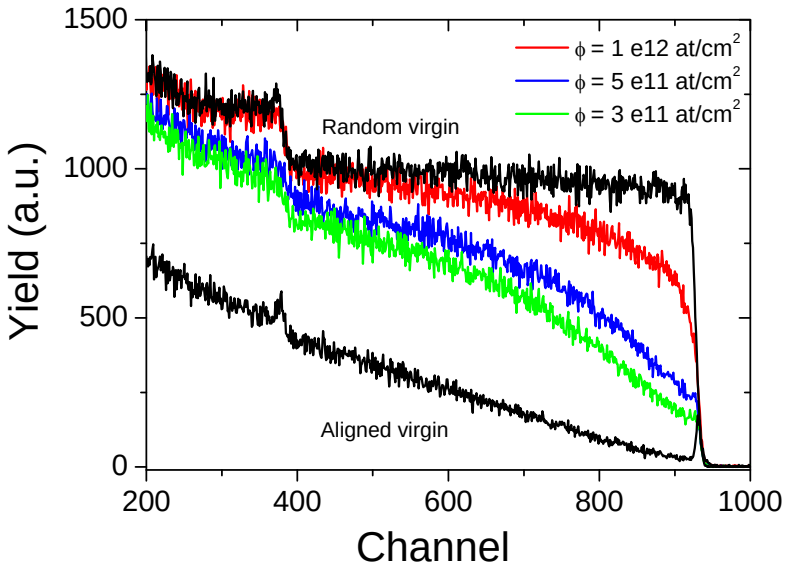

Fig. 2. RBS/C spectra for *z*-cut samples of $LiNbO_3$ irradiated with Br ions at 45 MeV incident energy at fluences from 3 e11 at/cm^2 to 1 e12 at/cm^2, indicated in the labels. The aligned and random spectra obtained on the virgin samples are presented for comparison. The Nb surface peak is located around energy channel 925. Analysis condition: 3-MeV $^4He^+$, detection angle = 170º.

backscattering yield with fluence is observed in channeling conditions, being related to damage extended defects induced by the irradiations, and necessarily imputable to the high electronic energy losses of the incident ions. This indicates a defect creation process in both oxygen and niobium sublattices. The sensitivity of $LiNbO_3$ to such kind of irradiations, characterized by high electronic stopping powers, has been reported by Canut et al. [31]. Due to the lack in RBS sensitivity for detecting low atomic masses, the disorder calculations have been carried out only from the niobium signal. The de-channeling yield χ_i of the irradiated sample was measured behind the Nb surface peak. By taking into account the minimum yield χ_v corresponding to virgin crystal in channeling conditions, and the χ_r, the yield of the randomly-oriented crystal; the relative disorder fraction (f_d) near the sample surface will be given by the classical expression [50]

$$f_d = \frac{\chi_i - \chi_v}{\chi_r - \chi_v} \qquad (1)$$

Such a procedure requires some comments:

(i) The disorder calculations do not take into account the Nb surface peak. This latter is clearly visible at the high-energy edge of RBS/C spectra, specially for the highest fluences. It indicates an excess of displaced Nb atoms from the surface to a few tens of nanometers.

(ii) The range of the incident Br 45 MeV ions exceeds the maximum depth probed by the 3-MeV $^4He^+$ analysis beam (≈ 2 μm). Consequently, except the above-mentioned increase of disorder at the surface, no deep evolution of f_d can be extracted from RBS/C data. In particular, the nuclear damage peak, located around the projected range (R_p) (see the values of **Table I**), cannot be evidenced by these channeling experiments.

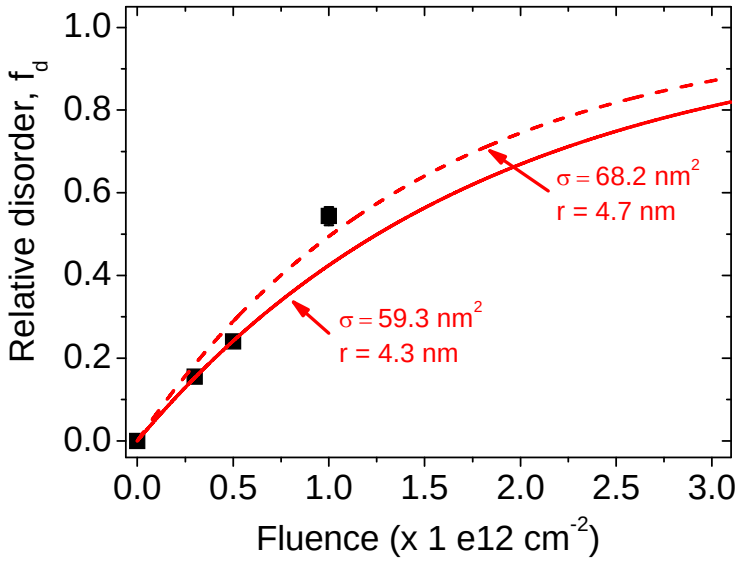

Fig. 3. Fluence dependence of the relative disorder fraction measured at the surface f_d in *z*-cut samples of irradiated $LiNbO_3$ with Br ions at 45 MeV. The solid and dashed lines correspond to the best fits of the experimental data by using a Poisson´s law. The solid line fits the f_d corresponding to lower fluences.

Ion	Energy (MeV)	Fluence (at/cm^2)	Damage cross section σ_e (nm^2)	Track radius (nm)
$^{79}Br^{8+}$	45	3 e11	59.3	4.3
		5 e11	59.3	4.3
		1 e12	68.2	4.7

Table II. Experimental damage cross section (σ_e), corresponding to a defect radius $r = (\sigma_e / \pi)^{1/2}$, from fittings of the experimental data by using the Poisson´s law parameters.

Fig. 3 represents the evolution of the disorder fraction (f_d) measured at the surface versus the irradiation fluence (ϕ), for the three cases under study. Assuming the absence of any annealing during the irradiation process, a *direct impact model* [51, 52] for defect creation predicts a kinetics which is given by

$$f_d = 1 - \exp(-\sigma_e \phi), \quad (2)$$

where σ_e, is the damage cross section. Satisfactory fittings of the experimental data were obtained by using the Poisson´s law (**Eq. 2**) and, consequently, from the analysis of the damage fraction versus fluence, it has been deduced the radii for cylindrical amorphous tracks. The mean track radius *r* of the damaged zones has been calculated from $\sigma_e = \pi r^2$ and varies from 4.3 to 4.7 nm. (see **Table II**). The resulting damage cross sections σ are listed in **Table II** too.

It is worthy to remark the following point, as it has been mentioned above, in the framework of *direct impact model* the damage cross sections and the track radii for each fluence

under study are obtained from the disorder fraction. However, we want to distinguish clearly two cases:

(i) firstly, when we are in the *isolated tracks regime*, lower fluences (3 e11 - 5 e11 at/cm^2), this behaviour is well fitted by the solid line (see **Fig. 3**), where the results of damage cross section (σ) and track radii (r) appear in **Table II**;

(ii) second, the case of starting the *overlapping track regime*, higher fluences (1 e 12 at/cm^2). For this case, the dashed red line is used to fit the highest fluence, showing a damage perhaps higher than it should be "expected" due to several factors: either the RBS/C experimental technique could overestimate the disorder fraction value for this fluence, or the linearity is starting to be lost due to some *sinergy* in the *overlapping regime*, as can be seen in the schematic snapshots shown in the following pages for both cases separately.

(iii) In addition, we have to remember our discussion, in **Chapter 5**, about the clear evidence of the cumulative behaviour through the experimental results on $LiNbO_3$. The growth of the normalized disordered area (f_d) as a function of fluence, for irradiation conditions below, as well as, above threshold (S_{th}) fits to an Avrami-like (sigmoidal) kinetics, $f_d = 1 - \exp\{-(\phi/\phi_0)^n\}$.

For irradiations well above threshold the measured Avrami curves correspond to the Poisson limit *(n = 1),* whereas for conditions below threshold, the Avrami curves present parameters n and ϕ_0 , that steadily increase on decreasing electronic stopping power. More specifically, above the stopping power threshold the amorphization kinetics roughly obeys a Poisson-type law, although some clear deviations appear. They are more significant as the stopping power decreases to approach the threshold value. In fact, a pure Poisson behaviour ($n = 1$) is only obtained for stopping powers higher than twice the threshold value as apparent (see **Table II** and **Fig. 9** in **Chapter 5**). In **Fig. 4** both fitting are shown.

It is necessary to comment that, taking into account some previous results [53], in the low fluence regime it should be possible to make the following approximation $f_d = \pi r^2 \phi$, and consequently, to deduce the mean track radius by a linear fit of all the experimental data. Nevertheless, we want to study separately each case since the beginning of the damage recovery process, trying to see if there is some kind of *fluence-induced effect* during the recrystallization transition.

In any case, these track radii values, obtained individually for each case separately, will be the initial points to study the evolution of the damage recovery through the following thermal annealing processes.

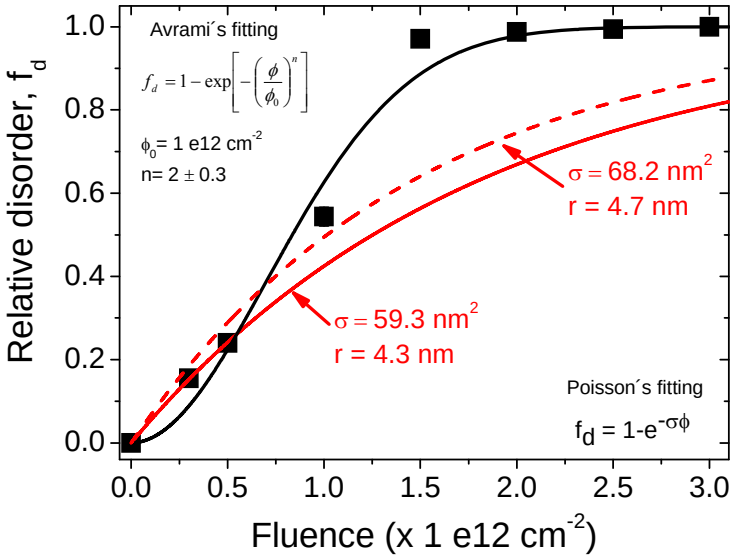

Fig. 4. Evolution of the disorder fraction (f_d) measured at the sample surface vs the irradiation fluence ϕ, in *z*-cut samples of irradiated $LiNbO_3$ with Br ions at 45 MeV. Avrami´s fitting (black solid line) and Poisson´s law fitting[3] (red lines) corresponding to the best fittings of the experimental data.

9.4. Recrystallization of single amorphous tracks.

9.4.1. Kinetics of isothermal annealing.

The aim is to measure the shrinking rate of the track cross-sections at the sample surface as a function of annealing time for several temperatures. **Fig. 5** shows as an example one set of RBS/C spectra corresponding to the annealing evolution for a temperature of 275 ºC and a fluence of 5 x10^{11} cm^{-2}. The kinetics of isothermal annealing on the fractional disordered area at several temperatures in the range 250-350 ºC is illustrated in **Fig. 6 (a)** corresponding to an irradiation fluence of ϕ = 3 ×10^{11} cm^{-2}. Similar results for samples irradiated at ϕ = 5 ×10^{11}cm^{-2} and ϕ = 1 ×10^{12} cm^{-2} are shown, respectively, in **Figs. 6 (b)** and **Fig. 6 (c)**[4]. The schematics next to the figures illustrate the damage morphology by showing a random MonteCarlo distribution of disks, having a radius of around 4.5 nm (as estimated from the results of **Fig. 6 (a)** for the lowest fluence), with the density corresponding to the fluence. They visualize how the track overlapping has clearly increased with fluence. From these data it is clear that the overall track cross-section decreases with annealing time, being slightly dependent on the irradiation fluence (the rate appears to decrease with increasing fluence). As we will see later, it appears more meaningful to plot the evolution of the track radius with annealing time.

[3] We have to point out that, the Poisson fit parameters shown in this case corresponds to *z*-cut $LiNbO_3$ irradiated samples, at variance to those corresponding to *z*-cut $LiNbO_3$ samples shown in **Chapter 5**. It is worthy to notice the anisotropic behaviour revealed from the comparison of both sets of parameters (not discussed here).

[4] Due to the time scales for each annealing process are very different, being very fast the isothermal processes at highest temperatures, it is necessary to make a zoom in the time scale (*x*-axis) with the aim of following accurately the behaviour of the disorder fraction and the track radii for each irradiation fluence. (see **Appendix II**.).

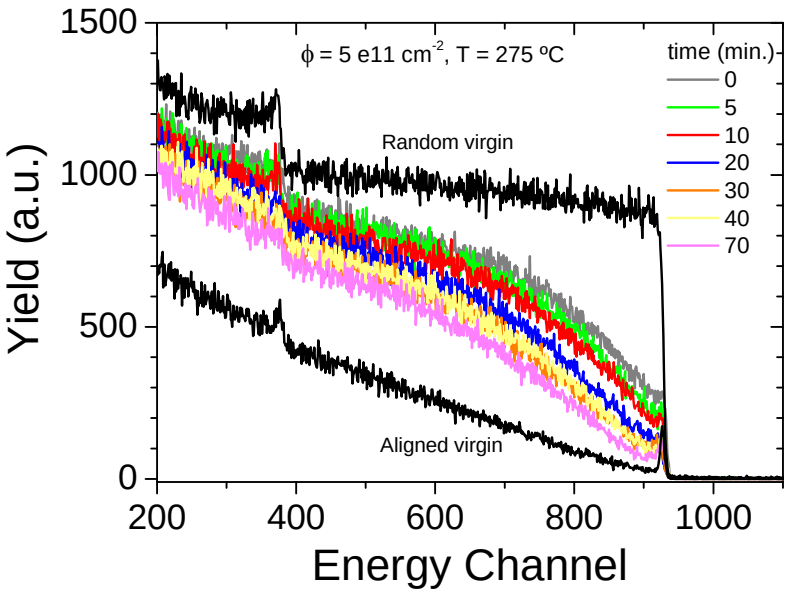

Fig. 5. RBS/C spectra measured, with an ion beam of He 3 MeV as a probe, for the case of an irradiated sample with a fluence of 5 e11 cm^{-2} (time = 0) and annealed in air at 275 ºC in six steps indicated in the Figure labels (time in minutes), and giving rise to a progressive decrease in the measured yield. The aligned and random spectra obtained on the virgin samples are presented for comparison.

To this end we have, initially, assumed that tracks are fully independent (not overlapped) and, thus, the disordered area is simply the cross-section of a track multiplied by the impact density ($f_d = \phi_e \pi r^2$). It is also assumed that the track cross-sections maintain the circular shape during the annealing as expected for tracks along the *z*-axis due to the axial crystal symmetry. Finally, it is assumed that the defective halo surrounding the amorphous tracks makes a negligible contribution to the de-channelled RBS yield. Using these approximations, one readily obtains the evolution of (core) track radius with annealing times from the measured amorphous area for the same temperatures and fluences as in **Fig. 5**. The results are shown in **Fig. 7 (a-c)**. Now, it becomes clear that the velocity of radial decrease, v = *dR / dt*, presents two well-defined linear regimes. There is a fast **initial stage (I)** until the radius shrinks to around or below 2.5 nm and, then, a **stage II** sets in where shrinking proceeds at a slower rate. Note that in the main stage I, the radial velocity at 350 ºC amounts to about 7 nm /min.

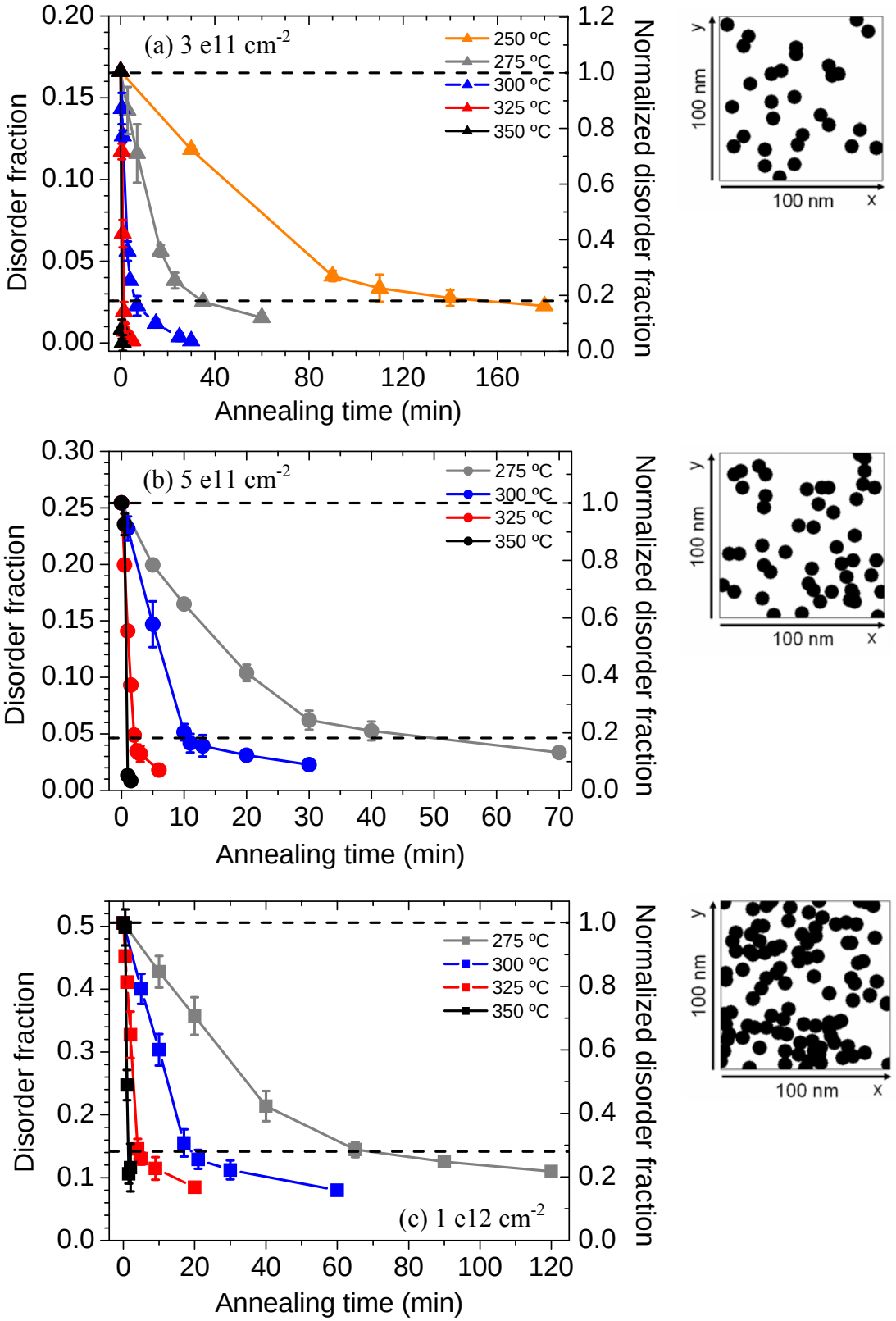

Fig. 6 (a-c). Disordered fraction obtained from RBS/C versus annealing time for the fluences **(a)** 3 x10^{11} cm^{-2}, **(b)** 5 x10^{11} cm^{-2} and **(c)** 1 x10^{12} cm^{-2}, and for the temperatures 250, 275, 300, 325 and 350 ºC, as indicated in the figures labels. The drawings show schematic illustrations of the covered area, for each of the three fluences, simulated with random impacts of estimated track radius of 4.4 nm.

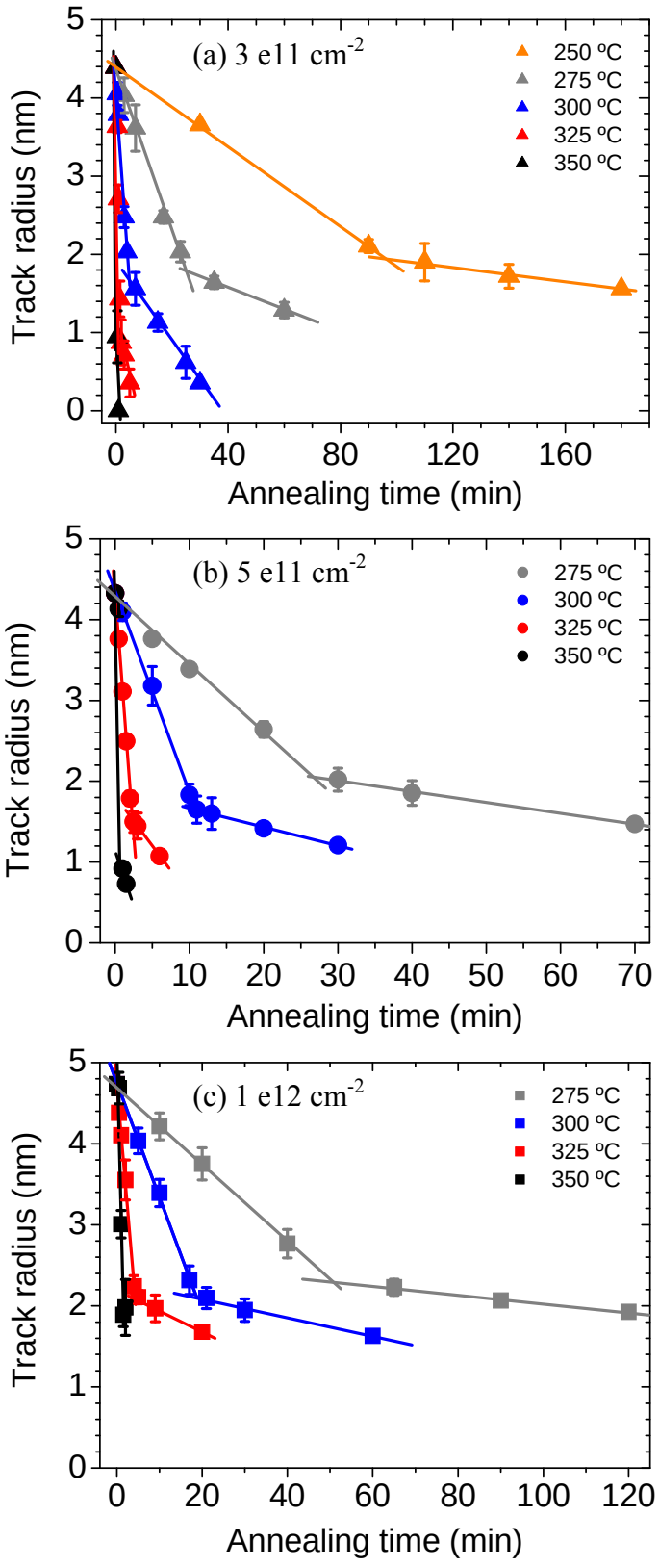

Fig. 7 (a-c). Evolution of the track radius with annealing time for the fluences **(a)** 3 x10^{11} cm^{-2}, **(b)** 5 x10^{11} cm^{-2} and **(c)** 1 x10^{12} cm^{-2}, and for the temperatures 250, 275, 300, 325 and 350 ºC, as indicated in the figures labels. The track radius is obtained for each case from the corresponding disordered fraction (shown in **Fig. 6**) as described in the text assuming a linear dependence of the cross-section of a track multiplied by the impact density.

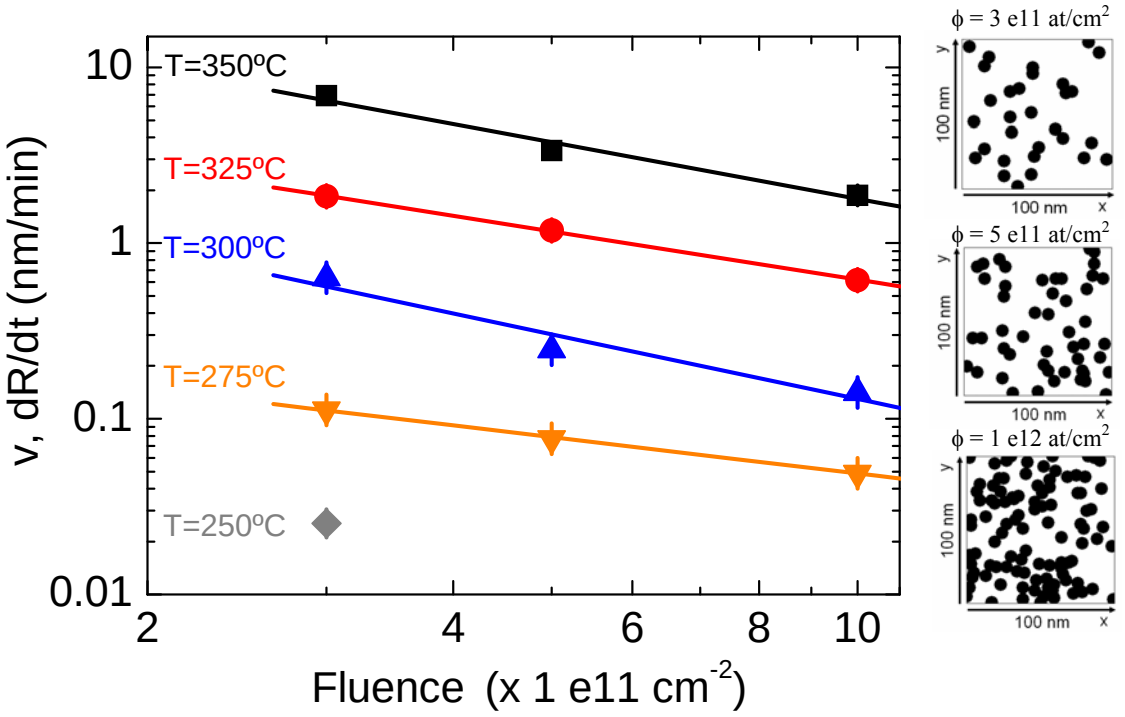

Fig. 8. Radial velocity of recrystallization as a function of fluence for the annealing temperatures indicated in the figure.

9.4.2. Stage I: Role of irradiation fluence.

Most reliable analysis of the kinetic behavior can be performed for the main and faster annealing **stage I**. From a comparison of the plots in **Fig. 7**, it can be appreciated that, for such a stage, the radial velocity **v** slightly decreases on increasing fluence. One should note from the insets that some overlapping already exists for 5×10^{11} cm^{-2} and it becomes serious for 1×10^{12} cm^{-2}. Therefore one should be cautious with the description of a proper track radius for the highest fluences. Nevertheless, keeping the analysis in terms of the (effective) track radius, **Fig. 8** illustrates the comparison of the velocities for the three investigated fluences. The reason of the dependence found is likely associated to the reduction of the crystalline-amorphous interface due to track overlapping. We will come back to this point later.

Since the recrystallization process appears to be thermally activated we have plotted in **Fig. 9 (a)** the radial velocity data for **stage I** as a function of temperature using the Arrhenius-type plot, $v = v_0 \cdot \exp\{-\varepsilon / kT\}$. All the data reasonably fit the Arrhenius dependence with an activation energy between $\varepsilon = 1.46$ eV and $\varepsilon = 1.58$ eV, slightly dependent on fluence. Since the differences are within the error range one may conclude that the activation energy is not substantially modified by fluence. Possible recrystallization mechanisms accounting for this behavior will be discussed below.

9.4.3. Slow annealing stage II.

One interesting result of our annealing experiments is the existence of a slower annealing stage (**II**) near the end of the recovery process, once the track radius has reached a

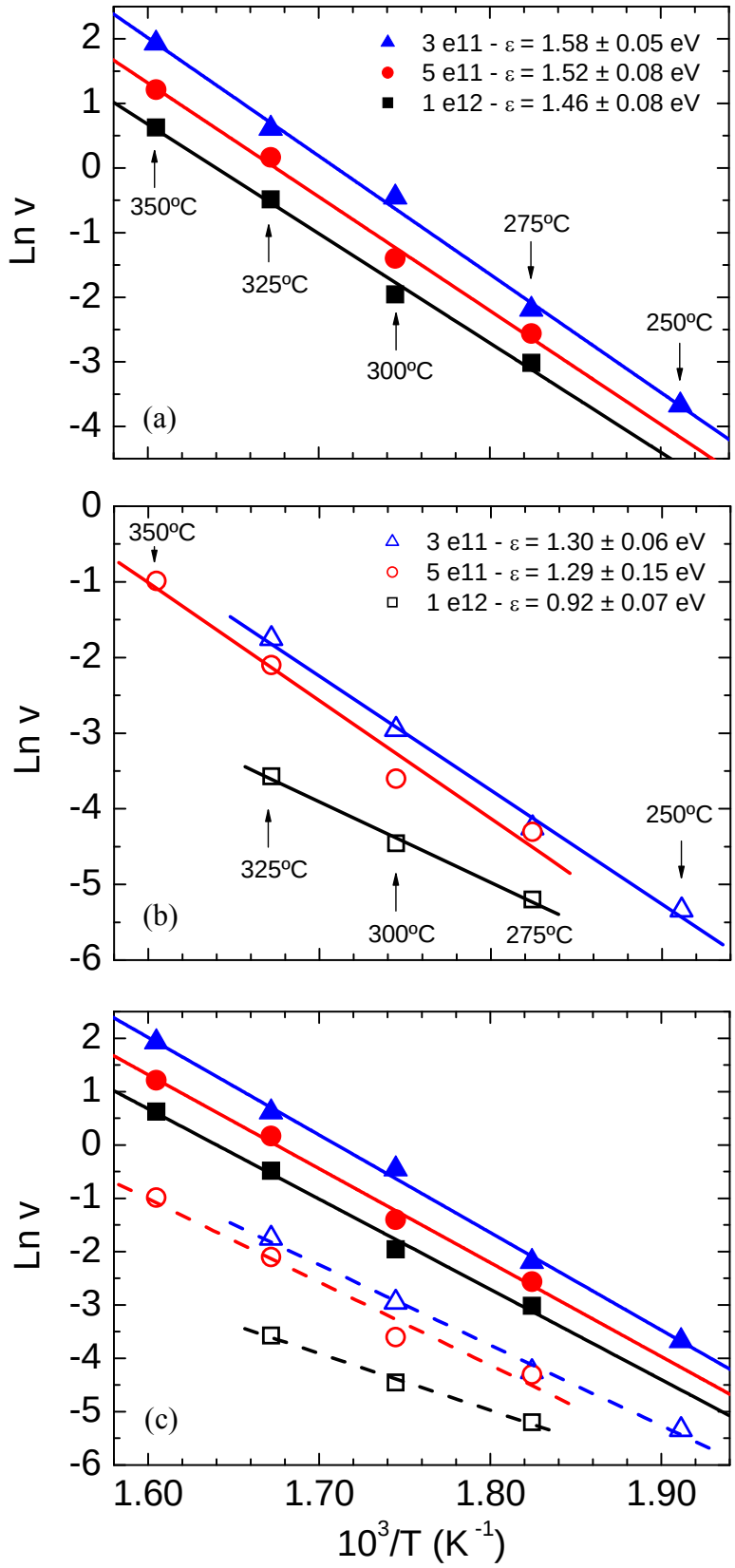

Fig. 9 (a-c). Arrhenius-type plot of the radial velocity data for the **stage I (a)** and **stage II (b)** for the three studied fluences indicated in the figure with their corresponding activation energies. **(c)** Both set of curves have been plotted together for comparison. **Stage I** (solid lines) and **stage II** (dashed lines).

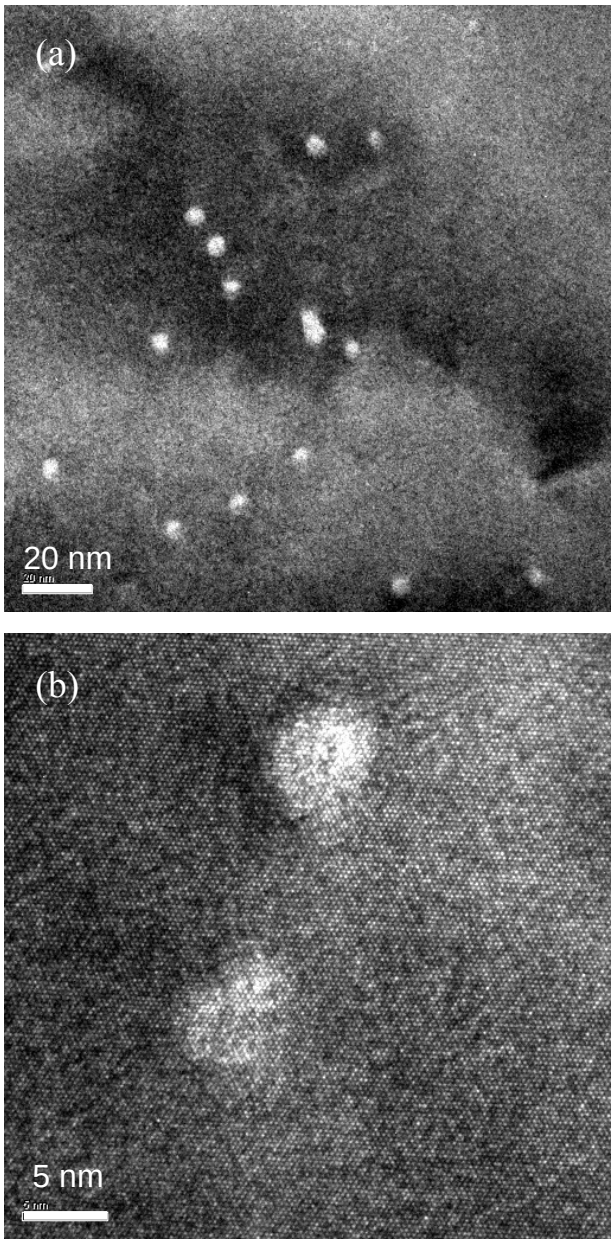

Fig. 10 (a, b). Bright field TEM images (two scales) of a $LiNbO_3$ sample irradiated with Br 45 MeV ions at a fluence of 3 $x10^{10}$ at/cm^2 after annealing in air for 30 min at 275 ºC. **(a)** several circular tracks can be observed in the statistical distribution of impacts; **(b)** High resolution image shows that the radius of the tracks (of about 2.5 nm) are consistent with data obtained from RBS/C.

value around or smaller than 2.5 nm. The data cover a limited number of data points with a higher relative error and so their analysis cannot be as conclusive as for the main annealing stage. Anyhow, the shrinking rate of **stage II** is also roughly linear and clearly smaller than that for **stage I**. Moreover it is thermally activated as inferred from the Arrhenius plot shown in **Fig. 9 (b)**. In **Fig. 9 (c)**, one sees that the radial velocities are a factor 2-3 smaller than for the main linear annealing stage, **Fig. 9 (a).** The data show large dispersion, although they approximately obey an Arrhenius-type law. The activation energies (between 0.92 eV and 1.30 eV) are not very different from those for **stage I**. In order to check that the structure of the track at the

inflexion point separating **stages I** and **II** is not anomalous TEM images have been obtained at that point and two of them are shown in **Fig. 10 (a, b)**. The shape is still circular and the radius is fairly consistent with the RBS/C data, although one should be cautious due to possible electron-induced recrystallization [54, 55].

9.5. Physical mechanisms.

It appears reasonable to start, first, with the recovery of individual amorphous tracks, where most complete information has been gathered. Moreover, they appear as the individual ingredients forming the homogeneous amorphous layers. In principle, we will here focus on the more reliable data for **stage I**. As in other solid-phase epitaxy processes [56]**,** one may assume that the recrystallization occurs at the crystalline-amorphous boundary (*interface-controlled process*). In fact, all data have been interpreted in accordance with this view considering that during the annealing the amorphous cores keep a circular cross section with a decreasing radius. On the other hand, it is expected that the basic Nb-O_6 octahedral unit stay essentially bound (rigid) in both crystalline and amorphous phases. The amorphous phase should only imply some random reordering of the crystalline octahedral arrangement. Therefore, one may think that the octahedra, lying in the amorphous phase close to the crystalline boundary, are those that may thermally accommodate into the crystalline structure and move the boundary. In other words, the rate of recrystallization is proportional to the number of octahedral sites at the boundary, i.e. to the perimeter of such a boundary. This view implies that the octahedral reordering is a **first-order local process** that does not depend on the long-range diffusion of point defects as vacancies or interstitials. In other words, the octahedra at the boundary sites behave independently of each other and have a definite frequency ν for recovery (re-orienting). This readily accounts for the constancy of the radial recrystallization velocity (v), and it is in accordance with more general formulations of solid-state epitaxy or epitaxial regrowth, such as the Kolmogorov-Johnson-Mell-Avrami (KJMA) model [57-60]. The linear boundary motion, or constant recrystallization rate, has also been invoked in the annealing of ion-beam irradiated ABO_3 oxides [37-41], mostly for the elastic nuclear collision regime.

The reorientation frequency should be an Arrhenius function of temperature $\nu = \nu_0 \exp\{-\varepsilon / kT\}$, ε being a certain energy barrier to be overcome for recovery. This is, in accordance with our assumption that, recovery is a local process as expected for a first-order phase transition (no long-range atomic motion or diffusion is involved). Then, the kinetics of recovery for the cross-section area σ of a single track with radius *R* would be

$$\frac{d\sigma}{dt} = 2\pi R\left(\frac{dR}{dt}\right) \qquad (3)$$

And, for the track radius, *R*,

$$\frac{dR}{dt} = -\nu\delta \qquad (4)$$

and, thus,

$$\frac{d\sigma}{dt} = -\nu(2\pi R)\delta = -(2\nu\pi^{1/2})\sigma^{1/2}\delta \qquad (5)$$

where v = $v\delta$, is the radial velocity of the track boundary, and, δ, some average value for the lattice parameter ($\delta \sim 0.5$ nm). In other words, integrating **Eq. (5)** one expects a linearly decreasing law for the time evolution of the radius: $R(t) = R_0 - \nu\,\delta\,t$, in accordance with the experimental data points, **Fig. 7**. For the main linear **stage I** of annealing, the value of the frequency ν amounts to around 10^{-3} s^{-1} at 275 ºC. Note that it is a rather low value that may correspond to some rotational frequency of the octahedra. How this rotation may occur, taking into account that the octahedra are anchored by the O corners, is not yet clear. The possible role of point defects such as O vacancies should also be elucidated. It is expected that the reorientation process would involve the overcoming of certain energy barriers and, so, its rate should be thermally activated. In fact, **Fig. 9 (a)** shows that, in spite of the limited temperature range, the data for v, and so for ν, presents a satisfactory fit to the Arrhenius plot. The energy barrier for recovery is in the range 1.46 - 1.58 eV, which appears reasonable for atomic jump processes. From the Arrhenius equation, $\nu = \nu_0 \exp\{-\varepsilon / kT\}$, one obtains a pre-exponential factor of around $\nu_0 \sim 10^{10}$ - 10^{11} s^{-1}.

9.5.1. Role of irradiation fluence.

We have advanced in **Section 7.4.2** that the decrease observed in the effective boundary velocity on increasing fluence should, likely, be due to a reduction in the extension of the crystalline-amorphous boundary (i.e. in the density of recrystallization sites). This argument may be put in a more quantitative form by using a simple MonteCarlo approach to describe the distribution of the amorphous sections of the tracks (disks) in a transversal plane (see more details in **Appendix III**). The overall perimeter of the distribution can be estimated from the morphologies illustrated in the schematics of **Fig. 6** by using a simple MonteCarlo code. The obtained dependence on track density (fluence) is displayed in **Fig. 11 (a, b)**. One sees an initial stage wherein the perimeter per track is constant as expected for fully isolated tracks. Around a certain critical fluence (≈ 3 x10^{11} cm^{-2}) the normalized perimeter (P_n) decreases with increasing fluence as a consequence of the track overlapping. As expected, the critical fluence, at which a change in behavior is observed, roughly corresponds to the impact density leading to optimum disk packing (coverage). In accordance with this view, the recrystallization velocity should decrease with increasing irradiation fluence. With the aim of checking this assumption, we have renormalized the recrystallization velocities in relation to the effective perimeter of the crystalline-amorphous boundary, **Fig. 12 (a)**. One sees that the accordance with experiment has improved but still there remains a significant discrepancy. One possible effect not considered so far, has to do with the role of overlapping defective halos around the track amorphous core [61], that may hinder the recrystallization process. In fact, as shown in **Fig. 12 (b)** the agreement with experiment can be achieve by artificially increasing the radius of the track core from 4.5 nm to around 5.5 nm or even 6.5 nm. The physical value of this assumption has to be explored in future work.

Finally, following with the idea of the recrystallization velocity should decrease with increasing irradiation fluence, it could be expected that at higher fluences there were a variation with time in the recrystallization rate (v), i.e., lower velocity at shorter times. Although it would be a small effect, this change in the behaviour of the beginning of the recovery process, which does not follows the rest of the behaviour; would suggest an extra energy barrier associated to

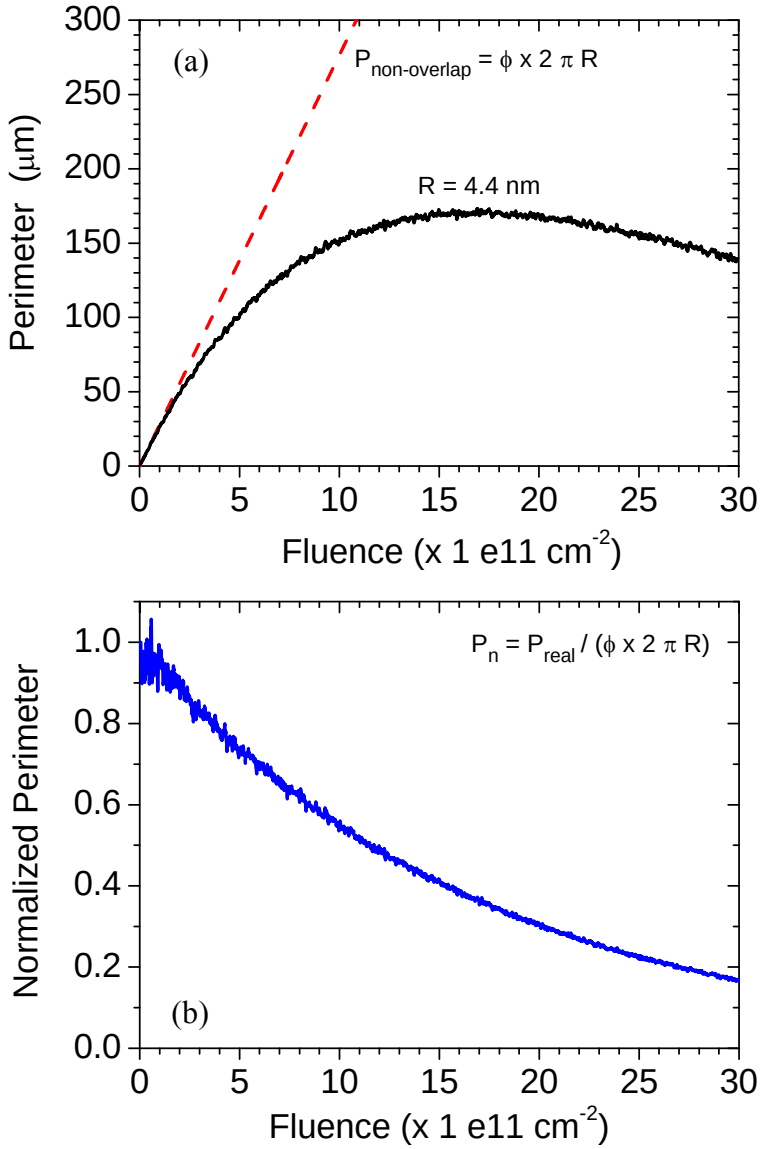

Fig. 11 (a, b). (a) Overall perimeter (P_{real}) as a function of fluence of a random track distribution of radius R = 4.4 nm numerically simulated with a MonteCarlo code (solid line). The linear dependence assuming non-overlapping tracks is shown as reference (dashed line). **(b)** Normalized perimeter (P_n) as a function of fluence.

the higher impact fluence. This could, perhaps, be interpreted as an "*incubation time*" or "*induction period*", being a property of the crystallization process and not related to the time required to raise the sample to the final annealing temperature. However, it seems a no observed effect, probably, because we are, in any case, at low irradiation fluences.

9.5.2. Slow annealing stage (II).

The occurrence of a slower annealing stage at the end of the recovery process cannot be well understood with the available information. In fact, one may consider that for track radii around or below 2 nm the discrete nature of the crystal lattice should be taken into account. On

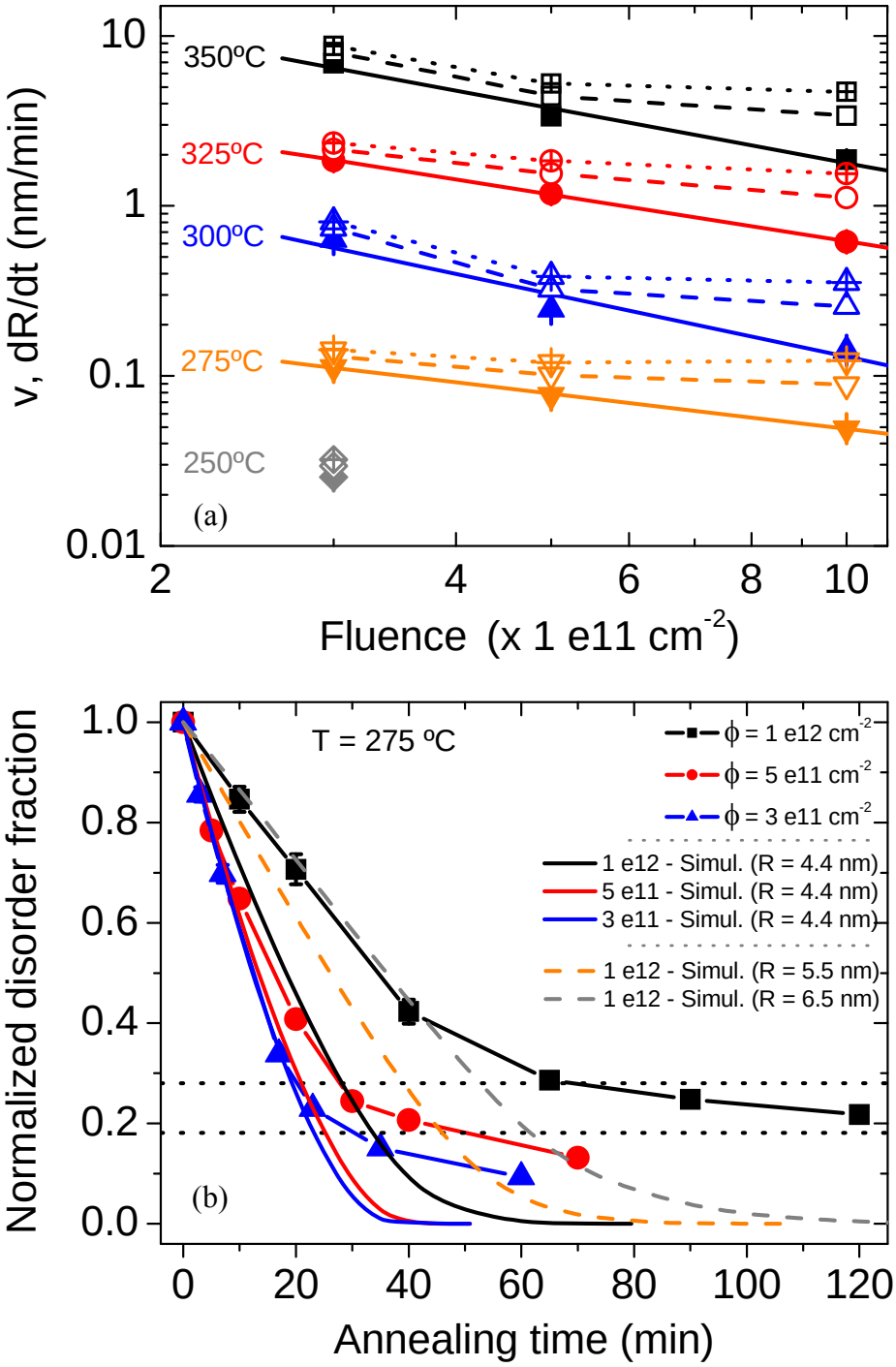

Fig. 12 (a, b). (a) Recrystallization velocity for the temperatures indicated in the figure renormalized to the effective perimeter for two different radii (4.4 and 5.5 nm). The solid symbols and lines are the experimental data also shown in **Fig. 8**. The open symbols correspond to the renormalized data. Dashed line corresponds to a radius of 4.4 nm and dotted line to a radius of 5.5 nm. **(b)** (Solid points) Normalized disorder fraction obtained from experimental RBS/C versus annealing time at 275 ºC for different fluences from **Fig. 6** (as indicated in the labels). (Solid and dashed lines) MonteCarlo simulations of the recrystallization process for different initial track radius (R = 4.4, 5.5 and 6.5 nm) and fluences, detailed in the labels.

the other hand, the normalized data also shown in **Fig. 6 (a)**, **6 (b)** and **6 (c)** (right axis) showing that the change from **stage I** to **stage II** seems to occur at a disorder percentage of about ~ 25 % (see dotted line in **Fig. 12 (b)**) independently of the fluence, may suggest a residual *track core* with a more stable structure, although this is difficult to justify unless additional experiments are carried out. It could be also argued that the recovered crystalline surrounding (halo) is more and more defective for decreasing track radii causing an enhancement of the channeled RBS yield over that one for the amorphous core. The use of an independent technique such as HRTEM observations and the appropriate data analysis would help to solve the problem.

9.6. Recrystallization of homogeneous amorphous layers.

According to current models of swift ion-beam amorphization, the formation of homogeneous amorphous layers results from the overlapping and accumulation of single tracks [62]. Therefore, one would expect coherent results for the annealing kinetics of both, tracks and layers. Optical (dark mode) techniques are particularly suitable to investigate amorphous layers that have been produced under moderate fluences inside the sample leaving crystalline the outermost surface layer. In this case the measurement of the propagating optical modes provides accurate and detailed information on the depth damage profile of the irradiated crystal. Buried layers have been produced [45] by irradiation with F ions at 20 MeV, whose stopping power curve as a function of depth presents a maximum inside the sample (below the surface, see **Fig. 1**). In this case a crystalline layer appears at the surface limited by the amorphous buried layer acting as an optical confinement medium because of its lower refractive index, as illustrated in the data of **Fig. 13**. The amorphous nature of the buried damaged layer is inferred from the measured refractive index profiles for both the TE and TM modes that decrease down to the amorphous value, 2.10 (at 633 nm wavelength) on reaching the outer amorphous boundary. This conclusion is also confirmed by the micro-Raman spectra showing the stacking of crystalline and amorphous layers [45]. Some exploratory isothermal annealing treatments (in air) were performed at several temperatures (up to 300 ºC) for 1 h. Our optical method yields the depth refractive index profile within the crystalline (waveguiding) layer and, thus, provides information on the motion of the crystalline-amorphous boundary. The observed effects are relatively minor and the main conclusions are:

i) The crystalline layer (waveguide) maintains essentially its thickness whereas the refractive index recovers substantially. The amorphous-crystalline boundary maintains its position, but boundary becomes sharper after annealing. This suggests that recrystallization has started close to the boundary but has not sufficiently progressed.

ii) The effects look similar for both X- and Z-cut samples.

In order to monitor in more detail the kinetics of the recrystallization process the samples irradiated with F (20 MeV) at 4 $x10^{14}$ cm^{-2}, have been kept at 350 ºC for different isothermal annealing times in air up to 10 h. The refractive index profiles obtained after different times for a *z*-cut sample are shown in **Figs. 13 (a, b)** for ordinary and extraordinary polarization, respectively. These profiles determine the high index values in the outer crystalline layer, wherein optical modes are propagated, and the index jump at the outer layer of the amorphous layer. Now, one clearly observes the inward motion of that boundary and the

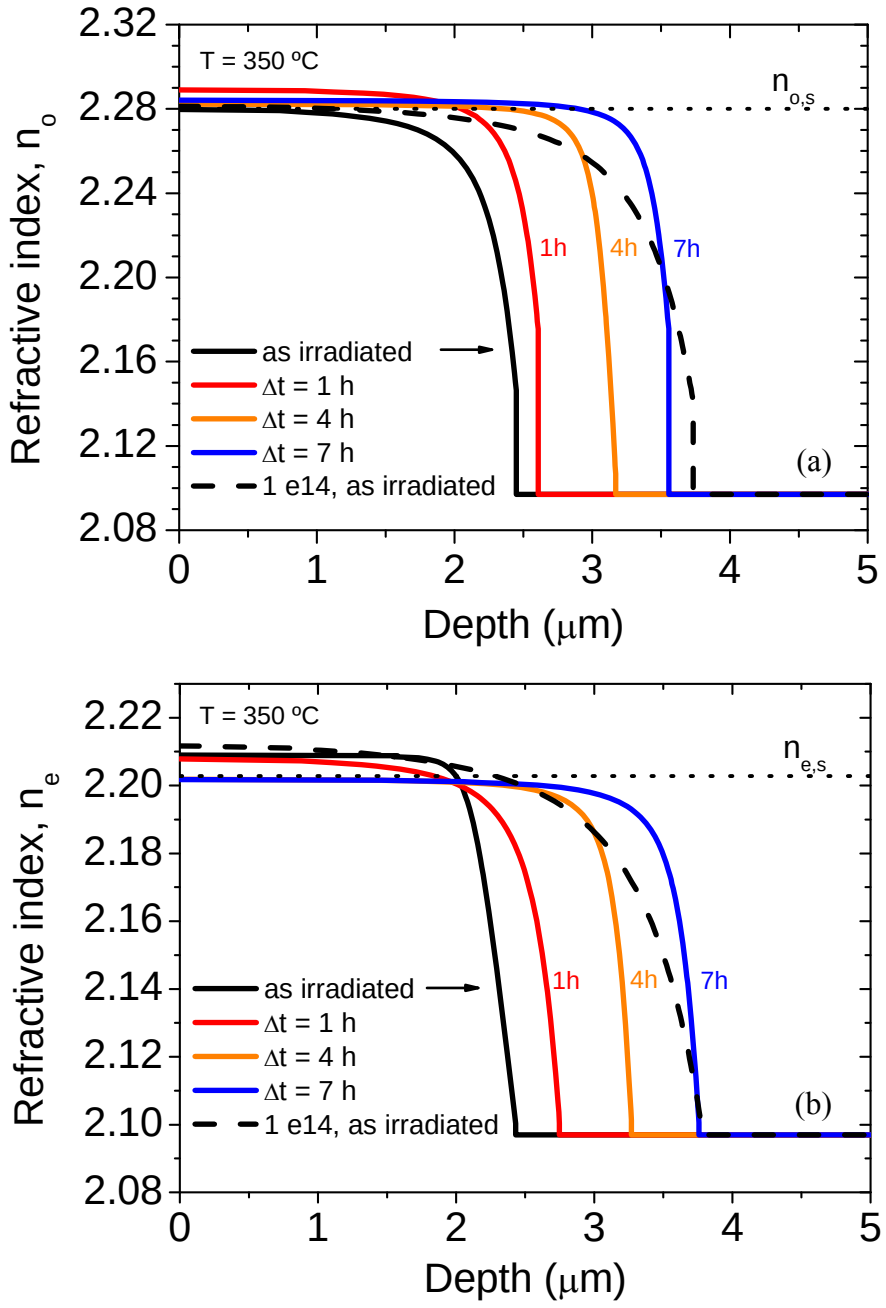

Fig. 13 (a, b). Refractive index (ordinary **(a)** and extraordinary **(b)**) profile evolution obtained after several steps (1, 4 and 7 h) of annealing in air at 350 ºC for a waveguide produced with F 20 MeV irradiation at a fluence of 4 x10^{14} cm^{-2} in the labels. In addition, (dashed line) the case as irradiated for 1 x10^{14} at/cm^2 (initial position of the amorphous boundary), is shown too. The substrate refractive indices of $LiNbO_3$ ($n_{o,\,s}$ and $n_{e,\,s}$) are shown as dotted lines.

corresponding widening of the waveguide at the surface. After 7 hours the position of the boundary reaches the initial position where amorphization was started (for fluences around $\phi \sim$ 1 x10^{14} cm^{-2}, also shown in **Fig. 13**). After 10 hours the profile has been so strongly modified that there is no left sign of any remaining waveguide. Similar results are found for *x*-cut samples. **Fig. 14** shows the thickness of the outer crystalline layer (waveguide) as a function of

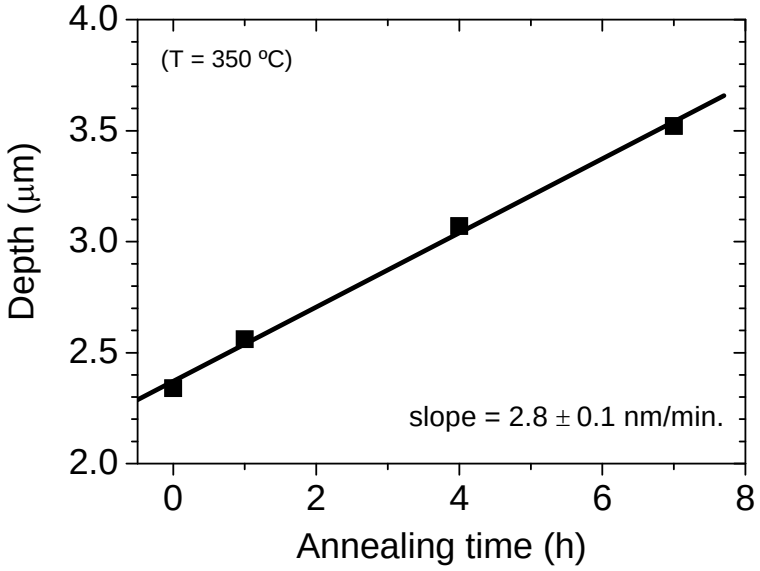

Fig. 14. Evolution of the crystalline-amorphous boundary position (depth) with annealing time at 350 ºC for the waveguide whose ordinary index profile is shown in **Fig. 13 (a)**.

annealing time. The dependence is essentially linear as found for the annealing of individual tracks and the linear recrystallization velocity is near 3 nm/min, not very different from the radial velocity for circular tracks. The same phenomenological model developed for isolated tracks can be applied to the recovery of full homogeneous layers. For a layer of initial thickness h, the kinetics is a simple extension of **Eq. (4)**, i.e.,

$$\frac{dh}{dt} = -v\delta \qquad (\mathbf{6})$$

predicting a linear motion of the boundary. Moreover the values obtained are quite consistent with those for single tracks (see **Section 7.5**). The linear boundary motion or constant recrystallization rate is typical of a simple solid-phase epitaxy [37, 63].

9.7. Comparison with the recrystallization of amorphous layers generated by elastic nuclear collision damage.

In relation to our work one should pay special attention to extensive work on perovskites and related oxides, using, both, light and heavy ions, mostly for applications to the storage and immobilization of radioactive waste [37-41]. The study has concentrated on the nuclear stopping regime or a mixed regime with a substantial contribution of nuclear collisions to the ion losses. The damage is initiated by the generation of primary atomic displacements (Frenkel pairs) as a result of the collisions of the incident ions. The process continues through the secondary displaced atoms within the material, leading to displacement cascades spike, whose accumulation finally causes an amorphous stage (see **Chapter 1**. *Section 1.3*). The overall process can be simulated by advanced MonteCarlo codes. Although the initiation of a definite amorphous phase is difficult to ascertain, it is generally accepted that it occurs for

fluences around or slightly above 1 dpa (displacements per atom). It appears to be a gradual (monotonic) process resulting from the accumulation of successive displacement spikes. Moreover, the detailed structure of such an amorphous phase is also controversial and maybe not unique.

In the case of electronic damage, each individual ion impact produces either isolated defects for electronic stopping powers below a well-defined threshold or an amorphous track above such threshold. Unfortunately, the atomic structure of the defects created by electronic excitation is not known and more research along the lines developed in ref [2] are required. Anyhow, for electronic excitation amorphization already occurs at the individual impact (track) level. This amorphization process appears to result from a phase transformation (either melting or a defect-driven transition) and has definite physical properties (refractive index, electronic properties...). This is a key difference with nuclear amorphization. On the other hand, the overall electronic damage after a multi-impact irradiation also results from the accumulation of the individual tracks. A detailed MonteCarlo analysis of the electronic damage morphology has been recently reported [62].

One main difficulty when trying to compare the recovery of the amorphous regions caused by nuclear collision or electronic damage is the fact that there are not clear-cut experiments where amorphization is exclusively produced by collision processes. In fact, experiments with light ions where electronic and nuclear damage regions are well separated hardly cause amorphization (except at very high fluences). So, the annealing data show a large variety of recovery temperatures that cannot be safely associated to an amorphous phase but to intermediate stages of disorder. On the other hand, many other experiments performed with heavy ions have been done at energies where electronic and nuclear effects are completely intermixed. Moreover one cannot ignore the role of the implanted ions reaching concentrations of 10^{-2} - 10^{-3} on the amorphization process as it has been clearly revealed [37, 63] (e.g. Pb at $E <$ 1 MeV). Anyhow, the available data depend strongly on ion and fluence. On the other hand the structure of the phases can be quite different. For electronic damage one can imagine some kind of mosaic structure made up of dislocated octahedra.

In particular, we can compare our data with those obtained [37, 63] in some perovskites after 0.5 MeV irradiation with Pb. They clearly show, by monitoring the recovery with RBS/C, that amorphous regions recrystallize epitaxially with motion of the boundary towards the surface. The recrystallization temperatures are similar as those corresponding to our experiments. Constant isothermal recrystallization rates are of the same order as those found in our experiments, e.g. 0.1 nm /s at 300 ºC and 0.3 nm /s at 350 ºC. One may suspect that the situation could be strongly influenced by electronic amorphization. On the other hand, activation energies are around 1 eV. All those similarities may suggest that the two processes cause a similar structure for the damage. This is consistent with the idea that basic transition metal octahedra are quite stable and amorphization can be understood as a random ordering of such octahedra.

9.8. Summary and conclusions.

In this work we have provided systematic data on the recrystallization kinetics of single amorphous tracks and homogeneous layers. The data for single tracks reveal that annealing is governed by interface processes, as for solid state epitaxy. The decrease in the radius of the tracks follows a linear dependence on annealing time, and it is constant for each temperature. Hence, the areal regrowth rate is not constant, neither proportional to the crystalline-amorphous boundary perimeter. The velocity of the crystalline-amorphous boundary moves at constant velocity v ~ 3 nm/min (at 350ºC) in a main annealing stage, but slows down dramatically for track radii of around 2 nm. The velocity is thermally activated, in accordance with an Arrhenius-type dependence, and an activation energy around 1.5 eV for the main initial stage has been found. For track radii smaller than ~2 nm the track shrinkage process slows down suggesting that other mechanisms should be taken into account.

For homogeneous amorphous layers the data can be described within the same physical process and provide consistent data with those obtained for individual tracks. The annealing of buried amorphous layers induces a reduction of their thicknesses in a similar temperature range. The displacement of the crystalline-amorphous boundary is also linear with annealing time and the crystallization rates are similar to those for tracks.

An universal scaling law has been found to describe the process, in this sense, a simple nucleation model is used to describe the observed phenomena; moreover a model that explains the recovery of the damage is proposed and discussed in terms of local reordering of the basic $Nb\text{-}O_6$ octahedral unit and epitaxial regrowth. From this, implies that the octahedral reordering is a first-order local process (interface-controlled regrowth) that does not depend on the long-range diffusion of point defects as vacancies or interstitials.

The comparison of these data with those previously obtained for the heavily-damaged (amorphous) layers produced by elastic nuclear collisions has been summarily described.

The results may have relevant implications for a number of applications. The control of track radii by suitable annealing treatments can be used to tailor the diameter of the nanopores after suitable chemical etching. Moreover, the control of track radii allows to tailor the dielectric constant and refractive index of the outer irradiated layer and, thus, the possibilities for integrated optics devices. Also, for the photonics field, the results found for homogeneous layers allow for an adequate control of the thickness of the outer waveguide layer and even the sharpness of the waveguide boundary [27]. Last, but not least, the annealing data are, indeed, very relevant in connection with the problem of radioactive waste disposal.

9.9. References.

[1] A. Rivera, J. Olivares, G. García, J. M. Cabrera, F. Agulló-Rueda and F. Agulló-López, *"Giant enhancement of material damage associated to electronic excitation during ion irradiation: The case of $LiNbO_3$"*, Phys. Status Solidi A 206 (2009) 1109-1116.

[2] C. S. Schnohr, P. Kluth, A. P. Byrne, C. J. Foran and M. C. Ridgway, *"Comparison of the atomic structure of InP amorphized by electronic or nuclear ion energy-loss processes"*, Phys. Rev. B 77 (2008) 073204.

[3] S. M. M. Ramos, R. Brenier, B. Canut, G. Fuchs, P. Thevenard, M. Trilleux, A. Meftah, M. Toulemonde, *"Europium diffusion enhancement in lithium niobate by GeV gadolinium ion irradiations"*, J. Appl. Phys. 77 (1995) 2952.

[4] B. Canut, S. M. M. Ramos, R. Brenier, P. Thevenard, J. L. Loubet, M. Toulemonde, *"Surface modification of $LiNbO_3$ single crystals by swift heavy ions"*, Nucl. Instrum. Methods B 107 (1996) 194 -198.

[5] F. Thibaud, J. Cousty, E. Balanzat, S. Bouffard, *"Atomic-force-microscopy observations of tracks induced by swift Kr ions in mica"*, Phys. Rev. Lett. 67 (1991) 1582-1585.

[6] J. Olivares, A. García-Navarro, G. García, A. Méndez and F. Agulló-López, *"Optical determination of three-dimensional nanotrack profiles generated by single swift-heavy ion impacts in lithium niobate"*, Appl. Phys. Lett. 89 (2006) 071923.

[7] P. Kluth, C. S. Schnohr, O. H. Pakarinen, F. Djurabekova, D. J. Sprouster, R. Giuliani, M. C. Ridway, A. P. Byrne, C. Trautmann, D. J. Cookson, K. Nordlund and M. Toulemonde, *"Fine Structure in Swift Heavy Ion Tracks in Amorphous SiO_2"*, Phys. Rev. Lett. 101 (2008) 175503.

[8] N. Itoh, D. M. Duffy, S. Khakshouri and A. M. Stoneham, *"Making tracks: electronic excitation roles in forming swift heavy ion tracks"*, J. Phys.: Condens. Matter 21 (2009) 474205.

[9] J. Olivares, G. García, F. Agulló-López, F. Agulló-Rueda, A. Kling, J. C. Soares, *"Generation of amorphous surface layers in $LiNbO_3$ by ion-beam irradiation: thresholding and boundary propagation"*, Appl. Phys. A 81 (2005) 1465-1469.

[10] G. García, F. Agulló-López, J. Olivares and A. García-Navarro, *"Monte Carlo simulation of damage and amorphization induced by swift-ion irradiation in $LiNbO_3$"*, J. Appl. Phys. 99 (2006) 053504.

[11] Z. G. Wang, Ch. Dufour, E. Paumier and M. Toulemonde, *"The S_e sensitivity of metals under swift-heavy-ion irradiation: a transient thermal process"*, J. Phys.: Condens. Matter 6 (1994) 6733.

[12] G. Szenes, *"General features of latent track formation in magnetic insulators irradiated with swift heavy ions"*, Phys. Rev. B 51 (1995) 8026-8029.

[13] M. Toulemonde, W. Assman, C. Dufour, A. Meftah, F. Studer, and C. Trautmann, in: *"Ion Beam Science: Solved and Unsolved Problems"*. P. Sigmund, (Ed.), *The Royal Danish Academy of Sciences and Letters*, Copenhagen, 2006, pp. 263.

[14] A. Kamarou, W. Wesch, E. Wendler, A. Undisz and M. Rettenmayr, *"Swift heavy ion irradiation of InP: Thermal spike modeling of track formation"*, Phys. Rev. B 73 (2006) 184107.

[15] N. Itoh, and A. M. Stoneham, *"Materials Modification by Electronic Excitation"*, Vol., (Ed.), Cambridge University Press, 2001.

[16] F. Agulló-López, A. Méndez, G. García, J. Olivares and J. M. Cabrera, *"Synergy between thermal spike and exciton decay mechanisms for ion damage and amorphization by electronic excitation"*, Phys. Rev. B 74 (2006) 174109.

[17] A. Rivera, A. Méndez, G. García, J. Olivares, J. M. Cabrera and F. Agulló-López, *"Ion-beam damage and non-radiative exciton decay in $LiNbO_3$"*, Journal of Luminescence 128 (2008) 703-707.

[18] H. J. Fecht, *"Defect-induced melting and solid-state amorphization"*, Nature 356 (1992) 133.

[19] D. Fink, P. S. Alegaonkar, A. V. Petrov, M. Wilhelm, P. Szimkowiak, M. Behar, D. Sinha, W.R. Fahrner, K. Hoppe and L. T. Chadderton, *"High energy ion beam irradiation of polymers for electronic applications"*, Nucl. Instr. Meth. B 236 (2005) 11-20.

[20] Z. Siwy, P. Apel, D. Baur, D. D. Dobrev, Y. E. Korchev, R. Neumann, R. Spohr, C. Trautmann and K. -O. Voss, *"Preparation of synthetic nanopores with transport properties analogous to biological channels"*, Surf. Sci. 532-535 (2003) 1061-1066.

[21] J. Chen, and R. Könenkamp, *"Vertical nanowire transistor in flexible polymer foil"*, Appl. Phys. Lett. 82 (2003) 4782.

[22] J. Chen, S. Klaumünzer, M. C. Lux-Steiner and R. Könenkamp, *"Vertical nanowire transistors with low leakage current"*, Appl. Phys. Lett. 85 (2004) 1401.

[23] M. Toulemonde, C. Trautmann, E. Balanzat, K. Horjt, A. Weidinger, *"Track formation and fabrication of nanostructures with MeV-ion beams"*, Nucl. Instr. Meth. B 216 (2004) 1-8.

[24] R. Sanz, J. Jensen, A. Johansson, M. Skupinski, G. Possnert, M. Boman, M. Hernández-Vélez, M. Vázquez and K. Hjort, *"Well-ordered nanopore arrays in rutile TiO_2 single crystals by swift heavy ion-beam lithography"*, Nanotechnology 18 (2007) 305303.

[25] M. L. Crespillo, M. Otto, A. Muñoz-Martín, J. Olivares, F. Agulló-López, M. Seibt, M. Toulemonde and C. Trautmann, *"Optimization of nanopores obtained by chemical etching on swift-ion irradiated lithium niobate"*, Nucl. Instr. Meth. B 267 (2009) 1035-1038.

[26] D. Kanjilal, *"Swift heavy ion-induced modification and track formation in materials"*, Current Science 80 (2001) 1560-1566.

[27] J. Olivares, G. García, A. García-Navarro, F. Agulló-López, O. Caballero and A. García-Cabañes, *"Generation of high-confinement step-like optical waveguides in $LiNbO_3$ by swift heavy ion-beam irradiation"*, Appl. Phys. Lett. 86 (2005) 183501.

[28] J. Olivares, M. L. Crespillo, O. Caballero-Calero, M. D. Ynsa, A. García-Cabañes, M. Toulemonde, C. Trautmann and F. Agulló-López, *"Thick optical waveguides in lithium niobate induced by swift heavy ions (~10 MeV/amu) at ultralow fluences"*, Optics Express 17 (2009) 24175-24182.

[29] C. A. Merchant, P. Scrutton, S. García-Blanco, C. Hnatovsky, R. S. Taylor, A. García-Navarro, G. García, F. Agulló-López, J. Olivares, A. S. Helmy and J. S. Aitchison, *"High Resolution refractive index and micro-raman spectroscopy of planar waveguides in $KGd(WO_4)_2$ formed by swift heavy ion irradiation"*, IEEE J. Quantum Electronics 45 (2009) 373-379.

[30] A. Majkić, M. Koechlin, G. Poberaj and P. Günter *"Optical microring resonators in fluorine-implanted lithium niobate"*, Optics Express 16 (2008) 8769.

[31] B. Canut, R. Brenier, A. Meftah, P. Moretti, S. Ould Salem, M. Pitaval, S. M. M. Ramos, P. Thevenard and M. Toulemonde, *"Latent track formation in $LiNbO_3$ single crystals irradiated by GeV Uranium ions"*, Rad. Eff. and Defect in solids 136 (1995) 307-310.

[32] S. M. M. Ramos, B. Canut, M. Ambri, C. Clement, E. Dooryhee, M. Pitavale, P. Thévenard and M. Toulemonde *"Europium diffusion enhancement in $LiNbO_3$ irradiated with GeV nickel ions: influence of the damage morphology"*, Nucl. Instr. and Meth. B 107 (1996) 254-258.

[33] S. S. M. Ramos, N. Bonardi, B. Canut and S. Della-Negra, *"Latent tracks in sapphire induced by 20-MeV fullerene beams"*, Phys. Rev. B 57 (1998) 189-193.

[34] K. Awazu, X. Wang, M. Fujimaki, T. Komatsubara, T. Ikeda and Y. Ohki, *"Structure of latent tracks in rutile single crystal of titanium dioxide induced by swift heavy ions"*, J. Appl. Phys. 100 (2006) 044308.

[35] A. Dunlop, G. Jaskierowicz and S. Della-Negra, *"Latent track formation in silicon irradiated by 30 MeV fullerenes"*, Nucl. Instr. and Meth. B 146 (1998) 302-308.

[36] G. G. Bentini, M. Bianconi, M. Chiarini, L. Correra, C. Sada, P. Mazzoldi, N. Argiolas, M. Bazzan and R. Guzzi, *"Effect of low dose high energy O^{3+} implantation on refractive index and linear electro-optic properties in X-cut $LiNbO_3$:Planar optical waveguide formation and characterization"*, J. Appl. Phys 92 (2002) 6477.

[37] C. W. White, L. A. Boatner, P. S. Sklad, C. J. McHargue, J. Rankin, G. C. Farlow and M. J. Aziz, *"Ion implantation and annealing of crystalline oxides and ceramic materials"*, Nucl. Instr. Meth. B 32 (1988) 11-22.

[38] A. Meldrum, S. J. Zinkle, L. A. Boatner and R. C. Ewing *"Heavy-ion irradiation effects in the ABO_4 orthosilicates: Decomposition, amorphization, and recrystallization"*, Phys. Rev. B 59 (1998) 3981–3992.

[39] Z. Zhang, I. A. Rusakova and W. K. Chu, *"RBS-channeling and TEM studies on the regrowth of low temperature argon ion amorphized lithium tantalate ($LiTaO_3$) single crystal"*, Nucl. Instr. Meth. B 136-138 (1998) 404-409.

[40] W. J. Weber, *"Models and mechanisms of irradiation-induced amorphization in ceramics"*, Nucl. Instr. Meth. B 166-167 (2000) 98.

[41] A. Meldrum, L. A. Boatner, W. J. Weber and R. C. Ewing, *"Amorphization and recrystallization of the ABO_3 oxides"*, J. Nucl. Mater. 300 (2002) 242-254.

[42] J. Ziegler, computer code SRIM version 2008, (http://www.srim.org).

[43] J. F. Ziegler, J. P. Biersack and U. Littmark, (Ed.), *The Stopping and Ranges of Ions in Solids*, Pergamon Press, New York, 1985.

[44] Centro de Microanálisis de Materiales. (http://www.cmam.uam.es).

[45] J. Olivares, A. García-Navarro, G. García, F. Agulló-López, F. Agulló-Rueda, A. García-Cabañes and M. Carrascosa, *"Buried amorphous layers by electronic excitation in ion-beam irradiated lithium niobate: structure and kinetics"*, J. Appl. Phys 101 (2007) 033512.

[46] P. D. Townsend, P. J. Chandler and L. Zhang, *"Optical Effects of Ion Implantation"*, Vol., (Ed.), Cambridge University Press, Cambridge, 1994.

[47] S. Klaumünzer, *"Ion hammering of silica colloids"*, Nucl. Instr. Meth. B 215 (2004) 345.

[48] K. S. Chiang, *"Construction of refractive-index profiles of planar dielectric waveguides from the distribution of effective indexes"*, J. Lightwave Technology 3 (1985) 385-391.

[49] P. Thévenard, G. Guiraud, C. H. S. Dupuy and B. Delaunay, *"Assumption of F-centre creation in lif bombarded with high-energy particles"*, Radiat. Eff. 32 (1977) 83-90.

[50] W. K. Chu, J. W. Mayer and M. A. Nicolet, *"Backscattering Spectrometry"*, Vol., (Ed.), Academic Press, New York, 1978.

[51] J. F. Gibbons, *"Ion implantation in semiconductors. Part II: Damage production and annealing"*, Proc. IEEE 60 (1972) 1062-1096.

[52] A. Meftah, J. M. Constantini, N. Khalfaoui, S. Boudjadar, J. P. Stoquert, F. Studer and M. Toulemonde, *"Experimental determination of track cross-section in $Gd_3Ga_5O_{12}$ and comparison to the inelastic thermal spike model applied to several materials"*, Nucl. Instrum. Methods B 237 (2005) 563-574.

[53] A. Meftah, J. M. Constantini, N. Khalfaoui, S. Boudjadar, J. P. Stoquert, F. Studer and M. Toulemonde, *"Experimental determination of track cross-section in GdGaO and comparison to the inelastic thermal spike model applied to several materials"*, Nucl. Instrum. Methods B 237 (2005) 563-574.

[54] A. Benyagoub, A. Audren, L. Thomé and F. Garrido, *"Athermal crystallization induced by electronic excitations in ion-irradiated silicon carbide"*, Appl. Phys. Lett. 89 (2006) 241914.

[55] Y. Zhang, J. Lian, C. M. Wang, W. Jiang, R. C. Ewing and W. J. Weber, *"Ion-induced damage accumulation and electron-beam-enhanced recrystallization in $SrTiO_3$"*, Phys. Rev. B 72 (2005) 094112.

[56] I. Markov, *"Crystal Growth for Beginners"*, Vol., (Ed.), 2nd Edition, World Scientific, Singapore, 2003.

[57] W. A. Johnson, and R. F. Mehl, Trans. Am. Inst. Miner. (Metall.) Eng. 135 (1939) 416.

[58] M. Avrami, *"Kinetics of Phase Change. I. General Theory"*, J. Chem. Phys. 7 (1939) 1103-1112.

[59] M. Avrami, *"Kinetics of Phase Change. II. Transformation-Time Relations for Random Distribution of Nuclei"*, J. Chem. Phys. 8 (1940) 212-224.

[60] M. Avrami, *"Kinetics of Phase Change. III. Granulation, Phase Change, and Microstructure"*, J. Chem. Phys. 9 (1941) 177-184.

[61] A. Rivera, J. Olivares, M. L. Crespillo, G. García, M. Bianconi and F. Agulló-López, *"Assessment of swift-ion damage by RBS/C: Determination of the amorphization threshold"*, Nucl. Instr. Meth. B 267 (2009) 1460-1463.

[62] A. Rivera, M. L. Crespillo, J. Olivares, G. García and F. Agulló-López, *"Effect of defect accumulation on ion-beam damage morphology by electronic excitation in lithium niobate: A MonteCarlo approach"*, Nucl. Instr. Meth. B 268 (2010) 2249–2256.

[63] C. W. White, L. A. Boatner, J. Rankin and M. J. Aziz, *"Ion implantation and annealing of $SrTiO_3$ and $CaTiO_3$"*, Mater. Res. Soc. Proc. 93 (1987) 9-14.

Chapter 10

Thick optical waveguides in lithium niobate induced by swift heavy ions (~10 MeV/amu).

10.1. Introduction.

Ion implantation of light ions (H or He) in the few-MeV energy range is a standard procedure to produce optical waveguides at visible and near-IR wavelengths in $LiNbO_3$ and in many other crystals [1-3]. At the end of their range (~ 1 μm), ions are implanted and severe structural damage is produced by elastic collisions with the atoms of the target material, leading to the formation of a buried layer having a lower density and refractive index than the virgin crystal. This buried layer behaves as an optical barrier creating a surface waveguide. For the formation of such a barrier fluences as high as 10^{16}-10^{17} at/cm^2 are required. At the typical currents obtained in ion accelerators the method becomes quite inefficient. The fact that the thickness of the optical barrier produced with MeV ions is limited to about 1 micron does not allow for full infrared light confinement. Propagation losses thus increase due to light tunnelling to the substrate modes (i.e. leaky modes). This problem could be overcome by using ions of larger energy and thus large range leading to thicker layers of modified material.

Nowadays, this method has been tested for $LiNbO_3$ demonstrating not only the feasibility but also a number of advantages, such as substantially reduced ion fluences [4]. The irradiation requires heavier projectiles (mass in the range 15 to 40 atomic units), and energies in the range of a few tens of MeV. For such high energies, the electronic energy deposition is dominant and responsible for structural modifications of the material [4-7]. The damage induced in the electronic energy loss regime has quite different features compared to defects produced by elastic collisions [8]. Track formation, i.e., the formation of columnar defects requires a well-defined electronic stopping power threshold value, and, on $LiNbO_3$, the damage cross-section of the tracks strongly increases with the energy loss (S_e). By analogy with the track morphology as depicted in Ref. [9], it is possible to define specific thresholds versus electronic energy loss [10] taking into account the *velocity effect* [11, 12]. At low velocity (~ 0.1 MeV/amu) threshold of damage creation is ~2 keV/nm and threshold of continuous track is ~7.5 keV/nm while at high energy (10 MeV/amu) the corresponding thresholds are ~6.5 and ~13 keV/nm, respectively. In between these two thresholds the damage in the track is inhomogeneous and not continuous. However, by accumulating high fluences homogeneous amorphous layers can be created due to track overlapping.

The idea behind the fabrication of an optical waveguide with high-energy ions is to bombard the material with ions having their electronic energy loss maximum at a certain depth inside the material. At and around this maximum, the damage threshold can be overcome producing an amorphous layer of lower refractive index. This buried layer constitutes an optical barrier for waveguiding at the surface. In first experiments, $LiNbO_3$ was bombarded with F ions of 22 MeV energy and maximum stopping power of about 3 keV/nm (i.e. below the threshold of continuous track damage). The irradiation produced useful waveguides with high refractive index jump (~10 %), step-like index profile (due to track overlapping) with low propagation losses and reasonably high nonlinear optical coefficients. The applied fluences were around 10^{14} cm^{-2}, which is compared to standard low-energy implantation, reduced by two orders of magnitude [4]. Following the same technique, lithium niobate ring resonators with 80 μm radius acting as wavelength filters at the 1.5 μm telecom wavelength have been fabricated [13].

Recently, swift ion irradiation in $LiNbO_3$ has received considerable attention due to its novel modification of structures and refractive indices of the crystal (**Chapter 3**. *Section 3.2.3*).

In these cases, the electronic energy deposition is dominant over the nuclear one, and the refractive index changes are mainly due to the electronic-damage-related structural modifications. In this sense, it is worthy to remark the intense effort performed by researchers with the aim of studying swift heavy ion-irradiated $LiNbO_3$ waveguides and related physical mechanisms. The electronic stopping power (S_e) of the incident ions is a key parameter that affects the structures and refractive indices of the $LiNbO_3$ substrate. As it has been discussed throughout the **Part I** of this Thesis, there is an *intrinsic* threshold value S_{th}, which strongly influences the formation of nanometer-sized amorphous tracks occurring during the irradiation process.

Coming from the latest results based on irradiations with ions, i.e. Si, Cl 40-45 MeV, such that S_e (of about 7 keV/nm) is higher than the amorphization threshold for individual nano-track formation (≥ 5-6 keV/nm) and simultaneously the maximum of S_e *(x)* is inside the crystal; then, in the (ultra-low) fluence regime of isolated impacts (~10^{11}-10^{12} cm^{-2}) to prevent full surface amorphization [14]. a nanostructured material is generated made of nanotracks embedded into the lithium niobate crystalline crystal whose diameter increase in depth, creating an effective optical layer which has a refractive index profile progressively decreasing from the surface allowing optical waveguiding. In this case, each nanometer-sized latent amorphous track creates a single ion impact with an isotropic refractive index ($n_o = n_e$ =2.1). The radius of each track increases monotonically with S_e, forming a depth-shaped distribution. Track structure has been ascertained to be composed of a pre-amorphous halo and an amorphous core. Also in this fluence regime, for heavy ions of lower energies when the maximum of S_e *(x)* is a not buried but is at the surface, it is possible to generate waveguides by refractive index enhancement after suitable annealing that recrystallizes the amorphous tracks through the pre-amorphous stage. This novel route for optical waveguide fabrication in lithium niobate using ultra low fluences implies an improvement in the fabrication time of a factor of 10^2-10^4. The linear and nonlinear optical properties have been measured and are reasonable high, so that some fundamental questions are still open such as the continuity of the tracks and the influence on optical properties like high waveguiding propagations losses due to internal scattering with the tracks, crystal strain, potential applications of Chlorine nanotracks waveguides, etc. Later on, the method was successfully applied to generate optical waveguides in another nonlinear optical crystal, $KGd(WO_4)_2$ [15, 16], slightly changing the irradiation conditions. This shows that the method could have a wide applicability to many other crystals with photonic interest.

On the other hand, and in addition, due to our colaborations with the swift heavy ions community, Prof. Marcel Toulemonde (GANIL) and Dr. Christina Trautmann (GSI), we think in the possibility of using a much higher energy for ion irradiation, e.g., several GeV, in order to form “thick” and “deep” waveguides (tens of microns) for applications in the infrared wavelength bands. Since $S_e >> S_{th}$, a lower dose is required for waveguide formation in $LiNbO_3$. Moreover, the main advantage of this procedure is that it dramatically reduces the required fluences, up to four orders of magnitude, compared to the traditional method for the implantation of light ions, thereby decreasing production time.

All of which leads us to consider the possibility of irradiating on purpose in the high stopping energy range (10-35 keV/nm) and at ultralow irradiation fluences (< 10^{12} cm^{-2}) performing experiments at GSI and GANIL. In this sense, we present here this first exploratory research in which heavy mass ions, Kr and Xe, having energies in the 1 GeV range have been

used to study the intrinsic potential of nanostructuring and to produce thick planar optical waveguides at the surface of lithium niobate.A study of the morphology of the tracks and their profiles in depth, combining various experimental techniques, including the measurement of refractive index profiles, and RBS/C measurements have been carried out. Such information is especially important to assess the potential for possible applications, and on the other hand for testing the theoretical models that describe the formation of the ion tracks.

Therefore, the purpose of this work has been to explore the use of the heavy ion irradiation method, in the electronic energy loss regime to even higher energies (~ 10 MeV/amu) and stopping powers. This would allow the fabrication of much thicker waveguides (up to tens of microns) with ultralow fluences ($< 10^{12}$ cm^{-2}). Such thick optical barriers may be useful in the mid-IR e.g. for astrophysical applications (or "Astrophotonics") [17, 18]. Moreover, in this energy range ion trajectories are more straight that would allow for better resolved waveguides patterns. In addition, at such high energies, the contribution of nuclear energy loss is extremely small and defects produced by elastic collisions are irrelevant for the major length of the ion trajectory. Therefore one would expect reduced optical losses after appropriate optimization. Although $LiNbO_3$ is not the most adequate material for applications going beyond 4 microns wavelength due to its large optical absorption, our experiments provide a demonstration test illustrating the potential of the method.

10.2. Waveguide preparation by swift heavy ion (SHI) irradiation.

The irradiations were performed at near normal incidence on *z*-cut $LiNbO_3$ samples at GANIL (Caen, France) and GSI (Darmstadt, Germany) with Kr and Xe ions, respectively. **Table I** lists the corresponding incident energies and ion ranges. Fluences applied ranged from 0.5 up to 8×10^{11} at/cm^2. The evolution of the electronic energy loss, calculated with the SRIM-2008 code [19, 20] as a function of penetration depth is shown in **Fig. 1**. The maximum value is reached at a depth of ~ 45 μm for Kr (809 MeV) and at ~35 μm for Xe (1432 MeV). In both cases, the energy loss is clearly above the expected amorphization threshold for a large fraction of the ion trajectory. The figure also includes the curve for 46-MeV Cl ions for comparison with earlier irradiations performed at CMAM (Madrid, Spain) [14].

It is worthy to mention that these low irradiation fluences were used in order to prevent breaking of the samples due to the total strain among the amorphous nanotracks embedded into the crystalline lithium niobate. At higher fluences the samples do not survive at all and the large thickness of the optical barrier originates an excessive strain producing a collapse of the sample. Moreover, a clear anisotropic behaviour of the strain is observed in the crystallographic orientation (*X*, *Z*-cut) of the irradiated samples for the same irradiation fluence (**Fig. 2**). On the other hand, must be mentioned that some strategies during the irradiation experiments can be carried out with the aim of tailoring the large thickness of the barrier, either by decreasing the ion energy or by irradiating at an angle, and therefore, this could diminish the total strain and would prevent breaking of the samples.

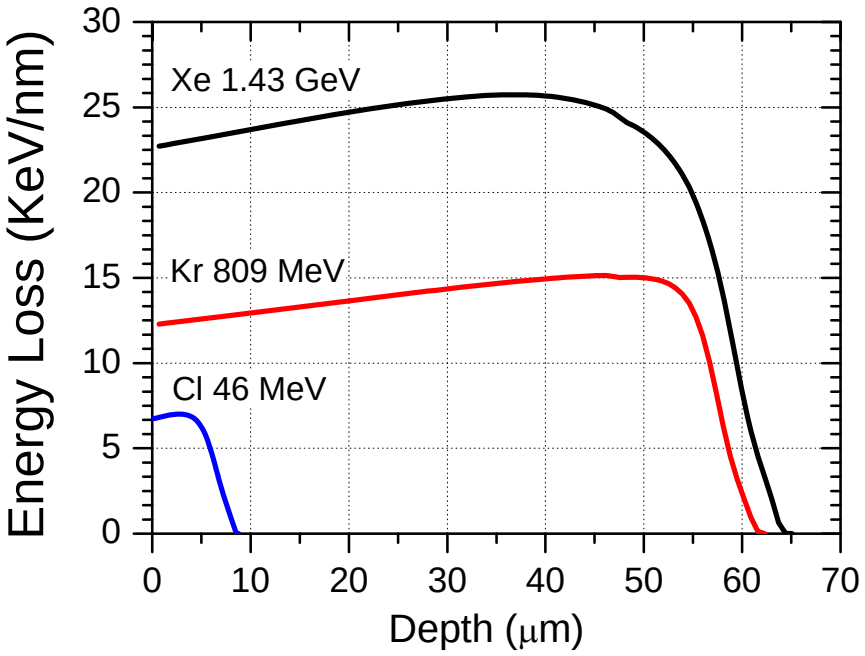

Fig. 1. Electronic energy loss of Kr (809 MeV) and Xe 1432 MeV as a function of penetration depth in $LiNbO_3$ obtained with the SRIM-2008 code [19, 20]. For comparison with earlier experiments [14], the case of Cl (46 MeV) is also shown.

Ion	Energy (MeV)	Energy (MeV/amu)	S_e surface (keV/nm)	S_e max. (keV/nm)	S_n max. (keV/nm)	R_p (μm)
^{78}Kr	809	10.4	12.3	15.1	0.5	62
^{129}Xe	1432	11.1	22.7	25.7	0.9	65

Table 1. Irradiation parameters including the electronic energy loss (S_e) at the sample surface and at the Bragg maximum as well as the maximum nuclear energy loss (S_n) and the projected ion range (R_p) according to the SRIM-2008 code [19, 20].

10.3. Optical characterization: refractive index profiles.

$LiNbO_3$ samples irradiated with high-energy Kr or Xe ions (**Table I**) indeed show a surface layer that acts as an optical waveguide. This behavior is illustrated in the optical micrographs of **Fig. 3** taken from the polished edge of a crystal exposed to 2×10^{11} Xe at/cm^2. The irradiated layer (left side) can clearly be seen in the transmission mode, **Fig. 3 (a)**, and in the dark-field reflexion mode (**R-DF**), **Fig. 3 (b)**. In the standard bright-field reflexion mode (**R-BF**, **3 (c)**) only a faint line defines the end of the ion range. The measured thickness of the irradiated layer is ~50 μm which is fair agreement with the ion range predicted by the SRIM-2008 code (cf. **Fig.1**).

The surface refractive index profile has been determined by the dark-modes technique at $\lambda = 633$ nm (see **Chapter 4**. *Section 4.7.3.1*). In all cases a quasi-continuum distribution of faint modes was observed for the ordinary refractive index. Due to the large thickness of the

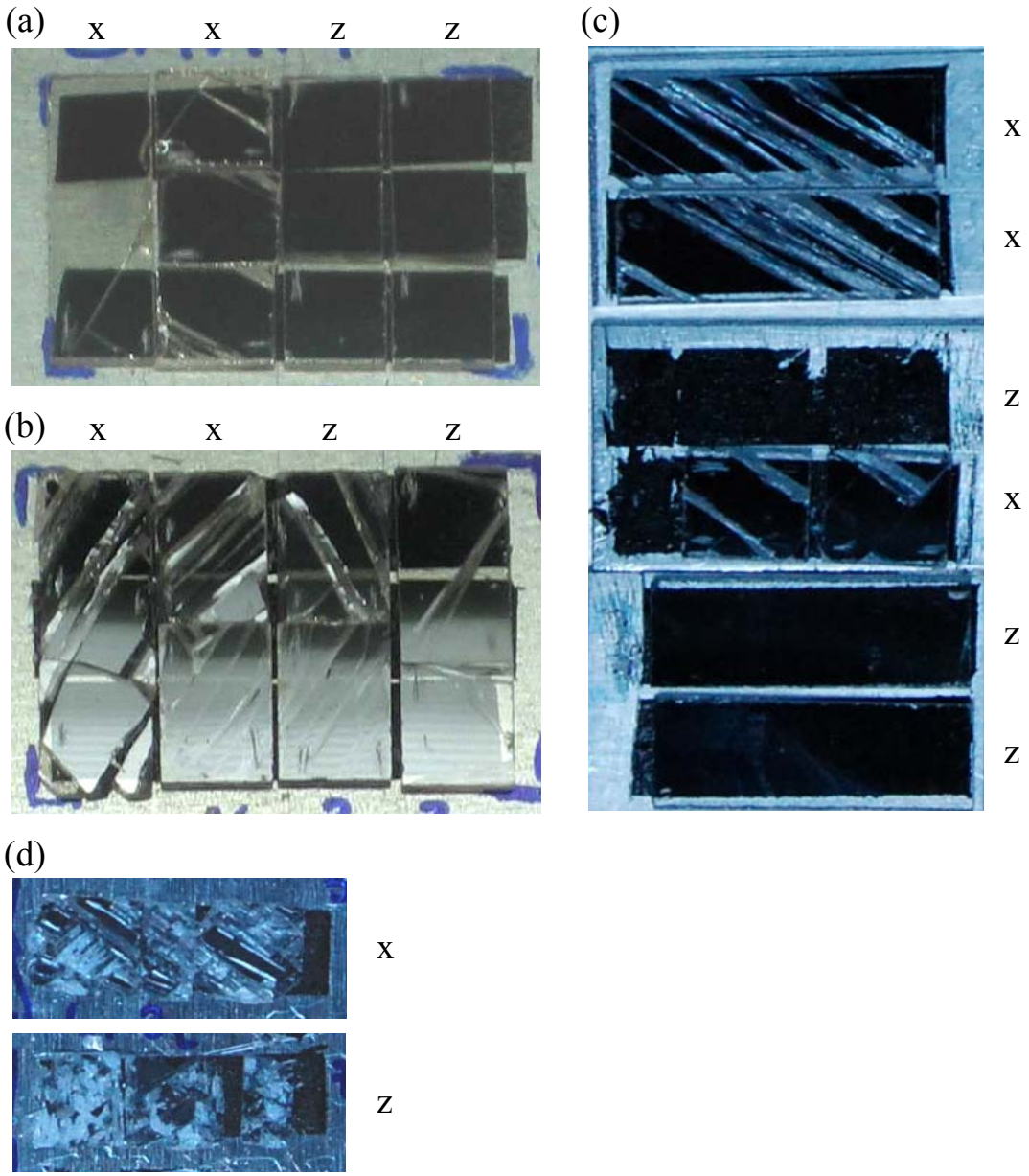

Fig. 2 Photographs of cracks developing at around ±45º on *X*-cut and *Z*-cut samples upon irradiation with 809 MeV Kr-ions at fluences of 2 x10^{11} cm^{-2} **(a)** and 4 x$10^{11}$$cm^{-2}$ **(b)**; and with Xe-ions of energy 1432 MeV at fluences of 2 x10^{11} cm^{-2} **(c)** and 8 x10^{11} cm^{-2} **(d)**. For comparison *Z*-cut samples are included. In the latter case surface damage is observed at high fluence (8 x10^{11} cm^{-2}) but follows no clear pattern unlike the *X*-cut samples. All the samples were glued on metallic holders by means of graphite tape.

waveguide the evanescent wave at the surface of the propagating modes for visible wavelength should be quite small decreasing the prism-coupling efficiency. In general, no modes could be observed for the extraordinary polarization with the prism coupling technique (see *Section 8.6. Discussion*), although propagation for both polarizations was possible by end-coupling through the polished edges. For the ordinary polarization we measured the first modes as well as the last mode (i.e. of effective index close to the barrier refractive index). Results for the samples irradiated with Kr ions are shown in **Fig. 4**, for the three fluences indicated.

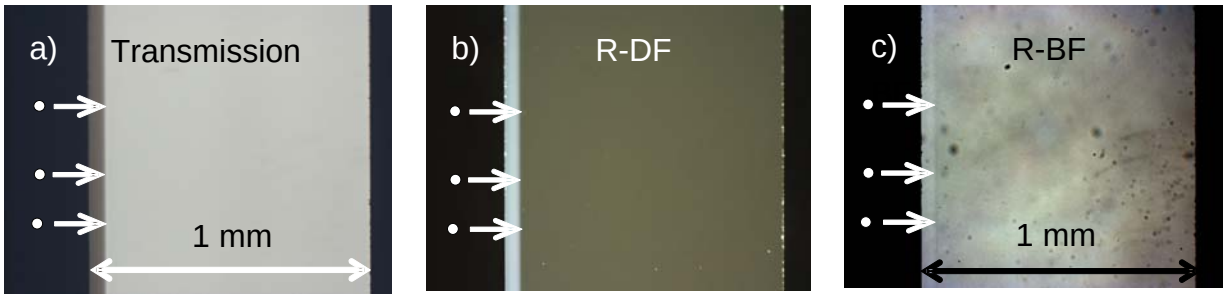

Fig. 3. Optical micrographs from the polished edge of 1-mm thick *z*-cut $LiNbO_3$ samples irradiated (from left to right) with Xe ions of fluence 2 x10^{11} cm^{-2} recorded in **(a)** transmission mode where the absorbing irradiated layer appears darker, **(b)** dark-field reflexion mode where the irradiated layer appears brighter than the substrate due to scattering centers, and **(c)** standard bright-field reflexion mode where a faint line at the depth of the end of ion range appears with different contrast.

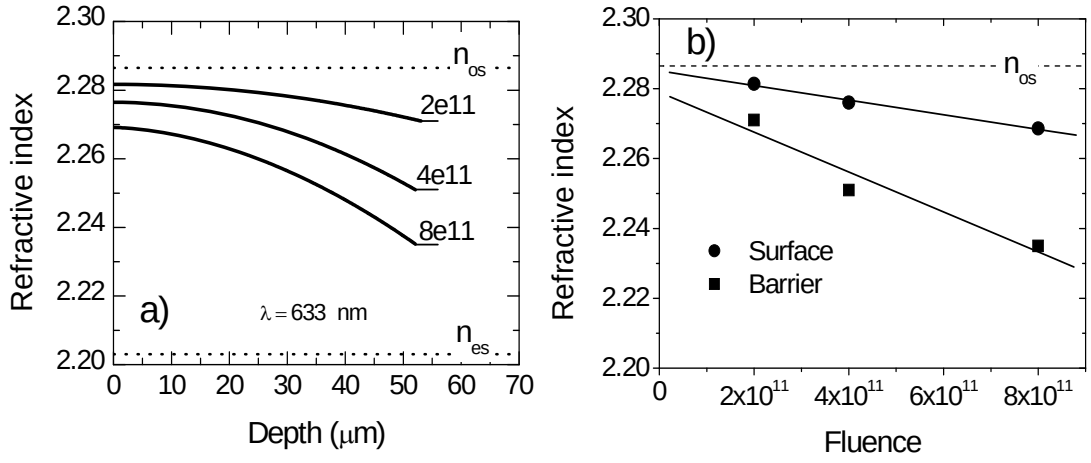

Fig. 4. (a) Refractive index profiles (λ = 633 nm) determined from the dark modes measured for samples irradiated with Kr (809 MeV) at the three fluences indicated (2 x10^{11}, 4 x10^{11} and 8 x10^{11} at/cm^2). The substrate refractive indices of $LiNbO_3$ (n_{os} and n_{es}) are shown as dotted lines. **(b)** Refractive index vs fluence determined at the surface from the index profiles (closed circles) and measured for the optical barrier layer (closed squares).

For the fluences 2 x10^{11} and 4 x10^{11} at/cm^2 35 and 43 evenly distributed modes were observed, respectively. With these data a linear function $N_m(m)$ of the mode effective index (N_m) vs mode number (m) was calculated and the refractive index profiles were reconstructed following a standard algorithm based on the Wentzel-Kramer-Brillouin (WKB) approximation valid for smooth index profiles [21] (see **Chapter 4**. *Section 4.7.3.1.2*). The sample irradiated with fluence 8 x10^{11} cm^{-2} broke before having done the mode counting, so its refractive index profile was simply plotted as a proportional one to the one obtained for the fluence 4 x10^{11} cm^{-2} using the measured surface and barrier refractive indices. The short horizontal lines at the end of each index profile, closed to the label (fluence in at/cm^2 units), represent the respective refractive indices of the effective substrate and optical barrier, i.e. when continuous light coupling takes place for any angle. The horizontal dotted lines represent the principal refractive

indices n_{os} (ordinary) and n_{es} (extraordinary) of the substrate. The refractive index values at the surface and at the barrier as a function of fluence as derived from **Fig. 4 (a)** are shown in **Fig. 4 (b)**. For an irradiation with 8 x10^{11} Kr at/cm^2, the overall refractive index jump reaches $\Delta n \sim 0.04$. For higher fluences, the samples break due to irradiation-induced stress. For fluences below 1 x10^{11} cm^{-2}, no modes could be observed.

10.4. Complementary RBS/C data.

Rutherford backscattering experiments in channeling configuration (RBS/C) is a powerful technique to measure the damage or disorder induced near the surface. With He of 2 MeV energy a thickness of about 2 μm can be probed. This information is useful as a cross-check for the optical data and allows for a more complete analysis of the results (see *Section 8.7. Summary and conclusions*). Basically, RBS/C data yield the damage fraction *f* generated at the surface as a function of electronic stopping power S_e and ion fluence ϕ. This fraction is readily derived from the de-channeling yield of an incident beam placed under channeling conditions. Usually, for cylindrical amorphous tracks of radius *r*, the analysis of the damage fraction versus fluence (ϕ) is performed using a Poisson law $f = 1 - exp(-\pi r^2 \phi)$ [22]. In the present experiment and taking into account previous results [14], in the low fluence regime it is possible to make the following approximation $f = \pi r^2 \phi$, and, consequently, to deduce the track radius by a linear fit as proposed in the **Figure 5 (b)**. Therefore, RBS/C experiments yield the track radius for any ion and energy.

Some complementary RBS/C experiments have been carried out in CMAM in the samples of this work and are shown in the **Figure 5 (a)** (the Kr case). It shows typical backscattering spectra obtained from a 2-MeV $^4He^+$ analysis of irradiated *z*-cut $LiNbO_3$ samples with Kr 809 MeV ions. Spectra recorded in channeling geometry, correspond to the three fluences studied (ϕ = 5 x10^{10}, 2 x10^{11} and 4 x10^{11} at/cm^2). The aligned and random spectra obtained on a virgin crystal are also presented for comparison. The damage fraction obtained are shown in **Fig. 5 (b)** and the surface track radius obtained with the analysis indicated is ≈ 2 nm, close to the literature values (see **Chapter 1**. *Section 1.4.2*. **Fig. 7**, Ref [12]).

The radius evolution versus the thickness, presented in **Figure 7 (a)** in the section related to the modelling of the refractive index (*Section 8.6*), is the result of a calculation of track radii using the inelastic thermal spike model (*i-TS*) developed by Meftah et al. [12] and applied in the present case of Kr irradiation.

10.5. Linear and nonlinear optical performance.

Relevant parameters for photonic applications include light propagation losses (see **Chapter 4**. *Section 4.7.3.2*) and second order nonlinear optical coefficients (d_{33} for $LiNbO_3$) (see **Chapter 2**. *Section 2.6.2*). Information about propagation losses was obtained by the light scattering method on samples ~2 cm long. Most reliable data for Xe-irradiated samples yield attenuation values in the range 2.6 to 4.5 dB/cm. Prior to this measurement, the samples were annealed in oxygen atmosphere (1 h, at 150 ºC) to remove absorption introduced by the ion irradiation. The refractive index profiles and the damage fraction measured by RBS/C remained unchanged after this annealing process. As example **Figure 6** shows the image for measuring

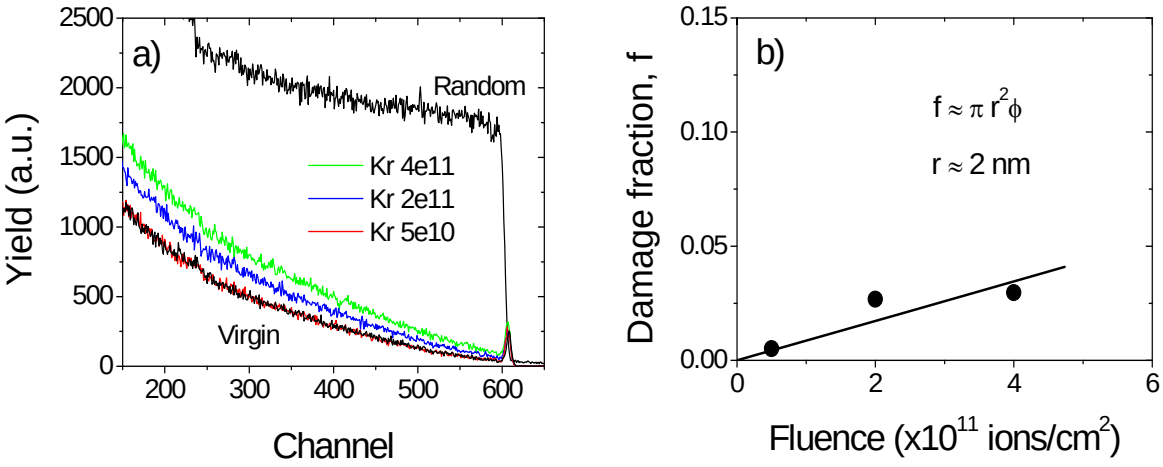

Fig. 5. (a) RBS spectra in channeling and random orientation measured with He (2 MeV) for *z*-cut samples irradiated with Kr ions at 809 MeV incident energy at different fluences (5 x10^{10}, 2 x10^{11} and 4 x10^{11} at/cm^2), indicated in the labels. The Nb surface peak is located around energy channel 600. **(b)** damage fraction (factor f) vs fluence obtained from the RBS/C spectra.

propagation losses of the waveguide in the case of 1-mm thick *z*-cut $LiNbO_3$ samples irradiated with ^{129}Xe 1432 MeV ions of fluence 2 x10^{11} cm^{-2}, where the light was in coupled with a rutile prism, and then propagated along the waveguide for around 20 mm.

The second harmonic generation (SHG) response has been measured in reflection geometry at a fundamental wavelength of 532 nm by the method described in Ref. [23]. The relative d_{33} coefficient amounts to 0.5-0.7 of the values for crystalline lithium niobate, and it is not much dependent on fluence, suggesting that light scattering by the amorphous tracks does not constitute the main mechanism for the losses. For samples irradiated with Xe ions, the coefficient remains at 90 % of the unirradiated value. These measured values are lower than expected if we take into account that, according to the RBS/C data, the amorphous fraction at the surface is less than 5 %. This could be due to partial ferroelectric domain reversal or depolarization around the amorphous tracks caused either by the strong electronic excitation or the high temperatures reached around each ion tracks [24]. It might be possible in the future to improve this performance by suitable annealing and/or repolarization treatments [25, 26].

10.6. Discussion: Modeling of the refractive index profiles.

Previous experiments have shown that the irradiation of lithium niobate with high energy heavy ions (E > 0.1 MeV/amu) generates along the ion trajectories axially symmetric amorphous tracks. The tracks have a diameter of a few nanometers and are embedded in the crystalline matrix. When the projectile penetrates into the target, the track radius thus first increases due to the increase in energy loss and to the *velocity effect* (i.e. the amorphization threshold is lower at lower ion velocity) and then decreases once the Bragg maximum has been surpassed. This is, just, the information contained in **Fig. 7 (a).**

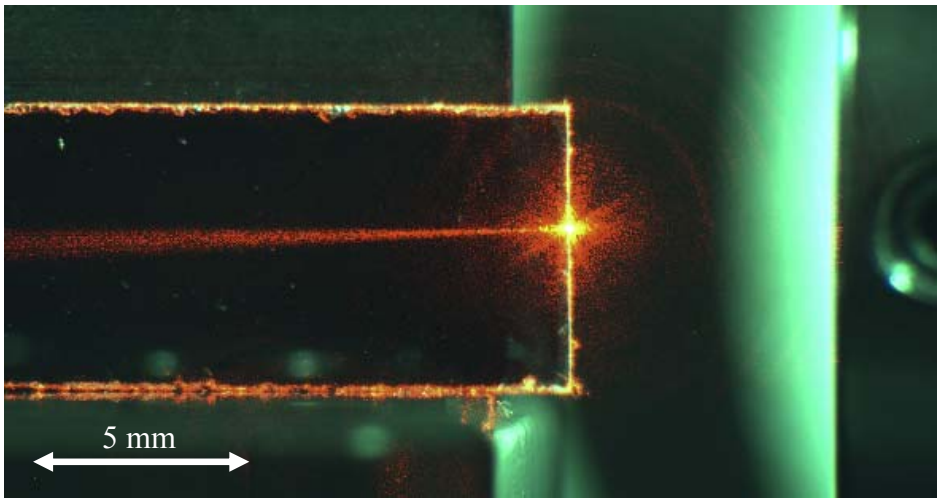

Fig. 6. Light propagation along the waveguide of z-cut $LiNbO_3$ sample irradiated with ^{129}Xe 1432 MeV ions at fluence 2 x10^{11} at/cm^2. Image used for the measurement of propagation losses of the waveguide with the scattering light technique.

We have then calculated the dependence of refractive index on depth by considering the irradiated $LiNbO_3$ crystal as an *effective dielectric medium* consisting of the isotropic amorphous tracks (dielectric constant $\varepsilon_a = n_a^2 = 4.41$) and the crystalline matrix (dielectric constant $\varepsilon_o = n_o^2 = 5.23$ (*ordinary*) and $\varepsilon_e = n_e^2 = 4.84$ (*extraordinary*)). It is assumed that the crystalline regions between the well-separated amorphous tracks keep the same refractive indices as the $LiNbO_3$ matrix, i.e., the effects of point defects and mechanical stresses are neglected. Under these conditions the dielectric constant of the effective medium for either ordinary or extraordinary polarization is

$$\bar{\varepsilon}_{e,o} = n_{e,o}^2 = f\varepsilon_a + (1-f)\varepsilon_{e,o} \qquad (1)$$

where f ($f = \phi\pi r^2$) is the amorphous fraction, ϕ the ion fluence and r the track radius.

The refractive index profiles derived from this analysis, are shown in **Fig. 7 (b)** for Kr at the fluences of 2 x10^{11} and 4 x10^{11} at/cm^2 together with the corresponding profiles optically determined (same as in **Fig. 4 (a)**). The profile calculated from the effective medium is in good agreement with the dark-mode data.

It may be surprising that dark modes have been rarely observed in this work for extraordinary light with the prism-coupling. One possible reason is that, according to the effective medium approach, the change in the refractive index is somewhat higher for the ordinary index (see **Fig. 7**). Since this effect is small one can also invoke a more significant but subtle effect. It has been shown that in addition to full amorphization for stopping powers above threshold, irradiation creates isolated defects that also modify the refractive indices [14]. Due to the structure of damage it has been found that even for the non-amorphized crystalline regions the ordinary refractive index experiences a small decrease whereas the extraordinary refractive index increases about twice such decrease in the ordinary index [27]. This will cause a reduction in the overall refractive index of the effective medium balancing or even surpassing the decrease caused by the amorphization. Further work by means of edge-polished micro-reflectance should

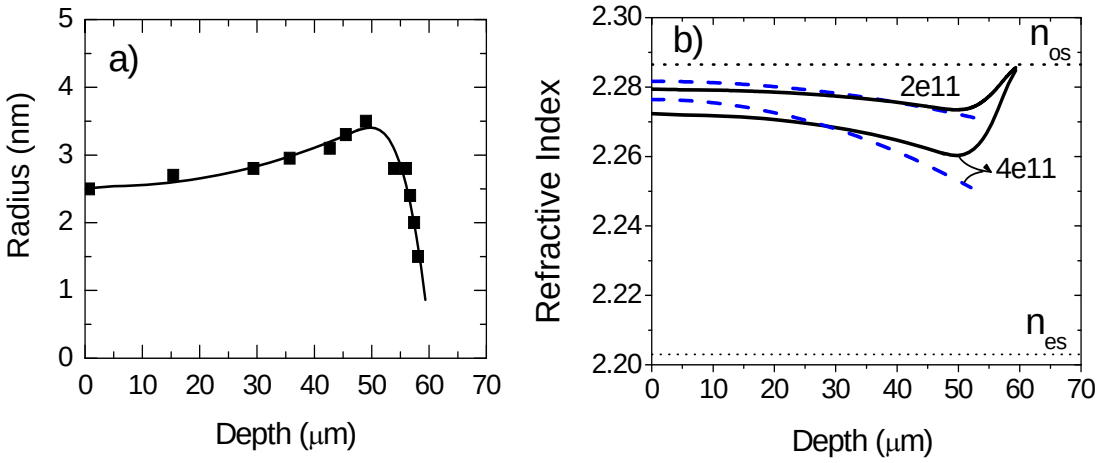

Fig. 7. (a) Track radius vs depth obtained (in the case of Kr 809 MeV irradiations) from a calculation using the inelastic thermal spike model (*i-TS*) developed by Meftah et al. [10] and **(b)** Theoretical refractive index profiles that would correspond to the track profile shown in **(a)** for the fluences of 2 x10^{11} and 4 x10^{11} cm^{-2}, calculated according to an *effective medium approach* as discussed in the text. The index profile optically determined for the same fluences are shown (dashed line).

be performed to clarify this behaviour. Such a detailed study including effects of strain/stress could also help to further improve the matching of the ordinary refractive index profile between the theoretical one and the measured one shown in **Fig. 7 (b)**.

Now it becomes clear that a surface layer of modified refractive index can be generated and should be responsible for light waveguiding. Our theoretical argument predicts a refractive index jump quite close to that of the experiment. Another simple and clear prediction, but relevant for the guided infrared applications, is the large thickness of the optical barrier that would provide enough optical confinement, as can be seen in **Fig, 7 (b)**.

10.7. Summary and conclusions.

The irradiation with swift heavy-mass ions such as Kr and Xe of energy around 10 MeV/amu and fluences as low as (2-8) x10^{11} cm^{-2} produces thick optical waveguides (~ 40 μm) keeping a significant fraction of the second-order non-linear optical response and presenting reasonably low propagation losses (~ 4 dB/cm) in the visible wavelength range. The waveguiding layer is a two-component medium consisting of nanometer-sized amorphous track cylinders aligned perpendicular to the surface and embedded in the essentially undisturbed crystalline lithium niobate matrix. The optical waveguiding can be understood in terms of an average effective medium. With increasing depth, the track diameter becomes slightly larger following the increase of the electronic stopping power and the decrease of the amorphization threshold. The modified layer is therefore also characterized by a damage fraction and refractive index which increases with depth. Preliminary experiments suggest the application of such waveguides in the medium infrared range for astrophysics and other fields. The performance should be significantly better for wavelengths in the mid-infrared where both scattering (due to

inhomogeneities) and absorption bands are known to be much weaker. The large thickness of the optical barrier should provide enough optical confinement. Certainly, the irradiated thickness could be easily decreased and tuned for realistic infrared applications in the wavelength range < 10 microns, either by decreasing the ion energy or by irradiating at an angle. This could decrease the total strain and would prevent breaking of the samples at higher fluences if these are required for specific tailoring of the index profile. Further work should be devoted to optimize the irradiation parameters (ion, energy, fluence, angle of irradiation) in order to tailor the refractive index profiles and to obtain higher refractive index jumps and better optical confinement.

10.8. References.

[1] P. D. Townsend, P. J. Chandler and L. Zhang, *"Optical Effects of Ion Implantation"*, Vol., (Ed.), Cambridge University Press, Cambridge, 1994.

[2] F. Chen, X. -L. Wang and K. -M. Wang, *"Development of ion-implanted optical waveguides in optical materials: A review"*, Opt. Mater. 29 (2007) 1523-1542.

[3] F. Chen, *"Photonic guiding structures in lithium niobate crystals produced by energetic ion beams"*, J. Appl. Phys. 106 (2009) 081101.

[4] J. Olivares, G. García, A. García-Navarro, F. Agulló-López, O. Caballero and A. García-Cabañes, *"Generation of high-confinement step-like optical waveguides in $LiNbO_3$ by swift heavy ion-beam irradiation"*, Appl. Phys. Lett. 86 (2005) 183501.

[5] G. G. Bentini, M. Bianconi, M. Chiarini, L. Correra, C. Sada, P. Mazzoldi, N. Argiolas, M. Bazzan and R. Guzzi, *"Effect of low dose high energy O^{3+} implantation on refractive index and linear electro-optic properties in X-cut $LiNbO_3$:Planar optical waveguide formation and characterization"*, J. Appl. Phys 92 (2002) 6477.

[6] J. Olivares, A. García-Navarro, G. García, F. Agulló-López, F. Agulló-Rueda, A. García-Cabañes and M. Carrascosa, *"Buried amorphous layers by electronic excitation in ion-beam irradiated lithium niobate: structure and kinetics"*, J. Appl. Phys 101 (2007) 033512.

[7] M. Bianconi, N. Argiolas, M. Bazzan, G. G. Bentini, M. Chiarini, A. Cerutti, P. Mazzoldi, G. Pennestri and C. Sada, *"On the dynamics of the damage growth in 5 MeV oxygen-implanted lithium niobate"*, Appl. Phys. Lett. 87 (2005) 072901.

[8] A. Rivera, J. Olivares, G. García, J. M. Cabrera, F. Agulló-Rueda and F. Agulló-López, *"Giant enhancement of material damage associated to electronic excitation during ion irradiation: The case of $LiNbO_3$"*, Phys. Status Solidi A 206 (2009) 1109-1116.

[9] M. Toulemonde, C. Trautmann, E. Balanzat, K. Horjt, A. Weidinger, *"Track formation and fabrication of nanostructures with MeV-ion beams"*, Nucl. Instr. Meth. B 216 (2004) 1-8.

[10] B. Canut, S. M. M. Ramos, R. Brenier, P. Thevenard, J. L. Loubet, M. Toulemonde, *"Surface modification of $LiNbO_3$ single crystals by swift heavy ions"*, Nucl. Instrum. Methods B 107 (1996) 194 -198.

[11] A. Meftah, F. Brisard, J. M. Constantini, M. Hage-Ali, J. P. Stoquert, F. Studer and M. Toulemonde, *"Swift heavy ions in magnetic insulators: A damage-cross-section velocity effect"*, Phys. Rev. B 48 (1993) 920-925.

[12] A. Meftah, J. M. Constantini, N. Khalfaoui, S. Boudjadar, J. P. Stoquert, F. Studer and M. Toulemonde, *"Experimental determination of track cross-section in $Gd_3Ga_5O_{12}$ and comparison to the inelastic thermal spike model applied to several materials"*, Nucl. Instrum. Methods B 237 (2005) 563-574.

[13] A. Majkić, M. Koechlin, G. Poberaj and P. Günter *"Optical microring resonators in fluorine-implanted lithium niobate"*, Optics Express 16 (2008) 8769.

[14] J. Olivares, A. García-Navarro, G. García, A. Méndez and F. Agulló-López, *"Optical determination of three-dimensional nanotrack profiles generated by single swift-heavy ion impacts in lithium niobate"*, Appl. Phys. Lett. 89 (2006) 071923.

[15] A. García-Navarro, J. Olivares, G. García, F. Agulló-López, S. García-Blanco, C. Merchant and J. Stewart Aitchison, *"Fabrication of optical waveguides in KGW by swift heavy ion beam irradiation"*, Nucl. Instr. and Meth. B 249 (2006) 177-180.

[16] C. A. Merchant, P. Scrutton, S. García-Blanco, C. Hnatovsky, R. S. Taylor, A. García-Navarro, G. García, F. Agulló-López, J. Olivares, A. S. Helmy and J. S. Aitchison, *"High Resolution refractive index and micro-raman spectroscopy of planar waveguides in $KGd(WO_4)_2$ formed by swift heavy ion irradiation"*, IEEE J. Quantum Electronics 45 (2009) 373-379.

[17] J. Bland-Hawthorn, and P. Kern, *"Astrophotonics: a new era for astronomical instruments"*, Opt. Express 17 (2009) 1880-1884.

[18] L. Labadie, and O. Wallner, *"Mid-infrared guided optics: a perspective for astronomical instruments"*, Opt. Express 17 (2009) 1947-1962.

[19] J. F. Ziegler, J. P. Biersack and U. Littmark, (Ed.), *The Stopping and Ranges of Ions in Solids*, Pergamon Press, New York, 1985.

[20] J. Ziegler, computer code SRIM version 2008, (http://www.srim.org).

[21] K. S. Chiang, *"Construction of refractive-index profiles of planar dielectric waveguides from the distribution of effective indexes"*, J. Lightwave Technology 3 (1985) 385-391.

[22] P. Thévenard, G. Guiraud, C. H. S. Dupuy and B. Delaunay, *"Assumption of F-centre creation in LiF bombarded with high-energy particles"*, Radiat. Eff. 32 (1977) 83-90.

[23] J. Rams, and J. M. Cabrera, *"Second harmonic generation in the strong absorption regime"*, J. Mod. Optics 47 (2000) 1659-1669.

[24] M. Toulemonde, C. Dufour and E. Paumier *"Transient thermal process after a high-energy heavy-ion irradiation of amorphous metals and semiconductors"*, Phys. Rev. B 46 (1992) 14362-14369.

[25] O. Caballero-Calero, M. Kösters, T. Woike, K. Buse, A. García-Cabañes and M. Carrascosa, *"Electric field periodical poling of lithium niobate crystals after soft-proton-exchanged"*, Appl. Phys. B 88 (2007) 75-78.

[26] O. Caballero-Calero, A. García-Cabañes, M. Carrascosa, F. Agulló-López, J. Villarroel, M. Crespillo and J. Olivares, *"Periodic poling of optical waveguides produced by swift-heavy ion irradiation in $LiNbO_3$"*, Appl. Phys. B. 95 (2009) 435-439.

[27] G. García, J. Olivares, F. Agulló-López, A. García-Navarro, F. Agulló-Rueda, A. García-Cabañes and M. Carrascosa, *"Effect of local rotations on the optical response of $LiNbO_3$: Application to ion-beam damage"*, Europhys. Lett. 76 (2006) 1123-1129.

Chapter 11

Conclusions.

In the following paragraphs, the main conclusions obtained throughout this Thesis work in the attempt at deepen our understanding about the ion beam damage due to electronic excitation, will be presented.

From the analysis of the kinetics of the evolution of the ion beam damage in the electronic regime, addressing with the contribution of the amorphous core and the defective point-like halo, it has to be pointed out:

- We have conclusively shown that the structural damage induced on dielectric materials by swift ions, in which the electronic stopping power is dominant, has some peculiar features such as, thresholding and cumulative character, at difference with the nuclear damage.
- It has been found that the cumulative damage behaviour under successive irradiation is not consistent with the Thermal Spike model. There is a clear transition from a Poisson-like ($n = 1$) amorphization kinetics behaviour for stopping powers well above threshold (typical of a direct process, *direct impact model,* as a result of track overlapping) to an Avrami-like (sigmoidal, $n > 1$) evolution below threshold, where no amorphization should be induced, so that a certain incubation fluence is need. The Avrami curves present parameters n and ϕ_0, that steadily increase on decreasing electronic stopping power.
- The amount of disorder that is assessed by RBS-C in $LiNbO_3$ has been analyzed using a recently proposed model - non-radiative exciton-decay model- to calculate the defect profile generated by every ion impact. The analysis describes the de-channeling caused at the surface by using a "filter" function. It is concluded that the amorphized area (core) of the track is markedly overestimated for stopping powers near the threshold value. The proposed scheme to describe the formation of the halo and predict its diameter, represents, just a first attempt, for a quantitative analysis of the problem.
- A MonteCarlo approach to the non-radiative exciton-decay model has been developed. It takes into account the statistical spatial distribution of the ion impacts at any depth in the sample. At variance with the previous analytical formulation, the new method is able to describe adequately the range of low irradiation fluences, where overlapping is still poor and statistical divergences of the true amorphized area, with regard to the average values, are quite significant.
- A validation of the Model has been shown through the well reproduction achieved of the experimental Avrami's and Poisson´s -type kinetics for amorphization. Moreover, the thickness of the layers having a mixed amorphous-crystalline composition has been obtained as a function of fluence.

Related to the nanopores obtained by chemical etching on ion irradiated $LiNbO_3$, it is worthy to remark:

- It is the first time observation of the well-faceted pore morphology in lithium niobate. Pores initially exhibit approximately axial symmetry, but under extended etching, they develop well-defined facets that correspond to particular crystalline planes.
- It has been confirmed dramatical variations of the nanopores dimensions and morphology strongly dependent on both, the concentration of the acid solution, the etching time, and the irradiation parameters.
- It has been found that thermal annealing treatments in the range of 150 ºC to 300ºC do not recover entirely the latent tracks. Furthermore, a clear elongation of the pore shape is enhanced, giving rise an anisotropic morphology.
- Two etching regimes with different morphologies and etching rates have been clearly identified:

  (1) The fast initial stage depends on the stopping power of the ion and could be associated to the track core including the highly defective surrounding halo.

  (2) The initial radial etch rate stage is followed by a linear slower stage, where the facets develop. The slow stage has a rate of a few nm/min depending on the concentration and composition of the acid solution and should correspond to the etching of crystalline $LiNbO_3$, i.e., the etching rate should be essentially equal to that of the bulk unirradiated material.
- It has been found that the irradiation fluence turns into a critical parameter. The higher fluences the higher etching rates, due to stress perpendicular to the ion tracks, leading to a very rough surface after the chemical process.
- Respect to the acid blends of HF and HNO_3, the etching rate was found to be linearly dependent on the acid concentration (c_{HF}), and constant over time. Hence, the pores grow linearly with etching time.
- The pores morphologies and depths obtained by AFM technique have been confirmed from HRTEM measurements, being in excellent accordance. In addition, valuable complementary structural information about the underlying ion tracks has been obtained.
- It has been demonstrated that desired pore structures can be tailored by fairly adjusting the irradiation and etching parameters. A clear different behaviour, related to the ions energies, have been shown by the structures revealed after etching from the swift heavy ions from GSI and Ganil Facilities, and the heavy ions (Bromine irradiations).

  (1) It seems that especially the projected range is responsible for a step-like increase of the pore diameters and the surface aspect ratio. A critical track length could not be determined, but the diameter was four times larger for Kr 809 MeV (L = 59 μm) ion tracks compared to Br 46 MeV (L = 4.5 μm)

irradiated material, both having approximately the same stopping power at the surface.

(2) In contra, the depth evolution was found to depend on the ion energy, the stopping power and on the amorphous track length. From our data it seems plausible to assume that the defect concentration governs the etch rate in depth, which presumably reaches a maximum around 12 keV/nm.

- It has been achieved a high degree of confidence in reproducing uniform nanopores in sizes and shapes, all of which, accompanied by the resulting optical grade flattened surfaces, turn them into very promising for nonlinear applications in optics and nanosensors.

According to the study of recrystallization kinetics of single amorphous tracks and homogeneous layers submitted to annealing treatments at different temperatures, the most remarkable conclusions are presented:

- It has been found that, the amorphous tracks present a clearly observable recrystallization rate above 250 ºC. The annealing phenomenon is governed by interface processes as for solid-phase epitaxy. The decrease in the radius of the tracks follows a linear dependence on annealing time, and it is constant for each temperature. Hence, the areal regrowth rate, essentially the number of Nb-O_6 octahedra recrystallizing per unit of time, is not constant, neither proportional to the crystalline-amorphous boundary perimeter.
- An epitaxial-like regrowth behaviour has been found, showing two clear distinct kinetics regimes in the diminishing of the track radius respect to the annealing time, for all the temperatures under study: a first main stage, in which the recrystallization rate, that is, the crystalline-amorphous boundary movement, is around ten times faster than the rate for the second stage, in which the slowing down (cross over) appears for track radii of around 2 nm.
- The velocity is thermally activated in accordance with an Arrhenius-type dependence and an activation energy around 1.5 eV for the main initial stage, has been found. For track radii smaller than ~2 nm the track shrinkage process slows down suggesting that other mechanisms should be taken into account.
- It has been confirmed that the annealing of buried amorphous layers induces a reduction of their thicknesses in a similar temperature range. The displacement of the crystalline-amorphous boundary is also linear with annealing time and the crystallization rates are similar to those for tracks.
- The recrystallization of buried amorphous layers can be described within the same physical process and provide consistent data with those obtained for individual tracks.
- An universal scaling law has been found to describe the process, and a simple nucleation model is used to describe the observed phenomena. In addition, a model that explains the recovery of the damage has been proposed and discussed in terms

of local reordering of the basic Nb-O_6 octahedral units and epitaxial regrowth. The octahedral reordering is a first-order local process, interface-controlled regrowth, that does not depend on the long-range diffusion of point defects as vacancies or interstitials.

- A great number of applications may be favoured by the relevant implications related to the obtained results:

  (1) The accurate control of track radii by suitable annealing treatments can be used to tailor the diameter of the nanopores after suitable chemical etching.

  (2) The control of track radii allows to tailor the dielectric constant and refractive index of the outer irradiated layer and, thus, the possibilities for integrated optics devices. Also, for the photonics field, the results found for homogeneous layers allow for an adequate control of the thickness of the outer waveguide layer and even the sharpness of the waveguide boundary.

Finally, respect to novel method proposed to fabricate thick optical waveguides in $LiNbO_3$ using the electronic damage produced by swift heavy ions at ultralow irradiation fluences, it is worthy to notice:

- Thick planar optical waveguides at the surface of lithium niobate have been successfully produced using heavy mass ions (Kr and Xe) with energies in the ~10 MeV/amu range. The obtained waveguides have a thickness of 40-50 micrometers, depending on ion energy and fluence, smooth profiles and refractive index jumps up to 0.04 (λ = 633 nm). They propagate ordinary and extraordinary modes with low losses keeping a high nonlinear optical response that makes them useful for many applications.
- It has been has been carried out a study of the morphology of the tracks and their profiles in depth, combining various experimental techniques, including the measurement of refractive index profiles and RBS/C measurements. Consistent values for the partial amorphization and refractive index change at the surface have been obtained.
- In addition of the dramatical reduction in the required fluences, and thereby decreasing production time, the waveguides produced by this way have an intrinsic potential of nanostructuring.
- This first test demonstration can be extended to other crystalline materials and suggest the application of such waveguides in the medium infrared range for astrophysics and other fields. The large thickness of the optical barrier should provide enough optical confinement. Moreover, the irradiated thickness could be easily decreased and tuned for realistic applications in the wavelength range < 10 microns.

Appendix I

Brief summary of Avrami kinetics.

We here summarize the main features of the Avrami amorphization kinetics used by most workers in the field. The Avrami law for the normalized amorphous area *S* as a function of the ion fluence ϕ writes:

$$S(\phi) = 1 - \exp\{-(\phi/\phi_0)^n\} \quad \textbf{(1)}$$

and it is represented in **Fig. 1**. It depends on two parameters, *n* and ϕ_0. Main features of this kinetics are:

a) For $n > 1$ the curve has a sigmoidal shape whose initial growth rate (at $\phi = 0$) is zero.

$$\frac{dS}{d\phi} = \frac{1}{\phi_0}\left[n\left(\frac{\phi}{\phi_0}\right)^{n-1}\right]\exp\left[-\left(\frac{\phi}{\phi_0}\right)^n\right] \quad \textbf{(2.a)}$$

$$\left(\frac{dS}{d\phi}\right)_0 = 0 \quad \textbf{(2.b)}$$

The exponent *n* measures the rate of disordering, $(dS/d\phi)_{\phi_0}$ = n / eϕ_0 , at the critical fluence ϕ_0 and represents the nonlinearity of the damage response. Moreover, ϕ_0 stands for the fluence required to reach a critical level of disorder causing S(ϕ_0)= 1-1/e ≈ 0.63 of the full random (amorphous) RBS yield.

On the other hand, it presents an inflexion point ($\frac{d^2S}{dS^2} = 0$) at $\rightarrow \phi_i$

$$\phi_i = \phi_0 \sqrt[n]{\frac{n-1}{n}} \quad \textbf{(3)}$$

that is not far from the value of the parameter ϕ_0 . At the inflexion point:

$$S(\phi_i) = 1 - \exp\{-(n-1)/n\} \quad \textbf{(4.a)}$$

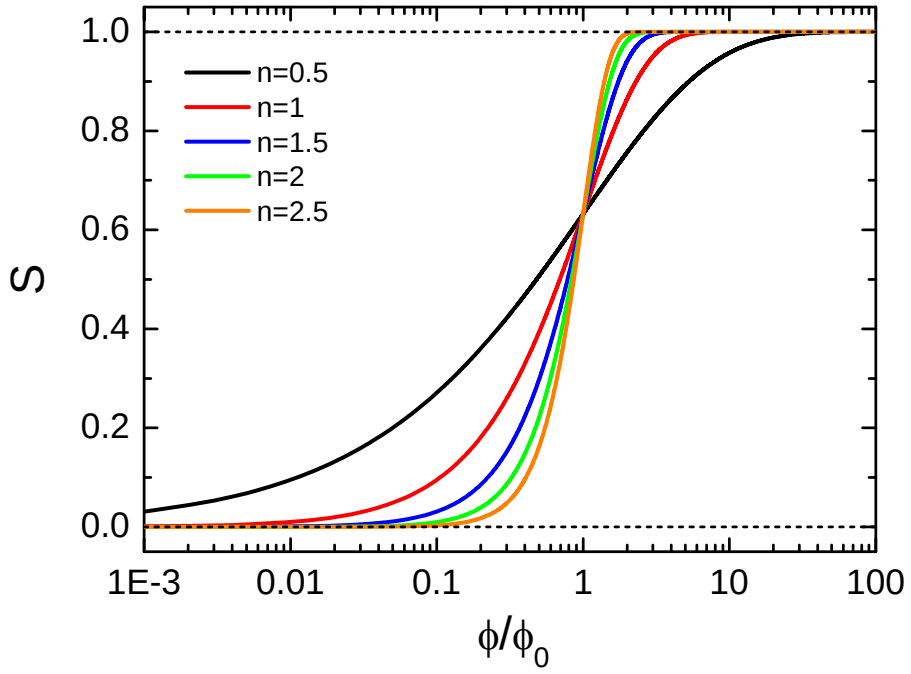

Fig. 1. Avrami curves, with ϕ normalized to the ϕ_0 value, for exponent n ranging from 0.5 to 2.5.

$$\left(\frac{dS}{d\phi}\right)_{\phi_i} = \frac{n-1}{\phi_i}\exp\{-(n-1)/n\}, \text{ or} \qquad \textbf{(4.b)}$$

$$\left(\frac{dS}{d\phi}\right)_{\phi_i} = \frac{n}{\phi_0}\left(\frac{n-1}{n}\right)^{\frac{n-1}{n}}\exp\{-(n-1)/n\} \qquad \textbf{(4.c)}$$

Note that the inflexion fluence (ϕ_i) moves from values close to 0 for n ≈ 1 to ϕ_0 for n >> 1. The corresponding normalized disordered areas (S(ϕ_i)) go from 0 to S ≈ 1-1/e ≈ 0.63 and the slopes of growth from $\left(dS/d\phi\right)_{\phi_i} \approx 1/\phi_0$ to $\approx (n-1)/e\phi_i$.

b) For $n = 1$ it evolves to a simple Poisson (exponential) curve. The curve shows a monotonic growth whose initial slope (at $\phi = 0$) is

$$S(\phi) = 1 - \exp\{-(\phi/\phi_0)\} \qquad \textbf{(5.a)}$$

$$\frac{dS}{d\phi} = \frac{1}{\phi_0}\exp\left[-\left(\frac{\phi}{\phi_0}\right)\right] \qquad \textbf{(5.b)}$$

$$\left(\frac{dS}{d\phi}\right)_0 = \frac{1}{\phi_0} \qquad \textbf{(5.c)}$$

Moreover, for the critical value of ϕ_0, $S(\phi_0) = 1\text{-}1/e \approx 0.63$, and its slope, $\left(dS / d\phi\right)_{\phi_0} = 1 / e\phi_0$.

c) Independently of the value of *n*, the function fulfils $S(\phi_0) = 1\text{-}(1/e)$, that is, if expressed as a function of the normalized variable ϕ/ϕ_0 , the family of curves spanned by the *n* parameter pivots on the single point (1, *1-1/e).*

Appendix II

Evolution of the disorder fractions and track radii during the thermal treatments.

The time scales for each annealing process are very different, being very fast the isothermal processes at highest temperatures. Hence, it is necessary to make a zoom in the time scale (*x*-axis) with the aim of following accurately the behaviour of the disorder fraction and the track radii for each irradiation fluence. The time scale has been accurate considered independent of the thermal treatment, trying to have enough experimental measurements points. With this purpose we present here for each irradiation fluence the adequate zooms in the evolution of the disorder fraction and track radii.

A. Disorder fractions.

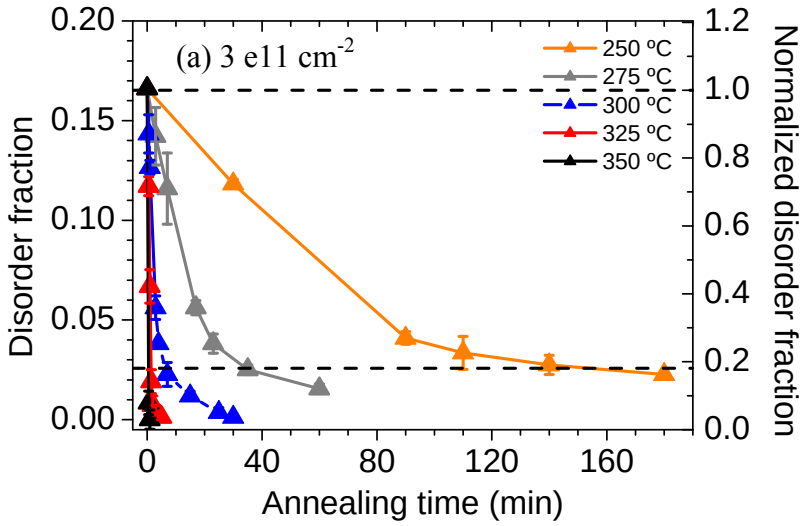

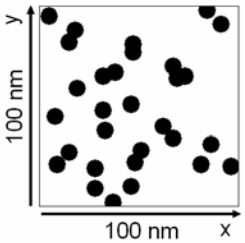

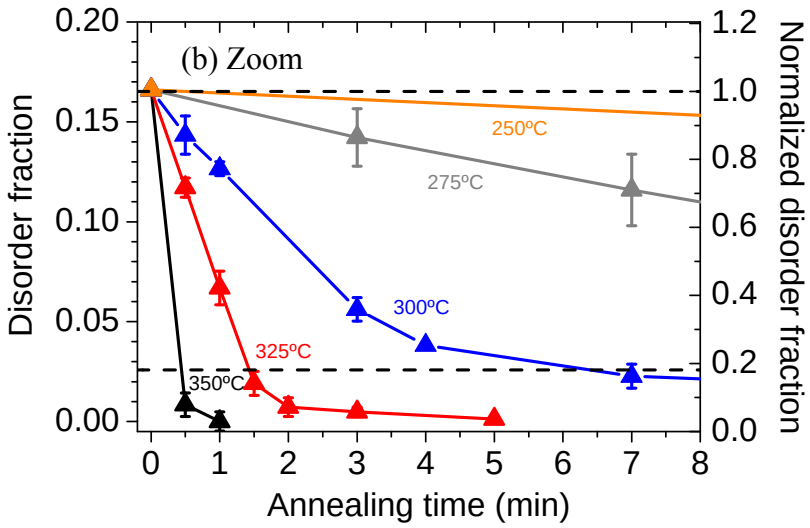

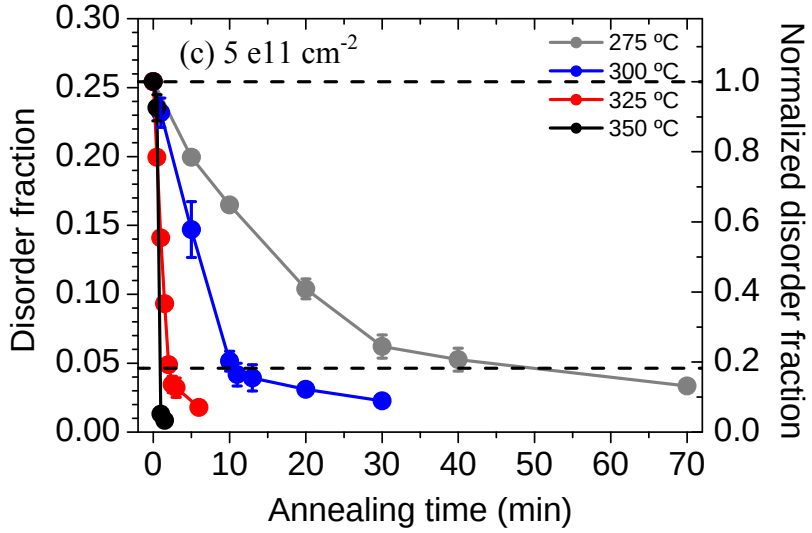
(c) 5 e11 cm-2
275 ºC
300 ºC
325 ºC
350 ºC
Disorder fraction
Normalized disorder fraction
Annealing time (min)
0.30
0.25
0.20
0.15
0.10
0.05
0.00
1.0
0.8
0.6
0.4
0.2
0.0
0
10
20
30
40
50
60
70

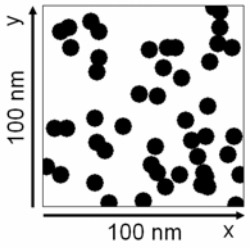
y
100 nm
100 nm
x

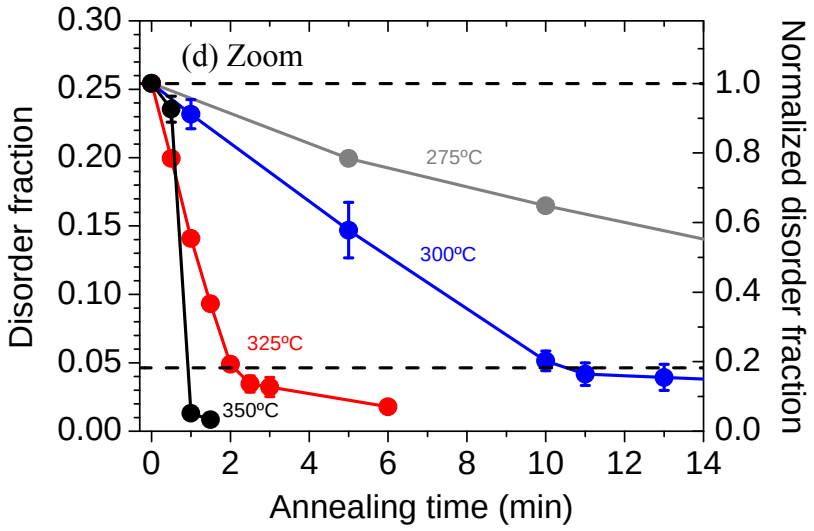
(d) Zoom
275ºC
300ºC
325ºC
350ºC
Disorder fraction
Normalized disorder fraction
Annealing time (min)
0.30
0.25
0.20
0.15
0.10
0.05
0.00
1.0
0.8
0.6
0.4
0.2
0.0
0
2
4
6
8
10
12
14

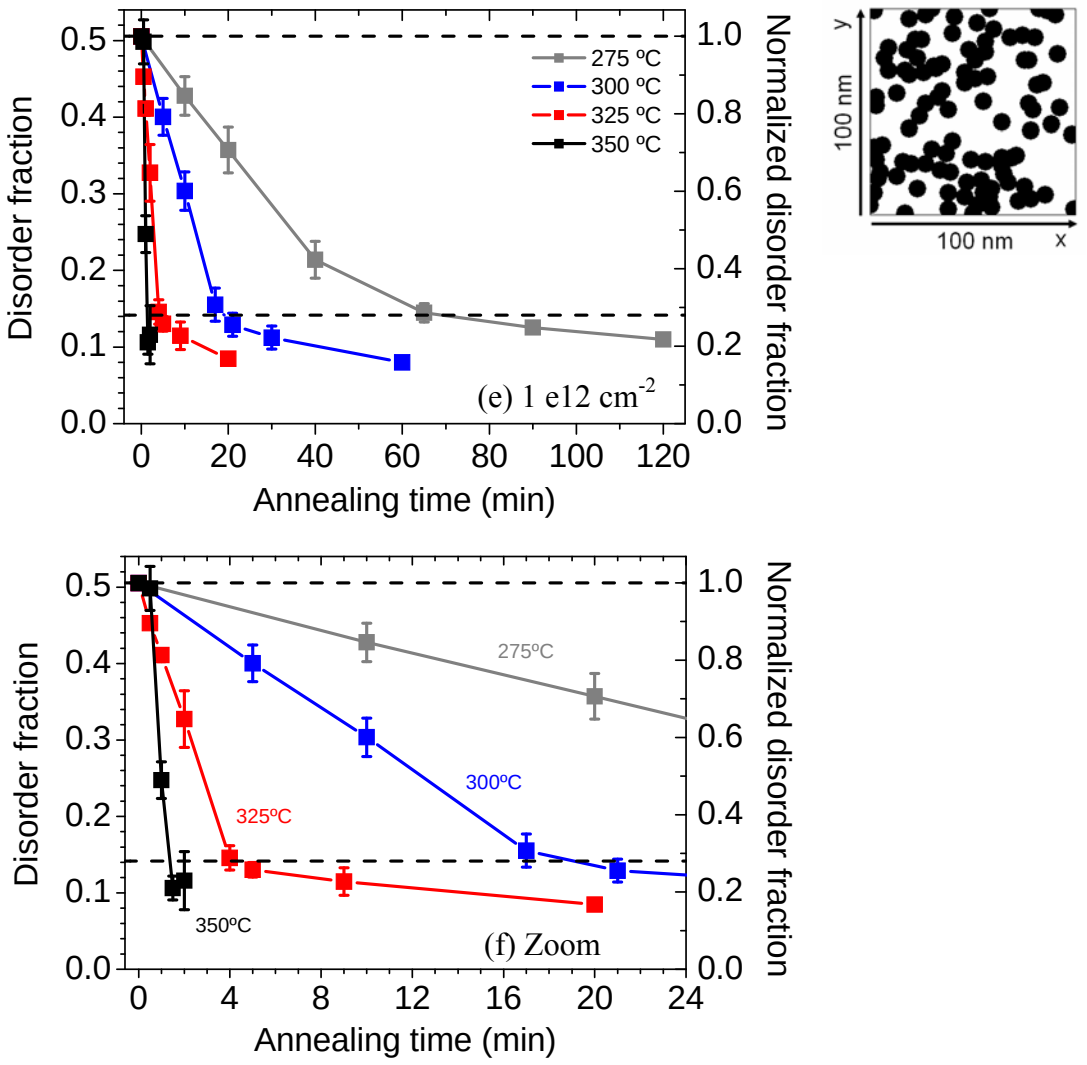

Fig. 1 (a-f). Disordered fraction obtained from RBS/C versus annealing time for the fluences **(a)** 3 x10^{11} cm^{-2}, **(c)** 5 x10^{11} cm^{-2} and **(e)** 1 x10^{12} cm^{-2}, and for the temperatures 250, 275, 300, 325 and 350 ºC, as indicated in the figures labels. **(b, d, f)** Show zooms in the adequate range for highest temperatures. The drawings next to the figures show schematic illustrations of the covered area, for each of the three fluences, simulated with random impacts of estimated track radius of 4.4 nm.

B. Track radii.

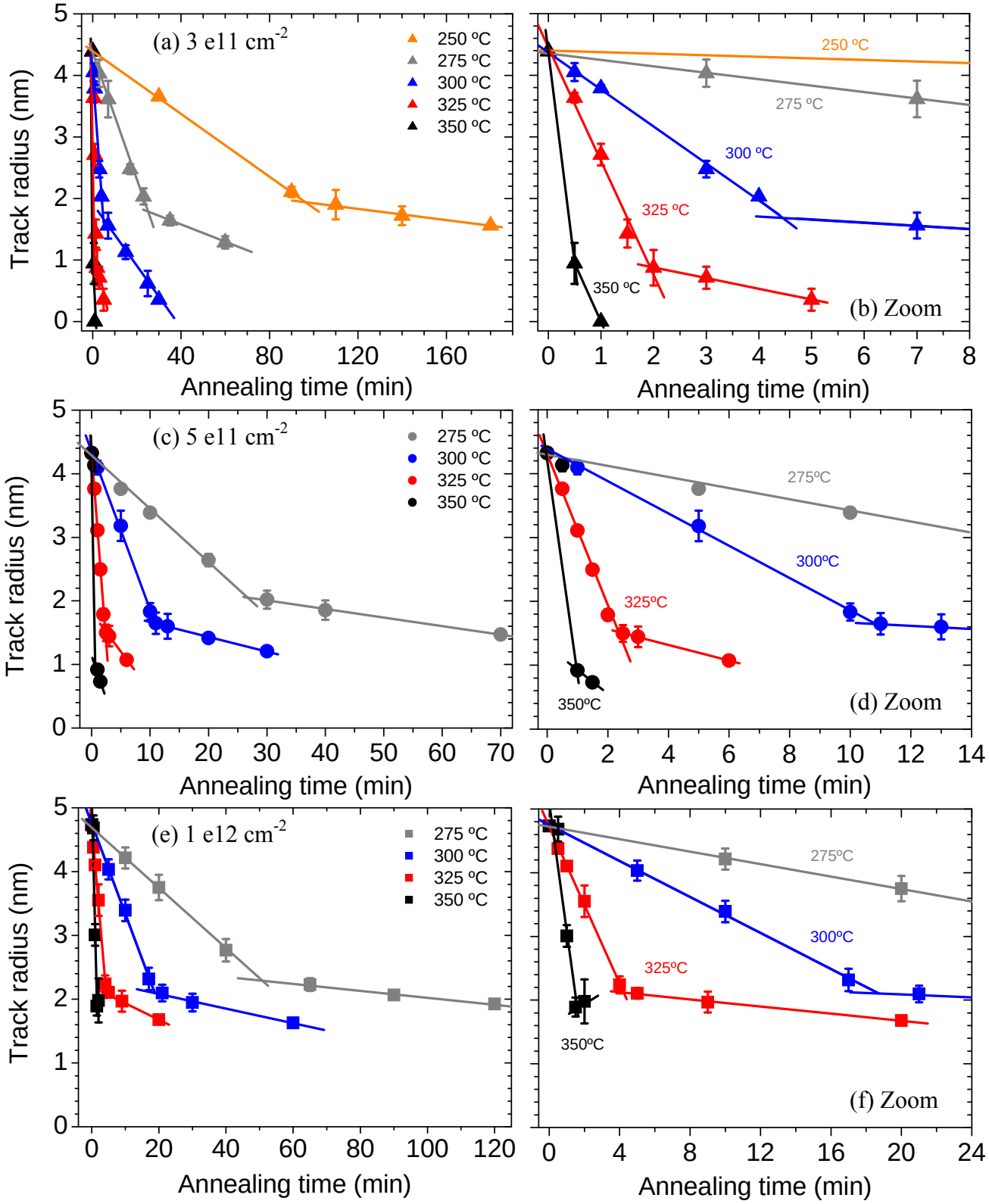

Fig. 2 (a-f). Evolution of the track radius with annealing time for the fluences **(a)** 3 x10^{11} cm^{-2}, **(c)** 5 x10^{11} cm^{-2} and **(e)** 1 x10^{12} cm^{-2}, and for the temperatures 250, 275, 300, 325 and 350 ºC, as indicated in the figures labels. The track radius is obtained for each case from the corresponding disordered fraction (shown in **Fig. 6**) as described in the text assuming a linear dependence of the cross-section of a track multiplied by the impact density. **(b, d, f)** Show zooms in the adequate range for highest temperatures.

Appendix III

A MonteCarlo approach to the recrystallization process.

An analytical approach of the recrystallization process would be a complicated task. Therefore, in order to account for the damage evolution in a multiple track scenario during the recrystallization process we have developed a MonteCarlo algorithm that operates as follows.

The disorder fraction (f_d) is restricted to a defined area of 100 x 100 nm. This area is numerically chosen as a 2-D matrix of 1000 x 1000 points. A number (N) of "black" disks of designed radius (R) are randomly distributed inside this matrix. It is important to state that boundary conditions are included in the code. By this way, if one disk is intersecting the area border, the rest of this disk is considered at the opposite side. A boundary condition as described, allows that all surface of a disk is included in the matrix. The disorder fraction is calculated by summing all the black points in the matrix divided by total matrix size (1000 x 1000 points). From a matrix size with this resolution allows us to calculate a disorder fraction whose behaviour fits in a reasonable way compared to the analytical Poisson curve.

The recrystallization process is taking place at the border between the tracks (black area) and the crystalline (unperturbed) zone, i.e., the amorphous-crystalline boundary. One "annealing step" consists in copying the original matrix into a second one removing the border points (first order neighbours); thus, this second matrix contains the image of the recrystallization process in one "time-step". The entirely process is obtained by repeating the step described before until the disorder fraction decrease till zero. At each step, the disorder fraction is calculated. In this manner, we obtain the simulation of the evolution of the disorder fraction (f_d) versus annealing time, i. e., the recrystallization process (**Fig. 1 (a, b)**).

It has been shown through the Chapter that a measurement of the border length (perimeter), when the overlapping takes place, can be very useful to understand the possible effect of the fluence into the slowing down observed in the experimental radial velocity of the track. I. e., the decrease observed in the effective boundary velocity on increasing fluence should, likely, be due to a reduction in the extension of the crystalline-amorphous boundary (in the density of recrystallization sites).

The value of the border length can be numerically calculated through a MonteCarlo approach, leading to a reasonable value. The calculation consists in generating an array of random N black disks of defined radius (R), and thus, with a defined area. A point belonging to this area is considered as a *border point* if it is situated inside of one of the random disks, but it stays at a certain small distance from an uncovered area. The MonteCarlo calculation of the border length consists in probing a lot of points (~ 1 x10^8), by this way we obtain an enough

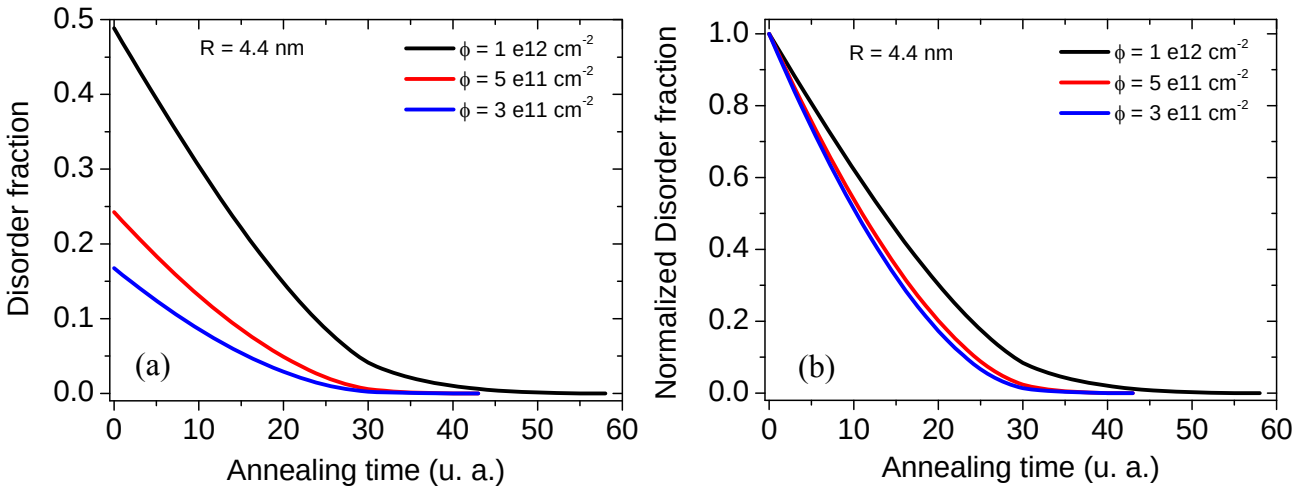

Fig. 1 (a, b). MonteCarlo simulations of **(a)** the evolution of the disorder fraction vs annealing time (u. a.) for the fluences 3 x10^{11} cm^{-2}, 5 x10^{11} cm^{-2} and 1 x10^{12} cm^{-2}, as indicated in the figures labels; **(b)** Normalized disorder fraction. The initial track radius is R = 4.4 nm.

high fraction of the points at the border line. The final value (perimeter length) is obtained after the application of the adequate proportional factor that relates physical lengths to the resulting quantity of border points. That is to say, in the isolated impacts regime of disks with a radius R (not overlapping is allowed), the overall perimeter will be (P = ϕ (N/area unit) x 2 πR), which will correspond through the MonteCarlo approach, to a defined summing of border points.

In **Fig. 2.** frames from the MonteCarlo simulation for the recrystallization have been selected in order to show the evolution of the process for the case of the fluence 1 x10^{12} cm^{-2} with initial track radius R = 4.4 nm. We have pointed out with red circles the way by which the clusters formed by multiple overlapped impacts develops.

With the aim of showing the effect in the disorder fraction (f_d) of increasing the initial track radius (R), which implies the reduction in the effective boundary perimeter, and hence, a slowing down effect in the recrystallization rate of the track radius, it is given in **Fig. 3 (a, b)** MonteCarlo simulations of the evolution of the normalized disorder fraction vs annealing time (u. a.) for different track radius. In addition, **Fig. 4 (a-e)** shows schematic illustrations (100 x 100 nm) of the covered area, for the fluence 1 x10^{12} cm^{-2}, simulated with random impacts of different track radius (R = 4.4 - 6.5 nm). The disorder fraction (f_d) is shown for each case in order to show the effect of increasing the track radius.

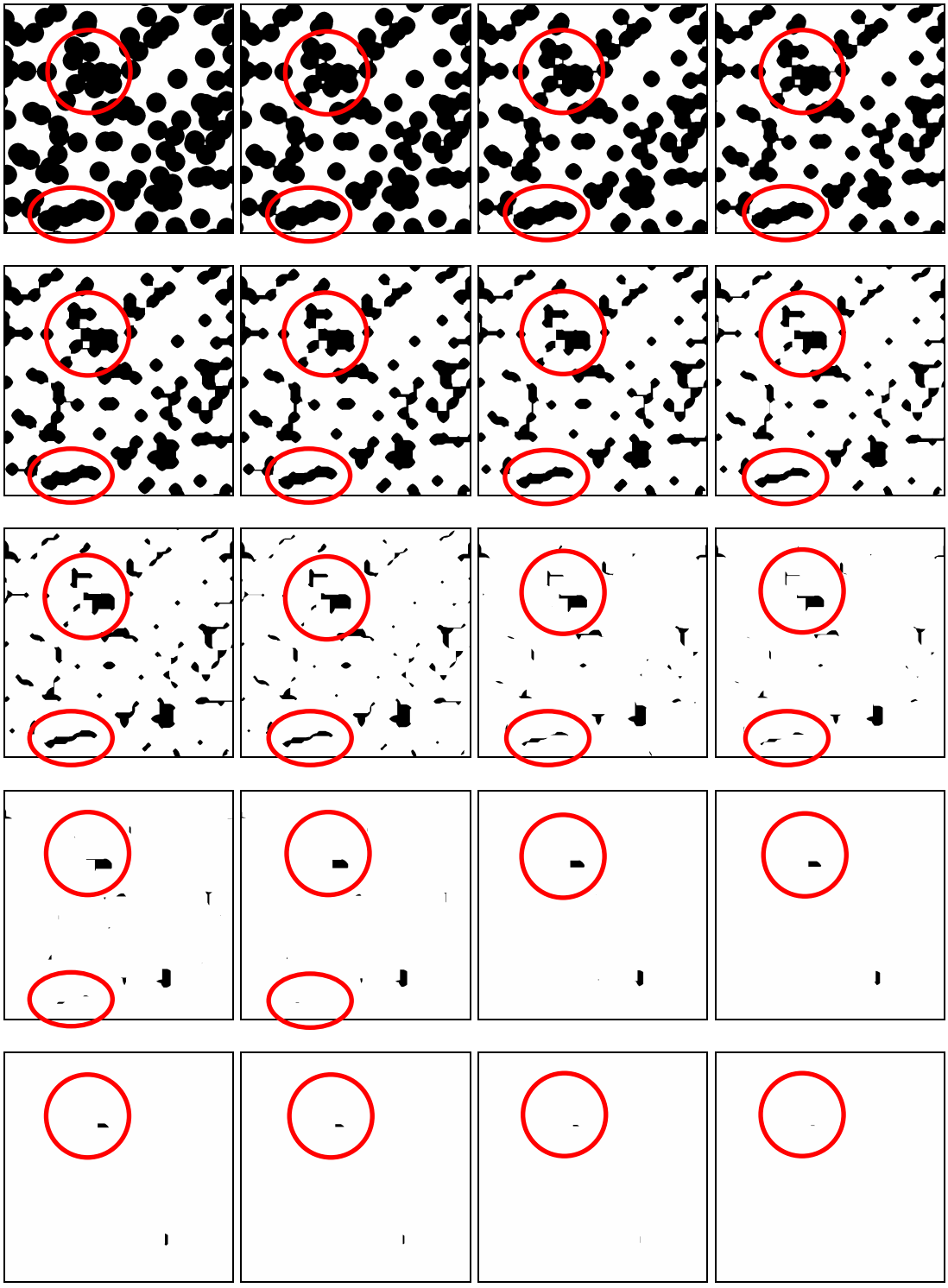

Fig. 2. Selected frames (from right to left) from the MonteCarlo simulation showing the evolution during the recrystallization process for the case of irradiation fluence of 1 x10^{12} cm^{-2} and initial track radius R = 4.4 nm. (Step time (u. a.) x 3). Initial disorder fraction f_d = 0.52. Red circles point out the evolution of selected impact clusters.

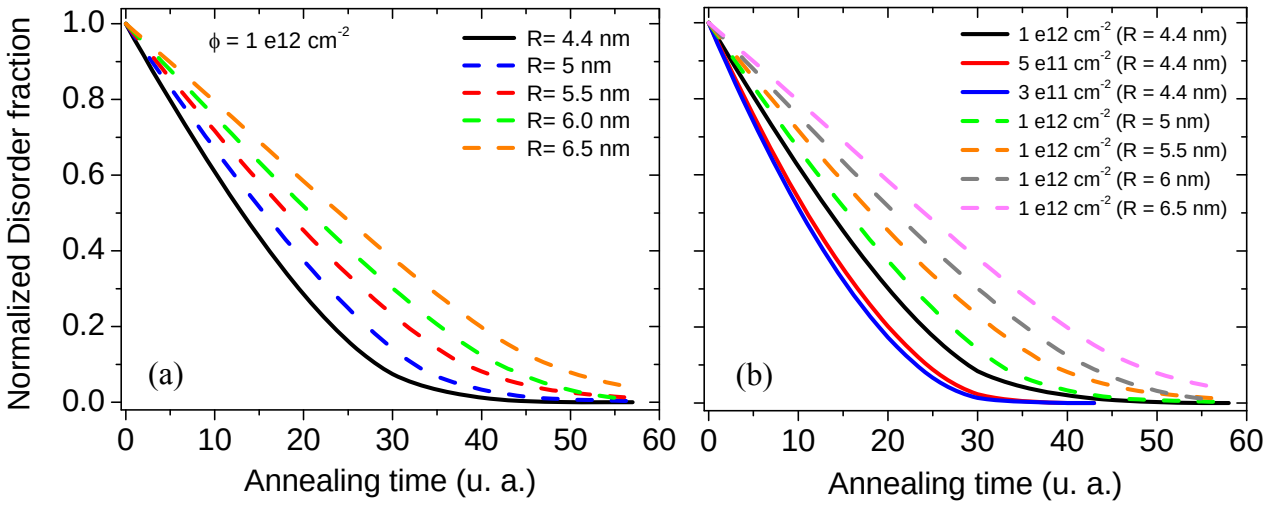

Fig. 3 (a, b). MonteCarlo simulations of the evolution of the normalized disorder fraction vs annealing time (u. a.). **(a)** Fluence 1 x10^{12} cm^{-2}, and different track radius (R), as indicated in the figures labels. **(b)** Different fluences (3 x10^{11} cm^{-2}, 5 x10^{11} cm^{-2} and 1 x10^{12} cm^{-2}) for the case of R= 4.4 nm (solid lines) shown in **Fig. 1 (b)**, and different initial track radius (R=5-6.5 nm) (dashed lines), as indicated in the figures labels, in order to show the effect in the f_d due to the increasing of the initial track radius (i. e., reduction in the effective boundary perimeter).

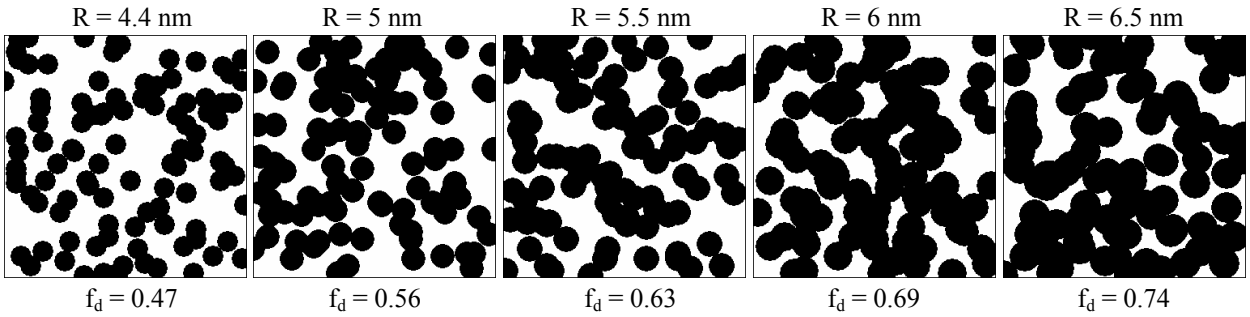

Fig. 4 (a-e). Schematic illustrations (100 x 100 nm) of the covered area, for the fluence 1 x10^{12} cm^{-2}, simulated with random impacts of different track radius (R = 4.4 - 6.5 nm). The disorder fraction (f_d) is shown for each case in order to show the effect of increasing the track radius.

Appendix IV

Abstract.

The aim of the Thesis is to understand and model the origin of the damage produced by high electronic excitation under energetic ion irradiation and, thus, try to apply this knowledge to design and fabricate optical layers by ion beam modification of the structural properties of lithium niobate. It discusses the different mechanism responsible for the observed damage and shows how it can be used for nanostructuring and photonic application in $LiNbO_3$. This Thesis shows the advantages of using ion beams in applied material science and nanotechnology.

This research has been carried out mainly at the Centro de Micro-Análisis de Materiales (CMAM) of the Universidad Autónoma de Madrid (Spain). However, beam time of other European research facilities, i.e. the Grand Accélérateur National d'Ions Lourds (GANIL) in Caen (France) and the GSI-Darmstadt (Germany), were also used.

The Thesis is divided into three parts. The first part contains an introduction to the field, to the investigated material $LiNbO_3$, and to the purpose of the current study. In the second part, the analytical techniques and instruments used for present research are presented. Finally, in the third part the results of this Thesis are presented and carefully discussed. At the end of the Thesis the main results and general conclusions drawn from this work are summarized.

The main results of this Thesis are based on essentially four important experimental investigations:

The first one explores the key problems related to the defects created by ion irradiation. This study tries to clarify the structure of the latent ion track and the determination of the amorphization threshold. A new theoretical model is presented to explain the experimental findings.

It has been developed the novel idea that point defects are produced around the ion trajectory whatever the electronic stopping power, and it has been proposed that these defects are produced as a consequence of the non-radiative decay of localized (or self-trapped) excitons. The proposed mechanism of damage growth under ion irradiation is more consistent than previous models based on the thermal spike or on simple excitonic mechanism, and it contains a convincing description of the formation of sub-threshold damage. In this last regime the use of a MonteCarlo code allowed for a deeper insight of the process.

The second investigation deals with a study on the morphology of the nanopores obtained after chemical etching of the damage induced in $LiNbO_3$ by ion irradiation for a variety of ions and energies. The role of etching time and etching agent on the pore morphology, diameter, depth, and shape was also studied.

The third experimental part is devoted to get a deeper understanding on the kinetics of annealing of the recrystallization properties of the damage when this is mainly constituted of amorphous nanotracks, and compared with the limit case of a fully amorphous to crystalline interface. Important information on the different stages during the recovery of the damage was obtained. An epitaxial-like regrowth behaviour has been found, showing two clear distinct kinetics regimes in the diminishing of the track radius respect to the annealing time. Systematic data on the recrystallization kinetics of isolated amorphous tracks and homogeneous layers, which have been generated in $LiNbO_3$ by high-energy irradiation using low or high ion fluences are obtained. In addition, an universal scaling law has been found to describe the process, and a simple nucleation model is used to describe the observed phenomena.

This is the first time by which a complete investigation of the annealing mechanism has been performed on ion implanted lithium niobate. The showed results are very important both to understand the nature of the defects and to engineer the damage for optical applications.

Finally, the work is completed with investigations on fabrication of very deep optical waveguides in $LiNbO_3$ using the ion-induced damage caused by swift heavy ions at ultralow irradiation fluences, much lower than normally used. This allows the creation of much thicker waveguides (up to tens of microns). Such thick optical waveguides may be useful in photonic devices for the mid-Infrared.

Appendix V

Abstract (translation)/ Resumen.

El objetivo de esta Tesis consiste en comprender y modelizar el origen del daño producido por la alta excitación electrónica durante la irradiación con iones energéticos y, de este modo, tratar de aplicar este conocimiento para diseñar y fabricar capas ópticas mediante la modificación por haz de iones de las propiedades estructurales del niobato de litio. Se discuten los diferentes mecanismos responsables del daño observado, y muestra cómo se puede utilizar para nanoestructuración y aplicación fotónica en $LiNbO_3$. Esta Tesis muestra las ventajas de la utilización de haces de iones en ciencia aplicada de materiales y nanotecnología.

Esta investigación ha sido llevada a cabo principalmente en el Centro de Micro-Análisis de Materiales (CMAM) de la Universidad Autónoma de Madrid (España). Sin embargo, tiempo de haz de otras instalaciones de investigación europeas, es decir, el Grand Accélérateur National d'Ions Lourds (GANIL) en Caen (Francia) y el GSI de Darmstadt (Alemania), también fue utilizado.

La tesis se divide en tres partes. La primera parte contiene una introducción al campo de estudio, al material investigado $LiNbO_3$, y al propósito de la presente investigación. En la segunda parte se presentan las técnicas analíticas e instrumentos utilizados para la presente investigación. Finalmente, en la tercera parte, se presentan los resultados de esta Tesis, siendo discutidos cuidadosamente. Al final de la Tesis se resumen los principales resultados y las conclusiones generales de este trabajo.

Los principales resultados de esta Tesis se basan esencialmente en cuatro investigaciones experimentales importantes:

El primero explora los principales problemas relacionados con los defectos creados por la irradiación con iones. Este estudio trata de aclarar la estructura de la traza latente iónica y la determinación del umbral de amorfización. Un nuevo modelo teórico se presenta para explicar los resultados experimentales.

Se ha desarrollado la novedosa idea de que los defectos puntuales se producen alrededor de la trayectoria del ion sea cual sea el poder de frenado electrónico, y se ha propuesto que estos defectos se producen como consecuencia del decaimiento no radiativo de los excitones localizados (o auto-atrapados). El mecanismo propuesto de crecimiento del daño bajo la radiación de iones es más consistente que los modelos anteriores basados en el mecanismo de pico térmico o en el simple mecanismo excitónico, y contiene una descripción convincente de la formación del daño por debajo del umbral. En este último régimen el uso de un código Monte Carlo permite una visión más profunda del proceso.

La segunda investigación tiene que ver con el estudio de la morfología de la nanoporos obtenidos tras ataque químico de los daños inducidos en $LiNbO_3$ por irradiación iónica de una gran variedad de iones y energías. El papel del tiempo de ataque y el agente químico sobre la morfología de los poros, el diámetro, la profundidad y la forma fueron también estudiados.

La tercera parte experimental está dedicado a obtener un conocimiento más profundo sobre la cinética de recocido de las propiedades de recristalización del daño cuando éste está constituido principalmente por nanotrazas amorfas, y comparada con el caso límite de una intercara cristalino-completamente amorfa. Información importante sobre las diferentes etapas en la recuperación del daño fue obtenida. Un comportamiento de recrecimiento epitaxial, ha sido encontrado, mostrando dos claros regímenes cinéticos distintos durante la disminución del radio de la traza respecto al tiempo de recocido. Una sistemática de datos sobre la cinética de la recristalización de las trazas amorfas aisladas y de las capas homogénea, que han sido generadas en $LiNbO_3$ por irradiación de alta energía utilizando baja o alta fluencia de iones, fue obtenida. Además, una ley de escalado universal, ha sido encontrada para describir el proceso, y un modelo de nucleación simple se utiliza para describir los fenómenos observados.

Esta es la primera vez en la una investigación completa a cerca del mecanismo de recocido ha sido realizada en niobato de litio implantado con iones. Los resultados mostrados son muy importantes tanto para comprender la naturaleza de los defectos como para el diseño del daño para aplicaciones ópticas.

Finalmente, el trabajo se completa con las investigaciones sobre la fabricación de guías de onda ópticas muy profundas en $LiNbO_3$ utilizando el daño inducido con iones pesados y rápidos, a fluencias de irradiación ultra bajas, mucho más bajas que las utilizadas normalmente. Esto permite la creación de guías de onda mucho más gruesas (hasta decenas de micras). Tales guías de onda ópticas gruesas pueden ser útiles en dispositivos fotónicos para el infrarrojo medio.

Appendix VI

Conclusions (translation)/ Conclusiones.

En los siguientes párrafos, las principales conclusiones obtenidas en este trabajo de Tesis en el intento de profundizar en nuestro conocimiento sobre el daño de haz de iones debido a la excitación electrónica, será presentado.

A partir del análisis de la cinética de la evolución del daño de haces de iones en el régimen electrónico, tratando con la contribución del núcleo amorfo y el halo de defectos puntuales, hay que señalar:

- Hemos demostrado de forma concluyente que el daño estructural inducido en materiales dieléctricos por iones rápidos, en el que el poder de frenado electrónico es dominante, tiene algunas características peculiares, como: la existencia de un umbral y el carácter acumulativo, a diferencia del daño nuclear.
- Se ha encontrado que el comportamiento de daño acumulativo bajo irradiaciones sucesivas no es consistente con el modelo del Pico Térmico. Hay una clara transición desde un comportamiento de la cinética de tipo Poisson ($n = 1$) para poderes de frenado muy por encima del umbral (típico de un proceso directo, *modelo de impacto directo*, como resultado de la superposición de trazas), a una evolución de tipo Avrami (sigmoidal, $n > 1$) por debajo del umbral, donde ninguna amorfización debería ser inducida, por lo que se necesita una determinada fluencia de incubación. Las curvas de Avrami presentan los parámetros n y ϕ_0, que aumentan mientras disminuye el poder de frenado electrónico.
- La cantidad de desorden que es evaluado por RBS-C en $LiNbO_3$ ha sido analizado mediante un modelo propuesto recientemente - modelo de decaimento excitónico no radiativo- para calcular el perfil de defectos generados por cada impacto de ion. El análisis describe la descanalización causada en la superficie mediante el uso de una función “filtro”. Se concluye que el área amorfizada (núcleo) de la traza está marcadamente sobreestimada para poderes de frenado cerca del valor de umbral. El esquema propuesto para describir la formación del halo y predecir su diámetro, representa un primer intento, para un análisis cuantitativo del problema.

- Una aproximación Monte Carlo al modelo de decaimiento excitónico no radiativo ha sido desarrollada. Tiene en cuenta la distribución especial estadística de los impactos de iones a cualquier profundidad en la muestra. En desacuerdo con la formulación analítica previa, el nuevo método es capaz de describir adecuadamente el rango de fluencias de irradiación bajas, donde la superposición sigue siendo insuficiente y divergencias estadísticas de la zona realmente amorfizada, con respecto a los valores medios, son muy significativas.
- La validación del modelo se ha demostrado a través de la Buena reproducción conseguida de la cinética de amortización experimental de tipo Avrami y Poisson. Por otra parte, el espesor de las capas que tienen una mezcla amorfa-cristalina en su composición ha sido obtenido en función de la fluencia.

Relacionado con los nanoporos obtenidos por ataque químico en $LiNbO_3$ irradiado con iones:

- Es la primera vez que se ha observado la bien faceteada morfología de los poros en niobato de litio. Los poros inicialmente muestran una simetría aproximadamente axial, pero bajo ataques prolongados, se desarrollan facetas bien definidas, las cuales se corresponden con determinados planos cristalinos.
- Se han confirmado variaciones dramáticas de las dimensiones y la morfología de los nanoporos dependientes en gran medida tanto, de la concentración de la solución del ácido, del tiempo de ataque, y de los parámetros de irradiación.
- Se ha encontrado que los tratamientos térmicos de recocido en el rango de 150 ºC a 300 ºC no recuperan por completo las trazas latentes. Por otra parte, un claro alargamiento en la forma de los poros es favorecido, dando lugar a una morfología anisotrópica.
- Dos regímenes de ataque con diferentes morfologías y velocidades de ataque han sido claramente identificados:

  (1) La etapa rápida inicial depende del poder de frenado del ion y podría estar asociada al núcleo de la traza incluyendo el halo circundante con alto grado de defectos.

  (2) La primera etapa de ataque radial es seguida por una fase lineal más lenta, donde las facetas se desarrollan. La etapa lenta tiene una velocidad de unos pocos nm/min dependiendo de la concentración y la composición de la solución ácida y debe corresponder al ataque químico del $LiNbO_3$ cristalino, es decir, la velocidad de ataque químico debe ser esencialmente igual a la del material no irradiado.
- Se ha encontrado que la fluencia de irradiación se convierte en un parámetro crítico. Cuanto más alta es la fluencias más alta es la velocidad de ataque, debido a la tensión perpendicular a las trazas de los iones, dando lugar a una superficie muy rugosa después del proceso químico.

- Respeto a las mezclas ácidas de HF y HNO_3, se ha encontrado que la velocidad de ataque es linealmente dependiente de la concentración del ácido (c_{HF}), y constante en el tiempo. Por tanto, los poros crecen linealmente con el tiempo de ataque.
- La morfología de los poros y las profundidades obtenidas mediante la técnica de AFM han sido confirmadas a partir de las mediciones de HRTEM, estando en excelente acuerdo. Además, valiosa información estructural de las trazas iónicas subyacentes ha sido obtenida.
- Se ha demostrado que las estructuras de poros buscadas pueden ser obtenidas a través del ajuste de los parámetros de la irradiación iónica y del ataque químico. Un comportamiento claramente diferente, relacionado con las energías de los iones, ha sido mostrado por las estructuras reveladas después del ataque de las irradiaciones con iones pesados y rápidos, y los iones pesados (irradiaciones con bromo).

  (1) Hay fuertes evidencias de que el rango de penetración de los iones es responsable del aumento abrupto observado por el diámetro de los poros y la relación de aspecto superficial. Una longitud de traza crítica no se pudo determinar, pero el diámetro es cuatro veces mayor para el caso de las trazas iónicas del material irradiado con iones de Kr 809 MeV (L = 59 μm) en comparación con las del Br 46 MeV (L = 4.5 μm), teniendo ambos aproximadamente el mismo poder de frenado en superficie.

  (2) Por el contrario, la evolución de la profundidad se encontró que dependía de la energía de los iones, el poder de frenado y la longitud de la traza amorfa. Parece razonable suponer que la concentración de defectos regula la velocidad de ataque en profundidad, la cual parece alcanzar un máximo alrededor de los 12 keV/nm.
- Se ha alcanzado un alto grado de confianza en la reproducción de nanoporos uniformes en tamaños y formas, todo lo cual, acompañado de las resultantes llanas superficies de grado óptico, las convierten en muy prometedoras para aplicaciones en óptica no lineal y nanosensores.

De acuerdo con el estudio de la cinética de recristalización de trazas amorfas aisladas y capas homogéneas sometidas a tratamientos de recocido térmico a diferentes temperaturas, las conclusiones más notables son:

- Se ha encontrado que, las trazas amorfas presentan una velocidad de recristalización claramente observable por encima de 250 ºC. El fenómeno del recocido se rige por los procesos de intercara como para la epitaxia en fase sólida. La disminución en el radio de la traza tiene una dependencia lineal con el tiempo de recocido, y es constante para cada temperatura.
- Un comportamiento similar al recrecimiento epitaxial se ha encontrado, mostrando dos claros regímenes distintos en la cinética de la disminución del radio de la traza respecto al tiempo de recocido, para todas las temperaturas del objeto de estudio: en primer lugar una etapa principal, en el que la velocidad de recristalización, es decir, el movimiento de la frontera amorfa- cristalina, es alrededor de diez veces más

rápida que velocidad para la segunda etapa, en la que una fuerte desaceleración aparece para valores del radio de traza en torno a 2 nm.

- La velocidad de recristalización ese encuentra térmicamente activada de acuerdo con una dependencia de tipo Arrhenius y, una energía de activación alrededor de 1.5 eV para la etapa inicial principal ha sido encontrada. Para radios de trazas más pequeños de ~ 2 nm el proceso de contracción de la traza se ralentiza, apuntandoa que otros mecanismos deben ser tenidos en cuenta.
- Se ha confirmado que el recocido de las capas amorfas enterradas induce una reducción de su espesor en un rango de temperatura similar. El desplazamiento de la frontera amorfa-cristalina es también lineal con el tiempo de recocido y las velocidades de cristalización son similares a las de las trazas.
- La recristalización de las capas amorfas enterradas puede ser descrita con el mismo proceso físico y proporcionan datos coherentes (velocidades de recristalización) con los obtenidos para las trazas.
- Una ley de escalado universal ha sido encontrada para describir el proceso, y un modelo de nucleación simple es utilizado para describir los fenómenos observados. Además, un modelo que explica la recuperación del daño ha sido propuesto y discutido en términos de reordenación local de las unidades octaédricas $Nb\text{-}O_6$ y recrecimiento epitaxial. El reordenamiento octaédrico es un proceso local de primer orden, recrecimiento controlado por el ancho de intercara, que no depende de la difusión a largo alcance de los defectos puntuales como las vacantes o intersticiales.
- Un gran número de aplicaciones puede ser favorecida por las relevantes implicaciones relacionados con los resultados obtenidos:

  (1) El control preciso de los radios des trazas a través de adecuados tratamientos de recocido pueden ser utilizados para ajustar el diámetro de la nanoporos después de un adecuado ataque.

  (2) El control de los radios de las trazas permite adaptar la constante dieléctrica y el índice de refracción de la capa exterior irradiada y, por tanto, las posibilidades para dispositivos ópticos integrados. Además, para el campo de la fotónica, los resultados encontrados para capas homogéneas permiten un adecuado control del espesor de la capa de guía de onda más externa e incluso la mejor definición (nitidez/abrutez) de la frontera de la guía de onda.

Por último, respecto al nuevo método propuesto para la fabricación de gruesas guías de onda ópticas en $LiNbO_3$ a través del daño electrónico producido por iones pesados y rápidos con fluencias de irradiación ultrabaja:

- Profundas guías de onda ópticas planas en la superficie de niobato de litio se han producido con éxito utilizando iones pesados (Kr y Xe) con energías en el rango de ~ 10 MeV/uma.. Las guías de onda obtenidas tienen un espesor entre 40-50 micras, dependiendo de la energía de los iones y la fluencia de irradiación, perfiles suaves y saltos de índice de refracción de hasta 0.04 (λ = 633 nm). Propagan modos

ordinarios y extraordinarios de bajas pérdidas manteniendo una alta respuesta no lineal óptica, lo cual hace que sean útiles para muchas aplicaciones.

- Se ha se ha realizado un estudio de la morfología de las trazas y sus perfiles en profundidad, a través de la combinación de diversas técnicas experimentales, incluyendo la medición de los perfiles de índice de refracción y medidas de RBS/C. Valores coherentes para la amorfización parcial y el cambio de índice de refracción en la superficie han sido obtenidos.
- Esta primera prueba demostrativa se puede extender a otros materiales cristalinos y sugiere la aplicación de tales guías de onda en el rango del infrarrojo medio para la astrofísica y otros campos. El gran espesor de la barrera óptica debe proporcionar suficiente confinamiento óptico. Por otra parte, el espesor irradiado puede ser fácilmente reducido y ajustado para aplicaciones realistas en el rango de longitud de onda < 10 micras.

Publications and Contributions.

1. List of publications related to this Thesis

As a result of the work described in this dissertation, the following papers have been published:

[1] O. Caballero-Calero, A. García-Cabañes, M. Carrascosa, F. Agulló-López, J. Villarroel, M. L. Crespillo and J. Olivares, *"Periodic poling of optical waveguides produced by swift-heavy ion irradiation in $LiNbO_3$"*, Appl. Phys. B. 95 (2009) 435-439.

[2] O. Caballero-Calero, A. García-Cabañes, M. Carrascosa, V. Bermúdez, M. L. Crespillo and J. Olivares, *"Fabrication of Periodically Poled Swift Ion-irradiation Waveguides in $LiNbO_3$"*, Ferroelectrics 390 (2009) 29-35.

[3] M. L. Crespillo, M. Otto, A. Muñoz-Martín, J. Olivares, F. Agulló-López, M. Seibt, M. Toulemonde and C. Trautmann, *"Optimization of nanopores obtained by chemical etching on swift-ion irradiated lithium niobate"*, Nucl. Instr. Meth. B 267 (2009) 1035-1038.

[4] J. Olivares, M. L. Crespillo, O. Caballero-Calero, M.D. Ynsa, A. García-Cabañes, M. Toulemonde, C. Trautmann and F. Agulló-López, *"Thick optical waveguides in lithium niobate induced by swift heavy ions (~10 MeV/amu) at ultralow fluences"*, Optics Express 17 (2009) 24175-24182.

[5] A. Rivera, J. Olivares, M. L. Crespillo, G. García, M. Bianconi and F. Agulló-López, *"Assessment of swift-ion damage by RBS/C: Determination of the amorphization threshold"*, Nucl. Instr. Meth. B 267 (2009) 1460-1463.

[6] J. Villarroel, M. Carrascosa, A. García-Cabañes, O. Caballero-Calero, M. L. Crespillo and J. Olivares, *"Photorefractive response and optical damage of $LiNbO_3$ optical waveguides produced by swift-heavy ion irradiation"*, Appl. Phys. B. 95 (2009) 429-433.

[7] N. Gordillo, A. Rivera, R. Grötzschel, F. Munnik, D. Güettler, M. L. Crespillo, F. Agulló-López and R. González-Arrabal, *"Compositional, structural and morphological modifications of N-rich Cu_3N films induced by irradiation with Cu at 42 MeV"*, J. Appl. Phys. D 43 (2010) 345301.

[8] J. Manzano, J. Olivares, F. Agulló-López, M. L. Crespillo, A. Moroño and E. Hodgson, *"Optical waveguides obtained by swift-ion irradiation on silica (α-SiO_2)"*, Nucl. Instr. and Meth. B 268 (2010) 3147-3150.

[9] A. Rivera, M. L. Crespillo, J. Olivares, R. Sanz, J. Jensen and F. Agulló-López *"On the exciton model for ion-beam damage: The example of TiO_2"*, Nucl. Instr. Meth. B 268 (2010) 3122-3126.

[10] A. Rivera, M. L. Crespillo, J. Olivares, G. García and F. Agulló-López, *"Effect of defect accumulation on ion-beam damage morphology by electronic excitation in lithium niobate: A MonteCarlo approach"*, Nucl. Instr. Meth. B 268 (2010) 2249–2256.

[11] M. L. Crespillo, O. Caballero-Calero, A. Rivera, V. Joco, P. Herrero, J. Olivares and F. Agulló-López, *"Recrystallization of amorphous nano-tracks and uniform layers generated by swift-ion-beam irradiation in lithium niobate"*, Appl. Phys. A 104 (2011) 1143-1152.

[12] G. García, A. Rivera, M. L. Crespillo, N. Gordillo, J. Olivares and F. Agulló-López, *"Amorphization kinetics under swift heavy ion irradiation: a cumulative overlapping-track approach"*, Nucl. Instr. Meth. B 269 (2011) 492–497.

[13] A. Rivera, G. García, J. Olivares, M. L. Crespillo and F. Agulló-López, *"Elastic (stress-strain) halo associated to ion-induced nano-tracks in $LiNbO_3$: role of crystal anisotropy"*, J. Appl. Phys. D (submitted).

2. Contributions to Congresses related to this Thesis.

[1] M. L. Crespillo, O. Caballero, J. Olivares, F. Agulló-López, C. Trautmann and M. Toulemonde *"Nanotrack profiles and threshold characterisation in lithium niobate by waveguide fabrication combination of optical and structural measurements."*, The Seventh International Symposium Swift Heavy Ions in Matter (SHIM 2008), Lyon (France), 2-5/06/08. Oral presentation.

[2] M. L. Crespillo, M. Otto, A. Muñoz-Martín, J. Olivares, F. Agulló-López, M. Seibt, M. Toulemonde and C. Trautmann, *"Optimization of nanopores obtained by chemical etching on swift-ion irradiated lithium niobate"*, The Seventh International Symposium Swift Heavy Ions in Matter (SHIM 2008), Lyon (France), 2-5/06/08. Poster presentation.

[3] M. Carrascosa, A. García-Cabañes, J. Villarroel, J. Olivares, O. Caballero-Calero, M. L. Crespillo, A. García-Navarro, F. Agulló-López and G. García, *"Novel nonlinear optical waveguides by swift ion irradiation"*, 9th European Conference on Applications of Polar Dielectrics, Roma (Italia), 25-29/08/08. Oral presentation.

[4] A. Rivera, J. Olivares, M. L. Crespillo, G. García, M. Bianconi and F. Agulló-López, *"Assessment of swift-ion damage by RBS/c: Determination of the amorphization threshold"*, The 16th International Conference on Ion Beam Modification of Materials (IBMM 2008), Dresden (Germany), 31/08/08-5/09/08. Oral presentation.

[5] J. Olivares, M. L. Crespillo, O. Caballero, F. Agulló-López and M. Carracosa, *"Novel optical waveguides by means of using electronic damage of swift heavy ions"*, The 16th International Conference on Ion Beam Modification of Materials (IBMM 2008), Dresden (Germany), 31/08/08-5/09/08. Poster presentation.

[6] M. L. Crespillo, M. Otto, A. Muñoz-Martín, J. Olivares, F. Agulló-López, M. Seibt, M. Toulemonde and and C. Trautmann, *"Optimization of nanopores generated by chemical etching of swift-ion irradiated $LiNbO_3$"*, The 16th International Conference on Ion Beam Modification of Materials (IBMM 2008), Dresden (Germany), 31/08/08-5/09/08. Poster presentation.

[7] N. Gordillo, R. González-Arrabal, M. S. Martín-González, D. Guettler, R. Groetzschel, M. L. Crespillo, J. Olivares, F. Agulló-López, F. Briones and D. O. Boerma, *"Irradiation induced changes in N-rich Copper thin layers"*, The 16th International Conference on Ion Beam Modification of Materials (IBMM 2008), Dresden (Germany), 31/08/08-5/09/08. Poster presentation.

[8] J. Villarroel, M. Carrascosa, A. García-Cabañes, O. Caballero, M. L. Crespillo and J. Olivares *"Non-linear photorefractive characterization of novel lithium niobate optical waveguides by swift ion irradiation"*, European Optical Society Annual Meeting. Photorefractive Materials, Effects, and Devices - Control of Light and MATTER 2008, Paris (France), 29/09/08-2/10/08. Poster presentation.

[9] O. Caballero-Calero, A. García-Cabañes, M. Carrascosa, F. Agulló-López, J. Villarroel, M. L. Crespillo and J. Olivares, *"Periodic poling of optical waveguides produced by swift-heavy ion irradiation in $LiNbO_3$"*, European Optical Society Annual Meeting. Photorefractive Materials, Effects, and Devices - Control of Light and MATTER 2009, Bad Honnef (Germany), 11-14/06/09. Poster presentation.

[10] J. Villarroel, M. Carrascosa, A. García-Cabañes, O. Caballero, M. L. Crespillo and J. Olivares, *"Photorefractive response and optical damage of $LiNbO_3$ optical waveguides produced by swift-heavy ion irradiation"*, European Optical Society Annual Meeting. Photorefractive Materials, Effects, and Devices - Control of Light and MATTER 2009, Bad Honnef (Germany), 11-14/06/09. Poster presentation.

[11] A. Rivera, M. L. Crespillo, J. Olivares, J. Jensen, R. Sanz and F. Agulló-López, *"Damage formation in rutile TiO_2 by swift heavy ion irradiation: Analysis with a non-radiative exciton decay model"*, Radiation Effects in Insulators (REI-15), Padova (Italy), 30/08/09 - 04/09/09. Poster presentation.

[12] J. Manzano, A. Zabot, M. L. Crespillo, J. Olivares, F. Agulló-López, A. Moroño and E. Hodgson, *"Optical waveguides obtained by swift-ion irradiation on silica"*, Radiation Effects in Insulators (REI-15), Padova (Italy), 30/08/09 – 04/09/09. Poster presentation.

[13] M. L. Crespillo, M. D. Ynsa, J. Olivares and F. Agulló-López, *"Recrystallization of amorphous tracks generated in lithium niobate by swift-ion beam irradiation"*, Radiation Effects in Insulators (REI-15), Padova (Italy), 30/08/09 - 04/09/09. Poster presentation.

[14] N. Gordillo, R. González-Arrabal, D. Güttler, R. Grötzschel, A. Rivera, M. L. Crespillo and F. Agulló-López *"Formation of Cu_2O and Cu nanostructures in N-rich Cu_3N films irradiated with Cu^{8+} at 42 MeV"*, 19th International Meeting on Ion Beam Analysis (IBA 2009), University of Cambridge (United Kingdom), 7-11/09/09. Poster presentation.

[15] M. L. Crespillo, *"Recrystallization of amorphous tracks generated in lithium niobate by swift-ion beam irradiation"*, Internal Seminar at the CMAM Accelerator (CMAM-UAM), Madrid, Centro de Microanálisis de Materiales (CMAM), 08/10/09. Oral presentation.

[16] A. Rivera, M. L. Crespillo, J. Olivares and F. Agulló-López, *"Exciton Model of Materials Damage by Ion Irradiation: Physical Bases"*, 2009 MRS Fall Meeting, Boston, MA (EEUU), 30/11/09 - 04/12/09. Oral presentation.

[17] A. Rivera, M. L. Crespillo, J. Olivares, J. Jensen, R. Sanz and F. Agulló-López, *"Damage Formation in Rutile TiO_2 by Swift Heavy Ion Irradiation: Analysis with a Non-radiative Exciton Decay Model"*, 2009 MRS Fall Meeting, Boston, MA (EEUU), 30/11/09-04/12/09. Poster presentation.

[18] J. Manzano, M. L. Crespillo, A. Zabot, J. Olivares, F. Agullo-Lopez, A. Morono and E. R. Hodgson, *"Optical Waveguides Obtained by Swift-ion Irradiation on Silica"*, 2009 MRS Fall Meeting, Boston, MA (EEUU), 30/11/09-04/12/09. Poster presentation.

[19] M. L. Crespillo, A. Rivera, J. Olivares and F. Agulló-López, *"Study of Crystallization Kinetics of Amorphous Layers and Tracks Generated in Lithium Niobate by Swift-ion Beam Irradiation"*, 2009 MRS Fall Meeting, Boston, MA (EEUU), 30/11/09-04/12/09. Poster presentation.

[20] J. Olivares, M. L. Crespillo, F. Agulló-López, P. Molina, K. Shimamura and E. Villora, *"Fabrication of optical waveguides in $BaMgF_4$ via electronic damage by high energy heavy ion irradiation"*, The 17th International Conference on Ion Beam Modification of Materials (IBMM 2010), Montreal (Canada), 22-27/08/10. Poster presentation.

[21] M. L. Crespillo, J. Olivares, O. Caballero-Calero, N. Gordillo, A. Rivera and F. Agulló-López, *"Recrystallization kinetics of amorphous tracks and homogeneous layers in LiNbO3 irradiated with swift heavy ions"*, The 17th International Conference on Ion Beam Modification of Materials (IBMM 2010), Montreal (Canada), 22-27/08/10. Poster presentation.

[22] A. Rivera, M. L. Crespillo, J. Olivares and F. Agulló-López, *"Amorphization induced by ion beams in dielectric crystals: competition between nuclear and electronic routes"*, E-MRS 2011 Spring Meeting, Congress Center. Nice (France), 09-13/05/11. Oral presentation.

[23] J. Olivares, M. L. Crespillo, J. Villarroel, M. Jubera, A. García-Cabañes, M. Carrascosa and F. Agulló-López, *"Novel methods to prepare optical waveguides by ion beam irradiation: an alternative to ion implantation"*, VII Reunión Española de Optoelectrónica (OPTOEL 2011), Santander (Spain), 29/06/11-1/07/11. Poster presentation.

[24] O. Caballero-Calero, J. Olivares, G. Martín, M. Carrascosa, A. García-Cabañes, M. L. Crespillo and F. Agulló-López., *"Channel waveguides produced by swift ion irradiation on proton exchanged LiNbO3 layers."*, 16th Internacional Conference on Radiation Effects in Insulators, Peking University, Beijing, (China). 14-19/8/2011. Poster presentation.

[25] M. L. Crespillo, J. Olivares, O. Peña-Rodríguez, A. Rivera and F. Agulló-López., *"Lattice swelling induced by swift-ion irradiation of lithium niobate: anisotropy, incubation and thresholding."*, 16th Internacional Conference on Radiation Effects in Insulators, Peking University, Beijing, (China). 14-19/8/2011. Poster presentation.

3. Other publications.

Additional publications in different related fields are:

[1] J. C. Guerra, S. Rodríguez, M. T. Arencibia and M. L. Crespillo, *"El ozono superficial y su papel en el sistema atmosférico"*, Información Tecnológica 14 (2003) 3-12.

[2] J. C. Guerra, M. T. Arencibia, S. Rodríguez y M. L. Crespillo, *"Técnicas de Medida de Ozono Atmosférico en Superficie. Instrumentos y Métodos de Calibración"*, Información Tecnológica 14 (2003) 13-18.

[3] M. L. Crespillo, J. L. Sacedón, B. A. Joyce and P. Tejedor *"Nanopatterning of GaAs(110) vicinal surfaces by hydrogen-assited MBE"*, Book Chapter: Kinetics-Driven Nanopatterning on Surfaces. MRS Series.MRS Proceedings 849 (2004) 41-46.

[4] M. L. Crespillo, J. L. Sacedón, B. A. Joyce and P. Tejedor, *"Kinetically-driven self-organization during hydrogen assisted MBE growth on GaAs(110)"*, Microelectronics Journal 36 (2005) 581-585.

[5] M. L. Crespillo, J. L. Sacedón and P. Tejedor, *"Terrace width distribution during unstable homoepitaxial growth of GaAs(110): An experimental study"*, Materials Science and Engineering C 26 (2006) 846-851.

[6] P. Tejedor, M. L. Crespillo and B. A. Joyce, *"Growth mode transitions induced by hydrogen-assisted MBE on vicinal GaAs(110)"*, Materials Science and Engineering C 26 (2006) 852-856.

[7] P. Tejedor, M. L. Crespillo and B. A. Joyce, *"Influence of atomic hydrogen on step stability during homoepitaxial growth on vicinal GaAs surfaces"*, Appl. Phys. Lett. 88 (2006) 063101.

[8] M. L. Crespillo, and P. Tejedor, *"AFM quantitative morphological analysis of the step bunching instability formed on GaAs(110) during H-assisted MBE"*, Book Chapter. AIP Conf. Proceedings.PHYSICS OF SEMICONDUCTORS: 28th International Conference on the Physics of Semiconductors- ICPS 2006. Vienna (Austria), 24-28 July 2006 893 (2007) 105-106.

[9] L. Diez-Merino, P. Tejedor and M. L. Crespillo, *"(As,Sb)In/GaInSb quantum well for infrared detection enhancement"*, Advances in Space Research 40 (2007) 704-707.

[10] P. Tejedor, L. Díez-Merino and M. L. Crespillo, *"H-assisted MBE growth of self-patterned InGaAs/GaAs(110) superlattices on stepped surfaces"*, Book Chapter. AIP Conf. Proceedings. PHYSICS OF SEMICONDUCTORS: 15th International Conference on Molecular Beam Epitaxy-ICMBE 2008. Vancouver (Canada), 3-8 August 2008. (2008) 101-102.

[11] P. Tejedor, M. L. Crespillo, L. Díez-Merino, I. Beinik and C.Teichert, *"Self-patterned InGaAs/GaAs (110) nanodot superlattices"*, Advanced Materials (submitted)

4. Other contributions to Congresses.

[1] J. C. Guerra, J. Meneses, M. T. Arencibia, M. L. Crespillo and E. Cuevas, *"Niveles críticos de ozono para la vegetación en la región subtropical sobre Canarias"*, 3º Asamblea Hispano-Portuguesa de Geodesia y Geofísica, Valencia (Spain), 4-8/02/02. Oral presentation.

[2] A. F. Rodríguez Hernández, E. Burunat, M. L. Crespillo, J. C. Albaladejo, M. Alonso Calvo, I. Lojo, L. F. Rodríguez Ramos, J. L. González Mora and H. M. Chulani, *"Comparative study of the acoustic response of the human ears, head and torso and its sculptural reproduction in silicon, oriented to the development of a sensory substitution device"*, XXXII Congreso de la Sociedad Española de Ciencias Fisiológicas joined to The Internacional Meeting of the Physiological Society, Tenerife, Islas Canarias (Spain), 13-17/02/03. Oral presentation.

[3] J. L. González Mora, L. F. Rodríguez Ramos, A. García Martín, A. de la Pedraja Pavón, A. Cruz López, A. Rodríguez Hernández, A, Moreno Suárez, A. Gil Aparicio, B. Mederos Díaz, B. Esteban Sánchez, B. Hernández Molina, C. Darias Armas, C. Serra Vallmitjana, C, Ferraz Castro, E. Burunat Gutiérrez, E. Ballesteros Ramírez, F. Martín del Rosario, H. Chulani, I. Lojo Ramírez, J. Pujol, J. López García, J. Maella Mareca, J. Ramón Muñiz Montes, J. Vicente Gigante Ripoll; J. García González, J. Carlos Albadalejo González, L. Magnoler, L. Díaz Saco, M. de los Ángeles Malfaz Vázquez, M. Ortiz Ramos, M. Suárez Valles, M. Alonso Calvo, M. Nedelec, M. A. Castellano Gil, M. Charcos Llorens, M. L. Crespillo Almenara, M. Núñez Pereira, M. Sánchez París, N. Armando Sosa García, R. Socas, R. Pérez Martín, R. López López, R. Armas Padrón, S. Alonso Pérez, U. Erdmenger and V. González Escalera, *"El Proyecto EAV como Proyecto Interdisciplinar"*, Congreso Internacional Virtual: "I N T A N G I B L E S, "I N T A N G I B L E S, PSICOLOGÍA, CONTABILIDAD, DERECHO, ECONOMÍA: nuevas perspectivas para la interdisciplinariedad", RedIris (Red Académica y de Investigación Nacional gestionada por el CSIC) (http://www.rediris.es/list/info/act-int.es.html), 23-27/06/03.SMS presentation in the framework of a Virtual Conference.

[4] M. L. Crespillo, *"Study of kinetically-driven self-organization during hydrogen assisted MBE growth on GaAs(110)"*, Internal Meeting of the L.A.S.M.E.A. (Laboratoire des Sciences et Matériaux pour l´Electronique et d`Automatique), Univ. Blaise Pascal. UMR 6602. C.N.R.S. Clermont-Ferrand. (France), 14/09/04. Oral presentation.

[5] M. L. Crespillo, J. L. Sacedón, B. A. Joyce and P. Tejedor, *"Nanopatterning of GaAs(110) vicinal surfaces by hydrogen-assited MBE"*, MRS Fall Meeting 2004, Boston, Massachussets (USA), 29/11/04-3/12/04. Oral presentation.

[6] M. L. Crespillo, J. L. Sacedón, B. A. Joyce and P. Tejedor, *"Kinetically-driven self-organization during hydrogen-assisted MBE growth on GaAs(110)"*, LDSD 2004 (The 5th International Conference on Low Dimensional Structures and Devices), Cancún (México), 12-17/12/03.Poster presentation.

[7] M. L. Crespillo, J.L. Sacedón and P. Tejedor, *"Terrace width distribution during unstable homoepitaxial growth of GaAs(110): an experimental study"*, E-MRS 2005. Spring meeting, Strasbourg (Francia), 31/05/05-3/06/05. Poster presentation.

[8] P. Tejedor, M. L. Crespillo and B. A. Joyce, *"Growth mode transitions induced by Hydrogen-Assisted MBE on vicinal GaAs(110)"*, E-MRS 2005. Spring meeting, Strasbourg (Francia), 31/05/05-3/06/05. Poster presentation.

[9] M. L. Crespillo, *"Self-organized growth of semiconductor structures on vicinal surfaces for optoelectronic applications"*, 1st Campus de Excelencia 2005, Tenerife, Canary Islands (Spain), 10-16/06/05. Invited Oral presentation.

[10] P. Tejedor, K. Vasco and M. L. Crespillo, *"Mecanismos de auto-organización atómica durante el crecimiento epitaxial en superficies nano y microestructuradas: Simulación numérica y experimentos"*, Workshop ICMM 2006. Jornadas Científica Internas, Madrid. Campus de Cantoblanco (Spain), 28/02/06-7/03/06. Oral presentation.

[11] L. Diez-Merino, P. Tejedor and M. L. Crespillo, *"(As,Sb)In/GaInSb quantum well for infrared detection enhancement"*, Committee on Space Research. 36th COSPAR Scientific Assembly, Beijing (China), 16-23/07/2006. Oral presentation.

[12] M. L. Crespillo, and P. Tejedor, *"AFM quantitative morphological analysis of the step bunching instability formed on GaAs(110) during H-assisted MBE"*, 28th International Conference on the Physics of Semiconductors (ICPS 28), Viena (Austria), 24-28/07/06.Oral presentation.

[13] M. L. Crespillo, and P. Tejedor, *"Time evolution of the step bunching instability and quantitative morphological analysis by AFM during H-assisted MBE growth on GaAs(110)"*, 14th International Conference on Molecular Beam Epitaxy (ICMBE 2006), Waseda University, Tokyo (Japan), 3-8/09/06. Poster presentation.

[14] M. L. Crespillo, and P. Tejedor, *"AFM quantitative morphological analysis of the step bunching instability formed on GaAs(110) during H-assisted MBE"*, Semestral Meeting of the Institute für Physik, Montanuniversität Leoben, Leoben, Montanuniversität Leoben, Institute für Physik (Austria), 19/10/06. Oral presentation.

[15] M. L. Crespillo, *"Ultimos avances en el estudio del crecimiento asistido con hidrógeno atómico de nanoestructuras semiconductoras autoorganizadas"*, 14º Jornadas Internas del Dpto. Física Aplicada (Módulo CIV). Facultad de Ciencias.Universidad Autónoma de Madrid (UAM), Dpto. Física Aplicada. Facultad de Ciencias. UAM. Madrid., 02/02/07. Oral presentation.

[16] M. L. Crespillo, I. Lejona and P. Tejedor, *"Comparative study of the step bunching instability evolution during GaAs(110) homoepitaxy by conventional and H-assisted MBE growth"*, E-MRS 2007 Spring Meeting, Strasbourg (France), 28/05/07-01/06/07. Invited Oral presentation.

[17] M. L. Crespillo, I. Lejona, C. Teichert and P. Tejedor, *"Advanced AFM Procedures for the Characterization of Self-Organized Multiatomic Step Arrays Formed On Vicinal GaAs(110) by H-Assisted MBE"*, E-MRS 2007 Spring Meeting, Strasbourg (France), 28/05/07-01/06/07. Poster presentation.

[18] L. Díez-Merino, I. Lejona, M. L. Crespillo, J. J. Pérez-Camacho and P. Tejedor, *"Growth of self-organized InGaAs/GaAs superlattices on GaAs(110) nanotemplates by H-assisted MBE"*, E-MRS 2007 Spring Meeting, Strasbourg (France), 28/05/07-01/06/07. Poster presentation.

[19] P. Tejedor, M. L. Crespillo, I. Lejona, F. Agulló-Rueda and I. R. Martín, *"Self-organization of short-period InGaAs/GaAs SLs on GaAs(110) nanotemplates by H-assisted Molecular Beam Epitaxy"*, Intel 12th EMEA Academic Forum, Budapest (Hungary), 12-14/06/07. Invited Poster presentation.

[20] P. Tejedor, and M. L. Crespillo, *"Nucleation kinetics of GaAs(110) on stepped surfaces: The role of atomic H as a surfactant"*, Intel 12th EMEA Academic Forum, Budapest (Hungary), 12-14/06/07. Poster Invited presentation.

[21] P. Tejedor, M. L. Crespillo, J. V. Anguita, J. J. Pérez-Camacho and P. Hudson *"Selective epitaxy of III-V compounds on nanostructured HfO_2/GaAs substrates for next generation non-planar transistor application"*, Intel 12th EMEA Academic Forum, Budapest (Hungary), 12-14/06/07.Poster Invited presentation.

[22] L. Díez-Merino, M. L. Crespillo and P. Tejedor, *"Nanoscale self-patterning of InGaAs/GaAs(110) superlattices by MBE"*, 29th International Conference on the Physics of Semiconductors (ICPS 29), Río de Janeiro (Brasil), 27/07/08-01/08/08. Oral presentation.

[23] M. L. Crespillo, C. Teichert and P. Tejedor, *"AFM characterization of GaAs(110) nanotemplates grown by surfactant mediated homoepitaxy"*, 29th International Conference on the Physics of Semiconductors (ICPS 29), Río de Janeiro (Brasil), 27/07/08-01/08/08. Poster presentation.

[24] M. L. Crespillo, C. Teichert and P. Tejedor, *"Effect of atomic hydrogen on the nucleation and surface morphology evolution of multiatomic step-GaAs(110) nanotemplates grown by MBE"*, 15th International Conference on Molecular Beam Epitaxy (MBE 2008), University of British Columbia, Vancouver (Canada), 3-8/08/08. Poster presentation.

[25] P. Tejedor, L. Díez-Merino and M. L. Crespillo, *"H-assisted MBE growth of self-patterned InGaAs/GaAs(110) superlattices on stepped surfaces"*, 15th International Conference on Molecular Beam Epitaxy (MBE 2008), University of British Columbia, Vancouver (Canada), 3-8/08/08. Poster presentation.

[26] P. Tejedor, and M. L. Crespillo, *"Surfactant-induced changes in GaAs(110) growth kinetics"*, 15th International Conference on Molecular Beam Epitaxy (MBE 2008), University of British Columbia, Vancouver (Canada), 3-8/08/08. Oral presentation.